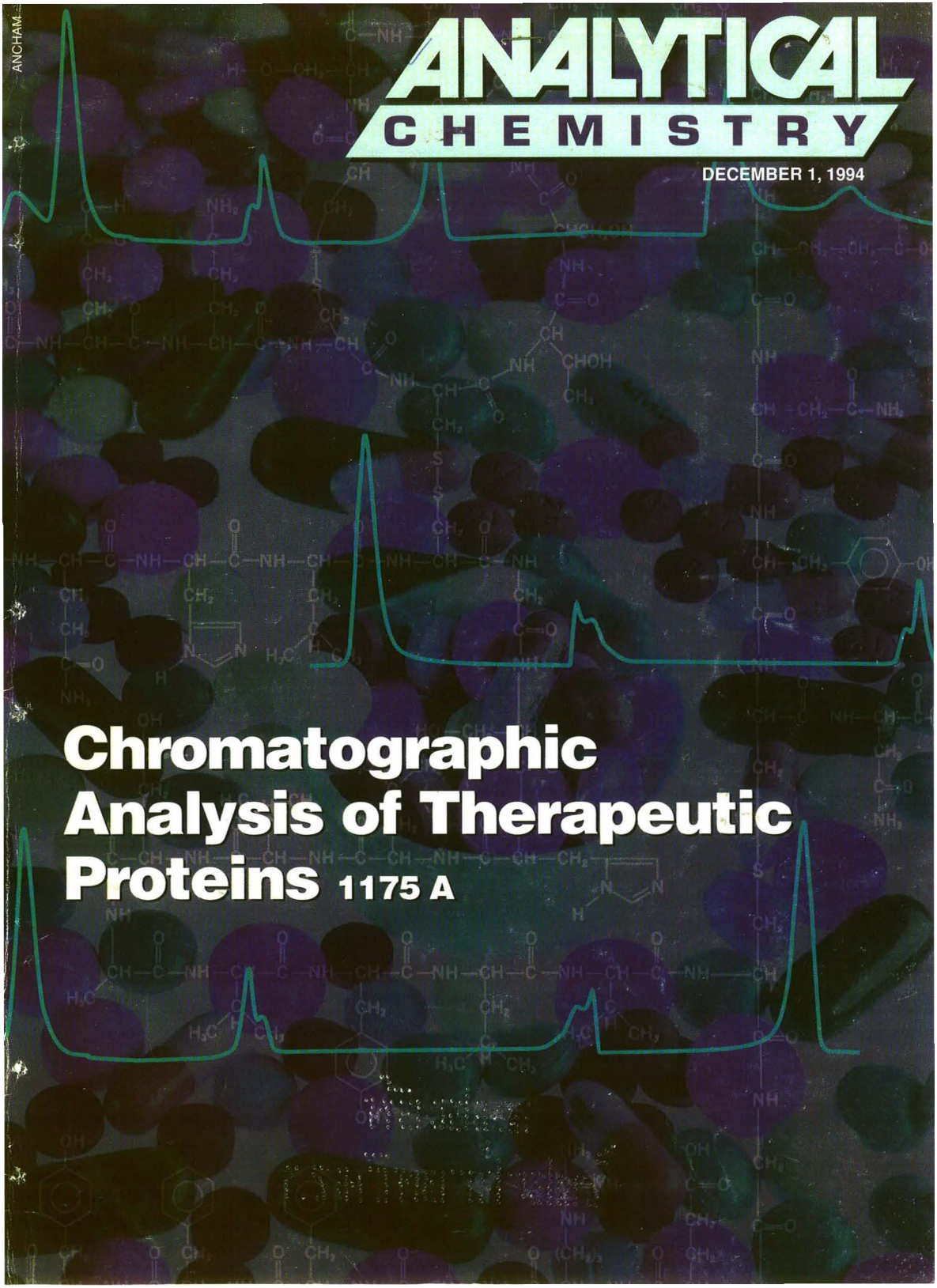
ANCHAM

ANALYTICAL CHEMISTRY

DECEMBER 1, 1994



Chromatographic Analysis of Therapeutic Proteins 1175 A

Pittcon®'95 Is The Answer To Many Of Your Research Problems.

The Question Is, "How Could You Risk Missing It?"

The Pittsburgh Conference and Exposition on Analytical Chemistry and Applied Spectroscopy Will Simplify Your Search for Answers to Your Technical Problems. Discover What Pittcon®'95 Has to Offer:

- A Superior Exposition with an Inclusive Collection of the Latest in Laboratory Equipment and Instrumentation
- A Technical Program that Features Over 200 World Renowned Scientists Delivering Invited Lectures, Plus Over 1500 Contributed Paper and Poster Presentations
- One-on-One Discussions and Demonstrations with Exhibitors Offering Insights into Difficult Analyses
- Opportunities to Exchange Ideas with Experts in Your Scientific Discipline
- Over 40 Inexpensive Short Courses, Including such Topics as "Introduction to Laboratory Data Management," "Basic Statistics," "Chemometrics" and "Setting Up Your Lab Safety Program"

Pittcon®'95 is the Premier Conference and Exposition on Laboratory Equipment and Chemical Analysis.

New Orleans
March 5-10 1995

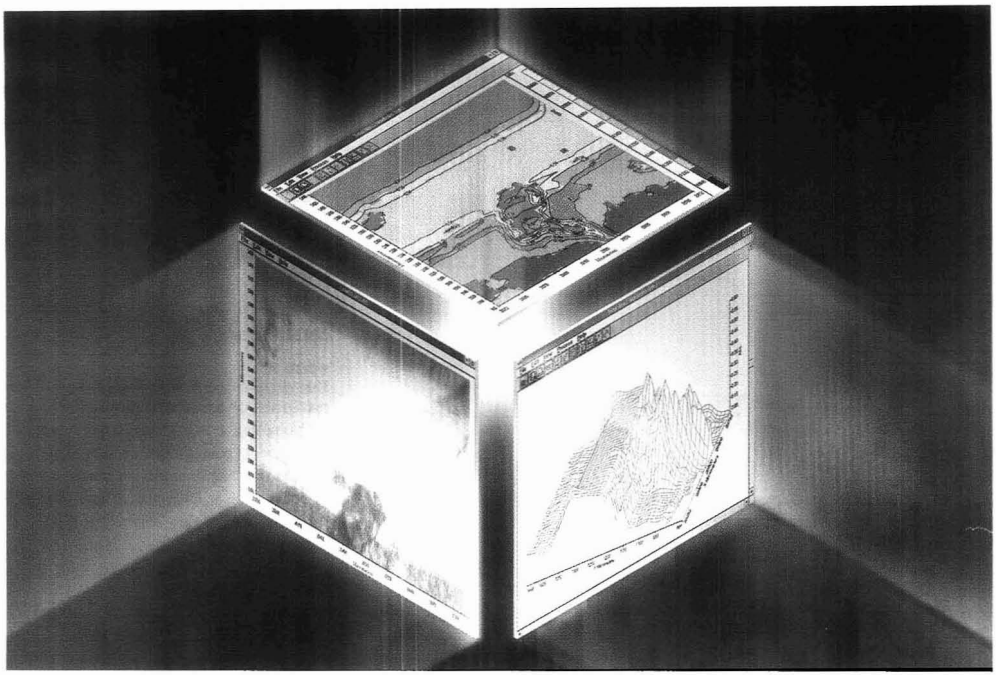
Pittcon® '95

Stimulating the Minds of
Today's and Tomorrow's Scientists

For further information, please contact:
Department 9528
The Pittsburgh Conference
Suite 332, 300 Penn Center Boulevard • Pittsburgh, PA 15235-5503
Phone: (412) 825-3220 TOLL FREE (800) 825-3221 • FAX:(412) 825-3224

Discover the Pittsburgh Conference on Analytical Chemistry and Applied Spectroscopy March 5-10, 1995, New Orleans, LA.

CIRCLE 4 ON READER SERVICE CARD



FT-IR with vision.

Perkin-Elmer launches interactive multimedia FT-IR.

For the first time, you can interact directly with a video image of a microscopic sample and acquire FT-IR spectra from areas of interest in real time, in a single operation. With the new *i*-Series Microscope and IMAGE software, you can also map chemical differences across a sample quickly and easily, with precise correlation of spectral and image data.

Work in a familiar Windows™ environment that complements the intuitive controls of the microscope and facilitates setup as well as data acquisition, analysis and storage.



Combined with Perkin-Elmer's exceptional FT-IR performance, this means a 15- to 25-fold time savings for mapping applications.

A vision of the future.

The new *i*-Series FT-IR Microscope and IMAGE software are the foundation of a new generation of FT-IR systems—and an exciting new way to work. For sales information or literature in the U.S., call 1-800-762-4000. Outside the U.S., contact your Perkin-Elmer representative.

ISO 9001 CERTIFIED

New *i*-Series FT-IR Microscope and IMAGE Software

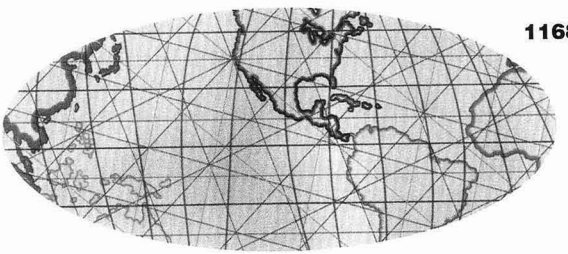
PERKIN ELMER

The Perkin-Elmer Corporation, 761 Main Avenue, Norwalk, CT 06859-0012, USA
Perkin-Elmer Ltd., Post Office Lane, Beaconsfield, Bucks HP9 1QA, UK. Bodenseewerk Perkin-Elmer GmbH, Postfach 10 17 61, D-88647 Ueberlingen, Germany
All analytical instruments and systems manufactured by Perkin-Elmer are certified under the quality requirements of ISO 9001.

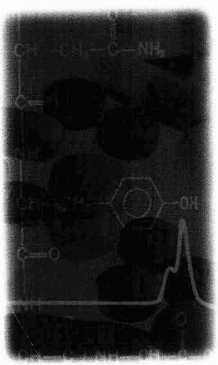
Windows is a trademark of Microsoft Corporation.

Circle No. 8 for Literature only. Circle No. 9 for Literature and Sales Call.

Contents

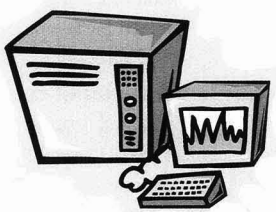


1168 A



1175 A

1183 A



REPORT

1168 A
Building cooperation on international chemical traceability.
As globalization of trade and interdependence among countries increases, CITAC seeks to consolidate existing measurement issues on an international level. Bernard King and Ronald Walker of the Laboratory of the Government Chemist review current CITAC initiatives and look at plans for the future.

REPORT

1175 A
ON THE COVER. **Chromatographic analysis of therapeutic proteins.**
As the cost of bringing new protein-based drugs to market soars, analysts turn to chromatographic methods to speed up the process. Bruce Jon Compton of AutoImmune and Lotte Kreilgaard of the Royal Danish School of Pharmacy and ZymoGenetics describe rapid LC methods that can be used to separate and characterize new protein- and peptide-based drugs without disrupting the unique three-dimensional structure on which their pharmacological activity is based.

EDITOR: **ROYCE W. MURRAY**
University of North Carolina

ASSOCIATE EDITORS: **Catherine C. Fenselau,** University of Maryland Baltimore County, **William S. Hancock,** Hewlett Packard, **James W. Jorgenson,** University of North Carolina, **Robert A. Osteryoung,** North Carolina State University, **Edward S. Yeung,** Iowa State University/Ames Laboratory

Editorial Headquarters
Research section
Department of Chemistry
Venable and Kenan Laboratories
University of North Carolina
Chapel Hill, NC 27599-3290
Phone: 919-962-2541
Fax: 919-962-2542
E-mail: Murray @ uncvx1.oit.unc.edu

Editorial Headquarters
A-page section
1155 Sixteenth St., N.W.
Washington, DC 20036
Phone: 202-872-4570
Fax: 202-872-4574
E-mail: acx96 @ acs.org

Managing Editor: Mary Warner
Senior Editor: Louise Voress
Associate Editor: Felicia Wach
Editorial Assistant: Deborah Noble
Contributing Editor: Marcia Vogel
Head, Graphics and Production: Leroy L. Corcoran
Division Art Director: Alan Kahan
Art Director: Peggy Corrigan
Designer: Michele Telschow
Production Editors: Kathleen Savory, Elizabeth Wood
Electronic Composition: Wanda R. Gordon

ANALYTICAL CHEMISTRY

DECEMBER 1, 1994
VOLUME 66 NUMBER 23

ANCHAM
66(23) 1147 A–1192 A/4121–4384 (1994)
ISSN 0003-2700

Registered in U.S. Patent and Trademark Office
©Copyright 1994 by the American Chemical Society

DEPARTMENTS

1157 A
In This Issue

1162 A
Editorial

Diversity. The breadth of electroanalytical chemistry ranges from the miniaturization of electrodes to scanning electrochemical microscopy to clinical sensors.

1163 A
Analytical Currents

1166 A
News

ATP awards to spur development of new technologies. • TJA to purchase Baird Analytical. • Kratos and Fisons at odds over patent. • ARI makes grants for instrumentation, renovation. • CAS and Dialog to cosponsor STAS. • Brookhaven to build facility to study ultrafast reactions. • Ignition facility to study fusion. • Digital signature for security. • Revised labeling requirements.

1172 A
Books

H. N. Cheng reviews a compendium of techniques used in polymer characterization. • Books received.

1181 A
Meetings

Conferences. • Short Courses.

1183 A
Focus

Used analytical instruments—Telling the cream puffs from the lemons. Used instruments can be a good deal if they're properly reconditioned and tested before you buy.

1186 A
New Products

A bridge designed to automatically transfer samples between a supercritical fluid extractor and a gas or liquid chromatograph, a quadrupole ion trap mass spectrometer that incorporates an rf waveform generator, and an NMR spectrometer intended for both routine analyses and methods development are featured. • Instrumentation. • Literature. • Catalogs.

1190 A
Information Express

RESEARCH

Accelerated Articles

4121
Glucopyranoside-Based Surfactants as Pseudostationary Phases for Chiral Separations in Capillary Electrophoresis
David H. Tickle, George N. Okafo, Patrick Camilleri, Rose F. D. Jones, and Anthony J. Kirby*

4127
Precolumn Reactions with Electrophoretic Analysis Integrated on a Microchip
*Stephen C. Jacobson, Roland Hergenröder, Alvin W. Moore, Jr., and J. Michael Ramsey**

Articles

4133
Oxygen Sensors Based on Luminescence Quenching: Interactions of Metal Complexes with the Polymer Supports
Wenying Xu, Robert Clayton McDonough, III, Brandi Langsdorf, J. N. Demas, and B. A. DeGraff*

continued on p. 1151 A

Publications Division
Director: Robert H. Marks
Head, Special Publications: Anthony Durniak
Head, Journals: Charles R. Bertsch
Head, Publications Marketing: David Schulbaum

Journals Dept., Columbus, Ohio
Editorial Office Manager: Mary E. Scanlan
Journals Editing Manager: Kathleen E. Duffy
Associate Editor: Lorraine Gibb
Assistant Editor: Stephanie L. Mallon

Advisory Board: Phyllis Brown, Bruce Chase, Joseph G. Gordon David M. Haaland, Joel M. Harris, Franz Hillenkamp, Kiyokatsu Jinno, Dennis C. Johnson, Richard A. Keller, Peter Kissinger, Gary E. Maciel, Scott M. McLuckey, Milos V. Novotny, Geraldine Richmond, Ralph Riggin, James A. Yergey *Ex Officio:* Henry Blount III

A-page Advisory Panel: Frank V. Bright, Raymond E. Clement, Therese M. Cotton, Norman J. Dovichi, Royce C. Engstrom, Mary Ellen P. McNally, John W. Olesik, J. Michael Ramsey, Robert D. Voyksner

Copyright Permission: An individual may make a single reprographic copy of an article in this publication for personal use. Reprographic copying beyond that permitted by Section 107 or 108 of the U.S. Copyright Law is allowed, provided that the appropriate per-copy fee is paid through the Copyright Clearance Center, Inc., 222 Rosewood Dr., Danvers, MA 01923. For reprint permission, write Copyright Administrator, Publications Division, ACS, 1155 Sixteenth St., N.W., Washington, DC 20036.

Analytical Chemistry (ISSN 0003-2700) is published semimonthly by the American Chemical Society, 1155 Sixteenth St., N.W., Washington, DC 20036. Second-class postage paid at Washington, DC, and additional mailing offices. Postmaster: Send address changes to *Analytical Chemistry*, Member & Subscriber Services, P.O. Box 3337, Columbus, OH 43210.

Canadian GST Reg. No. R127571347.

Metrohm Titrators for the real world!

Customize your workstation

Metrohm titrators, with buret resolution of 10,000 pulses, offer more features and lower prices than ever before. They provide precise and accurate analyses quickly, easily, and use minimum bench space. Brinkmann software lets you connect up to four titrators to a single PC and transfer data to your LIMS for GLP documentation. The wide choice of models and accessories lets you customize workstations for all your applications.

For more information, call
Brinkmann Instruments at 800-645-3050.
In Canada: 800-263-8715.



Outside U.S. and Canada: Metrohm Ltd., Switzerland
Phone 071/53 85 85 or Telefax 071/53 89 01

Metrohm

BRINKMANN Quality products for research and control.

AD 135-MET

CIRCLE 1 ON READER SERVICE CARD

Contents

4142
Laser-Induced Fluorescence Detection of a Single Molecule in a Capillary
*Yuan-Hsiang Lee, Russell G. Maus, Ben W. Smith, and James D. Winefordner**

4150
Solvent Effects in Determination of Anthracene on Solution Surfaces by Laser Two-Photon Ionization Technique
*Hangting Chen, Takanori Inoue, and Teiichiro Ogawa**

4154
Isotopic Analysis of Uranium Using Glow Discharge Optogalvanic Spectroscopy and Diode Lasers
C. M. Barshick, R. W. Shaw, J. P. Young, and J. M. Ramsey*

4159
Reduction of Fluorescence Interference in Raman Spectroscopy via Analyte Adsorption on Graphitic Carbon
*Mark R. Kagan and Richard L. McCreery**

4166
Membrane Inlet Mass Spectrometer for Rapid High-Precision Determination of N_2, O_2, and Ar in Environmental Water Samples
Todd M. Kana, Christina Darkangelo, M. Duane Hunt, James B. Oldham, George E. Bennett, and Jeffrey C. Cornwell*

4171
Electrospray Tandem Mass Spectrometry for Analysis of Native Muramic Acid in Whole Bacterial Cell Hydrolysates
Gavin E. Black, Alvin Fox, Karen Fox, A. Peter Snyder, and Philip B. W. Smith*

4177
Stable Isotope Methods for the Study of β-Carotene-d_8 Metabolism in Humans Utilizing Tandem Mass Spectrometry and High-Performance Liquid Chromatography
*Stephen R. Dueker, A. Daniel Jones, and Andrew J. Clifford**

4186
$^{176}Hf/^{177}Hf$ Determination in Small Samples by a Hot Temperature SIMS Technique
*Vincent J. M. Salters**

4190
Calcium Stoichiometry Determination for Calcium Binding Proteins by Electrospray Ionization Mass Spectrometry
*Peifeng Hu, Qi-Zhuang Ye, and Joseph Loo**

4195
Measuring the Resolving Power of Ion Mobility Spectrometers
William F. Siems, Ching Wu, Edward E. Tarver, Herbert H. Hill, Jr., Paul R. Larsen, and Dennis G. McMinn*

4202
Liquid–Solid Extraction and Fast Atom Bombardment High-Resolution Mass Spectrometry for the Determination of Hydroxyatrazine in Water at Low-ppt Levels
Zongwei Cai, V. M. Sadagopa Ramanujam, M. L. Gross, S. J. Monson, D. A. Cassada, and R. F. Spalding*

4210
Glycerol-Enhanced Separation of DNA Fragments in Entangled Solution Capillary Electrophoresis
*Jing Cheng and Keith R. Mitchelson**

4215
Theory of Field Programmed Field-Flow Fractionation with Corrections for Steric Effects
*P. Stephen Williams and J. Calvin Giddings**

4229
Chemometric Optimization of Azide Sensitivity in Reversed-Phase Ion-Interaction HPLC
E. Marengo, M. C. Gennaro, C. Abrigo, and A. Dinardo*

4236
Modeling Flow Profiles and Dispersion in Capillary Electrophoresis with Nonuniform Zeta Potential
Catherine A. Keely, Tom A. A. M. van de Goor, and Douglass McManigill*

4243
Effects of Linear Polyacrylamide Concentrations and Applied Voltages on the Separation of Oligonucleotides and DNA Sequencing Fragments by Capillary Electrophoresis
Takashi Manabe, Nong Chen, Shigeru Terabe, Masafumi Yohda, and Isao Endo*

4253
Retention Prediction Based on Molecular Interactions in Packed-Column Supercritical Fluid Chromatography
Darren M. Heaton, Keith D. Bartle, Anthony A. Clifford, Matthew S. Klee, and Terry A. Berger*

continued on p. 1153 A

Registered names and trademarks used in this publication, even without specific indication thereof, are not to be considered unprotected by law.

1994 subscription rates include air delivery outside the U.S., Canada, and Mexico. Canadian subscriptions are subject to 7% GST.

	Members	Nonmembers (personal)	Nonmembers (institutional)
U.S.	$ 37	$ 79	$ 481
Canada and Mexico	72	114	516
Europe	127	169	571
Other countries	154	196	598

Nonmember rates in Japan: Rates above do not apply to nonmember subscribers in Japan, who must enter subscription orders with Maruzen Company Ltd., 3–10, Nihonbashi 2-chome, Chuo-ku, Tokyo 103, Japan. Tel: (03) 272-7211.

For multi-year and other rates, call toll free 800-227-5558 in the U.S. and Canada; in the Washington, DC, metropolitan area and outside the U.S., call 202-872-4363; fax 202-872-4615.

Single issues, current year, $21.00 except review issue, $50.00, and LabGuide, $50.00; **back issues and volumes and microform editions** available by single volume or back issue collection. For information or to order, call the number listed for subscription orders by phone; or write the Microform & Back Issues Office at the Washington address.

Subscription orders by phone may be charged to VISA, MasterCard, or American Express. Call toll free 800-333-9511 in the continental U.S.; in the Washington, DC, metropolitan area and outside the continental U.S., call 202-872-8065. Mail orders for new and renewal subscriptions should be sent with payment to American Chemical Society, Department L-0011, Columbus, OH 43268-0011.

Changes of address must include both old and new addresses with ZIP code and a recent mailing label. Send all address changes to the ACS Columbus address. Please allow 6 weeks for change to become effective. **Claims for missing numbers** will not be allowed if loss was due to failure of notice of change of address to be received in the time specified; if claim is dated (a) North America—more than 90 days beyond issue date, (b) all other foreign—more than 180 days beyond issue date. Hard copy claims are handled at the ACS Columbus address.

ACS membership information: Lorraine Bowlin (202-872-4567)

Quality you can count on!

We're the Laboratory Products Association. When you buy from an LPA member company you can count on choosing from the best products & value, the broadest line of laboratory products, guaranteed delivery & service from well established & dependable companies. By purchasing from an LPA member company you tap an invaluable source of leading manufacturers & distributors serving the scientific community. Our membership is constantly growing & expanding its network of information & services; all with the goal of providing you with what you need.



and still counting...

LABORATORY PRODUCTS ASSOCIATION

225 Reinekers Lane, Suite 625
Alexandria, Virginia 22314
703 836 1360 ~ Fax 703 836 6644



CIRCLE 5 ON READER SERVICE CARD

Contents

4258
Determination of Chloride, Nitrate, Sulfate, Nitrite, Fluoride, and Phosphate by On-Line Coupled Capillary Isotachophoresis–Capillary Zone Electrophoresis with Conductivity Detection
Dušan Kaniansky, Imrich Zelenský, Anna Hybenová, and Francis I. Onuska*

4265
Determination of Urinary Albumin Using High-Performance Immunoaffinity Chromatography and Flow Injection Analysis
*Peggy F. Ruhn, Jay D. Taylor, and David S. Hage**

4272
Separation of Carrier-Free Holmium-166 from Neutron-Irradiated Dysprosium Targets
Ekaterina Dadachova, Saed Mirzadeh, Richard M. Lambrecht, Eric L. Hetherington, and F. F. Knapp, Jr.*

4278
Foam Flotation Enrichment of Enantiomers
Daniel W. Armstrong, Eve Y. Zhou, Shushi Chen, Kang Le, and Yubing Tang*

4283
Determination of the Active Hydrogen Content in Pyridine–Borane Complex by Schiff Base Reduction and High-Performance Liquid Chromatography
James A. Morley, Lee Elrod, Jr., and John F. Bauer*

4288
Prediction of Temperature Programmed Retention Indices for Polynuclear Aromatic Hydrocarbons in Gas Chromatography
Agneta K. Bemgard, Anders Colmsjö, and Kent Wrangskog*

4295
On-Line Coupling of Liquid Chromatography to Biochemical Assays Based on Fluorescent-Labeled Ligands
A. J. Oosterkamp, H. Irth, U. R. Tjaden, and J. van der Greef*

4302
Time-Resolved Immunofluorometric Determination of Specific mRNA Sequences Amplified by the Polymerase Chain Reaction
*Susan Bortolin and Theodore K. Christopoulos**

4308
Two-Dimensional High-Performance Liquid Chromatography Using Monodisperse Polymer Beads Containing Segregated Chemistries Prepared by Pore Size Specific Functionalization. Single-Column Combinations of Size Exclusion or Ion Exchange with Reversed-Phase Chromatography
*Vladimir Smigol, Frantisek Svec, and Jean M. J. Fréchet**

4316
Organic Gas Sorption Characteristics of Plasma-Deposited Amino Acid Films
Iwao Sugimoto, Masayuki Nakamura, and Hiroki Kuwano*

4324
Influence of Vapor Deposition Parameters on SERS-Active Ag Film Morphology and Optical Properties
*David J. Semin, and Kathy L. Rowlen**

4332
Alkali Metal, Alkaline Earth Metal, and Ammonium Ion Selectivities of Dibenzo-16-Crown-5 Compounds with Functional Side Arms in Ion-Selective Electrodes
*Akira Ohki, Jian Ping Lu, Xiaowu Huang, and Richard A. Bartsch**

4337
Eletrocatalysis of NADH Oxidation with Electropolymerized Films of 3,4-Dihydroxybenzaldehyde
*F. Pariente, E. Lorenzo, and H. D. Abruña**

4345
Measurement in Vitro of Human Plasma Glycerol with a Hydrogen Peroxide Detecting Microdialysis Enzyme Electrode
Lindy J. Murphy and Peter T. Galley*

continued on p. 1155 A

Instructions for authors of AC Research and guidelines for the Instrumentation, Report, Analytical Approach, and A/C Interface features are published in the Jan. 1 issue, p. 185. Please consult these instructions prior to submitting a manuscript for consideration for publication.

Manuscripts for publication in AC Research (4 copies of text and illustrative material) should be submitted to the Editor at the University of North Carolina address. Please include a signed copyright status form; a copy of this document appears on p. 191 of the Jan. 1 issue. Manuscripts for publication in the A-page section should be submitted to the Washington editorial staff.

Supplementary material is noted in the table of contents with a ■. It is available as photocopy ($10.00 for up to 3 pages and $1.50 per page for additional pages, plus $2.00 for foreign postage) or as 24X microfiche ($10.00, plus $1.00 for foreign postage). Canadian residents should add 7% GST. See supplementary material notice at end of journal article for number of pages. Orders *must* state whether for photocopy or for microfiche and give complete title of article, names of authors, journal, issue date, and page numbers. Prepayment is required and prices are subject to change. Order from Microforms & Back Issues Office at the ACS Washington address.

The American Chemical Society and its editors assume no responsibility for the statements and opinions advanced by contributors. Views expressed in the editorials are those of the editors and do not necessarily represent the official position of the American Chemical Society.

The paper used in this publication meets the minimum requirements of American National Standard for Information Sciences—Permanence of Paper for Printed Library Materials, ANSI Z39.48-1984.

Journals Department
American Chemical Society
2540 Olentangy River Road
P.O. Box 3330
Columbus, OH 43210
614-447-3600, Ext. 3171
TELEX 6842086 Fax 614-447-3745

Member & Subscriber Services
American Chemical Society
P.O. Box 3337
Columbus, OH 43210
614-447-3776
800-333-9511

Advertising Office: Centcom Ltd., 1599 Post Road East, P.O. Box 231, Westport, CT 06881

THE END OF INSCRUTABLE DISQUISITION.

The task of keeping up with the latest advances in chemical research can be daunting.

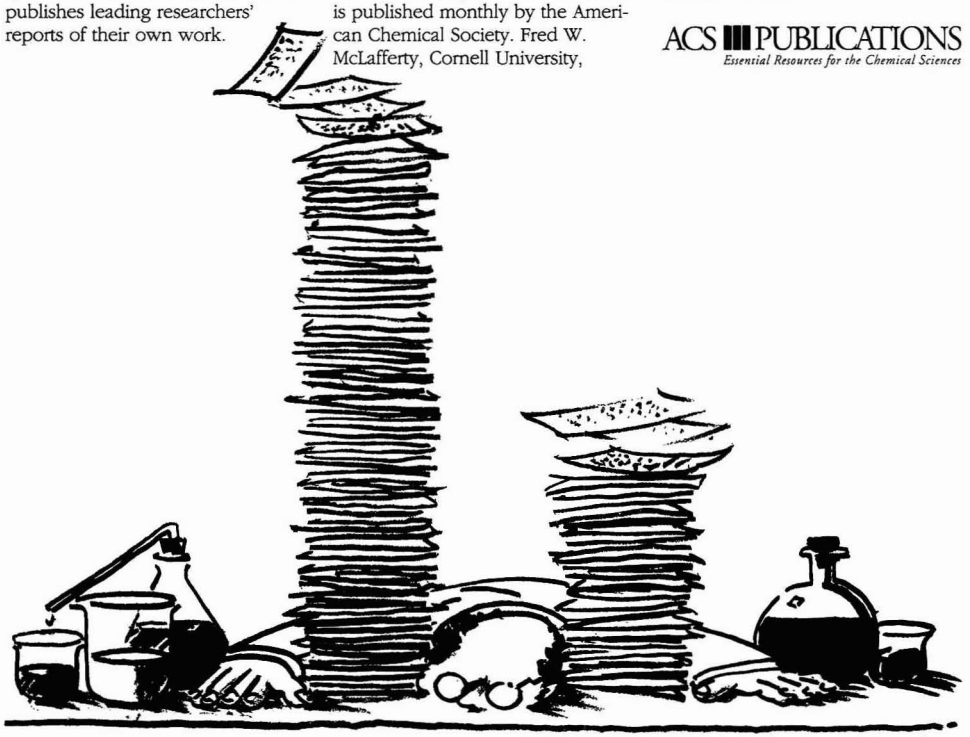
However, there is an easy way to gain a vital overview of basic research and applications in all areas of chemistry. Subscribe to *Accounts of Chemical Research* (ACR). ACR publishes leading researchers' reports of their own work.

Concise, critical articles help end controversies, relate recent advances to earlier work, and project their future significance.

Place your order today by calling 1-800-333-9511. Outside the U.S. call 614-447-3776.

Accounts of Chemical Research is published monthly by the American Chemical Society. Fred W. McLafferty, Cornell University, Editor. B.A. Baird, Cornell University, and J.E. McMurry, Cornell University, Associate Editors. Subscription rates in the U.S. for ACS Members are $29 for one year, $52 for two years. Nonmembers are $191 for one year. Call for rates outside the U.S.

ACS PUBLICATIONS
Essential Resources for the Chemical Sciences



Correspondence

4354
Determination of ppb-Level CO, CO_2, CH_4, and H_2O in High-Purity Gases Using Matrix Isolation FT-IR with an Integrating Sphere
Yoshimasa Ogawara, Albert Bruneau, and Takako Kimura*

4359
Detection of Alkylated Cellulose Derivatives in Several Archaeological Linen Textile Samples by Capillary Electrophoresis/Mass Spectrometry
Dmitri A. Kouznetsov, Andrey A. Ivanov, and Pavel R. Veletsky*

Technical Notes

4366
Determination of Absolute Mass Values in MALDI-TOF of Polymeric Materials by a Self-Calibration of the Spectra
Giorgio Montaudo, Maurizio S. Montaudo, Concetto Puglisi, and Filippo Samperi*

4370
Monitoring Formation of Diamine Process Intermediate by Reversed-Phase Liquid Chromatography
Barbara S. Lord and Rodger W. Stringham*

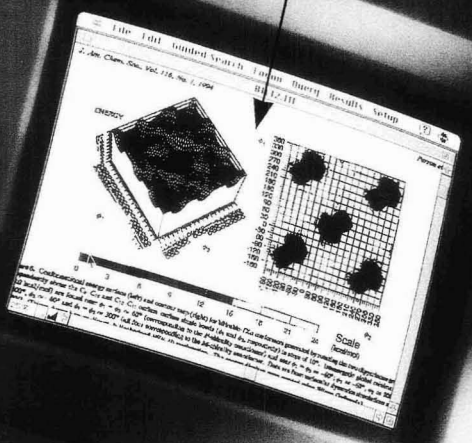
4375
Evaluation of an Automated Thermospray Interface for Coupling Electrothermal Atomization Atomic Absorption Spectrometry and Liquid Chromatography
C. Bendicho

4382
Labeling of Double-Stranded DNA by ROX-Dideoxycytosine Triphosphate Using Terminal Deoxynucleotidyl Transferase and Separation by Capillary Electrophoresis
*Daniel Figeys, Annika Renborg, and Norman J. Dovichi**

Author Index **4384**

Why Wait?

Access electronic journals with CJACS Plus. Available now!



The wait is over. CJACS Plus gives you online access to full page images from the Chemical Journals of the American Chemical Society — complete with figures, graphs, charts, photos and chemical structures — at your desktop! It's all part of the STN network. And it's all here now.

To find out more, call **800-753-4227** or 614-447-3731

ACS PUBLICATIONS
Essential Resources for the Chemical Sciences

CAS®
A Division Of The American Chemical Society
CAS operates STN in North America

In This Issue

Brief introductions to the research articles in this issue

Accelerated Articles

A pseudostationary phase for chiral CE

The ability of CE to differentiate enantiomers is attracting increasing interest because of the speed and efficiency of CE methods. Patrick Camilleri and co-workers at Cambridge University use a novel class of dodecyl β-D-glucopyranoside derivatives as pseudostationary phases for chiral separation in CE. When used above their critical micelle concentration, these surfactants provide selectivity for analytes of widely varying chemical structure, hydrophobicity, and ionic character. (p. 4121)

Precolumn reactions and CE on a chip

Microfabrication of analytical instrumentation has the potential for allowing the laboratory to be transported to the samples rather than vice versa. J. Michael Ramsey and colleagues at Oak Ridge National Laboratory construct a glass microchip to perform chemical reactions and capillary electrophoresis sequentially. The reaction and separation performances are evaluated by reacting amino acids with *o*-phthaldialdehyde to generate a fluorescent product that is detected with laser-induced fluorescence. Detection limits of 0.55 and 0.83 fmol are achieved for arginine and glycine, respectively. (p. 4127)



Calcium stoichiometry using ESIMS

Because the interaction of metal ions with proteins is essential to catalytic function and structural stability, determination of metal-binding stoichiometry is important for studies of protein function. Joseph A. Loo and colleagues at Parke-Davis Pharmaceutical Research use ESIMS to determine the calcium-binding stoichiometry of four proteins: bovine calmodulin and α-lactalbumin, rabbit parvalbumin, and human stomelysin. Using aqueous solutions for ESIMS allows gas-phase acquisition of metal-binding information that is consistent with that reported for solution-phase experiments. (p. 4190)

Glycerol enhances ESCE

Using glycerol as an additive in entangled solution CE can improve the efficiency for distinguishing mismatches in small DNA molecules. Keith R. Mitchelson and Jing Cheng of the University of Aberdeen (U.K.) investigate the effect of glycerol in ESCE with restriction fragments up to 1353 bp. Glycerol added to an entangled solution of (hydroxypropyl)methylcellulose (HPMC) in Tris-borate buffer improves separation by forming complexes with the borate and HPMC. (p. 4210)

CE of DNA sequencing fragments

Although linear polyacrylamide is a promising matrix for CE separation of DNA fragments, the mobility behavior of DNA fragments in this matrix has not been fully characterized. Takashi Manabe and colleagues at the Himeji Institute of Technology (Japan) and the Institute of Physical and Chemical Research (Japan) report on the separation and LIF detection of FITC-labeled oligonucleotides and DNA sequencing reaction products by CE with linear polyacrylamide as a sieving matrix. For large DNA fragments they find that the migration time interval between bands decreases linearly as DNA fragment size increases. (p. 4243)

LC and biochemical assays

Combining LC with biochemical detection (BCD) methods enhances the performance of both techniques and results in highly selective and sensitive analytical methods. H. Irth and colleagues at the University of Leiden (The Netherlands) report the on-line coupling of LC to a BCD technique based on the use of fluorescein-labeled ligands as reporter molecules. For the biotin/avidin model system, the researchers report a 160-fmol detection limit for biotin. (p. 4295)

Quantitating PCR products

Although the polymerase chain reaction (PCR) has had an enormous impact on the analysis of biological samples because it exponentially amplifies the mass of the analyte of interest, the techniques used for detecting PCR products are often qualitative and time-consuming. Theodore K. Christopoulos and Susan Bortolin of the University of Windsor (Canada) describe a time-resolved immunofluorescence method for the quantitative determination of PCR products. The PCR primers are labeled at their 5′ ends with biotin and a hapten that are incorporated in the amplified product. The phosphate ester of fluorosalicylic acid is used as a substrate, and the ternary complex formed is measured by time-resolved fluorometry. (p. 4302)

Labeling double-stranded DNA

Using intercalating dyes to detect double-stranded DNA separated by capillary electrophoresis is convenient, but different strands cannot be selectively labeled with different dyes because of the rapid equilibrium between free and bound dye. Norman J. Dovichi and colleagues at the University of Alberta (Canada) use terminal deoxynucleotidyl transferase to covalently label both blunt and sticky-end DNA fragments with a fluorescently labeled dideoxynucleotide. Although CE of the product using hydroxypropylmethylcellulose results in single peaks for each fragment, the higher resolution CE separation with non-cross-linked polyacrylamide shows that the product contains two components for each restriction digest fragment. (p. 4382)



NADH sensor

The redox activity of one of the most commonly used coenzymes in physiological processes, β-nicotinamide adenine dinucleotide (NADH), is difficult to characterize because of the high overpotential associated with NADH oxidation at bare electrode surfaces. H. D. Abruña of Cornell University and colleagues at the Universidad Autónoma de Madrid (Spain) describe the fabrication and performance of an electrocatalytic NADH sensor. The sensor is formed by oxidizing a quinone-containing compound, 3,4-dihydroxybenzaldehyde, on a glassy carbon electrode to create a stable redox-active film, and it exhibits submicromolar limits of detection. (p. 4337)

Measuring human plasma glycerol

Rapid determination of human plasma glycerol concentration may prove helpful in understanding non-insulin-dependent diabetes mellitus. Lindy J. Murphy and Peter T. Galley at St. Mary's Hospital (U.K.) describe a microdialysis electrode that can provide a response in 20 s. The electrode contains stationary glycerol kinase and glycerol phosphate oxidase and exhibits a linear response that is directly dependent on the concentration of ATP. (p. 4345)



MIMS of dissolved gases in water

Dissolved gases such as N_2, O_2, and Ar play an important role in marine and aquatic science in that deviations from equilibrium concentrations reflect biological activity and physical processes acting on the system. Todd M. Kana and colleagues at the University of Maryland modify a membrane inlet mass spectrometer to perform high-precision measurements of dissolved gases in water. The instrument pumps water through semipermeable microbore silicon tubing positioned inside an inlet vacuum line of a quadrupole mass spectrometer, and dissolved gas concentrations are determined in the multiple ion detection mode. (p. 4166)

Identifying bacteria with ESIMS

Although bacteria are traditionally identified on the basis of morphological and metabolic characteristics, such as by the use of a Gram stain, differentiation of bacteria from each other as well as from other microbes based on chemical composition is gaining popularity. Alvin Fox and colleagues at the University of South Carolina and Geo-Centers use ESIMS to determine the concentration of muramic acid, an unusual sugar found only in bacterial cell walls, in cell hydrosylates. The method can discriminate bacteria from fungi based on muramic acid content. (p. 4171)

Dating with high-temperature SIMS

Because the natural variation in $^{176}Hf/^{177}Hf$ is dependent on the time-integrated $^{176}Lu/^{177}Hf$ history of a geological sample, Hf isotopes are an important tool in dating events. Unfortunately, difficulties in separating Hf and its poor ionization efficiencies for thermal ionization MS have limited the use of Hf isotopes. Vincent J. M. Salters at Columbia University describes the use of "hot SIMS," which offers an improvement in ionization efficiencies of several orders of magnitude over conventional thermal ionization, to obtain a mass spectrum of sputtered ions that contains only a limited number of molecular ions. (p. 4186)

Differences between ion mobility spectrometers

Although peak shapes produced by ion mobility spectrometry have been analyzed and the effects of drift voltage, gate pulse width, temperature, and mobility on resolving power have been studied, the effects of specific instrument design characteristics such as the length and diameter of the drift region are not as well characterized. William F. Siems and colleagues of Washington State University and Gonzaga University fit IMS peak width data using a least-squares procedure to a semiempirical model with three adjustable parameters. The model's predictions correspond well to observed linewidths across a wide range of operating conditions, allowing the parameter values to be related to instrument design characteristics. (p. 4195)

The fate of atrazine

In the environment, atrazine is hydrolyzed to hydroxyatrazine under a wide range of conditions. However, the lack of quantitative methods for the determination of ultratrace quantities of HA has limited research on the fate of atrazine in water. M. L. Gross and colleagues of the University of Nebraska report on an isotope dilution and fast atom bombardment MS method for the determination of HA in water. An RSD of 10% and a relative error of < 10% is obtained for seven standard water samples containing HA at 100 pptr. The method can successfully determine HA and atrazine simultaneously in groundwater. (p. 4202)

A spray-on sense of smell

Biomimetic organic films are currently of interest as sensitive and specific gas sorption sensors and could eventually be used in artificial olfactory and taste detection systems. Iwao Sugimoto, Masayuki Nakamura, and Hiroki Kuwano of NTT Interdisciplinary Research Laboratories (Japan) use static SIMS to characterize the surface structure and gas sorption activity for organic films made by rf plasma sputtering of two amino acids, D-phenylalanine and D-glutamic acid, onto a nondoped silicon wafer. (p. 4316)

Analyzing ancient linens

Accurately analyzing archaeological textiles is important for determining the chemical mechanisms of textile aging as well as for gaining information about past technological processes. Dmitri A. Kouznetsov and colleagues at S. A. Sedov Biopolymer Research Laboratories (Russia) use CE/MS to examine the alkylated cellulose sequences in eight samples of light, undyed textile linen from between 1200 B.C. and A.D. 1500. Information on sample differences in alkyl group type and in the structure and abundance of the alkylated glucose residues can be correlated with the age and manufacturing location of the textiles. (p. 4359)

Absolute mass values by self-calibration

Although scientists have obtained good MALDI TOF spectra of polymeric samples, they are often unable to interpret

them because of difficulties in making the correct mass assignments and in discerning whether the polymer molecules desorb intact. Giorgio Montaudo and colleagues at the Universitá di Catania (Italy) and the Consiglio Nazionale delle Richerche (Italy) introduce a self-calibration method that allows determination of absolute mass values in these spectra. They use the technique to interpret each single peak in MALDI TOF spectra of poly(caprolactone) and poly(bis-phenol A carbonate) and establish that none of the peaks in the spectra corresponds to fragments. (p. 4366)



Eat your carrots

β-Carotene, an antioxidant precursor to vitamin A, has been proposed to have cancer- or aging-inhibition properties. Its metabolism in humans is not well characterized, however, and it is difficult to monitor because it is labile and associates with lipids. Andrew Clifford and co-workers at the University of California–Davis use SPE to isolate *all-trans*-β-carotene-d_8 and its metabolite retinol-d_4 in human plasma for determination by reversed-phase HPLC with spectrophotometric detection and by EI-MS/MS. (p. 4177)

FFF factors

Field-flow fractionation (FFF) techniques can be used to separate particulate or macromolecular mixtures on the basis of mass, size, thermal diffusion, or charge. Size separations, however, are susceptible to perturbations caused by the finite size of particles undergoing migration in the FFF channel. P. Stephen Williams and J. Calvin Giddings of the University of Utah explore the application of a first-order correction for particle size under conditions of both exponential and power-programmed field decay. Higher uniformity in fractionating power can be achieved by varying the parameters for power programming but not by changing those for exponential programming. (p. 4215)

Improving azide sensitivity

Sodium azide, widely used as an antimicrobial agent, has recently been recognized as a cancer-causing agent. M. C. Gennaro and colleagues at the Universitá di Torino (Italy) use an ordinary least squares method, an all-model search, the Fisher F test, and R2 values to optimize a reversed-phase ion interaction chromatography method for determining azide in the presence of many interferences. Under improved chromatographic conditions, a detection limit of 6.0 ppb is achieved. (p. 4229)

Modeling flow profiles and dispersion

In CE experiments at low pH, unusually high broadening of the sample peak cannot be accounted for by diffusion alone. Catherine A. Keely and colleagues of Hewlett Packard examine the contributions of flow profile in the capillary to band broadening and increased plate height. The theory is based on the expectation that the ξ potential changes along the length of the capillary because of electrical fields that exist across the wall of the capillary. Their discussion focuses on the case in which the radial voltage across the capillary wall is constrained to be a linear function of the length of the capillary. (p. 4236)

Predicting retention in SFC

Development of a chromatographic method for a new analyte often involves trial and error coupled with experience with similar compounds. Darren M. Heaton and coworkers at the University of Leeds (U.K.) and Hewlett Packard develop a model that can be used to predict retention of packed-column SFC based on multicomponent solubility parameters. Retention data are obtained for a series of aromatic molecules of form Ph-X on ODS-, phenyl-, nitrile-, and amino-bonded phases and bare silica. (p. 4253)

ITP stretches the dynamic range of CZE

Natural waters may contain low levels of anions such as nitrite, fluoride, and phosphate together with chloride, sulfate, and nitrate at much higher concentrations. Although CZE has speed and other advantages over ion chromatography for this type of analysis, its dynamic range is limited. Dušan Kaniansky and colleagues at Comenius University (Slovak Republic) and the National Water Research Institute (Canada) demonstrate a technique using capillary isotachophoresis (ITP) coupled with CZE that allows the determination of anions at low-part-per-billion concentrations in the presence of other anions at part-per-thousand concentrations. (p. 4258)

On-line volume correction for urinalysis

The presence of albumin and creatinine in urine can be an early indicator of kidney disease. Peggy Ruhn, Jay Taylor, and David Hage of the University of Nebraska describe an immunoaffinity chromatography system for urinary albumin determination that is coupled with a flow-injection analysis module for colorimetric determination of creatinine. The method's detection range spans the concentration range of clinical interest, and results are comparable with those of reference techniques. (p. 4265)

Purifying ^{166}Ho

Holmium-166 is used in a variety of radiotherapy applications because it emits high-energy β radiation without high-energy γ emission and because it decays to a stable element, making it relatively safe for others to be near the patient. Although ^{166}Ho with a high specific activity can be produced in a nuclear reactor from ^{166}Dy decay, the product often contains carrier ^{164}Dy. Saed Mirzadeh of Oak Ridge National Laboratory and colleagues at the Australian Nuclear Science and Technology Organization explore the use of two commercial cation exchangers and α-hydroxyisobutyric acid eluent for HPLC separation of ^{166}Ho from the carrier isotope. They report a 95% yield with low Dy breakthrough for the 2-h separation process. (p. 4272)

Separating enantiomers with bubbles

Adsorptive bubble separation methods such as foam, froth, and floc flotation have been used for many years for processing large amounts of materials at a relatively low cost. Daniel W. Armstrong and colleagues at the University of Missouri–Rolla investigate the possibility of using absorption bubble separation for process-scale enantiomeric separations. Foam-forming chiral collectors can be used in conjunction with an inexpensive glass device to enantiomerically enrich pharmaceutically important compounds as well as derivatized and underivatized amino acids. A variety of in-

teractions, including inclusion complex formation, ligand exchange, and steric interactions, are used to effect chiral separations in these systems. (p. 4278)

Determining active hydrogen content

Borohydrides and borane complexes are widely used as selective reducing agents in many chemical applications. The pyridine–borane complex (PBC), which is quite stable to hydrolysis, is an attractive reagent for large-scale reductions that are common in the pharmaceutical industry. James A. Morley, Lee Elrod, Jr., and John F. Bauer at Abbott Laboratories report on a simple method for quantitating the active hydrogen content in PBC that can be used to analyze an intermediate in the synthesis of a pharmaceutical product and to indicate the stability of the stored intermediate. The procedure exploits the ease with which Schiff bases are reduced by amine–boranes, uses HPLC to quantitate the reduction product, and offers speed and automation advantages over gasometric and volumetric procedures. (p. 4283)

Predicting GC retention of PAHs

Identification of many PAHs is difficult because of a lack of pure reference compounds. Agneta Bemgård, Anders Colmsjö, and Kent Wrangskog of the National Institute of Occupational Health (Sweden) relate temperature-programmed GC retention indices of nonsubstituted PAHs with calculated molecular properties. They use a partial least-squares regression equation with five descriptors (first-order valence molecular connectivity, ionization potential, length, height, and quadrupole moment) to predict retention. Peri-condensed PAHs are more accurately predicted than cata-condensed PAHs with the descriptor set used. (p. 4288)

Separation media with segregated chemistries

Multidimensional chromatography improves peak capacity as well as resolution in the separation of complex mixtures. Although these separations are often accomplished by column switching, stationary phases with both hydrophilic outer surfaces and hydrophobic pores have been developed. Jean M. J. Fréchet, Vladimir Smigol, and Frantisek Svec of Cornell University report on the preparation of media for separation of complex samples that require a combination of size exclusion or ion-exchange with reversed-phase chromatographic modes. They use a pore-size-specific functionalization process to prepare media with two segregated chemistries. Separation of proteins and alkylbenzenes documents the feasibility of the approach. (p. 4308)

A variety of side arms

Dibenzo-16-crown-5 compounds are efficient and selective agents for the solvent extraction of alkali metals and alkaline earth metals and their transport through liquid membranes. Richard A. Bartsch and colleagues of Texas Tech University investigate the influence of side-arm variation in dibenzo-16-crown-5 lariat ethers on their potentiometric responses to alkali metals, alkaline earth metals, and ammonium ions when incorporated into solvent polymeric membrane electrodes. Potentiometric responses are rationalized in terms of crown ether ring size, oxygen basicity, conformational positioning, and rigidity of the side arm. (p. 4332)

Monitoring a diamine process intermediate by LC

The synthesis of a new drug under development requires separation of a reaction mixture containing a hydrophobic solvent and precursor, a relatively hydrophobic intermediate, and a product containing two primary amine groups. The separation is complicated by the presence of two labile triethylsilyl ether protecting groups that dominate hydrophobic retention. Barbara S. Lord and Rodger W. Stringham at the DuPont Merck Pharmaceutical Co. report that the appropriate reversed-phase LC procedure requires both ionic and hydrophobic interactions. Ionic interactions, which appear to be necessary to reorient the amine portion of the molecules toward the chromatographic surface, must be moderated to minimize peak broadening. (p. 4370)



Exploring the role of polymer supports in sensors

Metal complexes used as sensors are supported on an inorganic or organic polymer matrix. In some cases, the matrix is a passive anchor, and in others, it plays an active role in the performance of the sensor. J. N. Demas and colleagues of the University of Virginia and James Madison University explore the relationship between polymer structure and design and the performance of an oxygen sensor. Domain models explain the variations in oxygen-quenching properties as a function of additives and cross-linkers. (p. 4133)

Detecting a single molecule in a capillary

Although detection of a single molecule in a flowing stream can be achieved using a variety of experimental schemes involving laser excitation and fluorescent detection, the overall detection efficiency is low because most molecules do not pass through the excitation laser beam. James D. Winefordner and colleagues at the University of Florida improve the efficiency of single-molecule detection by confining the molecules in a capillary tube, irradiating the entire internal diameter of the capillary with the excitation laser beam, and absorbing the laser specular scatter with a metal vapor filter. The measurement efficiency for the near-IR dye IR140 is estimated to be near unity. (p. 4142)

Anthracene on solvent surfaces

Laser two-photon ionization is a convenient and sensitive technique for detecting photoabsorbing molecular species. The detection of polycyclic aromatic hydrocarbons such as anthracene in the environment is important because this class of compounds can cause cancer. Teiichiro Ogawa, Hangting Chen, and Takanori Inoue of Kyushu University (Japan) report on their study of laser two-photon ionization of anthracene on the surface of various solvents and the effects of solvent polarity, dielectric constant, and electron mobility on the photoionization signal. (p. 4150)

Using OGS for isotopic analysis of uranium

Conventional methods for measuring isotope ratios require sophisticated instrumentation, such as a thermal ionization

or ion trap mass spectrometer. C.M. Barshick and colleagues at Oak Ridge National Laboratory investigate the potential of glow discharge atomization coupled with high-resolution optogalvanic spectroscopy for field measurement of uranium isotope ratios. A hollow cathode glow discharge is coupled with tunable lasers for isotopically selective excitation of gaseous uranium ions produced by cathodic sputtering, and optogalvanic detection of the discharge atom population allows identification of ^{235}U at depleted, natural, and enriched abundances in uranium metal and uranium oxide samples based on the spectral signatures of two transitions. (p. 4154)

Reducing interference in Raman spectroscopy

The combination of weak Raman scattering, instrumental complexity, and fluorescence interference has prevented Raman spectroscopy from being routinely applied for qualitative or quantitative analysis. Richard L. McCreery and Mark R. Kagan of the Ohio State University use an sp^2-hybridized carbon rod to absorb analytes from solution, effectively quenching fluorescence and allowing acquisition of Raman spectra with high S/N. The technique is applied to solutions of Rhodamine 6G, the near-IR laser dye IR125, bis-(methylstyryl)benzene, and fluoranthene. (p. 4159)

In search of film reproducibility

Vapor-deposited thin metal films are widely used in surface-enhanced Raman spectroscopy (SERS) because they are stable and easy to prepare and characterize. However, these films are prepared differently in every laboratory, resulting in unique morphology and optical properties. Kathy L. Rowlen and David J. Semin of the University of Colorado use optical absorption, atomic force microscopy, and SERS to investigate which variables of vapor deposition are important for generating reproducible silver films. Although the type of glass used appears to be important, pretreatment of the glass is not. Deposition rate, temperature, geometry, and postdeposition annealing are also discussed. (p. 4324)

Gases on a sphere

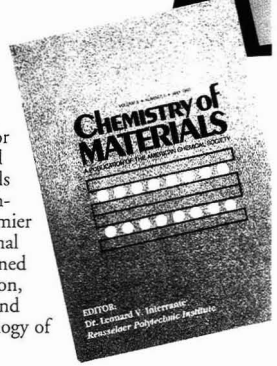
Although matrix isolation FTIR spectrometry has advantages over gas-phase FTIR spectrometry for determining impurities in high-purity gases, the flat substrate used in matrix isolation has a very short path length that results in insufficient sensitivity. Yoshimasa Ogawara and colleagues at Air Liquide Laboratories (Japan) use an integrating sphere to determine CO, CO_2, CH_4, and H_2O at part-per-billion levels in high-purity Ar and N_2. The results demonstrate increased sensitivity with a reduced sample volume compared with gas-phase FT-IR spectrometry. (p. 4354)

Hot shots for LC/AAS

Continuous-flow interfaces for HPLC with AAS suffer from low nebulization efficiency and can lower AAS sensitivity by causing dispersion and peak distortion. GFAAS systems provide high sensitivity but are usually incompatible with continuous-flow systems. C. Bendicho of the Universidad de Vigo (Spain) describes the use of an automated thermospray interface for pulsed deposition of LC eluates into a graphite tube platform. Total atomization times are shorter than those for conventional sample introduction methods. (p. 4375)

CHEMISTRY of MATERIALS...

All The Latest Directions And Innovations In Materials Chemistry!



Chemistry of Materials is an indispensible reference source for chemists, chemical engineers, materials scientists, and technologists...the premier international journal for anyone concerned with the preparation, characterization, and processing technology of new materials.

If you do materials-related R&D and want to be kept informed on the latest developments, return this coupon card today!

ACS PUBLICATIONS
Essential Resources for the Chemical Sciences

CHEMISTRY of MATERIALS **Subscription Certificate**
Editor: Dr. Leonard V. Interrante
Rensselaer Polytechnic Institute

❑ **Yes! I want to subscribe to this critical research publication. I don't risk a thing with ACS's prompt, pro-rata refund policy for all unmailed issues. Please enter my subscription for:**

One Year (12 issues)

	US	Canada & Mexico	Europe Air Service	All Other Countries Air Service
Member:	❑ $50	❑ $63	❑ $81	❑ $90
Nonmember:	❑ $420	❑ $433	❑ $451	❑ $460

Name: _____

Title: _____ Member #: _____

Employer: _____

Address: ❑ Home ❑ Business _____

City: _____ State: _____ Zip: _____

Country: _____

Telephone (Home): _____ (Work): _____

Employer's Business: ❑ Manufacturing ❑ Academic ❑ Government ❑ Other

Method of Payment (Check one.):

❑ Bill me ❑ Payment enclosed (Payable to the American Chemical Society)

❑ Charge my ❑ VISA ❑ MasterCard

Account #: _____

Expiration Date: _____

Signature: _____

***Chemistry of Materials*, American Chemical Society**
1155 Sixteenth Street, NW, Washington, DC 20036

Member rates are for personal use only. Subscriptions outside the U.S. Canada, and Mexico are delivered via air service. Journal subscriptions based on calendar year. Foreign payment must be made in US currency by international money order, UNESCO coupons, or US bank draft. Orders accepted through your subscription agency. For nonmember rates in Japan, contact Maruzen Co., Ltd. Please allow 45 days for delivery of your first issue. Redeem until December 31, 1994.

930/12/PH

7882J

Frontiers in Electroanalytical Chemistry

Electroanalytical chemistry is a broad subject that today encompasses much more than electroanalysis. Research and development done by electroanalytical chemists encompasses electron transfer chemistry of enzymes and of organometallic reagents, corrosion and coatings, solar energy conversion, catalytic reactions in fuel cells, and membrane-based separations. This diversity has developed over many years, and its growth continues. Electroanalytical chemistry also plays a large role in chemical analysis, particularly as embodied in ion-selective and enzyme electrodes. In this installment of my series of Frontiers in Analytical Chemistry editorials, I will point to some recent developments and opportunities in electroanalytical chemistry that seem especially exciting.

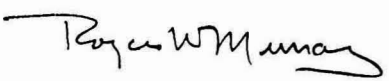
Electroanalytical chemistry, along with other areas of analytical chemistry, has a strong theme of miniaturization. Thinking small is good, and the act of making electrodes smaller than the eye can see has significant consequences. Microelectrodes have pushed the electrochemical kinetics timescale into the nanosecond regime and have opened up possibilities for electroanalysis of polymer solids and surfaces. Microelectrodes have become pioneer tools in small-space analysis; voltammetric measurements in single neurons have been reported, as has the time-resolved analytical detection of individual vesicles releasing their neurotransmitter contents at cell walls. A new form of microscopy, scanning electrochemical microscopy, offers chemically sensitive images on micrometer scales. The ultimate diminution of electrode size or diffusion path-length to values near molecular sizes promises a new and intimate view into interfacial chemistry fundamentals.

A modified electrode topic experiencing rapid progress is that of oriented molecular monolayers. These monolayers will be important because they allow the environment of electron transfer reactions to be controlled and manipulated on molecular scales. There are further prospects with organized monolayers for design of artificial receptor sites and a new generation of chemical sensors. Again, note the small-dimension theme.

The chemistry by which potentiometric responses can be evoked from ion-selective electrodes is rapidly expanding, so much so that I see them being referred to as species-selective electrodes because neutral molecular analytes are now targeted. These kinds of electrodes contribute mightily to all sorts of chemical analysis needs. Analyte selectivity is a major challenge in the world of sensors, and electroanalytical chemists are making fresh attacks on this problem by coupling redox enzymes with electrodes and by exploiting selective antigen–antibody binding reactions. There is a tremendous emphasis on glucose sensors, spurred by the relative sturdiness and consequent ease of use of the glucose oxidase enzyme as well as by the need for glucose sensors that can be used in clinical laboratories and by the individual diabetic patient for self-monitoring. Glucose sensor research combines clever schemes for glucose enzyme electrode electron transfer coupling with electrodes designed to be miniaturized, inexpensive and reliable to produce, and discarded after one measurement.

I have always felt the diversity of electroanalytical research and application to be a great strength, because it forces quite broad interdisciplinary interactions of its participants with other kinds of chemists and even nonchemists. A a result, the field is anything but insular, and it continues to contain bright opportunities for applications in analytical and other areas of chemistry.

Let's hear it for the electron pushers; they have a charged future.



P.S. I am grateful to a reader for pointing out that Vannevar Bush's report was presented to President Truman; President Roosevelt had passed away earlier in the spring of 1945. I'm glad to correct this factual error in last month's Editorial.

Synopses of significant analytical articles from other publications



Optimizing library search algorithms

Gas or liquid chromatography combined with low-resolution electron ionization MS is the method of choice for analysis of organic compounds in complex mixtures. Most instruments designed for this purpose are equipped with a computerized data system containing a searchable reference library of mass spectra that is commonly used to confirm a tentative identification or to suggest a list of candidate compounds that may have generated the spectrum. Donald R. Scott of the U.S. Environmental Protection Agency and Stephen E. Stein of the National Institute of Standards and Technology have optimized and tested five algorithms (probability-based matching, dot-product, similarity index, Euclidean distance, and absolute value distance) for library search identification of unknown compounds from their low-resolution mass spectra by matching test spectra against reference spectra in the NIST–EPA–NIH database.

The test set consisted of 12,592 alternate spectra of about 8000 compounds represented in the database. Most algorithms were optimized by varying their mass weighting and intensity scaling factors. The best-performing algorithm, with a 75% accuracy for rank, was the dot-product function, which measures the cosine of the angle between spectra represented as vectors. (*J. Am. Soc. Mass Spectrom.* **1994**, *5*, 859–66)

Boosting the performance of PB LC/MS

Researchers are interested in increasing the throughput of nonvolatile and thermally labile compounds in particle beam (PB) LC/MS, thereby increasing its sensitivity. A recent report that the transmission efficiency of benzidine could be dramatically increased by placing an ac corona discharge near the orifice of the thermospray nebulizer in a PB LC/MS interface attributed the increase to an aerosol neutralizing action of the corona discharge. These results prompted researchers William L. Budde, Thomas A. Bellar, and David D. Kryak of the U.S. Environmental Protection Agency to investigate the phenomenon with a different PB interface design.

They evaluated the performance of a system containing a helium-driven pneumatic nebulizer and a low-voltage dc glow discharge with 12 compounds separated using gradient elution LC. Signal enhancements observed with the dc glow discharge were significant but smaller than those caused by 0.01 M ammonium acetate in the mobile phase. Although the researchers were unable to prove the mechanism of improved transport efficiency, they concluded that the neutralization of charged particles is a viable hypothesis. (*J. Am. Soc. Mass Spectrom.* **1994**, *5*, 908–12)

LDI using fullerenes

MALDI MS, in which a time-of-flight mass spectrometer is used to mass analyze gas-phase protein ions, is a major tool in the investigation of bioorganic molecules. Gary D. Willett and colleagues at the University of New South Wales (Australia) have suggested that a layering technique using C_{60} as a substrate for laser desorption of large biological molecules could be a useful alternative to the well-known MALDI method.

Because fullerenes are insoluble in aqueous solution, a matrix layer is produced on a stainless steel sample holder by evaporation; the matrix layer is then coated with a solution containing the sample. A pulsed laser is used to irradiate the sample, and spectra are measured using a linear TOF mass spectrometer. The performance of the C_{60}-assisted laser desorption–ionization method is demonstrated using insulin, cytochrome *c*, and bovine serum albumin. (*Org. Mass Spectrom.* **1994**, *29*, 512–15)



Increased sensitivity for peptides

Electrospray ionization MS has become a useful method for analyzing peptides and proteins. Richard M. Caprioli and colleagues at the University of Texas Medical School have obtained zeptomole/attomole-per-microliter sensitivity for peptides using a micro-electrospray mass spectrometer.

The micro-electrospray source can integrate nanoliter flow-rate desalting and preconcentration techniques into the electrospray needle, effectively eliminating postcolumn dead volumes. It has been optimized for the specific analysis of neuropeptides such as neurotensin and methionine enkephalin. For neurotensin, the neuropeptide for which the method is most sensitive, a 10-μL injection of a solution containing 320 zmol/μL gave an $[M + 3H]^{3+}$ ion with a S/N > 8:1. Tandem MS analysis of the fragment ion at m/z 578.9 gave a S/N > 20:1 for a solution containing 32 amol of neurotensin. (*J. Am. Soc. Mass Spectrom.* **1994**, *5*, 867–69)



Imaging functional groups

Techniques that allow scientists to directly probe the spatial arrangement of functional groups causing observed interactions can provide information that is important in understanding problems ranging from lubrication and adhesion to biological recognition. Charles M. Lieber and colleagues at Harvard University and the Massachusetts Institute of Technology have used an atomic force microscope to make adhesive and friction force measurements between molecularly modified probe tips and organic monolayers that were lithographically patterned to pro-

duce a two-dimensional geometric distribution of distinct functional groups.

They used probe tips functionalized with hydrophobic or hydrophilic molecules to show that interactions between simple CH_3/CH_3, $CH_3/COOH$, and COOH/COOH functional groups correlate directly with friction images of sample surfaces patterned with these groups. By using this technique, one can produce friction images that correspond to the spatial distribution of functional groups on the sample surface and display predictable contrast. The researchers suggest that the approach, which they term chemical force microscopy, should also be useful in mapping the spatial distribution of functionalities such as charged or chemically reactive groups as well as more specific interactions such as those between complimentary and noncomplimentary oligonucleotides and ligand–receptor pairs. (*Science* **1994**, *265*, 2071–74)

Aza-arenes at the aqueous–silica interface

The carcinogenic and mutagenic properties and ubiquitous nature of aza-arenes necessitate the ability to predict the fate of this class of compounds in groundwater. The ability to predict solute transport requires an understanding of the interfacial interactions between the solute and the aquifer material. Jeanne E. Pemberton and colleagues at the University of Arizona have used in situ Raman spectroscopy to study the effect of pH on the solute–sorbent interactions and the nature of the adsorbed species at the aqueous–silica interface for acridine, quinoline, and pyridine.

Silica is used as the sorbent because it is well characterized and is a major component of aquifers. The researchers found that the neutral aza-arene hydrogen-bonds to surface sites in solutions in which the pH is above the pK_a of the compound. A protonated aza-arene/ClO_4^- ion pair interacts with surface sites in solutions in which the pH is below the pK_a of the compound. (*Appl. Spectrosc.* **1994**, *48*, 1043–53)

An ES interface as a nebulizer for ICP-AES

Because interest in using AES as a mode of detection for microseparations is growing, the use of nebulizers as interfaces is receiving increased attention. J. W. Elgersma and colleagues of the Vienna University of Technology (Austria) and the University of Amsterdam (The Netherlands) have reported on the use of an electrospray nebulizer to interface micro-HPLC with ICP-AES.

To test the interface, methanol and methanol–water solutions containing metal acetylacetonates were nebulized. The researchers found that the concentration detection limits were worse than those obtained with other nebulizers; however, the absolute detection limits were lower because of the low uptake rate of 10 μL/min. No signal drift was observed when a methanol test solution was nebulized for more than an hour. The contribution to peak width was too high for many applications; future work will attempt to reduce this problem. (*Spectrochim. Acta B* **1994**, *49*, 761–68)



EXAFS at the electrode interface

Determination of the structure of an electrode interface is important in determining the electrode's operating characteristics. T. E. Furtak and colleagues at the Colorado School of Mines and Rensselaer Polytechnic Institute have used extended X-ray absorption fine structure (EXAFS) spectroscopy to determine the structure of a copper monolayer–platinum electrode interface.

The EXAFS spectra of copper were measured at the K edge through a grazing incidence fluorescence detection experiment while the sample was under electrochemical control. With the X-ray electric field vector oriented parallel to the surface, information was obtained about the adsorbed monolayer in the plane of the surface; with perpendicular orientation, information was obtained about the substrate and the electrolyte. These results indicate that the neighbors of the copper are oxygen at 2.06 Å, platinum at 2.58 Å, and copper at 2.62 Å. (*J. Electrochem. Soc.* **1994**, *141*, 2369–73)



Column switching in CE

Column switching is commonly used in LC when a single column does not yield a sufficiently good separation. This technique has not been used in CE separations to date, however, because of the strict limit on system dead volume. Andreas Manz and colleagues at Ciba Geigy Ltd. and the University of Neuchâtel (Switzerland) have developed a technique for repeated column switching using a micro flow system etched in glass that eliminates unwanted sample components and allows separation of species with similar mobilities.

This technique, which the researchers refer to as synchronized cyclic CE, involves the use of a planar glass structure containing a separation channel that consists of four connecting capillaries arranged in a square as well as several channels that function as inlet and outlet channels and as buffer reservoirs. Separation is accomplished by voltage switching throughout the analysis cycle, and the component of interest is detected with laser-induced fluorescence. High plate numbers can be obtained using low voltages for the separation process. (*Sens. Actuators B* **1994**, *20*, 103–10)

The price of a jute bag

Jute fibers must be treated with some type of oil so that the fibers can be spun and made into bags that are used for shipping foods such as rice and coffee. Because using plant oils, rather than mineral oil, doubles the price of the bags, a method is needed to verify the absence of mineral oil. Konrad Grob and Christian Siegrist of Kantonales Labor report on a method that uses large-volume splitless injection onto a capillary column rather than the more traditional on-column injection.

In splitless injection, the sample is introduced into a packed vaporizing chamber. Heat is consumed as the solvent is evaporated, causing the site to cool and retain the higher boiling solute(s). The site then returns to the original temperature, volatilizing the solute, which is transferred to the column. To test injection performance, several *n*-alkane standards in pentane were injected. In the worst case, ~ 20% of the standard was lost by co-evaporation with the solvent. Injection of a 2-μL volume of a crude extract resulted in a measureable "hump" for a 100-mg/kg concentration of batching oil. After optimization, the researchers found that although the results demonstrate that the method is superior to off-line solvent evaporation, identification of the oil itself is a weakness in the method—the only evidence that the hump represents mineral oil is its shape and not having seen other material form a hump of similar shape. (*J. High Resolut. Chromatogr.* **1994**, *17*, 674–75)

BOTTOM LINE:

The more you read the higher you go.

Success for your company and your career means having the right information at the right time. And that's where *C&EN* comes in.

Week after week, *C&EN* delivers up-to-the minute news on every aspect of the chemical enterprise, from business to government, and research to education. Plus, you get an in-depth reporting of trends that puts it all in perspective.

You'll find practical information that enhances day-to-day business dealings, as well as long-range planning — information you can use to hold a competitive edge.

There's only one sure way to get the comprehensive chemistry news you need. Reading *C&EN* puts you on top. For subscription information, call toll-free:

1-800-333-9511.

Success for your company and your career.



CHEMICAL & ENGINEERING NEWS

C&EN

ATP awards to spur development of new technologies

The U.S. Department of Commerce has announced 41 awards totaling $170 million for research and development in information technology for health care, diagnostic technology for DNA, component-based software, and computer-integrated manufacturing for the electronics industry under the Advanced Technology Program (ATP). The goal of the ATP is to stimulate economic growth through the development of new industries. Administered by NIST, ATP makes the awards on the basis of rigorous review of the scientific and technical merit of each application and its potential benefits. Applicants must include a business plan for bringing the new technology to market once the technical obstacles have been overcome.

The goal of the information technology for health care program is to create fully integrated medical information systems across the health care industry, which would reduce costs and errors in handling medical information. Sixteen awards were made in this program for more than $72 million over five years, matched by more than $73 million in private-sector funds.

The goal of the diagnostic tools for DNA program is to develop compact, low-cost, automated DNA analytical technologies and equipment for fast, inexpensive detection and diagnosis of human, animal, and plant diseases. Thirteen awards were made in this program for more than $56 million over five years, matched by more than $54 million in private-sector funds.

The goal of the component-based software program is to develop reusable software elements suitable for automated assembly in a broad array of applications. Eleven awards were made in this program for more than $40 million over five years, matched by more than $41 million in private-sector funds.

The goal of the computer-integrated manufacturing for the electronics industry program is to develop a flexible, software-based framework to improve productivity, thereby allowing the electronics industry to easily



scale up and reconfigure its manufacturing operations. One award was made for more than $1.5 million over five years, matched by more than $1 million in private-sector funds.

ATP provides cost-sharing support to industry to allow exploration of promising, high-risk technologies that may form the basis for new and improved products, manufacturing processes, and services. These awards are the first to be given as part of the multiyear programs.

TJA to purchase Baird Analytical

Thermo Jarrell Ash Corp. (TJA, Franklin, MA), a subsidiary of Thermo Instrument Systems, has agreed to purchase the assets of the Analytical Instrument Division of Baird Corp. (Bedford, MA) for $13.5 million. Completion of the sale is expected this month.

This arrangement is expected to make TJA a leading supplier in instruments for elemental analysis, not only because of the resulting size of the company (which also includes Hilger) but also because of the complementary nature of the product lines involved. The companies expect to continue their individual product lines and customer service structures for the near future.

Kratos and Fisons at odds over patent

Kratos Analytical Ltd. (Manchester, U.K.) and Fisons plc (Ipswich, U.K.) are involved in a patent dispute over magnetic lens technology used in a surface analysis instrument. Kratos claims that the Fisons VG Escalab instrument infringes on its European patent EP 0 243 060, granted in 1991. Fisons says that Kratos's patent is narrow because it describes a particular arrangement of diaphragms in the magnetic lens and claims that its arrangement in the VG Escalab is different.

ARI makes grants for instrumentation, renovation

The National Science Foundation's Academic Research Infrastructure (ARI) program will award $52.8 million to 145 institutions to acquire or develop state-of-the-art instrumentation and to renovate research facilities. State-of-the-art instrumentation is "crucial to achieving scientific discoveries which enhance the nation's well-being and help ensure future prosperity" says Nathaniel Pitts, director of the Office of Science and Technology Infrastructure.

The ARI program was established by Congress as part of the Academic Research Facilities Modernization Act of 1988. More than 400 competitive proposals requesting nearly $175 million were submitted; only 43% received funding. Successful applicants are required to provide 30–50% in matching funds. The awards are targeted for institutions with

needs in the $100,000 to $2 million range, although smaller awards are made, such as the one granted to Indiana University for the acquisition of an electrochemical workstation. Awards generally are made for a maximum of three years; however, they may be extended to up to five years when new research instrumentation is being developed.

Among the recipients are Yale University for the acquisition of a high-field nuclear magnetic spectrometer, Union College for the development of the Center for Advanced Spectroscopic Techniques, and Miami University for the acquisition of a laser desorption time-of-flight mass spectrometer.

CAS and Dialog to cosponsor STAS

To standardize procedures used for searching and retrieving technical information from databases, Chemical Abstracts Service (CAS), Dialog Information Services, the Clearinghouse for Networked Information Discovery and Retrieval, and FIZ Karlsruhe are cosponsoring the publication of the Scientific and Technical Attribute Set (STAS). STAS, a list of standard data elements, their names and abbreviations, and a unique data element ID number, is designed to improve interoperability among consumers and providers of technical information using the Z39.50 protocol. Before STAS was developed, there was no standard way to refer to a large number of searchable and retrievable fields within scientific and technical databases.

CAS publishes *Chemical Abstracts*, operates the Chemical Registry System (with over 13 million entries), and produces a variety of online databases. Dialog Information Services, a Knight-Ridder company, produces more than 450 databases used by those in business, news, and scientific and technical fields.

Brookhaven to build facility to study ultrafast reactions

Brookhaven National Laboratory broke ground in October for the Pulse Radiolysis Facility (PRF), which will allow academic, industrial, and government researchers to study transient chemical species that live for only a few trillionths of a second. Previously, researchers used the 2 million eV Van de Graaff accelerator but were limited to species that live longer than one-millionth of a second. The facility will be used for basic research that is expected to eventually have practical applications in many areas. For example, as the process of electron transfer is better understood, so will the process of solar energy conversion.

Funded by the Department of Energy's Office of Basic Energy Sciences, the $3.6 million facility is based on a 10-million eV radio frequency photocathode electron gun housed in a reinforced underground concrete vault. The gun will be built by Northrop Grumman Corp., and the facility is expected to be completed by December 1995.

Ignition facility to study fusion

Secretary of Energy Hazel O'Leary has announced that Lawrence Livermore National Laboratory is the preferred site for a new multipurpose laser, the National Ignition Facility, which will be used to further the knowledge of fusion energy (e.g., processes that occur at the center of the sun).

The facility will consist of 192 lasers, focused on a ball bearing-sized capsule containing hydrogen. The goal of the project is to induce a fusion reaction that will produce more energy than it consumes. The hydrogen capsule could reach temperatures and pressures comparable to those found in stars. Alternative sites will be investigated, and a final decision will be made in about two years. The facility is expected to take seven years to build at an estimated cost of $900 million.

Digital signature for security

To encourage the use of digital signatures, NIST is seeking comments on a proposal for a pilot public key infrastructure program to implement the federal Digital Signature Standard (DSS). A digital signature allows the recipient of an electronic message or file to verify the sender's identity and the integrity of the file. DSS uses private digital keys, which are held by the user, and public keys, which are assigned and certified by a third party. In the future, a "public key infrastructure" will manage the certification of public keys on a large-scale basis. To reassure users of DSS that it does not infringe on other patents, the public key infrastructure contract will contain a clause stating that the government will assume liability for any patent infringement resulting from the performance of the contract, including use by private parties.

Revised labeling requirements

The American National Standards Institute's (ANSI) Board of Standards Review has approved revisions to ANSI Z29.1, the American National Standard for Hazardous Industrial Chemicals–Precautionary Labeling. The purpose of revising the standard is to assist label writers in developing more effective labels for use in a hazards communication program.

The revisions were based on suggestions offered by the Chemical Manufacturers Association (CMA), the general public, and other interested parties. The standard, last revised in 1988, includes labeling considerations for small packages, precautionary language that takes into account some industry practices that have become common since 1988, and updated definitions that reflect regulatory changes. An annex to the standard includes examples of label text, appropriate use of symbols, physical characteristics, a summary of the results of a label comprehension study, and environmental requirements.

Until publication of the final standard by ANSI, approved draft copies can be obtained from CMA Publications Fulfillment, 2501 M St., N.W., Washington, DC 20037 (202-887-1100; fax 202-887-1237). The cost is $12 for CMA members and $18 for nonmembers. For questions regarding content, contact Suzanne Croft at the address above (202-887-1292).

Report

BUILDING COOPERATION ON INTERNATIONAL CHEMICAL TRACEABILITY

As modern-day society becomes more sophisticated and dependent on advanced technology, its reliance on chemical analysis increases simultaneously. The ongoing development of instrumentation capable of providing fast and complex analyses prompts users of analytical data to expect accurate results more rapidly and at a lower cost. This process shows no sign of slowing and, as we move toward the start of the 21st century, analytical scientists face the serious challenge of satisfying the demands of the future. The increasing globalization of trade and a growing interdependence among countries on social issues such as environmental pollution illustrate the need for analytical data that are internationally comparable (*1*).

Substantial progress already has been made through organizations designed to facilitate collaboration on measurement issues. Support structures such as national institutes, professional and scientific bodies, and international organizations have existed for more than 150 years, and the pace of development is rapidly increasing. In Europe, for example, the European Analytical Chemistry Accreditation System (EURACHEM) was established in 1989 to provide a focus for analytical quality improvements in the European Community and European free trade area countries. For many years the Federation of European Chemical Societies (FECS) has provided a forum for national chemical societies to develop pan-European cooperation.

As globalization of trade and interdependence among countries increase, CITAC seeks to consolidate existing measurement issues on an international level

Similar developments are taking place in other parts of the world, and existing international organizations such as the International Bureau of Weights and Measures, the International Union of Pure and Applied Chemistry (IUPAC), the Association of Official Analytical Chemists (AOAC) International, and the International Laboratory Accreditation Conference (ILAC) also are expanding their activities.

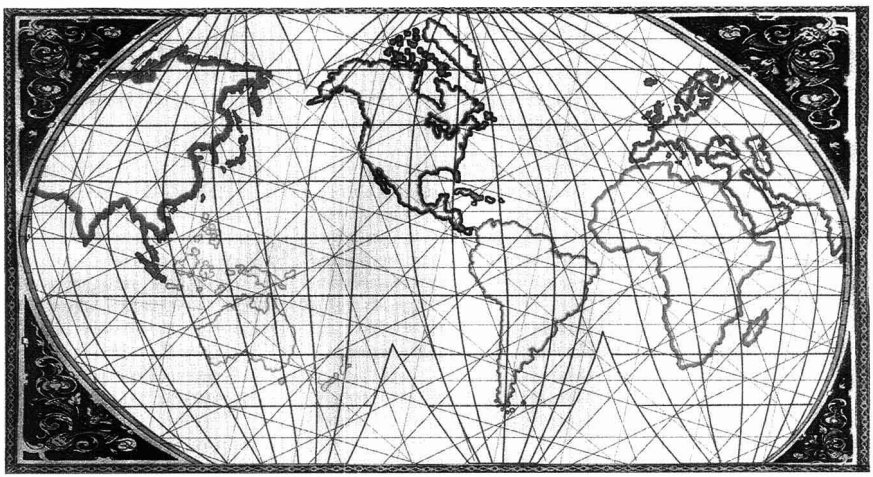
Despite this ongoing activity, a 1992 survey of senior analytical scientists from around the world indicated a need to consolidate these varied initiatives at the international level. As a result, two workshops were held in conjunction with Pittcon '93 and Pittcon '94 to discuss the development of an international chemical measurement system. A new working group called CITAC (Cooperation on International Traceability in Analytical Chemistry) was established as a result of these discussions and is currently undertaking a number of urgent tasks. In this article, we will review these initiatives and their status.

Atlanta workshop

An international group of analytical chemistry experts, including representatives from Western Europe, the United States, Russia, Japan, Canada, Australia, Africa, and South America, and delegates from the International Standards Organization (ISO), IUPAC, and AOAC International met in conjunction with Pittcon '93 to ex-

Bernard King
Ronald Walker
Laboratory of the Government Chemist

0003-2700/94/0366-1168A/$04.50/0
© 1994 American Chemical Society



plore how existing activities could be developed to meet the challenges of the 21st century.

The workshop began with keynote lectures that set the scene for constructive and lively discussions. They covered a number of broad-based topics, including the progress in establishing an international chemical measurement system (*1*). For example, we proposed that such a system be based on the principle of "fitness for purpose," ensuring that a product or service satisfies customer requirements with regard to technical specifications, time, and price. The need to address conceptual issues and to provide an organizational infrastructure that would ensure comparability of analytical data was also stressed. An overall structure was described, gaps in existing arrangements were identified, and additional activities were proposed. The discussion sessions also extended the initiatives regarding concepts and terminology, measurement uncertainty, traceability, and quality assurance proposed at the EURACHEM workshop in Belgium (*2*, *3*).

Responses from workshop participants reflected strong support for a new international initiative that would build on the work completed by other organizations, coordinate existing work so that duplication of effort is avoided, and start in a modest way by performing a small number of high-priority specific tasks. They also identified a number of possible collaborative tasks. Three groups were asked to consider gaps in the organizational infrastructure, what specific activities should be initiated now, how the work should be organized, who should be involved, and whether the EURACHEM workshop's recommendations on comparability and traceability are relevant at the world level.

Reports from these three groups provided the basis for a final plenary discussion and recommendations. Discussions revealed that delegates had very different ideas about the aims of the workshop and the meaning and significance of concepts such as traceability and comparability. For example, delegates from metrology institutes felt that establishing traceability to SI units was important, whereas delegates involved with "working-level" measurements in field laboratories felt that this was not of the highest priority; working-level comparability was often all that was required.

The groups concluded that although much valuable work was already being performed, improved coordination and cooperation among existing organizations were needed at the international level. The CITAC working group was established to provide a strategic plan and collaborative work program. Conferees felt that it was particularly important to establish traceability from the working level to internationally recognized reference materials and methods and, where feasible, to the chemical SI unit—the mole. Standardization of analytical quality practice and improvement in the comparability of measurements were also essential requirements. The CITAC working group also should provide a mechanism for improving cooperation among key organizations to improve communication, identify gaps, and minimize overlap.

CITAC tasks

A number of tasks were initiated during 1993 (*4*), including preparing a directory of certified reference materials (CRMs) currently under development, an ISO document on the quality system requirements of reference materials producers, a technical guide for quality assurance of chemical laboratories, a directory of chemical metrology activities, and defining the criteria for establishing traceability to the mole. Progress on these tasks was discussed at the second CITAC workshop held during Pittcon '94.

Directory of CRMs. This initiative was channeled through REMCO, the ISO committee that deals with reference material issues. Although a list of CRM producers

is not yet complete, more than 160 producers were identified and contacted; this resulted in a detailed listing of more than 1500 materials currently under development. Conferees agreed that the document should be revised on an annual basis and suggested that future revisions include information on the accreditation status of producers and specifications of the uncertainty of certified values. The directory will be of value not only to producers of CRMs, who need to avoid using valuable resources in a duplicative effort, but also to users of CRMs who need to be aware of available materials.

ISO document on the quality system requirements for producers of reference materials. Worldwide there are more than 100 recognized CRM producers, and many more commercial organizations produce chemical reference materials in one form or another. However, at present, there is little evidence of compliance with international quality system standards (e.g., ISO 9000, ISO Guide 25, and Good Laboratory Practices) for the production of these materials. This lack is troubling because reference materials provide a mechanism for providing traceability to national measurement standards. A draft guide has been prepared by several committees including CITAC, EURACHEM, EAL (European Accreditation for Laboratories), and REMCO. Following approval by REMCO, the document will be published as ISO Guide 34 and will provide detailed information at the technical level on the quality system requirements for producing appropriate reference materials.

International Guide to Quality in Analytical Chemistry: An Aid to Accreditation. Third-party assessment and registration are an important means of achieving the mutual acceptance of analytical data. Thus, it is important that at the international level both laboratories and accreditation authorities have adequate guidance on the specific requirements for chemical laboratories. CITAC is collaborating with ILAC, EURACHEM (*5*), EAL, and national accreditation authorities to provide this guidance. In addition to providing information such as organizational and staffing requirements, the guide will cover specific chemical issues such as achieving adequate calibration, traceability, and the use of computer-generated data. We anticipate that the guide will enable national accreditation authorities to standardize their interpretation of procedures and requirements, thereby achieving commonality on QA accreditation requirements for chemical laboratories throughout the world.

Directory of chemical metrology activities. This work aims to identify laboratories, committees, professional societies, and other organizations that are currently active in chemical metrology and the traceability of chemical measurements. These organizations are typically engaged in method development, reference material production, or interlaboratory measurement exercises. For example, the International Committee of Weights and Measures (CIPM) has recently initiated a study among national chemical metrology laboratories to assess the degree of comparability between chemical measurements made by these national institutes. The information in the directory will facilitate the linking of existing activities and identify areas in which work needs to be done. As such, it is a vital first step in establishing a truly integrated chemical measurement infrastructure.

Improved coordination and cooperation among existing organizations is needed at the international level.

Defining the criteria for establishing traceability to the mole. Traceability of physical measurements to the relevant SI base units (e.g., kg, s, m) has long been organized internationally and ensures that measurements at the working level are made on a sound basis. However, traceability to the mole does not yet commonly exist for routine chemical measurements. Many chemical measurements lack traceability because of insufficient information about the total uncertainty of the measurement process, a lack of high-quality reference materials (in turn because of a lack of primary methods), and no recognized system for comparability of traceable chemical measurements. Specialized work is ongoing at a number of chemical metrology institutes to improve the situation.

For example, the European Union's Institute for Reference Materials and Measurements (IRMM) is working to produce a primary elemental iron CRM whose atomic weight is known within a very narrow uncertainty range (for traceable conversions of mass to amount of substance). It is intended that this material will be interlinked with other iron matrix CRMs around the world. In addition, IRMM has established an international interlaboratory study to achieve comparability of analytical measurements for a range of real-world samples. On the basis of these and other activities, CITAC is evolving a pragmatic approach to establishing the links and defining the criteria necessary to achieve chemical traceability. Good progress is being made on all five tasks, and the work should near completion by the end of this year.

The CITAC working group also identified three additional initiatives in its March 1994 workshop: the uncertainty of chemical measurements, the establishment of quality system guidelines for nonroutine and R&D activities, and education and training.

Uncertainty of chemical measurements. Although much valuable work is being undertaken within the European arena to develop criteria for establishing the uncertainty of chemical measurements (*6*), this activity needs to be established on a worldwide level. At present, national standards organizations are having difficulty deciding on a unified, practical method of uncertainty estimation. The traditional approach focuses on methods of combining systematic and random effects on the result. More recently, it has been recognized that uncertainty components measured by repeated experiment and those derived by informed estimation or expert opinion are not strictly compatible; the first has a measure value and may have a measured distribution, whereas the "distribution function" appropriate to the second type is simply an expression of how firmly it is believed that the result will be in a specified range. This incompatibility

results in different views of the problem, to the extent that there are currently two draft documents in general circulation (*7*, *8*). However, the ISO draft (*8*) has been established as the preferred approach, and a draft EURACHEM/CITAC guide is under development.

Quality system guidelines for nonroutine and R&D activities. The present interpretation of quality system standards by the national accreditation authorities tends to be overly prescriptive and generally applicable only to specific types of well-established methods and tests. Generic guidelines need to be developed to cover research and development work. They would be applicable not just to accreditation standards (e.g., ISO Guide 25) but also to other types of quality systems such as total quality management.

Education and training. The majority of secondary schools and universities retain the traditional approach to the structure and syllabus for chemical education, namely the organic, inorganic, and physical branches of chemistry (*9*). More needs to be done at an international level to provide guidance on the importance of teaching analytical chemistry as a branch of chemistry, emphasizing the requirements to achieve valid analytical measurement. This topic is scheduled to be the subject of a workshop presented in conjunction with Pittcon '95 that will generate debate among employers and educators about the adequacy of chemistry graduates.

Future activities

Overall, the activities of the Chicago workshop generated considerable interest among conference delegates. To develop CITAC initiatives within the Far East and Pacific Rim countries, a two-day international CITAC symposium was held in Hong Kong in October in conjunction with the 1994 ILAC plenary meeting. In addition to involving many new people in the debate and discussing progress in CITAC tasks, the symposium considered new areas such as the QA of qualitative analysis, analytical requirements, and how to compare analytical results with limits given in regulations and specifications.

Plans also have been made for another CITAC workshop to be held in New Orleans in conjunction with Pittcon '95. In addition to the session on education and training mentioned above, a second session will review progress on all CITAC tasks and consider suggestions for new work. Additional information about CITAC is available from The CITAC Secretariat, Room B006, Laboratory of the Government Chemist, Queens Road, Teddington, Middlesex TWII 0LY, U.K. (fax 44 81 943 2767).

References

(1) King, B. *Analyst* **1993**, *118*, 587–91.
(2) de Bievre, P.; King, B.; Wegscheider, W. *Report of EURACHEM Workshop*, November 1992, Geel, Belgium; *Anal. Proc.*, in press.
(3) Walker, R. *Anal. Proc.* **1993**, *30*, 67.
(4) Walker, R. *Anal. Proc.* **1993**, *30*, 242.
(5) EURACHEM Guidance Document No. 1/WELAC Guidance Document GD2, Edition 1, April 1993.
(6) Ellison, S. *Anal. Proc.* **1993**, *30*, 499.
(7) Draft British Standard, Measurement Uncertainty, Document ref. 93/70, British Standards Institution (also issued as ISO Committee Document CD 12102.2), London, 1993.
(8) *Guide to the Expression of Uncertainty in Measurement,* 1st ed.; International Standards Organization: Geneva, Switzerland, 1993.
(9) Kellner, R. *Anal. Chem.* **1994**, *66*, 98 A–101 A.

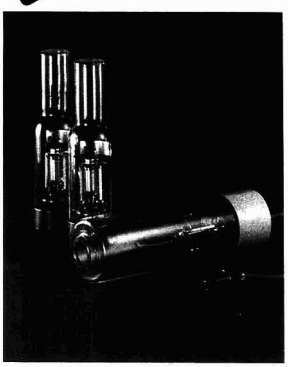




Bernard King (left) is director of analytical quality and government analyst of the Laboratory of the Government Chemist as well as director of the U.K. Valid Analytical Measurement Programme and chairman of the CITAC working group. His primary interests are in improving the validity of chemical measurements in the U.K. and developing an international chemical measurement system.

Ronald Walker is head of the certified reference materials and proficiency testing group at the Laboratory of the Government Chemist. He is also chairman of the U.K. CRM working group and is the U.K. representative on ISO-REMCO. His primary interest is in the development of certified reference materials and proficiency testing as key components in the improvement of analytical measurements.

GOOD NEWS FOR ATOMIC ABSORPTION SPECTROSCOPY



Hamamatsu Hollow Cathode Lamps are now available from major lab suppliers.

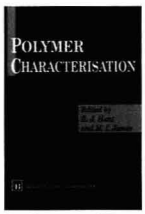
Hamamatsu single and multi-element Hollow Cathode Lamps offer superior stability, spectral purity and output intensity, even for such elements as arsenic and selenium. They are compatible with most commercial spectrophotometers, including Beckman, Zeiss and Perkin-Elmer. And best of all, they're available from your local lab supplier.

For Application Information, Call 1-800-524-0504 Ext. 100

HAMAMATSU

360 FOOTHILL ROAD
P.O. BOX 6910
BRIDGEWATER, NJ 08807
France (1) 49 75 56 80
Germany 08152/375-0
Spain 3 699 65 53
Italy (02) 935 81 733/734/740
Sweden Int + 46-8-7032950
UK 081-367-3560
© Hamamatsu Corporation, 1990

Analyzing Polymers



Polymer Characterisation
B. J. Hunt and M. I. James, Eds.
Blackie Academic and Professional
Division of Chapman & Hall
29 W. 35th St.
New York, NY 10001
1993, 362 pp., $100

This book is a useful compendium of techniques commonly employed in polymer characterization. The contributors (mostly British) present highly readable accounts of both solid and liquid characterization methods. The diversity of the subject matter can cause difficulty in producing such a book. Indeed, each of the techniques covered could be the subject for a separate book. In order for the book to be a reasonable length, the editors must achieve the proper blend of theory, experimental techniques, and applications that may be of interest to the readership. Although each chapter contains some discussions of theory and instrumentation, most of the contributors have chosen to emphasize the practical aspects of the techniques. Furthermore, some contributors have taken a pedagogical approach, whereas others have embarked upon a comprehensive review. As a result, the chapters are uneven in their approaches.

After an introductory chapter by the editors, Chapter 2 gives an excellent description of polymer separation procedures together with analyses of polymer additives that provide some practical schemes. These procedures, commonly used in industrial laboratories, are not usually given sufficient coverage.

Chapter 3 gives an overview of the use of both solid-state and liquid NMR spectroscopy in polymer studies. Chapter 4 provides a review of IR and Raman spectroscopy; a wide range of problems are included, with a comprehensive list of references.

In Chapter 5, methods for molecular weight determination, including end group assay, vapor-pressure osmometry, membrane osmometry, ebulliometry/cryoscopy, light scattering, viscometry, and ultracentrifugation are discussed. A useful addition is a list of commercial manufacturers of instrumentation for molecular weight determination.

Chapter 6 covers a wide variety of chromatographic techniques, including size exclusion chromatography, field-flow fractionation, hydrodynamic chromatography, TLC, GC, HPLC, and SFC. Because of the large number of topics covered, the treatments tend to be brief; interested readers will need to look in the references for additional details.

This book is a useful compendium of techniques commonly employed in polymer characterization.

Thermal analysis techniques, which are widely used in polymer characterization, are discussed in Chapter 7. Although a large number of thermal techniques are included, the literature covered is selective. Chapter 8 provides an excellent treatment of small-angle neutron scattering and reflectometry, including theory, experimentation, and examples. Chapter 9 gives a brief description of polymer rheology and mechanical testing. The approach is pedagogical; no attempt has been made to review the literature. Perhaps more examples of actual problems solved would illustrate the utility of the techniques.

Chapter 10 gives an elegant and well-referenced description of microscopic techniques (optical microscopy, scanning electron microscopy, and transmission electron microscopy) used in polymer studies. Staining, etching, and electron diffraction are included. Surprisingly, energy-dispersive X-ray (EDX) analysis is omitted. The book concludes with a good description of XPS (ESCA) and SIMS. Perhaps regrettable is the omission of wide-angle X-ray diffraction, which is commonly used to determine phase structures, or (more routinely) to obtain percent crystallinity in polymers.

This book is probably most useful for those looking for a review of a given topic. It has a subject index but no author index.

Reviewed by H. N. Cheng, Hercules, Wilmington, DE

BOOKS RECEIVED

Introduction to Open-Tubular Gas Chromatography
John V. Hinshaw and Leslie S. Ettre
Advanstar Communications
7500 Old Oak Blvd.
Cleveland, OH 44130
1994, 189 pp., $24.95 soft cover

This volume, dedicated to the memory of Marcel Golay, the inventor of open-tubular columns for GC, is intended for students and day-to-day users of open-tubular GC and includes topics that are essential for a practical working knowledge of the subject. Chapter topics include the evolution of open-tubular columns, the carrier gas, separation theory, band broadening and resolution, the stationary phase, variables of open-tubular GC systems, inlets, and detectors. A section on the literature of open-tubular columns provides a list of general references on open-tubular chromatography, including journals, textbooks, and proceedings of symposia, as well as a list of publishers. Symbols, acronyms, and abbreviations, as well as a subject index, are also included.

Mathematical Analysis by Spectral Orthogonality

John H. Kalivas and Patrick M. Lang
Marcel Dekker
270 Madison Ave.
New York, NY 10016
1993, 324 pp., $145

This book, volume 17 of the Practical Spectroscopy Series, contains chapters on basics of spectral orthogonality, assessment methodologies, approximation methodologies, and K-matrix and P-matrix analysis applications. Three appendices cover linear algebra (vector spaces and matrices), multivariate statistics, and additional applications. A subject index is included.

Advances in Chromatography, Vol. 34

Phyllis R. Brown and Eli Grushka, Eds.
Marcel Dekker
270 Madison Ave.
New York, NY 10016
1994, 456 pp., $165

This volume contains seven contributed chapters on high-performance CE of human serum and plasma proteins, analysis of natural products by GC/matrix-isolation IR, statistical analysis of peak overlap in chromatography, CE of carbohydrates, environmental applications of SFC, HPLC of homologous series of simple organic anions and cations, and uncertainty structure, information theory, and optimization of quantitative analysis in separation science. A subject index is included.

Fundamentals of Electrochemistry

V. S. Bagotzky
Plenum Press
233 Spring St.
New York, NY 10013
1993, 589 pp., $115

This book, translated from Russian by Klaus Miller, provides a rigorous outline of the basic concepts of modern theoretical and applied electrochemistry. It contains 23 chapters in 4 sections: basic concepts, properties of electrolytes and interfaces, electrochemical kinetics, and principles of applied electrochemistry. A list of relevant periodicals and books, an author index, and a subject index are included.

Data Analysis for the Chemical Sciences: A Guide to Statistical Techniques

Richard C. Graham
VCH
220 E. 23rd St.
New York, NY 10010
1993, 536 pp., $65

This textbook provides an introduction to univariate, bivariate, and multivariate statistical techniques. Ways to calculate the true value, dispersion, and frequency distribution of data points, calibration of instruments, and cluster analysis are described, and the life cycle of a set of data from initial design of the data acquisition program to production of the final report of similarities/differences between data sets is presented. Each of the 19 chapters contains solved problems; also included are extensive statistical tables and lists of statistical software for PCs.

Introduction to Modern Vibrational Spectroscopy

Max Diem
John Wiley & Sons
605 Third Ave.
New York, NY 10016
1994, 285 pp., $65

This textbook contains nine chapters: an introduction, results from quantum mechanics, polyatomic molecules, symmetry of molecular vibrations, introduction to Raman spectroscopy, instrumentation, vibrational spectra of selected small molecules, biophysical applications, and vibrational optical activity. Three appendices cover vibrational frequencies for some common groups, a refined set of Urey–Bradley force constants, and character tables for chemically important symmetry groups. A subject index is included.

Fundamentals of Electrochemical Science

Keith B. Oldham and Jan C. Myland
Academic Press
1250 Sixth Ave.
San Diego, CA 92101
1994, 474 pp., $45

This monograph was developed from the lecture notes of a one-semester course in electrochemistry taught at Trent University. Eleven chapters cover the conduction of electricity, ionic solutions, electrochemical cells, electrodes, electrode reactions, polarization, transport, steady-state voltammetry, the electrode interface, electrochemistry with periodic signals, and transient voltammetry. A subject index is included.

Charge-Transfer Devices in Spectroscopy

Jonathan V. Sweedler, Kenneth L. Ratzlaff, and M. Bonner Denton, Eds.
VCH
220 E. 23rd St.
New York, NY 10010
1994, 406 pp., $95

This volume describes the operation, uses, and characteristics of charge-transfer devices (CTDs), including system design and expected performance, in a variety of applications. Contributed chapters cover the history and principles of CTDs, specialized readout modes and spectrometers, arrays for detection beyond 1 μm intensified array detectors, CTD detectors for planar separations and electrophoresis, CCD array detectors for multichannel Raman spectroscopy, CTD detection in luminescence spectroscopy, 2D array detection for plasma diagnostics, and CTD detection in atomic emission spectroscopy. Each chapter contains an extensive list of references, most of which are current to the early 1990s. The book is illustrated with numerous figures and photographs, many of which are reproduced from the original research publications. A list of abbreviations and a subject index are included.

STAY AHEAD OF THE CURVE.

***Must Reading** for Fast Track Professionals*

Who reads Industrial & Engineering Chemistry Research?

Leading chemical engineers and industrial chemists worldwide.

Each month Industrial & Engineering Chemistry Research delivers up-to-the minute original studies and reports in the areas of kinetics and catalysis, materials and interfaces, process engineering and design and separation.

Peer-reviewed, quality information on:

- *Fundamental Research* — thermodynamics, transport phenomena, chemical reaction kinetics and engineering, catalysis, separations, and materials.
- *Process design and development* — new techniques in chemical equipment design, system analysis, process control, and scale-up procedures.
- *New Products* — involving chemical engineering processes for plastics, elastomers, fibers, fabrics, adhesives, coatings, paper, membranes, catalysts, lubricants, fertilizers, ceramics, aerosols, and liquid crystals.
- *Research Notes* — short reports on new ideas or data concerning fundamental concepts, products, and processes that are in the early stages of development.
- *Correspondence* — comments on, corrections to, reinterpretations, and rebuttals of previously published articles.
- *Reviews* — critical evaluations of the state of the art in timely areas of interest to readers.
- *Correlations* — concise papers based solely on correlations of existing data using an empirical or semiempirical mathematical framework.

Look to I & EC Research for vital information you need to stay *ahead of the curve*, and push into new frontiers.

Timely. Practical. Reliable. Comprehensive.

"Aggressive...innovative... indispensible" are how leading industrial and chemical engineers around the globe describe I & EC Research.



Don't miss a single issue. Call now!

Published by the American Chemical Society under the editorial leadership of Donald R. Paul, University of Texas, Austin.

Call Toll-Free 1-800-333-9511 in the U.S.

Outside the U.S.: 614-447-3776. Fax: 614-447-3671.
Or Write:
American Chemical Society • Member and Subscriber Services • P.O. Box 3337 • Columbus, OH 43210

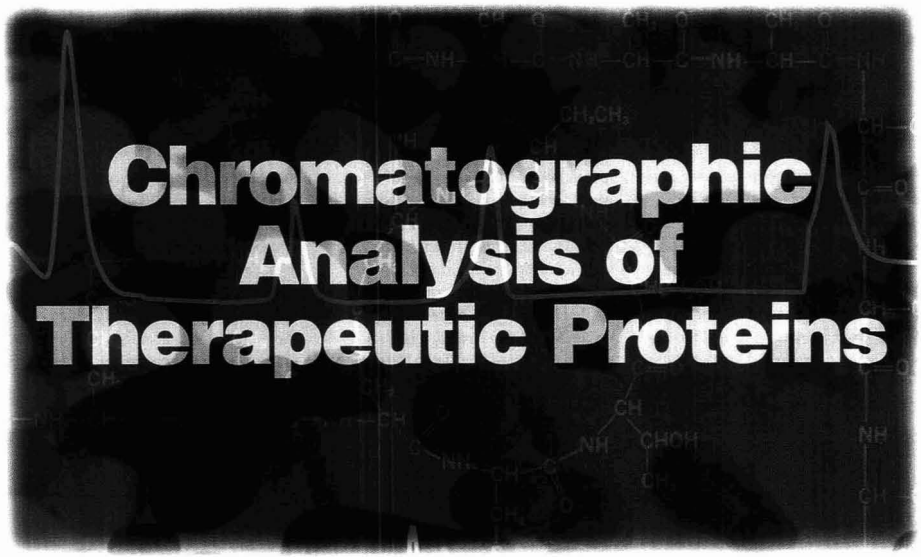
Printed	U.S.	Canada & Mexico	Europe*	All Other Countries*
ACS Members				
One Year	$ 65	$ 84	$112	$124
Two Years	$117	$155	$211	$235
Nonmembers	$613	$632	$660	$672

*Air Service Included

American Chemical Society
1155 Sixteenth Street, N.W.
Washington, D.C. 20036

ACS PUBLICATIONS
Essential Resources for the Chemical Sciences

Member subscription rates are for personal use only. Subscriptions are based on a calendar year. Foreign payment must be made in U.S. currency by international money order, UNESCO coupons, or U.S. bank draft, or order through your subscription agency. For nonmember rates in Japan, contact Maruzen Co., Ltd. This publication is available on microfilm and microfiche. The full text is available online on STN International.



Chromatographic Analysis of Therapeutic Proteins

As the cost of bringing new protein-based drugs to market soars, analysts turn to chromatographic methods to speed up the process

Development of new pharmaceuticals is increasingly expensive. Not only are the costs of R&D, laboratory testing, clinical trials, administration, and overhead escalating, but the maturing of the pharmaceutical industry itself is adding to the burden. Ten years ago, the rule of thumb was that development of a new drug cost about $200 million. Today that figure has doubled. A drug patent gives its owner exclusive rights to the invention for 17 years. Because it often takes as many as 12 years to bring a drug to market, it is crucial that product development proceed as efficiently as possible. Today the general rule for evaluating return on investment for pharmaceutical products is that for each day's delay in bringing the product to market, $1 million in sales is lost.

Analysis and purification are essential parts of drug R&D, manufacturing, and quality assurance. Using rapid analytical methods can significantly cut development time and boost profit. For example, rapid analysis makes it possible to evaluate pharmaceuticals before they degrade or lose activity. Fast analytical methods can provide better data by allowing replicate analyses to be performed in the time formerly required for a single run. Carrying out large screenings to evaluate candidate formulations or to develop sufficient data from which promising R&D leads can emerge might not be feasible without rapid analysis. The consequence of a test taking 2 min instead of 20 min may determine whether promising directions of research are uncovered and pursued or remain hidden.

Bruce Jon Compton
AutoImmune, Inc.
Lotte Kreilgaard
Royal Danish School of Pharmacy and Zymo Genetics, Inc.

Rapid LC applications

HPLC has become a principal tool for the rapid separation and characterization of many classes of pharmaceuticals, including those based on peptides and proteins. Most HPLC methods for biomolecules use an aqueous-based mobile phase; the stationary phase can vary, depending on the chromatographic mode. Aqueous solvents are used because, in general, nonaqueous solvents denature proteins by interfering with their uniquely folded structure.

With the emergence of new protein- and peptide-based drugs, it has become necessary to develop rapid LC methods that can separate and characterize these substances or be used for preparative purposes without disrupting the unique three-dimensional structure upon which pharmacological activity depends. In general, these methods include, but are not limited to, size exclusion chromatography (SEC), ion-exchange chromatography (IEC), hydrophobic interaction chromatography (HIC), reversed-phase LC (RPLC), and affinity chromatography (AC).

Each method has its strengths and weaknesses; the appropriate one is selected on the basis of the structure of the

0003-2700/94/0366-1175A/$04.50/0
© 1994 American Chemical Society

analyte and the application. In addition, the ability to scale chromatography in both time and capacity means that techniques used for analytical objectives can also play a role in process development.

SEC

SEC, also known as molecular sieve or gel filtration chromatography, was originally developed to measure polymer molecular weights. (SEC actually measures a molecule's hydrodynamic volume, which correlates with and can be used as a surrogate for molecular weight.) In SEC, the column packing is a porous material, and the dissolved analytes are carried into the stationary phase by the mobile phase. Analyte molecules too large to enter the pores are excluded and exit the column first. Pore residence time is inversely proportional to the log of solute molecular size, which results in solutes being sorted and eluted according to diminishing molecular size. By running a set of standards covering a desired molecular weight range, a linear calibration curve can be prepared that plots elution volume against the log of the molecular weight for globular proteins. This curve can then be used to determine analyte molecular weight from the corresponding elution volumes.

Initially, SEC was used to purify both synthetic polymers dissolved in nonaqueous media and DNA and proteins in aqueous media (*1*). Later, SEC was used on a small scale to characterize protein molecular weight (*2*). With the advent and widespread acceptance of sodium dodecylsulfate-polyacrylamide gel electrophoresis (SDS-PAGE) for protein molecular weight determination (*3*), SEC fell into disuse. Although SDS-PAGE is simpler to use and less expensive than other chromatographic methods, the sample treatment conditions under which SDS-PAGE analyses are carried out tend to denature the sample, making it unsuitable for the characterization of proteins in the native state (*4*). Thus attention once again turned to SEC because of its ability to characterize products using a wide range of flow rates, pHs, and solvent ionic strengths without altering the structural attributes of the sample.

A major application of SEC is the monitoring of product quality and stability. The stability of proteins and peptides depends on the formulation within which they are incorporated. Instability in a formulation often leads to molecular aggregation and precipitation, which are unacceptable because the pharmacological and other properties that determine a drug's safety and effectiveness (*5*) are altered, leading to loss of activity and possible health consequences. The extent of a protein's aggregation is a measure of its antigenicity (*6*), as demonstrated by cases in which diabetics reacted strongly to administration of insulin in aggregate form (*4*).

Precipitation of a protein within an unstable formulation can take place for a substantial amount of time before the change becomes obvious. However, incipient changes that lead to aggregation, such as dimerization, are often indicated by increases in molecular weight, which can be detected by SEC (*7*).

Normally, when a protein- or peptide-based drug is developed, an SEC analysis is included in the specification. Although aggregation can be measured by other methods, SEC is preferred because it not only detects the tendency to aggregate and provides molecular weight information on aggregate intermediates, but it can also be used to isolate such intermediates for further study. The resulting information can be used to better understand the mechanism of aggregation and speed the development of stable formulations. Figure 1 shows a comparison of size exclusion chromatograms for a normal and an aggregated sample of rhFXIII, a blood coagulation factor.

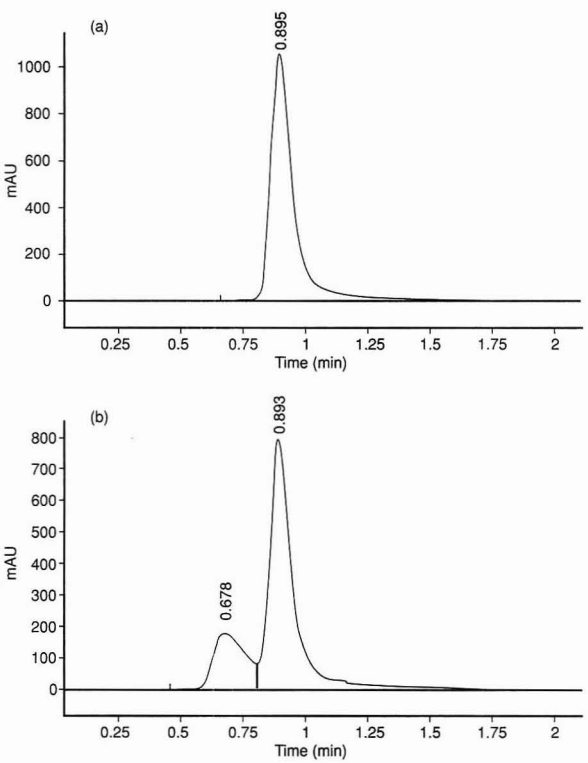


Figure 1. Comparison of size exclusion chromatograms of an (a) normal and (b) aggregated sample of rhFXIII.

The extra peak in (b) indicates the presence of aggregates in a thermally stressed sample.

The activity and stability of a pharmaceutical is typically evaluated over an extended period under a variety of conditions in hundreds of matrices, geometrically increasing the number of analyses required to properly evaluate the product. Screening times can be reduced by improving the various aspects of the chromatographic process.

Chromatographic resolution between two bands is related to the selectivity (determined by solute molecular weight and pore size and the homogeneity of the column packing), the number of theoretical plates (determined by factors such as particle and pore size and uniformity, column length, and packing efficiency) and the peak capacity (the number of column volumes within which two chromatographic bands are retained on the column).

In SEC, the peak capacity will always be < 1 and all solutes will elute within the total solvent volume in the column. This lack of capacity means that SEC has very low resolving power. A rapid SEC column will resolve a mixture into a maximum of seven peaks with approximately a twofold difference in molecular weight between the peaks. A consequence of the small elution volume differentials between analytes is that accurate measurement of elution volume is essential. For the same reason, increases in system dead volume can cause unacceptable peak broadening and overlap (*8*).

Factors that improve column efficiency by promoting equilibrium distribution of solute within the stationary phase or decreasing signal variance help sharpen peaks and improve separation. Column efficiency (expressed as the number of theoretical plates per unit length of column or height equivalent to theoretical plates, or HETP [*9*]) can be enhanced by using smaller and more uniform-sized packing particles (limited by the increase of back pressure as particle size is reduced by a power of 2), ensuring packing continuity over the length of the column, lengthening the column, and optimizing the flow rate of the eluent (*10–12*).

Many factors that affect column efficiency also affect signal variance, defined for a Gaussian peak as the standard deviation of the distribution squared. The total system variance is defined as the sum of the variance contributions of all system components (*13*), namely the variances from the dead volume, detector, injector, data system, and column variance (which is the sum of the variance contributions from the inhomogeneity of the column bed and particle and pore size).

As the variance in the system increases, chromatographic bands broaden, peak height is reduced, and sensitivity is lost. Peak broadening can eventually affect resolution as bands begin to overlap. The impact of dead volume is especially severe in SEC because all peaks elute within a single column volume of solvent. Speeding up chromatographic throughput can be accomplished by increasing column flow rate and reducing column length—changes that also reduce column efficiency.

In practice, these losses are compensated for by using packings with smaller and more uniform particle size, improved pore accessibility to solute, and greater mechanical stability, as well as by ensuring stationary phase continuity and homogeneity during column packing and subsequent use (*14–16*). The result is a microscale rapid SEC method with typical analysis times 1 order of magnitude faster than those of conventional SEC (Table 1). In addition, the reduction in system size means that microscale rapid SEC is considerably more economical to run and maintain than is conventional SEC.

The earliest SEC packings for use with proteins were soft gels prepared from cross-linked dextrans and agaroses (*17*). Because these materials are compressible, they cannot be used at HPLC pumping pressures. However, they do have a lower level of ion-exchange activity and therefore approach more closely an ideal noninteracting SEC stationary phase. With the growth of HPLC came the development of more mechanically robust silica-based packings (*14–16*). These packings can be manufactured with a smaller and more uniform particle size, enabling the development of shorter columns with higher efficiencies (*12*).

Notwithstanding the improvement in packing materials, problems in column preparation can adversely affect resolution and sensitivity. Commercial packers often prepare columns under high pressures, typically up to 12,000 psi, that can shatter the stationary phase or cause bed channels to form that allow solute to bypass the pores, a problem that defeats the chromatographic objective.

Table 1. Comparison of rapid and conventional SEC

Parameter	Rapid	Conventional
Packing size (μm)	5–	5
Column dimensions (mm)	4.6 × 150	7.8 × 300
Flow (mL/min)	1.0	1.0
Run time (min)	2.0	20
Injection volume (μL)	2.0	25
Sample runs per 6-h day	180	18
Buffer volume per sample (mL)	2.0	20

To avoid these pitfalls, we pack our own columns and compensate for any void formations before running the analysis. We use low-viscosity acetone to pack the column, then consolidate the bed using the mobile phase specified for the application, a preparatory option not available to vendors. Packing the column is also performed at a pressure only slightly greater than the anticipated operating pressure of the column, which facilitates the formation of a homogeneous and continuous phase over the entire length of the column.

Ideally, the SEC mechanism is controlled by solute diffusion between the mobile and stationary phases and by stereoregulated transfer into and out of particle pores. However, in the case of proteins and peptides, residual charges on the packing surface can interact with charges on the solute, enhancing retention and causing deviation from the expected linear relationship between the log of the molecular weight and elution volume. These effects can usually be moderated or eliminated by controlling solvent pH and ionic strength (*18–21*). At appropriate ionic strength, solvated ions screen the interaction between charged proteins and charges on the surface of the stationary phase. However, if the solvent's ionic strength is too high it can drive the protein out of the mobile phase and into the stationary phase in a fashion analogous to "salting out," where it may become hydrophobically bound (*21*).

In some SEC separations of proteins, a surfactant such as SDS or deoxycholic acid is added. These substances form a micelle-like sheath around the protein, screening out charge interactions with the stationary phase. Under certain conditions, surfactants can also coat the stationary phase and prevent aggregation-induced binding (*22*). However, using surfactants in SEC can be problematic. Once in the system, surfactants can complicate the chromatography by introducing an additional ion-exchange mechanism. For example, the hydrocarbon chains of SDS can interact hydrophobically with the stationary phase and cause the sulfonate end of the molecules to be positioned at the packing–solution interface, turning the stationary phase surface into a strong cation exchanger (*23*). Alternatively, once the surfactant forms a sheath around the protein, the hydrocarbon exterior of that sheath may interact hydrophobically with the stationary phase (*24*).

In our work, solvent pH and ionic strength are initially adjusted to be compatible with both the mode of chromatography and the protein of interest by the use of a universal buffer (*25*). This buffer can maintain constant ionic strength over a pH range of 2–11, making it possible to evaluate pH effects independent of solvent ionic strength.

Such studies show that pH can have a dramatic effect on the SEC behavior of proteins. In general, this behavior is determined by the solvent pH and the protein's isoelectric point (pI). At pHs below the pI, SEC interactions are often complicated by non-size exclusion mechanisms; at pHs equal to or above the pI, size exclusion effects predominate (*20, 21*). The likely explanation for the difference is the presence of silanol groups on the surface of silica-based packing particles. These groups ionize above pH 4, producing a negatively charged surface that can interact with proteins that are positively charged at pHs below their pI (*20, 21*).

When both the calibration and the analytical run are performed, deviations from linearity may be attributed to non-size exclusion effects that can be regulated by appropriate adjustment of pH and ionic strength (*18–21*). Given the large range of protein pIs, there will always be some proteins in a set of standards that do not fall on the calibration curve, and these data may be discarded. In our work with recombinant proteins, the molecular weight of the analyte is known in advance and its position on the calibration curve can be anticipated.

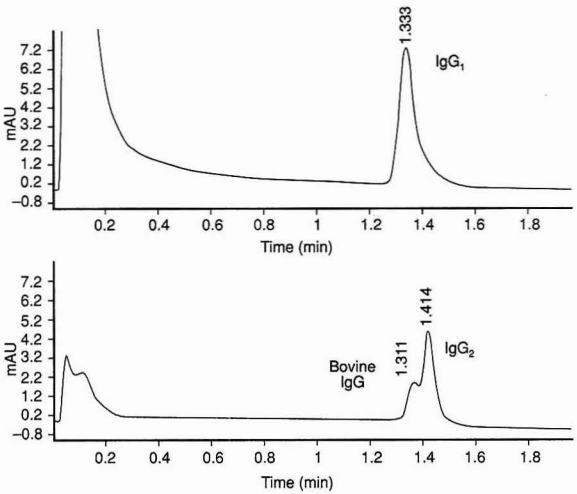


Figure 2. Separation and purification of two monoclonal antibody immunoglobulin class G samples using AC on protein A.

(a) IgG_1; (b) IgG_2. Although both compounds are in the same class, IgG_1 elutes prior to IgG_2 because it has a lower pI. The peak at 1.311 is a residue of the polyclonal bovine IgG from the fetal calf serum used to cultivate IgG-producing hybridomas. That peak also elutes prior to the IgG_2 because of its lower pI.

IEC

In SEC, the objective is to minimize charge interaction between the analyte and the column packing. In contrast, the IEC of proteins seeks to exploit this interaction. IEC is based on the exchange of charged analytes and counterions electrically bound to the charged functional groups in the stationary phase. After ion exchange takes place, the analytes remain bound to the charged column groups until displaced by an excess of counterion in the eluting solvent (*26*).

As with many other chromatographies, IEC was originally developed for nonbiologicals (*27*). The first IEC column packings for proteins were based on derivatized dextrans and agaroses (*28*). These were eventually replaced by aminated and sulfonated polystyrenes and by high-performance stationary phases based on silica that were capable of supporting the higher pumping pressure required for high-speed chromatography (*23, 24*). The most recent trend in IEC packings has been the development of a new class of pellicular resins (*29*).

Early pellicular packings were based on functionally derivatized glass beads ranging in size from 20 to 50 μm (*30*). The newer packings are surface-derivatized microparticulates ranging in size from 3 to 7 μm. The base packing material has also shifted from silica to polystyrene, which is easier to derivatize and can achieve higher ion-exchange capacities. Other developments in IE packings include particulate packings with flow-through pores and macroreticular resins based on acrylic polymers (*31*). The reduction in column size, increase in flow rates, and improvement in packing performance have enabled the reduction of typical IEC run times to between 1 and 5 min (*32*).

An important variation of protein IEC called chromatofocusing (CF) involves loading the protein on the stationary phase

in a selected pH buffer and then eluting with a pH gradient (*33*). Another version of this technique uses both a linear pH gradient and a salt to elute the analyte (*34*). The gradient solution is prepared by combining the requisite fractions of high- and low-pH eluents of an appropriate buffer. The sample is then loaded on the column at a specific pH, and the gradient is applied. When the gradient pH reaches the range of the bound protein's pI, the analyte elutes from the column (*34*). CF can achieve rapid resolution of protein isoforms and is useful in the study of protein stability, particularly if destabilization is associated with any change in the molecule's electric charge.

IEC has been applied to the separation of a variety of protein mixtures. For analytical separations, it can resolve proteins exhibiting microheterogeneity into their various isoelectrotypes. Because of its high capacity, IEC is often used as the "capture" step, the first step in a scheme that combines purification and concentration steps.

HIC and RPLC

HIC and RPLC are related techniques that have only recently been applied to proteins and peptides. Unlike SEC and IEC, RPLC can denature proteins and is therefore better suited to analytical rather than preparative applications. By contrast, HIC packings, though similar to those used in RPLC, are less hydrophobic and therefore operate under less denaturing conditions. Typically, HIC packings are made of derivatized silicas that have their surface silanol groups capped by short hydrocarbon or diol derivatives. The more hydrophobic the capping group, the greater the hydrophobicity of the packing surface (*35*). When the packing surface becomes sufficiently hydrophobic, it becomes better suited for RPLC.

Another important distinction between HIC and RPLC is the type of eluting solvents used. A typical HIC gradient begins with a very high ionic strength solvent such as 2 M aqueous salt and terminates with water. The combination of polar solvent gradients and mildly hydrophobic stationary phases makes HIC suitable for the separation of fairly large proteins (*28, 36*). An RPLC gradient typically starts where the HIC gradient leaves off, with an aqueous buffer, and terminates with a water-miscible organic solvent such as acetonitrile. (It is the organic solvents used in RPLC that tend to denature the proteins.)

HIC and RPLC are routinely applied to many peptide and protein separation problems. The RP mode is normally used for "impurity profiling" of an otherwise homogeneous protein. Once hydrolyzed to defined peptides, the protein can be characterized through its peptide map. The HIC mode is often applied to preparative separations of large proteins that normally denature using the RP mode.

AC

AC binding is based on the complementary relationship among structure, charge, and hydrophobicity between a protein and the stationary phase. AC packings are often designed to mirror the natural ligand to which the protein binds (*37*). Resolution in AC is much more dependent on selectivity than on column efficiency. Ideally, only the analyte of interest is retained and then eluted from the column in a sharp band using a step gradient.

Although not a common chromatographic tool, AC has some important specialized analytical and preparatory applications. For example, in the separation and quantitation of monoclonal antibodies, AC packings incorporate proteins that bind to the constant region of the antibody (*38*). AC can also be used to separate certain classes of enzymes such as proteases (*39, 40*) and, in conjunction with a pH gradient, to separate antibody isotypes. The latter technique represents a synergy of AC and CF methods in which the AC packing removes the antibody isoforms from the mobile phase and the pH gradient resolves them according to their pI as in Figure 2. AC/CF can be a useful tool for mass sample screening (*38*).

Multiple chromatographies

Combining chromatographies can be important for studying a protein or protein formulation. Purification regimes often incorporate orthogonal techniques that use different retention mechanisms to achieve a result unobtainable by one method alone. For example, in protein purification different chromatographic methods may be effective in removing different groups of impurities whereas others will concentrate the analyte. The orthogonal approach maximizes the quality of results and avoids the diminishing returns inherent in separations based on a

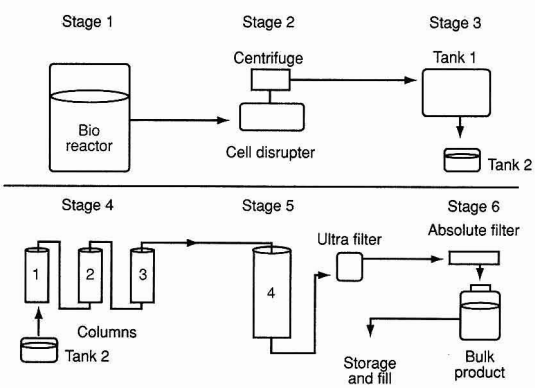


Figure 3. Production-scale purification of a recombinant protein.

After cultivation, recovery by centrifugation, and cell disruption, the product stream is concentrated and stored (stage 3, tank 2). The purification scheme involves HIC (column 1), IEC (column 2), and AC (column 3). This sequence takes advantage of the ionic strength of the process stream as it changes from high to low with each step. Polishing and buffer exchange is done using SEC (column 4) and, after sterile filtration, the bulk product is obtained.

single chromatographic mechanism. Figure 3 shows a generic protein pharmaceutical production stream using multiple compatible chromatographies.

In addition to the types of chromatographies used, the sequence of methods is also important. For example, in a purification scheme, SEC is most useful for buffer exchange and as a final polishing step for the removal of aggregates and particles. Unlike other chromatographic methods, SEC cannot be used to concentrate a sample or a process stream because there is no stationary phase binding. Therefore, SEC is used only after chromatographies that can concentrate the analyte, as demonstrated in Figure 3. Because chromatography is linearly scalable, processes can be rapidly optimized at the laboratory bench by using many of the methods described here in a preparative capacity. Refining process parameters before scale-up can eliminate much of the lost time and expense associated with process optimization during initial stages of pilot- and full-scale plant trials.

Future directions

A significant need in rapid microscale protein chromatography is the development of longer lasting stationary phases. The vast majority of columns are still based on silica and, with few exceptions, little has been accomplished in extending the useful life of these packings. In SEC, interesting developments include new packing materials based on zirconium oxide. Although inert to degradative conditions, zirconium oxide is a strong Lewis acid and therefore may react with certain functional groups on the protein.

Alumina is being considered as a replacement for silica for column packings, but it is uncertain whether this material will exhibit the undesirable properties typical of silica, such as metal binding and catalysis of protein oxidation (*41*). The development of macro particulate packings with through pores is of interest because, theoretically, this type of particle provides rapid mass transfer, thus increasing column efficiency (*31*). When appropriately derivatized, these particles may serve as the basis for a new generation of columns with even higher capacity and efficiency than are currently achievable.

Work also continues in the commercial sector to develop instruments better suited to rapid microscale chromatography. An important objective is to increase sample throughput without sacrificing sensitivity. At present, there are no instruments capable of injecting 1 µL reproducibly. In addition to improving sample injection, more work needs to be done on designing column configurations and detectors with lower dead volume.

References

(1) Determann, H. *Gel Chromatography*; Gross, E., trans.; Springer-Verlag OHG: Berlin, 1968; p. 968.
(2) Andrews, P. *Lab. Pract.* **1967**, *16*, 851.
(3) Weber, K.; Osborn, M. *J. Biol. Chem.* **1969**, *244*, 4406.
(4) Watson, E.; Kenny, W. C. *J. Chromatogr.* **1988**, *436*, 289.
(5) Working, P. K. In *Pharmaceutical Biotechnology*; Ferraiolo, B. L.; Mahler, M. A.; Gloff, C. A., Eds.; Plenum: New York, 1993; Vol. 1, p. 73.
(6) Brange, J.; Langjaer, L. In *Pharmaceutical Biotechnology*; Wang, Y. J.; Pearlman, R., Eds.; Plenum: New York, 1993; Vol. 5, p. 315.
(7) Scott, R.P.W.; Kucera, P. *J. Chromatogr.* **1979**, *169*, 51.
(8) Giddings, J. C. *Unified Separation Science*; John Wiley & Sons: New York, 1991; p. 96.
(9) Halaz, I.; Gorlitz, G. *Angew. Chem. Int. Ed. Engl.* **1982**, *21*, 50.
(10) Dawkins, J. V. *Pure Appl. Chem.* **1982**, *54*(2), 281.
(11) Cortes, H. J.; Pfeiffer, C. D. *Anal. Chem.* **1993**, *65*, 1476.
(12) Snyder, L. R.; Kirkland, J. J. *Introduction to Modern Liquid Chromatography*, 2nd ed.; John Wiley & Sons: New York, 1979; p. 33.
(13) Hashimoto, T.; Sasaki, H.; Aiura, M.; Kato, Y. *J. Chromatogr.* **1978**, *160*, 301.
(14) Krishen, A. *J. Chromatogr. Sci.* **1977**, *15*, 434.
(15) Chiantore, O.; Guaita, M. *J. Liquid Chromatogr.* **1982**, *5*(4), 643.
(16) Dubin, P. L. *Sep. Purif. Methods* **1981**, *10*(2), 287.
(17) Schluter, H.; Zidek, W. *J. Chromatogr.* **1993**, *639*, 17.
(18) Dubin, P. L.; Principi, J. M. *J. Chromatogr.* **1989**, *479*, 159.
(19) Kopaciewicz, W.; Regnier, F. E. *Anal. Biochem.* **1982**, *126*, 8.
(20) Herold, M. *Am. Lab.*, March 1993, p. 35.
(21) Strid, L. *FEBS Lett.* **1973**, *33*(2), 192.
(22) Davies, M. T. *Analyst* **1959**, *84*, 248.
(23) Kopaciewicz, W.; Rounds, M. A.; Fausnaugh, J.; Regnier, F. E. *J. Chromatogr.* **1983**, *266*, 3.
(24) Duncan, J. K.; Chen, A.J.C.; Siebert, C. J. *J. Chromatogr.* **1987**, *397*, 3.
(25) Snyder, L. R.; Kirkland, J. J. *Introduction to Modern Liquid Chromatography*, 2nd ed.; John Wiley & Sons: New York, 1979; p. 501.
(26) *Extraction Chromatography*; Braun, T.; Ghersini, C., Eds.; Elsevier: New York, 1975.
(27) Regnier, F. E. In *Methods in Enzymology*; Jakoby, W. B., Ed.; Academic: New York, 1984; Vol. 104, Part C; p. 170.
(28) Wilchek, M.; Miron, T.; Kohn, J. In *Methods in Enzymology*; Jakoby, W. B., Ed.; Academic: New York, 1984; Vol. 104, Part C; p. 3.
(29) Karger, B. L.; Snyder, L. R.; Horvath, C. *An Introduction to Separation Science*; John Wiley & Sons: New York, 1973; p. 369.
(30) Richey, J. S. In *Methods in Enzymology*; Jakoby, W. B., Ed.; Academic: New York, 1984; Vol. 104, Part C; p. 223.
(31) Liapis, A. I.; McCoy, M. A. *J. Chromatogr.* **1992**, *599*, 87.
(32) Kjellin, K. G.; Hallander, L. B. *Pathology* **1982**, *10*, 942.
(33) Kaltenbrunner, O.; Tauer, C.; Brunner, J.; Jungbauer, A. *J. Chromatogr.* **1993**, *639*, 41.
(34) Goheen, S. C.; Engelhorn, S. C. *J. Chromatogr.* **1984**, *317*, 55.
(35) Kunitani, M.; Johnson, D.; Snyder, L. R. *J. Chromatogr.* **1986**, *371*, 313.
(36) Geng, X.; Regnier, F. E. *J. Chromatogr.* **1984**, *296*, 15.
(37) Compton, B. J.; Lewis, M.; Whigham, F.; Gerald, J. S.; Countryman, G. E. *Anal. Chem.* **1989**, *61*, 1314.
(38) Small, D.A.P.; Atkinson, T.; Lowe, C. R. *J. Chromatogr.* **1981**, *216*, 175.
(39) Kasche, V.; Buchholz, K.; Galunsky, B. *J. Chromatogr.* **1981**, *216*, 169.
(40) Blackwell, J. A.; Carr, P. W. *J. Chromatogr.* **1992**, *596*, 27.
(41) Creedy, J. *Lab. Pract.* **1992**, *41*(6), 17.





Bruce Jon Compton received his B.A. degree in chemistry and biochemistry from the University of Hawaii in 1975 and a Ph.D. in analytical and clinical chemistry from McGill University in 1980. He recently joined Autoimmune (128 Spring St., Lexington, MA 02173) and is currently head of analytical development and quality control.

Lotte Kreilgaard received her M.S. degree in pharmacy from the Royal Danish School of Pharmacy in 1992. She is currently pursuing her Ph.D. at the same institution where her research is focused on the formulation and stability of therapeutic proteins. She is concurrently on the staff at Zymo Genetics (4225 Roosevelt Way N.E., Seattle, WA 98105).

Conferences



9th International Forum on Process Analytical Chemistry and 3rd International Conference: On-Site Analysis
Jan. 22–25, 1995. Houston, TX
Contact: InfoScience Services, Inc., Conference Division, 3000 Dundee Rd., Suite 313, Northbrook, IL 60062 (708-291-9161; fax 708-291-0097)

4th International Conference on Automation, Robotics, and Artificial Intelligence Applied to Analytical Chemistry and Laboratory Medicine
Feb. 7–10, 1995. Montreux, Switzerland
Contact: SCITEC, Av. de Provence 20, CH-1000 Lausanne 20, Switzerland (41-21-624-15-33; fax 41-21-624-15-49)

Pittcon '95
March 5–10, 1995. New Orleans, LA
Contact: Pittsburgh Conference, 300 Penn Center Blvd., Suite 332, Pittsburgh, PA 15235-5503 (412-825-3220; fax 412-825-3224)

86th AOCS Annual Meeting and Expo
May 7–11, 1995. San Antonio, TX
Contact: AOCS Education/Meetings Department, P.O. Box 3489, Champaign, IL 61826-3489 (217-351-8091; fax 217-359-2344)



Expoanalítica + Biociencia
April 3–6, 1995. Madrid, Spain
Contact: JBC Expoanalítica + Biociencia, Avda. Reina Ma. Cristina, Palacio no. 1, 08004 Barcelona, Spain (34-3-423-31-01; fax 34-3-423-63-48)

6th International Symposium on Pharmaceutical and Biomedical Analysis
April 23–26, 1995. St. Louis, MO
Contact: Shirley E. Schlessinger, Suite 1015, 400 E. Randolph Dr., Chicago, IL 60601 (312-527-2011)

Symposium on Validation Practice for Biotechnology Products
April 24–25, 1995. Gaithersburg, MD
Contact: James K. Shillenn, Bioprocessing Resource Center, Penn State University, 519 Wartik Laboratory, University Park, PA 16802-9959 (814-863-3650; fax 814-863-1357)

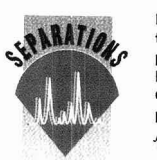
2nd National Conference on Laboratory Issues in Childhood Lead Poisoning Prevention
May 18–20, 1995. Atlanta, GA
Contact: Ann Ulm, ASTPHLD, 1211 Connecticut Ave., N.W., Suite 608, Washington, DC 20036 (202-822-5227; fax 202-887-5098)



187th Meeting of the Electrochemical Society
May 21–26, 1995. Reno, NV
Contact: The Electrochemical Society, 10 S. Main St., Pennington, NJ 08534-2896 (609-737-1902)



7th Sanibel Conference on Physics and Chemistry of Electrospray and Multiply-Charged Ions
Jan. 21–24, 1995. Sanibel Island, FL
Contact: ASMS, 1201 Don Diego Ave., Santa Fe, NM 87501 (505-989-4517; fax 505-989-1073)



HPCE '95: 7th International Symposium on High-Performance Capillary Electrophoresis
Jan. 29–Feb. 2, 1995. Wurzburg, Germany
Contact: Shirley E. Schlessinger, Suite 1015, 400 E. Randolph Dr., Chicago, IL 60601 (312-527-2011)

6th International Symposium on Chiral Discrimination
April 26–28, 1995. St. Louis, MO
Contact: Shirley E. Schlessinger, Suite 1015, 400 E. Randolph Dr., Chicago, IL 60601 (312-527-2011)

7th Symposium on Handling of Environmental and Biological Samples in Chromatography
May 7–10, 1995. Lund, Sweden
Contact: M. Frei-Häusler, IAEAC Secretariat, Postfach 46, CH-4123 Allschweil 2, Switzerland (fax 41 61 4820805)



1995 Winter Conference on Plasma Spectrochemistry
Jan. 8–13, 1995. Cambridge, England
Contact: Janice M. Gordon, Royal Society of Chemistry, Thomas Graham House, Science Park, Milton Rd., Cambridge CB4 4WF, U.K.

36th Experimental Nuclear Magnetic Resonance Conference
March 26–30, 1995. Boston, MA
Contact: ENC, 815 Don Gaspar Ave., Santa Fe, NM 87501 (505-989-4573; fax 505-989-1073)

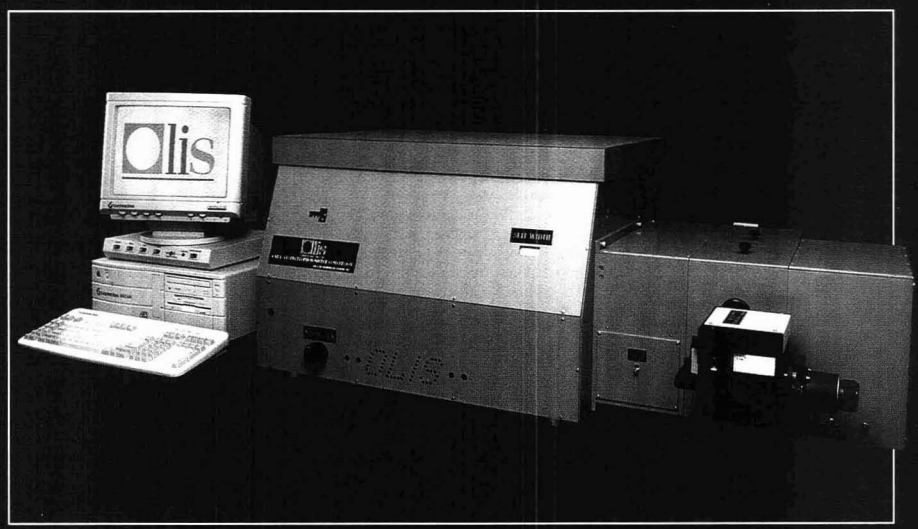
Short Courses

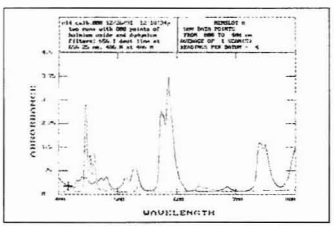
Time-Resolved Fluorescence Spectroscopy
Jan. 9–13, 1995. Baltimore, MD
Contact: J. R. Lakowicz, Department of Biological Chemistry, University of Maryland School of Medicine, 108 N. Greene St., Baltimore, MD 21201 (410-706-8409; fax 410-706-8408)

Supercritical Fluid Chromatography and Analytical Supercritical Fluid Extraction
Feb. 2, 1995. Cincinnati, OH
Contact: Doug Raynie, The Procter & Gamble Company, Miami Valley Laboratories, P.O. Box 398707, Cincinnati, OH 45239-8707 (513-627-1186; fax 513-627-1233)

Techniques for Polymer Analysis and Characterization
May 21, 1995. Sanibel Island, FL
Contact: Petr Munk, Department of Chemistry, University of Texas at Austin, Austin, TX (512-471-4179; fax 512-471-8696)

THE OLIS MODERNIZATIONS





OLIS software is mature, inclusive, and fundamental to the operation of the modernized spectrometer. All instrument settings, data collection, flexible data viewing and storing/retrieving, and contemporary data fitting are addressed by the comprehensive OLIS Spectroscopy Operating Systems.

Brilliant breakthroughs happen...

Manufactured in the years after WWII were some of the best UV/Vis and UV/Vis/NIR spectrophotometers ever made, based on monochromators designed by Arnold Beckman, Howard Cary, and Britton Chance. Directed by Richard DeSa, OLIS engineers and programmers modernize the Cary® 14, 15, 16, 17 & 118, as well as most of the Aminco line, again making them "the best spectrophotometers available." Useful computerization, reliable electronics, and the optics and housings that made "Cary®," "Beckman®," and "Aminco-Chance®" world-renowned, are available from us, today.

Please call ***1-800-852-3504*** *for technical and pricing details on a complete workstation from us or the modernization of your classic unit.*

***ours could** lead to yours.*

Olis

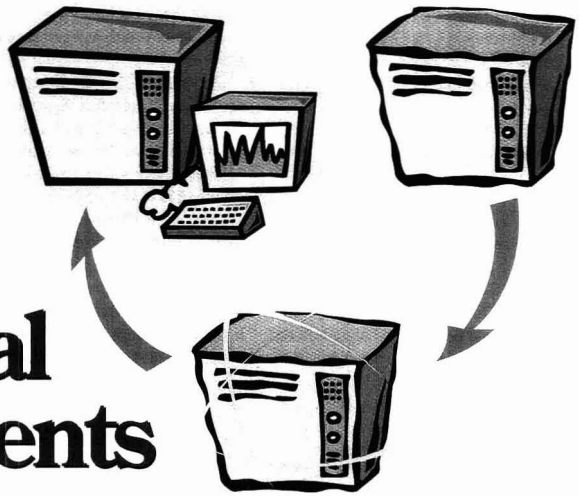
CIRCLE 10 ON READER SERVICE CARD

On-Line Instrument Systems, Inc.

130 CONWAY DRIVE, SUITES A & B • BOGART, GEORGIA 30622-1724

U.S. & Canada (800) 852-3504 • Worldwide (706) 353-6547 • Telefax (706) 353-1972

CARY is a registered trademark of Varian.
AMINCO is a registered trademark of SLM-Aminco.
BECKMAN is a registered trademark of Beckman Instruments, Inc.



Used Analytical Instruments

Telling the Cream Puffs from the Lemons

Used instruments can be a good deal if they're properly reconditioned and tested before you buy them

You want to open your own environmental contract lab. You have a staff of three, including yourself. When you get your first major client, you discover you need more equipment than your startup loan will cover—the GC/MS system alone would be more than half of your operating costs, but you can't do high-level work without it. And what about the atomic absorption spectrometer? The one you've found at auction after a local industrial plant closed has a chart recorder from the mid-1970s. No wonder it was going for $50.

In the 1990s, small or startup contract labs for analytical chemistry increasingly face the dilemma of acquiring advanced instruments they can't afford or being unable to offer competitively high-level analyses to their clientele. As a result, more and more labs are turning to the used-instrument dealers whose businesses have sprung up in the past decade or so. The advantages are obvious, but getting a good deal on a used instrument means looking for more than just a low price. "In some ways, buying a used instrument can be like buying a used car as far as reliability is concerned," says Sal Akhter, general manager for Spectra-Source (San Jose, CA).

Who offers what

Many of the used instrument dealers are small companies—with 10 or fewer employees—serving niche markets. Some specialize in only one brand of instrument. Alpha Omega Technologies (Neptune, NJ), for instance, reconditions and resells only Hewlett Packard instruments and peripherals made specifically for Hewlett Packard products by companies such as Tekmar. "We are the major reseller of Hewlett Packard instruments, supplies, and computer control systems for them," says Alpha Omega's president, Gerald Friedhoff. Within that limitation, however, the company reconditions and

sells instruments in several areas of analytical chemistry: gas and liquid chromatographs, GC/MS systems, UV–vis spectrometers, and diode array detectors.

At the other extreme is On-Line Instrument Systems (OLIS; Bogart, GA), which has been in business since the mid-1970s. According to company vice president Julie Ann DeSa Lorenz, OLIS sells nothing but dual-beam UV–vis, near-IR, CD, and stopped-flow optical spectroscopy systems (though no interferometers), but deals in whatever brand suits its needs, and often combines components from different manufacturers' instruments to create hybrids for customers. "Until three or four years ago, that was our main business," she says. "Since we came out with our own line of spectrophotometers, the used instruments are about half of our business."

Akhter says Spectra-Source also reconditions and resells instruments from a variety of manufacturers, specializing in chromatography systems (GC, LC, IC) from Hewlett Packard, spectrometers (IR, UV–vis, AAS, and ICP-AES) from Perkin Elmer, and NMR spectrometers from Varian. Although Hewlett Packard has authorized the company to resell some of its new products and supplies, "The company's focus remains primarily in reselling complete reconditioned systems," says Akhter.

Who's buying?

Each of these companies serves a different category of customers, although in the case of Spectra-Source and Alpha Omega, there is some overlap. Spectra-Source markets mainly to small, startup environmental contract labs and biotech/pharmaceutical labs. Alpha Omega serves "anyone from Fortune 100 companies and quality control labs for companies like Mobil and Exxon down to the startup labs for flavor and fragrance shops," according to Friedhoff.

Both companies offer leasing and rental options in addition to straight sales, and both have field service agreements with Hewlett Packard for their mostly commercial customer base as well as offering their own field and in-house service contracts at a discount from Hewlett Packard's contracts. OLIS, on the other hand, serves mainly academic researchers who want to upgrade their own instruments and young investigators looking to economize on their first grants. For them, says Lorenz, leasing equipment is much more difficult because of the way university grant administration and purchasing protocols are set up.

Although used analytical instrumentation's share of the total U.S. market is comparatively small—Friedhoff estimates it as 2–4% of new instrument sales—the number of buyers seems to be increasing. Friedhoff is unsure of the total market, but says Alpha Omega's used instrument business has been growing steadily since the company was started six years ago. Akhter says that in the four years Spectra-Source has been in business, the company's yearly earnings have increased from ~ $250,000 to roughly $2 million. "We have sold to nearly 400 customers and we maintain a database of about 3000 people who have shown interest in acquiring used instruments."

Even an extensive upgrade can be worthwhile if the original components are in good shape.

However, he notes that the market appears to be changing because of the downturn in the economy. "We used to serve both small and midsized environmental laboratories," he says. "But in the last year and a half, the medium-sized mom-and-pop operations have been eaten away by bigger labs. Now, four or five major lab chains own more than 70% of the industry, and the rest are small labs that thrive on local businesses and government contracts." The picture for the biotech sector is parallel, he adds, but the midsized labs are still hanging on.

The value of "value-added"

Obviously, knowing exactly where the instrument came from and what the reseller has done to it is important if you want to know the fair market value of the final product and whether it would be better to purchase a new one. Companies that offer reconditioning, upgrading, and service and maintenance contracts insist that these services can make or break the performance of a used instrument. "It's a matter of finding the right company," Akhter says. "We tell people these are high-tech instruments. Reconditioning them requires thorough knowledge and experience that most brokers don't possess."

The age of the original instrument can make even an extensive upgrade worthwhile if its components are in good shape. Lorenz notes that at OLIS, upgrading a Cary 14 with new electronics and a computer may cost the owner $20,000, but "a lot of them would rather do that than chuck their old spectrometer and have to pay $50,000 for a new one."

A used instrument typically goes for half the price of a new one, but because of depreciation, the more expensive it was to begin with, the greater the discount. A $300,000 instrument might depreciate to half its value within two years, whereas a $25,000 instrument might only depreciate to $18,000 in the same time. Akhter says Spectra-Source reconditions and sells instruments that are 5 or 6 years old on average; according to Friedhoff, the instruments Alpha Omega reconditions may be anywhere from 6 months to 12 years old. Lorenz says her company reworks older instruments such as Aminco (subsequently taken over by SLM, which was acquired by Milton-Roy) spectrometers from the 1970s.

Where do the used instruments come from? Many are sold off by companies that lease new instruments—after several years, the market value is diminished and not all of the leasing companies do reconditioning. Trade-ins are the other major source. Akhter and Friedhoff say their companies cooperate with the manufacturers' salespeople, who often refer customers to them to sell off old or obsolete equipment. But buying opportunities can turn up anywhere. Sometimes lab equipment is sold at auction when an industrial plant closes (unfortunately a recurrent phenomenon these days). Lorenz says the U.S. Department of Agriculture even called her office once to let her know

they would dump a number of older instruments if she didn't want them.

Depending on the company's objectives, a used instrument may be reconditioned to a usable level, customized, or brought up to the original manufacturer's specifications. Akhter says SpectraSource's reconditioning protocol includes an evaluation of whether an instrument should be refurbished or just cannibalized for parts; cleaning or repainting; optical assembly resurfacing or replacement; electronics upgrades; recalibration; and replacement of switches, knobs, or other worn-out parts as needed so that the instruments look like the new versions except for the older body design. Friedhoff says Alpha Omega's strategy is to incorporate new parts and software to add value to its used instruments; the company creates turnkey systems that may incorporate both new and used components.

Alpha Omega and Spectra-Source both bring Hewlett Packard instruments up to the manufacturer's specifications, and Spectra-Source does that for its other manufacturers' instruments as well. OLIS scavenges the optical benches from spectrometers, replaces the electronics in the older (pre-1980s) instruments, adds its own computer hardware and operating software, adds other components (e.g., adds a stopped-flow module from one manufacturer to a fluorescence spectrometer from another company that didn't offer a stopped-flow option), and sells the finished product as an OLIS instrument.

Akhter, Friedhoff, and Lorenz agree that the most significant upgrade for most of the instruments they deal in is modernization of computer control and data acquisition. For the most part, they say, the basic analytical instrumentation hasn't changed that much in the past decade (mass spectrometers and FT-IR spectrometers are two exceptions). However, the software and hardware technologies have improved so much that with the right retrofitted equipment and electronics, an older GC system or AA spectrometer can be made to work nearly as well as a current model and can perform more sophisticated analyses than it was designed to do.

Buying tips

Akhter points out that there are no official price guides or standards for used instruments. He cautions that a broker who does little or nothing to recondition instruments may charge the same price for them as a company that performs extensive reconditioning and upgrading. "There are companies out there that are reaping a 300–400% profit because they don't do anything to the instruments. We work on a margin of only 30–35% most of the time because our reconditioning process takes 5–10 days and we install new parts for the instruments, but we've retained 90% of our customers."

So how can you avoid getting ripped off when you buy a used instrument? Buying a used instrument may be like buying a used car, but whereas a used car may work for a few months and then show problems, a used analytical instrument usually shows its weaknesses up front. "Ask the vendor to fax you some test results for standards using the instrument you're about to purchase," Akhter advises. "That should give you a good idea of what shape it's in." "Customers should buy equipment that they know," adds Friedhoff. "They should get a detailed quotation from the vendor and clearly understand the warranty terms and conditions." A credit check through Dun & Bradstreet or TRW and a look at the company's literature and history can help you avoid fly-by-night operators. Finally, the support services offered by the company may provide some clues. "The key thing is to look for a quality job," Friedhoff says. "The dealer should offer the same warranty as for a new instrument." Spectra-Source, Alpha Omega, and OLIS all offer warranties of a year on reconditioned instruments as well as some in-house and on-site maintenance.

The used-instrument market is small but expanding, and doesn't appear to have peaked. "A lot more people should consider this option more actively," says Lorenz. "The I've-got-to-buy-new craze of the '80s is gone. We're all more concerned about throwing things away."

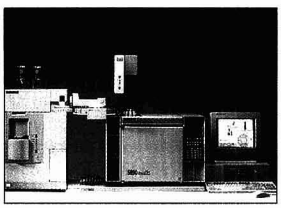
Deborah Noble



CIRCLE 7 ON READER SERVICE CARD

SFE/LC or SFE/GC

An optional hardware bridge with accompanying software is designed to integrate the HP 7680T supercritical fluid extractor with a liquid or gas chromatograph for applications such as monitoring polymer formulation in process laboratories. The bridge automates sample transfer between the extractor and the chromatograph and tracks all operations from sample thimble insertion into the extractor to final chromatographic analysis. The Windows-based bridge software controls the entire analytical system. Standard operating software for the SFE and chromatography modules can be used to set up methods. The bridge software links, sequences, and executes the SFE and chromatography methods. The integrated system can analyze both extracted and nonextracted samples in a chromatographic run, and each instrument can be operated independently of the other for flexibility in optimizing protocols. **Hewlett Packard ■ 404**



INSTRUMENTATION

SEM/XRF

The CryoX X-ray detector, designed for elemental microanalysis in a scanning electron microscope, contains a closed-cycle cryostat that requires no liquid nitrogen. The detector's modular components can be replaced individually during repair or servicing. **EDAX ■ 401**

IC

The Shodex CD-5 conductivity detector for IC has part-per-billion sensitivity and lower background noise than earlier models. It features a temperature-controlled flow cell, a digital display, and an autozero function. **JM Science ■ 402**

Arc/spark AES

The DV-6 arc/spark atomic emission spectrometer incorporates a high repetition rate spark source and is designed to improve precision and detection limits while reducing argon consumption. The optics in the 1-m spectrometer are thermostatted and have been re-engineered to improve detection of nitrogen, oxygen, and carbon. **Baird ■ 403**

Spectroscopy

The HPCell high-pressure cell system for fluorescence, absorption, or Raman spectroscopy accommodates pressures up to 3000 bar (43,500 psi). The system includes the pressure cell, a manual or computer-controlled pump for generating pressure, and software for system control and data acquisition. The system can be integrated with an ISS spectrofluorometer or used as a stand-alone accessory with other fluorometers. The cell is available with either three or four 10-mm-diameter quartz or sapphire windows placed to accommodate L- or T-format fluorescence measurements. **ISS ■ 405**

LITERATURE

SPM

Volume 94-2 of an applications newsletter on SPM features articles on surface characterization of epitaxial silicon by using a power spectral density function and on atomic force microscopy of the surface of hip socket replacements. The articles are illustrated with SPM images and computer screen shots. The newsletter also reports on the release of SPMLab software and other new products. **TopoMetrix ■ 406**

SPE

Three application notes, Nos. 37–39, describe the use of the Prospekt SPE sample preparation system in on-line HPLC analyses of clozapine in human serum, caffeine in cola, and a smooth-muscle relaxant drug in rat plasma. The notes are illustrated with chemical structures, sample chromatograms, and instrument schematics. **Spark Holland ■ 407**

Spectroscopy

Brochure describes the Model 2000-A Multi-Mode FT-IR system and the Model RA-4K-SP fluid sample cell, which provides pathlengths from 5 μm to 2 mm and operates at high temperatures and pressures. **Aabspec ■ 408**

Spectrophotometry

Guide presents accessories for the Spectronic Genesys 5 spectrophotometer and demonstrates them by showing accessory configurations with glassware and temperature-control instrumentation. **Milton Roy ■ 409**

Chiral HPLC

Guide to chiral column selection introduces the concepts of chirality and chiral separations by HPLC and describes techniques for method development and optimization. Pharmaceutical applications are presented with sample chromatograms and instrument parameters. The guide includes a table of Chirex stationary phases and applications. **Phenomenex ■ 410**

GC

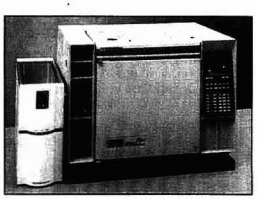
Bulletin No. 286 describes the EPC 1000 electronic pressure control module for GC, a stand-alone instrument that is designed to replace mechanical pneumatics for HP 5890 GC systems. The brochure lists performance specifications and is illustrated with sample chromatograms. **Alltech ■ 411**

Ion trap MS

The 3DQ Discovery is a quadrupole ion trap mass spectrometer incorporating a radio frequency waveform generator with user-selectable frequency range parameters. The waveform generator provides clean chemical ionization by reducing space charge interferences in the trap. The system can perform CI and EI switching within a run and accommodates a variety of inlet systems.

The Field-Noise Filter broadband waveform generator is controlled through a Windows-based user interface to eject ions of specified *m/z* and prevent the trap capacity from being overloaded. The user can program it to select ions with one or several *m/z* ratios or to select ions in one or more *m/z* ranges. Ions to be retained in the trap can be selected by specifying "notches" in the band of frequencies narrow enough to correspond to 1 Da. The spectrometer can perform EI, selected reagent ion CI, SIM, multiple ion monitoring, MS/MS, MS^n, and alternating CI and EI within a run.

The three posts that hold the ion trap together are heated; their contact with the end caps and ring electrode heats the trap directly and prevents samples from condensing on cold surfaces within the trap. The system provides unit mass resolution between 10 and 650 Da, and the mass scan rate can be specified in the range of 1000–25,000 Da/s. **Hitachi/Teledyne ■ 412**



CATALOGS

LC

Catalog No. 6 lists sample injectors for analytical-, micro-, or preparative-scale LC separations; high-pressure switching valves; low-pressure Teflon valves; and fittings, loops, filters, and valve accessories. Illustrations and descriptions are accompanied by specification tables. **Rheodyne ■ 413**

HPLC

Catalog lists instrumentation and accessories for HPLC, including complete chromatography systems, pumps and solvent delivery modules, injectors, column heaters and selectors, detectors, and fittings. **Rainin ■ 414**

Separations

Catalog lists IC, HPLC, CE, and SFC instrumentation and accessories as well as sample preparation stations, detectors, and chromatography modules. Liquid chromatographic accessories include pumps, postcolumn derivation cells, fittings, valves, and eluent delivery modules. SFC products include detectors, restrictors, SFC/GC columns, and an SFE system. **Dionex ■ 415**

For more information, please circle the appropriate numbers on one of our Reader Service Cards.

Walk-up NMR

The Gemini 2000 NMR spectrometer, intended for routine analyses and methods development in industrial and academic laboratories, is controlled by a Sun Microsystems SPARCstation that offers both simplified and advanced user interfaces. The system automates experiments such as COSY, DEPT, and HETCOR, and can produce simple ^1H NMR spectra in ≤ 4 min.

The simplified user interface provides drop-down menus and online help for parameter adjustment and instrument control. For methods development or for more advanced techniques such as indirect detection, solvent suppression, the use of pulsed-field gradients, and spin locking, the regular VNMR interface provides data analysis methods such as linear prediction, digital signal processing, deconvolution, and interactive free induction decay weighting. The digital signal processing software produces single or multidimensional spectra.

Probes for specific applications are available with the spectrometer. These include a pulsed-field gradient accessory for ^1H–^{13}C NMR and other heteronuclear correlation experiments, a probe that allows the user to obtain spectra from microgram and nanogram amounts of sample, and a probe that can be used for NMR of four different nuclei without the need for tuning. Oxford superconducting magnets for the spectrometer are available in the frequency range of 200–4000 MHz. Other components included in broadband configurations are high-power linear pulse amplifiers, computer-controlled pin-diode attenuators, and programmable filters. **Varian ■ 416**



Analytical instruments at ½ price!



Now you have all the options!

☑ Buy ☑ Lease ☑ Rent ☑ Trade ☑ Sell

Refurbished analytical instruments

International Equipment Trading, Ltd.

960 Woodlands Parkway • Vernon Hills, Illinois 60061

(708) 913-0777 Fax (708) 913-0785

CIRCLE 3 ON READER SERVICE CARD

COUNT THE WAYS

Do you know how many ways there are to fulfill your giving wishes—and at savings that may surprise you? As you make plans that will influence your tax picture next April 15, request a copy of our helpful booklet, "Your Guide to Effective Giving in 1994."

American Chemical Society
Development Office
1155 16th Street, NW
Washington, DC 20036

☐ Please send me a free copy of "Your Guide to Effective Giving in 1994."

Name _____

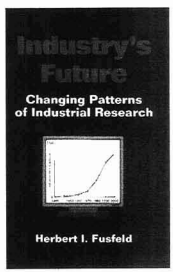
Address _____

City _____

State _____ Zip _____

Just Published!

Industry's Future: Changing Patterns of Industrial Research



This fascinating volume provides the readers with an understanding of the dynamic processes that make industrial research a principal driving force in creating technical change, producing economic growth, and strengthening the technical institutions in society.

It describes and analyzes the major factors that shape the conduct and organization of industrial research, including the internationalization of R&D, restructuring of industry, declining defense expenditures and the pressure to develop access to sources of technical change outside the corporation.

The volume presents approaches for improved industry relations with government and academia, discusses complex conditions for conducting industrial research effectively and analyzes potential new conditions that can shape future industrial research. The experiences of specific corporations with modern management of technology are also described.

Herbert I. Fusfeld

384 pages (1994)
Clothbound: ISBN 0-8412-2983-X
$39.95
Paperbound: ISBN 0-8412-2984-8
$24.95

Order from

American Chemical Society
Distribution Office Dept. 74
1155 Sixteenth Street, NW
Washington, DC 20036

Or Call TOLL FREE 1-800-227-5558
(in Washington, D.C. 872-4363)
and use your credit card!
FAX: 202-872-6067.

ACS Publications Catalog now available on internet: **gopher acsinfo.acs.org**

ACS PUBLICATIONS
Essential Resources for the Chemical Sciences

Laboratory Service Center

FREE DATA, FAST

To quickly amass data on all of the products you need, consult the Lab Data Service section on our *Analytical Chemistry* reader reply card insert.

Laboratory Service Center (Equipment, Materials, Services, Instruments for Leasing). Maximum space — 4 inches per advertisement. Column width, 2-3/16"; two column width, 4-9/16". Artwork accepted. No combination of directory rates with ROP advertising. Rates based on number of inches used within 12 months from first date of first insertion. Per inch: **1" — $200; 12" — $195; 24" — $190; 36" — $185; 48" — $180.**

Call or write Jane Gatenby

ANALYTICAL CHEMISTRY
1599 Post Road East
P.O. Box 231
Westport, CT 06881
203-256-8211 / FAX: 203-256-8175

Index to Advertisers

CIRCLE INQUIRY NO.	ADVERTISERS	PAGE NO.
7	Alpha Omega Technologies	1185A
1	Brinkmann Instruments, Inc. Lavey/Wolff/Swift Inc.	1150A
-	Hamamatsu SSD&W	1171A
3	* International Equipment Trading, Ltd.	1188A
2	Leco Corporation Lecom	OBC
5	LPA LaMotte Company	1152A
10	*OLIS: On-Line Instrument Systems	1182A
8, 9	*Perkin-Elmer Corporation Lena Chow Advertising	1147A
4	The Pittsburgh Conference	IFC

**See ad in 1995 LabGuide Edition.*

Advertising Management for the American Chemical Society Publications

CENTCOM, LTD.

President
James A. Byrne

Executive Vice President
Benjamin W. Jones

Joseph P. Stenza, *Production Director*

Laurence J. Doyle, *Director of Marketing*

1599 Post Road East
P.O. Box 231
Westport, Connecticut 06881-0231
(Area Code 203) 256-8211
Fax No. 203-256-8175

DIRECTOR, ADVERTISING SALES, LABORATORY PRODUCTS
Bruce E. Poorman

ADVERTISING PRODUCTION MANAGER
Jane F. Gatenby

SALES REPRESENTATIVES

Philadelphia, PA. . . . CENTCOM, LTD., The Meadows, 485 Devon Park Drive, Suite 106, Wayne, PA 19087. Telephone: 610-964-8061, FAX: 610-964-8071

New York/New Jersey . . . Dean A. Baldwin, John F. Raftery, CENTCOM, LTD., Schoolhouse Plaza, 720 King Georges Post Road, Fords, NJ 08863. Telephone: 908-738-8200, FAX: 908-738-6128

Westport, CT./Boston, MA. . . . Dean A. Baldwin, Michael J. Pak, CENTCOM, LTD., 1599 Post Road East, P.O. Box 231, Westport, CT 06881-0231. Telephone: 203-256-8211, FAX: 203-256-8175

Cleveland, OH. . . . Bruce E. Poorman, Dean A. Baldwin, CENTCOM, LTD., 19035 Old Detroit Road, Suite 203. Rocky River, OH 44116. Telephone: 216-331-5151, FAX: 216-331-3432

Chicago, IL. . . . Michael J. Pak, CENTCOM, LTD., 540 Frontage Rd., Northfield, IL. 60093. Telephone: 708-441-6383, FAX: 708-441-6382

Houston, TX./Atlanta, GA. . . . Edward M. Black, CENTCOM, LTD., P.O. Box 820966, Houston, TX 77082-0966. Telephone: 713-493-1560, FAX: 713-493-6673

San Francisco, CA. . . .Paul M. Butts, Bob LaPointe, CENTCOM, LTD., Suite 808, 2672 Bayshore Parkway, Mountain View, CA 94043. Telephone: 415-969-4604, FAX: 415-969-2104

United Kingdom, Scandinavia and Europe (Except: Germany, Switzerland, Austria, France, Italy, Spain) . . . Malcolm Thiele, Technomedia Ltd., Wood Cottage, Shurlock Row, Reading RG10 OQE, Berkshire, England. Telephone: 0734-343302, FAX: 0734-343848

Germany, Switzerland, Austria . . . IMP InterMediaPartners, GmbH, Deutscher Ring 40, 42327 Wuppertall, Germany. Telephone: (0202) 711091, FAX: (0202) 712431

France . . . Gerard Lecoeur, Aidmedia, 31–33 Grand rue de Saint-Rambert, 69009 Lyon, France. Telephone: 78-64-20-37, FAX: 78-83-56-67

Italy, Spain . . . Tess Serranti, Serranti Communications, 43 Van Sant Road, New Hope, PA 18938. Telephone: 610-598-0668, FAX: 610-598-0670

Hong Kong. . .SEAVEX, LIMITED, 503 Wilson House, 19 Wyndham Street, Central, Hong Kong, Telephone: 868-2010, FAX: 810-1283

Japan. . . Shigeyuki Yasui, Intercommunications (Japan), Inc. 2F Ginza ElwaBldg. 8-18-7 Ginza, Chuo-ku, Tokyo 104, Japan. Telephone: (03) 5565-0861, FAX: (03) 5565-0860.

Korea. . .DooBee International Limited, Center Building (Byulgwan), 1-11 Jeong-dong, Choong-ku C.P.O. Box 4557, Seoul, Korea, Telephone: 822-776-2096, FAX: 822-755-9860

Singapore.. . .SEAVEX, LIMITED, 400 Orchard Road, #10-01 Orchard Towers, Singapore 0923, Telephone: 734-9790, FAX: 732-5129

Taiwan. . .Epoch Limited, 2F No. 3, Lane 52, Nanking East Road, Section 4, P.O. Box 1642, Taipei, Taiwan, R.O.C. Telephone: 577-5441, FAX: 578-4308

South America . . .Bruce E. Poorman, CENTCOM, LTD., 19035 Old Detroit Road, Suite 203, Rocky River, OH 44116. Telephone: 216-331-5151,

ANALYTICAL CHEMISTRY Information Express

Get the product data you need fast...

By Phone: Use the reference list below, and contact the companies to fill an immediate need, or...
By Fax: Use the fax form on the opposite page to send a direct written request.

Company	Page	Issue	RSN	Data+	Phone	Fax	Contact
Aabspec	1186 A	12/1/94	408	●	516-783-9380	516-781-4934	
Able Technologies	1096 A	11/1/94	412		800-637-3609	914-496-8532	Debra Noeldechen
Aldrich Chemical	OBC	11/1/94	1	●	414-273-3850	414-273-2094	Rich Gross
Alltech Associates	1186 A	12/1/94	411	●	708-948-8600	708-948-1078	Laura Inkley
Alpha Omega Technologies	1185 A	12/1/94	7	●	800-842-5742	908-919-0459	Ed Zachowski
Baird Analytical	1186 A	12/1/94	403	●	617-276-6163	617-276-6510	Robin Tamulynas
Baltek	983 A	10/1/94	409		44-625-434127	44-625-616916	Helen Williams
J. T. Baker	922 A	10/15/94	9	●	908-859-2151	908-859-9318	William Broad
Brinkmann Instruments	1150 A	12/1/94	1	●	800-645-3050	516-334-7506	C. Shevchenko
Burleigh Instruments	879 A	9/1/94	407	●	716-924-9355	716-924-9072	Brian Samoriski
ChemService	1141 A	11/15/94	1	●	800-452-9994	610-692-8729	Ron Gray
Cole Parmer	1096 A	11/1/94	414	●	800-323-4340	708-647-9660	Gary Hermann
Dionex	1187 A	12/1/94	415	●	800-346-6390	408-739-4398	Nancy Jensen
Directed Energy	872 A	9/1/94	19	●	303-493-1901	303-493-1903	Ronald Sherwood
EDAX	1186A	12/1/94	401	●	201-327-6611		Alan Hutchings
EG&G Instruments (Princeton)	804 A	8/1/94	10–11	●	609-530-1000	609-883-7259	Ruth Rearick
EG&G Ortec	1095 A	11/1/94	402	●	800-251-9750	615-483-0396	Sanford Wagner
Finnigan MAT	944–945 A	10/1/94	6	●	408-433-4800	408-433-4823	Nancy Williams
Fisons Instruments	1046 A	11/1/94	5–9	●	508-524-1000	508-524-1100	Cathy Schaub
Galileo Electro-Optics	982 A	10/1/94	406	●	508-347-9191	508-347-3849	Laurie Placella
Graseby Nutech	983 A	10/1/94	408	●	800-637-6312	919-544-3770	Chris Dale
Hamamatsu	1171 A	12/1/94	none	●	800-524-0504	908-231-1218	Robert Wisner
Hellma	982 A	10/1/94	403	●	718-544-9166	718-263-6910	Debra Aronowitz
Hewlett Packard	1096 A	11/1/94	413	●	415-857-5603	415-857-8228	Doug Forsyth
Hiden Analytical	816 A	8/1/94	404		44-925-445225	44-925-416518	Ian D. Neale
Hitachi/Teledyne	1186 A	12/1/94	412	●	408-955-7047		Susanne Lee
InterAction Chromatography	983 A	10/1/94	410		408-894-9200	408-894-0405	David Hometchko
International Equipment Trading	1188 A	12/1/94	3	●	708-913-0785	708-913-0777	Turgay Kaya
Isco	1108 A	11/15/94	4	●	402-464-0231	402-464-0318	Gary Bakken
ISS	1186 A	12/1/94	405	●	217-359-8681	217-359-7879	Vijai Tyagi
J&W Scientific	878 A	9/1/94	404	●	916-985-7888	916-985-1101	Brenda Meadows
JM Science, Inc.	1186 A	12/1/94	402	●	716-774-8706	716-774-8708	
JEOL USA	1104 A	11/15/94	5	●	508-535-5900	508-536-2205	Brian Musselman
Krejci Engineering	1104 A	11/15/94	401		42-504-298	42-5-572667	
Labsphere	982 A	10/1/94	405	●	603-927-4266	603-927-4694	Joan A. Beaulieu
Leco	OBC	12/1/94	2	●	616-983-5531	616-983-4117	W. Stockwell
LPA	1152 A	12/1/94	5		703-836-6444	703-836-1360	William Strackbein
Macherey Nagel	1113 A	11/15/94	2		49-02421-6980	49-02421-62054	
Maxtek	867 A	9/1/94	8	●	310-320-6604	310-320-6609	Valli K. Febbraro
Metorex	878 A	9/1/94	402		800-229-9209	503-385-6750	James Pasmore
Metrohm	942 A	10/1/94	2		41-071-538-585	41-071-538-901	R. Steiner
Milton Roy	1186 A	12/1/94	409	●	716-248-4000	716-248-4014	Lynn Kobel
Nicolet Instrument	1023 A	10/15/94	4	●	608-271-3333	608-273-5046	Joni Hansen
NovaChem B.V.	983 A	10/1/94	411		31-85-2190	31-85-212332	
Ocean Optics	879 A	9/1/94	408		813-733-2447	813-733-3962	Michael Morris
On-Line Instrument Systems	1182 A	12/1/94	10	●	706-353-1972	703-353-6547	Julie D. Lorenz
Packard	1095 A	11/1/94	405	●	800-323-1891	203-235-1347	Christian Petrilli
Parr Instrument	878 A	9/1/94	403	●	309-762-7716	309-762-9453	W. Sherman Ha
Perkin Elmer	1147 A	12/1/94	8–9	●	800-762-4000	203-762-6000	Mary Cooke-Kager
PerSeptive Biosystems	1095 A	11/1/94	403	●	617-621-1787	617-621-2575	Denise Boyd
Phenomenx	1186 A	12/1/94	410	●	310-212-0555	310-328-7768	Tom Cleveland
Pittsburgh Conference	IFC	12/1/94	4		412-825-3220	412-825-3224	Daniel A. Wilson
Protein Solutions	879 A	9/1/94	409		800-446-4752	804-296-2306	David Dolak
Radiometer Analytical SA	817 A	8/1/94	408	●	33-78-03-38-38	33-78-68-88-12	Patricia Dalmas
Rainin	1187 A	12/1/94	414	●	510-654-9142		
Restek	982 A	10/1/94	407	●	800-356-1688	814-353-1309	Pamela Reynolds
Rigaku/USA	982 A	10/1/94	402	●	508-777-2446	508-777-3594	Alan Robson
Rheodyne	1187 A	12/1/94	413	●	415-434-4321		Al Young
Rosemount Analytical	816 A	8/1/94	401	●	216-684-4423	216-684-4458	Blaine Shank
Scientific Instrument Services	817 A	8/1/94	406	●	908-788-5550	908-806-6631	Theresa Neilsen
Seradyne Particle Technologies	1095 A	11/1/94	407	●	800-428-4007	317-266-2991	
Sigma-Aldrich Techware	OBC	11/15/94	10	●	414-273-3850	414-273-2094	Rich Gross
SLM-Aminco	885 A	9/15/94	7	●	800-637-7689	716-248-4014	Jill Koepke
Spectra-Tech	982 A	10/1/94	404	●	203-357-7055	203-357-0609	Debbie Esposito
Spark Holland	1186 A	12/1/94	407	●	31-5910-31700	31-5910-30035	Gerard Haak
SynChrom	1095 A	11/1/94	408	●	800-283-4752	317-447-5703	Teresa Dawson
Techne	981 A	10/1/94	5	●	609-452-9275	609-987-8177	P. H. Summers
Tekmar	879 A	9/1/94	406	●	800-543-4461	513-247-7050	Christine Wagner
Teledyne	IFC	9/1/94	18	●	415-962-6526	415-967-4353	Sharon Gomez
Thermo Separations	1095 A	11/1/94	406	●	800-424-7666	510-490-8182	Marianne Hartfield
TopoMetrix	1186 A	12/1/94	406	●	408-982-9700	408-982-9751	Tim Van Slambrouck
Upchurch Scientific	817 A	8/1/94	410	●	800-426-0191	800-359-3460	Amy King
Varian	1187 A	12/1/94	416	●	415-424-6786		Kathy McKinney
VCH	1050 A	11/1/94	3		49-6207-606740	49-62016-06184	Christine Schweikart
VHG Labs	1096 A	11/1/94	411	●	603-622-7660	603-622-5180	Lynne Hajjar
Waters	1101 A	11/15/94	3	●	508-478-2000	508-872-1990	Kathy Fernandes
Whatman	1043 A	11/1/94	10	●	800-922-0361	201-472-6949	Sharman Pate
Wheaton	OBC	9/1/94	6–7	●	609-825-1100	609-825-9035	Frank Norman
John Wiley & Sons	841 A	9/1/94	2		212-850-6137	212-850-6264	S. Nelson

Data+ Column: A bullet indicates that additional product and company information is available in the 1995 *Analytical Chemistry* LabGuide Edition.
RSN: Reader Service Number

PRODUCT DATA SERVICE

VALID THROUGH APRIL, 1995

ANALYTICAL CHEMISTRY

DECEMBER 1, 1994

Please circle the appropriate Reader Service Numbers to receive additional information.

Please help us determine your future laboratory buying trends. Which of the following products do you use, buy, specify, recommend or purchase? Circle all appropriate numbers on the attached reply card.

327 AA Spectroscopy
328 Analytical Services
329 Baths/Circulators
330 Biotechnology
331 Books/Periodicals
332 Centrifugation
333 Chemicals/Gases/Solvents
334 Computers/Software
335 Cooling/Freezing/Refrig.
336 Databases, Online
337 Densitometry
338 Detectors
339 Dryers/Evaporators
340 Electrochemistry
341 Elemental Analysis
342 Filtration
343 Flow Meters/Regulators
344 FT-IR Spectroscopy
345 Furnaces/Ovens
346 Gas Chromatography
347 General Lab Equipment
348 Heating/Temperature
349 Ion Chromatography
350 Lab Furniture/Hoods
351 Labware/Apparatus
352 Lasers/Fiber Optics
353 Liquid Chrom./HPLC
354 Mass Spectrometry
355 Microscopy
356 Capillary Electrophoresis
357 Mix/Stir/Blend/Grind
358 NMR Spectroscopy
359 Particle Size Analysis
360 Plasma Spectroscopy
361 pH/Ion Meters/Titrators
362 Pumping Monitoring
363 Recording/Integrating
364 Robotics/Automation
365 Sampling/Dispensing
366 Supercritical Fluid Chrom.
367 Spectrofluorometry
368 Stills/Purification
369 Surface Analysis
370 Thermal Analysis
371 Thin Layer Chrom.
372 UV-Vis Spectroscopy
373 Valves/Tubes/Fittings
374 Viscometry
375 Water/Moisture Analysis
376 Weighing/Balances
377 X-Ray Diffraction
378 X-Ray Spectroscopy

1	2	3	4	5	6	7	8	9	10	11	12	13	14	15	16	17
18	19	20	21	22	23	24	25	26	27	28	29	30	31	32	33	34
35	36	37	38	39	40	41	42	43	44	45	46	47	48	49	50	51
52	53	54	55	56	57	58	59	60	61	62	63	64	65	66	67	68
69	70	71	72	73	74	75	76	77	78	79	80	81	82	83	84	85
86	87	88	89	90	91	92	93	94	95	96	97	98	99	100	101	102
103	104	105	106	107	108	109	110	111	112	113	114	115	116	117	118	119
120	121	122	123	124	125	126	127	128	129	130	131	132	133	134	135	136
137	138	139	140	141	142	143	144	145	146	147	148	149	150	151	152	153
154	155	156	157	158	159	160	161	162	163	164	165	166	167	168	169	170
171	172	173	174	175	176	177	178	179	180	181	182	183	184	185	186	187
188	189	190	191	192	193	194	195	196	197	198	199	200	201	202	203	204

PRODUCT DATA SERVICE				327	328	329	330	331	332	333	334	335	336	337	338	339	340
341	342	343	344	345	346	347	348	349	350	351	352	353	354	355	356	357
358	359	360	361	362	363	364	365	366	367	368	369	370	371	372	373	374
375	376	377	378													

NEW PRODUCTS			401	402	403	405	406	407	408	409	410	411	412	413	414	415
416	417	418	419	420	421	422	423	424	425	426	427	428	429	430	431	432
433	434	435	436	437	438	439	440	441	442	443	444	445	446	447	448	449
450	451	452	453	454	455	456	457	458	459	460	461	462	463	464	465	466
467	468	469	470	471	472	473	474	475	476							

NAME (PLEASE PRINT)

TITLE

COMPANY

ADDRESS MAIL STOP

CITY STATE ZIP

TELEPHONE FAX

A. PRIMARY FIELD OF WORK

01 ☐ Energy
02 ☐ Environmental
03 ☐ Medical/Clinical
04 ☐ Drug/Toiletries
05 ☐ Forensic/Narcotic
06 ☐ Biotechnology
07 ☐ Metals
08 ☐ Pulp/Paper/Wood
09 ☐ Soaps/Cleaners
10 ☐ Paint/Coating/Inks
11 ☐ Electrical/Electronic
12 ☐ Instrument Dev./Design
13 ☐ Plastic/Polymer/Rubber
14 ☐ Agriculture/Food/Bev.
15 ☐ Inorganic Chemicals
16 ☐ Organic Chemicals

B. MY PRIMARY AREA OF EMPLOYMENT IS:

INDUSTRIAL
17 ☐ Research & Development
18 ☐ Quality/Process Control
MEDICAL/HOSPITAL
19 ☐ Research & Development
20 ☐ Clinical/Diagnostic
GOVERNMENT
21 ☐ Research & Development
COLLEGE/UNIVERSITY
22 ☐ Research & Development
23 ☐ Teaching
INDEPENDENT/CONSULTING
24 ☐ Research & Development
25 ☐ Analysis/Testing

C. INTENSITY OF PRODUCT NEED

26 ☐ Purchasing Immediately 27 ☐ Within 3-6 months 28 ☐ Within 6-12 months 29 ☐ Future project

D. Is this your personal copy of Analytical Chemistry?

☐ Yes ☐ No

FAX EXPRESS

FOR FASTEST SERVICE, USE THIS CARD TO FAX YOUR REQUEST DIRECTLY TO THE ADVERTISER.
PLEASE PHOTOCOPY THIS CARD FOR MULTIPLE USE.

TO: _____

FROM: _____

FAX: ( ) _____ DATE : _____

MY NEED IS:
☐ Immediate
☐ 6 - 12 Mos.
☐ 12 + Mos.

I WANT TO KNOW MORE, PLEASE...
☐ Send Literature
☐ Have a Salesman Call
☐ Send Name of Nearest Dealer
☐ Send Me a Price Quote

Description: _____

_____

Quantity: _____

I saw your... ☐ Advertisement ☐ Editorial Listing Regarding...
_____ on page _____ of the (date) _____ issue of AC

NAME:
TITLE:
COMPANY:
MAILSTOP:
STREET:
CITY: STATE: ZIP:
PHONE: FAX:

NO POSTAGE NECESSARY IF MAILED IN THE UNITED STATES

BUSINESS REPLY MAIL
FIRST CLASS MAIL PERMIT NO 307 PITTSFIELD MA

POSTAGE WILL BE PAID BY ADDRESSEE

ANALYTICAL CHEMISTRY
PO BOX 5511
PITTSFIELD MA 01203-9384

PRODUCT DATA SERVICE

Please help us determine your future laboratory buying trends. Which of the following products do you use, buy, specify, recommend or purchase? Circle all appro-priate numbers on the attached reply card.

327 AA Spectroscopy
328 Analytical Services
329 Baths/Circulators
330 Biotechnology
331 Books/Periodicals
332 Centrifugation
333 Chemicals/Gases/Solvents
334 Computers/Software
335 Cooling/Freezing/Refrig.
336 Databases, Online
337 Densitometry
338 Detectors
339 Dryers/Evaporators
340 Electrochemistry
341 Elemental Analysis
342 Filtration
343 Flow Meters/Regulators
344 FT-IR Spectroscopy
345 Furnaces/Ovens
346 Gas Chromatography
347 General Lab Equipment
348 Heating/Temperature
349 Ion Chromatography
350 Lab Furniture/Hoods
351 Labware/Apparatus
352 Lasers/Fiber Optics
353 Liquid Chrom./HPLC
354 Mass Spectrometry
355 Microscopy
356 Capillary Electrophoresis
357 Mix/Stir/Blend/Grind
358 NMR Spectroscopy
359 Particle Size Analysis
360 Plasma Spectroscopy
361 pH/Ion Meters/Titrators
362 Pumping Monitoring
363 Recording/Integrating
364 Robotics/Automation
365 Sampling/Dispensing
366 Supercritical Fluid Chrom.
367 Spectrofluorometry
368 Stills/Purification
369 Surface Analysis
370 Thermal Analysis
371 Thin Layer Chrom.
372 UV-Vis Spectroscopy
373 Valves/Tubes/Fittings
374 Viscometry
375 Water/Moisture Analysis
376 Weighing/Balances
377 X-Ray Diffraction
378 X-Ray Spectroscopy

ANALYTICAL CHEMISTRY
FAX EXPRESS

FOR FASTEST SERVICE, USE THIS CARD TO FAX YOUR REQUEST DIRECTLY TO THE ADVERTISER.
PLEASE PHOTOCOPY THIS CARD FOR MULTIPLE USE.

TO: _____

FROM: _____

FAX: ( ) _____ DATE : _____

I saw your... ☐ Advertisement ☐ Editorial Listing Regarding...
_____ on page_____of the (date)_____issue of AC

NAME:
TITLE:
COMPANY:
MAILSTOP:
STREET:
CITY: STATE: ZIP:
PHONE: FAX:

MY NEED IS:
- ☐ Immediate
- ☐ 6 - 12 Mos.
- ☐ 12 + Mos.

I WANT TO KNOW MORE, PLEASE...
- ☐ Send Literature
- ☐ Have a Salesman Call
- ☐ Send Name of Nearest Dealer
- ☐ Send Me a Price Quote

Description: _____

_____

Quantity:_____

Accelerated Articles

Anal. Chem. **1994**, *66*, 4121–4126

Glucopyranoside-Based Surfactants as Pseudostationary Phases for Chiral Separations in Capillary Electrophoresis

David C. Tickle,† George N. Okafo,‡ Patrick Camilleri,*,‡ Rose F. D. Jones,† and Anthony J. Kirby†

University Chemical Laboratory, Cambridge University, Lensfield Road, Cambridge, UK CB2 1EW, and SmithKline Beecham Pharmaceuticals, The Frythe, Welwyn, Herts, UK AL6 9AR

Dodecyl β-D-glucopyranoside monophosphate and monosulfate anionic surfactants have been synthesized and used successfully in micellar electrokinetic capillary chromatography for the separation of enantiomers. These surfactants have low critical micelle concentrations of about 0.5 and 1.0 mM, respectively. The methodology developed is applicable to chiral molecules differing widely in chemical structure, hydrophobicity, and acidity. The use of these surfactants extends the usefulness of CE as a tool for chiral separations, complementary to other techniques such as thin-layer chromatography and high-performance liquid chromatography.

The ability to differentiate between enantiomers is of primary importance especially in the analysis of biologically active molecules. Well-established "wet" techniques such as high-performance liquid chromatography (HPLC)[1,2] and thin-layer chromatography (TLC)[3] have been used extensively over the past 20 years for enantioselective separations. Important recent developments in the application of different modes of CE are capillary zone electrophoresis (CZE),[4,5] micellar electrokinetic capillary chromatography (MECC),[6–8] and capillary gel electrophoresis[9] for the resolution of enantiomers. Chiral separations by CE in particular are attracting much current interest.[10,11] In all these techniques, enantiomeric discrimination requires analytes to interact reversibly with a chiral environment.

Oligosaccharide- or protein-based chiral stationary phases are most commonly used for chiral separation by HPLC. In our experience it is often necessary to screen a wide range of normally expensive chromatography columns before a successful chiral resolution method is obtained. The lifetimes of these columns are often short, and reproducibility between one column and another cannot be guaranteed.

Although immobilized chiral selectors have been used[12,13] in CE, most successful enantiomeric separations have been achieved by the addition of chiral "selectors" to the buffer medium. Chiral mobile phase additives in CZE have included cyclodextrins,[5,8] crown ethers,[14] macrocyclic antibiotics,[15] proteins,[16] and synthetic chelating reagents.[17] The most popular additives for chiral separation by MECC have been either naturally occurring chiral surfactants on their own[7] or cyclodextrins in combination with either chiral[18] and achiral[19] surfactants, in particular sodium

† Cambridge University.

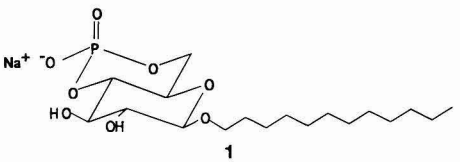
‡ SmithKline Beecham Pharmaceuticals.

(1) Allenmark, S. G. *Chromatographic Enantioseparation: Methods and Applications*; Ellis Horwood: Chichester, UK, 1988.
(2) Krstulovic, A. M., Ed. *Chiral Separations by HPLC: Applications to Pharmaceutical Compounds*; John Wiley & Sons: New York, 1989.
(3) Lepri, L.; Coas, V.; Desideri, P. G.; Santianni, D. *Chromatographia* **1993**, *36*, 297–301.
(4) Fanali, S. *J. Chromatogr.* **1991**, *545*, 437–444.
(5) Nielen, M. W. F. *Anal. Chem.* **1993**, *65*, 885–893.
(6) Nishi, H.; Fukujama, T.; Terabe, S. *J. Chromatogr.* **1991**, *553*, 503–516.
(7) Nishi, H.; Fukujama, T.; Matsuo, M.; Terabe, S. *J. Chromatogr.* **1990**, *515*, 223–243.
(8) Quang, C.; Khaledi, M. G. *Anal. Chem.* **1993**, *65*, 3354–3358.
(9) Cruzado, I. D.; Vigh, G. *J. Chromatogr.* **1992**, *608*, 421–425.
(10) Okafo, G. N.; Camilleri, P. Separation of Enantiomers in Capillary Electrophoresis. In *Capillary Electrophoresis: Theory and Practice*; Camilleri, P., Ed.; CRC Press: Boca Raton, FL, 1993; Chapter 5.
(11) Terabe, S.; Otsuka, K.; Nishi, H. *J. Chromatogr.* **1994**, *666*, 295–319.
(12) Li, S.; Lloyd, D. K. *Anal. Chem.* **1993**, *65*, 3684–3690.
(13) Mayer, S.; Schurig, V. *J. High Resolut. Chromatogr.* **1993**, *16*, 915–917.
(14) Kuhn, R.; Stoklin, F.; Erni, F. *Chromatographia* **1992**, *33*, 32–39.
(15) Armstrong, D. W.; Rundlett, K.; Reid, G. L. *Anal. Chem.* **1994**, *66*, 1690–1695.
(16) Barker, G. E.; Russo, P.; Hartwick, R. A. *Anal. Chem.* **1992**, *64*, 3024–3028.
(17) Gassman, E.; Kuo, J. E.; Zare, R. N. *Science* **1985**, *230*, 813–814.
(18) Okafo, G. N.; Camilleri. P. *J. Microcolumn Sep.* **1993**, *5*, 149–153.
(19) Otsuka, K.; Kawahara, J.; Tatekawa, K.; Terabe, S. *J. Chromatogr.* **1991**, *559*, 209–214.

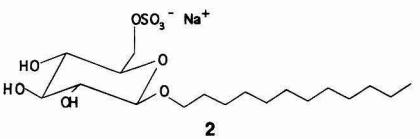
0003-2700/94/0366-4121$04.50/0 © 1994 American Chemical Society

dodecyl sulfate (SDS). Sodium dodecyl valinate has also been used as a chiral recognition reagent in conjunction with SDS.[20] In general, the development of chiral selectivity by CE has provided a approach to chiral analysis complementary to TLC and HPLC.

Long-chain alkyl glucopyranoside uncharged surfactants have been used previously in MECC[21] but not for chiral separations. In this paper, we introduce a novel class of dodecyl β-D-glucopyranoside derivatives (structures **1** and **2**) that differ in



1



2

the type of ionic substituent in the 6-position of the sugar residue. When used above their critical micelle concentration they provide good selectivity for analytes of widely varying structure, hydrophobicity, and ionic character. The simplified MECC methodology involved avoids the use of a comicellar phase system and requires a single mobile phase additive (buffer constituents and cosolvent apart) for chiral separations.

EXPERIMENTAL SECTION

Materials. All chemicals used in the synthesis of **1** and **2**, 1,1′-dinaphthyl-2,2′-diyl hydrogen phosphate, 3,4-dimethyl-5,7-dioxo-2-phenylperhydro-1,4-oxazepine, 2,2′-dihydroxy-1,1′-dinaphthyl, and Troger's base were purchased from Aldrich Chemical Co. (Gillingham, UK) and were the highest purity grade available. Buffer constituents and methanol used in MECC were of ANALAR grade (Sigma Chemical Co., Poole, Dorset, UK). Dansylated amino acids, mephenytoin, ephedrine, hexobarbital, phenobarbital, and metoprolol were also obtained from Sigma. Cromakalin, fenoldopam, and hydroxymephenytoin were prepared at Smith-Kline Beecham. Dodecyl β-D-glucopyranoside used in the initial step for the preparation of both **1** and **2** was synthesized by the method of Havlinova.[22] The synthetic procedures for the remaining steps are outlined below.

***n*-Dodecyl β-D-Glucopyranoside 4,6-Phenyl Phosphate.** To a stirred solution of *n*-dodecyl β-D-glucopyranoside (1.047 g, 3.0 mmol) in 20 mL of dry dichloromethane was added dry triethylamine (1.6 mL, 1.1 equiv). The solution was then cooled to 0 °C and phenyl dichlorophosphate (0.5 mL, 1.1 equiv) added; the reaction was then allowed to proceed at room temperature for 3 h. The mixture was concentrated in vacuo and the residue purified by flash column chromatography (SiO_2, CH_2Cl_2/MeOH, 90:10) to yield the two enantiomers of the phenyl phosphate as white needles: 0.869 g, 60.8%); R_f (CH_2Cl_2–MeOH, 90:10) 0.41; δ_H (250 MHz, $CDCl_3$) 7.4–7.1 (5 H, m, Ph), 4.55–4.15 (5 H, m, $H_{anomeric}$, $CHCH_2OP$ and CHOP), 3.87–3.67 (2 H, m, 2 CHOH), 3.59–3.41 (2 H, m, OCH_2R), 3.22 (1 H, s, OH), 2.04 (1 H, s, OH), 1.62–1.55 (2 H, m, OCH_2CH_2R), 1.4–1.15 (18 H, m, $OC_2H_4C_9H_{18}$-CH_3), 0.87 (3 H, t, *J* 6.5 Hz, CH_3); δ_C (250 MHz, $CDCl_3$) 150.01, 130.42, 130.06, 129.90, 125.79, 125.55, 120.28, 120.21, 119.62, 119.54 ($C_{aromatic}$, two isomers), 103.29, 103.14 ($C_{anomeric}$), 80.62, 80.52 (CHOP), 79.30, 73.35, 73.21, 70.83, 70.70 (OCH_2R), 69.06, 68.94 (CH_2OP), 66.06, 65.97, 31.90, 29.62, 29.55, 29.34, 25.85, 22.67, 14.10; δ_P (250 MHz, H decoupled, $CDCl_3$) −151.47, −154.06; δ_P (250 MHz, H coupled, $CDCl_3$), −151.48 (dd, *J* 39, 20 Hz), −154.07 (d, *J* 57.5 Hz).

***n*-Dodecyl β-D-Glucopyranoside 4,6-Hydrogen Phosphate, Sodium Salt (1).** *n*-Dodecyl β-D-glucopyranoside 4,6-phenyl phosphate (0.482 g, 1 mmol) was dissolved in 35 mL of a 1,4-dioxane/water mixture (70% dioxane), the pH of the solution adjusted to 10 using crushed NaOH, and the solution stirred overnight. The solution was concentrated in vacuo to approximately 10 mL and neutralized using 1 M HCl. The resulting solution was then lyophilized to yield a white powder, which was washed with ether and absolute ethanol to yield the phosphate **1** as flakes (0.532 g, 67.5%): δ_H (250 MHz, D_2O), 4.45 (1 H, d, *J* 7.5 Hz, $H_{anomeric}$), 4.3–4.0 (2 H, m, CH_2OP), 3.95 (1 H, t, *J* 9 Hz,CHOP), 3.85–3.5 (4 H, m, $CHCH_2OP$ and OCH_2R), 3.36 (1 H, t, *J* 9 Hz, H-2), 1.7–1.5 (2 H, m, OCH_2CH_2R), 1.4–1.1 (18 H, m, $OC_2H_4C_9H_{18}$-CH_3), 0.9–0.8 (3 H, m, CH_3); δ_C (250 MHz, D_2O) 102.72, 77.64, 72.84, 72.62, 69.99, 66.38, 31.40, 29.39, 29.30, 29.08, 28.97, 25.30, 22.05, 13.24; δ_P (250 MHz, H decoupled, D_2O) −142.01 (1 P, s); δ_P (250 MHz, H coupled; D_2O) −142.02 (1 P, d, *J* 49.5 Hz); $[\alpha]_D^{25°C}$ = −33.1 (1 mg/mL, water).

***n*-Dodecyl β-D-Glucopyranoside 6-Hydrogen Sulfate, Monosodium Salt (2).** Sulfur trioxide pyridine complex (1.1 g, 6.92 mmol) was added to a stirred solution of *n*-dodecyl β-D-glucopyranoside (2.09 g, 6 mmol) in 20 mL of dry pyridine under argon at 0 °C. After 2 h at 0 °C, the reaction was stirred overnight at room temperature. The mixture was concentrated in vacuo, the residue was purified by flash column chromatography (SiO_2, $CHCl_3$/MeOH, 90:10) and then dissolved in water, the pH was raised to 9 using crushed NaOH, the resulting precipitate was filtered off, and the liquid was lyophilized to yield monosulfate **2** as white flakes (1.87 g, 69.4%): R_f ($CHCl_3$/MeOH, 90:10) 0.04; δ_H (250 MHz, D_2O), 4.33 (1 H, d, *J* 12.5 Hz, $H_{anomeric}$), 4.27–4.06 (2 H, m, CH_2OS), 3.84–3.66 (1 H, m, $OCH_AH_BC_{11}H_{23}$), 3.62–3.28 (4 H, m, 4 CH), 3.23–3.16 (1 H, m, $OCH_AH_BC_{11}H_{23}$), 1.60–1.50 (2 H, m, $OCH_2CH_2C_{10}H_{21}$), 1.21–1.15 (18 H, m, $OC_2H_4C_9H_{18}CH_3$), 0.83–0.74 (3 H, m, CH_3); δ_C (400 MHz, D_2O) 101.38 ($C_{anomeric}$), 74.25 (CHOH), 72.44 (CHOH), 71.71 (CHOH), 69.29 ($OCH_2C_{11}H_{23}$), 67.63 (CHOH), 65.21 (CH_2OS), 30.65, 28.60, 28.51, 28.23, 28.18, 27.93, 24.40, 21.32, 12.55; *m /z* (negative ion FAB) 427 (100, M − Na^+), 97 (72, HSO_4^-); $[\alpha]_D^{25°C}$ = −23.1(1 mg/mL, water).

Equipment. All MECC separations were performed on a Beckman P/ACE Model 2100. The dimensions of the fused silica capillary were 57 cm × 50 μm i.d. (effective length, 50 cm). The running buffer consisted of 30 mM sodium dihydrogen phosphate, 10 mM boric acid, and either 40 mM of **1** or 45 mM of **2** adjusted to pH 8.0 using dilute NaOH. Methanol, 0–10% was also added. The separation voltage was either 20 or 28 kV at a constant

(20) Dobashi, A.; Ono, T.; Hara, S.; Yamaguchi, J. *Anal. Chem.* **1989**, *61*, 1984–1986.
(21) Smith, J. T.; El Rassi, Z. *J. Microcolumn Sep.* **1994**, *6*, 127–138.
(22) Havlinova, B; Kosik, M.; Kovak, P.; Blazej, A. *Tenside, Surfactants, Deterg.* **1978**, *5*, 72–74.

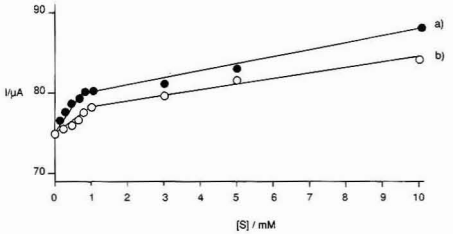


Figure 1. Variation of current with concentration of (a) **1** and (b) **2**. 25 kV was applied to a capillary 57 cm in total length and 50 μm i.d.

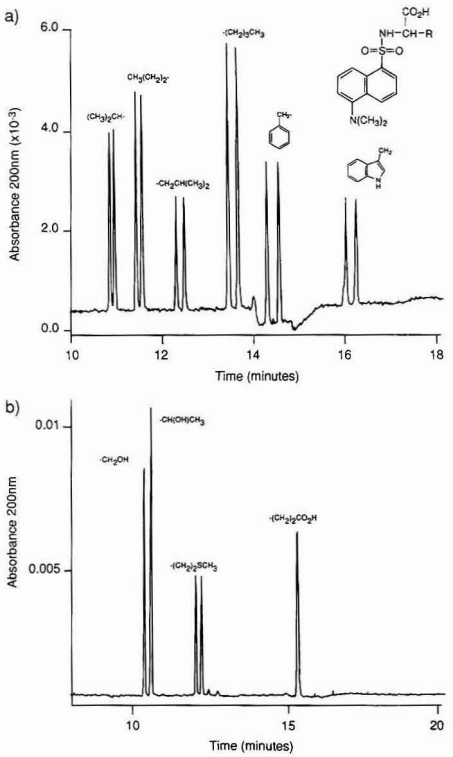


Figure 2. Electropherograms of racemic mixtures of dansylated amino acids. Conditions: buffer, phosphate/borate (pH 8) containing **1** (45 mM); capillary, 57 cm in length (50 cm to the detector) and 50 μm i.d.; applied voltage, 20 kV; temperature, 25 °C.

temperature of 30 °C. Samples were monitored by UV at either 214 or 254 nm and injected as solutions in a 90:10 methanol/water mixture by applying hydrodynamic pressure (0.5 psi) for 1 s.

RESULTS AND DISCUSSION

The use of SDS, above its critical micelle concentration, is very frequently the method of choice in MECC for the separation of

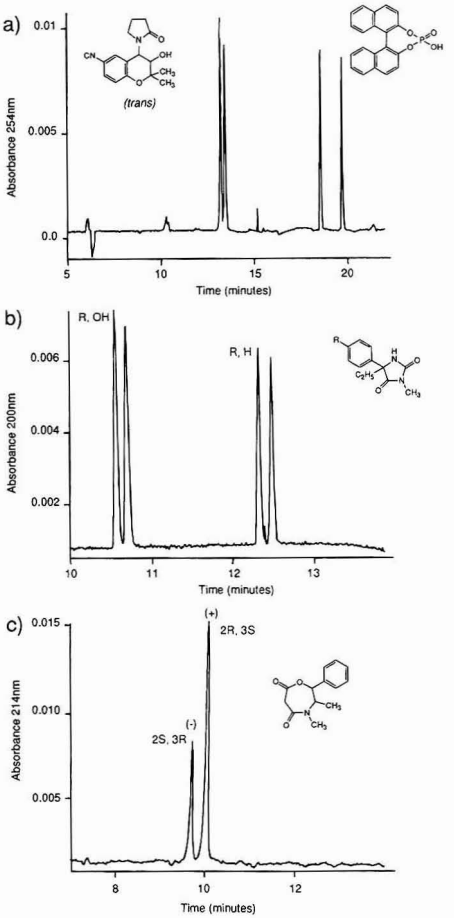


Figure 3. Electropherograms showing the resolution of the enantiomers of (a) cromakalin and 1,1′-dinaphthyl-2,2′-diyl hydrogen phosphate, (b) mephenytoin and hydroxymephenytoin, and (c) 3,4-dimethyl-5,7-dioxo-2-phenyperhydro-1,4-oxazepine. Conditions are the same as in Figure 2.

both ionic and nonionic analytes. Solute selectivity results from partitioning between the micellar phase (moving toward the detector under the influence of electroosmotic flow) and the surrounding aqueous medium. As this anionic surfactant is achiral it cannot be used alone in MECC to achieve resolution of enantiomeric species.

Molecules containing chiral glucopyranoside residues have been added to SDS to create a stereoselective environment. For instance, the addition of cyclodextrins[5,8] (nonionic cyclic oligosaccharides made up of D-(+)-glucopyranose units linked by α-(1,4) bonds) to this surfactant has been found to increase the selectivity of this MECC system. Triterpene glucosides such as glycyrrhizic acid (a tricarboxylic acid) and β-escin (a dicarboxylic acid) have also been used in mixed micellar systems with SDS to induce

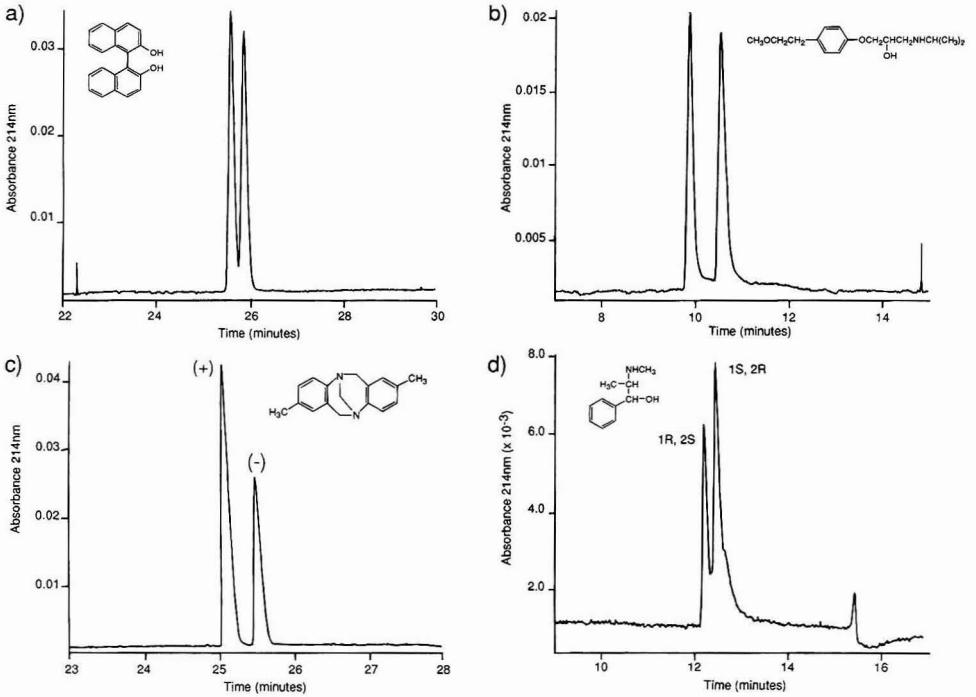


Figure 4. Separation of the enantiomers of (a) 2,2′-dihydroxy-1,1′-dinaphthyl, (b) metoprolol, (c)Troger's base, and (d) ephedrine, using 10% methanol in the buffer which contained **1** (45 mM). Conditions are the same as for Figures 2 and 3 except that the voltage is 28 kV.

chiral discrimination.[23] In all these cases the number of parameters to be considered for a successful chiral separation is larger than when a chiral surfactant is used alone.

We designed β-D-glucopyranoside anionic surfactants **1** and **2** as chiral mobile phase additives for MECC. These two molecules are very similar in structure: both contain a D-glucose residue bonded to a long-chain hydrocarbon group via a glycosidic linkage. The anionic character of these molecules is due to replacement of the hydroxy group at the 6-position in the glucose ring by either a sulfate or a phosphate group, respectively. Linking the phosphate group in **1** to the hydroxy group in the 4-position of the glucose ring results in a more rigid bicyclic structure, and a dialkyl phosphate with a low pK_a in the range of 1–2 comparable with that of the sulfate group in **2** or in SDS.

The critical micelle concentration (cmc) of these two surfactants was determined in phosphate/borate buffer (pH 8) by measuring current at different concentrations. The mobility of the single molecules in an electric field is expected to differ from that of their aggregated (micellar) forms. A break in the current–concentration profile can therefore be related to cmc. Every point shown in Figure 1 is an average of two determinations. cmc values for **1** and **2** determined by this method were found to be about 0.5 and 1.0 mM, respectively. These values are ~1 order of magnitude lower than that determined for SDS by using either the same method or spectrofluorometric methods[24,25] under similar pH and buffer conditions.

The sodium salts of both **1** and **2** are soluble in water at concentrations above 100 mM. The absence of a chromophore makes these compounds ideal for use in capillary electrophoresis and allows direct detection at wavelengths as low as 200 nm. To test the potential of these surfactants as chiral selectors, when used above their critical micelle concentration, we have used capillary electrophoresis in the MECC mode to analyze enantiomeric mixtures of a number of solutes varying in structural complexity, hydrophobicity, and ionic character. The methodology developed for these micellar separations is simple and only involves the addition of either **1** or **2** to a buffer at pH 8 . The concentration of surfactant varied between 30 and 50 mM. A cosolvent such as methanol was at times added to enhance enantiomeric resolution. Unlike the case of a number of other surfactant chiral selectors, the use of a comicellar system with an achiral surfactant such as SDS was not necessary.

Typical electropherograms obtained using either **1** or **2** as the micellar constituent are shown in Figures 2–5. Structures of the chiral compounds analyzed have been included in these figures. From our experience to date with these surfactants it appears that **1** has the greater potential as a chiral selector. This may be due

(23) Ishihama,Y.; Terabe, S. *J. Liq. Chromatogr.* **1993**, *16*, 933–944.

(24) Camilleri, P.; Okafo, G. N. *J. Chem. Soc., Chem. Commun.* **1992**, 530–532.

(25) Brito, R. M. M.; Vaz, W. L. C. *Anal. Biochem.* **1986**, *152*, 250–261.

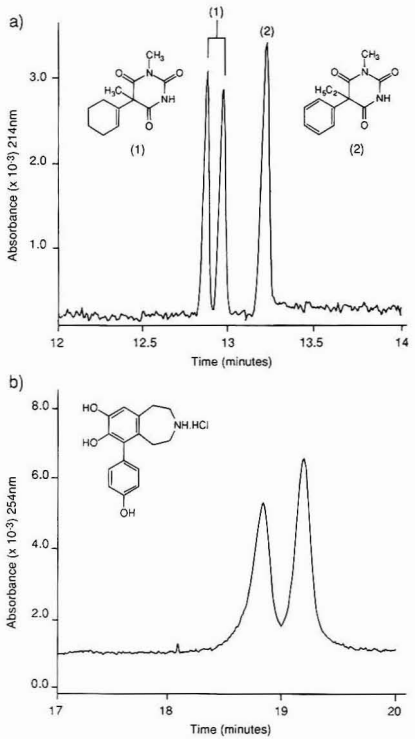


Figure 5. Analysis of racemates of (a) hexobarbital and phenobarbital and (b) fenoldopam, using **2** (30 mM) in the separation buffer (pH 8). The remaining conditions are the same as in Figure 2.

to the fixed orientation of the phosphate substituent with respect to the glucose ring. The orientation of the sulfate group in **2** is more variable. Nevertheless it will be shown that when it proves impossible to resolve certain mixtures of enantiomers with **1**, chiral selectivity may be achieved successfully when **2** is included in the mobile phase. The duration of analysis is less than 30 min for all the pairs of enantiomers successfully resolved. Moreover, most of the enantiomeric separations achieved in the present study have been reported previously for a variety of other chiral selectors. Thus, Mayer and Schurig[26] recently compared the separation of enantiomers of a number of analytes using native β- and γ-cyclodextrin, permethylated β-cyclodextrin, and sulfonated β-cyclodextrin. These authors found big variations in the chiral selectivity of these cyclic oligosaccharides. The wide applicability of **1** and **2** as chiral selectors may be due to the flexible nature of the corresponding micelles compared to the more rigid structure of cyclodextrins.

The baseline resolution of the enantiomers of a mixture of seven dansylated D,L-amino acids, using **1** as the chiral selector, is shown in Figure 2a. Under the pH conditions used, these derivatives are negatively charged. As expected in a micellar system, migration of the pairs of enantiomers is related to their respective hydrophobicity. Thus, dansylated valine migrates fastest and the tryptophan derivative slowest. It is also interesting that, for the two pairs of amino acids valine/norvaline and leucine/norleucine, branching in the alkyl group leads to faster migration. It is well-known that secondary and tertiary alkyl groups contribute to a lesser extent to hydrophobicity compared to their straight-chain isomers.[27] The excellent resolution of these dansylated amino acids may also be related to differences in charge density.

Figure 2b shows the migration behavior of racemic mixtures of another four dansylated amino acids. Of these only the enantiomers of the methionine derivative can be resolved, under the same conditions as in Figure 2a. The lack of resolution in the case of dansylated D,L-serine and D,L-threonine is probably due to the more hydrophilic nature of these molecules and to adverse interaction of the hydroxy group with the micellar selector. The long migration time of dansylated D,L-glutamic acid and the failure to resolve the enantiomers of this molecule is a strong indication of electrostatic repulsion between this dianionic species and the micellar phase. This molecule is apparently migrating under free zone capillary electrophoresis conditions. It was not possible to resolve the enantiomers of the four dansylated amino acids in Figure 2b and racemic mixtures of dansylated D,L-valine and D,L-norvaline using surfactant **2** as the chiral selector.

The potential for chiral selectivity of **1** is further demonstrated in the electropherograms in Figure 3, which shows the resolution of enantiomeric mixtures related to another acidic analyte and four neutral solutes. Racemic samples were analyzed in the case of cromakalin, 1,1′-dinaphthyl-2,2′-diyl hydrogen phosphate, and the anti-convulsant drug mephenytoin and its principal metabolite hydroxymephenytoin. For 3,4-dimethyl-5,7-dioxo-2-phenylperhydro-1,4-oxazepine an approximate 2:1 mixture of the 2*R*,3*S* to the 2*S*,3*R* enantiomers was used. Baseline separation was obtained in almost all these mixtures. Although the inclusion of **2** still produced excellent resolution in the case of hydroxymephenetoin and the binaphthyl and oxazepine derivatives, the rest of the racemates in Figure 3 were not resolved by this surfactant.

Figure 4 shows the electropherograms of enatiomeric mixtures of another four compounds (2,2′-dihydroxy-1,1′-dinaphthyl, metoprolol, Troger's base, and ephedrine), which could only be resolved by using **1** as a mobile phase additive. For optimum separation of these enantiomers, the addition of 10% methanol was necessary in all cases. Besides improving the solubility of these solutes, the presence of this organic modifier reduced migration time by altering electroosmotic flow and the affinity characteristics of the micelle for analytes.[28] Although it is difficult to predict the basicity and charge of molecules in a micellar medium, the presence of relatively small amounts of methanol may increase the concentration of neutral species in the surrounding aqueous phase, thus favoring interaction with the chiral micelle.

The enantiomeric mixtures of the two solutes, hexobarbital and fenoldopam, could only be resolved when **2** was added to the separation buffer (Figure 5). The electropherogram in Figure 5a shows that chiral resolution is very sensitive to structure, resolving the enantiomers of hexo- and not phenobarbital. Moreover, resolution may also be related to some interaction specific to the sulfate group of this surfactant. It has been reported that the addition of D-camphor-10-sulfonate to a mixture of

(26) Mayer, S.; Schurig, V. *Electrophoresis* **1994**, *15*, 835–841.

(27) Hansch, C; Leo, A. In *Substituent Constants for Correlation Analysis in Chemistry and Biology*; John Wiley & Sons: New York, 1979.

(28) Nielsen, K. R.; Foley, J. P. In *Capillary Electrophoresis: Theory and Practice*; Camilleri, P., Ed.; CRC Press: Boca Raton, FL, 1993; Chapter 4.

γ-cyclodextrin and SDS greatly improves the resolution of the enantiomers of thiopental and pentobarbital.

The "tailing" characteristics of the electropherogram in Figure 5b may be due to the abundance of hydrogen bonding in fenoldopam. A similar situation is observed when the enantiomers of the latter compound are resolved by using HPLC with a cellulose based chiral stationary phase.[29]

CONCLUSION

The two anionic glucopyranoside surfactants reported in this paper appear to be effective chiral selectors for the MECC resolution of a variety of enantiomeric mixtures. Other advantages of these molecules are their high solubility in aqueous media, low cmc, and low absorbance at wavelengths above 200 nm. The discovery of the substantial chiral selectivity of this class of surfactants opens up new opportunities in the screening of other sugar-based molecules where interaction with chiral solutes can be enhanced or modified by altering the nature of the negatively charged carbohydrate "head" and/or the length of hydrocarbon "tail". Unlike naturally occurring surfactants, in particular cyclodextrins and bile salts, which are available in one stereoisomeric form, **1** and **2** can be readily synthesized in both the D- and L-forms. This may be analytically desirable, especially when an accurate estimate of a low-level enantiomer impurity is needed, but this follows the main antipode. We are actively carrying out a synthesis program aimed at preparing other molecules with broad and complementary selective properties.

Received for review August 29, 1994. Accepted October 3, 1994.[⊗]

(29) Camilleri, P.; Dyke, C. A.; Paknoham, S. J.; Senior, L. A. *J. Chromatogr.* **1990**, *498*, 414–416.

[⊗] Abstract published in *Advance ACS Abstracts*, November 1, 1994.

Anal. Chem. **1994,** *66,* 4127–4132

Precolumn Reactions with Electrophoretic Analysis Integrated on a Microchip

Stephen C. Jacobson, Roland Hergenröder, Alvin W. Moore, Jr., and J. Michael Ramsey*

Chemical and Analytical Sciences Division, Oak Ridge National Laboratory, P.O. Box 2008, Building 4500S, MS 6142, Oak Ridge, Tennessee 37831-6142

A glass microchip was constructed to perform chemical reactions and capillary electrophoresis sequentially. The channel manifold on the glass substrate was fabricated using standard photolithographic, etching, and deposition techniques. The microchip has a reaction chamber with a 1 nL reaction volume and a separation column with a 15.4 mm separation length. Electrical control of the buffer, analyte, and reagent streams made possible the precise manipulation of the fluids within the channel manifold. The microchip was operated under a continuous reaction mode with gated injections to introduce the reaction product onto the separation column with high reproducibility (<1.8% rsd in peak area). The reaction and separation performances were evaluated by reacting amino acids with *o*-phthaldialdehyde to generate a fluorescent product which was detected by laser-induced fluorescence. Control of the reaction and separation conditions was sufficient to measure reaction kinetics and variation of detection limits with reaction time. Half-times of reaction of 5.1 and 6.2 s and detection limits of 0.55 and 0.83 fmol were measured for arginine and glycine, respectively.

The microfabrication of analytical instrumentation will potentially enable the laboratory to be transported to the samples rather than vice versa. Miniature chemical instrumentation can be based on conventional laboratory approaches to chemical measurement problems. Many laboratory-based procedures require sample manipulation prior to the actual measurement, and many analyses are fully automated to circumvent operator bias. Similarly, a portable instrument should have these sample preparatory steps incorporated into the design and function of the instrument. In addition, micromachined chemical instruments as opposed to single-analyte chemical sensors should be able to identify and quantify all members of a desired class of compounds using a single device. The approach taken is to micromachine a channel manifold in a monolithic device that includes all desired fluid manipulation for complete chemical analysis. Chemical separation techniques including capillary electrophoresis,[1–6] free-flow electrophoresis,[7] open channel electrochromatography,[8] and capillary electrophoresis with postcolumn derivatization[9] have been demonstrated using microfabricated devices.

To demonstrate a reactor/analyzer microchip, we chose the relatively simple reaction of amino acids with *o*-phthaldialdehyde (OPA), which yields a fluorescent product.[10] For capillary electrophoresis, both pre- and postseparation labeling using OPA have been studied.[11] The reaction is moderately fast (a half-time of reaction for alanine at room temperature of ≈4 s [12]), but the fluorescent product can be short lived (≈10 min for glycine[13]). This reaction is fast enough to perform postcolumn labeling when the analysis time is long compared to the reaction time, but as analysis times decrease, the postcolumn labeling becomes less attractive. Both detection limits and separation efficiency suffer due to "slow" product formation when high-speed analysis is performed.[9] Analysis times on microchip electrophoresis devices can be significantly faster than the OPA reaction times; separation times for microchip electrophoresis as short as 150 ms have been reported.[6] Precolumn derivatization becomes the desired method if the electrophoretic analysis can be performed before the product degrades and without hindering the quality of the separation.

In this paper, a simple channel manifold was fabricated on a glass microchip to perform on-line precolumn reactions coupled with electrophoretic analysis of the reaction products. Here, the reactor is operated continuously with small aliquots introduced periodically onto the separation column to be analyzed. The operation of the microchip consists of three elements: derivatization of the amino acids with OPA, injection of the sample onto the separation column, and separation/detection of the components of the reactor effluent. Each of these elements is evaluated.

EXPERIMENTAL SECTION

The microchips were fabricated using standard photolithographic, wet chemical etching and bonding techniques.[14] A

(1) Harrison, D. J.; Manz, A.; Fan, Z.; Lüdi, H.; Widmer, H. M. *Anal. Chem.* **1992,** *64,* 1926.
(2) Manz, A.; Harrison, J.; Verpoorte, E. M. J.; Fettinger, J. C.; Paulus. A.; Lüdi, H.; Widmer. H. M. *J. Chromatogr.* **1992,** *593,* 253.
(3) Seiler, K.; Harrison, D. J.; Manz, A. *Anal. Chem.* **1993,** *65,* 1481.
(4) Harrison, D. J.; Fluri, K.; Seiler, K.; Fan, Z.; Effenhauser, C. S.; Manz, A. *Science* **1993,** *261,* 895.
(5) Jacobson, S. C.; Hergenröder, R.; Koutny, L. B.; Warmack, R. J.; Ramsey, J. M. *Anal. Chem.* **1994,** *66,* 1107.
(6) Jacobson, S. C.; Hergenröder, R.; Koutny, L. B.; Ramsey, J. M. *Anal. Chem.* **1994,** *66,* 1114.
(7) Raymond, D. E.; Manz, A.; Widmer, H. M. *Anal. Chem.* **1994,** *66,* 2858.
(8) Jacobson, S. C.; Hergenröder, R.; Koutny, L. B.; Ramsey, J. M. *Anal. Chem.* **1994,** *66,* 2369.
(9) Jacobson, S. C.; Koutny, L. B.; Hergenröder, R.; Moore, A. W., Jr., Ramsey, J. M. *Anal. Chem.* **1994,** *66,* 3472.
(10) Roth, M. *Anal. Chem.* **1971,** *43,* 880.
(11) For example: Rose, D. J.; Jorgenson, J. W. *J. Chromatogr.* **1988,** *447,* 117. Pentoney, S. L., Jr.; Huang, X.; Burgi, D. S.; Zare, R. N. *Anal. Chem.* **1988,** *60,* 2625. Nickerson, B.; Jorgenson, J. W. *J. Chromatogr.* **1989,** *480,* 157. Albin, M.; Weinberger, R.; Sapp, E.; Moring, S. *Anal. Chem.* **1991,** *63,* 417.
(12) Butchner, E. C.; Lowry, O. H. *Anal. Biochem.* **1976,** *76,* 502.
(13) Lindroth, P.; Mopper, K. *Anal. Chem.* **1979,** *51,* 1667.
(14) For example: Ko, W. H.; Suminto, J. T. In *Sensors*; Gopel, W., Hasse, J., Zemmel, J. N., Eds.; VCH: Weinhein, Germany, 1989; Vol. 1, pp 107–168.

0003-2700/94/0366-4127$04.50/0 © 1994 American Chemical Society

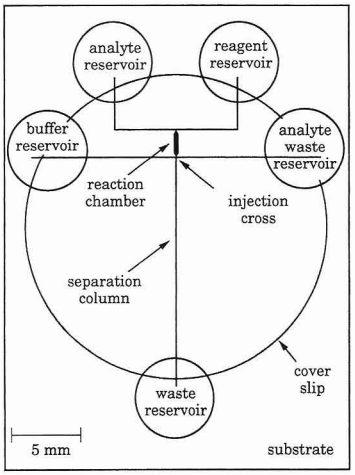
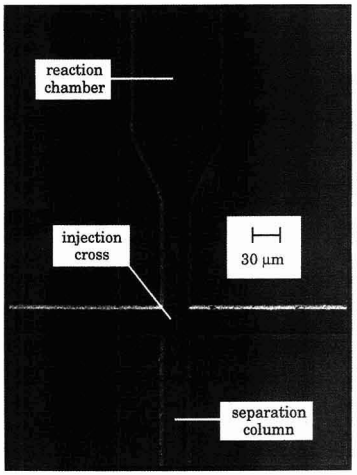


Figure 1. Schematic of the microchip with integrated precolumn reactor. The reaction chamber is 2 mm long, and the separation column is 15.4 mm long.

photomask was fabricated by sputtering chrome (50 nm) onto a glass slide and ablating the microchip design (Figure 1) into the chrome film using a CAD/CAM excimer laser machining system (ArF, 193 nm; Resonetics, Inc.). The column design was then transferred onto the substrates using a positive photoresist (Shipley 1811). The channels were etched into the substrate in a dilute, stirred HF/NH_4F bath. To form the closed network of channels, a cover plate was bonded to the substrate over the etched channels by use of a direct bonding technique.[5] Cylindrical glass reservoirs were affixed on the substrate using epoxy. Platinum electrodes provided electrical contact from the power supply (Spellman CZE1000R) to the solutions in the reservoirs.

The reaction chamber was designed to be wider than the separation column to give lower electric field strengths in the reaction chamber and thus longer residence times for the reagents. Figure 2a shows a scanning electron microscope (SEM) image of the injection cross and the lower portion of the reaction chamber prior to bonding of the cover plate. The image has the same orientation as the microchip schematic in Figure 1. The reaction chamber is 96 μm wide at half-depth and 6.2 μm deep, and the separation column is 31 μm wide at half-depth and 6.2 μm deep. Figure 2b shows an SEM image of the cross section of the separation channel. The microchip was broken perpendicular to the separation column $\approx$1 mm downstream from the injection cross. The isotropic etch of the glass substrate, i.e., uniform etch in all directions, is evident in the trapezoidal geometry of the cross section.

Column performance and separations were monitored on-microchip using a single-point detection scheme via laser-induced fluorescence (LIF). An argon ion laser (351.1 nm, 10 mW; Coherent Innova 90) was used for excitation and focused to a spot onto the microchip using a lens (100 mm focal length). The fluorescence signal was collected using a 20$\times$ objective lens, followed by spatial filtering (0.6 mm diameter pinhole) and spectral filtering (440 nm bandpass, 10 nm bandwidth), and measured using a photomultiplier tube (PMT; Oriel 77340). The schematic



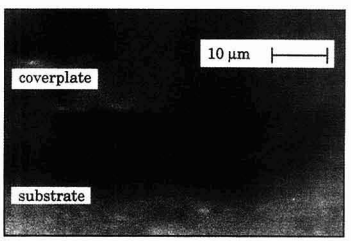


Figure 2. (a, top) Scanning electron microscope (SEM) image of injection cross. The broader channel is the lower portion of the reaction chamber. The separation channel is 6.2 μm deep and 31 μm wide, and the reaction chamber is 6.2 μm deep and 96 μm wide. The SEM is in the same orientation as Figure 1. (b, bottom) SEM image of cross section of separation column after bonding of coverplate to the substrate.

in Figure 3a shows the data acquisition/voltage switching apparatus, which is computer controlled using programs written in-house in Labview 3.0 (National Instruments). The compounds used for the experiments were arginine (0.48 mM), glycine (0.58 mM), and *o*-phthaldialdehyde (5.1 mM; Sigma Chemical Co.). The buffer in all of the reservoirs was 20 mM sodium tetraborate with 2% (v/v) methanol and 0.5% (v/v) 2-mercaptoethanol. 2-Mercaptoethanol is added to the buffer as a reducing agent for the derivatization reaction.[10]

Figure 3b shows the ratio of the potentials at each of the reservoirs for a given potential applied to the system. This configuration allowed the lowest potential drop across the reaction chamber (25 V/cm for 1.0 kV applied to the microchip) and the highest across the separation column (300 V/cm for 1.0 kV applied to the microchip) without significant bleeding of the product into the separation column. The voltage divider used to establish the potentials applied to each of the reservoirs had a total resistance of 100 with 10 MΩ divisions. The sample and reagent are electroosmotically pumped into the reaction chamber with a volumetric ratio of 1:1.06. Therefore, the solutions from the analyte and reagent reservoirs are diluted by a factor of $\approx$2. Buffer

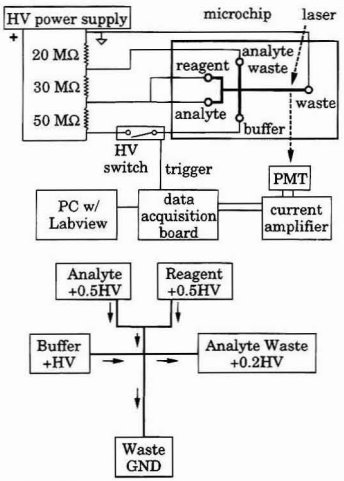


Figure 3. (a, top) Diagram of the high-voltage switching apparatus and detection/data acquisition system. (b, bottom) Block diagram of flow pattern for precolumn reactor microchip with the relative potentials applied at each reservoir (arrows depict direction of flow).

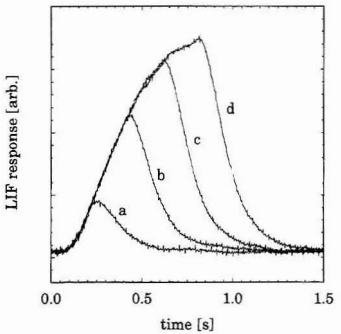


Figure 4. Series of injection profiles for injection times of (a) 0.2, (b) 0.4, (c) 0.6, and (d) 0.8 s with E_{inj} = 0.6 kV/cm and L_{obs} = 0.05 mm.

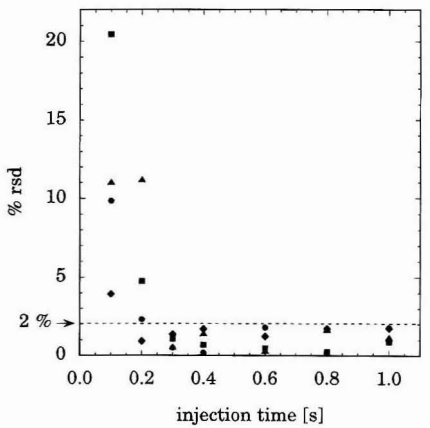


Figure 5. Reproducibility of injections as percent relative standard deviation (% rsd) of the peak area with injection time for arginine (◆) and glycine (●) at E_{inj} = 1.2 kV/cm and for arginine (▲) and glycine (■) at E_{inj} = 0.6 kV/cm with L_{obs} = 0.05 mm. Dashed line represents 2% rsd.

was simultaneously pumped by electroosmosis from the buffer reservoir toward the waste and analyte waste reservoirs. This buffer stream prevents the newly formed product from bleeding into the separation column. A gated injection scheme, described previously,[9] is used to inject effluent from the reaction chamber onto the separation column. The potential at the buffer reservoir is simply floated (opening of the high-voltage switch in Figure 3a) for a brief period of time (0.1–1.0 s), and sample migrates into the separation column as in an electrokinetic injection.[15] To break off the injection plug, the potential at the buffer reservoir is reapplied (closing of the high-voltage switch in Figure 3a). The length of the injection plug is a function of both the time of the injection and the electric field strength. With this configuration of applied potentials, the reaction of the amino acids with the OPA continuously generates fresh product to be analyzed.

RESULTS AND DISCUSSION

Fluid manipulation, including sample injections, is performed by simply controlling the potentials applied to the reservoirs; i.e., no valves or pumps are required. This allows reagents to be mixed accurately and samples to be injected reproducibly onto the separation column. Using the gated injection scheme described above, Figure 4 shows four injections of glycine derivatized with OPA for increasing injection times of 0.2, 0.4, 0.6, and 0.8 s with an injection field strength of 0.6 kV/cm. The injection field strength is the electric field strength in the separation column during the injection; i.e., the high-voltage switch in Figure 3a is open. Similar profiles were obtained for arginine. The injections were observed in the separation column 0.05 mm downstream from the injection cross using the single-point detection scheme. The peak fronts coincide as expected, and the durations of the injection profiles correspond to the injection times.

A significant shortcoming of many capillary electrophoresis experiments has been the poor reproducibility of the injections. Here, because the microchip injection process is computer controlled, and the injection process involves the opening of a single high-voltage switch, the injections can be accurately timed events. Figure 5 shows the reproducibility of the amount injected (percent relative standard deviation, % rsd, for the integrated areas of the peaks) for both arginine and glycine at injection field strengths of 0.6 and 1.2 kV/cm and injection times ranging from 0.1 to 1.0 s. For injection times of ≥0.3 s, the percent relative standard deviation is below 1.8%. This is comparable to reported values for commercial, automated capillary electrophoresis instruments.[16] However, injections made on the microchip are ≈100 times smaller in volume, e.g., 100 pL on the microchip versus 10 nL on a commercial instrument. Part of this fluctuation is due to the stability of the laser, which is ≈0.6%. For injection times of

(15) Jorgenson, J. W.; Lukacs, K. D. *Anal. Chem.* **1981**, *53*, 1298.

(16) For example, Hewlett-Packard reports 1–2% rsd for peak area measurements.

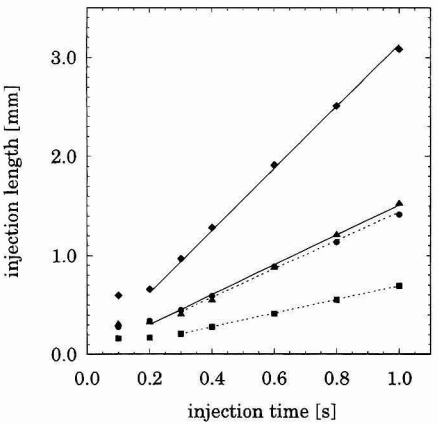


Figure 6. Variation of injection widths with injection time for arginine (◆) and glycine (●) at E_{inj} = 1.2 kV/cm and for arginine (▲) and glycine (■) at E_{inj} = 0.6 kV/cm with L_{obs} = 0.05 mm. Lines represent best fit for injection times of ≥0.2 s for arginine and ≥0.3 s for glycine.

≥0.3 s, the error appears to be independent of the compound injected and the injection field strength.

In Figure 6, the injection plug lengths at half-height are plotted versus the injection time. For injection times of ≥0.2 s for arginine and ≥0.3 s for glycine at the two selected injection field strengths, the lengths of the injected plugs are a linear function of the injection times and injection field strengths. Because the injection is electrophoretically biased, and arginine has a higher electrophoretic mobility than glycine, injection widths are linear at shorter injection times for arginine. The injection widths are not proportional to the injection times for shorter injection times. The injection cross region has a finite width, and once filled with analyte, the area must be swept clean after the injection. Lines with a *y*-intercept equal to zero are fitted to the data for injection times of ≥0.2 s for arginine and ≥0.3 s for glycine. The slopes of the lines are 3.13 and 1.51 mm/s for arginine with injection field strengths of 1.2 and 0.6 kV/cm, respectively, and 1.44 and 0.692 mm/s for glycine with injection field strengths of 1.2 and 0.6 kV/cm, respectively. For both arginine and glycine, the slopes for the injection field strength of 1.2 kV/cm are 2 times greater than at 0.6 kV/cm. For the experiments described below, the injector was operated in the reproducible (Figure 5) and linear ranges (Figure 6), and the injection times were scaled to give comparable peak widths and, thus, injection volumes for separations performed at different separation field strengths. The electrophoretic bias in the injections requires the injection time to be long enough to inject accurately the compound with the lowest electrophoretic mobility, e.g., glycine. This, in turn, means compounds with a higher electrophoretic mobility, e.g., arginine, are injected in relative excess.

Figure 7 shows the overlay of three electrophoretic separations of arginine and glycine after on-microchip precolumn derivatization with OPA with a separation field strength of 1.8 kV/cm and a separation length of 10 mm. The separation field strength is the electric field strength in the separation column during the separation; i.e., the high voltage switch in Figure 3a is closed. The field strength in the reactor is 150 V/cm. The reaction times

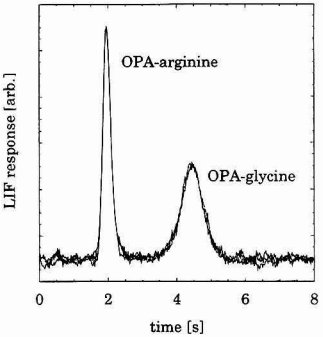


Figure 7. Overlay of three electropherograms of arginine and glycine using precolumn derivatization with *o*-phthaldialdehyde with E_{sep} = 1.8 kV/cm and L_{sep} = 10 mm.

for the analytes are inversely related to their mobilities; e.g., for arginine the reaction time is 4.1 s and for glycine the reaction time is 8.9 s. The volumes of the injected plugs were 150 and 71 pL for arginine and glycine, respectively, which correspond to 35 and 20 fmol of the amino acids injected onto the separation column. The gated injector allows rapid sequential injections to be made. In this particular case, an analysis could be performed every 4 s. The observed electrophoretic mobilities for the compounds are determined by a linear fit to the variation of the linear velocity with the separation field strength. The slopes were 29.1 and 13.3 $mm^2/(kV \cdot s)$ for arginine and glycine, respectively. No evidence of Joule heating was observed, as indicated by the linearity of the velocity versus field strength data. A linear fit produced correlation coefficients of 0.999 for arginine and 0.996 for glycine for separation field strengths from 0.2 to 2.0 kV/cm.

With increasing potentials applied to the microchip, the field strengths in the reaction chamber and separation column increase. This leads to shorter residence times of the reactants in the reaction chamber and faster analysis times for the products. By varying the potentials applied to the microchip, the reaction kinetics can be studied. The variation in amount of product generated with reaction time is plotted in Figure 8. The response is the integrated area of the peak corrected for the residence time in the detector observation window and photobleaching of the product (discussed below). The offset between the data for the arginine and the glycine in Figure 8 is due primarily to the difference in the amounts injected, i.e., different electrophoretic mobilities, for the amino acids. A 10-fold excess of OPA was used to obtain pseudo-first-order reaction conditions. The slopes of the lines fitted to the data correspond to the rates of the derivatization reaction. The slopes are 0.13 s^{-1} for arginine and 0.11 s^{-1} for glycine, corresponding to half-times of reaction of 5.1 and 6.2 s, respectively. These half-times of reaction are comparable to the 4 s previously reported for alanine.[12] We have found no previously reported data for arginine or glycine.

The reaction time varies with the potential applied to the microchip. For lower field strengths in the reaction chamber, the reaction time is longer and should yield more product and larger signals. In Figure 9, the mass detection limits (signal-to-noise ratio (S/N) equal to 2) are estimated for a series of reaction times for arginine and glycine. For longer reaction times, the mass detection limits improve as expected. Detection limits of 0.55 fmol

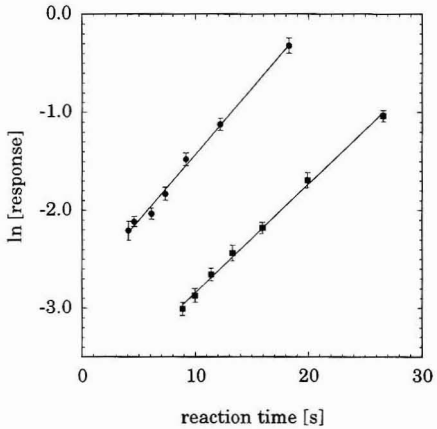


Figure 8. Variation of product formation (ln [response]) with reaction time for arginine (●) and glycine (■) derivatized with *o*-phthaldialdehyde. Lines represent linear fits. Error bars are $\pm\sigma$ for three runs.

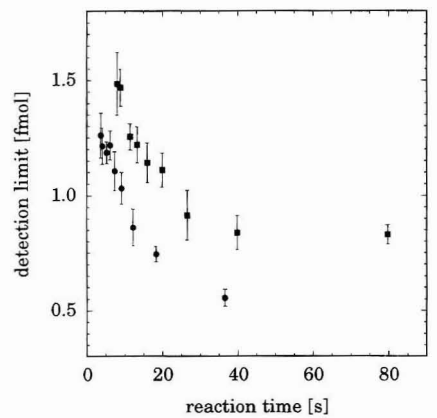


Figure 9. Variation of detection limits (S/N = 2) with reaction time for arginine (●) and glycine (■) derivatized with *o*-phthaldialdehyde. Error bars are $\pm\sigma$ for three runs.

for arginine and 0.83 fmol for glycine are reached for reaction times of 36 and 80 s, respectively. The difference in detection limits between arginine and glycine is assumed to be differences in relative fluorescence and in separation efficiency. The source of the limiting background for this experiment is fluorescence from the glass substrate. Detection limits could be improved by using fused silica substrates, which would minimize the background fluorescence.

Photobleaching can affect quantitative results in fluorescence measurements. The degree of photobleaching was estimated by determining the photochemical lifetimes of the fluorescent products. The fluorescence signal was measured as a function of the residence time in the detector observation window by running a frontal electropherogram of the individual products. The fluorescence signal, S, for the continuous stream measurements is

$$S = kI\sigma_F N e^{-\Delta t/\tau} \quad (1)$$

where k is a geometrical factor, I is the intensity of the laser ($\approx$400 W/cm^2), σ_F is the fluorescence cross section, N is the number of molecules in the detection volume, Δt is the detector residence time (0.01−0.1 s for arginine and 0.02−0.25 s for glycine), and τ is the photochemical lifetime. k, I, σ_F, and N are constant for the experiments. The residence time of the product in the detection volume is known, and thus, the photochemical lifetime, τ, of the reaction product can be estimated by use of a linear fit of the variation of ln S with Δt. The photochemical lifetimes are 51 ms for arginine and 58 ms for glycine under these experimental conditions. The products are known to have poor stability,[13] and not surprisingly, the photochemical lifetimes are short compared to the longer observation times. Accurate quantitative measurements must take account of the photobleaching effect.

To improve the peak capacity of the separation, the band dispersion needs to be minimized. For electrophoretic separations the total plate height can be expressed as

$$H_{total} = H_{inj} + H_{det} + H_{diff} \quad (2)$$

where H_{inj}, H_{det}, and H_{diff} are the contributions to the plate height from the injection plug length, the detector observation length, and axial diffusion, respectively. The contributions from the injection plug length and the detector observation length are time independent, and the contribution to the plate height from axial diffusion is time dependent. Effects such as Joule heating are not considered because the variation of the linear velocity with the separation field strength is linear, as mentioned above.

The contributions to the plate height from the injection plug length and the detector observation length are[17]

$$H_{inj} = l_{inj}^2/(16L_{sep}) \quad (3)$$

$$H_{det} = l_{det}^2/(16L_{sep}) \quad (4)$$

where l_{inj} and l_{det} are the lengths of the injection plug and detector observation, respectively, and L_{sep} is the separation length. The contributions from the injection plug length (see injection profiles in Figure 4) and detector observation length are written as Gaussian functions. The lengths of the injection plug and the detector observation are constant for all experiments. If these time-independent contributions predominate in their contribution to the plate height, then the total plate height decreases as the separation length increases.

The contribution to the plate height from axial diffusion is[18]

$$H_{diff} = 2D_m/(\mu E) \quad (5)$$

where μ is the effective electrophoretic mobility of the analyte, E is the electric field strength, and D_m is the diffusion coefficient of the analyte in the buffer. The contribution from axial diffusion to the plate height is reduced by increasing the separation field strength and, consequently, reducing the analysis time.

(17) Sternberg, J. C. *Adv. Chromatogr.* **1966**, *2*, 205.
(18) Giddings, J. C. *Dynamics of Chromatography, Part I: Principles and Theory*; Marcel Dekker: New York, 1965; Chapter 2.

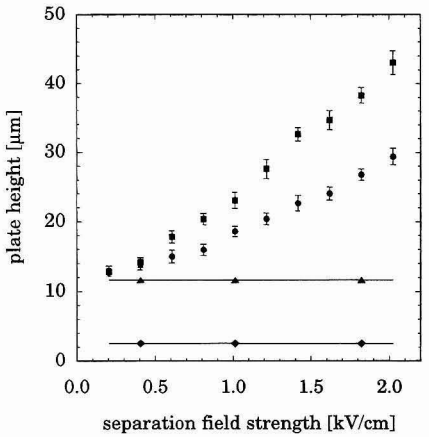


Figure 10. Variation of plate height with the separation field strength for arginine (●) and glycine (■) derivatized with *o*-phthaldialdehyde with L_{sep} = 10 mm. The contribution to the plate height from the injection and detection is calculated from eqs 3 and 4 for arginine (▲) and glycine (◆). Error bars are $\pm\sigma$ for three runs.

In Figure 10, the total plate height versus the electric field strength is plotted along with the calculated contributions from the injection plug length and the detector observation length. The time-independent contributions differ for arginine and glycine because the injections have an electrophoretic bias, and consequently, compounds with a greater electrophoretic mobility will have a larger contribution to the plate height. The injection plug lengths at half-height were 0.80 and 0.37 mm for arginine and glycine, respectively, which correspond to H_{inj} equal to 11.6 and 2.5 μm. These contributions are substantial, but in order to run the injector in the linear, reproducible regime for all separation field strengths, longer injection times were required. The detector observation length, i.e., the laser spot size, was $\approx$50 μm, which corresponds to H_{det} equal to 21 nm. In the range of separation field strengths used, the contribution from axial dispersion is small relative to the other contributions to the total plate height and is not discussed further. Unfortunately, as the field strength increases, the total plate height increases. This behavior is reminiscent of liquid chromatography, where mass transfer in the mobile and/or stationary phases dominates at high mobile phase velocities. The contribution from mass transfer to the plate height is a linear function of the mobile phase velocity:

$$H_{mt} = Cu \tag{6}$$

where

$$u = \mu E \tag{7}$$

u is the linear velocity of the mobile phase and C is the coefficient of mass transfer. Typically, in capillary electrophoresis, contributions to the plate height from mass transfer are neglected because there should be no interaction of the analyte with the walls of the capillary. However, in Figure 10 the magnitude of this contribution is surprisingly large especially for small molecules which tend to have little or no interaction with the walls.

An alternative explanation might be that the source of band broadening is due to inhomogeneity of the channel surface, especially at the channel walls. As seen in the SEM image in Figure 2a, the separation channel walls have a noticeable roughness. These etch defects derive primarily from the imperfections in the photomask. The photomask that was generated using UV ablation of a thin chrome film had an edge smoothness of $\pm$ 1 μm on a 25 μm wide line. This roughness in the mask is then transferred to the photoresist during exposure and, subsequently, etched into the substrate. In Figure 10, the plate height increases with increasing electric field strength. If related to the surface roughness, the magnitude of such a contribution is difficult to quantitate since the exact nature of the channel surface is not known. Prior work at comparable separation field strengths yielded more favorable results and agrees with eq 2.[6] However, in that work, an e-beam written photomask, which had edge smoothness more than 1 order of magnitude better, was used for the microchip fabrication. The threshold of roughness that can be tolerated for the photomask and thus the channel wall is under further investigation.

CONCLUSION

Chemical reactions followed by analysis of the products have been demonstrated on a single microchip. Devices can be tailored to accommodate any such reaction to be performed in a miniaturized environment. The reactor volumes and separation lengths can be optimized accordingly. Electroosmotically driven flow enables buffer, analyte, and reagent streams to be controlled precisely in the channel manifold of the microchip without the use of valves or pumps. The gated injector allows continuous loading of sample and rapid sequential injections to be made. Low dead volume connections between channels can be easily fabricated allowing pre- and postseparation reactions to be incorporated on-microchip. Having an electrode placed at the injection cross would allow independent control of the potentials in the reaction chamber and separation column. To have a long reaction time for the chemical reaction, the field strength in the reaction chamber should be minimized, but for capillary electrophoresis, the resolution between compounds increases with increasing electric field strength. With the current design, a compromise must be reached with the potentials applied to the microchip so that the OPA has sufficient time to react with the amino acids without seriously impeding the quality of the separation.

ACKNOWLEDGMENT

This research was sponsored by the U.S. Department of Energy (DOE), Office of Research and Development. Oak Ridge National Laboratory is managed by Martin Marietta Energy Systems, Inc. for the U.S. Department of Energy under contract DE-AC05-84OR21400. Also, this research was sponsored in part by an appointment for S.C.J. to the Alexander Hollaender Distinguished Postdoctoral Fellowship Program sponsored by the U.S. DOE and for A.W.M. and R.H. to the ORNL Postdoctoral Research Associates Program. These postdoctoral programs are administered by the Oak Ridge Institute for Science and Education and ORNL.

Received for review August 1, 1994. Accepted September 26, 1994.[⊗]

[⊗] Abstract published in *Advance ACS Abstracts,* October 15, 1994.

Anal. Chem. **1994,** *66,* 4133–4141

Oxygen Sensors Based on Luminescence Quenching: Interactions of Metal Complexes with the Polymer Supports

Wenying Xu,[†] Robert Clayton McDonough, III,[†] Brandi Langsdorf,[†] J. N. Demas,*[,†] and B. A. DeGraff*[,‡]

Departments of Chemistry, University of Virginia, Charlottesville, Virginia 22901, and James Madison University, Harrisonburg, Virginia 22807

Oxygen quenching of $[Ru(Ph_2phen)_3]Cl_2$ (Ph_2phen = 4,7-diphenyl-1,10-phenanthroline) has been studied in a diverse series of polymers, most with a common poly(dimethylsiloxane) (PDMS) component. Systematic variations in the polymer properties have been made in order to delineate the structural features important for satisfactory use of supports for oxygen sensors. Most measurements were made using homo- or copolymers containing a PDMS region, although some measurements were made on small ring siloxane polymers. In particular, quenching behavior was examined as a function of polymer structure as well as the type of and amount of polar copolymer cross-linkers. Cross-linkers were added to enhance the solubility of oxygen probes in an otherwise nonpolar polymer. In addition, hydrophobic silica was added to alter quenching properties. Domain models are used to explain the variations in oxygen quenching properties as a function of additives and cross-linkers. These considerations have led to the most sensitive ruthenium-based sensor reported to date. The relative affinity of the different domains for the complex and the efficacy of the domains for oxygen quenching control the overall behavior of the sensing response. Guidelines for design of suitable polymer supports for oxygen sensors are proposed.

Luminescent transition metal complexes can be used as photosensitizers in such areas as solar energy conversion,[1] chemi- and electroluminescent systems,[2] binding to heterogeneous media,[3] and macromolecular probes.[4,5] $Ru^{II}(L)_3^{2+}$ complexes (L = 2,2′-bipyridine, 1,10-phenanthroline, or substituted derivatives) have been the most frequently used in these applications due to strong visible absorption, high photochemical stability, efficient luminescences, and relatively long lived metal to ligand charge transfer (MLCT) excited states.[6–8] These systems have shown considerable promise in the area of sensors, particularly as quenching-based oxygen sensors[9–16] and possibly as sensors for pH, CO_2,[17,18] and temperature.[19]

The emitting-state energies and excited-state redox properties of the sensitizers can be very sensitive to variations in the metal, coordinating ligands, and solvent. Solvents and substituents have been used to control the relative positions of different excited states and to "tune" photophysical and photochemical properties.[7] Many of these luminescent species exhibit a wide variety of energetically accessible charge transfer (CT), ligand field (LF), and intraligand (IL) excited states. These excited states have different orbital parentage and, thus, quite different excited-state characteristics. Since the photophysical properties of the metal complexes are determined predominantly by the lowest energy excited states, the rational design of new and more useful photosensitizers and probes necessitates an intimate understanding of their excited-state energetics and dynamics; in this area,

† University of Virginia.
‡ James Madison University.

(1) *Energy Resources through Photochemistry and Catalysis*; Grätzel, M., Ed.; Academic Press: New York, 1983.
(2) Tokel-Takvoryan, N. E.; Hemingway, R. E.; Bard, A. J. *J. Am. Chem. Soc.* **1973**, *95*, 6582–2847.
(3) Kalyanasundaram, K. *Photochemistry in Microheterogeneous Systems*; Academic Press: New York, 1987.
(4) Hartshorn, R. M.; Barton, J. K. *J. Am. Chem. Soc.* **1992**, *114*. 5919–5925.
(5) Sacksteder, L.; Lee. M.; Demas, J. N.; DeGraff, B. A. *J. Am. Chem. Soc.* **1993**, *115*, 8230–8238.
(6) Watts, R. J. *J. Chem. Educ.* **1983**, *60*. 834–842 and remainder of issue.
(7) Juris, A.; Balzani, V.; Barigellitti, F.; Campagna, S.; Belser, P.; von Zelewsky, A. *Coord. Chem. Rev.* **1988**, *84*, 85–277.
(8) Demas, J. N.; DeGraff, B. A. In *Advances in Fluorescence Spectroscopy*; Lakowicz, J., Ed.; Plenum Press: New York, in press; Vol. 4.
(9) Lippitsch, M. E.; Pusterhofer, J.; Leiner, M. J. P.; Wolfbeis, O. S. *Anal. Chim. Acta* **1988**, 205, 1–6.
(10) Kaneko, M.; Takekawa, T.; Asakura, T. *Makromol. Chem., Macromol. Symp.* **1992**, *59*, 183–197.
(11) Demas, J. N.; DeGraff, B. A. *Anal. Chem.* **1991**, *63*, 829A–837A.
(12) Li, X.-M.; Ruan, F.-C.; Wong, K.-Y. *Analyst* **1993**, *118*, 289–292.
(13) MacCraith, B. D.; McDonagh, C. M.; O'Keeffe, G.; Keyes, E. T.; Vos, J. G.; O'Kelly, B.; McGilp, J. F. *Analyst* **1993**, *118*, 385–388.
(14) Berndt, C. W.; Lakowicz, J. R. *Anal. Biochem.* **1992**, *201*, 319–325.
(15) Demas, J. N.; DeGraff, B. A. *Makromol. Chem., Macromol. Symp.* **1992**, *59*, 35–51.
(16) Sacksteder, L.; Demas, J. N.; DeGraff, B. A. *Anal. Chem.* **1993**, *65*, 3480–3483.
(17) Orellana, G.; Moreno-Bondi, M. C.; Segovia, E.; Marazuela, M. D. *Anal. Chem.* **1992**, *64*, 2210–2215.
(18) Wolfbeis, O. S.; Weis, L.; Leiner, M. J. P.; Ziegler, W. *Anal. Chem.* **1988**, *60*, 2028–30.
(19) Demas, J. N.; DeGraff, B. A. *Proc. SPIE–Int. Soc. Opt. Eng.* **1992**, *1796*, 71–80.

0003-2700/94/0366-4133$04.50/0 © 1994 American Chemical Society

metal complexes are relatively well understood. We have discussed such designs in reference to sensors.[8]

Virtually all complexes used as sensors will be supported on an inorganic or organic polymer matrix. In some cases the support is a passive anchor, while in others it has an active role. Indeed, the support may have quite stringent criteria for suitable performance. For example, in oxygen sensors, a high diffusion coefficient is necessary for rapid response, a highly locally effective quenching around the oxygen probe is necessary for good sensitivity, and considerable interest in physiological monitoring necessitates a high degree of biocompatibility. In addition, the sensor support must lend itself to convenient and robust attachment to a sensor probe such as a fiber-optic sensor.

Unfortunately, unlike our knowledge of solution properties of metal complexes, our understanding of the detailed role of the polymer support in controlling photophysical behavior is still very much in its infancy. This is true not only for metal complexes but also for analogous systems based on luminescent organic molecules. Our goals were to explore systematically the interplay of polymer structure and design and oxygen sensor performance. In this paper we are interested primarily in the interactions of the support with metal complexes. Therefore, we used a single metal complex, $[Ru(Ph_2phen)_3]Cl_2$ (Ph_2phen = 4,7-diphenyl-1,10-phenanthroline). This complex has one of the highest responses for oxygen quenching that we have observed, has a long unquenched lifetime and quantum yield (about 5 μs and 0.5, respectively), is highly colored (30 000 molar extinction coefficient at 460 nm), and is reasonably photochemically stable.[20,21]

In particular, there were two areas that we wished to consider in our design and understanding of the polymer support. Given the insolubility of our metal complex luminescent oxygen sensors in pure nonpolar poly(dimethylsiloxane) (PDMS) polymers, we were very interested in ways of adding polar functionality to the polymer in order to increase compatibility of our complexes or other sensor materials with the polymers without degrading the other features. Further, we were intrigued by the question of the effect of fillers, such as silica, on sensor performance. Previously, it has been shown that our earlier work with a commercial RTV rubber support was affected by the presence of a silica filler in the polymer.[22] As expected, the nature of the polymer and silica additive has a profound effect on sensor response. We present a domain model that accounts for most of these properties of polymer supported and mixed silica polymer systems with this inorganic oxygen sensor probe.

EXPERIMENTAL SECTION

Absorption and Emission Spectra. Absorption spectra were measured using a Hewlett-Packard 8452A diode array spectrophotometer. Room temperature corrected fluorescence spectra were taken on a Spex Fluorolog 2 spectrofluorometer using visible excitation. Emission spectra were corrected for polymer background.

Room temperature τ values were measured using a pulsed N_2 laser (337 nm) decay system.[23] A Tektronix 2222 digital oscilloscope was used for most measurements, although a few were carried out using a faster Tektronix TDS-540. The emissions were monitored at 620 nm. Both single exponential and multiexponential luminescence decay curves were observed for different samples. Complex decays were fit by nonlinear least-squares[24] methods to the sum of up to three exponentials (eq 1). $D(t)$ is

$$D(t) = \sum_{i=1}^{3} K_i \exp(-t/\tau_i) \tag{1}$$

the luminescence intensity at time t, and the K and τ terms are the preexponential weighting factors and the excited-state lifetimes, respectively.

Oxygen quenching studies were carried out by either evacuating the sample cell or blowing nitrogen, air, or oxygen over the samples. Equilibration was insured by making measurements until stable data were obtained.

Ideally, intensity quenching data should follow Stern–Volmer quenching kinetics, given by

$$I_0/I = 1 + K_{SV}[Q] \tag{2a}$$

$$K_{SV} = k_2\tau_0 \tag{2b}$$

where I is the emission intensity at a quencher concentration [Q], K_{SV} is the Stern–Volmer quenching constant, and k_2 is the bimolecular quenching constant. The subscript 0 denotes the value in the absence of quencher. A linear plot of $(I_0/I) - 1$ versus [Q] should result. Since the solubility of oxygen in the polymers is unknown, we adopt the standard procedure of using the oxygen partial pressure in place of oxygen concentration. K_{SV} then has units of reciprocal pressure.

In polymer systems, persistent microheterogeneity frequently causes different sites to be quenched differentially with a resultant downward curved Stern–Volmer plot. We have found a two-site model[21] to have excellent predictive value for quenching in microheterogeneous solids. The two-site Stern–Vomer equation is

$$\frac{I_0}{I} = \frac{1}{\dfrac{f_{01}}{1 + K_{SV1}[O_2]} + \dfrac{f_{02}}{1 + K_{SV2}[O_2]}} \tag{3}$$

where f_{0j} is the fraction of each of the two sites contributing to the unquenched intensity and the K_{SV} values are the quenching constants for the two sites. Since $f_{02} = 1 - f_{01}$, this is a three-parameter model. Some of the more extensive data sets were fit by either a linear one-site or this nonlinear two-site Stern–Volmer equation.

Materials. The ruthenium complex was the same sample as used earlier.[20] All reagents were of the highest purity available. The silica was Cab-O-Sil TS-720, a hydrophobic, amorphous, fumed silica from Cabot Corp. with a surface area of 100 M^2/g. Most of the OHs on the SiOHs have been replaced by $O[Si(CH_3)_2O]_nSi(CH_3)_3$. This silica is so hydrophobic that it forms a surface coating on water and cannot be pressed into it. The sodium tetrakis(*m*-(trifluoromethyl)phenyl)borate was from Fluka. The

(20) Bacon, J. R.; Demas, J. N. *Anal. Chem.* **1987**, *59*, 2780–2785.
(21) Carraway, E. R.; Demas, J. N.; DeGraff, B. A.; Bacon, J. R. *Anal. Chem.* **1991**, *63*, 337–342.
(22) Klimant, I.; Leiner, M. J. P. *Abstracts, 1st European Conference on Optical Chemical Sensors and Biosensors*, Graz, Austria, April 12–15, 1992; p 131.
(23) Leasure, R. M.; Sacksteder, L.; Nesselrodt, D.; Demas, J. N.; DeGraff, B. A. *Inorg. Chem.* **1991**, *30*, 3722–3728.
(24) Demas, J. N.; Demas, S. E. *Interfacing and Scientific Computing on Personal Computers*; Allyn & Bacon: New York, 1990.

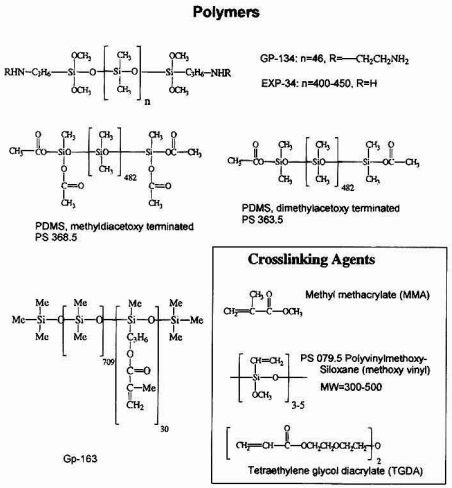


Figure 1. Structures of the different PDMS prepolymers along with the cross-linking agents.

$[Ru(bpy)_3]^{2+}$ salt of this anion was prepared by aqueous metathesis. Poly(dimethylsiloxane) was from Huls and had viscosities of 1, 5, 50, and 500 cP.

Amine-Terminated Polymers. We examined two amine-terminated polymers with similar amine-terminated end functionality but differing lengths of PDMS intermediate sections. The prepolymers were GP-134 and EXP-34 amine functional silicone fluids from Genesee Polymer Corp. These polymers are shown in Figure 1. Atmospheric moisture hydrolyzes the methoxy group to form silanol groups. Silanol groups condense with silanol or methoxy groups to liberate water or methyl alcohol and give new siloxane bonds. The amines catalyze this reaction. Reaction continues until essentially all methoxy groups are hydrolyzed. Soft, clear, rubbery films result. Thickness can be adjusted by using a solvent, such as an aliphatic hydrocarbon, to dilute the prepolymer. Curing time was temperature dependent and took about 16–24 h at room temperature, 4 h at 70 °C, and 2 h at 90 °C. Curing takes longer when hexane is used as a dilutant. The prepolymer density is 0.93 g/cm^3, with 0.9 mequiv of base per gram. Because the prepolymer shows a rapid conversion to a cross-linked silicone rubber on exposure to atmospheric moisture, containers were tightly sealed and pressurized slightly with dry nitrogen. Also, nitrogen protection was used during all transfers.

For EXP-34, the curing method was the same as for the GP-134 prepolymer. Curing took 2 days at room temperature for 0.3–0.5 mm thickness film; however, this is much longer than that for GP-134 under the same curing conditions. This is consistent with the greater percentage of hydrophobic PDMS, which retards moisture penetration.

PDMS Methyldiacetoxy-Terminated Oligomer. This oligomer, PS 368.5 from Huls, was cured with atmospheric moisture at room temperature for 24–72 h depending upon sample thickness (0.3–2 mm). The prepolymer is terminated at each end with two hydrolyzable acetoxy groups, which permits chain extension and cross-linking. The resulting film is transparent and rubbery with good mechanical properties. Typically a pure 0.3 mm film cured in about 6 h at 60 °C. Cab-O-Sil-impregnated films took much longer. A 0.3 mm film with 2–5 wt % Cab-O-Sil took 1 week to cure. For preparation of silica-containing films, the silica was mixed into the oligomer and allowed to stand until bubble-free before polymerization. The mixture exhibited only a slight cloudiness before polymerization.

For a more hydrophobic polymer, we also used the oligomer PS 363.5, which has only one acetoxy at each end. The pure oligomer water cures to a very viscous liquid. Apparently, the absence of two acetoxy groups at each end prevents cross-linking and rubber formation. To obtain varying degrees of PDMS, we polymerized rubbers from mixtures of PS 368.5 with PS 363.5. While rubbers with up to 1:3 ratios (w/w) of PS 368.5 to PS 363.5 formed, they became increasingly difficult to polymerize; mechanically sound rubbers could not be obtained at higher than 1:3 in a reasonable curing time. With ruthenium, only a 2:1 mixture was studied.

For the moisture-cured polymers, films were prepared by coating the prepolymer onto Teflon plates with a Teflon standoff to control sample thickness. The surfaces were leveled with a razor blade. Films were typically air-cured at room temperature with ambient humidity.

Methacryloxy Siloxane Polymers. The macro monomer or oligomer Gp-163, a methacryloxy functional silicone fluid, was from Genesee Polymer Corp. (Figure 1). Gp-163 is a modified PDMS containing (methacryloxy)propyl side chains in place of some methyl groups. The methacryloxy groups were distributed randomly on the chain rather than as a block copolymer. The mole percentage of methacryloxy was 6%.

These were polymerized either as the homopolymer or with different cross-linking agents. The cross-linking agents are also shown in Figure 1. Polymerization of the homopolymer was carried out by using a radical initiator such as benzoyl peroxide (BPO) from Aldrich (0.3%) or 2,2-azobisisobutyronitrile (AIBN) from Polyscience Inc. The reaction took 16–20 h at 100 °C under nitrogen with a BPO initiator or at 70 °C with an AIBN initiator. The homopolymer network was a transparent rubbery polymer.

The copolymers made from Gp-163 with the tetra(ethylene glycol) diacrylate (TGDA) from Aldrich will be referred to as the acrylate TGDA copolymer. AIBN initiator was dissolved in the TGDA and then mixed with Gp-163. The mixture was placed in a mold with two pieces of Teflon, and the thickness was adjusted by a Teflon spacer and then tightly clamped. Polymerization was carried out under nitrogen to avoid air inhibition. After polymerization was completed, the films were released from the Teflon mold and washed three times in methylene chloride, each for 1 h, to eliminate unreacted monomer and initiator. The films were vacuum-dried at room temperature for 30 min to 3 h, depending on thickness. The copolymers were transparent to cloudy, depending on composition; with less than 3 wt % of TGDA, the polymer was transparent, but beyond 5% copolymers became cloudy white. A polymer made from pure TGDA was brittle, rigid, and transparent.

The copolymer networks made from Gp-163 with MMA (Aldrich) will be referred to as the acrylate MMA copolymer. The MMA was inhibited with 10 ppm of hydroquinone monomethyl ether, MEHQ. The inhibitor was removed by passing the MMA through a 9 in. long and 0.8 in. diameter disposable inhibitor remover column (Aldrich). BPO, 0.3 wt % based on the total weight of monomers, was first completely dissolved in the MMA,

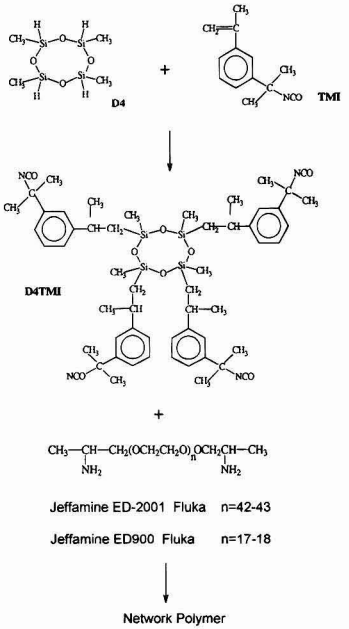


Figure 2. Synthesis and structures of the cyclic siloxane polymers.

and then Gp-163 was added. Composition was based on the weight of the cross-linker over the total weight. Polymerization was carried out in a temperature-controlled oven under a continuous N_2 stream. The polymerization temperature was controlled in steps: 60 °C for 4 h, 100 °C for 10 h, and finally 120 °C for 2 h. The film was extracted three times for 2 h each with CH_2Cl_2. Films were slowly dried in air and then in a vacuum oven for 2 h. The copolymer is transparent and rubbery for less than 10 wt % MMA.

The copolymer networks made from Gp-163 with the PS 079.5 from Huls will be referred to as the acrylate vinylsiloxane copolymer. BPO (0.3 wt % based on the total weight of monomers) was dissolved in the PS 079.5 at 70 °C and then mixed with Gp-163. The mixture was allowed to stand for a few minutes to eliminate bubbles and then transferred to a Teflon mold. Polymerization conditions and treatment of the sample after polymerization were similar to those for the acrylate MMA copolymer. With the vinylsiloxane system, the alkoxy groups are potentially cross-linkable by moisture after radical polymerization, although we noticed no changes in properties on standing.

Siloxane Ring Polymers. The structures and synthesis of these polymers are shown in Figure 2. *m*-TMI from American Cyanamid was distilled under reduced pressure. A fraction at 110 °C under 6 Torr was collected. 2,4,6,8-Tetramethylcyclotetrasiloxane (D4H) was from Huls. The procedure for preparing D4TMI is similar to that given elsewhere.[25] In a typical experiment, 5 g of D4H was mixed with 25 g of freshly distilled *m*-TMI. In a three-neck flask, 0.25 mL of a 3% solution of platinum divinyltetramethyldisiloxane in xylene (Huls) was added. The mixture was heated under N_2 at 50 °C for 18 h, and small additional amounts of catalyst were added to complete the reaction. ^{1}H NMR of the product showed complete disappearance of the 4.61 ppm SiH peak. Purification was modified from the literature.[25] The reaction mixture was mixed with dried hexane and 6–8 g of carbon black, stirred for 6 h, and filtered to give a colorless solution. Hexane was removed on a Rotovap. Finally, any remaining *m*-TMI was removed under high vacuum at 110 °C for 10 h.

Preparation of D4TMI–PEG–Jeffamine Network. D4TMI and Jeffamine with equal equivalents of NCO and NH_2 were dissolved separately in CH_2Cl_2 (ca. 15 wt %). Both solutions were cooled in ice, and the Jeffamine solution was mixed into the D4TMI solution, allowed to gel in an ice bath, and set at room temperature for 24 h to complete gel formation. IR showed the absence of NCO peaks. The gel was extracted with THF, CH_3OH, and acetone and dried.

Sensor Preparation. In Cab-O-Sil-doped samples, the silica was mixed with the prepolymer before polymerization. To prepare polymer-supported Ru(II) complexes, 0.1 mg of $Ru(4,7\text{-}Ph_2\text{-}phen)_3Cl_2{\cdot}6H_2O$ was dissolved in about 3 mL of CH_2Cl_2. The polymerized films (5–7 mm × 5–7 mm × 0.2–0.5 mm) were immersed in the solution for 15–30 min to give transparent orange films. The films were rinsed in cold CH_2Cl_2 to remove any surface complex and dried slowly in a CH_2Cl_2 atmosphere and finally at 60 °C in vacuum. Sensor films were kept dry and in the dark until used.

For the pure silica samples, the procedure described earlier for hydrophilic silicas was used.[26] The metal complex was adsorbed onto the silica from CH_2Cl_2 solution. The doped silica was dried and then pressed in an IR press to give a nearly clear disk. The disk was very porous, as judged from the almost instantaneous response to changes in oxygen pressures.

RESULTS

Solid $Ru(4,7\text{-}Ph_2phen)_3Cl_2{\cdot}6H_2O$. The solid complex has a nonexponential decay, which appeared to be independent of the presence or absence of oxygen. The three exponential fits yielded lifetimes of ~60, ~250, and ~600 ns with preexponential weights of 0.2, 0.4, and 0.4. The preexponential factor weighted mean lifetime was about 300 ns and independent of oxygen concentration.[21]

Pure PDMS. We were unable to solubilize our Ru complex in linear dimethylsiloxane polymers. This was true with chloride or perchlorate counterions. We also attempted unsuccessfully to solubilize $Ru(bpy)_3^{2+}$ as the salt with the extremely hydrophobic phenylborate anion. Thus, it is reasonable to assume that our chloride salts will not dissolve in a region of the polymer that consists predominantly of hydrophobic PDMS.

In none of the polymers described below do we see evidence for phase separation of the metal complex. No microcrystals are seen under the microscope. Further, for systems where the complex was insoluble in the support, we frequently get a very different purple color as opposed to the red or orange color in homogeneous solutions or in the polymers studied here.

Amine Siloxane Polymer with Silica. Figure 3 shows the quenching for the pure Gp-134 amine siloxane and the same

(25) Zhou, G. B.; Smid, J. *J. Polym. Sci., Part A: Polym. Chem.* **1991**, *29*, 1097–1105.

(26) Carraway, E. R.; Demas, J. N.; DeGraff, B. A. *Langmuir* **1991**, *7*, 2991–2998.

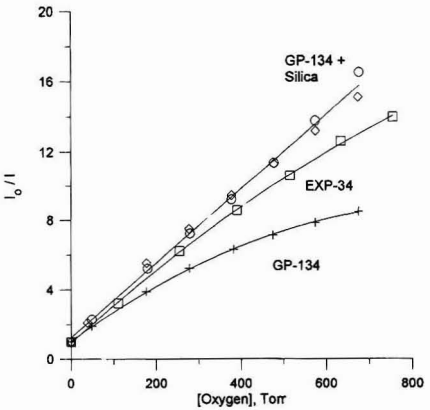


Figure 3. Oxygen quenching of $[Ru(Ph_2phen)_3]^{2+}$ in amine siloxane polymers with and without silica. (+) Shorter chain PMDS with no silica; (□) longer chain PMDS with no silica; (◇) 0.9% by weight of silica; (○) 4.8% by weight silica. The bottom two curves are best fit by the two-site quenching model. For Gp-134, $f_{01} = 0.06$, $K_{SV1} = 0$ Torr^{-1}, $K_{SV2} = 0.0216$ Torr^{-1}. For EXP-34, $f_{01} = 0.017$, $K_{SV1} = 0$ Torr^{-1}, $K_{SV2} = 0.0227$ Torr^{-1}. The upper line is the best linear least-squares fit to both sets of data for the two silica loadings ($K_{SV} = 0.0214$ Torr^{-1}).

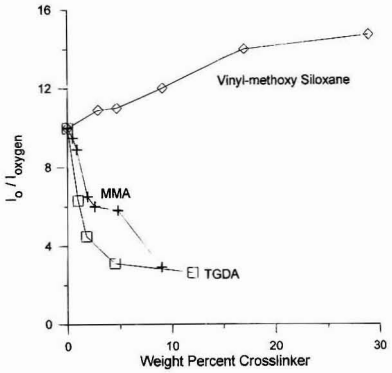


Figure 4. Oxygen quenching of $[Ru(Ph_2phen)_3]^{2+}$ in acrylate siloxane polymers with different cross-linkers. (◇) Vinyl siloxane polymer; (+) MMA cross-linker; (□) TGDA cross-linker. The lines are shown only to allow following trends and have no physical significance.

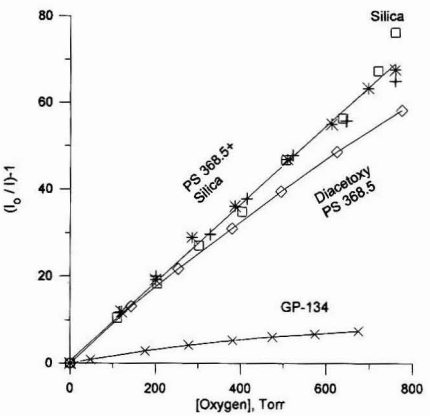


Figure 5. Oxygen quenching of $[Ru(Ph_2phen)_3]^{2+}$ in a pure hydrophobic silica disk (□) , pure diacetoxy polymer (◇), and the diacetoxy polymer with 2% (+) and 5% (*) of added silica. Shown for comparison is the GP-134 (×). The solid line for the pure diacetoxy is a two-component Stern–Volmer fit. The solid line for the pure silica and the doped diacetoxy polymer is a linear least-squares fit to the combined data ($K_{SV} = 0.0898$ Torr^{-1}). The solid line for the PS 368.5 is a two-site fit with $f_{01} = 0.002$, $K_{SV1} = 0$ Torr^{-1}, $K_{SV2} = 0.0865$ Torr^{-1}.

polymer doped with 0.9 and 4.8 wt % of silica. Up to 20 wt % silica, the behavior is similar to and indistinguishable from that of the 0.9 and 4.8 wt % samples. Clearly, the pure polymer shows a very nonlinear Stern–Volmer plot, while the silica-doped systems are more nearly linear and have much larger responses.

Figure 3 also shows the pure EXP-34 polymer, which has a higher percentage of PDMS regions. This polymer has a higher and more nearly linear response than the pure GP-134 polymer but is more curved and has a poorer response than the silica-doped Gp-134.

The solid lines in Figure 3 are the best fits. A two-site model was used for the polymers without silica. For Gp-134, $f_{01} = 0.06$, $K_{SV1} = 0$ Torr^{-1}, $K_{SV2} = 0.0216$ Torr^{-1}. For EXP-34, $f_{01} = 0.017$, $K_{SV1} = 0$ Torr^{-1}, $K_{SV2} = 0.0227$ Torr^{-1}. All the silica-doped data are combined to yield a single-component Stern–Volmer quenching constant $K_{SV} = 0.0214$ Torr^{-1}. Thus, the curvature of both pure polymers is due to a small amount of unquenched emission. The higher sensitivity and more nearly linear plot of the EXP-34 versus Gp-134 is due to the smaller amount of unquenched component.

Acrylate Siloxane Polymers. The pure acrylate polymer shows a nearly linear Stern–Volmer plot. The Stern–Volmer plot was unaffected by addition of silica loading up to 20 wt %.

Figure 4 shows the quenching performance of the acrylate polymer with varying amounts of different cross-linkers. Rather than complete Stern–Volmer plots, which were nearly linear, only the I_0/I_{oxygen} is shown .

There is a pronounced dependence on the wt % for the different cross-linkers. The vinylsiloxane is the only cross-linker that shows enhanced quenching with increasing cross-linker concentration. Not shown on the plot is the point for 80 wt % TGDA, where $I_0/I_{oxygen} = 1.1$.

Silica and Diacetoxysiloxane. Figure 5 shows the nearly linear Stern–Volmer plot for the pure silica. The upward hook at the highest oxygen pressures is probably due to an incorrect assumption about the baseline contribution from the cloudy silica; the sample emission intensity is quite low at higher oxygen pressures, and a very small underestimation of the blank would cause an upward trend. Also shown are the pure diacetoxy polymer and the silica-doped diacetoxy polymer. The silica-doped silicone is indistinguishable from the pure silica, and the pure silicone is very slightly lower in response and has a slight downward curvature not present in the silica systems. Given the difficulties of making measurements at these high degrees of quenching, the differences between the silicone and silica samples are near the limits of measurement, although there does appear

to be a discernible difference in both degree of quenching and shape of the Stern–Volmer curves.

The doped silicone data and the pure silica data are indistinguishable and are fit by a single-component Stern–Volmer plot with $K_{SV} = 0.0898$ Torr^{-1}. Assuming a two-site model for the slightly curved pure silicone, we obtain fitting parameters of $f_{01} = 0.002$, $K_{SV1} = 0$, $K_{SV2} = 0.0865$ Torr^{-1}. Thus, even a very small amount of an unquenched component can produce noticeable nonlinearity in the Stern–Volmer plots.

While sensors made from the diacetoxy-terminated prepolymer gave excellent Stern–Volmer plots and near single exponential decay times, the 2:1 mixture of PS 368.5 and PS 363.5 is more complex. The mixture showed poorer lifetime quenching than pure PS 368.5 as well as a nonlinear Stern–Volmer plot and highly nonexponential decay curves. In particular, there is a substantial contribution of 200–500 ns components, which are not strongly affected by oxygen. This behavior is similar to that observed for the solid $Ru(4,7\text{-}Ph_2phen)_3Cl_2{\cdot}6H_2O$. This value suggests that, with increasing amounts of PDMS, we exceed the solubility limits of the complex and are looking at unquenchable aggregated or precipitated solid complex separating from the polymer, even though there is no visible precipitation. Because of the much greater inhomogeneity of the mixed polymers, we did not pursue this area further.

Ring Polymers. The Stern–Volmer quenching constant for the D4-900 polymer was 0.0017 Torr^{-1}, and that for the D4-2000 polymer was 0.0023 Torr^{-1}. These corresponded to I_0/I_{oxygen} of about 1.5–2, which is very inferior to the PDMS-based systems. The response times were much slower than those for the PDMS-based polymers (about 5–10 times). The plots were reasonably linear and somewhat upward curved at higher oxygen pressures. The oxygen quenching showed some hysteresis, which may have arisen from the very hydrophilic character of the polymer and variations in hydration during measurements on our vacuum system. Because of these factors, one should not place too great a weight on the quenching constants.

Photochemistry. We did not directly study the photochemistry, but it became clear that the amine polymer did exhibit photodecomposition under room lights after a week or two. Photochemistry manifested itself by the appearance of small red spots in the film. These spots were not due to coalescence of the complex into microcrystals since extraction of the films with dichloromethane removed all of the complex from the film except for the red spots, which remained unaffected. The spots were nonluminescent.

DISCUSSION

Polymer Characteristics. All polymers shared the same polydimethylsiloxane (PDMS) backbone except the ring polymers, which had a PDMS-like region. PDMS has one of the highest oxygen diffusion coefficients of any polymer and provided potentially good regions for oxygen quenching. In addition, all of the polymers provided pendant or terminal functionality that permitted cross-linking. Further, all the polymers contained polar regions for solubilizing the somewhat polar ionic metal complex. Some of the structural variables were the amount of polar functionality versus the nonpolar PDMS portion. Further, variations in the polymer polarity could be controlled by varying the amount and polarity of the copolymer cross-linker.

The amine functionality provided a polar solubilizing region. The two amine polymers differed substantially in the ratio of polar functionality to nonpolar backbone. This provides a good test of the contribution of the PDMS to oxygen diffusion and quenching in mixed polymers. The polymerized acrylate regions in acrylate copolymers provide a good polar region for solubilizing the complex, which dissolves readily in pure MMA or poly(MMA). The ethylene oxide component of the TGDA also provides a more hydrophilic region than any of the other copolymers since pure poly(ethylene oxide) is highly water soluble. The vinylsiloxane cross-linker provides a very hydrophobic region, but being a siloxane polymer probably gives it good oxygen transport properties.

The diacetoxy polymer is the one oddity. Condensation of SiOH groups at the acetoxy or hydrolyzed acetoxy ends will yield SiOSi chains. This should be essentially a continuation of the PDMS backbone, which will be very nonpolar. However, the complex is fairly soluble in the films, and this indicates a reasonable polarity. There will be some unterminated SiOH components, and it must be the clustering of these that produces domains of adequate size and polarity to solubilize the metal complex. Apparently, mixing in monoacetoxy-terminated PDMS (PS 363.5) reduces the ratio of unterminated OH groups to dimethysiloxanes, decreases polymer polarity, and reduces the solubility of the complex to where it begins to precipitate as microcrystals.

The reason for selecting the ring polymers was twofold. First, there seemed to be nothing known about the oxygen transport and quenching properties of molecules in the cyclic siloxane systems. Second, these polymers swell in water. This feature, along with the very hydrophobic silicone core, offered the opportunity to build supports that could anchor hydrophobically a sensor while providing water access to the bulk of the polymer. Thus, these systems might prove especially useful in pH-sensitive systems, where a hydrophobic probe with a pH-sensitive group is anchored by hydrophobic interactions rather than by covalent attachment, which would be much more difficult to engineer.

Domain Model. The major variation in the polymers was the extent and nature of the polar functionality. Our results can be explained on the basis of a domain model where there is a tendency for polar groups to cluster and nonpolar regions to separate from the polar regions. Specifically, our systems are characterized by three types of regions or domains. First, we have a largely hydrophobic domain whose major constituent is PDMS. Second, we can have more polar regions contributed by the cross-linker. Third, we introduce phase heterogeneity with the incorporation of insoluble silica particles.

With silica-doped polymers, we create microscopic domains on which the complex can be adsorbed (Figure 6A). From earlier work we know that our metal complexes are heavily oxygen quenched when supported on hydrophilic fumed silica.[26] Thus, if the complex is adsorbed on the silica, luminescence quenching could be enhanced. The polymer environment then merely acts as a protective overcoat and oxygen transport medium for the sensor portion of the system.

Since the complex is not soluble in the pure PDMS region, one of the reasons for using polar cross-linkers or copolymers was to increase the polarity of the support and enhance solubility of the complex. In this way it is possible to get polar domains into an otherwise nonpolar polymer. This is shown schematically in Figure 6B, where we show polar domains in the nonpolar matrix. There will be transition regions, as indicated by the less

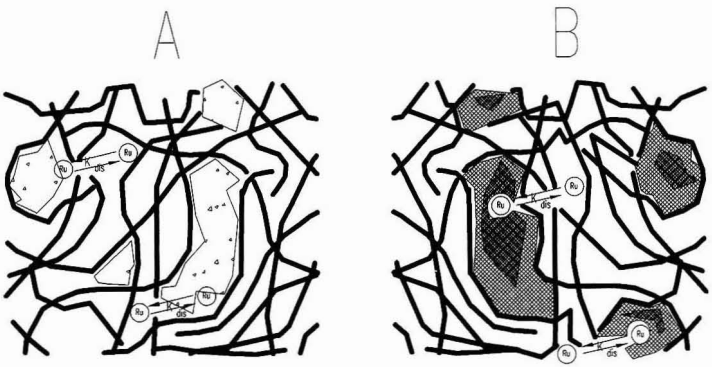


Figure 6. (A) Model for silica doped polymers showing distribution of complex between silica and polymer phases. (B) Model for two-component polymer systems showing distribution of complex between hydrophobic PDMS regions (heavy lines) and more polar domains indicated by cross-hatching.

heavily shaded areas. At higher loadings the transition regions will become smaller relative to the highly polar regions.

Silica Support. We use the domain model of Figure 6A to explain the silica results. The metal complex can partition between the polymer phase and the silica particles. For a given distribution coefficient, K_{dis}, the greater the percentage of silica, the greater the fraction of the complex that will bind to the silica.

For pure silica without any polymer, I_0/I_{oxygen} is about 65. This is the best solid support that we have found in terms of sensitivity. However, the silica is fragile and not completely clear, which limits its usefulness.

For the shorter chain silica–amine polymer system (Figure 3), it is clear that the complex has a very strong preference for binding to the silica versus the polymer support itself. With the addition of only 0.9 wt % silica, the binding to the silica has saturated, and no further addition of silica even up to 20 wt % (not shown to prevent clutter) affects the luminescence quenching properties. An interesting point is that the I_0/I_{oxygen} in the silica polymer is 16, which is quite different from the 65 for the pure silica. Thus, the metal complex, even though it is bound on the silica particles, feels the presence of the polymer, and its quenching properties are altered from those of the pure silica. This is not unreasonable since the polymer can overlay the silica surface on which the complex is adsorbed. This will change the local environment and give a different degree of quenching than is observed for molecules adsorbed on a silica surface exposed directly to gas. We can rule out the possibility that the complex is adsorbed in a polymer-free region of the silica. If this were the case, then the quenching would be identical to that of the pure silica.

For the 6% homoacrylate polymer, there is no evidence for silica binding. For up to 20 wt % silica, the I_0/I_{oxygen} does not change from that for the pure polymer. While it is possible that the silica-supported complex has the same degree of quenching as the polymer-dissolved complex, this would be a fortuitous combination of properties, and we consider it unlikely. We therefore assume that the polar complex stays in the more polar acrylate regions of this polymer.

For the diacetoxy-terminated polymer there appears to be a slight reduction of I_0/I_{oxygen} for the polymer versus the pure silica. However, the silicone has a superb response in terms of both linearity of the Stern–Volmer plot and the I_0/I for oxygen. For the silica-doped diacetoxy polymer, the response is the same as that for the pure silica, although the differences between pure silicone and the silica polymer systems are small. We suggest that the metal complex may be partitioning onto the silica, which slightly improves its performance over the pure silicone, but the differences are too small to be absolutely certain. However, since the pure silicone support sensor performance is so good, there would be little incentive for going to a binary silica system with the increased fabrication problems.

Amine Polymers. The two amine polymers exhibit nonlinear Stern–Volmer quenching plots, but the polymer with the higher percentage of PDMS shows about twice the I_0/I_{oxygen} of the lower percentage PDMS polymer. We attribute the enhanced sensitivity to the higher percentage of the complex exposed to the PDMS richer environment, which enhances diffusion through the regions around the metal complex. Further, the longer chains will prevent coalescence of the amines into larger polar regions, and these smaller regions will permit closer interaction of the bulk PDMS and greater quenching. It is clear from the two-site quenching fits that the major difference between these two polymers is a reduction of the unquenched component in the higher percentage PDMS EXP-34. This is consistent with our model for reduced quenching in the polar region.

Copolymer Results. With the exception of the vinylsiloxane cross-linker, the TGDA and MMA copolymer systems all showed decreased oxygen quenching sensitivity with increasing wt % of the copolymer. The vinylsiloxane shows a significant improvement in I_0/I_{oxygen} with increasing wt % of the vinylsiloxane copolymer. We explain the TGDA and MMA copolymer results with the domain model of Figure 6B. With increasing amounts of the polar cross-linker, the polar domains grow. With increasing polar domains, the metal complex partitions into these regions, and as they become larger, the local diffusion coefficient decreases and the degree of quenching falls. This is especially true at 80 wt % TGDA cross-linker, where the apparent quenching decreases by 100 times $((I_0/I_{oxygen}) - 1$ at 1 atm of oxygen) over that of the pure monomer.

The enhanced quenching observed for the vinylsiloxane cross-linker can be ascribed to two factors. First, a siloxane polymer itself is being added which could have better quenching properties than the starting polymer. Second, the available acrylate polar domains are being diluted or disrupted with the vinylsiloxane. This will have the effect of forcing any metal complex into closer proximity with siloxane regions and thus enhancing quenching. We cannot give weights to the contribution from each of these two mechanisms. We could not polymerize and study the pure vinylsiloxane polymer.

Diacetoxy Polymer. The data for this polymer indicate that even a relatively small polar region can profoundly affect metal complex solubilization. The metal complex is completely insoluble in a pure PDMS. Yet it clearly dissolves in the polymerized diacetoxy polymer, which at most has a few unterminated SiOH groups for the polar region. Thus, amazingly little polarity is required to dissolve the oxgyen sensor molecule. Alternatively, it may just be that the cation exchange character of the few surviving SiOH groups is responsible for solubilization. From the two-component fitting, it is clear that the diacetoxy-terminated polymer has essentially only one site with the observed curvature resulting from only a 0.2% contribution of an unquenched component.

The extremely high degree of quenching exceeds that observed for any of the supports studied here or earlier. The results are consistent with the known superb oxygen diffusion properties of pure or doped PDMS.[27,28] We note that this is clearly a cross-linked polymer. Polymerization of a similar polymer with only a single acetoxy at each end, which can only yield a linear polymer, never achieves more than a very viscous liquid state; this is unlike the rubbery polymer from the diacetyoxy prepolymer. It would appear that the best responses are obtained the more closely the polymer approaches pure PDMS. Therefore, further attempts should be directed toward polymers with still higher PDMS percentages.

Unfortunately, the mixed diacetoxy−monoacetoxy-terminated PDMS suggests that we are near the solubility limit for this metal complex, and further increases in the nonpolar PDMS region degrade performance by precipitating the metal complex. We do not consider this system further in regard to the Ru(II) complex.

Ring Polymers. The K_{SV} values for both ring polymers are similar even though the lengths of the poly(ethylene oxide) linkages differ by a factor of 2. Indeed, the polymer with the shorter linker seems to show a somewhat lower K_{SV}. We had expected the Ru complex to reside in the ethylene oxide region, which from Figure 4 appears to be a poorly quenching region. Thus, we anticipated that the $n = 17-18$ polymer would be a better sensor support than the $n = 42-43$ polymer because of the greater proximity of the oxygen probe to the siloxane region. If anything, the reverse is true. This difference may be due to binding in the amide region of the core and n-dependent variations in structure of this star-type polymer. Conclusions cannot be drawn at this time, and work with related polymers is anticipated to unravel this behavior.

However, while the degree of quenching is nowhere near as great as that for the PDMS systems, we do get a reasonable degree of oxygen quenching, even for a polymer that is predominantly poly(ethylene oxide)-like. This result shows that the D4 siloxane ring system is good for promoting oxygen quenching similar to PDMS. Indeed, the D4 systems are comparable in quenching behavior to ethylene oxide cross-linked acrylate siloxane with 10−20 wt % of the cross-linker. This result suggests that the ring siloxanes with connecting groups that are more compatible with good oxygen quenching should be explored.

Lifetimes. We did not do exhaustive lifetime measurements on all the polymers. We found the decay kinetics of the amine polymers to be complex and requiring two or three exponentials to obtain good fits. τ_M varied in a fashion consistent with dynamic quenching, but the complexity of the fitting precluded a definitive resolution of this question. The complex decays were also consistent with the curvature of the Stern−Volmer plots. Curved intensity plots are proof of heterogeneity in the quenching, and it would be likely under these conditions to have multiple exponential decays.

We also examined the lifetime quenching in the diacetoxy polymer. Here the Stern−Volmer intensity plot is nearly linear, which suggests minimal environmental heterogeneity. The decay in nitrogen was essentially a pure single exponential, while the air decays contain a small contribution from a second component. The unquenched lifetime was 5.10 μs (with about 1% total emission contribution from a 0.8 μs component). The 5.10 μs value is close to the longest value observed for this complex at room temperature in any media. The main air-quenched lifetimes were 0.30 μs and 2.4 μs, with the latter contributing about 1.5% in the preexponential factor. This result suggests that a small percentage of the complex exists in a site that is quenched poorly. Using the primary component, the τ_0/τ data match the I_0/I data for this particular sample, showing that quenching is essentially purely dynamic. The near single exponential behavior is consistent with the near absence of heterogeneity as shown by the nearly linear Stern−Volmer quenching plots.

The exceptionally good linearity of response in the diacetoxy polymer, coupled with the excellent response and near single exponential decays in this system, suggests that it has great promise as an oxygen sensor.

Photochemistry. RuL_3 complexes are substitutionally photolabile in solutions.[29] The relatively low photochemical degradation efficiencies observed with bidentate ligands appear to be a consequence of the fact that only one end of the ligand is initially dissociated. The second covalent bond can then keep the ligand in close enough proximity to the metal to allow self-healing before the second bond can rupture thermally. It is known that if a good coordinating group is in close proximity to the complex following the initial single-ended dissociation, this other group can compete for the free site and, once reacted, block self-healing. Thus, this blocking can significantly increase decomposition efficiency. For example, this enhancement has been observed for $[Ru(bpy)_3](SCN)_2$ in CH_2Cl_2, where efficient ion pair formation allows the SCN^- ion to react in the ion pair to form $Ru(bpy)_2(SCN)_2$.[30]

We believe that a similar effect occurs in our amine polymer, which contains free NH_2 or NH groups in the polar binding region for the metal complex. Amines are good coordinating groups for Ru(II), and, on displacement of one end of the bidentate ligand, the amines probably can successfully compete with the self-healing

(27) Cox, M. E. *J. Polym. Sci., Part A: Polym. Chem.* **1986**, *24*, 621−636.
(28) Cox, M. E.; Dunn, B. *J. Polym. Sci., Part A: Polym. Chem.* **1986**, *24*, 2395−2400.
(29) Watts, R. J.; Harrington, J. S.; Van Houten, J. *J. Am. Chem. Soc.* **1977**, *99*, 2179−2187.
(30) Hoggard, P. E.; Porter, G. B. *J. Am. Chem. Soc.* **1978**, *100*, 1457−1463.

step. The result would be a Ru(II) covalently linked to the polymer by a coordinating amine. The covalent linkage would prevent the complex from being extracted from the polymer, as is observed. An amine-coordinated $Ru(II)L_2$ complex would have longer wavelength absorptions, which are consistent with the red color and loss of luminescence. For example, $[Ru(phen)_2en]^{2+}$ (en = ethylenediamine) is red in solution and nonluminescent at room temperature.[31]

CONCLUSIONS

Our results suggest certain rules of design that should be kept in mind when selecting polymeric probe supports for oxygen sensors.

One should be careful of many commercial polymers since they can be filled, which can radically affect performance. Ideally, any polymer of an undefined structure should be avoided because of the unpredictable, and probably unguaranteed, consistency of the polymer for sensor applications.

Pure homogeneous polymers can be formulated to give very acceptable sensor responses even without the addition of a heterogeneous component such as silica. Indeed, the very best unfilled Ru(II) polymer system is the diacetoxy polymer.

However, for polymers that yield poor quenching performance because the sensor probe partitions into regions of poor quenching ability, performance can be enhanced by adding a heterogeneous component, which selectively adsorbs the sensor and gives good response. In the extreme case of a polymer that does not dissolve the sensor at all, the heterogeneous support can carry the sensor into the protective polymer environment.

In systems with heterogeneous components, such as silica, there can be specific interactions between the polymer and the silica. Therefore, the response can deviate from that observed for the pure silica support.

Copolymers can be used to tailor the properties of a sensor support. For example, addition of polar cross-linkers can be used to increase the solubility of polar molecules in nonpolar polymers. However, care must be taken not to introduce domains that solubilize the sensor but shut off quenching due to poor local oxygen diffusion or solubility around the oxygen probe.

Just because a polymer is a good solvent for the sensor does not preclude severe heterogeneity as shown by nonlinear Stern–Volmer response. Finally, polymers containing good coordinating groups such as NH_2 may enhance photoinstability by substituting into the metal coordination sphere and should probably be avoided for this reason.

The two-site model used earlier provides an excellent modeling equation for quantitatively fitting intensity quenching data. However, because it will quantitatively fit more complex systems, one should use its fitting parameters cautiously for detailed mechanistic interpretations.

ACKNOWLEDGMENT

We gratefully acknowledge support by the National Science Foundation (CHE 88-17809 and 91-18034), a grant from the Howard Hughes Medical Institute through the Undergraduate Biological Sciences Education Program for support of R.C.M., and an NIH Biomedical Research Support Grant BRS-5-36187. We thank Mindy Whaley, who helped with some of the solid-state lifetime measurements. We thank Hewlett-Packard for the gift of the 8452A spectrophotometer and Henry Wilson for his kind assistance. We thank Cabot Corp. for the gift of the Cab-O-Sil TS-720.

Received for review May 31, 1994. Accepted September 7, 1994.®

(31) Demas, J. N.; Crosby, G. A. *J. Am. Chem. Soc.* **1971**, *93*, 2841–2847.

® Abstract published in *Advance ACS Abstracts*, October 15, 1994.

Anal. Chem. **1994,** *66,* 4142–4149

Laser-Induced Fluorescence Detection of a Single Molecule in a Capillary

Yuan-Hsiang Lee, Russell G. Maus, Ben W. Smith, and James D. Winefordner*

Department of Chemistry, University of Florida, Gainesville, Florida 32611-7200

The objective of this work is to develop a novel laser-excited spectrometric method to reliably detect a single molecule in a flowing stream which is confined in a capillary. An argon ion-pumped Ti–sapphire laser tuned to a rubidium atomic transition line at 780.023 nm is used to excite the fluorescence of IR140 molecules in a capillary. A focused laser beam illuminates the whole capillary inner diameter to achieve near unity spatial probing efficiency. A rubidium metal vapor filter, based on the resonance absorption of an atomic metal vapor, absorbs the laser specular scatter from the capillary while passing the molecular fluorescence. The photoelectron signal is measured during the transit time of a single molecule through the 1.05-pL probe volume. A digital weighted quadratic summing filter is used to extract the individual photon bursts from single molecules. The measurement efficiency for the near-infrared dye IR140 is estimated to be near unity. The average number of photoelectrons from a single IR140 molecule is estimated to be 5.9, 7.0, and 8.5 for laser powers of 50, 100, and 150 mW, respectively.

Detection of a single molecule in a flowing stream has been obtained with a variety of experimental schemes, all involving efficient laser excitation and fluorescent detection.[1–3] As a molecule passes through a focused laser beam, it is repeatedly cycled between the ground electronic state and the excited electronic state with the emission of a photon on each cycle, producing a photon burst.

This paper addresses an important concept in single-molecule detection, which is how to improve the efficiency of detecting all the molecules in a *sample* in contrast to just those that pass through the *probe volume.* In previous experiments for single-molecule detection, most molecules did not pass through the excitation laser beam and as a result the overall detection efficiency was low. Our unique approach is to confine the molecules in a capillary tube, to irradiate the entire internal diameter of the capillary with the excitation laser beam, and to absorb the laser specular scatter with a metal vapor filter.

Sensitive fluorescence detection in solution is limited by the background noise sources from the optics and the solvent. The central problem of isolating the molecular fluorescence from background luminescence and Raman scatter is overcome by reducing the probe volume to the smallest possible size. The reduction in the probe volume can be achieved by optically restricting the illuminated and/or observed volume, by physically decreasing the size of sample confinement, or by a combination of these techniques. Various experimental schemes, such as sheath flow cell and electrodynamic levitated microdroplets, have been applied as the sample confinement for single-molecule detection.

By flowing the molecules in a sample stream, Keller et al.[1] utilized laser-induced fluorescence (LIF) to observe the photon burst from a single molecule. With an electrodynamic trap to confine a single molecule in a microdroplet, Ramsey et al.[2] were also able to detect a single molecule with a signal-to-noise ratio of 3. Soper et al.[3] have demonstrated the detection of near-infrared (near-IR) molecules (IR132) traveling through a focused Gaussian laser beam with 97% detection efficiency. Using a very simple capillary-based experimental system, we have used a diode laser to induce fluorescence of near-infrared fluorophors in a flowing stream and have detected 10^3–10^4 molecules in a single probing.[4,5] With the development of more versatile laser sources, this capillary-based scheme might be easily applied to practical analytical detection in such methods as capillary zone electrophoresis and capillary liquid chromatography or in any analytical technique involving an extremely small sample volume. However, detection of a single molecule with near 100% measurement efficiency has not been achieved because of the need to decrease the spatial probing efficiency to a value considerably below unity in order to minimize the laser scatter and background noise.

In this work, the emphasis is placed on the reliable measurement of a single molecule in a capillary. A major advantage of this approach is that the capillary will facilitate the analysis of extremely small volumes of solution. Furthermore, the extremely small physical dimensions encountered in a capillary column also require that detection be performed on-column, which excludes the utilization of sheathed flow cells and other types of external flow cells.

In addition, the use of a near-IR laser as an excitation source for laser-induced fluorescence is attractive since absorption is negligible for almost every type of matter, such as flow cell material, solvent, and most impurities. This is advantageous because background fluorescence from these materials does not impose limitations on achieving a low detection limit.

However, studies at the single-molecule level using a quartz ultramicrocapillary tube for sample confinement have not been done, in large part because of the difficulty in discriminating against the high level of laser specular scatter caused by the

(1) Shera, E. B.; Seitzinger, N. K.; Davis, L. M.; Keller, R. A.; Soper, S. A. *Chem. Phys. Lett.* **1990**, *174*, 553–557.
(2) Whitten, W. B.; Ramsey, J. M.; Arnold, S.; Bronk, B. V. *Anal. Chem.* **1991**, *63*, *1027*–1031.
(3) Soper, S. A.; Mattingly, Q. L.; Vegunta, P. *Anal. Chem.* **1993**, *65*, 740–747.
(4) Johnson, P. A.; Barber, T. E.; Smith, B. W.; Winefordner, J. D. *Anal. Chem.* **1989**, *61*, *861*–863.
(5) Lehotay, S. J.; Johnson, P. A.; Barber, T. E.; Winefordner, J. D. *Appl. Spectrosc.* **1990**, *44*, 1577–1579.

0003-2700/94/0366-4142$04.50/0 © 1994 American Chemical Society

capillary. Rejection of laser specular scatter has been one of the most important considerations for ultratrace analysis using LIF. An ideal optical filter for laser specular scatter would have to show nearly full absorption at the laser wavelength while maintaining transparency over the luminescence band. The metal vapor filter (MVF) is a promising optical filter for rejecting narrow-band laser specular scatter based on the resonance absorption of an atomic vapor. The MVF is simply a heated quartz cell with parallel windows containing an inert gas and a volatile metal with a resonance atomic absorption line at the laser wavelength. This MVF, depending on its composition, is heated to an appropriate temperature in order to produce a sufficient number density of metal atoms to absorb efficiently all detectable laser specular scatter. Therefore, the metal atoms in the MVF provide a nearly perfect optical filter for laser specular scatter as long as the laser can be tuned to the metal vapor absorption peak and the laser line width is narrower than the absorption bandwidth of the MVF. Compared with conventional laser line rejection filters, such as a monochromator and notch filter, MVFs offer such advantages as low cost, high absorbance, large signal collection solid angle, narrow absorption bandwidth, and high signal throughput. Recently, several MVFs have been demonstrated to be effective in eliminating laser specular scattering for Raman spectroscopy.[6,7]

The intent of this study is to develop a novel LIF spectroscopic technique to reliably detect a single near-IR molecule (IR140) flowing through a small probe volume within a capillary. The laser is tuned to the rubidium atomic transition line at 780.023 nm and focused onto the uncoated part of a capillary. A heated rubidium metal vapor filter absorbs the laser specular scatter while passing the molecular fluorescence. The excitation source is a Ti–sapphire ring laser with a line width narrower than the rubidium atomic absorption bandwidth. The detector is a single-photon avalanche photodiode with high photon detection efficiency and low dark count rate. Because of the importance of the metal vapor filter, the transmission characteristic of the Rb MVF is evaluated theoretically and experimentally. A weighted quadratic summing filter is applied to extract the photon bursts from individual molecules as they pass through the laser beam. Detection of a single molecule in a capillary with high measurement efficiency is demonstrated.

CONCEPT OF SINGLE MOLECULE DETECTION

The ability to detect single molecules is largely governed by the signal-to-noise ratio (S/N) of the measurement. Kaiser has developed a statistical approach for the detection limit, which is defined as the concentration or amount of an analyte that gives a S/N of m, where m is the statistical confidence level.[8] The limit of detection (LOD, $m = 3$) corresponds to a S/N = 3, and the limit of guarantee (LOG, $m = 6$) to a S/N = 6. The reciprocal of S/N times 100 is the percentage relative standard deviation (% RSD) of the measurement. It is assumed that the noise is the same on the blank and on the analyte measurements near the detection limit. The limit of detection X_d is associated with an α – chance of false positive detection (mistaking a blank measurement for the analyte). The analyte is present at a concentration or amount that gives a signal at the limit of guarantee X_g that is associated with a β – chance of false negative detection (mistaking the presence of analyte for the blank). Thus, these two approaches to detection limit (LOD and LOG) are figure of merits describing the detection power of an analytical method. The value of the detection limit indicates the level of analyte that is discerned from the background noise. If measured carefully, the LOD and LOG can give an objective comparison of the detection power of different analytical methods. The LOD has a low probability of false positives (α, type I error), 0.14%, but a high probability of false negatives (β, type II error), 50%. The LOG is a more conservative analytical figure of merit which has very low probability of a false positives (α, type I error), below 0.14%, and a low probability of a false negatives (β, type II error), ~0.14%. This means that when the analyte is present in the sample at the LOD value, fully 50% of the measurement will fall below X_d, even though there is only a 0.14% probability that the measurement of a blank will give a false positive. On the other hand, if the analyte is present at the LOG value, measurement of the analyte will be always detected above X_d at the 99.86% confidence level.

The first theoretical treatment for the concept of detection limit was developed by Alkemade.[9,10] In terms of intrinsic and extrinsic detection limits, Winefordner et al.[11,12] and Stevenson and Winefordner[13–15] have shown theoretically that LIF is the only viable approach for single-molecule detection. Methods that have achieved single-molecule detection using LIF are usually based on a "cyclic" interaction of molecule and laser, and each molecule produces a relatively large number of photons during its interaction with the laser. An ideal technique for single-molecule detection will meet the following demands simultaneously: (i) Intrinsic noise dominates extrinsic noise. (ii) The efficiency of detection, ϵ_d, and the efficiency of measurement, ϵ_m, are both unity.

Noise in a measurement can be classified as either extrinsic or intrinsic. Extrinsic noise is the excess noise that arises owing to a nonspecific background signal that is present even in the absence of analyte. Extrinsic noise sources are determined by such instrumental factors as dark current, source light scatter, background emission from concomitants, and nonselective detection of molecules in blank. Intrinsic noise represents the ultimate limit of an analytical method and is determined by the statistical nature of the measurement process, such as the discrete nature of matter, fluctuations in the low number of analytes in the probe volume, and shot noise in analyte signal production. As intrinsic noise arises from the detection of analytes, it cannot be removed. In a counting measurement, it may be possible to reduce all extrinsic noise sources to the extent that the probability of registering one or more counts from the blank is negligible during the sampling interval. For such an intrinsic noise limit measurement, the only noise on the signal is due to the statistical nature of the analyte detection process itself. Signal noise in an extrinsic noise limited experiment is due to contributions from both extrinsic and intrinsic noise sources.

Alkemade defined the detection efficiency as the probability that any given species appearing in the probe volume produces

(6) Indralingam, R; Simeonsson, J. B.; Petrucci, G. A.; Smith, B. W.; Winefordner, J. D. *Anal. Chem.* **1992**, *64*, 964–967.
(7) Pelletier, M. J. *Appl. Spectrosc.* **1993**, *47*, 69–74.
(8) Kaiser, H. *Two Papers on the Limit of Detection of a Complete Analytical Procedure*; Jafner Publishing: New York, 1969.
(9) Alkemade, C. Th. *J. Appl. Spectrosc.* **1981**, *35*, 1–14.
(10) Alkamade, C. Th. In *Analytical Applications of Lasers*; Pipmeier, E. H., Ed.; Wiley-Interscience: New York, 1986; Chapter 4.
(11) Winefordner, J. D.; Stevenson, C. *Spectrochim. Acta* **1993**, *44B*, 757–767.
(12) Winefordner, J. D.; Petrucci, G. A.; Stevenson, C. L.; Smith, B. W. *J. Anal. At. Spectrom.* **1994**, *9*, 131–143.
(13) Stevenson C. L.; Winefordner, J. D. *Appl. Spectrosc.* **1992**, *46*, 715–724.
(14) Stevenson, C. L.; Winefordner, J. D. *Appl. Spectrosc.* **1992**, *46*, 407–419.
(15) Stevenson, C. L.; Winefordner, J. D. *Appl. Spectrosc.* **1991**, *45*, 1217–1224.

Table 1. Required Sensitivities for Limit of Detection (LOD) and Limit of Guarantee (LOG)

mean blank, X_b (counts)	mean sensitivity, X_t (counts) LOD = 1 molecule $\alpha \leq 0.0014$	LOG = 1 molecule $\beta \approx 0.0014$
0.00	1	6.6
0.05	2	8.9
0.25	4	12.4
1.00	5	15
5.00	9	23
10.00	12	29
100.00	32	69

an event during the transit time.[9,10] The probe volume was determined by the geometry of the (intersecting) laser beam and by the part of the irradiated region that is "seen" by the detector. In this approach, the transit time was determined by the pulse duration or the width of the time gate in case a time-gating circuit is applied, whichever is the shorter. Multiple probings were obtained by firing many laser shots. In addition, Alkemade was concerned only with those cases when there were no extrinsic noise sources.

Winefordner et al.[11,12] and Stevenson and Winefordner[13–15] have developed a theory to take into account the transit time of a single molecule within the probe volume and the presence of extrinsic noise sources. When compared with Alkemade's concepts, Winefordner's are more general in two important aspects: (1) Detection efficiency is defined with respect to a transit time of the molecules in the probe volume, not simply over a single "probing" of the laser pulse. (2) Detection efficiency considers the need to detect the signal due to analytes over the extrinsic noise.

Therefore, the detection efficiency is defined as the probability that a given analyte appearing in the probe volume produces a signal that is detected above the background noise (if any) during the transit time of the analytes within the observation region. Table 1 gives the measurement sensitivity, X_t, required to detect single molecules by using LIF at various mean blank signal levels ($\alpha \leq 0.0014$ for LOD and $\beta \approx 0.0014$ for LOG).[11,12] For example, at the intrinsic noise limit ($X_b = 0$), values of $X_t = 1$ count molecule^{-1} and $X_t = 6.6$ counts molecule^{-1} are needed to detect a single molecule for the LOD and LOG, respectively. This means that, in order to detect every molecule that crosses the laser with 99.86% confidence (LOG), each molecule must emit enough photons so that, on average, 6.6 counts are registered for the molecule by the detector. As the background level increases, e.g., to 1 count, the number of analyte counts from a single molecule above the blank increases to 5 counts molecule^{-1} (total 5 + 1 counts molecule^{-1}) at the LOD and 15 counts molecule^{-1} (total 15 + 1 counts molecule^{-1}) at the LOG.

The overall measurement efficiency, ϵ_m, is defined as the probability that a given analyte in the sample is detected above the background noise in the observation region. The measurement efficiency, ϵ_m, is related to the detection efficiency, ϵ_d, by the following equations:

$$\epsilon_m = \epsilon_T \epsilon_P \epsilon_d \quad (1)$$

$$\epsilon_p = \epsilon_s \epsilon_t \quad (2)$$

where ϵ_T is the transfer efficiency of the sample from the point of introduction to the probing region and ϵ_P is the probing efficiency, which is composed of a spatial probing efficiency, ϵ_s, and a temporal probing efficiency, ϵ_t. The spatial probing efficiency, ϵ_s, accounts for the loss of analyte species not passing through the laser excitation and/or observation region. The temporal probing efficiency, ϵ_t, is unity for a continuous wave source or a pulsed source that is at a repetition rate sufficiently high such that each analyte interacts with at least one laser pulse while passing through the observation region. Unlike ϵ_d, the value of ϵ_m is related to analyte concentration in the sample and may be less than unity even if $\epsilon_d = 100\%$ since ϵ_m accounts for analyte losses between the sample and the detection region and for insufficient spatial and temporal probing of analytes.

Even if single-molecule detection with high detection efficiency has been achieved in the sheath flow cell, the measurement efficiency may be far less than unity. For example, a sample stream flowing through a square flow cell has been used to minimize the laser specular scatter caused by the optical materials.[16–19] However, the laser beam only probed a small portion of the sample stream to reduce the Raman and background scatter from the solvent and the optical materials. A spatial filter placed before the detector only imaged a small region of probe volume to reduce the amount of laser scatter generated at the air–glass interface. Therefore, the spatial probing efficiency for single-molecule detection in a sheathed flow cell was very low, which means that only a fraction of those molecules passing through the flow cell were detected even though the detection efficiency was near unity.

In this work, the laser beam illuminates the whole sample stream, which is confined in a capillary, as compared to many of the previous studies involving sheathed flow cells, where the spatial probing efficiency was much less than unity. Thus, every molecule passing through the capillary flow cell in our case should be detected with near-unity measurement efficiency (ϵ_m).

EXPERIMENTAL SECTION

Instrumentation. A schematic diagram for the single-molecule detection apparatus is shown in Figure 1. All lines output from an argon ion laser (Spectra Physics 2060, Mountain View, CA) are used to pump a single-mode, tunable, continuous-wave titanium–sapphire laser in the ring configuration (Schwartz Electro-Optics, Inc., Orlando, FL). The laser spectral line width is less than 10 MHz.[20] A weak, broad-band background fluorescence from the Ti–sapphire crystal is further attenuated with a narrow-band pass interference filter (0.18 nm fwhm at 780.1 nm, Omega Optical, Brattleboro, VT). The sample is contained in a fused silica capillary (inner diameter 11 μm, outer diameter 139 μm, and length 10 cm; Polymicro Technology, Phoenix, AZ), and flow is controlled by a mechanical microliter syringe pump (Harvard Apparatus 975, South Natick, MA). From the known volume of solution introduced with the gas-tight microliter syringe

(16) Dovichi, N. J.; Martin, J. C.; Jett, J. H.; Trkula, M.; Keller, R. A. *Anal. Chem.* **1984**, *56*, 348–354.
(17) Nguyen, D. C.; Keller, R. A.; Jett, J. H.; Martin, J. C. *Anal. Chem.* **1987**, *59*, 2158–2161.
(18) Nguyen, D. C.; Keller, R. A.; Trkula, M. *J. Opt. Soc. Am. B* **1987**, *4*, 138–143.
(19) Jett, J. H.; Keller, R. A.; Martin, J. C.; Marrone, B. L.; Moyzis, R. K.; Ratliff, R. L.; Seitzinger, N. K.; Shera, E. B.; Stewart, C. C. *J. Biomol. Struct., Dyn.* **1989**, *7*, 301–309.
(20) Schwartz Electro-Optics, Inc., Titanium–sapphire tunable lasers data sheet, 1990.

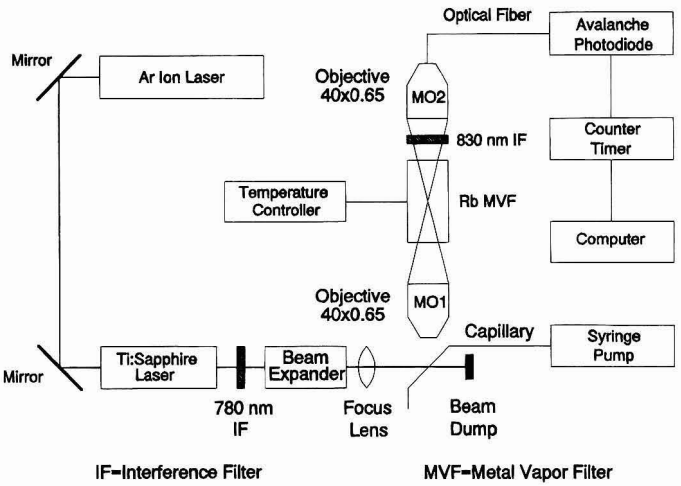


Figure 1. Experimental arrangement for detecting a single molecule in a capillary.

and time of introduction, the measured volume flow rate is found to be very close to the value specified by the manufacturer. To obtain a stable slow flow rate, a 30-min waiting time is normal before making the measurement. A "fluorescence window" is created by removing a section of the polyimide coating on the capillary with concentrated sulfuric acid at 100 °C. The laser is directed through a 20× beam expander (Melles Griot, Irvine, CA) and focused by a camera lens (1:1.4, $f = 55$ mm) onto the uncoated part of the capillary. By translating a razor blade across the laser beam with a microtranslation stage (Newport 461-XY-M, Irvine, CA) and monitoring the laser power on a photodiode, the $1/e^2$ laser beam diameter on the capillary is determined to be 11 μm. Since the focused laser beam and the capillary inner diameter are the same, the system is very sensitive to changes in the optical alignment. As an approximation, the probe volume is defined as a cylinder whose radius is equal to the capillary inner radius and whose height is equal to twice the radius of the focused laser beam. From the capillary inner diameter and laser beam diameter, the probe volume is estimated to be 1.05 pL. The fluorescence and the laser scatter are collected at a right angle by using a microscope objective (40 × 0.65, Melles Griot, Irvine, CA) and passed through the Rb MVF. For the absorbance measurements of the Rb MVF at different temperatures, the capillary is replaced with a mirror at 45° in order to direct the laser beam through the Rb MVF. The commercially available metal vapor cell (Opthos, Rockville, MD) consisted of a quartz cylinder (length 10 cm, diameter 2.5 cm) with parallel quartz windows on both ends. An excess of rubidium metal (500 mg) was distilled into the evacuated cell such that sufficient metal would be present to give saturated metal vapor at all temperatures used in this work. Nitrogen gas at 200 Torr (at room temperature) was used as a fill gas in order to quench the atomic resonance fluorescence and broaden the absorption bandwidth of the Rb MVF. To avoid window discoloring due to the attack of hot Rb metal vapor, the Rb MVF is held inside a cylindrical forced hot nitrogen heating device, as shown in Figure 2. The nitrogen, which is heated by a furnace (Lindberg 55035, Watertown, WI) whose temperature is controlled to within

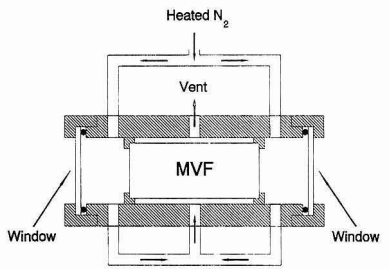


Figure 2. Cutaway view for the design of rubidium metal vapor filter.

±1 °C, flows past both windows and recycles back to the body of the MVF. In this way, the flat window faces of the MVF are kept warmer than the center of the MVF, preventing metal vapor from condensing onto the windows, which would reduce the signal throughput and the transmittance of the MVF. The Rb MVF used in this work has functioned flawlessly for over 1 year. A bandpass interference filter (10 nm fwhm at 830 nm, Corion, Holliston, MA) is placed after the Rb MVF to block the Raman scattering at 860 nm from the solvent.[21] With a second microscope objective (40 × 0.65, Melles Griot, Irvine, CA), the output from the Rb MVF is then refocused onto a fiber pigtail (100-μm core diameter, Canstar, ON, Canada), which is prealigned to the avalanche photodiode. The avalanche photodiode (EG&G Optoelectronics Canada SPCM-200, Vaudreuil, Canada) is a single-photon counting module with 25% photon detection efficiency at 830 nm and a dark count rate of 25 counts s^{-1}.[22] The digital output pulses from the avalanche photodiode are interfaced to a computer-controlled counter/timer board (Keithley Metrabyte CTM-05, Tauntor, MA) for further data analysis.

To tune the Ti–sapphire laser to the Rb transition line at 780.023 nm, the Rb MVF is heated to 100 °C and laser scatter

(21) Lehotay, S. J. Ph.D. Dissertation, University of Florida, Gainsville, FL, 1992.
(22) EG&G SPCM-200-PQ-F830 data sheet, 1993.

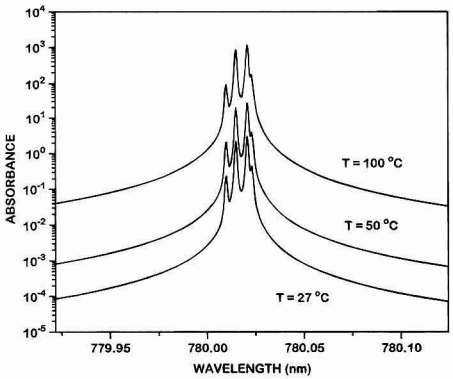


Figure 3. Calculated rubidium Voigt absorption profile of the 780.023-nm rubidium line at different temperatures. Path length is 10 cm, and nitrogen pressure is 200 Torr at 25 °C.

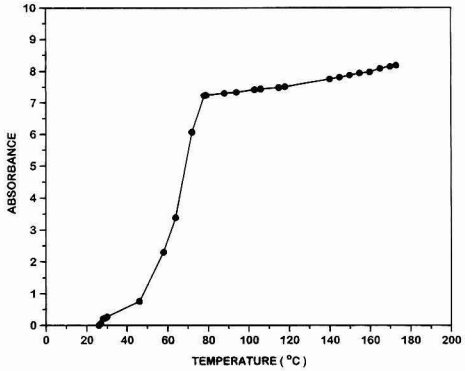


Figure 4. Experimental results for absorption of rubidium metal vapor filter at 780.023 nm. Path length is 10 cm, and nitrogen pressure is 200 Torr at 25 °C.

from the capillary is passed through the Rb MVF onto the avalanche photodiode. The Ti–sapphire laser is then tuned to maximum absorbance of the Rb MVF by slowly adjusting the intracavity birefringent filter. Fine tuning is done by tilting the intercavity Fabry Perot etalon to further maximize absorbance. The maximum absorbance is more like a plateau than a peak because the Fabry Perot etalon can be adjusted significantly before the laser is tuned off-wavelength and the absorbance decreased sharply. The calculated laser line width (fwhm) at 780.023 nm is less than 0.081 pm when the Ti–sapphire laser is operated in the ring configuration with a 10-MHz spectral line width.[10]

Reagents and Chemicals. The IR140 [Exciton Chemical Co., Inc., Dayton, OH; chemical name, 5,5′-dichloro-11-(diphenylamino)-3,3′-diethyl-10,12-ethylenethiatricarbocyanine perchlorate; CAS no. 53655-17-7; fw = 779] is dissolved in methanol (Optima grade, Fisher Scientific, Orlando, FL). Sample solutions at different concentrations are prepared from serial dilution of a 1.5×10^{-5} M stock solution and analyzed on the same day. The fluorescence maximum for IR140 in methanol is 833 nm with excitation at 780.023 nm.

RESULTS AND DISCUSSION

Characterization of Rb Metal Vapor Filter. Because of its role in absorbing the laser specular scatter, the Rb MVF is one of the most critical components for detecting single molecules in a capillary. The rubidium atom has two main isotopes, ^{85}Rb and ^{87}Rb, which exist naturally in the ratio of 0.727:0.273.[23] Each isotope has its own hyperfine structure. The melting point for rubidium is 39 °C, so it is easy to produce a sufficient number density of atoms at a moderate temperature. From the oscillator strength and number density of each electronic transition,[24] the absorption profile of Rb can be simulated at various conditions. Based on Puerta and Martin's approximation,[25] Figure 3 shows the calculated Voigt absorption profile, a convolution of Gaussian and Lorentzian profiles, of Rb at 27, 50, and 100 °C. As Figure 3 shows, increasing the cell temperature has a large effect on the absorbance, which essentially mirrors the increasing Rb metal vapor number density. The presence of more than one peak for each absorption profile is due to the hyperfine structure of the overall transition. The Voigt absorption bandwidth is estimated to be 21 pm at 780.023 nm, which is close to the measured value.[26] Ideally, once the narrow laser line is tuned to the absorption peak of the Rb MVF at 100 °C, an absorbance of several thousand could be reached. By calibrating with neutral density filters, the transmitted signal through the Rb MVF is measured at different temperatures. The measured transmittance is then converted to absorbance. The result is shown in Figure 4, where the absorbance of the laser scatter is plotted as a function of temperature. The maximum absorbance of ~8 at 170 °C is believed to be limited by a weak, broad-band laser background from the Ti–sapphire crystal.

Single-Molecule Detection. To achieve single-molecule detection with near unity measurement efficiency, the capillary must be fully illuminated with the focused laser beam. Dovichi et al.[16] and Soper et al.[3] have described the algorithm for the parabolic flow within the sample stream. The average linear flow velocity of molecules flowing through the capillary can be estimated from the volume flow rate and the cross-sectional area of the capillary (9.5×10^{-7} cm^2). The average molecular transit time through the probe volume can be simply determined using the equation[16]

$$\text{average transit time} = \frac{\pi \times \text{laser beam diameter}}{4 \times \text{average linear flow velocity}} \quad (3)$$

The calculated transit time is ~0.8 ms when the volume flow rate of the syringe pump is set at 0.061 μL/min. Possible deviations from the molecular transit time in the probe volume are the uncertainties of the small capillary inside diameter, distorted laser beam shape within the cylindrical capillary, and Brownian diffusion. Desorption of molecules from the capillary walls, left over from a previous experiment at high concentrations, could lead to more detected molecules than expected. Alterna-

(23) Beacham, J. R.; Andrew, K. L. *J. Opt. Soc. Am.* **1971**, *61* (2), 231–235.
(24) Gallagher, A.; Lewis, E. L. *J. Opt. Soc. Am.* **1973**, *63* (3), 864–869.
(25) Puerta, J.; Martin, P. *Appl. Opt.* **1981**, *20* (22), 3923–3928.
(26) Barber, T. E. Ph.D. Dissertation, University of Florida, Gainsville, FL, 1992.

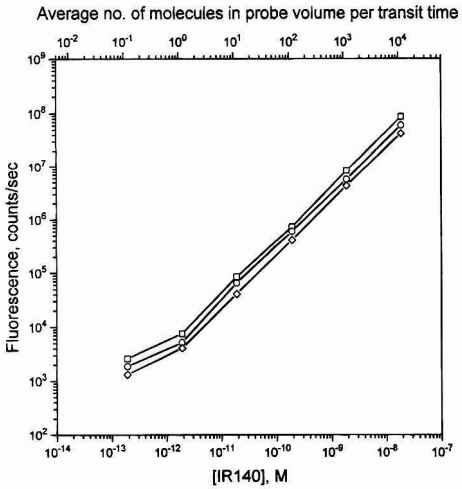


Figure 5. log–log plot of the IR140 fluorescence emission versus the sample concentration with a transit time of 0.8 ms at different laser powers: 150 (□), 100 (○), and 50 mW(◇).

tively, the number of molecules detected would be less than the number of molecules expected due to sample adsorption on the walls of the capillary.

The average photodestruction probability of the flowing molecules can be evaluated by measuring the dependence of fluorescence intensity on the flow velocity of fluorescent molecules through a laser beam.[27] When the laser power is 150 mW, the fluorescence signal from the IR140 decreases to 85% of the maximum value when the volume flow rate is decreased from 1.26 to 0.061 μL/min. The corresponding transit time of IR140 molecules in the probe volume increases from 0.039 ms to 0.8 ms when the volume flow rate is decreased over this range, thus indicating that the majority of the molecules are not photodestructed during their travel through the laser beam.

Figure 5 shows the log–log calibration curves of IR140 over various concentration ranges. These calibration curves are obtained at three different laser powers while the molecular transit time is 0.8 ms. The signal from IR140 molecules is linear for at least 4 orders of magnitude from 1.9×10^{-12} to 1.9×10^{-8} M. Within this linear concentration range, the average number of molecules present in the probe volume per transit time are from 1.2 to 12 000. For an IR140 concentration of 1.9×10^{-12} M and a transit time of 0.8 ms, there are ~1500 molecules that actually travel through the probe volume within a 1-s integration time.

To assure that only one molecule resides within the probe volume at any given time, the probability of two or more than two molecules occupying the probe volume must be minimized. Assuming the number of molecules in the probe volume during the transit time follows the Poisson distribution, the probability that n molecules occupy the probe volume simultaneously is given by

(27) Mathies, R. A.; Stryer, L. In *Applications of Fluorescence in the Biomedical Sciences*; Tylor, D. L., Waggoner, A. S., Lanni, F., Murphy, R. F., Birge, R., Eds.; Alan R. Liss, Inc.: New York, 1986; pp 129–140.

Table 2. Probability for Different Numbers of Molecules Occupying the Probe Volume at Any Given Time[a]

no. of molecules in probe vol	probability
0	0.887
1	0.106
2	0.006
3	~0.000

[a] [IR140] = 1.9×10^{-13} M; probe volume, 1.05 pL.

$$P(N_{t+k} - N_t = n) = \frac{(k\lambda_p)^n e^{-k\lambda_p}}{n!} \quad (4)$$

where N_t is the number of molecules arrived at time t, k is the number of time segment per transit time, and λ_p is the average number of molecules in probe volume per time segment.

At an IR140 concentration of 1.9×10^{-13} M, the average number of molecules in the probe volume (1.05 pL) is 0.12. For the present experimental parameters, since the transit time of single IR140 molecules through the probe volume is 0.8 ms, therefore $k = 4$ and $\lambda_p = 0.03$ for a counter with a 200-μs time segment (integration time). In other words, when a single molecule flows through the probe volume with a 0.8-ms transit time, the emitted photons should be distributed over four consecutive time segments. Table 2 gives the probability for different numbers of molecules occupying the probe volume at any given time. Most of time, there is no molecule in the probe volume ($P(n=0) = 0.887$). The probability of one molecule occupying the probe volume is $P(n=1) = 0.106$ while the probability of multiple occupancy ($P(n \geq 2) = 0.006$) is relatively low and can be neglected.

It is possible to estimate the average number of events expected as a single IR140 molecule passes through the focused laser beam. Here, the number of events is the number of time segments with any signal counts from single IR140 molecules. The number of events, N_{ev}, for all molecules traveling through the probe volume during the measurement time T can be estimated from

$$N_{ev} = \frac{N_p T k}{t_r} \quad (5)$$

where N_{ev} is the number of events from molecules during the measurement time, N_p is the average number of molecules in probe volume, and t_r is the transit time of a single molecule in probe volume.

The calculated total number of events, N_{ev}, is 120 during a typical experimental run ([IR140] = 1.9×10^{-13} M, $N_p = 0.12$, T = 200 ms, $k = 4$, and $t_r = 0.8$ ms). Within the 200-ms measurement time, ~30 molecules will pass through the probe volume.

To obtain photon bursts from individual single molecules, various signal processing methods have been proposed for the continuous detection and monitoring of molecules entering the probe volume.[1,3,13–15,28,29] The individual photon bursts are analyzed and searched within the data stream in order to obtain direct

(28) Soper, S. A.; Davis, L. M.; Shera, E. B. *J. Opt. Soc. Am. B* **1992**, *9*, 1761–1769.

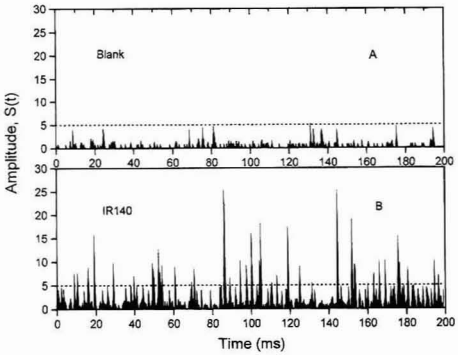


Figure 6. Photon burst data for the methanol blank (A) and for a 1.9×10^{-13} M IR140 solution (B) subjected to the weighted quadratic summing (WQS) filter algorithm with $k = 4$. The IR140 molecules is excited with 100-mW laser power at a flow rate of 0.061 μL/min (transit time, 0.8 ms). The raw data are taken in a 200-μs integration time. Within the 200-ms sampling time, ~30 molecules pass through the probe volume. The discriminator threshold (dashed lines) was set at $S(t) = 5$. The number of events that exceeded this threshold for the dye solution is found to be 110.

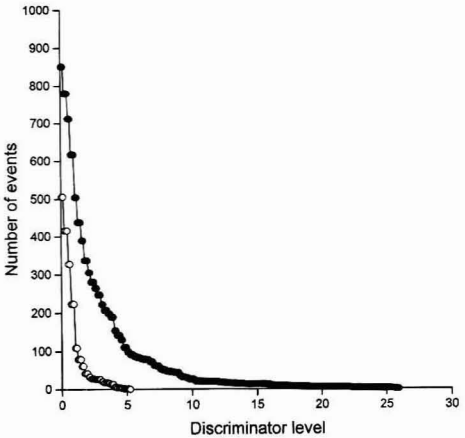


Figure 7. Cumulative number of events exceeding the discriminator threshold versus discriminator for a 1.9×10^{-13} M IR140 solution (●) and for the methanol blank (○). The experimental conditions are the same as those in Figure 6. When the discriminator level is set to 5, there are 110 events detected from the IR140 molecules while only 1 event from the methanol blank.

evidence for single-molecule sensitivity. To enhance the visibility of photon bursts from single molecules, the weighted quadratic summing (WQS) filter, a modified sliding sum method, has been evaluated and demonstrated to be an efficient photon burst indicator of a passing single molecule in previous single-molecule detection experiments. The raw data are squared and processed with the WQS filter algorithm, which is given by

$$S(t) = \sum_{\tau=0}^{k-1} w(\tau)\ \mathrm{d}(t+\tau)^2 \qquad (6)$$

where k covers time intervals that are approximately equal to the transit time of a single molecule through the probe volume, $w(\tau)$ is a weighing factor, and $\mathrm{d}(t+\tau)$ is the raw data point at time $t + \tau$. Due to the lack of knowledge in the actual laser excitation profile within the capillary and the photon emission profile from single molecules, different weighing factors might give an optimized S/N ratio depending on the experimental conditions. As the molecules cross the laser beam, the fluorescence signal increases slowly, followed by an abrupt cessation, when the molecule is photodecomposed. To best discriminate the time-correlated fluorescence signal from the random background noise, the weighing factor, $w(\tau)$, is chosen as an asymmetric triangular ramp,[1,3]

$$w(\tau) = \frac{(\tau+1)}{k} \qquad (7)$$

Figure 6 shows the WQS filtered data for a 1.9×10^{-13} M IR140 solution and the methanol blank. The large-amplitude bursts from IR140 solution are clearly evident for individual single molecules passing through the center of laser beam. The variation in the burst amplitude arises from the molecules flowing through different parts of the Gaussian intensity laser profile. When the molecules travel through the edges of the laser beam, they experience fewer excitation cycles and thus emit fewer photons. Variation in the solvent blank photoelectron bursts is due to fluctuations of background and dark counts.

In order to evaluate the detection efficiency for the near-IR dye molecules, a plot of the cumulative number of WQS filtered events exceeding a discriminator threshold is constructed for the solvent blank and the dye solution. Figure 7 shows the cumulative number of filtered events exceeding a discriminator threshold for a 1.9×10^{-13} M IR140 solution and the methanol blank when excited with 100-mW laser power. Since the spatial probing efficiency is near unity, the measurement efficiency is defined as the ratio of measured to expected total number of events for molecules flowing through the capillary. To minimize the false positive probability, the discriminator threshold is set at $S(t) = 5$, indicated as the dashed line in Figure 6. The number of events that exceed the threshold for the IR140 molecules is found to be 110, while 1 event is due to blank. Since the expected number of events during this 200-ms measurement time is ~120, the measurement efficiency is calculated to be slightly less than 100%, which is believed due to errors in the estimation of analyte concentration and the probe volume and/or due to sample adsorption on the walls of the capillary. To designate photon bursts from individual single molecules, the raw data are compared with WQS filtered data. The corresponding four consecutive raw data points with WQS amplitude higher than the specific discriminator threshold are binned to four (200 μs × 4) within the 200-ms measurement time. The total photoelectron counts of these four consecutive raw data points give the size of the photon burst from this specific single molecule. Table 3 summarizes the total number of events and average detected photo-

(29) Soper, S. A.; Davis, L. M.; Fairfield, F. R.; Hammond, M. L.; Harger, V. A.; Jett, J. H.; Keller, R. A.; Martin, J. C.; Nutter, H. L.; Shera, E. B.; Simpson, D. J. In *Optical Methods for Ultrasensitive Detection and Analysis: Techniques and Applications*; Feary, B. L., Ed. *Proc. SPIE-Int. Soc. Opt. Instrum. Eng.* **1991**, *1435*, 168–178.

Table 3. Number of Fluorescent Events at Different Laser Powers

	laser power (mW)		
	50	100	150
discriminator	3.1	5.0	7.1
measured events	112	110	116
expected events	120	120	120
av photoelectrons per molecule[a]	5.9	7.0	8.5

[a] Average number of photoelectrons per molecule is calculated as $(\sum C_i)/N$, where N is the number of molecules with WQS amplitude higher than the discriminator level and C_i is the photon counts from an individual molecule using the raw data.

electrons from a single molecule with excitation at different laser powers. A higher discriminator threshold is required when the laser power is increased while maintaining similar detection efficiency. It is found that the average number of photoelectrons detected from a single IR140 molecule while traveling through the probe volume per transit time are 8.5, 7.0, and 5.9 for 150-, 100-, and 50-mW laser powers. Ideally, when a single molecule passes through the laser beam, the distribution of emitted photons should mirror the Gaussian profile of the laser beam. Unfortunately, if the size of photon burst from a single molecule is small, as in this work, the Poisson noise will severely distort the Gaussian distribution. The other complication with the present experimental configuration is that some molecules pass through the edge of the laser beam. This makes the exact counting of single molecules more difficult. Since the average number of background counts per transit time is less than 1 count within these three laser powers, 5 or more signal counts justify the use of the LOD concept, but do not justify the case of the LOG.

Table 4 compares the near-IR single-molecule detection of IR132 and IR140. Although the average photon yield per molecule is lower for IR140 with similar photon detection efficiency, the measurement efficiency is 4 orders of magnitude higher because the whole capillary inner diameter is fully illuminated with the laser beam to assure near unity spatial probing efficiency.

CONCLUSIONS

In summary, this work has demonstrated the photon burst detection of single near-IR molecules (IR140) with high efficiency. There are several components that are interesting and relevant in the area of single-molecule detection. For example, the use of the metal vapor filter and the high spatial probing efficiency produced by irradiating the entire inner diameter of the capillary are unique. This approach depends heavily on the use of a novel

Table 4. Comparison of Near-Infrared Single-Molecule Detection for IR132 and IR140

parameter	IR132[a]	IR140
excitation wavelength (nm)	800	780
observed wavelength[b] (nm)	840 (30)	830 (10)
photon detection efficiency	0.007	0.007[c]
probe volume (pL)	0.8	1.05
transit time (ms)	10	0.8
av photoelectron per molecule	18 (±4)	8.5[d]
detection efficiency (%)	97 (±7)	97
spatial probing efficiency (%)	0.01	100
measurement efficiency (%)	0.0097	97

[a] Data taken from ref 3. [b] The number in parenthesis is fwhm spectral bandpass. [c] The photon detection efficiency is calculated from the product of the geometric collection efficiency of MO1 (10%), the transmission efficiency of MO1 (90%), the transmission efficiency of rubidium metal vapor filter (90%), the transmission efficiency of the band-pass filter for the fluorescence emission of the dye (50%), the geometric collection efficiency of MO2 (90%), the transmission efficiency of MO2 (90%), the transmission efficiency of optical fiber (90%), and the quantum efficiency of the avalanche photodiode at 830 nm. [d] Laser power, 150 mW.

metal vapor filter to minimize laser scatter from the capillary reaching the detector. The measured absorbance of the rubidium metal vapor filter at 170 °C is determined to be ~8. The maximum absorbance is believed to be limited by the background fluorescence from the Ti−sapphire laser. The use of near-IR excitation and detection will benefit ultrasensitive fluorescence detection due to the reduced background noise sources from impurities. The fluorescence signal versus concentration plot has good linearity for at least 4 orders of magnitude from 1.9×10^{-12} to 1.9×10^{-8} M. To enhance the detection of single molecules, a digital weighted quadratic summing filter is applied to extract the individual photon bursts from the raw data. The development of on-column capillary detection with single-molecule-level sensitivity would have a major impact on numerous analytical applications, including cell sorting and sizing, immunoassay, DNA sequencing, and miniaturized chemical separation techniques involving capillary electrophoresis, packed capillary liquid chromatography, and open tubular capillary liquid chromatography.

ACKNOWLEDGMENT

The authors thank Dr. D. Hueber and Dr. S. J. Lehotay for helpful discussions in this work. We also acknowledge the University of Florida, Division of Sponsored Research, for partial financial support of this work.

Received May 26, 1994. Accepted September 7, 1994.[⊗]

[⊗] Abstract published in *Advance ACS Abstracts,* October 15, 1994.

Anal. Chem. **1994,** *66,* 4150−4153

Solvents Effects in Determination of Anthracene on Solution Surfaces by Laser Two-Photon Ionization Technique

Hangting Chen,† Takanori Inoue, and Teiichiro Ogawa*

Department of Molecular Science and Technology, Kyushu University, Kasuga-shi, Fukuoka 816, Japan

The photoionization charge (area of the signal) of anthracene on the solution surface has been measured for various solvents using the third harmonic of an NdYAG laser (355 nm). The charge was quadratically proportional to the laser pulse energy, indicating a two-photon process. It saturated quickly at a higher bias voltage. It increased drastically with increasing dielectric constant of the solvent when the solvent was polar. It increased with increasing electron mobility of the solvent when the solvent was nonpolar. Water, which has the largest dielectric constant among the solvents used, gave the largest signal and the lowest detection limit.

The laser two-photon ionization technique has been a convenient and sensitive method for detecting photoabsorbing molecular species.[1] In a sequential two-photon process, an analyte molecule absorbs a first photon to be excited to a resonant state, and the excited molecule absorbs a second photon to be selectively ionized in the presence of a large amount of transparent solvent or bulk molecules. The conductivity method is sensitive for detecting ions and electrons thus produced. Highly sensitive detections have been carried out in nonpolar solvents.[2−6] on a metal surface[7−9] and on a water surface.[10−12]

A large leakage current has been detrimental for highly sensitive detection in polar solvents.[13−15] Although the effect of polar solvents has been investigated with a flow cell,[13,16] it has been impossible to carry out a highly sensitive determination in water in spite of the importance of water for practical applications. This disadvantage has been overcome by using the surface of the solution,[10−12] because an air gap between the positive electrode and the solution surface can cut off the leakage current (a dc component) effectively and because electrons can, nevertheless, be liberated from the solution surface and pass through the air gap to the positive electrode. The detection limits of aromatic molecules excited by a nitrogen laser (337 nm) were as low as sub-ppb levels for aromatic molecules on the water surface, and these values were close to those obtained in the nonpolar hydrocarbon solvents.[11]

Photoionization from a solution surface has been investigated in a vacuum with special devices: a rotating disk electrode[17,18] for surface photoelectron spectroscopy and a liquid jet[19,20] for time-of-flight ion detection. These techniques have indicated the translational energy of the ejected species. Meanwhile, the present technique can provide information on the in situ solution in ambient air.

Water is the only solvent so far used for surface photoionization in ambient air. It is an important subject to study the effect of solvents and to clarify important factors for efficient photoionization from a solution surface. In solution experiments, the photoionization signal increases with increasing electron mobility of the solvent.[21]

Polycyclic aromatic hydrocarbons are important environmental pollutants and have cancer-inducing effects. There are intensive needs for highly sensitive detection of these toxic compounds. Laser-induced fluorescence is the most popular technique for this purpose,[22] and use of a diode laser has simplified the apparatus.[23,24] Sharp spectra of these molecules have been obtained by a supersonic jet technique in order to increase selectivity.[25]

In the present paper, we are reporting laser two-photon ionization of anthracene on the surface of various solvents and the effect of the solvent polarity, the dielectric constant, and the electron mobility on the photoionization signal. Their implications for analytical applications will be discussed.

EXPERIMENTAL SECTION

The experimental apparatus was essentially identical with that described previously.[10−12] Briefly, the third harmonic of an

† On leave from the Chungchun Institute for Applied Chemistry, Changchun, Jilin, China.

(1) Yamada, S.; Ogawa, T. *Prog. Anal. Spectrosc.* **1986**, *9*, 429
(2) Voigtman, E.; Jurgensen, A.; Winefordner, J. D. *Anal. Chem.* **1981**, *53*, 1921.
(3) Yamada, S.; Kano, K.; Ogawa, T. *Bunseki Kagaku* **1982**, *31*, E247.
(4) Yamada, S.; Hino, K.; Kano, K.; Ogawa, T. *Anal. Chem.* **1983**, *55*, 1914.
(5) Yamada, S.; Sato, S.; Kawazumi, H.; Ogawa, T. *Anal. Chem.* **1987**, *59*, 2719.
(6) Ogawa, T.; Kise, K.; Yasuda, T.; Kawazumi, H.; Yamada, S. *Anal. Chem.* **1992**, *64*, 1217.
(7) Ogawa, T.; Yasuda, T.; Kawazumi, H. *Anal. Sci.* **1992**, *8*, 81.
(8) Ogawa, T.; Yasuda, T.; Kawazumi, H. *Anal. Chem.* **1992**, *64*, 2615.
(9) Kawazumi, H.; Yasuda, T.; Ogawa, T. *Anal. Chim. Acta* **1993**, *283*, 111.
(10) Masuda, K.; Inoue, T.; Yasuda, T.; Nakashima, K.; Ogawa, T. *Anal. Sci.* **1993**, *9*, 297.
(11) Inoue, T.; Masuda K.; Nakashima, K.; Ogawa, T. *Anal. Chem.* **1994**, *66*, 1012.
(12) Ogawa, T.; Chen, H.; Masuda, K.; Inoue, T. *Anal. Sci.* **1994**, *10*, 219.
(13) Voigtman, E.; Winefordner, J. D. *Anal. Chem.* **1982**, *54*, 1834.
(14) Yamada, S.; Ogawa, T.; Zhang, P. *Anal. Chim. Acta* **1986**, *183*, 251.
(15) Johnson, M. E.; Voigtman, E. *Anal. Chem.* **1992**, *64*, 551.
(16) Voigtman, E.; Snyder, P. A. *Anal. Instrum.* **1990**, *19*, 1.
(17) Nemec, L.; Gaehrs, H. J.; Chia, L.; Delahay, P. *J. Chem. Phys.* **1977**, *66*, 4450. Watanabe, I.; One, K.; Ikeda, S. *Bull. Chem. Soc. Jpn.* **1991**, *64*, 352.
(18) Moberg, R.; Bökman, F.; Bohman, O.; Siegbahn, H. O. G. *J. Chem. Phys.* **1991**, *94*, 5226.
(19) Nishi, N.; Koga, K.; Ohshima, C.; Yamamoto, K.; Nagashima, U.; Nagami, K. *J. Am. Chem. Soc.* **1988**, *110*, 5246.
(20) Mafune, F.; Takedo, Y.; Nagata, T.; Kondow, T. *Chem. Phys. Lett.* **1992**, *199*, 615; **1994**, *218*. 234.
(21) Ogawa, T.; Sato, M.; Tachibana, M.; Ideta, K.; Inoue, T.; Nakashima, K. *Anal. Chim. Acta*, in press.
(22) Imasaka, T.; Ishibashi, N. *Prog. Quantum Electron.* **1990**, *14*, 131.
(23) Imasaka, T.; Ishibashi, N. *Anal. Chem.* **1990**, *62*, 363A.
(24) Imasaka, T. *Anal. Sci.* **1993**, *9*, 329.
(25) Imasaka, T.; Tsukamoto, A.; Ishibashi, N. *Anal. Chem.* **1988**, *60*, 1362.

0003-2700/94/0366-4150$04.50/0 © 1994 American Chemical Society

NdYAG laser (Spectra Physics GCR11; 355 nm, 60 mJ, 10 Hz) was focused by a quartz lens ($f = 900$ mm) softly on the solution surface; the incident angle to the surface normal was set at 85°. Typical laser pulse energy used was 0.8 mJ/pulse, because the signal-to-noise ratio was best at this pulse energy.[12] A stainless steel container (0.5 mL) held the sample solution, served as the negatiave electrode, and was connected to a current amplifier (Keithley 427). A disk electrode was located 6 mm above the solution surface and was positively biased (2 kV/6 mm) by a high-voltage power supply unit (Ikegami HD2.5K-M).

The photoionization signal was fed to a digital storage scope (Iwatsu DS-6411). The data were analyzed with a microcomputer (NEC PC9801RX). The laser pulse energy was monitored simultaneously with the the storage scope to calibrate its fluctuation.

The water was distilled, deionized, filtered, and distilled in a quartz vessel. Hydrocarbon solvents were used as received: ethanol, octane, hexane, trimethylpentane, cyclohexane, benzene, toluene, and xylene were guaranteed reagent from Kishida Chemicals; butanol, pentanol, and acetic acid were a special grade from Wako Pure Chemical Ind.; and ethylene glycol was a special grade from Nacalai Tesque. Anthracene (research grade; Kishida Chemicals) was used without further purification. It was dissolved in the solvents by ultrasonic vibration and measured with an UV/visible spectrophotometer (Hitachi U-3200) in order to determine the molar absorptivity and with a fluorescence spectrophotometer to confirm the concentration.

RESULTS AND DISCUSSION

Photoionization Signal. Upon laser irradiation, an analyte molecule absorbs two photons sequentially and produces a geminate ion−electron pair in the bulk solution.[1] The electron and the cation in the geminate pair may recombine or escape toward the electrode. There is a substantial difference in the laser photoionization process in the bulk solution and on the solution surface. In a nonpolar solution, electrons thus created are captured by neutral analytes or impurities (such as oxygen in the case of experiments in ambient air) and become anions; most signals used for analytical applications are conductivity signals due to cations and anions.[1] On the solution surface, electrons escape from the surface and pass to the positive electrode, although some of them are captured by ambient oxygen molecules to create oxygen anions, and the time profile of the photoionization signal showed a fast and a slow component.[10,11]

A reflected beam at 355 nm can penetrate about 200 Å (depth at half-intensity) from the surface into the solution. Because a two-photon process is proportional to the square of the laser pulse energy as described below, the possibility of photoionization of an analyte molecule located about 100 Å below surface is about half as much as that of an analyte molecule on the surface layer. Although the escape probability of electrons of a few electronvolts has never been measured in any condensed phase, the escape depth of those of 5 eV in metallic solid is about 50 Å.[26] Therefore, we would expect that the "surface" probed in the present technique is the region from the borderline of the two phases to the depth at most 100 Å below it.

The area of the photoionization profile represents the charge created in the photoionization process and was taken as the photoionization signal throughout the present study. Signals from 32 laser shots were accumulated for a measurement. Five independent measurements were averaged as a data point.

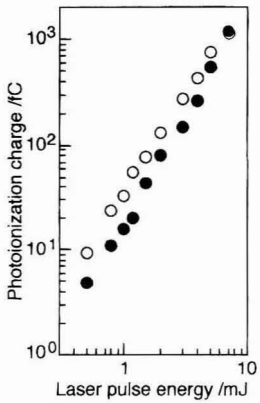


Figure 1. Laser pulse energy dependence of the photoionization charge of anthracene (10^{-5} M) in benzene excited at 355 nm: ○, anthracene in benzene; ●, pure benzene.

Effect of Pulse Energy on Photoionization Charge. The photoionization charge of anthracene was quadratically proportional to the laser pulse energy, as typically shown in Figure 1 for anthracene (10^{-5} M) in benzene. The two-photon energy of the third harmonic (355 nm) of an NdYAG laser is 7.0 eV, and the ionization threshold of anthracene is 6.14 eV[27] in trimethylpentane. Although the ionization threshold may differ slightly according to the solvent used, the difference may be small. We could expect that the ionization of an anthracene molecule should be a stepwise two-photon process for all the solvents used in the present study. The photoionization signal of pure benzene was also quadratically proportional to the laser pulse energy. Photoionization of pure benzene seems to be a simultaneous two-photon process because benzene is transparent at 355 nm.

The fluctuation of the blank signal (the signal from the pure solvent) was the largest source of noise and was related to the detection sensitivity. The signal/blank (S/B) ratio for anthracene in benzene was 3.7 for laser pulse energy from 0.1 to 1.5 mJ. At higher energies, the signal of anthracene tended to saturate and the S/B ratio decreased; an intense laser did not necessarily give a better signal-to-noise ratio. Thus the laser pulse energy was set at 0.8 mJ/pulse for most of the experiments.

The photoionization charge depended on the incident angle of the laser beam with respect to the surface normal. At an incident angle of 85° as used in the present study, the photoionization proceeds mainly on the surface because most of the laser beam is reflected at the surface. In this case, the signal is proportional to the analyte concentration over its wide concentration range.[12]

Influence of Bias Voltage upon Photoionization Charge. The photoionization signal can be directly related to the bias voltage between the positive electrode and the solution container if the escape probability of electrons from the surface depends on it. The bias voltage can alter the time profile of the photoionization signal because electrons migrate faster and arrive at the

(26) Brundle, C. R. *J. Vac. Sci. Technol.* **1974**, *11*, 212.

(27) Holroyd, R. A.; Preses, J. M.; Zenos, N. *J. Chem. Phys.* **1983**, *79*, 483.

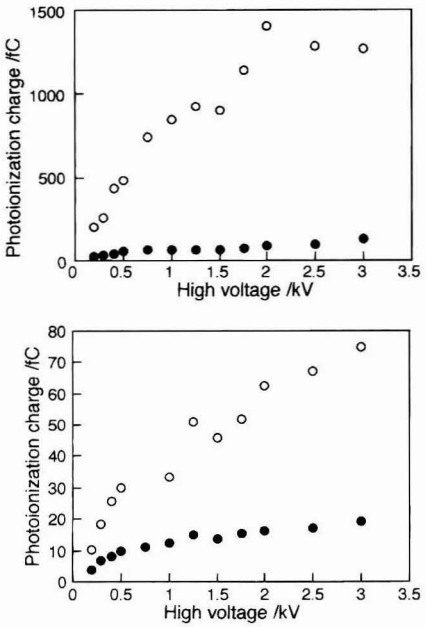


Figure 2. Dependence of the photoionization charge on bias voltage. Laser pulse energy, 0.8 mJ/pulse: (top) ○, anthracene (1×10^{-6} M) in water; ●, water. (bottom) ○, anthracene (1×10^{-5} M) in octane; ●, octane.

positive electrode before being captured by oxygen molecules at a larger bias voltage; this effect should not affect the photoionization charge if the collection efficiency of electrons is unity. In the case of photoionization in the bulk nonpolar solution, the photoionization signal was roughly proportional to the bias voltage,[4] as was expected from the Onsager equation.[28]

The bias voltage dependence of the photoionization charge is shown for anthracene (1×10^{-5} M) on water and on octane in Figure 2. The signal was not proportional to the bias voltage and leveled off at a higher bias voltage; this finding disagrees with that in bulk solution. This disagreement implies that the photoionization mechanism is more complicated on the surface and that the escape probability of electrons depends on the bias voltage in a complicated manner.

Effect of Solvent Properties on Photoionization Charge. The photoionization charge of anthracene on various solvents is summarized in Table 1, together with the dielectric constant and the electron mobility of the solvents. The solvents used in the present study should have a relatively high boiling point so that evaporation of solvent, hence change in the concentration during a measurement, should be negligible. The photoionization signal of pure solvents is also summarized in Table 1; a solvent which produces a large photoionization charge by itself tends to give a large photoionization charge of the solute.

The dependence of the photoionization signal of anthracene on the dielectric constant of various solvents is shown in Figure 3. Polar and nonpolar solvents seem to show a different dependence. Nonpolar solvents, which have dielectric constants of about 2, did not show any correlation. Instead, polar solvents showed a definite dependence on the dielectric constant; the signal increased with increasing dielectric constant of the solvent. This dependence would be due to surface excess concentration and decrease in photoionization threshold in more polar solvents. Anthracene is hardly soluble in polar solvents, and its surface concentration tends to increase with the dielectric constant of the solvent. The photoionization threshold decreases for solvents with large dielectric constants because the polarization energy of the ion and the electron affinity are larger in such solvents[27] and ions created in photoionization processes can be effectively stabilized. Thus, electrons created in solvents with larger dielectric constant have larger excess energy and can escape from the surface more easily.

The photoionization signal on the nonpolar solvents depended on the electron mobility as shown in Figure 4. Yamada et al.[30] studied the effect of electron mobility of nonpolar solvents on the

Table 1. Photoionization Signals of Anthracene on the Surface of Various Solvents

solvent	photoionization charge[a] solvent (fC)	photoionization charge[a] solution[b] (fC)	dielectric const[29] at 25 °C	electron mobility[29] (cm^2/Vs)
water	168	10900	78.5	
ethylene glycol	70	293	37.7	
ethanol	12	39	24.6	0.0003
butanol	0.8	9.5	17.5	
pentanol	1.7	9.8	13.9	
acetic acid	1.6	6.0	6.15[c]	
2,2,4-trimethylpentane	156	265	1.94[c]	5.3
octane	9.8	45	1.95[c]	
hexane	25	31	1.88	0.09
cyclohexane	114	254	2.02	0.45
benzene	67	174	2.27	0.11
toluene	20	81	2.38	0.063
p-xylene	21	156	2.27[c]	0.062

[a] Measured at 0.8 mJ/pulse and 2 kV/6 mm. [b] Measured for 1×10^{-5} M solution except water where measured at 1×10^{-6} M and multiplied by 10. [c] Measured at 20 °C.

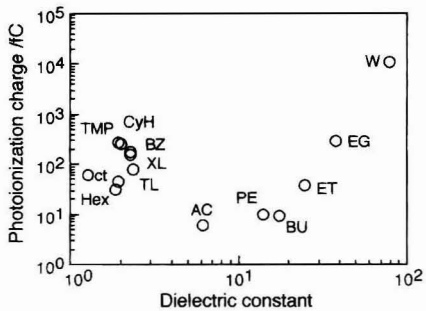


Figure 3. Dependence of photoionization charge of anthracrene (10^{-5} M) on dielectric constant of solvents excited at 355 nm at 0.8 mJ/pulse. Key: W, water; EG, ethylene glycol; ET, ethanol; BU, butanol; PE, pentanol; AC, acetic acid; TL, toluene; XL, *p*-xylene; BZ, benzene; Hex, hexane; Oct, octane; CyH, cyclohexane; TMP, 2,2,4-trimethylpentane.

(28) Onsager, L. *Phys. Rev.* **1938**, *54*, 554.

(29) *Kagaku Binran* (Tables of Chemical Constants), 4th ed.; Chemical Society of Japan: Maruzen: Tokyo, 1993; Vol. I, p 604; Vol II, pp 415, 498.

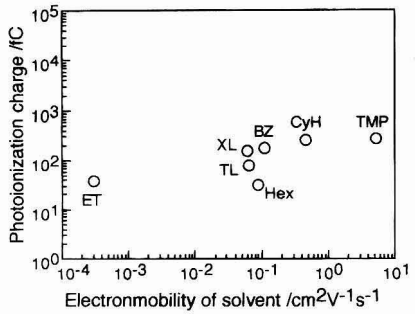


Figure 4. Dependence of photoionization charge of anthracene (10^{-5} M) on electron mobility of solvents excited at 355 nm at 0.8 mJ/pulse. Key: ET, ethanol; TL, toluene; XL, *p*-xylene; BZ, benzene; Hex, hexane; CyH, cyclohexane; TMP, 2,2,4-trimethylpentane.

Table 2. Detection Limits (ng/mL) of Anthracene at 355 nm Excitation

solvents	on surface	in bulk solution[21]
water	0.53	*a*
ethylene glycol	55	
2,2,4-trimethylpentane	44	0.0030
dodecane	120	
hexane	130	0.014
cyclohexane	530	
benzene	140	
toluene	210	

[a] A highly sensitive determination in bulk water is impossible due to its large leakage current.

fast signal of photoionization in the bulk solution and found that the peak height of the fast signal increased with increasing electron mobility. Ogawa et al.[21] found that this was also the case for the total photoionization signal in the bulk solution. The present result showed a similar dependence for an analyte on the solution surface.

In the case of surface experiments, once an electron escapes from the surface, its motion should have nothing to do with the solvent properties. Thus, the dependence on dielectric constant and electron mobility should be related to the probability of electron emission from the solution surface. The electron emission should be much easier for solvents with a large dielectric constant or with a large electron mobility.

Calibration Curve and Detection Limit. The observed photoionization signal (S) consisted of the signal of anthracene (S_a) and the solvent blank (S_b):

$$S_a = S - S_b \quad (1)$$

The signal-to-noise ratio (S/N) should be represented as follows:

$$S/N = S_a/\sigma_b \quad (2)$$

where σ_b is the standard deviation of S_b. The analytical curves were linear over a concentration range of 1–3 orders of magnitude above the detection limits. The linear range depended on the solvent, and water, which gave the largest signal, gave the widest linear range.

The detection limits were obtained as a concentration where the signal-to-noise ratio was 3. Detection limits of anthracene in several solvents are shown in Table 2 and are compared with those obtained in bulk solution.[21]. The best detection limit was obtained as 0.53 ppb on a water surface. The surface technique is very successful in detection limit only for water.

ACKNOWLEDGMENT

The authors thank Dr. Iwao Watanabe of Osaka University for his useful comments.

Received for review July 11, 1994. Accepted September 8, 1994.[⊗]

[⊗] Abstract published in *Advance ACS Abstracts,* October 15, 1994.

(30) Yamada, S.; Yoshida, S.; Kawazumi, H.; Nagamura, T.; Ogawa, T. *Chem. Phys. Lett.* **1985**, *122*, 391.

Anal. Chem. **1994,** *66,* 4154–4158

Isotopic Analysis of Uranium Using Glow Discharge Optogalvanic Spectroscopy and Diode Lasers

C. M. Barshick,* R. W. Shaw, J. P. Young, and J. M. Ramsey

Chemical and Analytical Sciences Division, Oak Ridge National Laboratory, Oak Ridge, Tennessee 37831-6375

A hollow cathode glow discharge has been coupled with tunable lasers for isotopically selective excitation of gaseous uranium atoms produced by cathodic sputtering. A CW argon ion laser-pumped titanium:sapphire ring laser and a semiconductor diode laser were employed. Optogalvanic detection of the discharge atom population allowed identification of ^{235}U at depleted, natural, and enriched abundances in uranium metal and uranium oxide samples based on the spectral signatures of two transitions. Isotope ratio measurements were precise from run to run (internal precision) to better than ±1% relative standard deviation at 1σ; external precision (sample to sample) was on the order of ±3% relative standard deviation at 1σ. As in mass spectrometry, the most accurate analysis will be obtained when a bias correction is employed to correct for day to day variations in the laser and discharge conditions.

Conventional methods for measuring isotope ratios require sophisticated instrumentation well suited to an analytical laboratory. In particular, thermal ionization mass spectrometry, while a very accurate and precise[1–3] technique for measuring isotope ratios, typically requires extensive sample preparation and is too cumbersome for any setting other than a laboratory. One exception to this generalization is the ion trap mass spectrometer that is currently being employed for field measurements of organic pollutants.[4] Although a similar instrument has been proposed for measuring the concentrations and isotopic abundances of inorganic analytes in contaminated soils,[5,6] little has been done with this instrument other than proof of principle experiments in the laboratory.

As an alternative to the use of conventional mass spectrometers, we have been pursuing glow discharge atomization coupled with high-resolution optogalvanic spectroscopy (OGS) for quantification of uranium isotope ratios.[7] Further, we wish to make use of diode lasers for excitation. This approach has been considered by others,[8] but we have focused on demountable discharge cells[9] for practical isotope ratio measurements for realistic samples. While our eventual goal is a fieldable instrument, this report describes our laboratory-based results to date. A field instrument does not require the accuracy and precision of a laboratory mass spectrometer but must be sensitive to changes in sample isotopic composition, be free from interferences, and have sufficient precision for a decision to be made about the fate of the field sample, i.e., does the sample warrant further laboratory analysis? The technique ideally should require a minimum of sample preparation and should at the same time be amenable to a variety of sample types. We are conducting experiments to determine whether the technique described herein meets these requirements for field use.

In a glow discharge, the cathode is bombarded by energetic gas phase ions. This produces a population of gaseous cathodic ions directly amenable to isotopic analysis using a mass spectrometer (glow discharge mass spectrometry, GDMS).[10] Neutrals are produced as well and are amenable to a variety of other techniques, including absorption,[11] emission,[12] and laser-induced fluorescence[13] spectroscopies. In the technique pursued here, the sputtered atoms are resonantly excited to a higher lying energy level, from which they may be ionized by collisions. The change in the discharge voltage brought about by disruption of the ionization equilibrium serves as an indicator of optical absorption and is the basis of optogalvanic signal collection.[14]

Semiconductor diode lasers are coherent light sources that generally operate in the near-infrared portion of the electromagnetic spectrum. They are conveniently tunable by electronic means and are rugged enough for field use. Gagne and coworkers[15] as well as others[16,17] have performed a number of fundamental spectroscopic investigations of uranium in this

(1) Heumann, K. G. In *Inorganic Mass Spectrometry*; Adams, F., Gijbels, R., Van Grieken, R., Eds.; John Wiley & Sons: New York, 1988.
(2) Dubois, J. C.; Retail, G.; Cesario, J. *Int. J. Mass Spectrom. Ion Processes* **1992**, *120*, 163.
(3) Turner, P. J. In *Applications of Plasma Source Mass Spectrometry II*; Holland, G., Eaton, A. N. Eds.; Royal Society of Chemistry: Cambridge, U.K., 1993.
(4) Wise, M. B.; Thompson, C. V.; Buchanan, M. V.; Merriweather, R.; Guerin, R. *Spectroscopy* **1993**, *8*, 14.
(5) Duckworth, D. C.; Barshick, C. M.; Smith, D. H. *J. Anal. At. Spectrom.* **1993**, *8*, 875.
(6) Duckworth, D. C.; Barshick, C. M.; Smith, D. H.; McLuckey, S. A. *Anal. Chem.* **1994**, *66*, 92.
(7) Keller. R. A.; Engleman, R., Jr.; Zalewski, E. F. *J. Opt. Soc. Am.* **1979**, *69*, 738.
(8) Lipert, R. J.; Lee, S. C.; Edelson, M. C. *Appl. Spectrosc.* **1992**, *46*, 1307.
(9) Tong, W. G.; Shaw, R. W. *Appl. Spectrosc.* **1986**, *40*, 494.
(10) King, F. L.; Harrison, W. W. In *Glow Discharge Spectroscopies*; Marcus, R. K., Ed.; Plenum Press: New York, 1993.
(11) Ohls, K. *Fresenius' Z. Anal. Chem.* **1987**, *327*, 111.
(12) Broekaert, J. A. C. In *Glow Discharge Spectroscopies*; Marcus, R. K., Ed.; Plenum Press: New York, 1993.
(13) Van Dijk, C.; Smith, B. W.; Winefordner, J. D. *Spectrochim. Acta* **1982**, *37B*. 759.
(14) King, D. S.; Schenck, P. K.; Smyth, K. C.; Travis, J. C. *Appl. Opt.* **1977**, *16*, 2617.

0003-2700/94/0366-4154$04.50/0 © 1994 American Chemical Society

Table 1. Isotopic Abundances (%) of Samples Studied

sample	^{233}U	^{234}U	^{235}U	^{236}U	^{238}U
enriched	<0.001	0.063	9.967	0.059	89.911
natural		0.005	0.720		99.275
depleted			<0.3		>99.5

spectral range, and data concerning isotope shifts and relative intensities of many optical transitions are available. We have narrowed our present consideration to two particular uranium transitions originating at low-lying initial states and with wavelengths of 778.42 and 776.19 nm.

In this paper, we report spectral and isotope ratio results for these two uranium transitions. The emphasis has been on demonstrating the usefulness of the technique for distinguishing samples based on their ^{235}U content (e.g., depleted versus enriched). Isotope ratio measurements have been limited to preliminary studies of accuracy and precision to determine the utility of this method.

EXPERIMENTAL SECTION

The preliminary spectroscopy was facilitated through the use of a commercial depleted uranium (0.3% ^{235}U) hollow cathode lamp (Model 3QQAY/U, Cathodeon, Ltd.) with a cylindrical metal cathode that is open at both ends. For all of the other studies, glow discharge cathodes were prepared in the shape of hollow cylinders 4.85 mm in diameter × 2.54 mm in length with an i.d. of 2.38 mm. These cathodes were fabricated by machining uranium metal into the desired shape or by pressing uranium powder in a hollow cathode die[18] at 3.4×10^{-7} Pa for 5 min. The pressed samples comprised pure uranium metal powder and uranium oxide powder (natural and depleted compositions) homogenized with silver powder (325 Mesh, 99.99+%, Aldrich Chemical Co., Milwaukee, WI) in a 50/50 wt % ratio.

Caution! Uranium metal is pyrophoric when finely divided. Because uranium is radioactive, special precautions are necessary. Uranium is an α emitter, and care should be taken to minimize ingestion and inhalation. Uranium also emits low to moderate levels of β and γ radiation, and care should be taken to minimize exposure. Anyone contemplating research with uranium is well advised to seek the help of a health physicist.

Table 1 shows the isotopic compositions of the samples used. The cathodes were held in a stainless steel ring that was welded to a 1.59 mm diameter rod (see Figure 1). The bulk of the sample holder was shielded with a quartz tube that was required to keep the discharge from arcing near the high-voltage feedthrough. A discharge formed over the entire cathode and holder ring. Uranium atoms were measured at the center of the cylinder bore, where the atom density is reported highest.[19,20]

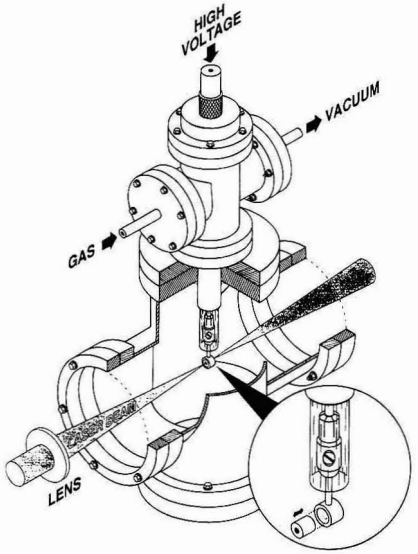


Figure 1. Demountable hollow cathode glow discharge cell.

The discharge support gas for this study was argon, maintained at 500–900 Pa in the source. Flow rates were approximately 2–3 cm^3(STP) min^{-1}. During the analysis, the cathode was held at constant current, ranging from 20–50 mA. At these pressures and currents and with a 5 kΩ ballast resistor in the circuit, the applied voltage ranged from 250 to 500 V. This relatively large discharge power range was necessary to facilitate signal collection for a variety of samples that included uranium metal enriched to 10% ^{235}U and depleted uranium oxide with approximately 0.3% ^{235}U.

Figure 1 is a drawing of the discharge cell showing the demountable cathode as an inset. Pumping was provided by a 0.4 L/s mechanical pump, and the ultimate base pressure was <0.1 Pa. Sample manipulation was accomplished by means of a direct insertion probe (DIP) fed through an O-ring seal; this arrangement also facilitated rapid sample exchange. The discharge voltage was introduced coaxially via the DIP. The vacuum chamber housing served as the counter electrode.

The goal of the project is to use diode lasers for excitation; they suffer, however, from limited tuning range and mode-hopping problems that hamper the acquisition of survey spectra. Therefore, a CW argon ion laser-pumped titanium:sapphire ring laser (Inova-100 argon ion laser and Model 899-29 titanium:sapphire ring laser, Coherent Laser Group, Santa Clara, CA) was used for exploratory spectroscopy. Scans of 30 GHz span were accomplished under computer control.

The diode laser system used for later work was a single longitudinal mode AlGaAs laser (Model ML-64110N, Mitsubishi Electric Corporation, Tokyo, Japan) with a nominal room temperature output at 777 nm of 30 mW. The diode laser was used in conjunction with commercial control electronics (Model LDM-4412 laser diode mount, Model LDT-5910 thermoelectric tem-

(15) Demers, Y.; Gagne, J. M.; Dreze, C.; Pianarosa, P. *J. Opt. Soc. B* **1986**, *3*, 1678. Piyakis, K. N.; Gagne, J. M. *J. Opt. Soc. B* **1989**, *6*, 2289. David, E.; Gagne, J. M. *Appl. Opt.* **1990**, *29*, 4489.
(16) Blaise, J.; Radziemski, L. J., Jr. *J. Opt. Soc. Am.* **1976**, *66*, 644.
(17) Engleman, R.; Palmer, B. A. *J. Opt. Soc. Am.* **1980**, *70*, 308. Palmer, B. A.; Keller, R. A.; Engleman, R. Informal Report No. LA-8251-MS; Los Alamos Scientific Laboratory, Los Alamos, NM, 1980.
(18) Marcus, R. K. Ph.D. Dissertation, University of Virginia, Charlottesville, VA, 1986.
(19) Caroli, S.; Alimonti, A. Petrucci, F. In *Improved Hollow Cathode Lamps for Atomic Spectroscopy*; Caroli, S., Ed.; Ellis Horwood Limited Publishers, Halsted Press: New York, 1985.
(20) Caroli, S.; Senofonte, O. In *Glow Discharge Spectroscopies*; Marcus, R. K., Ed.; Plenum Press: New York, 1993.

perature controller, and Model LDX-3620 ultra-low-noise current source, ILX Lightwave Corp., Bozeman, MT). According to the manufacturer's specifications, the temperature controller provided ±0.005 °C stability, and the power supply noise was 2 μA rms or less. For the 778 nm spectral study, the diode laser was maintained at 47.4 °C, yielding a power at the sample of approximately 3 mW (150 W/cm^2) at currents around 105 mA. For the 776 nm spectral study, the diode laser was maintained at 25.0 °C, with an approximate power at the sample of 8 mW (400 W/cm^2) at 130 mA.

The diode laser frequency was scanned using a sawtooth signal generator (Model 164, Wavetek Corp., San Diego, CA); a 4.8 mA current scan (corresponding to 14.1 GHz) was used for the 778 nm line and 7.5 mA (21.9 GHz) for the 776 nm line. Wavelengths were determined with wavemeters with readout accuracy of ±0.001 nm.

The CW laser light was chopped at 1000 Hz with a mechanical chopper (Model SR540, Standford Research Systems, Inc., Sunnyvale, CA). The ac component of the cathode voltage was split between a digital oscilloscope (Model 2246A, Tektronix Inc., Beaverton, OR) and a lock-in amplifier (Model SR510, Stanford Research Systems; 1 s time constant). The output from the lock-in was digitized by the same computer that was used to control the titanium:sapphire laser or by a separate computer for the case of diode laser scans.

The lasers used in this investigation were class 4 (titanium: sapphire) and class 3b (diode) devices. Safe operating practices consistent with these classifications are required.

RESULTS AND DISCUSSION

Survey Spectra. Several hundred uranium transitions have been identified in the diode laser accessible wavelength range of 670 nm to 1.5 μm.[15-17] We have examined a number of these as possible excitation candidates for isotopic analysis. Two well-suited transitions are illustrated in Figure 2. These data were obtained using titanium:sapphire laser excitation and a 10% enriched ^{235}U metal sample in the demountable discharge cell. The uranium line at 778.42 nm (Figure 2A) corresponds to excitation from the odd parity metastable level at 620 cm^{-1} (f^3ds^2 $^5K°_5$) to the level at 134 63 cm^{-1} (f^3s^2p $^5K_5$). The observed ^{238}U linewidth was 925 MHz fwhm for an optical excitation power density of approximately 1 × 10^5 W/cm^2. At this intensity, there was some degree of line broadening that, as anticipated, was reduced at lower powers. The reported isotope shift for this transition is +3 GHz.[16] Due to hyperfine splitting, the ^{235}U signal comprises many unresolved lines. Figure 2B illustrates another measured line corresponding to excitation from the 7005 cm^{-1} metastable level (f^3ds^2 $^3K°_6$) to the level at 19 885 cm^{-1} (f^3dsp $^5M_7$). Since the isotope shift for this line (−12.6 GHz) is larger than for the former transition, the ^{235}U signal can be measured unambiguously (without overlap with ^{238}U). The line width was comparable to that observed in Figure 2A (800 MHz fwhm) for a comparable laser power density (1 × 10^5 W/cm^2).

Real-world samples are unlikely to be in the form of metal, nor do we expect them to be enriched to 10% ^{235}U. It is more likely that uranium will be of natural abundance, and the sample will exist as some inorganic molecule (oxide, fluoride, etc.) Figure 3 illustrates a spectrum obtained using the demountable hollow cathode fitted with a pressed electrode formed from 50% uranium oxide powder (U_3O_8, natural abundance) and 50% silver powder.

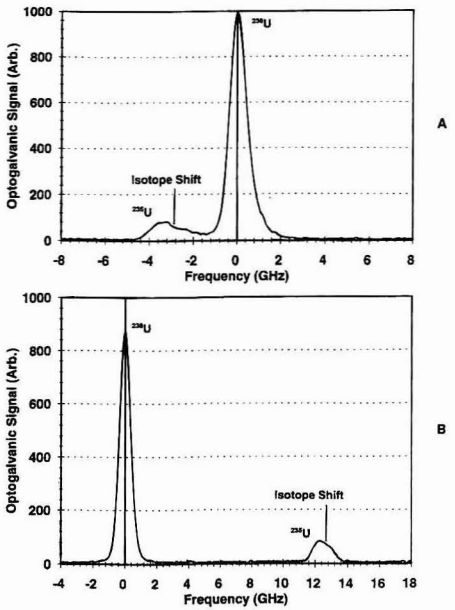


Figure 2. Uranium optogalvanic spectra recorded using a 1 × 10^5 W/cm^2 titanium:sapphire ring laser tuned to two transitions: (A) 778.42 and (B) 776.19 nm. In A, the discharge conditions were 870 Pa argon, 20 mA, and 300 V. In B, the discharge conditions were 670 Pa argon, 20 mA, and 400 V. The sample was uranium metal enriched to 9.97% ^{235}U.

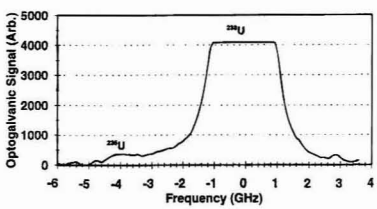


Figure 3. Uranium optogalvanic spectrum recorded using a 1 × 10^5 W/cm^2 titanium:sapphire ring laser tuned to 778.42 nm. The discharge conditions were 900 Pa argon, 40 mA, and 600 V. The sample was uranium oxide powder (natural abundance U_3O_8) mixed with silver powder in a 50/50 wt % ratio.

The sensitivity was purposely increased to drive the ^{238}U signal off-scale. A spectral feature at the frequency corresponding to the unresolved hyperfine structure of ^{235}U is seen in the low-energy line wing. Much of the uranium sputtered from uranium oxide could have been in molecular form (e.g., UO or UO_2)[21,22] and would have been transparent to a laser tuned to a uranium atomic line. The result reported here is significant in that in this discharge, ground-state or low-lying uranium atoms are present in sufficient density for useful measurements of isotope ratios. A ^{235}U spectral feature similar to that shown in Figure 3 has also been recorded using a commercial depleted uranium lamp. The

(21) Mei, Y.; Harrison, W. W. *Spectrochim. Acta* **1991**, *46B*, 175.
(22) Tong, S. L.; Harrison, W. W. *Spectrochim. Acta* **1993**, *48B*, 1237.

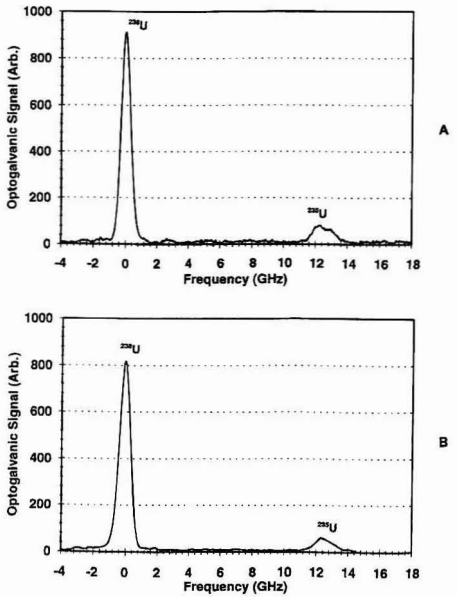


Figure 4. Uranium optogalvanic spectra recorded for the 776.19 nm line. (A) Titanium:sapphire laser at approximately 300 W/cm^2. (B) Diode laser at approximately 400 W/cm^2. The sample was the same in both cases, enriched uranium metal (9.97% ^{235}U). The discharge conditions were the same in both cases, 800 Pa argon, 20 mA, and 300 V.

spectra shown in Figures 2A and 3 indicate that it is quite easy to distinguish between a 10% enriched cathode and a natural abundance cathode; distinguishing between a depleted cathode and a natural cathode is a more rigorous task.

Diode Laser Spectra. The spectra presented in the previous figures were recorded using a high-power titanium:sapphire laser. For a fieldable analytical device, diode lasers with milliwatt outputs would be used. Prior to using a diode laser, an experiment was performed wherein the titanium:sapphire laser power was attenuated to a few milliwatts to evaluate the practicality of employing laser power in the range of diode lasers for optogalvanic measurements. Figure 4A illustrates a spectrum of the 776 nm transition recorded for the enriched uranium metal sample. The titanium: sapphire laser power was attenuated to approximately 6 mW (300 W/cm^2). In Figure 4B, the diode laser operating at approximately 8 mW was employed to acquire the same spectrum. Note that the two spectra are quite similar. This was an anticipated result, since the linewidths of both lasers are at least an order of magnitude narrower than the spectral line width, which is dominated by Doppler broadening (ca. 600–800 MHz). Similar spectral results were obtained in comparing the two lasers at the 778 nm uranium transition. It is certainly obvious that diode laser excitation can be employed in identifying these isotopes of uranium.

Diode Laser Isotope Ratio Measurements. A preliminary study to measure accurate uranium isotope ratios using diode laser optogalvanic spectroscopy has been undertaken. We have carried out studies of both the precision and the accuracy of ratio measurements on the 10% ^{235}U-enriched uranium sample using diode laser excitation of the 778 and 776 nm transitions. Accuracy was found to vary considerably depending on whether the well-resolved spectrum (776 nm) or the partially resolved spectrum (778 nm) was used. For integrated area measurements (calculated from the sum of the areas of the trapezoids formed by the data points) using the 776 nm transition, the measured ^{235}U composition ranged from 7.0% to 9.0%. The precision of the ratio measurement was followed for a 3 day period by carefully measuring the peak intensities (the absolute maximum plus 10 points encompassing 0.000 13 nm on either side of the maximum) of the isotopes at the stronger 778 nm transition. As compared to integration of peak areas, the peak height approach is simpler and yields a realistic measure of precision; the measured ratio, however, will be inaccurate due to the ^{235}U hyperfine splitting. Ten ratio measurements were made each day. Single day precision varied from ±0.8% to ±2.2% at 1σ. Sample to sample precision was approximately ±3.1%. Although this precision does not approach that which is attainable using conventional mass spectrometry, these results should be satisfactory for a fieldable isotope ratio instrument designed to determine gross differences in isotopic composition.

The measurement accuracy will be improved with the addition of a bias correction. However, the bias correction for this technique will be numerically different than that for glow discharge mass spectrometry, where the parameters influencing a few tenths of a percent per mass bias are still under investigation.[23,24] Optogalvanic bias correction factors will probably be the result of several parameters that include discharge pressure and current effects, as well as laser conditions. These and other effects associated with OGS and the glow discharge will be the subject of a subsequent evaluation to determine the practical limits of this technique.

CONCLUSIONS

Optogalvanic spectra have been recorded for uranium atoms sputtered from uranium metal and uranium oxide cathodes to test the feasibility of a practical isotope ratio measurement instrument. Isotopic signatures have been observed for two transitions (778.42 and 776.19 nm) using a demountable hollow cathode glow discharge cell. Metals were run directly, and insulating metal oxides were mixed with a conducting silver host matrix prior to analysis. An atom population of sufficient density for OG detection was generated by sputter atomization even though uranium has a pronounced oxygen gettering ability. At the reported level of spectral resolution and for the low-abundance isotope, the most difficult challenge will be extracting the signal corresponding to the minor isotope from the wing of the major isotope line and the baseline noise. Quantification and accuracy studies are continuing using both the titanium:sapphire and the diode lasers. Preliminary measurement precision using the diode laser source was as good as ±1% internal (run to run) and ±3% external (sample to sample) relative standard deviation at 1σ. These data substantiate the claim that glow discharge optogalvanic spectroscopy using diode lasers is a viable technique for uranium isotopic analysis. Further development is needed to determine whether field use will be feasible.

(23) Donohue, D. L.; Petek, M. *Anal. Chem.* **1991**, *63*, 740.
(24) Riciputi, L. R.; Duckworth, D. C.; Barshick, C. M.; Smith, D. H. *Int. J. Mass Spectrum. Ion Processes*, submitted.

ACKNOWLEDGMENT

The authors wish to acknowledge the help of J. B. Treen of the Office of Radiation Protection, Oak Ridge National Laboratory, for his assistance in sample preparation. Research was sponsored by the U.S. Department of Energy, Office of Research and Development. Oak Ridge National Laboratory is managed by Martin Marietta Energy Systems, Inc., for DOE under Contract DE-AC05-84OR21400.

Received for review August 11, 1994. Accepted September 7, 1994.[⊗]

[⊗] Abstract published in *Advance ACS Abstracts,* October 15, 1994.

Anal. Chem. **1994,** *66,* 4159–4165

Reduction of Fluorescence Interference in Raman Spectroscopy via Analyte Adsorption on Graphitic Carbon

Mark R. Kagan and Richard L. McCreery*

Department of Chemistry, The Ohio State University, 120 West 18th Avenue, Columbus, Ohio 43210

Raman spectra of normally fluorescent materials were obtained by quenching the fluorescence through adsorption on carbon surfaces. Energy transfer from the excited state to the carbon surface greatly reduced the fluorescence of rhodamine 6G and the near-IR laser dye IR125, and Raman spectra with high S/N were obtained from the adsorbed molecules. Strong resonance enhancement of Raman scattering was observed, and monolayer films of R6G were observed. R6G exhibited Langmuirian adsorption behavior, with saturation coverage occuring at ~0.5 mM in methanol. The technique was also successfully applied to bis(methylstyryl)benzene (BMB) and fluoranthene, which are less fluorescent but also much weaker scatterers. Since the laser wavelengths yielding resonance enhancement are in the same range as those producing fluorescence, adsorption to carbon permits elimination of fluorescence without loss of resonance enhancement. The porous graphite substrate has the added advantage of high microscopic surface area, low elastic background, and propensity to adsorb a wide range of organic materials. With care, it was possible to observe Raman features from monolayers of materials having cross sections comparable to that of benzene, such as the 1205 cm^{-1} peak of BMB.

Raman spectroscopy has several attractive features as an analytical technique: high information content and molecular specificity, compatibility with common optical materials, including optical fibers, linearity of signal with concentration, and the ability to selectively monitor resonance-enhanced scatterers.[1–5] In cases involving surface and resonance enhancement, Raman spectra can be obtained on very small amounts of analyte, often at nanomolar levels in solution[6] or submonolayers on surfaces.[7–10] However, Raman scattering has not been used widely as an analytical technique for several fundamental and practical reasons. The generally low cross sections for Raman scattering lead to very weak signals for most samples. Until the devlopment of CCD detectors and efficient Raman spectrometers, Raman instrumentation was expensive and difficult to use compared to UV–visible or FT-IR spectrometers. Even when the instrumental difficulties and small cross sections are accommodated, fluorescence interference is often a severe problem. Even weak fluoresence from the analyte or impurities in the sample is often much stronger than the Raman scattering, resulting in a large background. Once the shot noise on the fluorescence background becomes large relative to the Raman signal, the fluorescence can no longer be subtracted effectively. The combination of weak scattering, instrumental complexity, and fluorescence interference has prevented Raman spectroscopy from being applied routinely for qualitative or quantitative analysis.

Several approaches for reducing fluorescence have been described, including UV excitation,[11] time-resolved detection,[12,13] quenching with added reagents, and photolytic destruction of fluorescent impurities.[14] Of particular relevance here are surface quenching and near-IR excitation. When an analyte is deposited on a metal, the fluorescence is quenched by energy transfer from the excited state to the metal.[15–17] If the metal surface is rough, the Raman intensity can be surface enhanced,[18] although roughened metals can also lead to enhanced fluoresence.[16,19,20] A different approach is excitation with near-infrared (780–1064 nm) lasers. FT-Raman with 1064 nm excitation has proven very useful, mainly because the longer laser wavelength excites fluorescence in many fewer samples.[21–23] This broader applicability has stimulated the development of commercial FT-Raman systems by at least five manufacturers. Operation in the 780–830 nm range also results in reduction of fluorescence, while also permitting lower detection limits through the use of silicon-based CCD detectors.[24–26]

(1) Campion, A.; Perry, S. *Laser Focus World* **1990** (August), 113–123.
(2) Packard, R. T.; McCreery, R. L. *Anal. Chem.* **1989**, *61*, 775A–789A.
(3) Grasselli, T. G.; Bulkin, B. J. *Analytical Raman Spectroscopy*; Wiley: New York, 1991.
(4) Campion, A.; Woodruff, W. H. *Anal. Chem.* **1987** *59*, 1299A–1308A.
(5) McCreery, R. L. CCD Array Detectors for Multichannel Raman Spectroscopy. In *Charge Transfer Devices in Spectroscopy*; Sweedler, J., Ratzlaff, K., Denton, M. Eds.: VCH: New York, 1994; pp 227–279.
(6) Schwab, S. D.; McCreery, R. L. *Appl. Spectrosc.* **1987**, *41*, 126–130.
(7) Van Duyne, R. P. In *Chemical and Biological Applications of Lasers*; Moore, L. B., Ed.; Academic: NewYork, 1979; Vol. 4, Chapter 4.
(8) Campion, A.; Brown, J.; Grizzle, W. H. *Surf. Sci.* **1982**, *115*, L153–L158.
(9) Dierker, S. B.; Murray, C. A.; LeGrange, J. D.; Schlotter, N. E. *Chem. Phys. Lett.* **1987** *137*, 453–457.
(10) Bryant, M.; Pemberton, J. *J. Am. Chem. Soc.* **1991**, *113*, 3629–3637.
(11) Asher, S. *Anal. Chem.* **1993**, *65*, 59A–66A.
(12) Gustafson, T. L.; Lytle, F. E. *Anal. Chem.* **1982**, *54*, 634–637.
(13) Burgess, S.; Shepherd, I. W. *J. Phys. E* **1977**, *10*, 617.
(14) Strommen, D.; Nakamoto, K. *Laboratory Raman Spectroscopy*; Wiley: New York, 1984; pp 94–95.
(15) Chance, R. R.; Prock, A.; Silbey, R. *Adv. Chem. Phys.*, **1978**, *37*, 1–65.
(16) Ritchie, G.; Burstein, E. *Phys. Rev. B* **1981**, *24*, 4843–4846.
(17) Tanimura, K.; Kawal, T.; Sakata, T. *J. Phys. Chem.* **1980**, *84*, 751–756.
(18) Chang, R. K.; Furtak, T. E. *Surface Enhanced Raman Spectroscopy*; Plenum: New York, 1982.
(19) Aussenegg, F. R.; Leitner, A.; Lippitsch, M. E.; Reinisch, H.; Riegler, M. *Surf. Sci.* **1987**, *189/190*, 935–945.
(20) Garoff, S.; Stephens, R. B.; Hanson, C. D.; Sorenson, G. K. *Opt.Commun.* **1982**, *41* (4), 257–262.
(21) Chase, D. B. *J. Am. Chem. Soc.* **1986**, *108*, 7485–7488.
(22) Chase, D. B. *Anal. Chem.* **1987**, *59*, 881A–889A.
(23) Schrader, B.; Hoffman, A.; Simon, A.; Sawatzki, J. *Vib. Spectrosc.* **1991**, *1*, 239–250.

0003-2700/94/0366-4159$04.50/0 © 1994 American Chemical Society

Avoidance of fluorescence by long-wavelength excitation is not without a cost in sensitivity, however. Normal Raman scattering intensity decreases with $1/\lambda^4$, leading to a factor of 18 less scattering at 1064 nm than at 514.5 nm. Silicon CCD detectors have a lower quantum efficiency in the 800–1000 nm region than in the visible and cannot detect light above 1.1 μm at all. The available detectors for FT-Raman have good quantum efficiency (~0.7), but high dark signal and accompanying noise. Finally, resonance Raman enhancement depends on the same electronic transitions as fluorescence, so avoiding fluorescence by using a longer excitation wavelength will generally negate resonance enhancement.

The present experiments were undertaken in an attempt to maintain the relatively high sensitivity of visible excitation and CCD detectors while at the same time suppressing fluorescence. An sp^2-hybridized carbon rod was used to adsorb several analytes from solution, some of which were highly fluorescent. Not only does the carbon substrate quench fluorescence, but it also should preconcentrate the analyte when strong adsorption occurs. The advantages of the technique for routine Raman analysis are discussed.

EXPERIMENTAL SECTION

Sample Preparation. Spectroscopic graphite rods (type U-5, Carbone of America, Ultra Carbon Division, Bay City, MI) were dry polished first with 180 grit and then 600 grit silicon carbide grinding paper (Buehler). After sonication to remove any polishing debris followed by 10 min of heating in a Bunsen burner flame (sample placed in a covered crucible to prevent contamination by flame gases), the carbon rod was submerged in the analyte solution for a measured amount of time. For all cases except fluoranthene, the rod was gently rinsed with solvent after removal from the analyte solution in order to minimize multilayer adsorption. The R6G (Lambda Physik), IR125 (Exciton), fluoranthene (Aldrich), and 1,4-bis(2-methylstyryl)benzene (BMB, Aldrich), were used without additional purification. The solvents used in these studies were reagent grade acetone, anhydrous methanol, and carbon tetrachloride. The analyte solutions in which the carbon rods were dipped ranged in concentration from 10^{-8} to 10^{-2} M, as noted for each experiment.

Figure 1A shows the apparatus used for 514.5 nm excitation. A 25 cm focal length, single-stage spectrometer with $f/4$ optics (Chromex, Albuquerque, NM) was coupled to a CCD detector (TEK CB/AR with 512 × 512 pixels, 13 mm × 13 mm active area, Photometrics CH260 camera head (Tucson, AZ)). The detector was operated at −110 °C, and all spectra were collected by binning the CCD in the vertical direction, yielding 512 spectral resolution elements. A 1200 lines/mm grating (optimized at 750 nm) or an 1800 lines/mm grating (optimized at 500 nm) was used, yielding a spectral resolution of 2–4 cm^{-1}. The typical slit width employed was 50 μm while the laser power was 10–20 mW at the sample. The argon ion laser was a Coherent 70-4 "Innova". Since the Chromex Raman One spectrograph comes with lenses L3 and L4 permanently mounted, the samples could have been placed at the position where the CdS band reject filter is shown in Figure 1A, eliminating the need for lenses L1 and L2. The more complex optical arrangement containing the additional lenses, L1 and L2,

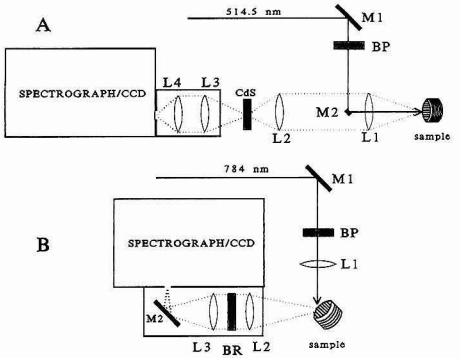


Figure 1. Apparatus for Raman spectroscopy with 514.5 (A) and 784 nm (B) lasers: (A) L1, 30 mm diameter × 120 mm focal length lens; L2, 30 mm diameter × 110 mm focal length lens.; BP, bandpass filter; M1, plane mirror; M2, 2 mm × 2 mm plane mirror; L3 and L4, 25 mm diameter × 75 mm focal length lenses. (B) L1, 12 mm diameter × 25 mm focal length lens; M1 and M2, plane mirrors; L2 and L3, 25 mm diameter × 75 mm focal length lenses.

was chosen because it allowed an epi-illuminated, 180° backscattered collection geometry to be used. In this geometry, the same lens, L1, is used to focus both the excitation laser beam and to collect the scattered sample radiation. This configuration leads to relatively simple and reproducible sample positioning. The band gap of the CdS filter (Cleveland Crystals, Inc.) is such that it strongly absorbs 514.5 nm light, while transmitting light Raman shifted by >300 cm^{-1} at a level of ~60%.

The apparatus for spectroscopy with a 784 nm laser is shown in Figure 1B. A different version of the Chromex spectrograph with a side-mounted filter compartment was employed. This spectrograph employed a 600 lines/mm grating with a 500 nm blaze. All other features of the spectrograph were the same as described previously. The CCD used was an EEV05-10 with 296 × 1152 pixels (0.66 cm × 2.59 cm active area). Once again, the detector was operated at −110 °C, and all spectra were collected by binning the CCD in the vertical direction (short axis), yielding 1152 resolution elements. The 784 nm radiation was provided by an argon ion pumped Ti–sapphire laser (Coherent Model 890). Rejection of elastic scatter was achieved by replacing the CdS crystal with a holographic Notch Plus filter (Kaiser, Ann Arbor, MI). The slit width used in these experiments was 100 μm, yielding resolution of 6.6 cm^{-1}.

In the near-IR experiments, the epi-illuminated, 180° backscattered collection geometry was not used. Instead, the band reject filter was placed between L2 and L3, while the sample was positioned as shown in Figure 1B. The position of M1 and the band pass filter were adjusted to allow the excitation laser beam to pass through an additional lens, L1, that focused it onto the sample. The resulting excitation and collection axes were at ~90° with respect to each other. While the 90° arrangement is more difficult to align than the 180° geometry, the Raman spectra obtained with either geometry were qualitatively identical.

The Raman shift axis was calibrated with known naphthalene frequencies and is accurate to ±2 cm^{-1}. The intensity axis was not corrected for the instrument response function.

(24) Wang, Y.; McCreery, R. *Anal. Chem.* **1989**, *62*, 2647–2651.
(25) Harris, T. D.; Schnoes, M. L.; Seibles, L. *Anal. Chem.* **1989**, *61*, 994–998.
(26) Newman, C. D.; Bret, G. G.; McCreery, R. L. *Appl. Spectrosc.* **1992**, *46*, 262–265.

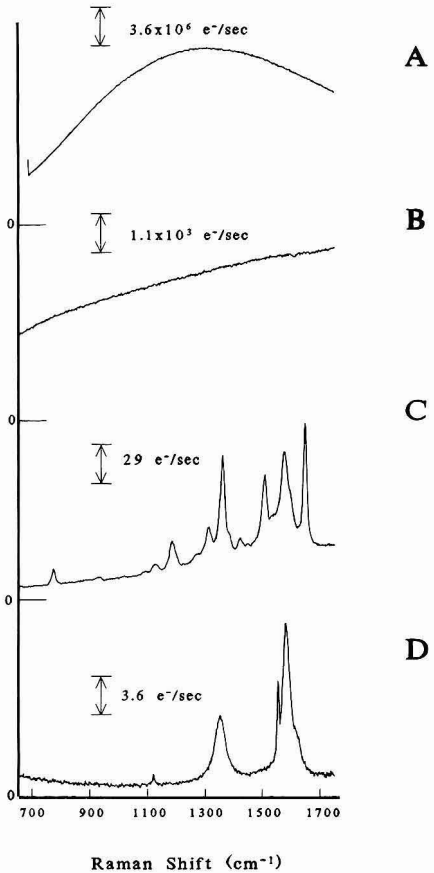


Figure 2. (A) Raman spectrum of 50 nM solution of R6G in methanol. Laser power, 10 mW. (B) Raman spectrum of R6G solid. Laser power, 10 mW. (C) Raman spectrum of R6G adsorbed on carbon. Laser power, 15 mW. Carbon submerged into an unstirred 2.4 mM solution of R6G in methanol for 60 min and then rinsed in pure methanol before drying in air. (D) Raman spectrum of carbon rod preceding R6G adsorption. Laser power, 15 mW. Excitation wavelength was 514.5 nm in all four spectra.

RESULTS

Rhodamine 6G (R6G) is a common laser dye with an absorption maximum at 530 nm and an emission maximum at 590 nm. As shown in Figure 2A and B, R6G is strongly fluorescent when excited by 514.5 nm light, either as a solid or as a dilute solution. Spectra C and D were obtained under identical conditions from a carbon rod before (D) and after (C) immersion in 2.4 mM R6G in methanol. The fluorescence is greatly reduced for R6G adsorbed to the carbon. The peak heights in Figure 2C are much larger than the <1 e^-/s observed for a monolayer of nitrobenzene on metals (e.g, Ni)[8] because of resonance enhancement of the R6G. Figure 3 shows spectra for R6G solid and MeOH solution obtained with a 784 nm laser in order to avoid fluorescence. While the band positions are approximately the same for the adsorbed

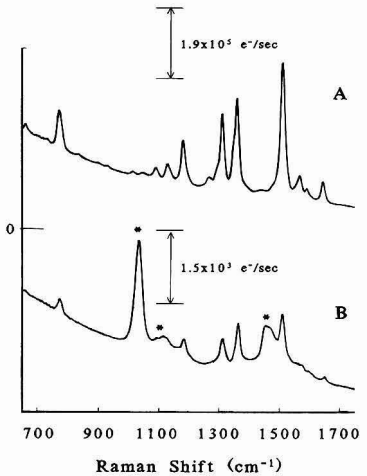


Figure 3. (A) Raman spectrum of R6G solid, obtained with 100 mW of 784 nm light. (B) Raman spectrum of 9.5 mM solution of R6G in methanol; same laser conditions. Asterisks indicate solvent peaks.

R6G at 515 nm and the solid R6G at 784 nm, there are significant differences in relative intensity. Since the spectra were not corrected for instrument response function, some of the intensity variation is attributable to the variation in detector response between the two wavelength regions. However, the large difference between closely spaced peaks (e.g., 1513 and 1645 cm^{-1}) must be due to differences in resonance enhancement or the influence of the carbon surface. Frequencies for the observed Raman bands are listed in Table 1.

IR125 is a near-IR laser dye with an absorption maximum of 795 nm and an emission maximum of 838 nm in chloroform. Figure 4 shows spectra of IR125 solid and methanol solution, both exhibiting strong fluorescence when excited at 784 nm. After adsorption to a carbon rod, the Raman spectrum is revealed, with a small contribution from the carbon itself. IR125 was also strongly fluorescent when excited with a 514.5 nm laser, so Raman spectra of the unadsorbed dye could not be obtained. Spectra of R6G and IR125 adsorbed on carbon, but obtained with excitation away from their absorption maxima, are shown in Figure 5.

The quantitative reproducibility of the surface spectra was assessed by examining five carbon rods and two locations on each rod. The geometry of Figure 1A permitted reproducible sample placement and minimized the variation of sample and beam alignment. The area of the 1580 cm^{-1} carbon band on fresh carbon surfaces for 10 measurements is listed in Table 2. The 3.8% relative standard deviation indicates good reproducibility of sample placement and good sample homogeneity. Table 2 also lists 10 signals for the 775 cm^{-1} band of adsorbed R6G. The higher standard deviation is probably due to nonuniformity of R6G coverage. A working curve for R6G was constructed by absorption from methanol solutions of varying R6G concentration for 5 min onto freshly prepared carbon rods, followed by a methanol rinse. The area of the 1182 cm^{-1} band vs R6G concentration is shown in Figure 6. The line is a fit to the Langmuir adsorption equation, and the flat plateau above 600 μm indicates monolayer coverage.

Table 1. Raman Shift Frequencies

excitation at 514.5 nm			excitation at 784 nm		
solid	solution	adsorbed on carbon	solid	solution	absorbed on carbon
		Rhodamine 6G			
		771–777[a]	773		
			1012		
			1046		
			1090		
		1121–1130[a]	1129		
		1179–1187[a]	1182	1184	
			1268		
		1312	1313	1313	
			1362	1365	
		1500–1508[a]	1513	1511	1512
			1568		
			1591		
		1636–1649[a]	1645	1650	
		Fluoranthrene			
		1017			
1098	1098	1099			
		1135			
1268	1265	1267			
1371	1373	1371			
1420	1419	1419			
1453	1456	1454			
1611	1613	1613			
		IR125			
					664
		723			726
					832
					893
		943			938
					1009
					1035
					1092
		1126			1132
		1147			1144
		1166			1165
		1202			1204
					1258
					1293
					1355
					1420
		1448			1444
					1461
		1522			1519
					1538
					1593
					1621
		BMB			
1050					
1104					
1178	1178	1177			
1205	1207	1205			
1290					
1316					
1334					
1555		1551			
1591	1594	1591			
1627	1627	1621–1627[a]			

[a] Peak position varied with coverage and surface preparation.

As shown in Figure 7, it was possible to obtain R6G spectral features from a carbon rod following adsorption from 60 nM R6G.

Fluoranthene and BMB are not resonant at 514.5 nm and are much weaker scatterers than R6G or IR125. Solid and solution spectra of fluoranthene are shown in Figure 8A and B, both exhibiting significant fluorescence. After adsorption onto carbon from a 10 mM solution in acetone, spectrum C results. The Raman to fluorescence ratio at 1613 cm^{-1} has increased from 0.11

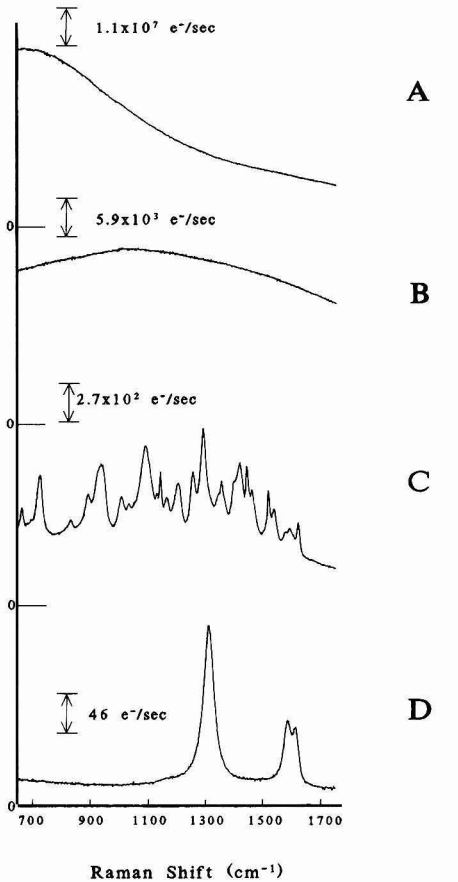


Figure 4. (A) Raman spectrum of 0.93 mM solution of IR125 in methanol. Laser power, 30 mW. (B) Raman spectrum of IR125 solid. Laser power, 30 mW. (C) Raman spectrum of IR125 adsorbed on carbon. Laser power, 100 mW. Carbon was submerged in an unstirred 0.62 mM solution of IR125 in methanol for 5 min and then rinsed in pure methanol before drying. (D) Raman spectrum of carbon preceding adsorption. Laser power, 100 MW. Excitation wavelenth was 784 nm for all four spectra.

in solution to 1.4 on the carbon. BMB yields spectra for monolayers on carbon, with the peak frequencies shown in Table 1.

Considering qualitative issues first, it is clear that adsorption on carbon greatly reduces fluorescence for R6G and IR125. Fluorescence quenching by energy transfer to metal surfaces occurs over a distance of 1–60 nm,[27,28] so both monolayer and multilayer films should be quenched up to an as yet undetermined film thickness. Compared to metals, we would expect carbon to adsorb a wider range of analytes. The dispersion, acid–base, covalent, and electrostatic interactions that are possible between

(27) Cnossen, G.; Drabe, K. E.; Wiersma, D. A. *J. Chem. Phys.* **1993**, *998*, 5276–5280.
(28) Ohshima, S.; Kajiwara, T.; Hiramoto, M.; Hashimoto, K.; Sakata, T. *J. Phys. Chem.* **1986**, *90*, 4474–4476.

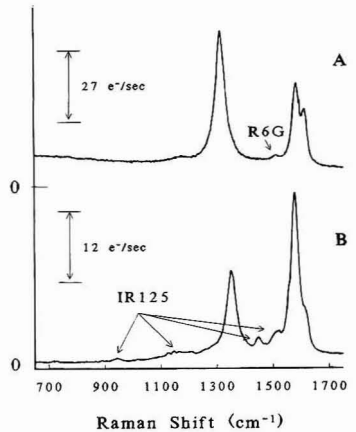


Figure 5. (A) Raman spectrum of R6G adsorbed on carbon. Excitation wavelength was 784 nm (100 mW). Carbon was submerged in an unstirred 9.5 mM solution of R6G in methanol for 222 min and then rinsed in pure methanol before drying. (B) Raman spectrum of IR125 adsorbed on carbon. Excitation wavelength was 514.5 nm (10 mW). Carbon was submerged in an unstirred 0.62 mM solution of IR125 in methanol and then rinsed in pure methanol before drying in air.

Table 2. Reproducibility of Graphitic Carbon and Adsorbed R6G[a] Raman Signal Intensities[b]

sample no.[c]	spot no.[d]	1582 cm^{-1} carbon band intensity (e^-/s)	775 cm^{-1} R6G band intensity (e^-/s)
1	1	504	
1	2	485	
2	1	512	
2	2	514	
3	1	512	
3	2	536	
4	1	503	
4	2	508	
5	1	545	
5	2	545	
6	1		48.1
6	2		51.5
7	1		57.6
7	2		56.7
8	1		40.9
8	2		59.7
9	1		59.3
9	2		114
10	1		56.3
10	2		89.0
mean ± SD		516 ± 19.6	63.3 ± 21.71

[a] The sample was prepared by submerging a carbon rod into a 0.17 mM solution of R6G in methanol followed by a 5 min submersion in pure methanol. [b] Excitation wavelength was 514.5 nm (20 mW at sample), integration time, 180 s. [c] Ten different pieces of carbon were sampled. [d] Two different regions on each piece of carbon were sampled.

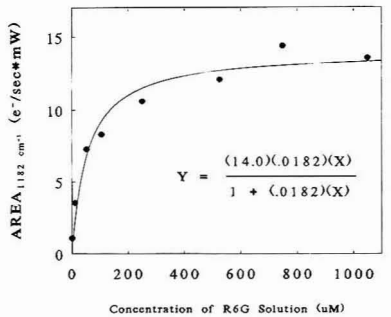


Figure 6. Intensity of the R6G 1182 cm^{-1} band on carbon rods following adsorption of R6G from solutions of varying concentration in methanol. Rods were dipped in the R6G solutions for 5 min and then rinsed once by immersion in MeOH. Each point is an average of two or three runs at a given concentration. Laser power, 15–20 mW. The solid line is a fit to the Langmuir isotherm equation, as shown.

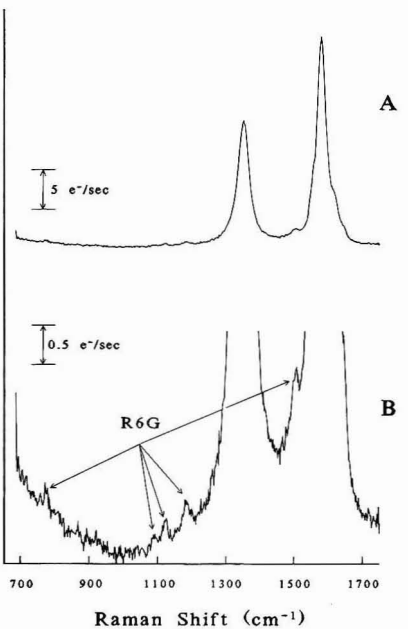


Figure 7. (A) Raman spectrum of R6G adsorbed on carbon. Excitation wavelength, 514.5 nm. Laser power, 10 mW. Carbon was submerged into an unstirred 50 nM solution of R6G in methanol for 210 min and allowed to dry without rinsing. Excitation wavelength, 514.5 nm (10 mW). (B) A 10-fold magnification of (A).

carbon surfaces and adsorbates are more varied than those for metals, leading to the wide use of carbon as an adsorbant.[29–31] Furthermore, the common occurrence of pores in carbon, particularly when activated, increases adsorption by increasing surface area. Although SERS substrates such as silver, copper,

(29) Bansal, R. C.; Donnet, J.-B.; Stoechli, F. *Active Carbon*; Dekker: New York, 1988; Chapter 4.

(30) Arnett, E. M.; Hutchinson, B. J.; Healy, M. H. *J. Am. Chem. Soc.* **1988**, *110*, 5255–5260.

(31) Suffet, I. H.; McGuire, M. J. *Activated Carbon Adsorption of Organics from the Aqueous Phase*; Ann Arbor Science Publishers, Inc.: Ann Arbor, MI, 1980.

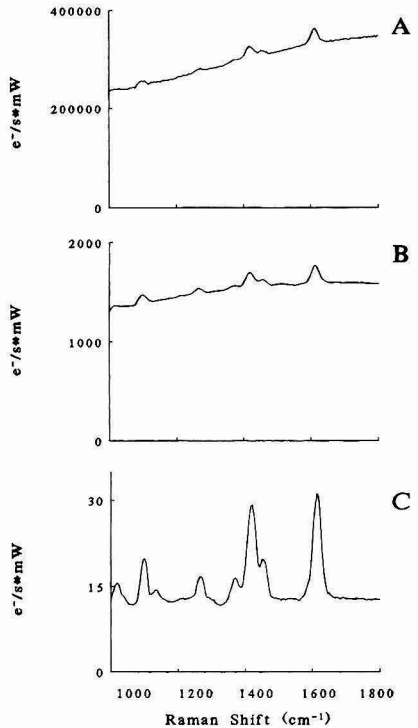


Figure 8. Spectra of fluoranthene as a solid (A), a 10 mM solution in CCl_4 (B), and adsorbed on carbon (C). Adsorption occurred from 10 mM solution in acetone. Laser power was 10 mW at 514.5 nm, and CCl_4 and carbon background spectra were subtracted in spectra B and C, respectively. The signal strength of the 1613 cm^{-1} peak is high for an unenhanced monolayer and implies either a preresonant condition or a multilayer film.

and gold yield major sensitivity enhancements,[18,32,33] they do not adsorb as wide a range of materials as carbon and are therefore not as general. Furthermore, minor impurity levels can reduce or prevent adsorption to SERS active surface and drastically affect SERS intensity.

The shapes of the R6G working curve in Figure 6 and a similar curve obtained for BMB provide strong evidence that the R6G and BMB spectra (at least) were obtained from monolayers. There are several cases of frequency shifts upon adsorption, relative to the bulk or solution values. For example, the 1513 cm^{-1} band observed in the bulk R6G spectrum obtained at 784 nm has also been observed by CARS at 1517 cm^{-1},[34] but for the adsorbed R6G excited at 514.5 nm, the peak shifts to as low as 1500 cm^{-1}. These peak shifts are evidence for monlayer adsorption. In addition, the adsorption of R6G and IR125 from dilute solution followed by a solvent wash is unlikely to yield multilayers. For either the mono- or multilayers considered here, it is clear that the fluorescence is quenched.

The expected Raman scattering from an absorbate has been considered by several authors, but a useful form is given by eq 1

$$S = P_D \beta_S D_S \Omega A_D T Q t \tag{1}$$

for a flat surface,[5] where S is the signal measured at CCD (electrons) integrated over Raman line, P_D is the laser power density (photons s^{-1} cm^{-2}), $\beta_s$is the cross section of a molecule on a surface (cm^2 $molecule^{-1}$ sr^{-1}), D_s is the number density of analyte on a surface (molecules cm^{-2}), Ω is the collection angle of spectrometer, measured at the sample (sr), A_D is the sample area monitored by spectrograph (cm^2), T is the spectrometer transmission (unitless), Q is the detector quantum efficiency (photoelectrons $photon^{-1}$), and t is the measurement time, (s).

For a flat surface and monolayer coverage of benzene (β = 2.0×10^{-29} cm^2 $molecule^{-1}$ sr^{-1}), eq 1 predicts a signal of ~0.1 e^-/s for the conditions employed. As noted earlier, the much larger signal observed in Figure 2C is due to resonant enhancement.

An estimate of the resonance enhancement of β can be made by comparing Figures 2C and 5A, in which adsorbed R6G is observed at 514.5 and 784 nm. Ignoring the small change in sampling depth of the carbon between 514.5 and 784 nm, the carbon Raman scattering intensity will track the carbon cross section as the laser wavelength is varied. Thus the carbon band at 1580 cm^{-1} can be used as an internal standard, and eq 2 applies

$$\frac{S_s^1}{S_c^1} = \frac{\beta_s^1 D_s^1}{\beta_c^1 D_c^1} \tag{2}$$

if all instrumental parameters are constant. The superscript 1 refers to a given laser wavelength and the subscripts S and C refer to the adsorbate and carbon substrate, respectively. Equation 2 can be evaluated at two laser wavelengths and ratioed, with

$$\frac{S_s^1/S_c^1}{S_s^2/S_c^2} = \frac{\beta_s^1 \beta_c^2 D_s^1}{\beta_s^2 \beta_c^1 D_s^2} \tag{3}$$

$D_c^1 = D_c^2$ yielding eq 3. Thus, if the same sample is examined at both wavelengths, the sample Raman intensity relative to the carbon band is a function of the relative adsorbate and carbon cross sections and number densities. Equation 3 assumes only that the sampling depth is the same for both wavelengths. The cross section of graphite has not been determined rigorously as a function of wavelength, but some results are available. By comparing the graphite scattering intensity to the scattering from Na_2SO_4 in a graphite/Na_2SO_4 pellet, Wang et al. estimated that the glassy carbon cross section deviated from υ^4 behavior by less than a factor of 3 between 409 and 782 nm.[36] Thus, we estimate the β_c^2/β_c^1 term in eq 3 to equal $(515/784)^4$ or 0.19.

Figures 4C and 5B compare the spectra of IR125 at 784 and 515 nm, respectively. Application of eq 3 with $D_s^1 = D_s^2$ indicates that the IR125 cross section is 79 times larger at 784 nm than at

(32) Moody, R. L.; Vo-Dinh, T.; Fletcher, W. H. *Appl. Spectrosc.* **1987**, *41*, 966–969.
(33) Mullen, K.; Carron, K. T. *Anal. Chem.* **1991**, *63*, 2196–2199.
(34) Matsubara, S.; Takahashi, H. *Chem. Phys. Lett.* **1984**, *108*, 475.
(35) Fryling, M.; Frank, C. J.; McCreery, R. L. *Appl. Spectrosc.* **1993**, *47*, 1965–1974.
(36) Wang, Y.; Alsmeyer, D.; McCreery, R. L. *Chem. Mater.* **1990**, *2*, 557–563.

515 nm for the 944 cm^{-1} band, 81 times larger for the 729 cm^{-1} band, and 86 times larger for the 1208 cm^{-1} band. Thus there is clearly a significant increase in resonance enhancement at the longer laser wavelength. Figure 5A was obtained with a relatively thick R6G film in order to yield sufficient signal. As a result, eq 3 yields a lower limit for β_s^1/β_s^2 if D_s^1 is assumed to equal D_s^2. Comparison of Figures 2C and 5A, combined with eq 3 leads to the semiquantitative estimate that the adsorbed R6G (1515 cm^{-1} band) cross section at 514.5 nm is at least 630 times that at 784 nm. This factor represents the minimum gain in sensitivity due to resonance enhancement from using 514.5 nm excitation rather than 785 nm. Speaking more generally, resonance enhancement necessarily involves excited electronic states which can also lead to fluorescence. By shifting the laser toward the red, one can diminish fluorescence but also decrease resonance enhancement. By quenching the fluorescence on the carbon surface, resonance enhancement and accompanying sensitivity can be maintained.

The generality of the use of carbon surfaces as supports for Raman samples depends on two major factors: the range of molecules that adsorb and their Raman cross sections and number densities. As noted earlier, a wide range of materials adsorb to carbon, particularly organics. The observation of adsorbed R6G after carbon immersion in a 50 nM solution raises the possibility of using adsorbate Raman for trace analysis. At monolayer coverage, the 1205 cm^{-1} band of BMB yields a detectable signal with an intensity of approximately 0.1 e^-/s-mW. This is within a factor of 10 of that predicted for a monolayer of benzene observed at 992 cm^{-1}.[37] Thus, strongly resonant adsorbates such as R6G at 514.5 nm were easily detected at monolayer levels, while much weaker scatterers yield easily observed Raman features. The suitability of the approach for a wider range of adsorbates is currently being assessed.

(37) Fryling, M. A., private communication.

CONCLUSIONS

The ability of a graphitic carbon surface to provide high-quality Raman spectra of adsorbed molecules that exhibited only fluorescence when sampled as bulk solids or in solution was demonstrated. Laser dyes probed with excitation wavelengths close to their absorption maxima were used in this study to produce a "worst case" scenario of fluorescence interference. Although it has previously been shown that metals such as silver and aluminum also possess the ability to quench fluorescence efficiently, carbon offers several potentially significant advantages. First among these advantages is carbon's superior affinity for organic absorbates. This could be crucial for solution phase trace analyses where the surface coverage of a particular analyte will increase for a higher adsorption equilibrium constant. A second advantage of graphitic carbon over metals is its availability in very high surface area "activated" forms. This should increase the number of adsorption sites and reduce saturation and competitive adsorption effects. The results also indicate that features with Raman cross sections comparable to that of benzene, such as the 1205 cm^{-1} band of BMB, can be observed at monolayer levels on carbon surfaces.

ACKNOWLEDGMENT

This work was supported by the Division of Analytical and Surface Chemistry of the National Science Foundation.

Received for review May 20, 1994. Accepted September 18, 1994.®

® Abstract published in *Advance ACS Abstracts*, October 15, 1994.

Anal. Chem. **1994,** *66,* 4166–4170

Membrane Inlet Mass Spectrometer for Rapid High-Precision Determination of N_2, O_2, and Ar in Environmental Water Samples

Todd M. Kana,* Christina Darkangelo, M. Duane Hunt, James B. Oldham, George E. Bennett, and Jeffrey C. Cornwell

Horn Point Environmental Laboratory, University of Maryland System, P.O. Box 775, Cambridge, Maryland 21613

A membrane inlet mass spectrometer was modified to perform rapid, high-precision measurements of dissolved N_2, O_2, and Ar in water. The instrument pumps water at <1 mL min^{-1} through semipermeable microbore silicone tubing positioned inside an inlet vacuum line of a quadrupole mass spectrometer. Precise pumping and temperature control of the water sample contribute to high signal stability and reproducibility. Dissolved gas concentrations are determined from intensities of the mass spectrometer signals in the multiple ion detection mode. Precision (coefficient of variation) is <0.5% for N_2, O_2, and Ar concentrations and <0.05% for N_2/Ar and O_2/Ar ratio data. Deviation from expected values was between 0.5 and 1.5% for air-equilibrated water of widely ranging temperature and salinity. Advantages of the instrument over existing methods include rapid throughput (~20–30 samples h^{-1}), lack of sample water preparation (e.g., no degassing step), small sample size (<10 mL), and high-precision measurement of both concentration and gas ratio data. A limitation of the present instrument is the difficulty in measuring water with significantly supersaturated gas concentrations. An example of the utility of the instrument is described for the measurement of denitrification in estuarine sediment.

Dissolved gases play an important role in marine and aquatic science. Deviations from equilibrium concentrations are common and reflect biological activity and physical processes acting on the system. Of the three most concentrated gases in aerobic waters, N_2 and O_2 are affected by both biological and physical processes, whereas Ar is affected strictly by physical processes. This distinction has enabled limnologists and oceanographers to separate physically driven processes, such as bubble release or injection, from biological processes, such as net biological oxygen exchange.[1-3] In some cases, only small fractional (<1%) deviations from equilibrium occur and it is necessary to measure dissolved gases with high precision. For that, mass spectrometers, which provide highly precise gas ratio data (e.g., N_2/Ar ratios), are usually used.

The principal methods of analysis of the major dissolved gases include gas chromatography (GC) or mass spectrometry (MS). GC provides direct concentration data while MS provides gas ratio data, which can be converted to concentration data with the independent measurement of concentration of one of the component gases (e.g., O_2). Gas chromatography offers a precision of measurement in the range of 0.3–1% for N_2, O_2, and Ar extracted from water.[1] Mass spectrometry, on the other hand, yields precision on the order of 0.05% for gas ratios (e.g., N_2/Ar or O_2/Ar).[3] Both GC and MS require injection of a gas sample that was previously extracted from the water sample in a separate batch process. This separate extraction step adds time and can limit overall precision of the gas analysis.[3]

The instrument described here is a type of membrane inlet mass spectrometer (MIMS)[4,5] optimized for high-precision measurement of the dominant dissolved gases in water. It uses a capillary bore silicone tube interface in a configuration modified from a design reported previously by Bier and Cooks.[6] We considered desirable characteristics of the instrument to include high-precision measurement of dissolved N_2, O_2, and Ar concentrations and selected gas ratios (e.g., N_2/Ar), rapid end-to-end sample analysis, and small sample volume requirement. These were met by incorporating components that provided temperature and flow control of the water sample and trapping of interfering gases. Compared to other methods of measuring the dominant dissolved gases in water, the MIMS instrument is unique in the fact that it analyzes a water sample directly, thus avoiding a separate time-consuming degassing step. Degassing the water sample is done via the membrane interface, and gases are analyzed in-line by the mass spectrometer. Response time of the analyzer is rapid and throughput of 20–30 samples h^{-1} is possible. Moreover, precision of estimates of N_2, O_2, and Ar concentrations and gas ratios compare favorably with those obtained with existing optimized GC and MS methods.

MATERIALS AND METHODS

Instrumentation. A membrane inlet mass spectrometer was modified from existing types by including a highly stable flow of water across the membrane, temperature control of the water in the membrane, and cryogenic trapping of water vapor and other compounds (e.g., CO_2) that may interfere with the detection of the gases of interest. Our evaluation considered measurement of N_2, O_2, and Ar, only, although this technique may also be appropriate for measurement of other dissolved gases.

* E-mail: kana@hpel.umd.edu.

(1) Craig, H.; Hayward, T. *Science* **1987,** *235,* 199–202.
(2) Devol, A. H. *Nature* **1991,** *319,* 319–321.
(3) Emerson, S.; Quay, P.; Stump, C.; Wilbur, D.; Knox, M. *Global Biogeochem. Cycles* **1991,** *5,* 49–69.
(4) Kotiaho, T.; Lauritsen, F. R.; Choudhury, T. K.; Cooks, R. G.; Tsao, G. T. *Anal. Chem.* **1991,** *63,* 875–883.
(5) Degn, H.; Cox, R. P.; Lloyd, D. *Methods Biochem. Anal.* **1985,** *31,* 165–194.
(6) Bier, M. E.; Cooks, R. G. *Anal. Chem.* **1987,** *59,* 597–601.

0003-2700/94/0366-4166$04.50/0 © 1994 American Chemical Society

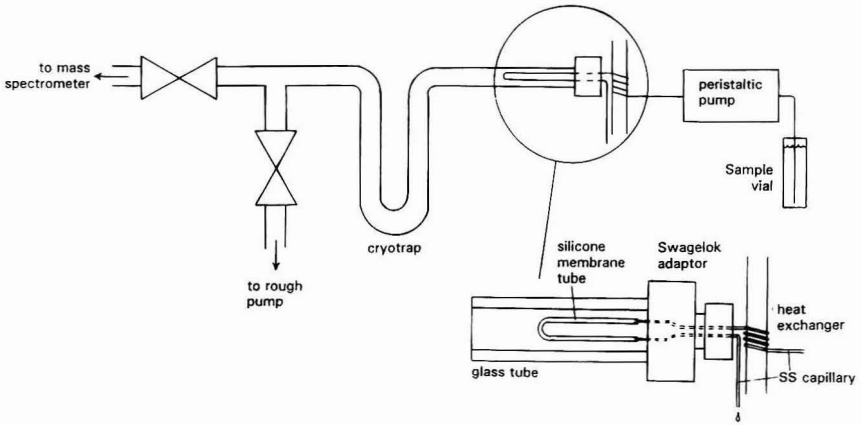


Figure 1. Schematic of the sample pumping system and vacuum interface to the quadrupole mass spectrometer.

The instrument consists of the following functional systems: water pumping, vacuum inlet, MS detector, and computer controller. The water pumping system (Figure 1) uses a peristaltic pump (Rainin Rabbit) operating at a constant speed (~0.75 mL/min). The water line upstream of the membrane interface consists of stainless steel (SS) capillary tubing connected to Viton pump tubing. Viton pump tubing provides a more rapid equilibration of the system than PVC tubing because of its lower gas permeability and reduced carryover of gases between samples. The stainless steel capillary that leads from the pump to the membrane inlet is wrapped and cemented around a 6.4 mm diameter copper tube through which thermostated water flows. This serves as a heat exchanger which stabilizes sample temperature to within 0.1 °C. The selected temperature is arbitrary, though it is usually set to a value close to 20 °C. After the heat exchanger, the capillary immediately extends through a vacuum lock (Swagelok fitting) and is connected to a 5 cm long section of 0.3 mm i.d. (0.15 mm wall thickness) silicon tubing (Silastic, Dupont). The silicone tubing serves as a semipermeable membrane interface. Sample water exits the vacuum lock through a second stainless steel capillary.

The vacuum inlet system (Figure 1) is built around a section of 9 mm diameter glass tubing bent to form a U-tube with horizontal exits. Gases that diffuse through the membrane located at one end of the tube pass through a liquid nitrogen trap (U-tube) to remove water vapor and CO_2 before entering the mass spectrometer. (CO_2 can affect N_2 analyses because of its CO (mass 28) fragment.)

Gases were detected using a quadrupole mass spectrometer (Balzers QMG420 with cross-beam ion source and secondary electron multiplier) operating in multiple ion detection mode. A pumping speed of 9 L s^{-1} was determined by a 1 cm orifice located above a 50 L s^{-1} turbomolecular pump. The ion source was tuned to provide relatively broad peaks with near-flat tops. Masses 28, 32, and 40 were detected sequentially in a repetitive cycle (~1.5 Hz) and signals were analyzed using customized software. Time trends of the mass signals and ratios of selected pairs are displayed as boxcar averages of 50 data points. Included is a visual display of each mass signal and calculated ratio magnified by ignoring the two most significant digits of each datum and scaling the remainders between 0 and 1. This provided an accurate visual assessment of the stability of the signal at a resolution of 10^4. Termination of an individual analysis was on operator command based on a visual assessment of signal stability. On termination of a sample analysis, the 50 point moving average of each signal and ratio was recorded. Sample changeover involved stopping the peristaltic pump for 2–4 s while vials were exchanged.

Sampling. Water samples were collected in 8 mL screw-capped vials using Teflon-faced silicone septa as closures. Vials were filled by siphon to overflowing, capped with no head space, and stored under water at room temperature until analysis. Samples remained uncontaminated by leakage through the septa for at least 24 h, but were generally analyzed within a few hours of collection. Samples were analyzed by inserting a stainless steel dip tube to the base of an uncapped vial, thus drawing off water from the base only. This extended the length of time the instrument could dwell on a sample before surface contact with air altered the gas composition of the water that was sampled. A high depth/diameter ratio of the sample vial is preferred. Other methods of sample withdrawal were investigated in an effort to increase the analysis time before contamination occurred, including the use of 125 mL conical flasks and injection of cold brine as a displacement solution in closed septa vials. Those changes were advantageous in situations where sample-to-sample gas compositions differed greatly and analysis time needed to be extended to several minutes. For all analyses reported here, samples were withdrawn using the simple open vial method.

Standards. Standards consisted of air-equilibrated water maintained at constant temperature and salinity for >72 h. Salinity gradients were made with either NaCl in deionized water or diluted ocean water. Water was maintained in either temperature-controlled environment rooms or jacketed flasks regulated by thermostated water. Flasks were covered with plastic wrap or loosely stoppered to maintain 100% relative humidity and limited air exchange. Dissolved gas concentrations were determined from equations derived by Weiss.[7] Variable O_2 standards were prepared

(7) Weiss, R. F. *Deep-Sea Res.* **1970**, *17*, 721–735.

by adding different amounts of sodium dithionite to water standards. Vials were immediately capped, mixed, and analyzed by the standard protocol.

Sediment Core Denitrification Experiment. The instrument was used to measure metabolic processes within a brackish water sediment system. Sediment samples were collected in triplicate from an experimental pond on the campus of Horn Point Environmental Laboratory using a 15 cm diameter cylindrical plexiglass coring device. Approximately 10–15 cm deep cores with overlying water (~2 L) were transferred to a filled aquarium inside a temperature-controlled (20 °C) environment room. Each core was fitted with inlet and outlet tubes to provide continuously flowing water at 3 mL m^{-1}, representing a turnover time of ~11 h inside each core. Feed water was collected from the ponds at least 24 h before use, filtered using 5 μm mesh, and stored in the environment room with gentle bubbling. The head-space water was stirred continuously (60 rpm) using a magnetic bar.

Duplicate water samples (8 mL) were collected from inlets and outlets at daily intervals and analyzed immediately for N_2, O_2, and Ar concentrations and N_2/Ar and O_2/Ar ratios. Data were analyzed by using differences in N_2/Ar ratios between inlet and outlet water. Ar concentration was assumed to be at equilibrium with the water at the measured temperature and salinity. N_2 flux (F) was calculated as $F = (C_i - C_o)V/A$, where C_i and C_o are the concentrations (μmol/L) of N_2 in the inlet and outlet, respectively, V is the flow rate (L/h), and A is the sediment surface area (m^2).

RESULTS AND DISCUSSION

The original design criteria—high-precision, high-throughput, and small sample size—were met with the instrument as described here. Several components contributed to the high precision including, a stable liquid pump, sample temperature control, and cryotrapping. The peristaltic pump operated in a range where the signal intensity depended on pump speed. Short-term stability was high, but drift in the signal intensity on the order of a few percent or less per hour occurred due to "aging" of the pump tubing. This invariably caused lower signals over time (ratio data were generally unaffected, however). Drift in the concentration data was accounted for by periodically analyzing standards and correcting for changes in instrument sensitivity during the course of an analysis run. The time required for mass signals to stabilize depended on flow rate. In general, increased flow rate reduced the time to steady state. But increasing flow also decreased the time that a vial sample could be analyzed before air-contaminated water reached the dip tube. A flow of ~0.75 mL m^{-1} was a suitable compromise, resulting in sample turnaround as brief as 90 s.

Precision and accuracy were evaluated on temperature and salinity standards. The practical lower limit of a temperature standard was ~10 °C when the instrument was operated at room temperature (~24 °C). This was due to the negative pressure developed in the capillary tube leading to the pump and the resultant outgassing of the supersaturated water in the feed line. Results of five temperature standards using full strength seawater are presented in Table 1. For measurement of concentration, coefficients of variation (CV) averaged 0.20% for five temperatures and three gases. Coefficients of variation of N_2/Ar and O_2/Ar ratios averaged 0.068%. Accuracy was assessed by standardizing the instrument at a single temperature (20.9 °C). Concentration values were generally within 1.5% of expected, and ratios were within 0.5% of expected. In a similar exercise, variable salinity water of constant temperature was analyzed (Table 2). Measurement precision (CV) was comparable to variable temperature standards, averaging 0.20% for the three gases and six salinities and 0.030% for the N_2/Ar and O_2/Ar ratio measurements.

Table 1. Dissolved Gas Analysis of Seawater (36 ppt Salinity)[a]

	temp, °C				
	12.7	17.6	20.9	30.6	39.3
N_2					
mean (μM)	473.0	432.7	415.7	359.3	325.6
CV (%)	0.05	0.13	0.44	0.07	0.25
expected (μM)	479.7	439.3	415.7	359.3	320.3
Δ (%)	−1.41	−1.49	0	0.01	1.65
O_2					
mean (μM)	260.5	236.4	225.6	190.5	169.3
CV (%)	0.08	0.15	0.39	0.10	0.48
expected (μM)	264.6	239.9	225.6	191.5	168.3
Δ (%)	−1.58	−1.47	0	−0.51	0.62
Ar					
mean (μM)	12.82	11.60	11.05	9.35	8.31
CV (%)	0.05	0.10	0.37	0.10	0.21
expected (μM)	12.94	11.75	11.05	9.40	8.26
Δ (%)	−0.94	−1.27	0	−0.46	0.66
N_2/Ar					
mean (μM)	36.89	37.30	37.61	38.41	39.16
CV (%)	0.03	0.02	0.08	0.02	0.08
expected (μM)	37.08	37.39	37.61	38.23	38.79
Δ (%)	−0.52	−0.24	0	0.45	0.96
O_2/Ar					
mean (μM)	20.32	20.38	20.41	20.37	20.36
CV (%)	0.05	0.06	0.03	0.00	0.31
expected (μM)	20.45	20.42	20.41	20.38	20.38
Δ (%)	−0.66	−0.23	0	−0.07	−0.07

[a] The analyzer was calibrated using 20.9 °C water. Quadruplicate samples were analyzed in the following order: 20.9, 39.3, 30.6, 17.6, and 12.7 °C. Run time for completion of the 20 samples was 32 min. The percent deviation (Δ) between the mean value and expected value was calculated as (mean − expected)/expected × 100.

The influence of different O_2 concentrations on the N_2 signal and N_2/Ar ratio was investigated by altering the amount of O_2 in water standards equilibrated at constant temperature (Figure 2). Over the range of 0–100% O_2 saturation, the N_2 signal increased proportionally 2.5%, while the N_2/Ar ratio remained constant.

The application that we present deals with the measurement of denitrification, a microbial process that reduces NO_3^- to N_2 and that is often associated with anaerobic marine sediments. Developing methods that directly measure the end product has been hampered by the low flux of N_2 compared to its background concentration. This requires routine precision at better than 1%. Hence, alternative methods have been employed which either require inhibitors or other manipulations that modify the system and/or place it in a non-steady-state mode which variably cause alterations in the in situ denitrification flux.[8] By exploited the high-precision measurement capability of the instrument, we could utilize an experimental design that offered the advantage of manipulating the system among various steady-state conditions.

Figure 3 illustrates the result of a continuous-flow experiment on triplicate brackish pond sediment cores with overlying water. Net N_2 evolution (net denitrification) ranged between 1 and 60 μmol m^{-2} h^{-1} depending on the addition of nitrate or nitrate plus acetate (an energy source). These fluxes are in the range of denitrification rates found in estuarine sediments measured by other techniques.[9] In our experiment, flow rate was adjusted to

(8) Seitzinger, S. P.; Nielsen, L. P.; Caffrey, J.; Christensen, P. B. *Biogeochemistry* **1993**, *23*, 147–167.

Table 2. Dissolved Gas Analysis of Water of Differing Salinities (20 °C)[a]

	salinity, ppt					
	0	2.25	4.5	9.0	18.0	36.0
N_2						
mean (μM)	524.2	523.8	516.4	503.9	480.6	439.5
CV (%)	0.22	0.04	0.21	0.15	0.30	0.16
expected (μM)	531.2	523.6	516.1	501.4	473.4	421.9
Δ (%)	−1.31	0.04	0.06	0.49	1.53	4.19
O_2						
mean (μM)	279.7	279.9	276.4	270.1	258.1	237.6
CV (%)	0.24	0.04	0.18	0.13	0.24	0.12
expected (μM)	283.6	279.9	276.2	269.0	255.1	229.3
Δ (%)	−1.39	−0.00	0.06	0.42	1.21	3.62
Ar						
mean (μM)	13.70	13.71	13.53	13.23	12.67	11.69
CV (%)	0.22	0.03	0.20	0.12	0.26	0.14
expected (μM)	13.91	13.73	13.54	13.18	12.50	11.24
Δ (%)	−1.49	−0.17	−0.09	0.30	1.39	4.08
N_2/Ar						
mean (μM)	38.21	38.16	38.13	38.05	37.89	37.57
CV (%)	0.003	0.014	0.027	0.034	0.039	0.020
expected (μM)	38.19	38.15	38.11	38.03	37.87	37.55
Δ (%)	0.06	0.04	0.06	0.05	0.07	0.06
O_2/Ar						
mean (μM)	20.39	20.40	20.41	20.39	20.35	20.31
CV (%)	0.052	0.006	0.027	0.014	0.040	0.033
expected (μM)	20.39	20.39	20.40	20.40	20.40	20.41
Δ (%)	−0.02	0.00	0.06	−0.02	−0.24	−0.48

[a] Duplicate samples were analyzed in ascending order of salinity followed by the analysis of a second set of duplicate samples in random order. The analyzer was calibrated using 2.25 ppt water at the beginning and middle of the run. N_2/Ar and O_2/Ar data were corrected for analyzer background according to equation $(G - G_b)/((G/[G/A]) - A_b)$, with G the gas (N_2 or O_2) concentration signal, G_b the analyzer background signal, A the argon concentration signal, A_b the argon background signal, and $[G/A]$ the gas ratio value from the sample run. The percent deviation (Δ) between the mean value and expected value was calculated as (mean − expected)/expected × 100.

maintain the O_2 concentration in the overlying water at ~50% of saturation (data not shown), which had the desirable effect of maintaining oxygenated headwater throughout the 16 day experiment. This parameter constrained the ΔN_2 to a value between 0 and 1% owing to the significantly lower denitrification flux compared to respiratory flux in the system. Therefore, resolution of the change in N_2 required use of N_2/Ar ratios that could be measured with higher precision than N_2 concentrations alone. This is the first demonstration of the use of direct N_2 production measurements in steady-state sediment cores.

We have identified both advantages and disadvantages of the MIMS instrument over conventional methods for measuring dissolved N_2, O_2, and Ar. The MIMS instrument offers significantly higher analysis speed with >100 analyses per day being readily attainable. This has advantages in environmental studies where spatial and temporal variability can be high and intensive sampling is desirable. Additionally, it can be exploited where rapid, near real-time data are beneficial, such as in kinetic experiments or where contingency-based decisions would improve efficiency of sampling, such as in shipboard oceanographic projects. (Our mass spectrometer has been operated aboard oceanographic research vessels, indicating the potential for using the instrument at sea.)

The MIMS instrument also provides data equivalent to two different instruments, a GC and an MS. Generally, for the highest precision work, dual-inlet isotope ratio mass spectrometers have

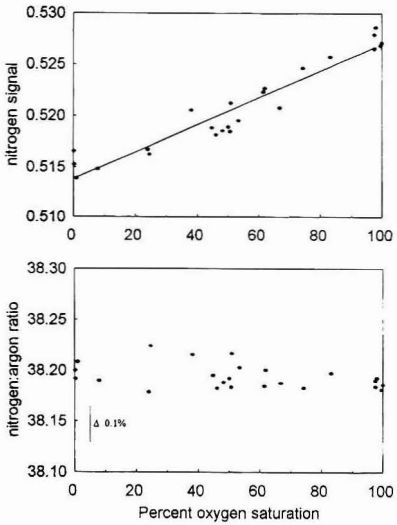


Figure 2. Effect of different oxygen concentrations on the measurement of N_2 (top panel) and N_2/Ar ratios (bottom panel). Line corresponds to the linear best fit.

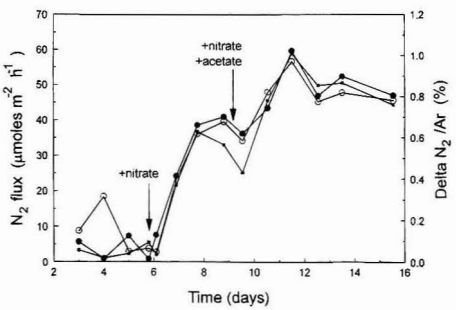


Figure 3. Time course of triplicate sediment cores exposed to continuous-flow conditions. See text for details.

been used, although the level of precision is ultimately limited by the step involving degassing of the water sample and not the analysis of the gas itself. Such mass spectrometers are not widely available owing to their expense and technical requirements. The quadrupole mass spectrometer used in the instrument is significantly less expensive to purchase and maintain and can be assembled as a benchtop instrument.

Limitations of the instrument include its difficulty in measuring supersaturated water and lack of absolute standards based on gravimetrically or volumetrically prepared standards. Bubbles originating from outgassing of supersaturated water cannot be tolerated in the silicone capillary tubing because they perturb the uniform gas flow across the membrane. The instrument operated at room temperature, which limited cool water standards to a temperature of >9 °C. Such samples could withstand warming and the negative pressure developed within the capillary dip tube without outgassing, whereas cooler water standards outgassed in the fluid inlet line. Supersaturated water is also found in aquatic

(9) Seitzinger, S. P. *Limnol Oceanogr.* **1988**, *33*, 702–724.

samples that have high oxygen production rates or bubble injection (e.g., under dams). Those samples can also be difficult to measure with the instrument although we have successfully measured 27 °C pond samples with 200% oxygen saturation. It should be possible to extend the capability of the instrument for measuring low-temperature samples (0−10 °C) by operating the peristaltic pump and inlet tubes at subambient temperature by use of a refrigeration box.

Calibration of the instrument depends on standards consisting of air-equilibrated water of known temperature and salinity. This type of standard will have an effect on the accuracy of measurement depending on how rigorously the standards are prepared. In general, one can expect the solubility values derived from published tables or regression equations to be accurate to within a few tenths percent for equilibrated water under standard conditions (100% relative humidity and 1 atm). Therefore, measurements by the MIMS instrument cannot exceed this level of accuracy. In the present experiments, atmospheric pressure was not measured or controlled over the head space of the standard water samples. This would affect estimates of concentration but not ratios, as changes in pressure would affect gases similarly. Yet, the lack of pressure measurement or control should not affect our determination of accuracy statistics since all standards from a given temperature or salinity gradient were sampled at the same time resulting in, at worst, a deviation from the true value by some constant value. Standards used in this study were all exposed to a similar atmospheric pressure history. Nevertheless, it is apparent that when high accuracy is required, pressure control or measurement during the preparation of standards is necessary.

We believe the instrument described here offers significant advantages over existing methods when high precision and/or rapid analysis is desired. We have demonstrated its ability to measure small differences in N_2 in environmental samples in a rapid and convenient way. The continuous-flow inlet, described here, is rudimentary and can be modified in various ways, for example, to provide automated sample handling or continuous monitoring of one or more experimental systems (e.g., tanks). Additionally, the quadrupole mass spectrometer can measure other dissolved gases (e.g., CO_2 and CH_4, among others) and isotopes (e.g., $^{18}O_2$ and $^{15}N_2$, among others) as previously demonstrated with existing membrane inlet mass spectrometers.

ACKNOWLEDGMENT

This research was supported by grants from the Maryland Water Resources Research Center, the Environmental Protection Agency MEERC program, and The National Science Foundation REU program. This is contribution 2553 from the Center for Environmental and Estuarine Studies.

Received for review May 31, 1994. Accepted August 24, 1994.[⊗]

[⊗] Abstract published in *Advance ACS Abstracts,* October 1, 1994.

Anal. Chem. **1994,** *66,* 4171–4176

Electrospray Tandem Mass Spectrometry for Analysis of Native Muramic Acid in Whole Bacterial Cell Hydrolysates

Gavin E. Black, Alvin Fox,* and Karen Fox

School of Medicine, University of South Carolina, Columbia, South Carolina 29208

A. Peter Snyder

Development and Engineering Center, U.S. Army Chemical Research, Aberdeen Proving Ground, Maryland 21010-5423

Philip B. W. Smith

Gunpowder Branch, Geo-Centers, Inc., P.O. Box 68, Aberdeen Proving Ground, Maryland 21010-0068

Muramic acid is an amino sugar found in eubacterial cell walls and not elsewhere in nature. This study explored the use of electrospray tandem mass spectrometry (ESI MS/MS) in analysis of underivatized muramic acid in bacterial hydrolysates. Fungal hydrolysates were used as negative controls. The only processing used was hydrolysis in sulfuric acid followed by extraction with an organic base (*N,N*-dioctylmethylamine) to remove the acid prior to ESI MS/MS analysis. Compared with pure muramic acid, bacterial hydrolysates produced more complex ESI mass spectra, such that the protonated molecular ion at *m/z* 252 was barely detectable. In contrast, product ion spectra of *m/z* 252 were identical among pure muramic acid, Gram positive bacteria, and Gram negative bacteria. However, no characteristic product ion spectrum was manifested from *m/z* 252 in fungal samples. This allowed ready, visual differentiation of bacteria and fungi. Multiple reaction monitoring (MRM) following muramic acid fragmentations (*m/z* 252 → 144 and *m/z* 252 → 126) increased sensitivity and allowed quantitative differentiation when compared with the MRM of the internal standard *N*-methyl-D-glucamine (*m/z* 196 → 44). ESI MS/MS required minimal sample preparation and allowed rapid sample throughput for analysis of muramic acid in whole bacterial cell hydrolysates.

Conventionally, microbes are identified by morphological and metabolic characteristics. For example, the Gram stain and other microscopic tests can readily differentiate bacteria and fungi. Bacteria can be classified into two broad categories based on this stain, Gram positive and Gram negative. Staining characteristics are thought to be related to differences in cell wall structure. In recent years, there has been considerable interest in bacterial differentiation based on chemical composition using mass spectrometry.[1–3]

Bacterial cell wall composition fall into two categories. Gram positive type indicates a thick peptidoglycan (PG) with no outer membrane, whereas Gram negative type has inner and outer membranes with a thin PG.[4] The so-called "Gram type" does not always correlate with classic Gram-staining characteristics. Indeed, it is best to consider the biochemical information inferred by Gram type as distinct from morphological information provided by the Gram stain.

PG is a polymer that has a glycan backbone consisting of repeating units of *N*-acetylmuramic acid and *N*-acetylglucosamine. Muramic acid (MA) is an unusual sugar not found elsewhere in nature.[5–7] Considerable heterogeneity exists in MA content among bacteria. Indeed, Gram positive bacteria can often have similar levels of MA compared to Gram negative bacteria. Due to this heterogeneity, MA levels do not strictly correlate with Gram-staining characteristics. Furthermore, some eubacteria do not contain MA,[6] while fungi lack both PG and MA.

Classical methods for determination of MA are based on colorimetry. These procedures do not readily distinguish muramic acid from other amino sugars and amino acids at the levels found in bacterial cells. Chromatographic methods are certainly superior to colorimetric approaches. However, definite identification of sugars is not possible without the mass spectrometer. For example, using both colorimetric and chromatographic methods, it has been debated for many years whether the Gram negative bacteria *Chlamydia* contain MA. By use of gas chromatography/mass spectrometry (GC/MS), *Chlamydia* were shown to lack MA.[6] In this work, other bacteria were used as positive controls and fungi served as negative controls. Unfortunately, due to the complexity of the hydrolysis/derivatization procedure, it has been difficult to apply GC/MS analysis of MA (or other neutral and aminosugars)[8,9] outside of a few research centers.

* Fax number, (803) 733-3192; e-mail address, afox@med.scarolina.edu.,

(1) Odham, G.; Larsson, L.; Mårdh, P.-A. *Gas Chromatography/Mass Spectrometry Applications in Microbiology*; Plenum Press: New York, 1984.

(2) Fox, A.; Morgan, S. L.; Larsson, L.; Odham, G. *Analytical Microbiology Methods: Chromatography and Mass Spectrometry*; Plenum Press: New York, 1990.

(3) Fenselau, C. *Mass Spectrometry for the Characterization of Microorganisms*; American Chemical Society: Washington, DC, 1994.

(4) Eudy L.; Walla M.; Morgan S. L.; Fox, A. *Analyst* **1985**, *110*, 381–385.

(5) Fox, A.; Schwab, J. H.; Cochran, T. *Infect. Immun.* **1980**, *29*, 526–531.

(6) Fox, A.; Rogers, J. C.; Gilbart, J.; Morgan, S.; Davis, C. H.; Knight, S.; Wyrick, P. B. *Infect. Immun.* **1990**, *58*, 835–837.

(7) Findlay, R. H.; Moriarty, D. J. W.; White, D. C. *Geomicrobiol. J.* **1983**, *3*, 135–150.

0003-2700/94/0366-4171$04.50/0 © 1994 American Chemical Society

Pyrolysis GC/MS is an attractive technique for Gram typing, in terms of both rapidity of analysis and automation. The differentiation of group B streptococci from other streptococcal groups was acheived by the identification of a characteristic dehydration product (dianhydroglucitol) generated from the simpler sugar glucitol.[10] However, MA (like many other compounds) is destroyed during the extremely high temperatures required for on-line depolmerization and volatilization during pyrolysis.[4]

Electrospray liquid chromatography/mass spectrometry (ESI LC/MS) is a possible alternative to GC/MS of MA. Unfortunately, the technical difficulties of routine analysis of native sugars by LC/MS have not yet been fully solved. Excellent chromatography of native sugars can be obtained with anion exchange LC at highly alkaline pH using a pulsed amperometric detector. The high ionic strength solutions often necessary for LC of sugars are not directly suited to MS, and even the use of on-line suppressors which make eluent suitable for MS can cause loss of some charged sugar species.[11,12] Decreased sensitivity can also occur due to suppression of ESI by contaminating ions from the LC mobile phase. Excellent sensitivity may be achievable using ESI tandem mass spectrometry (MS/MS) analysis since problems with the chromatography solvent entering the MS can be eliminated.[13]

This study attempted to differentiate a group of Gram negative/Gram positive bacteria from fungi using ESI MS/MS. The only sample preparation used was hydrolysis to release MA from cell wall polymers prior to analysis. Our aim was to develop a method that avoided both the complexities of derivatization/pyrolysis for sample volatilization in GC/MS and the technical problems associated with LC/MS for routine sugar analysis.

EXPERIMENTAL SECTION

Preliminary experiments were performed on an API III (Sciex, Thornhill, Canada) and the remainder on a Quattro (VG BioTech, Cheshire, England) with comparable results. Both instruments were triple–quadrupole mass spectrometers equipped with electrospray ionization sources. Both systems used a 50% acetonitrile/water mobile phase, the former acidified with 1% acetic acid. The API III solvent delivery was maintained at 7 μL/min by a Harvard Apparatus (Harvard Apparatus, MA) syringe pump. Solvent delivery for the Quattro was achieved by a Pharmacia (Uppsala, Sweden) P-500 fast protein liquid chromatography (FPLC) pump operating at 17 μL/min. A Rheodyne (Cotati, CA) Model 7125 sample injector with a 10 μL sample loop was used to introduce samples into the solvent flow. Nitrogen was used as nebulizing and bath gas delivered at flow rates of 15 and 350 L/min, respectively. The collision cell hexapole region of the API III used a pressure of 3×10^{-5} Torr with argon, whereas the Quattro was maintained at a pressure of 4×10^{-4} Torr with argon and used a collision energy of 20 eV. Both Quattro quadrupoles were calibrated using a solution of 40 ng/μL poly(ethylene glycol) 400 (380–420) in 50% acetonitrile and 1 mM ammonium acetate. In order to prevent carryover, a minimum of three injections of acetonitrile/water/acetic acid (50:50:1) were injected between each sample.

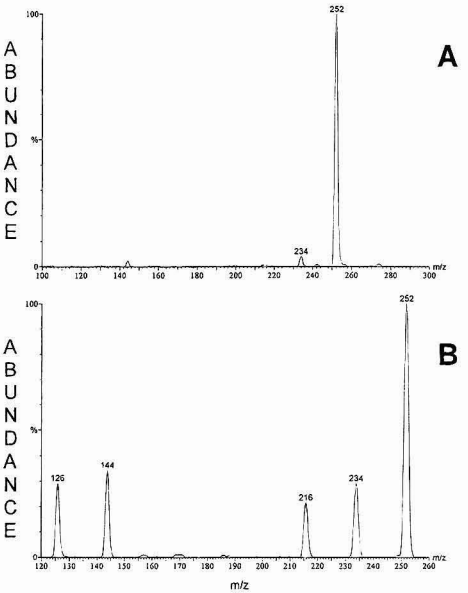


Figure 1. ESI mass spectrum of the protonated molecular ion of muramic acid ($MH^+ = m/z$ 252) (A), and the ESI product ion mass spectrum (B) exhibiting characteristic ions at m/z 126 and 144, in addition to ions at m/z 216 and 234 formed by dehydration reactions.

Four different data collection functions were used, each set to require 1.0 s of analysis time: function 1, ESI mass spectrum scanning from m/z 100 to 300; function 2, product ion mass spectrum of the protonated molecular ion of MA ($MH^+ = m/z$ 252) after collision-induced dissociation (CID) scanning from m/z 50 to 260; function 3, multiple reaction monitoring (MRM) following from m/z 252 → 144 and m/z 252 → 126 ion dissociations, which are specific for MA, with a dwell time of 0.5 s per dissociation; function 4, MRM following the transition m/z 196 → 44, which is specific for *N*-methyl-D-glucamine (MeGlN) ($MH^+ = m/z$ 196). Quattro resolution was 1.5 Da at half peak height for both quadrupoles, with an acquisition step size of 8 points/Da.

MA was purchased from Sigma (St. Louis, MO); MeGlN was obtained from Aldrich (Milwaukee, WI); glacial acetic acid and sulfuric acid were Ultrex grade (J. T. Baker, Phillipsburg, NJ), and glass distilled chloroform and acetonitrile (Burdick & Jackson, Muskegon, MI) were used as supplied from the manufacturer. *N,N*-Dioctylmethylamine (Fluka, Ronkonkoma, NY) was only available as reagent grade and was preextracted twice with double distilled water to remove contaminants.

Representative Gram positive and Gram negative bacteria and fungi included the following (Gram positive bacteria) *Staphylococcus epidermidis*, *Bacillus subtilis*, *Corynebacterium haemolyticum*, *Clostridium perfringens*, and *Bacillus anthracis*; (Gram negative bacteria) *Neisseria sicca*, *Flavobacterium meningosepticum*, *En-*

(8) Fox, A.; Morgan, S. L.; Gilbart, J. In *Analysis of Carbohydrates by GLC and MS*; Biermann, C. J., McGinnis, G. D., Eds.; CRC Press: FL, 1989; Chapter 5, p 87.
(9) Fox, A.; Black, G. In *Mass Spectrometry for the Characterization of Microorganisms*; Fenselau, C., Ed.; American Chemical Society: Washington, DC; 1994; Chapter 8, p 107.
(10) Smith, C. S.; Morgan, S. L.; Parks, C. D.; Fox, A.; Pritchard, D. G. *Anal. Chem.* **1987**, *59*, 1410–1413.
(11) Simpson, R. C.; Fenselau, C. C.; Hardy, M. R.; Townsend, R. R.; Lee, Y. C.; Cotter, R. J. *Anal. Chem.* **1990**, *62*, 248–252.
(12) Conboy, J. J.; Henion, J. *Biol. Mass Spectrom.* **1992**, *21*, 397–407.
(13) Duffin, K. L.; Henion, J. D.; Shieh, J. J. *Anal. Chem.* **1991**, *63*, 1781–1788.

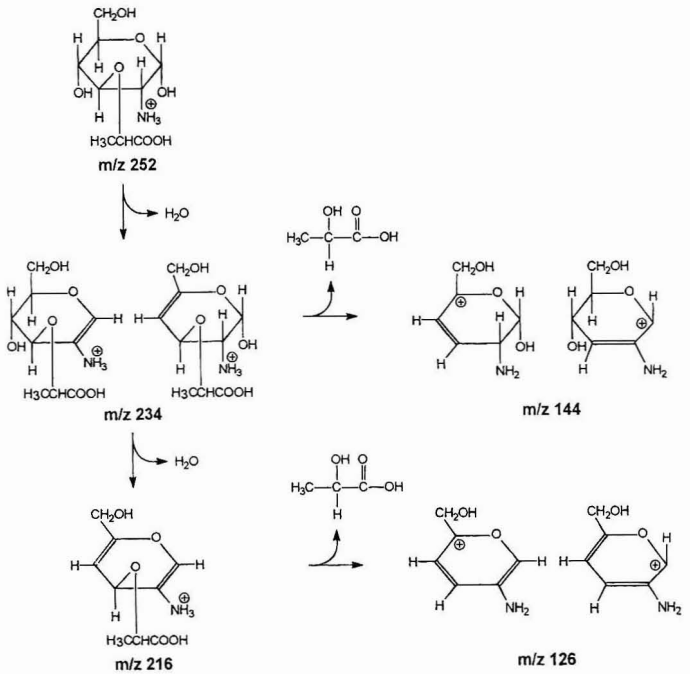


Figure 2. Interpretation of ESI MA product ions produced by dehydration and fragmentation reactions, including the characteristic loss of lactic acid.

terobacter cloacae, Shigella sonnei, Escherichia coli, Aeromonas hydrophilia, Klebsiella pneumoniae, and *Legionella pneumophila*; (fungi) *Aspergillus fumigatus, Cladosporium* sp., *Cryptococcus neoformans, Microsporum canis, Nigrospore* sp., and *Saccharomyces cerevisiae.* Microbes were grown in the appropriate liquid media, washed three times in water, and sterilized by autoclaving prior to lyophilization.

Samples of 5–20 mg were suspended in 500 μL of 2 N H_2SO_4 and hydrolyzed for 3 h at 100 °C. All samples were analyzed in duplicate. Samples were cooled, and 100 μg of MeGlN was added as an internal standard for quantitation. External standards consisted of mixtures of 50 μg of MA and 100 μg of MeGlN treated identically to samples, except with no heating. Samples were neutralized by addition of 1.25 mL of a 50% *N,N*-dioctylmethylamine/chloroform mixture. The aqueous phase was extracted twice with 1.5 mL of chloroform to remove residual *N,N*-dioctylmethylamine. A 200 μL aliquot of aqueous phase was added to 200 μL of acetonitrile and acidified with 4 μL of 10% acetic acid.

A standard curve using MA ranging in concentration from 0 to 250 ng/μL and a constant amount of MeGlN (100 ng/μL) was used to test the quantitative nature of the technique. The possible role of sulfate ions (from sulfuric acid for hydrolysis) and residual *N,N*-dioctylmethylamine (used for neutralization) on ionization efficiency was addressed by comparing MS signal intensities of sets of mixtures of MA and MeGlN: aqueous solutions without acidification or neutralization, solutions with neutralization, and solutions with neutralization and acidification.

To determine MA concentration in the samples, the ratio of MRM signals for MA and MeGlN (function 3 and function 4) in the sample was compared to the same ratio in the external standards. The concentration was divided by the weight of sample analyzed and the resulting weight of muramic acid expressed as percent dry weight of the microbial cells.

RESULTS AND DISCUSSION

The purpose of this study was to develop a method for rapid quantification of MA in hydrolysates of whole bacterial cells to provide chemotaxonomic information. Analysis of fungal hydrolysates (which lack MA) served as negative controls. As MA is a component of cell wall polysaccharides, it must first be released by hydrolysis. Concentrated mineral acid, used for hydrolysis, is unsuitable for ESI MS/MS analysis and was readily removed with a water-immiscible organic base, *N,N*-dioctylmethylamine.

The ESI mass spectrum of MA contained a prominent protonated molecular ion at m/z 252 (see Figure 1) and a small dehydration species (m/z 234). The m/z 252 product ion mass spectrum is also shown in Figure 1. Fragmentation of the protonated molecular ion includes single or double dehydrations resulting in m/z 234 and 216, in addition to loss of the lactic acid moiety, which result in fragments m/z 144 and 126 (see Figure 2). Dehydration reaction fragments are observed in the product ion mass spectra of many classes of compound and thus are not suitable for ESI MS/MS characterization analyses. Therefore, m/z 144 and 126 were chosen as distinctive product ions of MA.

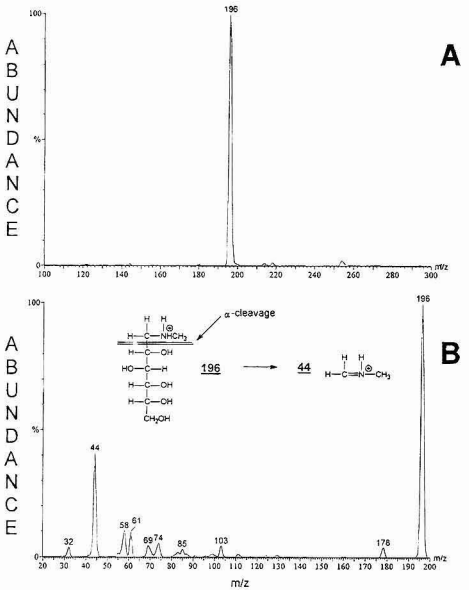


Figure 3. ESI mass spectrum of the protonated molecular ion of methylglucamine ($MH^+ = m/z$ 196) (A), and its ESI product ion mass spectrum (B), including the α-cleavage reaction which forms the characteristic methyliminium ion at m/z 44.

The MA product ions were identical on both the Sciex and VG Quattro instruments, as well as comparable to fragments generated by others using plasmaspray and thermospray.[14] The abundance of the protonated molecular ion in ESI was increased over that of plasmaspray or thermospray. The MS/MS was tuned to maximize the protonated molecular ion of MA in the ESI mass spectrum and m/z 144 and 126 in the product ion spectrum.

The ESI mass spectrum of MeGlN had a protonated molecular ion at m/z 196 and generated few prominent fragment ions after CID (see Figure 3). The only prominent fragment was the methyliminium ion (m/z 44). This fragment ion is produced by α-cleavage between C1 and C2 (the most common fragmentation of amines), where C1 bears the protonated amino group.

The MA standard curve consisted of seven replicate samples (including a blank) with a concentration range of 7.8–250 ng/μL. All samples contained 100 ng/μL MeGlN as an internal standard. The plot of MA concentration versus MA/MeGlN MRM signal ratio gave an excellent linear response ($r^2 > 0.99$). Although, ESI MS/MS is generally used as a qualitative technique, others have also shown concentration-dependent responses.[13] MS and MS/MS responses were reproducible between samples, and over the several days of experiments.

As noted above, samples and standards were hydrolyzed in sulfuric acid and neutralized with *N,N*-dioctylmethylamine. MA and MeGlN in water alone exhibited higher signals when compared to samples that had been acidified and neutralized. To address this, MRM signal intensities of sets of mixtures of MA and MeGlN were compared, including aqueous solutions without acidification or neutralization, solutions with neutralization alone, and solutions with neutralization and acidification (see Table 1). In one set of experiments MeGlN was added before any treatment, whereas in the second set of experiments MeGlN was added afterward. In both cases, neutralization with *N,N*-dioctylmethylamine reduced the signal for both MA and MeGlN. Acidification, in addition to neutralization, reduced the signal even further. Overall suppression was comparable regardless of when MeGlN was added. This suggested that suppression of signal, rather than physical loss of compounds, had occurred. Others have previously noted the difficulties of ESI MS analysis of carbohydrates due to ion suppression.[12]

Table 1. Suppression of Multiple Reaction Monitoring after Acidification and Neutralization

	aqueous solution	neutralization	acidification and neutralization
MeGlN Added before Acidification or Neutralization			
muramic acid	3.01×10^4	9.19×10^3	2.79×10^3
	2.33×10^4	1.06×10^4	4.31×10^3
methylglucamine	3.61×10^6	3.20×10^5	9.49×10^4
	2.82×10^6	3.71×10^5	9.60×10^4
MeGlN Added after Acidification or Neutralization			
muramic acid	3.16×10^5	1.78×10^5	3.69×10^4
	3.19×10^5	2.04×10^5	3.65×10^4
methylglucamine	1.87×10^6	8.60×10^5	5.52×10^4
	1.89×10^6	8.48×10^5	5.62×10^4

ESI mass spectra of microbial hydrolysates exhibited more complex patterns than did mixtures of authentic MA and MeGlN and did not allow differentiation of bacteria and fungi. Figure 4 compares the ESI mass spectra from a representative Gram positive bacterium, *S. epidermidis*, a Gram negative bacterium, *E. cloacae*, and a fungus, *A. fumigatus*. The presence of the m/z 252 protonated molecular ion of MA was often difficult to visually ascertain, although the m/z 196 molecular ion of MeGlN was clear in every sample. In bacterial samples containing at least 0.2% dry cell weight MA, product ions of m/z 252 were readily detected in the full-scan product ion mass spectra and were identical to those of pure MA fragments (Figure 5). The product ion mass spectra of the fungal samples analyzed did not contain characteristic MA fragment ions (see Figure 5). Samples below 0.2% MA did not produce visually identifiable m/z 144 or 126 fragment ions.

MRM provided considerably better detection of MA and MeGlN than observation of product spectra. Identification of MA from whole cell hydrolysates using MRM was possible at levels of 1 part per 2000. All samples containing the internal standard, MeGlN, showed a clear signal for the transition m/z 196 → 44. In samples not containing MeGlN, no signal for that transition was observed. MRM signals for the transitions m/z 252 to 144 and 126, characteristic for MA, were identified in every bacterial sample analyzed, and quantitative analyses resulted in values of 0.06–1.04% MA on a dry weight basis. The MRM transitions used for MA were used to scan fungal samples and resulted in a baseline level, identical to the signal observed for solvent alone. This allowed ready differentiation of bacterial and fungal samples (see Figure 6 and Table 2). However, the MA MRM response for one gram negative bacterial sample, *L. pneumoniae*, approached the range found in the fungal samples.

(14) Elmroth, I.; Larsson, L.; Westerdahl, G.; Odham, G. *J. Chromatogr.* **1992**, *598*, 43–50.

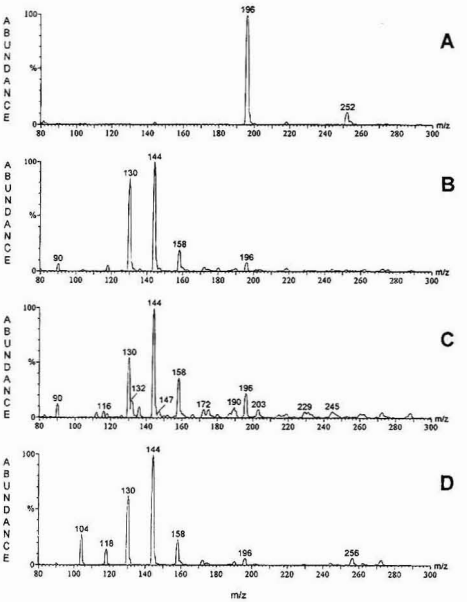


Figure 4. ESI full-scan mass spectra of an authentic MA and MeGlN mixture (A) and hydrolyzed whole cells of *S. epidermidis* (a Gram positive bacterium) (B), *E. cloacae* (Gram negative) (C), and *A. fumigatus* (fungus) (D).

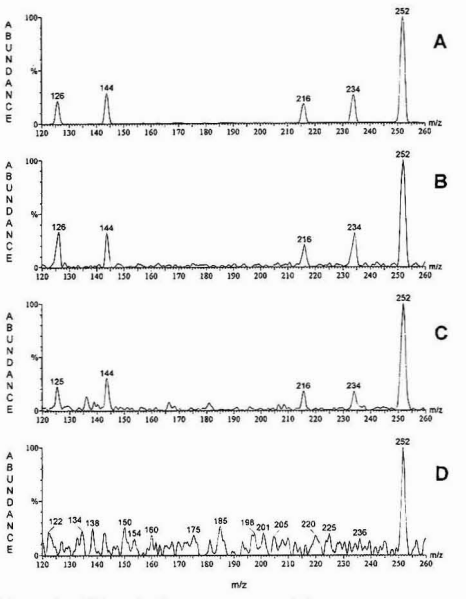


Figure 5. ESI product ion mass spectra of the samples described in Figure 4.

CONCLUSIONS

Use of ESI MS/MS for the quantitation of muramic acid (a marker for cell wall PG) in hydrolysates of whole microbial cells was demonstrated. ESI MS/MS, compared to ESI MS, allowed ready visual discrimination of bacteria and fungi based on the presence of MA in the former. Certain unusual eubacteria (such as chlamydia) do not contain MA. In a wider sense, it is well established that MA is only found in the kingdom Eubacteria, not Archaebacteria. The content of MA provides information on the chemical composition (PG) among microbes that is not readily apparent by using traditional microbiological approaches.

MA is present at different levels in most eubacteria, however, other markers are less widely distributed among different microbial species or genera. There is a great diversity of sugars, both common and uncommon, found in bacteria. For example, most members of the Gram negative *Legionellaceae* contain the rare aminodideoxyhexoses quinovosamine and fucosamine.[15,16] Members of the Gram positive genus *Bacillus* contain the uncommon aminohexose mannosamine.[17] The alditol acetate procedure for whole-cell carbohydrate profiling by GC/MS was used to identify these sugars. In fact, these compounds, like MA, contain amino functions that would make them amenable to ESI ionization. Whether ESI MS/MS can provide carbohydrate profiles similar to GC/MS for these and other sugars, remains to be explored in future work.

Many sugars found in microorganisms need to be chromatographically resolved from other coexisting isomers to provide chemotaxonomic information. The presence of galactosamine enables differentiation of *B. anthracis* and *Bacillus cereus*.[17] Without chromatographic resolution it would be extremely difficult to discriminate galactosamine from the mannosamine present in both species. In this instance, chromatographic separation is essential and MS/MS would be inadequate. However, as demonstrated here, ESI MS/MS is more easily applied than GC/MS to analysis of charged species (as is the case for amino or acidic sugars, such as are found in the teichuronic acid of bacilli). MS/MS would provide profiling of compounds based on separation by molecular weight. Such profiling could provide complementary information, but would not replace GC/MS.

Compared to more conventional GC/MS analysis of bacterial carbohydrates, ESI MS/MS is simpler in terms of both sample preparation and speed of sample analysis. An ESI MS/MS analysis takes a couple of minutes versus 30–50 min for a typical GC/MS run. These considerations would be extremely important if this approach were to be adapted for rapid or routine bacterial identification.

The current work was concerned with identification of a compound found in pure bacterial cultures. Detection of bacteria, or their chemical components, in complex matrices is more difficult since bacterial markers are only present at trace levels. In the current ESI MS/MS work, the concentration of muramic acid was 0.05–1.04% and analysis was of 5–10 mg of sample. GC/MS studies have detected MA in animal serum after injection with bacterial PG subunits (muramyl dipeptide) at concentrations of

(15) Fox, A.; Lau, P.; Brown, A.; Morgan, S. L.; Zhu, Z.-T.; Lema, M.; Walla, M. D. *J. Clin. Microbiol.* **1984**, *19*, 326–332.
(16) Fox, A.; Rogers, J. C.; Fox, K. F.; Schnitzer, G.; Morgan, S. L.; Brown, A.; Aono, R. *J. Clin. Microbiol.* **1990**, *28*, 546–552.
(17) Fox, A.; Black, G. E.; Fox, K.; Rostovtseva, S. *J. Clin. Microbiol.* **1993**, *31*, 887–894.

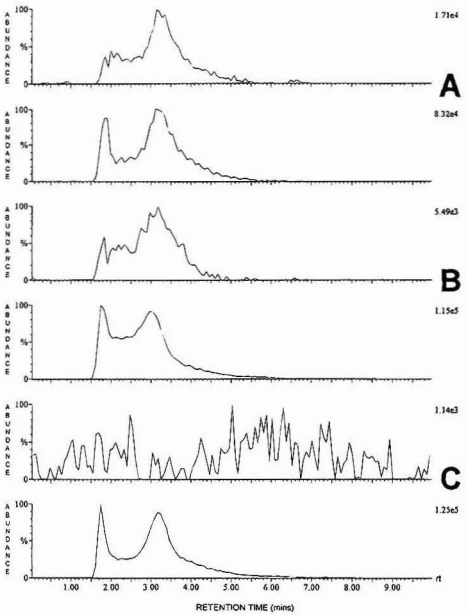


Figure 6. Pairs of MRM tracings for MA (top) and MeGIN (bottom) for a Gram positive bacterial sample, *S. epidermidis*, (A), a Gram negative bacteria, *E. cloacae*, (B), and a fungus, *A. fumigatus*, (C).

100 ng/mL (1 part in 10 million).[18] MA from endogenous bacteria in house dust has been found at levels of 4 ng/mg (1 part in 250 000) using GC/MS and GC/MS/MS. With current methodology, GC/MS sensitivity for trace detection of compounds from complex matrices is superior by several orders of magnitude over ESI MS/MS.[19] ESI MS/MS is useful, however, for the rapid identification of compounds present at more elevated levels.

In summary, the simplicity and rapidity of ESI MS/MS for the discrimination of bacteria from fungi based on MA content suggests the applicability of this approach with other compounds. Further research exploring compounds amenable to ESI MS/MS analysis, which could provide chemotaxonomic differentiation, will be vital before widespread use of this technique is possible.

(18) Fox, A.; Fox, K. *Infect. Immun.* **1991**, *59*, 1202–1205.
(19) Fox, A.; Wright, L.; Fox, K. F. *J. Microbiol. Methods*, in press.

Table 2. Levels of Muramic Acid in Bacteria and Fungi[a]

	% dry wt
Gram positive	
S. epidermidis	1.036
B. subtilis	0.806
C. haemoliticum	0.266
C. perfringens	0.188
B. anthracis	0.135
mean	0.486
Gram negative	
N. sicca	0.781
F. meningosepticum	0.347
E. ccloacae	0.308
S. sonnei	0.300
E. coli	0.188
A. hydrophilia	0.125
K. pneumoniae	0.201
L. pnuemophila	0.063
mean	0.289
fungi	
A. fumigatus	0.010
C. neoformans	0.024
Cladosporium sp.	0.022
M. canis	0.051
Nigrosporium sp.	0.013
S. cerevisiae	0.018
solvent	0.050
mean	0.027

[a] As determined by multiple reaction monitoring.

ACKNOWLEDGMENT

Thanks are extended to William E. Cotham and Michael D. Walla in the Mass Spectrometry Facility, Department of Chemistry and Biochemistry, of the University of South Carolina (Columbia, SC 29208) for help and advice. This work was supported by the Army Research Office (Grant DAAL03-92-0255), a training award from the Army Research Office DoD EPSCoR program, and an equipment grant (DAAH0493-G-0506).

Received for review May 9, 1994. Accepted August 26, 1994.[⊗]

[⊗] Abstract published in *Advance ACS Abstracts*, October 1, 1994.

Anal. Chem. **1994,** *66,* 4177–4185

Stable Isotope Methods for the Study of β-Carotene-d_8 Metabolism in Humans Utilizing Tandem Mass Spectrometry and High-Performance Liquid Chromatography

Stephen R. Dueker,[†] A. Daniel Jones,[§] Gary M. Smith,[‡] and Andrew J. Clifford*,[†]

Departments of Nutrition and Food Science and Technology and Facility for Advanced Instrumentation, University of California, Davis, California 95616

This report presents analytical methods for the isolation and quantification of *all-trans*-β-carotene-d_8 in human plasma following a 73 μmol oral dose. Retinol-d_4 derived from β-carotene-d_8 was also determined in the same plasma. Plasma samples drawn over a 24 day period were analyzed. β-Carotene and retinol were isolated and purified for analysis using a solid phase extraction protocol with aminopropyl-bonded silica sorbent. Ratios of β-carotene-d_8/β-carotene were determined using reversed-phase HPLC with spectrophotometric detection, which fully resolved the isotopomers, and by tandem mass spectrometry (MS/MS) with electron ionization. Results obtained from MS/MS and HPLC analysis showed close agreement and demonstrated improved selectivity relative to analysis using a single mass analyzer. Retinol-d_4 was converted to its *tert*-butyldimethylsilyl ether and analyzed by gas chromatography/mass spectrometry using selected ion monitoring. The ability to resolve the β-carotene isotopomers by HPLC makes it feasible for investigators without mass spectrometers to investigate the dynamics of absorption and metabolism of β-carotene-d_8 in humans.

β-Carotene is a metabolic precursor of vitamin A and is believed to have other biological functions including antioxidant activity. Intense interest in β-carotene developed after it was proposed that it might inhibit carcinogenesis in humans.[1] Despite the recognized importance of carotenoids in human physiological functions, many aspects of the absorption and metabolism of β-carotene and other carotenoids in humans are not well understood. Progress here has been hindered by lack of a suitable animal model that mimics human β-carotene metabolic dynamics, scarcity of carotenoids labeled with stable isotopes, and technical difficulties associated with development of analytical methods for monitoring the distribution and fate of carotenoids labeled with stable isotopes.

Parker et al. recently reported results from a human study using per-^{13}C-labeled β-carotene and high-precision isotope ratio mass spectrometry. They reported that 64%, 21%, and 14% of the absorbed ^{13}C entered the plasma as retinyl ester, retinol, and unaltered β-carotene, respectively, following a 1.87 μmol oral dose.[2] Two previous experiments using radioactive β-carotene found that 8.7–52.5% of the radioactivity of an administered dose of radioactive β-carotene was recovered in lymph.[3,4] Of this, 2–30% was associated with β-carotene, and most of the remaining label was associated with retinyl esters. No other human studies using labeled β-carotene appear in the literature.

Carotenoids consist of a diverse group of hydrocarbons including numerous *cis*-isomers, and many carotenoids and carotenoid oxidation products have been identified in human plasma.[5] Studies of the uptake and metabolism of stable isotope labeled β-carotene require that it be isolated from carotenoids and other endogenous substances that could interfere with the analysis. Concentrations of β-carotene in human blood plasma are ~0.3 μmol/L. β-Carotene exhibits a strong characteristic absorbance at 453 nm (in EtOH) which facilitates its determination in biological fluids and tissues using reversed-phase HPLC. Mass spectrometric analysis of β-carotene requires more rigorous isolation procedures to remove other lipids, such as fatty acid esters of glycerol and cholesterol, which occur in high concentrations in human plasma.

This report describes stable isotope methods for the analysis of β-carotene-d_8 and its metabolite, retinol-d_4, in human plasma following a 73 μmol oral dose. The isotopic ratios of β-carotene-d_8/β-carotene in the isolated plasma β-carotene are determined using two independent methods: (1) reversed-phase HPLC with spectrophotometric detection and (2) tandem mass spectrometry (MS/MS) with electron ionization and selected reaction monitoring. A solid phase extraction (SPE) protocol for isolating total β-carotene and total retinol from human plasma is also presented in this paper. An application of the extraction and analysis protocols is demonstrated by following the appearance and disappearance of β-carotene-d_8 and retinol-d_4 in plasma. The availability of stable isotope-labeled β-carotene and routine analytical methods for measuring it in plasma offer great promise for investigating the absorption and metabolism of β-carotene in humans. Protocols for the chemical synthesis of β-carotene-d_8 have been described recently.[6]

[†] Department of Nutrition.
[‡] Department of Food Science and Technology.
[§] Facility for Advanced Instrumentation.

(1) Peto, R.; Doll, R.; Buckley, J. D.; Sporn, M. B. *Nature* **1981**, *290*, 201–208.
(2) Parker, R. S.; Swanson, J. E.; Marmor, B.; Goodman, K. J.; Spielman, A. B.; Brenna, J. T.; Viereck, S. M. *Ann. N. Y. Acad. Sci.* **1994**, *691*, 86–95.
(3) Goodman, D. W.; Blomstrand, R.; Werner, B.; Huang, H. S.; Shiratori, T. *J. Clin. Investig.* **1966**, *45*, 1615–1623.
(4) Blomstrand, R.; Werner, B. *Scand. J. Clin. Lab. Invest.* **1967**, *19*, 339–345.
(5) Khachik, F.; Beecher, G. R.; Goli, M. B.; Lusby, W. R.; Smith, J. C., Jr. *Anal. Chem.* **1992**, *64*, 2111–2122.

0003-2700/94/0366-4177$04.50/0 © 1994 American Chemical Society

EXPERIMENTAL SECTION

Apparatus. Extract-Clean NH2 solid phase extraction cartridges (500 mg, 2.8 mL) and Adsorbosphere NH2 and Adsorbosphere HS ODS HPLC columns (150 mm long × 4.6 mm i.d., 3 μm particle size) were from Alltech Associates Inc. (Deerfield, IL). A 16-port vacuum manifold (Alltech Associates Inc.) was used to regulate the flow rate of solvents through the SPE cartridges at <5 mL/min. The liquid chromatograph was a Varian Model 5000 (Varian Associates, Palo Alto, CA) connected to a Lee Model 501 UV–visible detector (Lee Scientific, Salt Lake City, UT). ^{1}H NMR spectra of β-carotene-d_8 were acquired in C^2HCl_3 at 5 °C using a 70° flip angle and a 5.02 s recycle time with a GE Ω-300 spectrometer (GE NMR Instruments, Fremont, CA). A 8192-point time domain data block was used, and the data were zero-filled once during processing, which employed a line broadening of 0.1 Hz. Tandem mass spectrometry experiments were performed on a ZAB-2F-HS mass spectrometer (VG Analytical, Wythenshawe, U.K.) with 100 eV electron ionization (EI) and an accelerating potential of 8000 V. The source temperature of the mass spectrometer was kept at 250 °C to minimize memory effects due to condensation of β-carotene in the source. The slits of the mass spectrometer were adjusted to provide only slight attenuation of the ion beam, and the resolution ($M/\Delta M$) of the mass spectrometer was determined to be 500 (10% valley definition) at the single-focus detector and 1000 at the double-focus detector. Retinol-d_4 and retinol were measured using a Hewlett Packard Model 5890 gas chromatograph (Hewlett-Packard, Palo Alto, CA) fitted with a 15 m long × 0.15 mm i.d. capillary column with a 0.15 μm film (DB-23, J & W Scientific, Folsom, CA) and directly interfaced to a Trio-2 quadrupole mass spectrometer (VG Masslab, Altrincham, U.K.) operating in the selected ion monitoring mode following a protocol developed in this laboratory.[7,8]

Chemicals: *all-trans*-β-Carotene-*10,10′,19,19,19,19′,19′,19′*-d_8 (β-carotene-d_8) was purchased from Cambridge Isotope Labs (Woburn, MA) where it was synthesized as previously described.[6] Unlabeled *all-trans*-β-carotene was obtained from Sigma Chemical Co. (St. Louis, MO). HPLC grade solvents were obtained from Fisher Scientific (St. Louis, MO).

^{1}H NMR Analysis of β-Carotene-d_8. β-Carotene-d_8 in C^2HCl_3 was analyzed by ^{1}H NMR spectroscopy at 300 MHz and 5 °C using a GE Ω-300 spectrometer. Integration was performed on ^{1}H spectra taken at 300 MHz with the integral of the 16,16′,17,17′ methyl group resonances at 1.03 ppm assigned a value of 12 protons. Unlabeled β-carotene in C^2HCl_3 was also analyzed by ^{1}H NMR spectroscopy at 500 MHz and 15 °C using a GE Ω-500 spectrometer to verify the assignments reported by Vetter et al.[9] A double-quantum-filtered phase-sensitive COSY experiment[10] showed that the doublet arising from the 10,10′ protons overlapped with the AB quartet of the 7,7′ and 8,8′ protons (data not shown).

Reagent Purification and Preparation of Standards. Samples containing β-carotene were handled in amber vials and shielded from light to minimize isomerization and degradation. The β-carotene-d_8 was ~98% chemically pure as purchased as determined by HPLC, but it did contain β-carotene-d_7 (16.4%) and β-carotene-d_6 (3.5%) based on FAB/MS data supplied by the vendor. The β-carotene-d_8 was used as purchased without further purification. The unlabeled β-carotene was purified on an ODS phase Adsorbosphere HS column with an isocratic mobile phase of CH_3CN:2-propanol:CH_3OH (68:20:12 v:v:v) pumped at 0.9 mL/min. The *all-trans*-β-carotene peak was collected, concentrated to near dryness under argon, and resuspended in EtOH to a final concentration of 1.8–3.6 μmol/L; the extinction coefficient used was 140 642 $M^{-1}cm^{-1}$ at 453 nm. Five β-carotene isotopomer standards were made by adding a fixed amount of β-carotene to varying amounts of β-carotene-d_8; the molar ratios of β-carotene-d_8/β-carotene in the five carotene isotopomer standards were 0.0426, 0.1278, 0.453, 1.278, and 2.557.

Extraction of β-Carotene and Retinol from Plasma. A 1 mL volume of EtOH was added to 1 mL of plasma in a 16 × 125 mm screw-cap culture tube, the mixture was vortexed for 30 s, and lipophilic substances were extracted with 4 mL of hexane. The hexane layer was transferred to a new culture tube and dried under argon. Saponification of the lipid extract was then performed to facilitate the separation of β-carotene and retinol from lipids with similar physical properties. The residue was suspended in 1.2 mL of EtOH, to which was added 500 μL of 5.3 mol/L KOH in H_2O and 100 μL of 5.5 mmol/L pyrogallol in EtOH. The tube was purged with argon and capped, and the sample was heated at 70 °C for 1 h.

The tube was allowed to cool to room temperature, 1 mL of H_2O was added, and the saponified mixture was extracted with 4 mL of hexane. The hexane layer was transferred to a new tube, concentrated to ~100 μL under argon, and applied to an NH2 SPE cartridge previously conditioned with hexane. The sorbent was rinsed with 4 mL of hexane; the first 1.2 mL (of rinse) was discarded, and carotenes that were eluted in the following (remaining) 2.8 mL (of rinse) were collected in a glass vial containing 45 nmol of butylated hydroxytoluene (BHT) and stored at −20 °C until being analyzed for β-carotene-d_8 and β-carotene by HPLC (without further purification) or by MS/MS (after further purification).

The NH2 SPE cartridge was then washed with 20 mL of hexane:ethyl acetate (95:5 v:v), and the retinol was eluted with 3 mL of hexane:ethyl acetate (75:25 v:v) into a glass vial containing 45 nmol of BHT and dried under argon. The residue was resuspended in 500 μL of CH_3CN, transferred to a reaction vial, and concentrated to dryness under argon. The sample was then derivatized and analyzed for retinol-d_4 and retinol as previously described.[7,8] Since each plasma sample was saponified, the retinol-d_4 and retinol values include both free and esterified retinol.

The concentrations of total β-carotene and retinol were determined[11] in a 100 μL aliquot from the plasma pool before it was processed for analysis of isotopic enrichment. The concentrations of total β-carotene and retinol were also determined in the 2.8 mL hexane rinse and the 3.0 mL hexane:ethyl acetate (75:25 v:v) eluant, respectively, from the NH2 SPE after a 1 mL aliquot of the plasma pool was processed. Recovery was calculated as the amounts of β-carotene and retinol rinsed and eluted, respectively, from the NH2 SPE cartridge expressed as percentages of those present in the plasma prior to processing.

(6) Bergen, H. R. *Methods Enzymol.* **1992**, *213*, 49–53.
(7) Handelman, G. L.; Haskell, M. J.; Jones, A. D.; Clifford, A. J. *Anal. Chem.* **1993**, *65*, 2024–2028.
(8) Dueker, S. R.; Lunetta, J. M.; Jones, A. D.; Clifford, A. J. *Clin. Chem.* **1993**, *39*, 2318–2322.
(9) Vetter, W.; Englert, G.; Rigassi, N; Schwieter, U. In *Carotenoids;* Isler, 0., Gutman, H., Solms, U., Eds.; Birkhauser Verlag: Basel, Switzerland, 1971; pp 189–266.
(10) Rance, M.; Sorensen, O. W.; Bodenhausen, G.; Wagner, G.; Ernst, R. R.; Wuthrich, K. *Biochim. Biophys. Acta* **1983**, *117*, 479–486.
(11) Zulim, R. A.; Lunetta, J. M.; Corso, F. A.; Dueker, S. R.; Schneider, P. D.; Joyce, V.; Rippon, M. B.; Wolfe, B. M.; Clifford, A. J. *Cancer,* submitted.

Analysis of β-Carotene Isotopomers by HPLC. The 2.8 mL eluant from the NH2 SPE cartridge containing plasma carotenes was dried under argon, redissolved in 80 μL of CH_3CN, and separated on a reversed-phase HPLC system of two columns of Adsorbosphere HS ODS connected in series using an isocratic mobile phase of CH_3CN:H_2O:ammonium acetate (82:18:0.01 v:v:w) at 0.9 mL/min. The absorbance at 450 nm was monitored, and peak areas for β-carotene-d_8 and β-carotene were integrated using a Lab Calc software package (Chrom 1-AT, Galactic Industries Corporation, Salem, NH). The five β-carotene/β-carotene-d_8 calibration standards were also analyzed on this HPLC system, and peak areas were integrated to establish a standard β-carotene isotopomer HPLC calibration curve.

Further Purification of Plasma Carotene for MS/MS Analysis. The 2.8 mL eluant from the NH2 SPE cartridge containing plasma carotenes was concentrated to ~100 μL under argon and further purified (to remove interfering lipids) by normal-phase HPLC on an Adsorbosphere NH2 HPLC column using hexane for 2 min, followed by a 4 min linear gradient to 2-propanol:hexane 25:75 (v:v) at 1.2 mL/min. β-Carotene eluted between 1.5 and 1.8 min and was collected in an amber vial containing 45 nmol of BHT. It was dried under argon and rechromatographed on an Adsorbosphere HS ODS column using CH_3CN:2-propanol:MeOH (68:20:12 v:v:v) at 0.9 mL/min. The all-*trans*-β-carotene isotopomers eluted between 13 and 14 min, and this fraction was collected, concentrated to 20 μL under argon, and stored in an amber vial at −20 °C until being analyzed for β-carotene-d_8 and β-carotene by MS/MS.

Analysis of β-Carotene Isotopomers by MS/MS. Aliquots (2−4 μL of the further purified plasma extract) were loaded onto the filament of a direct exposure probe which was introduced directly into the mass spectrometer. Fragmentation of both isotopomers was established by performing linked metastable scans at constant B/E to establish the principal fragments (m/z 452 and m/z 444) formed from the molecular ions of β-carotene-d_8 and β-carotene, respectively. Rapid evaporation of the loaded sample was effected by passing a current of 1 A through the probe filament immediately upon introduction to the ion source of the mass spectrometer. These conditions caused the β-carotene to evaporate rapidly, giving a detected peak with a width of 5 s or less. β-Carotene-d_8 and β-carotene were detected by selected reaction monitoring of the first field-free region metastable transitions, m/z 544.5 → 452.4 and m/z 536.4 → 444.4, respectively, via linked switching of magnetic and electric field strengths under control of the VG 11/250 data system. Alternating detection of the two metastable reactions was performed using a sampling time of 0.200 s and a delay of 0.040 s between channels. The probe was cleaned between analyses by inserting the probe tip into the flame generated by a gas burner for 3−5 s. Analysis of blank samples containing no β-carotene failed to show detectable memory effects. The five β-carotene isotopomer standards were also analyzed on this MS/MS system, and the integrated areas of the signal for each channel were measured to establish a standard β-carotene isotopomer MS/MS assay curve.

Human Plasma Specimens. An informed, consenting, healthy 53-year old male weighing 94 kg swallowed a gelatin capsule (No. 000, Eli Lilly and Co., Indianapolis, IN) containing 73 μmol of β-carotene-d_8 dissolved in ~2 g of olive oil with a light breakfast (a bran muffin and a cup of coffee). The subject ate lunch and dinner 3 and 8 h later, respectively. Blood samples (~25 mL) were drawn into glass tubes containing K_3-EDTA just before and again at 0.5, 1, 2, 5, 7, 9, 12, and 24 h and at 2, 3, 4, 6, 8, 10, 12, 16, 20, 24, 36, 43, 57, 71, 85, 99, and 113 days after ingesting the β-carotene-d_8. All blood draws after the first day were taken before breakfast. Extra blood (~50 mL) was drawn on day 16 for the recovery and reproducibility experiments. Plasma was separated by centrifugation and stored as 2 mL aliquots at −70 °C. Total β-carotene and retinol was measured in all the plasma specimens.[11]

Reproducibility of Recovery and of HPLC Analysis of β-Carotene Isotopomers. Four aliquots of day 16 plasma were extracted, saponified, and processed through the NH2 SPE cartridges and analyzed for β-carotene-d_8 and β-carotene each day for three days to determine the reproducibility of our HPLC method. Four additional aliquots from the same pool were extracted, saponified, and processed through the NH2 SPE cartridges and analyzed for total β-carotene and total retinol[11] each day for 3 days to determine the recovery of β-carotene and retinol. The amount of total β-carotene and total retinol recovered from the NH2 SPE cartridges was expressed as a percent of amounts in the plasma aliquots prior to processing in calculating recovery.

The reproducibility of our HPLC analysis of β-carotene-d_8 and β-carotene in plasma was calculated using a 2-factor ANOVA to determine the within-day and between-day variability. The reproducibility of our sample preparation protocol for isolating β-carotene and retinol from plasma was also calculated using a 2-factor ANOVA to determine the within-day and between-day variability.

Repeated HPLC injections ($n = 4$) of an isotopomer standard solution containing 18.66 pmol of β-carotene-d_8 plus 597 pmol of β-carotene (molar ratio of β-carotene-d_8/β-carotene = 0.031) were performed to determine the lower limits of measurement. As little as 1.87 pmol of β-carotene-d_8 was injected onto the HPLC system to determine the lower limits of detection.

Comparison of HPLC and MS/MS Methods for Plasma Analysis. Plasma samples from all 10 blood draws during the first 48 h after the subject ingested β-carotene-d_8 were analyzed for β-carotene-d_8 and β-carotene using our HPLC and MS/MS methods to provide a direct comparison of the two methods. These data were analyzed by correlation analysis.

Calculation of β-Carotene-d_8/β-Carotene and Retinol-d_4/Retinol Ratios in Plasma. Integrated peak area ratios for β-carotene-d_8/β-carotene for the five β-carotene isotopomer standards (x-variable) versus the molar ratios of β-carotene-d_8/β-carotene (y-variable) were plotted, and a calibration curve was calculated by linear regression. Regression equations were calculated for the HPLC peak areas and independently for the MS/MS peak areas. Integrated peak area ratios for β-carotene-d_8/β-carotene (and retinol-d_4/retinol) for each plasma sample were substituted into the appropriate regression equation, and the molar ratios of β-carotene-d_8/β-carotene (and of retinol-d_4/retinol) were calculated for unknowns.

RESULTS

^{1}H NMR of β-Carotene-d_8. Spectra were obtained in the absence of added antioxidant, and spontaneous decomposition of the carotene could be observed in the NMR tube within 1 h, even at 5 °C. The low but progressively increasing level of decomposition products contributed to a cluttered baseline in some regions and decreased the precision of the integrals obtained. Nonetheless, ^{1}H NMR spectroscopy demonstrated clearly that the β-car-

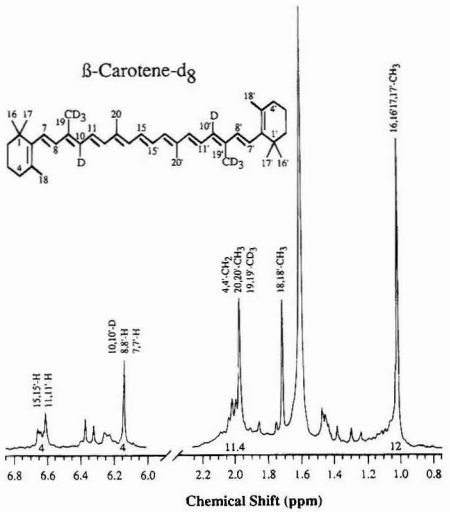


Figure 1. ^{1}H NMR spectrum of β-carotene-d_8. The spectrum was acquired in C^2HCl_3 at 5 °C using a 70° flip angle and a 5.02 s recycle time. A 8192-point time domain data block was used, the data were zero-filled once during processing, and a line broadening of 0.1 Hz was used. Relevant assignments are indicated. Integrals are reported relative to the resonance at 1.03 ppm, which was assigned an intensity of 12 protons. The strong resonance at 1.7 ppm arises from traces of H_2O condensate in the C^2HCl_3, picked up while pipetting cold C^2HCl_3.

otene-d_8 was specifically deuterated at the 10,10′ olefinic and 19,19′ methyl group positions on the basis of the following observations. The spectrum of the β-carotene-d_8 (Figure 1) shows that the height and width of the methyl resonance at 1.95 ppm are indistinguishable from those of the six-carbon resonance of the 18,18′ methyl groups at 1.7 ppm, attesting to the absence of the 19,19′ methyl groups. The integral in this region should theoretically correspond to only 10 protons if the 19,19′ methyl groups were fully deuterated. Integral values ranging from 11.3 to 11.5 were found experimentally for the β-carotene-d_8, most likely because of the low, broad signals in the baseline which contribute significantly to integrated intensity but not to peak height. Even if the additional intensity were attributed entirely to residual protons on the 19,19′ methyl groups, the extent of deuteration could be no lower than 75% (integral = 11.5).

Likewise, the integral of the β-carotene-d_8 spectrum near 6.12 ppm contains only the 7,7′ and 8,8′ protons, which are essentially degenerate at 300 MHz. The 10,10′ protons, which should appear as a doublet flanking the 7,7′ and 8,8′ protons, are absent, and the integrals in this region ranged from 3.5 to 4 protons, indicating essentially complete deuteration of the 10,10′ olefinic positions. Although partially obscured by the 15,15′ resonances, the resonances of the 11,11′ protons at 6.6 ppm show multiplicity characteristic of coupling to a deuteron and a proton rather than to two nonequivalent protons.

These ^{1}H NMR spectra clearly demonstrate that the 10,10′ olefinic positions of the β-carotene-d_8 were fully deuterated. The spectra also demonstrate that the 19,19′ methyl group positions of the β-carotene-d_8 were at least 75% deuterated.

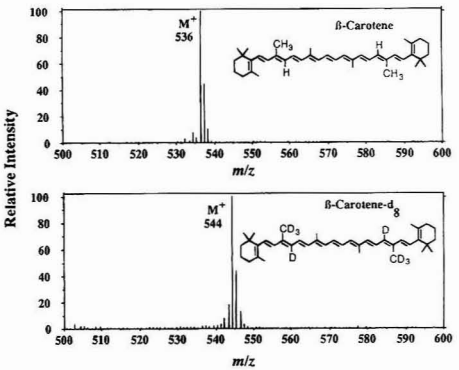


Figure 2. Molecular ion region of 100 eV mass spectra of β-carotene and β-carotene-d_8.

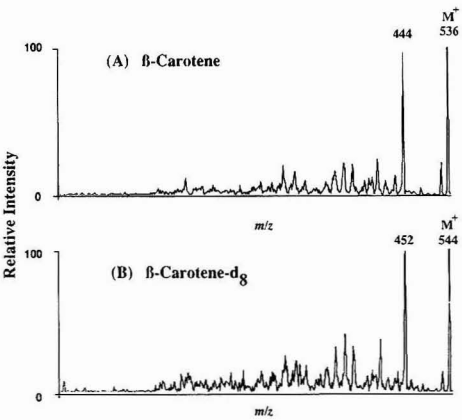


Figure 3. Spectra of product ions generated from first field-free region decomposition of molecular ions of (A) unlabeled β-carotene (precursor at m/z 536.4) and (B) β-carotene-d_8 (precursor at m/z 544.5). Spectra were acquired by performing scans of constant B/E without added collision gas.

Mass Spectra, Principal Fragments, and MS/MS of β-Carotene Isotopomers. The molecular ion regions of the electron ionization mass spectra for β-carotene-d_8 and β-carotene are shown in Figure 2. Molecular ions appear at m/z 536 and 544 for β-carotene and β-carotene-d_8, respectively. The β-carotene-d_8 was ~98% chemically pure by HPLC and 80.1% isotopically pure, containing 16.4% β-carotene-d_7 and 3.5% β-carotene-d_6. Constant B/E-linked metastable ion scans (Figure 3) of the β-carotene-d_8 and β-carotene revealed that the principal fragments formed from the molecular ions of these compounds were m/z 452 and 444, respectively, representing the well-known loss of toluene (C_7H_8) from the polyene chain of many carotenoid compounds.[12] Fragmentation of β-carotene-d_8 was analogous to that of β-carotene, with the principal fragment ion corresponding to loss of C_7H_8, and smaller amounts (~20% as much) of a product ion corresponding to loss of C_7H_7D were observed.

(12) Budzikiewicz, H. In *Carotenoid Chemistry and Biochemistry*; Britton,G., Goodwin, T. W., Eds.; Pergamon Press: Oxford, U.K., 1982; pp 155–165.

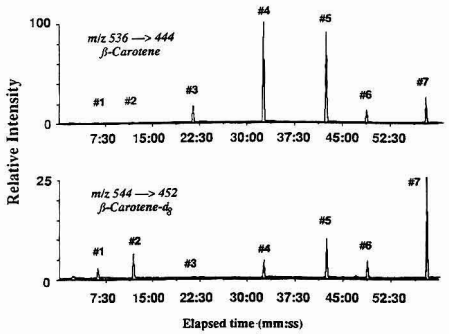


Figure 4. Ion current profiles measured during selected reaction monitoring of the transitions m/z 536.4 → 444.4 (β-carotene) and 544.5 → 452.4 (β-carotene-d_8) for isotopomer standards and analyses of β-carotene in several plasma extracts collected at different times after administration of β-carotene-d_8. The first two injections (1 and 2) contained only β-carotene-d_8 and showed no peaks in the m/z 536.4 → 444.4 channel. The third sample (3) contained only unlabeled β-carotene and showed no peaks in the m/z 544.5 → 452.4 channel. The last four samples (4–7) were extracts of serial plasma samples taken from the volunteer who ingested β-carotene-d_8 and showed peaks in both channels. All peaks (top and bottom panels) are normalized to the peak 4 in the top panel. Sharp symmetrical peaks were observed when interfering substances had been adequately removed. Variability in the absolute peak height is attributed to variations in the amount of solution loaded onto the direct exposure probe filament.

Quantitative analysis of labeled and unlabeled β-carotene was performed using rapid evaporation from the desorption chemical ionization probe and selected reaction monitoring of the metastable loss of C_7H_8 from the molecular ions of both isotopomers. The ion current profiles obtained during the analysis of several samples are shown in Figure 4. Measurement of isotopomer ratios was possible for quantities of about 100 pmol of β-carotene loaded onto the probe filament.

HPLC of β-Carotene Isotopomers. HPLC traces of β-carotene isotopomers in plasma drawn before (bottom trace) and 6 days after (top trace) the subject ingested β-carotene-d_8 are shown in Figure 5. No interferences were present between α-carotene (t_R = 72.1 min) and β-carotene (t_R = 78.9 min). The upper trace shows baseline resolution of β-carotene-d_8 (t_R = 76.5 min) from β-carotene (t_R = 78.9 min). The ratio of the integrated areas of the β-carotene-d_8/β-carotene peaks in the top trace was 0.443, demonstrating that 30.7% (0.443/1.443 × 100) of the β-carotene in this plasma sample was deuterated. Similar traces, but without the α-carotene peaks, were observed with the β-carotene isotopomer standards (traces not shown).

HPLC and MS/MS Calibration Curves for β-Carotene Isotopomer Standards. Calibration curves for the HPLC and MS/MS analysis of the β-carotene isotopomer standards are shown in Figure 6. The HPLC calibration curve is described by the equation $y = 0.003 + 1.066x$, $R^2 = 1.000$. The MS/MS calibration curve is described by $y = 0.022 + 0.724x$, $R^2 = 0.999$.

HPLC and MS/MS Analysis of Nine Plasma Samples. A plot of the molar ratios of β-carotene-d_8/β-carotene in nine plasma samples that were determined by HPLC (y-axis) and by MS/MS (x-axis) is shown in Figure 7. The slope of the line is 0.984 + 0.030, and the R^2 value is 0.995, demonstrating excellent agreement between the HPLC and the MS/MS methods for determining the molar ratios of β-carotene-d_8/β-carotene in plasma.

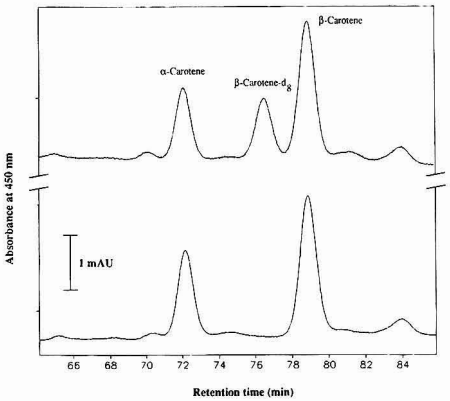


Figure 5. HPLC chromatogram showing resolution of β-carotene from β-carotene-d_8. Detection was by absorbance at 450 nm.

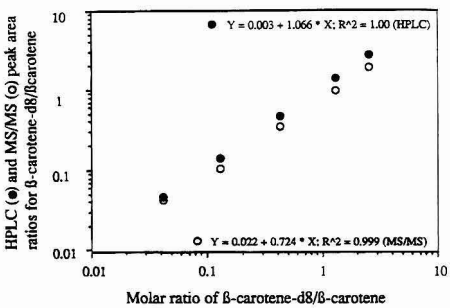


Figure 6. Calibration curves for determination of β-carotene-d_8/β-carotene generated using standard mixtures of β-carotene-d_8 and β-carotene. Mixtures were prepared by adding a varying amounts of β-carotene-d_8 to fixed amounts of β-carotene as described in the text. For HPLC analysis, ratios of the areas of peaks for β-carotene-d_8 (t_R = 76.5 min) and β-carotene (t_R = 78.9 min) were calculated (●). Analysis using MS/MS was performed by calculating the ratios of peak areas for the transitions m/z 544 → 452 (β-carotene-d_8) and m/z 536 → 444 (β-carotene), shown as ○.

Reproducibility of Extraction and HPLC Analysis of Plasma. The reproducibility of the HPLC method for determining the molar ratios of β-carotene-d_8/β-carotene in separate aliquots from a pool of plasma made from blood drawn 16 days after the subject ingested β-carotene-d_8 is shown in Table 1. At this time, the molar ratio of β-carotene-d_8/β-carotene was ~0.12. The coefficient of variation (CV) for the extraction–saponification–NH2 SPE isolation and HPLC analysis of individual aliquots from this pool of plasma was 3.25% (CV = SD/mean × 100). The within-day CV for individual analysis of four separately extracted plasma samples was 2.84%. These results demonstrate that our HPLC analytical protocol was reproducible with an overall CV of <4% at levels of enrichment found 16 days after the subject ingested 73 μmol of β-carotene-d_8.

As little as 1.87 pmol of β-carotene-d_8 was detectable with our HPLC system. Repeated HPLC analysis (n = 4) of an isotopomer

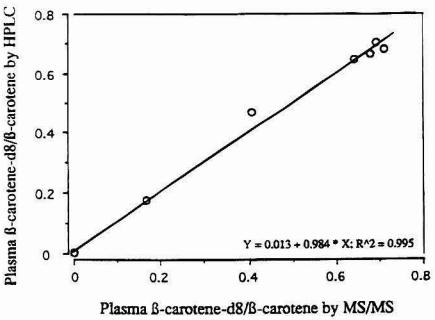


Figure 7. Comparison of molar ratios of β-carotene-d_8/β-carotene in extracts of human plasma as determined by HPLC and MS/MS as described in the text. The adult male subject ingested 73 μmol of β-carotene-d_8, and plasma was isolated from blood drawn just before and at 0.5, 1, 2, 5, 7, 9, 12, and 24 h after the subject ingested the dose. Isotopomer ratios determined for plasma from blood drawn just before and at 0.5 and 1 h after the subject ingested β-carotene-d_8 did not detect the deuterated isotopomer and appear as a single circle near the origin.

Table 1. Isotope Dilution Analysis of β-Carotene-d_8 and β-Carotene Using HPLC and Recoveries of Total β-Carotene and Retinol in Separate Aliquots of Pooled Plasma

day	sample description	β-carotene-d_8/ β-carotene	recovery of total: plasma β-carotene	recovery of total: plasma retinol
1	plasma aliquot 1[a]	0.118	80.5	64.3
1	plasma aliquot 2	0.121	78.5	66.2
1	plasma aliquot 3	0.122	78.1	62.3
1	plasma aliquot 4	0.121	79.1	
2	plasma aliquot 5	0.109	81.0	81.3
2	plasma aliquot 6	0.122	78.3	65.6
2	plasma aliquot 7	0.124	76.5	68.8
2	plasma aliquot 8	0.118	80.4	
3	plasma aliquot 9	0.117	81.2	68.1
3	plasma aliquot 10	0.119	79.5	67.5
3	plasma aliquot 11	0.121	78.6	64.8
3	plasma aliquot 12	0.119	80.2	
	mean	0.119	79.3	66.2
	CV, %	3.25	1.76	3.19

[a] β-Carotene and retinol were extracted and isolated by solid phase extraction from 12 separate aliquots of plasma from a common pool on three different dates. The ratios of β-carotene-d_8/β-carotene in each β-carotene isolate were determined by HPLC as described in the methods. The ratios of retinol-d_4/retinol in each retinol isolate can be determined as we have previously described.[7,8]

standard containing 18.66 pmol of β-carotene-d_8 plus 597 pmol of β-carotene (molar ratio of β-carotene-d_8/β-carotene = 0.031) gave a relative standard deviation of 8.51% in the experimentally determined ratio. This means that ~23.5 pmol of β-carotene-d_8 in a plasma could be measured with a CV of ~8.5% using our HPLC system if we assume a β-carotene recovery of ~79% with our extraction protocol.

The efficiency and reproducibility of the extraction–saponification–NH2 SPE method for isolating β-carotene and retinol from separate aliquots of a single plasma pool are also shown in Table 1. Average recovery of β-carotene was 79.3%, and the CV was 1.76%. The within-day CV for β-carotene recovery of four

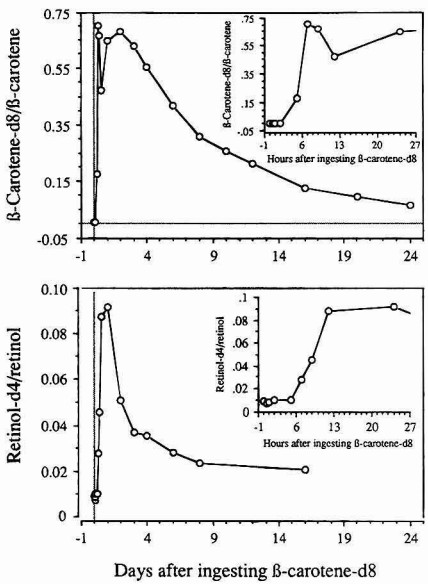


Figure 8. Ratios of β-carotene-d_8/β-carotene (upper trace) and retinol-d_4/retinol (lower trace) determined in serial plasma after ingestion of 73 μmol of β-carotene-d_8. Ratios of β-carotene-d_8/β-carotene were determined using the HPLC method described in the text.

separately extracted plasma samples was 1.7%. Average recovery of retinol was 66.2%, and the coefficient of variation was 3.19%. The within-day CV for retinol recovery of four separately extracted plasma samples was 1.9%.

***β*-Carotene-d_8/β-Carotene and Retinol-d_4/Retinol Profiles in Plasma.** Changes in the ratio of β-carotene-d_8/β-carotene (determined by HPLC) and retinol-d_4/retinol (determined by GC/MS) in plasma after administration of 73 μmol of β-carotene-d_8 are shown in Figure 8. The β-carotene-d_8/β-carotene ratio reached a sharp peak at ~7 h, a valley at 12 h, a broad peak at 1–2 days, a rapid fall over the next 5 days, and a terminal slow fall over the following 2 weeks. The retinol-d_4/retinol profile showed a single peak at ~24 h and a pharmacokinetic pattern similar to that previously described.[13]

DISCUSSION

The trans-β-carotene-*10,10′,19,19,19,19′,19′,19′*-d_8 was selected over other labeled carotenoids because central cleavage would yield retinol-*10,19,19,19*-d_4, which could be measured using previously established methods.[7,8] The protocol developed here allowed us to determine the overall pattern of appearance and disappearance of β-carotene-d_8 and of retinol-d_4 in plasma after the subject ingested β-carotene-d_8. We could also compare the retinol-d_4 pattern in the present experiment with that of a previous experiment where the same subject ingested retinyl-d_4 acetate.[13]

Extraction of β-Carotene and Retinol from Plasma. A major challenge in the isolation and purification of β-carotene-d_8

(13) Song K. S.; Muller, H. G.; Clifford, A. J.; Furr, H. C.; Olson, J. A. *Biometrics*, in press.

is the removal of relatively large quantities of triglyceride (~4 g/L compared to ~1.3 μmol/L retinol and ~0.3 μmol/L β-carotene) that occur in this biological fluid. Thus, the overall strategy used in developing our protocol was to find cleanup steps that exploited the chemical differences between β-carotene, retinol, and the many classes of lipids present in plasma.

Precipitation of plasma proteins with EtOH was necessary to break noncovalent associations of proteins with retinol and β-carotene (and nonpolar lipids). Solubilized lipids were then extracted into hexane. The lipid in the hexane extract was saponified, and the neutral lipids including retinol and β-carotene were reextracted with hexane. Retinyl esters were converted to retinol during the saponification step. The great selectivity of the NH2 SPE sorbent toward minor differences in structure among compounds enabled it to remove most other lipids including sterols such as cholesterol. To facilitate adsorption of β-carotene and retinol to the sorbent, the hexane extract of the saponified material was applied to the NH2 sorbent in hexane so as not to disrupt any interactions between retinol and the sorbent by a more polar solvent. The hexane rinse of the column removed β-carotene because of its weak affinity for the sorbent and its high solubility in hexane.

Adding BHT to the vial containing β-carotene rinsed from the NH2 SPE cartridge is important to stabilize it during handling. Many products of β-carotene oxidation have been characterized recently.[14] We have frequently observed the presence of β-carotene oxidation products, even in β-carotene obtained from commercial sources. Further oxidation occurs over just a few hours in normal laboratory environments, particularly if carotenoids are not protected from light. We have also observed oxidation of less-reactive retinoids during storage unless BHT or other antioxidants were present, and our use of BHT in this study was a precaution based upon our earlier experiences.

About 20% of the β-carotene present in the original plasma was lost through the NH2 SPE step. Therefore, of the β-carotene present in the original plasma, ~80% was recovered after the NH2 SPE step.

Washing the NH2 SPE cartridge with hexane:ethyl acetate (95:5 v:v) removed cholesterol and any residual triglyceride and diglyceride.[15] Retinol was then eluted from the NH2 SPE cartridge with hexane:ethyl acetate (75:25 v:v). Adding BHT to the vial containing retinol eluted from the NH2 SPE cartridge is important to minimize oxidative decomposition of retinol.[8] About 34% of the retinol present in the original plasma was lost through the NH2 SPE step. Therefore, of the retinol present in the original plasma samples, ~66% was recovered after the NH2 SPE step. The 66% recovery of retinol in the present experiment is slightly greater than the 50% recovery with a simpler version (no saponification) of this protocol.[8]

MS/MS of β-Carotene Isotopomers. The eluant fraction (from the NH2 SPE cartridge) containing plasma carotenes required additional purification to remove lipids before it could be successfully analyzed by MS/MS. Single stage MS analysis using probe introduction often showed the presence of contaminants including cholesterol esters (characterized by a peak at m/z 367) and fatty acyl esters of glycerol (numerous peaks between m/z 520 and 560, some of which interfered with the β-carotene molecular ions). Purification was achieved by successive HPLC separations using first an Adsorbosphere NH2 column followed with another separation using an Adsorbosphere HS ODS. Without these two separation steps, analysis by MS/MS and selected reaction monitoring revealed impurities that yielded substantial ion currents for the transitions (m/z 536 → 444 and 544 → 452) and interfered with the detection of β-carotene and β-carotene-d_8 by MS/MS. Interfering substances were judged to be present when the volatilization profiles as detected by the mass spectrometer showed the presence of material which evaporated more slowly than β-carotene. Recovery of *all-trans*-β-carotene through these two HPLC steps was essentially quantitative (data not shown), and isolated β-carotene was found to be of sufficient purity for MS/MS analysis.

The β-carotene-d_8 and β-carotene isotopomers exhibited major fragment ions at m/z 452 and 444, respectively, corresponding to the characteristic loss of toluene (92 Da) from the polyene chain of many carotenoid compounds.[12] Fragmentation of the molecular ion of β-carotene-d_8 was analogous to that of β-carotene, as we had anticipated from earlier MS studies of β-carotene-d_{40} and β-carotene.[16] Overall, the MS/MS findings were in good agreement with β-carotene metastable ions previously reported.[17]

As shown in Figure 6, the slope of the MS/MS calibration curve is 0.724. In other words, the loss of C_7H_8 from the molecular ion of β-carotene-d_8 is 72.4% as efficient as loss of the same neutral fragment from the molecular ion of unlabeled β-carotene. Three interacting factors (isotopic purity of β-carotene-d_8 and the loss from β-carotene-d_8 that is accounted for by C_7H_8 versus C_7H_7D, which lower the slope, and the lower resolution of the mass spectrometer for precursor and product ions, which raise the slope) account for this phenomenon. First, the isotopic purity of the β-carotene-d_8 is only ~80% (80% by MS, 77% by ^{1}H NMR), the balance being either β-carotene-d_7 or β-carotene-d_6, which would not be detected for the transition m/z 544 → 452. Second, only ~80% of the loss from the β-carotene-d_8 molecular ion was C_7H_8 (the remainder was C_7H_7D). These two factors would suggest that the slope of the MS/MS calibration curve should be only 0.64 (0.8 × 0.8) rather than 0.724. However, it should be remembered that although the mass spectrometer resolution was 1000 at the double-focus detector, resolution of precursor and product ions is substantially less,[18] with the result that these ions are expected to contribute to the transition m/z 544 → 452 due to contributions from adjacent peaks with different isotopic compositions. Resolution of the fragment (product) ion at m/z 452 was experimentally determined to be 300 ($M/\Delta M$ defined at full width at half-maximum) for β-carotene-d_8.

HPLC of β-Carotene Isotopomers. The β-carotene-d_8 and β-carotene (in the plasma carotene fraction rinsed from NH2 SPE cartridge with hexane) were fully resolved by isocratic reversed-phase HPLC as shown in Figure 5. The baseline separation of β-carotene-d_8 from unlabeled β-carotene allowed reliable measurements of the ratios of β-carotene-d_8/β-carotene to be made by HPLC, which was important for the strong correlation between

(14) Yamauchi, R.; Miyake, N.; Inoue, H.; Kato, K. *J. Agric. Food Chem.* **1993**, *41*, 708–713.

(15) Kaluzny, M. A.; Duncan, L. A.; Merritt, M. V.; Epps, D. E. In *Proceedings of the Second International Symposium on Sample Preparation and Isolation Using Bonded Silicas;* Van Horne, K. C., Ed.; Sorbent Extraction Technology Handbook; Analytichem International: Harbor City, CA, 1985; pp 82–84.

(16) Svec, W. A.; Harkness, A. L.; Strain, H. H.; Katz, J. J. *Org. Mass Spectrom.* **1972**, *6*, 843–851.

(17) Rose, M. E. In *Carotenoid Chemistry and Biochemistry;* Britton, G., Goodwin, T. W., Eds.; Pergamon Press: Oxford, U.K., 1982; pp 167–174.

(18) Glish, G. L.; McLuckey, S. A. *Proc. 36th ASMS Conf. Mass Spectrom. Allied Topics* **1988**, 825–826.

the HPLC and MS/MS methods shown in Figure 7.

The retention times of β-carotene-d_8 and unlabeled β-carotene were 76.5 and 78.9 min, respectively; this corresponded to a 20 s shortening of the t_R for replacement of a single proton with a deuteron (difference of 78.9 less 76.5 divided by 8, assuming the relationship is linear). Because the β-carotene-d_7 contributed only a small amount (16.4%) of the material in the β-carotene-d_8 peak and because the difference in t_R between β-carotene-d_8 and β-carotene-d_7 was small (20 s) relative to the width at half-height of the β-carotene-d_8 peak (1 min), the β-carotene-d_7 was expected to contribute only a minor amount to broadening of the β-carotene-d_8 peak. This expectation was confirmed by the symmetrical appearance of the β-carotene-d_8 peak.

Furthermore, when we determined the chemical purity of the β-carotene-d_8 using HPLC, we observed only one peak even though β-carotene-d_7 was seen to be present at m/z 543 in the electron ionization mass spectrum (Figure 2, bottom panel) of another aliquot of the same β-carotene-d_8 sample. Therefore, we assume that the HPLC peak at $t_R = 76.5$ min (labeled β-carotene-d_8 in Figure 5) includes overlapping contributions from β-carotene-d_8 and β-carotene-d_7. Furthermore, chromatographic separation of isotopomers is usually minor even in the best of separations (e.g., capillary GC) when the difference is only replacement of a single proton by a deuteron, particularly for a molecule the size of β-carotene.

Finally, the mechanism by which deuteration alters the t_R of carotenes is unclear at present. Molecular mass is not changed appreciably by deuteration, and therefore the difference in mass between labeled and nonlabeled β-carotene would not be expected to account for the resolvability of the isotopomers. On the other hand, isotopic substitution might stabilize a particular family of conformations that alters the interaction of β-carotene-d_8 with the reversed-phase column. Such a change could be subtle and could represent only a small shift in the population of conformers. Such a change could effect a small reduction in the hydrophobic surface area available to bind the stationary phase. A change in hydrophobic surface area could alter the t_R according to the stoichiometric displacement model of reversed-phase chromatography.[19] According to this rationale, substitution at olefinic positions would be more important than that at the methyl group positions in determining t_R. For instance, the presence or absence of a deuteron at the 10 or 10′ olefinic position would be expected to have a greater effect on t_R than the presence or absence of one of the three deuterons at the 19 or 19′ methyl groups; C^2HH_2 is more similar to CH_3 than is olefinic CH to C^2H. Under these conditions, the β-carotene-d_8 peak in Figure 5 includes overlapping contributions from β-carotene-d_8, β-carotene-d_7, and β-carotene-d_6.

Differences in retention times for β-carotene-d_8 (76.5 min) and β-carotene (78.9 min) are attributed to a small isotope effect upon the partitioning of the two isotopomers between the stationary and the mobile phase. This isotope effect can be used to advantage in analyzing plasma (and tissue) samples for β-carotene-d_8 and β-carotene using HPLC, which is one of the primary methods for separation, purification, and analysis of carotenoids and retinoids. Since chromatographic separation of isotopomers was only possible by careful selection of mobile phase and long chromatographic analyses, it is anticipated that such fractionation is of minor importance in vivo. The HPLC method allows analysis of isotopomers of β-carotene to be made without sophisticated MS/MS equipment and dedicated and highly trained personnel. Finally, though we have been able to elute β-carotene using short capillary GC columns, previous studies in our laboratory have shown that GC/MS is not well suited for the analysis of β-carotene because isomerization causes extensive band broadening and a significant decrease in method sensitivity (unpublished data).

Suitability of the Methods for Pharmacokinetic Studies. The β-carotene-d_8/β-carotene ratios in blood plasma specimens drawn at various times during the first 24 days of a 113 day period following ingestion of 73 μmol of β-carotene-d_8 are shown in the top panel of Figure 8. The β-carotene-d_8/β-carotene ratios show a sharp peak at 7 h, a valley at 12 h, and a broad peak at 1−2 days. As blood is a physically heterogeneous fluid, the sharp peak at 7 h may reflect a transient surge of β-carotene-d_8 labeling of different phases within the blood such as chylomicrons and very low density lipoproteins (VLDL) while the broad peak at 1−2 days reflects β-carotene-d_8 labeling of low density lipoproteins (LDL).[20] The valley at 12 h represents liver processing of the β-carotene-d_8-labeled chylomicron remnants and VLDL.

The retinol-d_4/retinol ratios are shown in the bottom panel of Figure 8. The magnitude of the retinol-d_4/retinol ratio at peak labeling was ~9 times less than that of β-carotene-d_8/β-carotene. Plasma retinol levels are typically greater (4.5 times) than β-carotene concentrations, 1.3 vs 0.3 μmol/L, suggesting that the smaller retinol-d_4/retinol ratio (compared to β-carotene-d_8/β-carotene ratio) reflected a greater dilution of retinol-d_4 within a larger retinol pool. The ratios of retinol-d_4/retinol peaked at ~24 h and then dropped sharply over the next day, and by the eighth day, very little labeling was evident. The timing of the retinol-d_4/retinol peak in the present study coincides well with the timing of the retinol-d_4/retinol peak when retinyl-d_4 acetate was ingested by the same subject in a previous study.[13] This suggests that the pharmacokinetics of retinol are similar when it is ingested as retinyl acetate or as its precursor β-carotene. The present protocols should be useful in investigating the conversion of newly ingested β-carotene to retinal, retinol, and possibly other key metabolites in blood and urine.

The 73 μmol dose of β-carotene-d_8 was chosen because it was expected to double the concentration of total β-carotene in plasma,[21,22] to provide plasma samples with β-carotene-d_8/β-carotene ratios within the range of our standard isotopomer assay curve, and to be within the range of β-carotene intake (30−335 μmol/day) regularly used in the ongoing clinical trials with antioxidants.[22] Consequently, our protocols are appropriate for investigating the pharmacokinetics of β-carotene at intakes regularly used in clinical trials with antioxidants. Our protocols are also appropriate for investigating the basis for the well-known hyper and hypo responses to oral intakes of β-carotene.[23,24] Finally, plots of the plasma concentrations of β-carotene-d_8 (β-carotene-d_8/β-carotene ratios times total β-carotene concentration) by time since dose can be fitted with a variety of mathematical

(19) Geng, X.; Regnier, F. E. *J. Chromatogr.* **1985**, *332*, 147−168.

(20) Cornwell, D. G.; Kruger, F. A.; Robinson. H. B. *J. Lipid Res.* **1962**, *3*, 65−70.

(21) Brown, E. D.; Micozzi, M. S.; Craft, N. E.; Bieri, J. G.; Edwards, B. K.; Rose, A.; Taylor, P. R.; Smith, J. C., Jr. *Am. J. Clin. Nutr.* **1989**, *49*, 1258−1265.

(22) Dimitrov, N. V.; Meyer, C.; Ullrey, D. E.; Chenoweth, W.; Michelakis, A.; Malone, W.; Boone, C.; Fink, G. *Am. J. Clin. Nutr.* **1988**, *48*, 298−304.

(23) Nierenberg, D. W.; Stukel, T. A.; Baron, J. A.; Dain, B. J.; Greenberg, E. R.; The Skin Cancer Prevention Group. *Am. J. Clin. Nutr.* **1991**, *53*, 1443−1449.

(24) Canfield, L. M.; Bulux, J.; de Serrano, J. Q.; Rivera, C.; Lima, A. F.; Lopez, C. Y.; Perez, R.; Khan, L. K.; Harrison, G.; Solomons, N. W. *Am. J. Clin. Nutr.* **1991**, *54*, 539−547.

models [25] to describe the dynamics of absorption and metabolism of β-carotene in humans.[26]

A final note of caution for laboratories wishing to measure ratios of labeled/unlabeled carotenoids in human plasma. This study demonstrated that significant amounts of other lipids remain in plasma extracts even after extensive sample purification, and selective modes of detection such as spectrophotometric absorbance at 450 nm or MS/MS analyses were necessary to eliminate signals from remaining impurities. This finding reinforces the importance of verifying that the chemical purity of samples is adequate for the analysis before ratios of isotopomers are measured.

(25) Berman M.; Weiss, M. F. *SAAM Manual.* DHEW Publication 78-180; National Institutes of Health, Bethesda, MD; U.S. Government Printing Office: Washington, DC, 1978.

(26) Zeng, S.; Furr, H. C.; Olson, J. A. *Am. J. Clin. Nutr.* **1992**, *56*, 433–439.

ACKNOWLEDGMENT

The authors are grateful to Drs. Rebecca Zulim and Francesca Corso for drawing the blood samples. This research has been supported by the National Institutes of Health (Grant RO1-DK-43098) and bridging funds from the Office of the Vice Chancellor for Research at UCD. The VG ZAB mass spectrometer was purchased in part with NIH funds. The NMR instruments were purchased in part with NIH (Grant NIH IS10-RR04795) and NSF (NSF BBS8804739) funds.

Received for review May 13, 1994. Accepted August 24, 1994.[⊗]

[⊗] Abstract published in *Advance ACS Abstracts,* October 1, 1994.

Anal. Chem. **1994,** *66,* 4186–4189

$^{176}Hf/^{177}Hf$ Determination in Small Samples by a High-Temperature SIMS Technique

Vincent J. M. Salters*

Lamont-Doherty Earth Observatory, Columbia University, Palisades, New York 10964

This paper describes a new method for the analysis of the Hf isotopic composition in geological materials. This technique requires the separation and purification of Hf out of a complex matrix. The resulting Hf separate contains less than 0.2% Zr and less than 0.01% Ti. In the new mass spectrometric technique, called "hot-SIMS", the sample is held at a high temperature while being bombarded by a primary beam. The hot-SIMS technique has several orders of magnitude better ionization efficiency than conventional thermal ionization. Also, due to the high temperature at which the sample is held, the mass spectrum of the sputtered secondary ions contains only a limited amount of molecular ions; the formation of hydrides, especially, is inhibited by the high temperatures. This new technique now allows routine high-precision $^{176}Hf/^{177}Hf$ determination on 50 ng of hafnium separate. Samples down to 15 ng can be analyzed at a lower precision level.

^{176}Lu decays to ^{176}Hf with a half-life of 35.7 Ga. The natural variation in $^{176}Hf/^{177}Hf$ is thus dependent on the time-integrated $^{176}Lu/^{177}Hf$ history of the sample. This makes Hf isotopes an important tool in dating events on a geological time scale. However, the difficulty of the analysis has limited the use of Hf isotopes. The problems with analyzing Hf isotopes are 2-fold: First, Hf, in nature, and in the laboratory, behaves very similar to Zr, which makes it difficult to separate. Most materials still have the same Hf/Zr ratio as the initial Hf/Zr ratio of the earth 4.55 Ga ago. The purity of the Hf separate affects the ionization efficiency of Hf, the purer the Hf the higher the ionization efficiency. Second, the ionization potential of Hf is relatively high, resulting in poor ionization efficiencies for thermal ionization. Previous techniques were able to measure $^{176}Hf/^{177}Hf$ on Hf separates down to 1 μg of Hf with a precision between 0.007% and 0.04%.[1–3] Natural levels of Hf in basalts range from 1 to 5 ppm, which requires 1 g of material to be processed for thermal ionization mass spectrometric measurements.

This paper presents a new and improved chemical separation technique for Hf and an improved mass spectrometric technique for high-precision determination of $^{176}Hf/^{177}Hf$. This new technique is an enormous improvement over the old thermal ionization technique in that ionization efficiencies are ~2 orders of magnitude better than the thermal ionization technique. This now allows determination of Hf isotopic composition on Hf separates down to 15 ng in size, which was heretofore beyond our analytical capabilities. The mass spectrometry is done on the Lamont Isolab[4] by the "hot-SIMS" technique, where the sample is held at a high temperature while being bombarded by 15 kV Ar^+ ions. However, the increased ionization efficiency of the hot-SIMS technique compared to thermal ionization is not restricted to Hf alone. All other species present on the filament ionize better too, thus requiring a purer Hf separate and improved Hf chemistry. Specifically, isobaric interferences of $^{90}Zr^{12}C_8$ at mass 176 and $^{48}Ti^{12}C_{11}$ at mass 180 need to be avoided. The chemistry described above is designed to produce these higher degrees of purity of the Hf separate. The new separation chemistry, not much more complicated than previous techniques,[2,3] achieves an almost 100% effective separation between Hf and Zr and Hf and Ti, while using smaller volumes of concentrated acids. Hf separates as small as 50 ng can now be analyzed for $^{176}Hf/^{177}Hf$ with a routine precision between 0.007% and 0.015%. This paper describes the new technique and reports reproducibility for both standards and natural samples.

DISSOLUTION AND SEPARATION CHEMISTRY

The separation of Hf out of the complex matrix of a rock powder was investigated by addition of radioactive ^{181}Hf to the rock powder. ^{181}Hf was produced at the nuclear reactor at MIT by neutron addition through irradiation of preconcentrated ^{180}Hf (>95% ^{180}Hf). ^{181}Hf activity in the different fractions was determined using a NaI detector. This method requires only small additions (<10 ng) of Hf to the sample, and Hf concentrations can be determined in both liquids and solids independent of matrix complexity. Other analytical techniques (atomic absorption or inductive coupled plasma mass spectrometry) are less sensitive (higher doping levels are needed) and require longer time for analyses. Throughout the chemistry only ultrapure reagents and always double subboiling distilled acids are used. *(CAUTION: Mineral acids, such as HNO_3, HCl, HF, and $HClO_4$ are irritants to the eyes, skin, and mucous membranes. Perchlorates can form explosive mixtures in combination with organic materials. In addition, effects of direct exposure to HF can go unnoticed for several hours. Proper precaution is required for handling of any of the above materials.)*

Theoretically, separation of Hf and Zr from the sample matrix is easily achieved with a AG 50W-X8 cation exchange column. However, dissolved Hf and Zr associate strongly with fluoride ions

* Present addrsss: National High Magnetic Field Laboratory and Department of Geology, Florida State University, Tallahassee, FL, 32310-4005.

(1) Corfu, F.; Noble, S. R. *Geochim. Cosmochim. Acta* **1992,** *56,* 2081–2097.
(2) Patchett, P. J.; Tatsumoto, M. *Contrib. Mineral. Petrol.* **1980,** *75,* 263–267.
(3) Salters, V. J. M.; Hart, S. R. *Earth Planet. Sci. Lett.* **1991,** *104,* 364–380.
(4) England, J. G.; et al. *Int. J. Mass Spectrom. Ion Processes* **1992,** *121,* 201–240.

0003-2700/94/0366-4186$04.50/0 © 1994 American Chemical Society

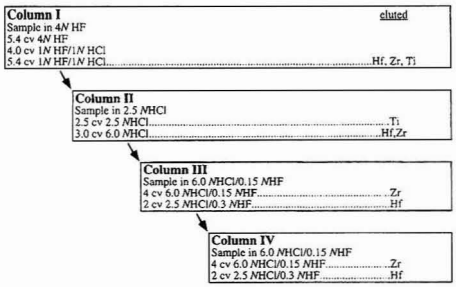


Figure 1. Elution scheme.

and form a Hf–F_x complex (or Zr–F_x). The distribution coefficient (D = {concentration of element in resin}/{concentration of element in solution}) for this complex on AG 50W-X8 is close to zero, while Hf in a chloride solution will adhere to the resin. Also, in theory, Hf and Zr are easily separated from the sample matrix precipitation of zirconium tetramandelate.[5,6] However, the presence of fluoride inhibits the formation of mandelate salts. Dissolution of the rock powder with concentrated HF obviously introduces a large amount of fluoride ions. The bulk and complexity of the matrix inhibits the effective and complete evaporation of HF even at high temperatures (150–200 °C) in the presence perchloric or sulfuric acid. Therefore, cation exchange resins can only be used after Hf is separated from the bulk of the matrix and the fluoride can be evaporated quantitatively.

An alternative way of bringing rock powder in solution is by fusing a sample with flux, thereby making the sample soluble in hydrochloric acid. A minimum sample to flux ratio of 1:5 is needed to allow dissolution and then a large volume of hydrochloric acid is required (50–100 mL of 2.5 N HCl), which introduces high blank levels.

With the present technique, 100 mg of rock powder is dissolved in 4 mL of concentrated hydrofluoric acid in a clean airflow box as follows: concentrated HF is added to the sample and allowed to react at room temperature in an open 15 mL Savillex Teflon reaction vessel. After 12 h the vessel is closed, and the temperature is raised to 100 °C, and the rest of the sample is completely dissolved in the next 24 h. At that time the vessel is opened and the sample is dried at 100 °C. The precipitated salts are partly dissolved in 0.2 mL of 4 N HF, which is added at room temperature and allowed to sit for at least 2 h. The sample is ultrasonically agitated, centrifuged, and decanted; the residue is repeatedly treated with 0.1 mL batches of 4 N HF until a total of 0.6 mL is collected. If the temperature of the sample was over 100 °C during the dry-down stage, some Hf will stay in the residue.

The Hf is separated from the bulk sample and purified by three different ion exchange columns (see Figure 1 and Table 1). The first column separates a Hf–Zr–Ti fraction from the bulk sample. The 0.6 mL sample solution is loaded on a Dowex1-X8 (200–400 mesh) anion exchange column 19 cm long and 0.5 cm in diameter. The sample is rinsed on the column with another 2 × 0.2 mL 4 N HF after which the bulk of the matrix is eluted with first 20 mL of 4 N HF followed by 20 mL of 1.0 N HCl/1.0 N HF. The Hf concentrate is eluted with 15 mL of 1.0 N HCl/1.0 N HF. (The column is cleaned with 12 mL of concentrated HF, twice with 12 mL of 8 N HNO3, backwashed with 8 mL of 4 N HF, and conditioned once with 8 mL 4 N HF.)

(5) Belcher, C.; Sykes, A.; Tatlow, J. C. *Anal. Chim. Acta* **1954**, *10*, 34–47.
(6) Hahn, R. B.; Baginski, E. S. *Anal. Chim. Acta* **1956**, *14*, 45–47.

Table 1. Ion Exchange Columns

column	resin type	h (cm)	vol (cm^3)
I	AG 1-X8, 200–400 mesh (anion)	19	3.7
II	AG50-X8, 200–400 mesh (cation)	10	2.0
III	HDEHP on Teflon beads (anion)	12	2.4
IV	HDEHP on Teflon beads (anion)	12	2.4

Concentrated perchloric acid (0.1 mL) is added to the Hf fraction from the first column, and the sample is dried to a small drop at 100 °C in a clean airflow box. At this point the temperature is raised to 150 °C, and the rest of the perchloric acid is slowly evaporated. When almost dry, a second 0.1 mL of perchloric acid is added and the sample is again heated till almost dry. This step is repeated once more. It is important to not dry the sample completely because once dry it will not redissolve in hydrochloric acid. The fluoride ions are evaporated during the repetitive drying of the sample, and after the last dry down the sample cooled and dissolved in 0.3 mL of 2.5 N HCl. Incomplete dissolution in HCl at this stage indicates the presence of HfO_2 and a drop of HF is added the dissolve the HfO_2, after which the dry-down procedure has to be repeated from the beginning. Drying the sample in a PFA-type Teflon beaker creates unusually large samples which sometimes do not dissolve in HCl. I attribute this to leaching of organic material out of the PFA by the perchloric acid, resulting in an increase in the bulk of the sample. In addition, organic material is not effectively separated from the Hf on the ion exchange columns and the columns themselves can be a source for organic material, both resulting in impure Hf separates. Therefore the Ti–Hf–Zr fraction from the first column needs to be dried in PTFE-type Teflon, which is more resistant to perchloric acid.

The resin bed of the second column is 10 cm long and 0.5 cm in diameter and is used to separate Ti from Hf and Zr. Ti needs to be separated from Hf quantitatively because $^{48}Ti^{12}C_{11}$ is an isobaric interference on ^{180}Hf. The column material is AG 50W-X8 cation resin. A 30 μL aliquot of Ultrex concentrated hydrogen peroxide is added to the sample solution. The hydrogen peroxide will form an orange-brown complex with titanium.[2] The formation of this orange-brown complex (exact color is dependent on the amount of Ti present) is a qualitative check of the chemistry up until this point. Incomplete expulsion of the fluoride ions will result in only a pale yellow or even a colorless solution. If this occurs, the dry-down sequence with perchloric acid has to be repeated.

This second column is essentially similar to the technique described by Patchett and Tatsumoto.[2] The Hf separate is loaded on the column in 0.3 mL of 2.5 N HCl and rinsed on the column with another 0.4 mL of hydrochloric acid. Ti is eluted as an orange $Ti{\cdot}(H_2O_2)_x$ complex in 5 mL of 2.5 N HCl. Hf and Zr are eluted in 5 mL of 2.5 N HCl/ 0.30 N HF and dried on a hot plate in a clean airflow box at 100 °C. This column step ensures $^{48}Ti/^{180}Hf$ signal intensity ratios of less than 2 in the mass spectrometer. The $^{48}Ti/^{180}Hf$ ratio in geological materials varies from 6900 to 12 000, which combined with the 10 times higher ionization efficiency of Ti over Hf indicates that more than 99.998% of the Ti is routinely

separated from the Hf. (The column is cleaned by 10 mL of 4 N HF followed by 2 × 10 mL of 6.0 N HCl, after which it is backwashed with 8 mL of 2.5 N HCl.)

The third column procedure is adapted in part from Fujimaki et al.[7] and is used to separate Hf from Zr. The third column bed is 12 cm long and 0.5 cm in diameter. The column has a long stem to ensure a pressure head of at least 20 cm. The pressure is kept relatively constant by a reservoir at the top of the column. A hole, ~1 cm above the resin, is used to load the sample and to drain the excess acid out of the reservoir. During sample elution and cleaning, the hole is closed by Teflon tape wrapped around the column. The column material is (bis(2-ethylhexyl)orthophosphoric acid (HDEHP) coated on Teflon beads. A description of the material can be found in Zindler.[8] The column is packed to a flow rate of 10 mL of H_2O/h with a 20 cm pressure head. The pressure head assures a faster flow rate, but consequently, the column needs to be calibrated by time instead volume. The dried-down Hf–Zr separate from the second column is redissolved in 0.2 mL of 6.0 N HCl/0.15 N HF, which is loaded on the column and rinsed on the resin bed with 3 × 0.2 mL of 6.0 N HCl/0.15 N HF.

This column is calibrated by time instead of volume. The sample is eluted with 6.0 N HCl/0.15 N HF until just before the Hf comes off the column (after 2–3 h). The excess acid is drained through the hole just above the resin, and the hole is closed by wrapping Teflon tape around the column. The Hf fraction is eluted and collected in ~60 min with 2.5 N HCl/0.30 N HF. (The column is cleaned with 10 mL of 4 N HF and 2 × 10 mL 6.0 N HCl.) The exact HF normality is not important in this separation step as long as the Hf stays on the column for at least 2 h. The behavior of Hf and Zr is extremely sensitive to flow rate and HF normality. The HF–HCl mixture is made up in a 20 L batch, and the columns are calibrated with each new batch. After collection, the Hf fraction is dried down in a clean airflow box at 100 °C. This column step is repeated once to achieve optimum separation of Hf and Zr. It has been found that the ion exchange procedure with the HDEHP–Teflon columns produces a more complete separation of Hf from Zr than either the technique described by Patchett and Tatsumoto[2] using cation columns or the separation technique described by Strelow and Bothma[9] using anion columns. Both Hf and Zr have a strong affinity for fluoride, which makes it difficult to assure complete removal of fluoride from the samples. In contrast to the old separation methods, this new technique does not require the removal of fluoride ions before the sample is loaded on the third ion exchange column. This makes the new technique more robust and allows a more reproducible Hf–Zr separation.

The procedure results in $^{90}Zr/^{180}Hf$ intensity ratios in the mass spectrometer that are consistently less than 0.14, indicating 99.7% of the Zr is routinely removed from the Hf fraction ($^{90}Zr/^{180}Hf$ is ~55 in nature). $^{48}Ti/^{180}Hf$ ratios in nature are ~9250, while the $^{48}Ti/^{180}Hf$ intensity ratios in the mass spectrometer are consistently less than 0.3. The total procedural blank is in the order of several picograms (always less than 10 pg) and does not affect the isotope ratio. Based on tests with radioactive ^{181}Hf, less than 1 ppm of the loaded sample is present on any of the ion exchange columns after the first cleaning step and the largest blank contribution is from the reagents. Yield of the total chemistry as measured both by isotope dilution analyses and as determined with radioactive ^{181}Hf range from 80 to 95%.

Table 2. Peak Switching Routine for Fractionation Corrected $^{176}Hf/^{177}Hf$ Analysis

Faraday cup position	Hi1	Hi2	Hi3
nominal amu collected			
position 1	175	176	177
position 2	176	177	178
position 3	177	178	179
position 2	176	177	178
position 1	175	176	177

MASS SPECTROMETRY

Hf is loaded on a five pass zone refined Re filament 30 μm thick and 760 μm wide. The loading procedure is as follows: first two stripes of Parafilm are melted on the filament ~400 μ apart. The area between the two stripes is squared by melting one more stripe of parafilm. The sample is dissolved in 1 μL of 0.15 N HF/0.3 μL of colloidal graphite (20 mg/mL), and 0.5 μL of 0.25 N H_3PO_4 is added. The mixed sample solution is deposited onto the filament between the Parafilm stripes in small increments. Each increment is dried down slowly at a current of ~1.0 A. After the complete sample is loaded, the filament is slowly brought to a dull red glow. The filament is kept at this temperature for 2 s. The addition of colloidal graphite results in the formation of hafnium carbide when the filament is heated. The hafnium carbide is extremely refractory, and it avoids the evaporation of the Hf before the high temperatures required for optimum ionization efficiency are attained (~1700–1900 °C during data acquisition).

The mass spectrometric measurement of the isotopic composition of Hf is performed on the Lamont Isolab.[4] This is a double-focusing forward geometry mass spectrometer with secondary ionization capability. The Ar^+ primary beam is produced by a cold cathode duoplasmatron and is focused to an ~100 μm diameter by two sets of Einzel lenses. Impurities in the primary beam are reduced by a Wienfilter which limits the mass spectrum of the primary beam to between 36 and 44.

The determination of Hf isotopes is done by the hot-SIMS (secondary ionization mass spectrometry) technique. Under vacuum the sample on the filament is heated to 1900°C while being bombarded by 15 kV Ar^+ ion beam. The sputtered secondary ions are accelerated and focused by a lens system similar to that of a conventional thermal ionization mass spectrometer. The ion beam is energy filtered by an electrostatic analyzer, and a 20 eV wide energy spread of the ions passes through. The electrostatic analyzer is followed by a conventional magnetic sector, and the ion beams of the different isotopes are collected simultaneously in Faraday cups according to a multidynamic collection scheme (see Table 2). There are several advantages of the high temperatures at which the sample is kept. First, the high temperature reduces the number of molecular ions and eliminates the formation of hydrides. Since hydride correction is extremely difficult for the Hf mass spectrum, the successful elimination of hydrides is the key to obtaining the correct isotope ratios. Second, the

(7) Fujimaki, H.; Tatsumoto, M.; Aoki, K. *J. Geophys. Res.* **1984**, *89*, 662–672.
(8) Zindler, A. Geochemical processes in the earth's mantle and the nature of crust–mantle interactions: Evidence from studies of Nd and Sr isotope ratios in mantle derived igneous rocks and lherzolite nodules. Massachusetts Institute of Technology, Cambridge, MA, 1980.
(9) Strelow, F. W. E.; Bothma, C. J. C. *Anal. Chem.* **1967**, *39*, 595–599.

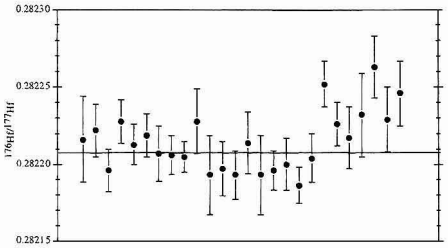


Figure 2. Standard values obtained on JMC 475. Over the first 3 years the $^{176}Hf/^{177}Hf$ averaged 0.282 207. After repair of the collector block the value for the standard changed to 0.282 236 for $^{176}Hf/^{177}Hf$.

high-temperature SIMS increases the ionization efficiency of Hf by a factor of 3 as compared to cold SIMS. The achieved ionization efficiency of the hot-SIMS technique is 1 ion in 500 atoms, which is a marked improvement over previous methods of 1 ion in 40 000 atoms.[2]

Total Hf ion beams of 0.5–1.0 nA for 2–3 h are routine for 150 ng of Hf standard JMC 475, which is 2 orders of magnitude better than thermal ionization techniques.[1,2] The ion beams of the three individual isotopes are simultaneously collected, and a multidynamic peak switching routine (see Table 2) is used in which Faraday cup, amplifier bias, and signal instabilities are canceled out. $^{176}Hf/^{177}Hf$ is corrected for fractionation using $^{177}Hf/^{178}Hf = 0.6816$, which corresponds to $^{179}Hf/^{177}Hf = 0.7325$ as used by Patchett.[2] The resulting, in-run precision, is consistently better than 0.008% (2σ level, whereby σ signifies the standard deviation of the mean).

External precision of the standard JMC-475 is better than 0.01% at the 2σ level, while the average of the standard ($^{176}Hf/^{177}Hf$ = 0.282 207) is very close to the accepted value ($^{176}Hf/^{177}Hf$ = 0.282 200) before 1993 (see Figure 2). In 1993, some repairs and modifications were performed on the collector block of the mass spectrometer and after these repairs the standard value changed to $^{176}Hf/^{177}Hf = 0.282\,237$. The shift in the standard value is expected after changes to the mass spectrometer. The reproducibility of the internal standard (AUG-7; see Table 3) is still excellent after correction with the appropriate standard value. The last two AUG-7 values were obtained after the shift in the standard. Duplicates and triplicates of samples (see Table 3) are all within the 2σ internal run precision of each other. The new technique also reproduces $^{176}Hf/^{177}Hf$ of samples analyzed by thermal ionization in other laboratories (see Table 3).

Table 3. Reproducibility and Comparison with Other Laboratories[a]

sample no.	$^{176}Hf/^{177}Hf$	absolute $2\sigma \times 10^6$	lab
AUG-7	0.283 270	±26	LDEO
AUG-7	0.283 281	±24	LDEO
AUG-7	0.283 259	±17	LDEO
AUG-7	0.283 259	±20	LDEO
AUG-7	0.283 257	±23	LDEO
AUG-7	0.283 273	±20	LDEO
2392-9	0.283 215	±22	LDEO
2392-9	0.283 207	±14	LDEO
KbH 57W	0.283 58	±170	LDEO
KbH 57W	0.283 41	±202	LDEO
77SL13	0.284 96	±170	LDEO
77SL13	0.284 66	±268	LDEO
WIC 020	0.283 121	±35	LDEO
WIC 020	0.283 100	±60	MPI
WIC 020	0.283 070	±40	MPI
NTP-8	0.282 389	±28	MIT
NTP-8	0.282 361	±18	LDEO

[a] Results of multiple analysis of a Aleutian arc basalt (AUG-7), which is used as an in-house rock standard, and duplicate analysis of mid-ocean ridge basalt 2392-9 and of peridotites (KbH57W and 77SL13), both with the hot-SIMS technique. Also samples analyzed with the thermal ionization technique at the Massachusetts Institute of Technology (MIT) and at Max-Planck Institute (MPI), Mainz, and with the new technique at LDEO (Lamont Doherty Earth Observatory) are compared.

In summary, the new technique allows high-precision determination of Hf isotope ratios on samples as small as 50 ng of Hf (2σ <0.01%), and on amounts of Hf as small as 15 ng, the $^{176}Hf/^{177}Hf$ can be determined with less precision. This now allows determination of Hf isotope ratios in materials such as mafic and ultramafic rocks as well as natural waters.

ACKNOWLEDGMENT

John England is thanked for his help in keeping the Lamont Isolab in good shape during the first years of this research. Kate Verraneault is thanked for improving the English of the manuscript. Linda Godfrey and two anonymous reviewers are thanked for their comments. This research was supported by NSF Grants EAR 90-17404 and EAR 92-19261 to V.J.M.S.

Received for review May 25, 1994. Accepted August 24, 1994.[⊗]

[⊗] Abstract published in *Advance ACS Abstracts,* October 1, 1994.

Anal. Chem. **1994,** *66,* 4190–4194

Calcium Stoichiometry Determination for Calcium Binding Proteins by Electrospray Ionization Mass Spectrometry

Peifeng Hu, Qi-Zhuang Ye, and Joseph A. Loo*

Parke-Davis Pharmaceutical Research, Division of Warner-Lambert Company, 2800 Plymouth Road, Ann Arbor, Michigan 48105

Electrospray ionization mass spectrometry was used for the determination of calcium-binding stoichiometry for calcium-binding proteins. Bovine calmodulin, bovine α-lactalbumin, and rabbit parvalbumin were found to bind specifically to 4, 1, and 2 Ca^{2+} ions, respectively, in agreement with previously reported results obtained by using other physical methods. This mass spectrometry method could also be applied to proteins that bind more than one type of metal ion. The Zn^{2+}- and Ca^{2+}-binding stoichiometries for human stromelysin catalytic domain were determined to be 3 and 2, respectively.

The structure of proteins does not always adequately define the function of protein systems. "The biological activities of proteins are (also) mediated by their interactions with their environment: with water, salts, membranes, other proteins, nucleic acids, and the numerous other large and small molecules in living systems. All of these interactions arise from a limited set of fundamental noncovalent forces, but with many variations on a theme, so it is important to understand the physical basis of the interactions." [1] The interaction with metal ions, essential to catalytic function and structural stability, is an integral component of many enzymes (metalloenzymes).[2]

Techniques used to study the interaction between metal ions and biological materials include absorption spectroscopy, circular dichroism,[3] electron paramagnetic resonance spectroscopy,[4] and nuclear magnetic resonance (NMR) spectroscopy.[3,5] A rapidly emerging method for investigating interactions between metal ions and biological molecules is mass spectrometry (MS). To detect these interactions by mass spectrometry, a methodology is needed to transfer the interacting complex from an aqueous environment to the gas phase without disrupting or changing the *specificity* of the association in solution. At the very least, for the method to provide useful information to the protein scientist, the data from a mass spectrometry experiment should *correlate* well to the solution-phase interaction.

Electrospray ionization mass spectrometry (ESI-MS),[6,7] which analyzes materials from solution, is generating increasing interest as a bioanalytical method because of its ability to efficiently ionize large molecular weight biomolecules and its potential for studying protein complexes with other molecules. The gentleness of the ionization/desorption event allows fragile complexes to remain intact for detection by the mass analyzer.[8,9] The potential of ESI-MS to determine peptide–metal ion stoichiometry in a rapid and sensitive fashion is also promising. The ESI-MS results of Hutchens and co-workers,[10,11] investigating the interactions of Cu^{2+} and Zn^{2+} with cysteine (sulfur)- and histidine-containing polypeptides, suggest that ESI mass spectra reflect the *specific* association of the metal(s) with the peptide and can clearly be differentiated from nonspecific interactions due to clustering or adduct formation. Fenselau and co-workers[12] developed an ESI-MS strategy that provides analysis of metal ions in native and reconstituted metallothionein proteins. Seven metal ions (Zn^{2+} or Cd^{2+}) were observed to associate with the fully reconstituted protein. This observation agrees well with the results of solution studies, and it was therefore suggested that metallothionein proteins retain their conformation in the gas phase. Acidic iron-binding proteins have also been investigated. Intact metal-loaded proteins were detected by negative ion ESI-MS.[13]

In this report, we describe the application of electrospray ionization mass spectrometry to determine the calcium-binding stoichiometry of Ca^{2+}-binding proteins. Four calcium-binding proteins, bovine α-lactalbumin, bovine calmodulin, rabbit parvalbumin, and human stromelysin catalytic domain (SCD), were studied by ESI-MS. The first three proteins have been well characterized by various methods.[14,15] Their metal-binding properties and functions are summarized in Table 1. Calmodulin and parvalbumin are members of the family of "EF-hand" calcium-binding proteins.[14] Stromelysin, an important matrix metallopro-

(1) Creighton, T. E. *Proteins: Structure and Molecular Properties,* 2nd ed.; W. H. Freeman and Co.: New York, 1993; p 507.
(2) Glusker, J. P. In *Advances in Protein Chemistry;* Anfinsen, C. B., Edsall, J. T., Eisenberg, D. S., Richards, F. M., Eds.; Academic Press: San Diego, CA, 1991; Vol. 42, pp 1–76.
(3) *Metallobiochemistry, Part C, Spectroscopic and Physical Methods for Probing Metal Ion Environments in Metalloenzymes and Metalloproteins;* Riordan, J. F., Vallee, B. L., Eds.; Academic Press: San Diego, CA, 1993; Vol. 226.
(4) *Metallobiochemistry, Part D, Physical and Spectroscopic Methods for Probing Metal Ion Environments in Metalloproteins;* Riordan, J. F.; Vallee, B. L., Eds.; Academic Press: San Diego, CA, 1993; Vol. 227.
(5) Bertini, I.; Turano, P.; Vila, A. J. *Chem. Rev.* **1993**, *93*, 2833–2932.
(6) Meng, C. K.; Mann, M.; Fenn, J. B. *Z. Phys. D—At., Mol. Clusters* **1988**, *10*, 361–368.
(7) Smith, R. D.; Loo, J. A.; Ogorzalek Loo, R. R.; Busman, M.; Udseth, H. R. *Mass Spectrom. Rev.* **1991**, *10*, 359–451.
(8) Ganem, B.; Li, Y. T.; Henion, J. D. *J. Am. Chem. Soc.* **1991**, *113*, 7818–7819.
(9) Smith, R. D.; Light-Wahl, K. J. *Biol. Mass Spectrom.* **1993**, *22*, 493–501.
(10) Hutchens, T. W.; Nelson, R. W.; Allen, M. H.; Li, C. M.; Yip, T.-T. *Biol. Mass Spectrom.* **1992**, *21*, 151–159.
(11) Hutchens, T. W.; Nelson, R. W.; Yip, T.-T. *FEBS Lett.* **1992**, *296*, 99–102.
(12) Yu, X.; Wojciechowski, M.; Fenselau, C. *Anal. Chem.* **1993**, *65*, 1355–1359.
(13) Petillot, Y.; Forest, E.; Mathieu, I.; Meyer, J.; Moulis, J.-M. *Biochem. J.* **1993**, *296*, 657–661.
(14) McPhalen, C. A.; Strynadka, N. C. J.; James, M. N. G. In *Advances in Protein Chemistry;* Anfinsen, C. B., Edsall, J. T., Eisenberg, D. S., Richards, F. M., Eds.; Academic Press: San Diego, CA, 1991; Vol. 42, pp 77–145.
(15) Dieter, P.; Marme, D. *The History of Calcium-Binding Proteins;* CRC Press, Inc.: Boca Raton, FL, 1988; Vol. 1, pp 1–9.

0003-2700/94/0366-4190$04.50/0 © 1994 American Chemical Society

Table 1. Properties of Ca^{2+}-Binding Proteins

protein	M_r	no. of calcium ions	$K_d(Ca^{2+})$, M	role of calcium
bovine calmodulin	16 791.5	4	10^{-5}–10^{-6}	enzyme regulation
rabbit parvalbumin	11 976.7	2	10^{-8}–10^{-9}	calcium buffer
bovine α-lactalbumin	14 182.2	1	10^{-6}–10^{-7}	stabilization

teinase believed to be involved in connective tissue degradation, is not stable for study due to self-degradation.[16] The catalytic domain of human stromelysin was expressed to further the study on stromelysin, because this protein retains the catalytic activity but lacks the instability of stromelysin.[17] Our mass spectrometry results on calmodulin, parvalbumin, and α-lactalbumin agree with published results. The Zn^{2+}-binding stoichiometry of SCD agrees with the results of recently completed atomic absorption (AA) experiments.[18]

EXPERIMENTAL SECTION

Calcium-binding proteins purchased from commercial vendors typically contain various levels of ubiquitous metal ions, e.g., Na^+, which interfere with the electrospray ionization process. Stromelysin catalytic domain sample was prepared in a buffer containing 50 mM Tris·HCl, 1 μM Zn^{2+}, and 10 mM Ca^{2+} ions. The salts and buffer materials in the samples were removed through the use of a microcentrifuge filter unit with a molecular weight cutoff of 5000 (Ultrafree-MC, Millipore, Bedford, MA). The protein retained by the membrane in the centrifuge unit was washed with water three times and reconstituted to a concentration of approximately 1 μg/μL. Samples for mass spectrometric analysis were prepared by taking 25 μL of the salt-free protein solution and adding appropriate amounts of 10 mM calcium acetate solution and water to make a final volume of 50 μL. A syringe pump (Harvard Apparatus, South Natick, MA) controlled the analyte delivery rate to the ESI source at 1 μL min^{-1}. Parvalbumins were analyzed in 2.5 mM ammonium bicarbonate solution.

Bovine calmodulin, rabbit parvalbumin, and bovine α-lactalbumin (type III) were purchased from Sigma Chemical Co. (St. Louis, MO). The expression and purification of SCD have been described previously.[17]

ESI-MS analyses were performed with a Finnigan MAT 900Q forward geometry double focusing mass spectrometer (Bremen, Germany) equipped with a 20 kV dynode/electron conversion multiplier and a position-and-time-resolved ion counting (PATRIC) array detector.[19,20] The PATRIC array detector was used for data acquisition in this work. Mass spectra were typically acquired at 20 s/decade.

An electrospray ionization interface based on a heated glass capillary inlet (0.5 mm i.d. × 6.2 mm o.d. × 218 mm length) was used.[6] Droplet desolvation was accomplished by a countercurrent stream of warm nitrogen (~60 °C) and by collisions in the electrospray interface controlled by adjustment of the voltage difference between the tube lens at the metalized exit of the glass capillary and the first skimmer element of the ESI interface. SF_6 flow coaxial to the spray was also used to suppress possible corona discharges.[21]

RESULTS AND DISCUSSION

Selection of Solvent and Ionization Modes. Proteins carry either a positive or a negative charge depending on the solution pH (provided the pH is not at the isoelectric point, pI, of the protein). Water is the native environment where proteins associate with other biological molecules to function. Because preserving solution associations before a phase change is a prerequisite for successful detection of the complex in the gas phase by ESI-MS, aqueous solutions should be preferable to those containing excessive amounts of organic solvent (although it does not exclude the possibility of complex dissociation in the gas phase). In this work, water with or without low concentration buffer (e.g., 2.5 mM ammonium bicarbonate, pH 8) was used as the solvent.

Since the electrospray ionization process produces multiply charged ions, ESI-MS analyses rely on the multiple protonation or deprotonation of the protein molecule. Whether positively or negatively charged species are detected depends on the instrument polarity. The addition of a small amount of acid promotes the detection of molecules as positive ions, and the addition of base aids the detection of negative ions.[22,23] Protonation and deprotonation of proteins in solution, however, can alter the higher order structure of proteins and can be detrimental to noncovalent interactions in solution.[9,12,13,19] For optimum sensitivity, the chosen instrument polarity should be the same as that of the solution protein ions. The alternative approach, i.e., positive ions in solution are detected as gas-phase negative ions or vice versa, would involve protonation and metal attachment or deprotonation necessary to change the polarity of the molecule. This may prevent the successful detection of the targeted complex, although it has not been previously discussed in the literature. Calcium-binding proteins are a group of very acidic molecules with pI values ranging from 4 to 4.5. Within the pH range (6.5–8) used in this work, where the proteins binds to Ca^{2+} ions with maximum affinity, the protein molecules have a net negative charge. For the above-mentioned reasons, negative ion electrospray MS was chosen for the analysis of calmodulin, parvalbumin, and α-lactalbumin.

The choice of negative ion electrospray for the analysis of calcium binding proteins was also found to be practically necessary. To maintain the neutrality of the solution, positive counterions must accompany the ionized carboxylate groups in the protein molecules. As long as the pH of the solution remains above the isoelectric points of these proteins, these counterions can be replaced by other positive ions but cannot be removed by separation methods. If these proteins are to be analyzed by positive ion electrospray mass spectrometry, not only do the negatively charged groups need to be neutralized by counterions, but also the molecules must be charged by metal binding or protonation. As revealed in the positive ion ESI spectrum from

(16) Woessner, J. F., Jr. *FASEB J.* **1991**, *5*, 2145–2154.
(17) Ye, Q.-Z.; Johnson, L. L.; Hupe, D. J.; Baragi, V. *Biochemistry* **1992**, *31*, 11231–11235.
(18) Soler, D.; Auld, D.; Van Wart, H.; Ye, Q.-Z. *Biochem. Biophys. Res. Commun.* **1994**, *201*, 917–923.
(19) Loo, J. A.; Giordani, A. G.; Muenster, H. *Rapid. Commun. Mass Spectrom.* **1993**, *7*, 186–189.
(20) Loo, J. A.; Ogorzalek Loo, R. R.; Andrews, P. C. *Org. Mass Spectrom.* **1993**, *28*, 1640–1649.
(21) Ikonomou, M. G.; Blades, A. T.; Kebarle, P. *J. Am. Soc. Mass Spectrom.* **1991**, *2*, 492–496.
(22) Loo, J. A.; Ogorzalek Loo, R. R.; Light, K. J.; Edmonds, C. G.; Smith, R. D. *Anal. Chem.* **1992**, *64*, 81–88.
(23) Kelly, M. A.; Vestling, M. M.; Fenselau, C. C. *Org. Mass Spectrom.* **1992**, *27*, 1143–1147.

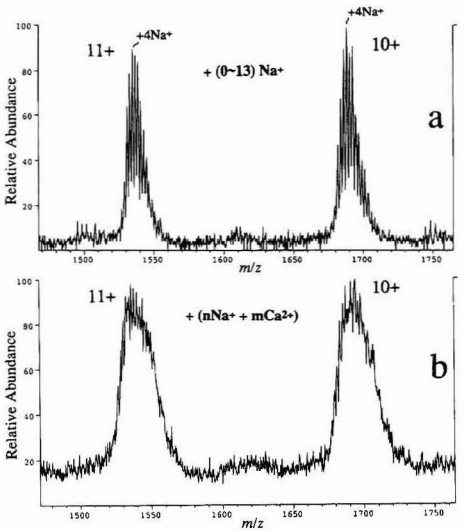


Figure 1. Positive ion electrospray mass spectra of calmodulin in (a) water and (b) 1 mM calcium chloride.

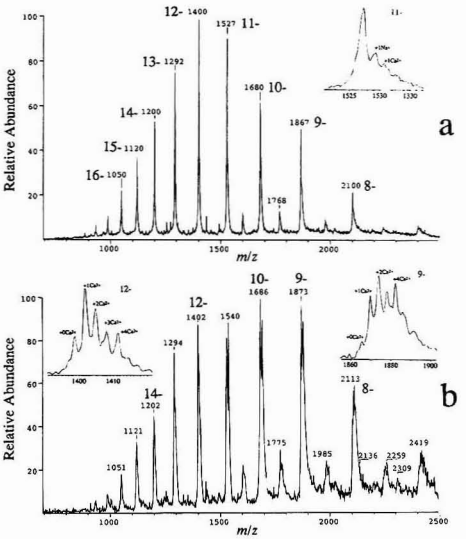


Figure 2. Negative ion electrospray mass spectrum of bovine calmodulin in (a) water and (b) 1 mM calcium acetate.

an aqueous calmodulin solution (Figure 1a), calmodulin can carry as many as 13 sodium ions with the molecules bearing six sodium ions to be the most abundant. (The source of the sodium is unknown, but sodium is ubiquitous.) Loading of calcium ions onto the protein does not necessarily exclude sodium binding, for the ions may not compete for the same sites, particularly for the sodium ions that are attached at sites away from calcium sites. Consequently, both sodium and calcium ions bind to the same molecule. Binding by different combinations of sodium and calcium ions makes it very difficult to interpret the exact number of calcium ions a calmodulin molecule carries without ultra-high-resolution analysis (Figure 1b).[24] Similar Na^+ attachment was also observed for α-lactalbumin and parvalbumin when they were analyzed by positive ion ESI-MS in aqueous solution. Stromelysin catalytic domain is, however, an exception, which can be analyzed by positive ion ESI-MS in aqueous solution without observable Na^+ attachment.

The detection of acidic proteins as negative ions should reduce the likelihood of observing nonspecific metal ion binding because metal attachment is not necessary for charging these proteins. Indeed, a much cleaner negative ESI spectrum (Figure 2a) was produced for the same calmodulin solution used for obtaining the spectra in Figure 1. Deprotonated calmodulin ions are the most abundant species, accompanied by less abundant species carrying one sodium or one calcium ion. The presence of Ca^{2+}-carrying species indicates the incompleteness of decalcification. Sodium attachment to α-lactalbumin and parvalbumin was also negligible when they were analyzed by negative ion ESI-MS (Figures 3a and 4a).

Stoichiometry Determination for Calmodulin, Parvalbumin, and α-Lactalbumin. When a divalent calcium metal ion

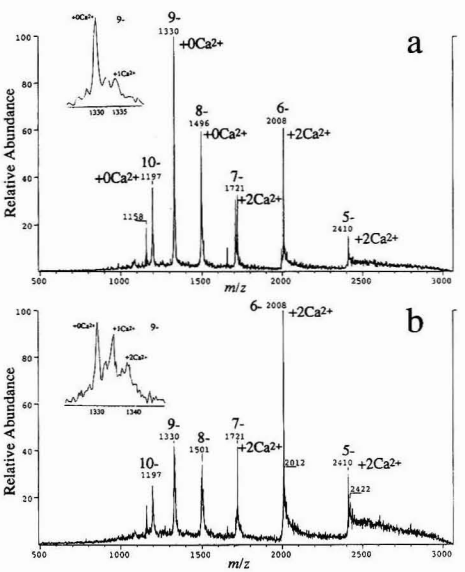


Figure 3. Negative ion electrospray mass spectra of rabbit parvalbumin in (a) water and (b) 1 mM calcium acetate.

is incorporated into a protein molecule, two protons are displaced to maintain charge balance. The net mass increase of the protein is the mass of the metal ion minus 2 Da. The number of bound Ca^{2+} ions (n) is correlated with the mass (M) of the ions carrying a net charge z by the formula $[M + n\mathrm{Ca} - (2n + z)\mathrm{H}]^{z-}$. The negative ion ESI spectra of calmodulin, rabbit parvalbumin, and α-lactalbumin with and without added calcium are given in Figures

(24) Beu, S. C.; Senko, M. W.; Quinn, J. P.; Wampler, F. M., III; McLafferty, F. W. *J. Am. Soc. Mass Spectrom.* **1993**, *4*, 557–565.

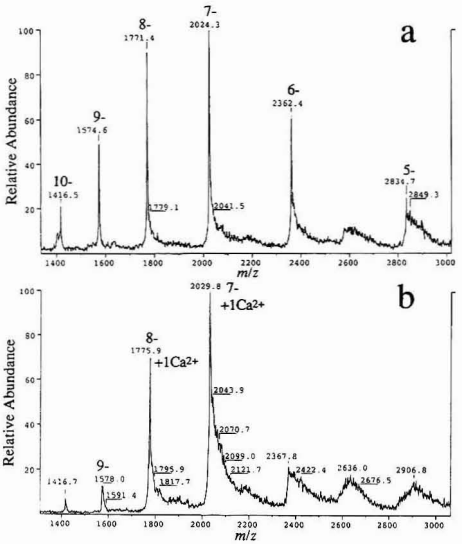


Figure 4. Negative ion electrospray mass spectra of bovine α-lactalbumin in (a) water and (b) 1 mM calcium acetate.

Table 2. Measured and Theoretical Mass to Charge Ratios for Ca^{2+}-Binding Proteins Carrying Various Numbers of Ca^{2+} Ions[a]

protein	Ca_0	Ca_1	Ca_2	Ca_3	Ca_4	charge
calmodulin	1678.1 (1678.1)	1681.7 (1681.9)	1685.5 (1685.7)	1689.3 (1689.5)	1693.2 (1693.3)	10−
rabbit parvalbumin	1709.9 (1709.9)	1715.0 (1715.3)	1720.8 (1720.8)			7−
bovine α-lactalbumin	2025.0 (2025.0)	2030.5 (2030.4)				7−

[a] The numbers in parentheses are theoretical values. The m/z scale was calibrated to the apoprotein (Ca_0) value.

2−4. Determining the calcium-binding stoichiometry from these spectra is rather straightforward. The data in Figures 2a, 3a, and 4a provide the masses of the protein molecules without bound Ca^{2+} in various charge states. The m/z shifts of the corresponding charge states due to calcium binding allow the determination of the number of metal ions bound (see Table 2). Calmodulin binds to a maximum of four calcium ions, whereas parvalbumin and α-lactalbumin bind to a maximum number of 2 and 1, respectively. For both calmodulin and parvalbumin, partially loaded molecules are also present. Calmodulin was found in all five forms that contain 0−4 calcium ions. All three forms of parvalbumin with different extents of calcium loading were present (0, 1, and 2 calcium ions), with the abundance of the 1 Ca^{2+} species to be extremely low. The presence of these partially loaded species is evidence of the calcium-binding equilibrium, and the relative abundances of these species provide insights about the Ca^{2+}-binding properties of the proteins.[25] It is also shown that only a small population of Ca^{2+}-bound α-lactalbumin and calmodulin were

(25) Hu, P.; Loo, J. A. *Biochemistry*, submitted.

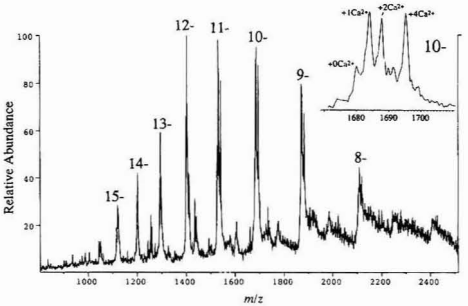


Figure 5. Negative ion electrospray mass spectrum of calmodulin that was saturated with 10 mM calcium chloride and desalted by filtration (see text for discussion).

present in the samples, but a substantial population of the commercial preparation of parvalbumin exists as fully Ca^{2+}-loaded form.

The concentration of Ca^{2+} ion is an important factor for an unambiguous stoichiometry determination. Calcium ion titrations were carried out for both calmodulin and α-lactalbumin. With a protein concentration of approximately 4×10^{-5} M, it was found that 5×10^{-4} M Ca^{2+} concentration was sufficient for saturating α-lactalbumin, while 1×10^{-3} M Ca^{2+} was necessary for fully Ca^{2+}-loaded calmodulin to be a major species. If the calcium concentration was low (e.g., 2×10^{-4} M calcium acetate, at which the Ca^{2+} to calmodulin ratio was ca. 4:1), a majority of calmodulin molecules were observed to carry zero, one or two calcium ions. A small population of calmodulin molecules was loaded with four calcium ions. If, however, the Ca^{2+} ion concentration is too high (e.g., 5 mM), a majority of calmodulin molecules bind to four calcium ions, but a small amount of nonspecific Ca^{2+} attachment (e.g., 5 Ca^{2+} ion binding) can also occur. The calcium ion concentration appropriate for this work was found to be 1 mM. At this concentration, calmodulin molecules carrying different numbers of Ca^{2+} (0−4) are simultaneously observed, and the tendency for nonspecific binding is reduced (Figure 2b).

Experimentally, Ca^{2+} incorporation onto calmodulin can be done by another method. The protein was dissolved in 10 mM calcium acetate solution to saturate the calcium sites. The bulk unbound calcium ions along with other salts in the sample are removed by membrane filtration according to the method described in the Experimental Section. This method has some advantages over the one adopted for general use in this work for stoichiometry determination. Because the bulk calcium ions are removed (low free Ca^{2+} concentration in the sample for ESI-MS analysis), nonspecific calcium binding is avoided, and the solution is more favored for electrospray ionization analysis (Figure 5). A disadvantage of this method is that the concentration of calcium ion in the final solution for electrospray analysis is difficult to control, which in turn affects the reproducibility unless a strict solution volume control at every step of the filtration is adopted.

A word of caution should also be added for the proteins that bind to more than one calcium ion. The relative abundances of molecular ions that carry different numbers of calcium ions vary with the number of charges on the molecules. The envelopes of the various species peak at different charge states (Figures 2b and 3b). One extreme is rabbit parvalbumin, which has two

envelopes that are nearly completely separated from each other (Figure 3). In general, the addition of calcium to apoproteins shifts the charge distribution to higher *m/z* (lower charge states). This could be misleading, because the higher charged states may contain mostly underloaded species. Nevertheless, misassignments can easily be avoided by taking into consideration the full spectrum and identifying the envelopes that are comprised of the species loaded with the greatest number of calcium ions.

Although Ca^{2+}-binding stoichiometry can be determined by this strategy, the Ca^{2+} affinity of the proteins studied is not appropriately reflected by the relative population of the species loaded with various numbers of Ca^{2+}. For example, the generally accepted K_d value for calmodulin ranges from 10^{-4} to 10^{-6}. Incomplete Ca^{2+}-loaded molecules (1, 2, and 3 Ca^{2+}, see above discussion) are still observed at the Ca^{2+} concentration level of 1 mM, where the Ca^{2+} to calmodulin molar ratio is ca. 16:1. Also, for bovine α-lactalbumin, a Ca^{2+} concentration higher than 0.5 mM is necessary for complete conversion of the apoprotein to the Ca^{2+} bound form. This difference needs to be addressed further by more precisely controlled experiments.

Metal Binding to Human Stromelysin Catalytic Domain. We attempted to determine the metal-binding stoichiometry for stromelysin catalytic domain, which requires both Zn^{2+} and Ca^{2+} for activity.[17] At the time of this work, it was known that SCD has a much higher Zn^{2+} affinity than Ca^{2+} affinity. The binding stoichiometry for both Ca^{2+} and Zn^{2+} remained unknown. An aqueous sample of SCD (40 μM) was analyzed by positive ion ESI because SCD is not as acidic as the other proteins studied and is less prone to nonspecific metal attachment. The measured and theoretical (in parentheses) mass to charge ratios for the three components of the 9+ charge state are 2189.6 (2190.0), 2193.9 (2194.2), and 2198.4 (2198.4) respectively, corresponding to $(SCD + 3Zn^{2+} + H_2O + 3H)^{9+}$, $(SCD + 3Zn^{2+} + Ca^{2+} + H_2O + H)^{9+}$, and $(SCD + 3Zn^{2+} + 2Ca^{2+} + H_2O - H)^{9+}$ (also see Figure 6a). Therefore, SCD binds to a maximum of 3 Zn^{2+} and 2 Ca^{2+} ions. The metal binding, particularly Zn^{2+} binding, is readily disrupted by the addition of acetic acid to 1% (v/v) (Figure 6b) so that some of the SCD molecules are associated with one Ca^{2+} or Zn^{2+}. The results for Zn^{2+} binding agree with recently conducted atomic absorption experiments by Auld and co-workers.[18] The zinc metal to SCD ratio was found to be consistently larger than 2 but smaller than 3 by AA. It was concluded in their report that SCD may have a third low-affinity Zn^{2+} site.

It is interesting to note that from the ESI mass spectra, SCD molecules appear to retain one H_2O molecule. This observation is supported by previous studies on Zn^{2+} proteins. All *catalytic site* Zn^{2+} ions have one water molecule as their fourth ligand, and the water molecule serves an important role in the functional mechanism.[16,26] The coordination to the metal ion may be the key factor that distinguishes this water molecule from the other solvent water molecules. However, more work is necessary to unambiguously identify the presence of coordinated water.

Another property of SCD revealed in our data is its relative metal affinity. SCD binds Zn^{2+} ions tightly, and therefore all molecules carry 3 Zn^{2+} ions. The number of the less tightly bound

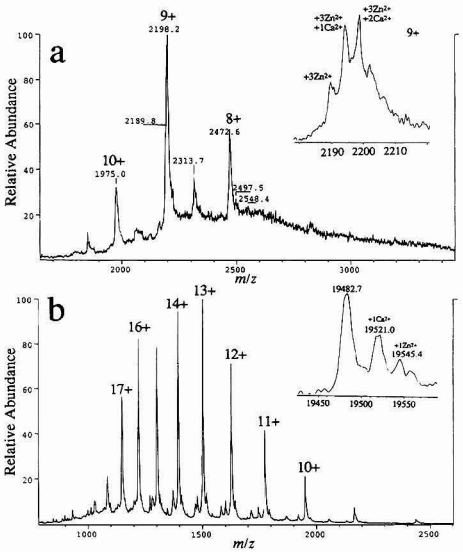


Figure 6. Positive ion electrospray mass spectra of stromelysin catalytic domain in (a) water and (b) 1% acetic acid.

Ca^{2+} ions carried by SCD is variable (0, 1, or 2), most likely because the sample preparation proceedure removed Ca^{2+} ions from some of the protein molecules. It may also be possible that the zinc metal ions are burried inside the molecule, while calcium ions bind to the surface of the molecule so that zinc metal is better retained than calcium.

CONCLUSION

Metal stoichiometry for calcium-binding proteins can be determined by electrospray ionization mass spectrometry. It is shown that for proteins, such as stromelysin catalytic domain that binds to more than one type of metal ion, the stoichiometries of each metal can also be determined concomitantly. The proper selection of ionization polarity and metal ion concentration not only helps to preserve the specific associations found in solution but also reduces the likelihood of observing nonspecific interactions that may occur in the ionization process. The use of aqueous solutions for ESI-MS experiments allows the acquisition by a gas-phase methodology of metal-binding information that is consistent with that reported from solution-phase experiments, thus waiving special sample requirements (e.g., crystal for X-ray crystallography). This mass spectrometric method also has the advantage that precise stoichiometry can be obtained when not all protein molecules are fully loaded. Other methods, such as atomic absorption, may yield noninteger numbers of metal ions per protein molecule under similar circumstances because they register the average metal content per protein molecule.

Received for review May 31, 1994. Accepted September 13, 1994.[⊗]

(26) Vallee, B. L.; Auld, D. S. *Acc. Chem. Res.* **1993**, *26*, 543–551.

[⊗] Abstract published in *Advance ACS Abstracts*, October 15, 1994.

Anal. Chem. **1994**, *66*, 4195–4201

Measuring the Resolving Power of Ion Mobility Spectrometers

William F. Siems,* Ching Wu, Edward E. Tarver, and Herbert H. Hill, Jr.

Department of Chemistry, Washington State University, Pullman, Washington 99164-4630

Paul R. Larsen and Dennis G. McMinn

Department of Chemistry, Gonzaga University, Spokane, Washington 99258-0001

Ion mobility spectrometry peak width data are fitted by a least-squares procedure to a semiempirical model having three adjustable parameters. Peaks are wider than contributions from initial pulse width and diffusion predict, and it is suggested that the additional width is due mainly to electric field inhomogeneity and Coulombic repulsion. The effects of operating conditions and instrument dimensions on resolving power are discussed. It is proposed that increased inhomogeneity of the electric field results in lower measured mobility values, as well as lower resolving power.

For ion mobility spectrometry (IMS),[1] as for any separation technique, the ability of an instrument to resolve closely spaced peaks is of considerable interest. While IMS peak shapes have been analyzed[2] and the effects of drift voltage, gate pulse width, temperature, and mobility on resolving power have been studied,[3] the effects of specific instrument design characteristics such as length and diameter of the drift region have been less well characterized. The earlier studies used mathematical models based on idealized conceptions of electric field uniformity and pulse shape, and while there has been good qualitative agreement between the models and experiment, quantitative agreement has been less satisfactory. We have followed and expanded on a suggestion of Revercomb and Mason[4] by fitting measured peak width data against theoretical pulse width and diffusion width variables. The resulting slope and intercept values become empirical parameters in our revised model. The model's predictions correspond well to observed line widths across a wide range of operating conditions, and the parameter values can be related to instrument design characteristics and used to discuss differences between instruments.

The most useful definition of resolving power, R, for IMS is the single-peak-based quotient

$$R = t_d/w \tag{1}$$

where t_d is the drift time of an ion of interest and w is the temporal peak width measured at half-height. The drift time of an ion is related in theory to the length of the drift space in centimeters, L, the voltage drop across the drift space, V, and the mobility of the ion in cm^2/Vs, K:

$$t_d = L^2/KV \tag{2}$$

Equation 2 is a rearranged form of the fundamental mobility equation $v_d = KE$, where v_d is the drift velocity in cm/s and E is the electric field strength in V/cm.

The major factors determining IMS peak shape are the initial shape of the bundle of ions admitted to the drift region and the diffusional broadening of the bundle as it travels to the collector. If an initial pulse gated into the drift region were of Gaussian shape with width at half-height t_g, then the peak gathered at the collector would also be Gaussian with width at half-height w and

$$w^2 = t_g^2 + t_{diff}^2 \tag{3}$$

where t_{diff} is the width at half-height of the Gaussian peak that would be produced by diffusional broadening of an infinitely narrow initial pulse. The initial pulse is in fact not Gaussian. In the first place, the gating control is usually generated as a step function. Spangler and Collins[2] achieved close fits of experimental peak shapes by convoluting a step function, representing initial pulse shape, with a Gaussian function representing diffusional broadening. On the other hand, although the voltage applied to a gate can closely approximate a step function, Aronson's mathematical model of gating has shown that ion density across a closed gate drops to zero considerably less rapidly than a step function[5] and that this profile is retained by the leading edge of an ion bundle that is admitted to the drift region when the gate opens. This same study showed that the trailing edge of an ion pulse, created as an open gate suddenly closes, also slopes less abruptly than a step function. Further, the position and slope of the leading and trailing edges were found to depend on the details of the gating (gate closure field, wire diameter, and spacing).

Another imperfection of eq 3 is its neglect of the diffusion that takes place while an ion pulse is being collected, which causes the trailing edges of all ion peaks to be slightly more diffuse than their leading edges. With these caveats about peak shape in mind, we chose eq 3 as the starting point for this study.

(1) For an introduction to ion mobility spectrometry, see: Hill, H. H., Jr.; Siems, W. F.; St. Louis, R. H.; McMinn, D. G. *Anal. Chem.* **1990**, *62*, 1201A–1209A and references listed therein.
(2) Spangler, G. E.; Collins, C. I. *Anal. Chem.* **1975**, *47*, 403–407.
(3) Rokushika, S.; Hatano, H.; Baim, M. A.; Hill, H. H., Jr. *Anal. Chem.* **1975**, *57*, 1902–1907.
(4) Revercomb, H. E.; Mason, E. A. *Anal. Chem.* **1975**, *47*, 970–983.
(5) Aronson, E. A. Technical Report No. SAND87-0072; Sandia Corp.: Albuquerque, NM, 1987.

0003-2700/94/0366-4195$04.50/0 © 1994 American Chemical Society

The spatial spreading of an ion peak, arriving at the collector t_d seconds after being admitted to the drift space as an extremely narrow pulse, is governed by its diffusion coefficient, D (in cm^2/s):

$$\sigma_{space} = (2Dt_d)^{1/2} \quad (4)$$

In the low electric field generally employed in IMS, the diffusion coefficient has a simple connection to mobility, expressed in the Einstein relation

$$D = kTK/q \quad (5)$$

where k is the Boltzmann's constant, q is the charge on the ion, and T is the absolute temperature. Inserting eqs 2 and 5 into eq 4 gives

$$\sigma_{space} = \left[\frac{2kT}{qV}\right]^{1/2} L \quad (6)$$

The spatial spreading of the ion pulse is related to the temporal duration measured at the collector by[4]

$$\frac{\sigma_{space}}{L} = \frac{\sigma_{time}}{t_d} \quad (7)$$

Finally, using eq 7 and the usual relation between the standard deviation and peak width at half-height ($t_{diff} = (8 \ln 2)^{1/2}\sigma_{time}$), we arrive at

$$t_{diff} = \left[\frac{16 \ln 2kT}{qV}\right]^{1/2} t_d \quad (8)$$

The resulting model equation for measured peak widths,

$$w^2 = t_g^2 + \frac{16 \ln 2\, k}{q} \frac{Tt_d^2}{V} \quad (9)$$

is equivalent to Spangler and Collins's eq 12 (aside from the Townsend energy factor),[2] Revercomb and Mason's eq 82,[4] and Rokushika et al.'s eq 13 (aside from an extra factor of 2 chosen by those authors for reporting peak widths).[3]

Spangler and Collins[2] measured Cl^- peak widths at 160.3 °C and E = 214 V/cm using initial pulse widths between 0.05 and 1.00 ms. To achieve a good fit between predicted and measured values, they increased the diffusional contribution to peak width by using a modified form of the Einstein relation which included η, the Townsend energy factor:[6]

$$D = \frac{\eta kTK}{q} \quad (10)$$

The Townsend factor takes into account that the ions may be at a higher effective temperature than the drift gas, since the ions are continually receiving energy from the electric field and hence may not be in thermal equilibrium with their surroundings. The best fit between prediction and experiment was obtained by the authors with $\eta = 2.7$. However, because η is known to be close to 1 for ions under conditions common in IMS experiments (see ref 6, p 533), such a high value cannot be correct, and there must be another explanation for the additional peak broadening observed.

Rokushika et al. studied resolving power for the $H(H_2O)_n^+$ reactant ion as a function of temperature, electric field, and initial pulse width and resolving power for a series of methyl ester product ions as a function of mobility.[3] While good qualitative agreement with the predictions of eq 9 was obtained, measured values of resolving power were in all cases lower than theoretical by about 33%. In discussing possible reasons for peak widths greater than theoretical predictions, the authors dismissed ion–molecule reactions in the drift space and mutual Coulombic repulsion between like-charged ions. In fact, the earlier work of Spangler and Collins[2] and a recent argument by Spangler[7] have shown that Coulombic repulsion, although less important than diffusional broadening, does contribute measurably to peak widths, and that the effect becomes more pronounced as the initial pulse width increases. Nevertheless, Coulombic broadening cannot account for discrepancies of the magnitude reported by Rokushika et al. It is interesting to note that these are of the same magnitude as those treated earlier by Spangler and Colins with introduction of the η parameter,[2] a result which might be expected given the similarity of the instruments employed in the studies (built by Franklin GNO in one case and its successor, PCP Inc. of West Palm Beach, FL, in the other). Finally, Rokushika et al. suggest without discussion that the discrepancy in peak widths could be due to the difficulty of achieving a smooth electric field throughout the drift region, an idea with which we concur and will discuss further below.

Revercomb and Mason have suggested that gating behavior could be studied by plotting w^2 vs t_d^3 or $1/V^3$ (equivalent since $t_d \propto 1/V$) for a single ion, while keeping t_g constant. If the initial pulse shape were Gaussian, the plot would be a straight line, and deviations from linearity would give information about the initial distribution.[4] Realizing that semiempirical fitting of line width data could help us evaluate the contributions of various physical processes to measured values, we have substituted the following expression for eq 9:

$$w^2 = \gamma + \beta t_g^2 + \alpha \frac{Tt_d^2}{V} \quad (11)$$

Here α, β, and γ are parameters that can be adjusted to give the best fit to parameters t_g, V, and T and the measured values t_d and w. The third term is the "diffusion" contribution to pulse width, although it may include other effects with the same voltage dependence as diffusion (increased effective temperature of the ions or electric field inhomogeneity, for example). A plot of w^2 vs Tt_d^2/V (which we refer to as the diffusion parameter) would have a slope $\alpha = 0.957 \times 10^{-3}$ if eq 9 were obeyed exactly, whereas if other broadening processes are operative, a larger value would be obtained for the slope. The second term is the "gate width" contribution to peak width, although it could include other broadening processes that increase along with increasing gate width (Coulombic repulsion, for example). A plot of w^2 vs t_g^2

(6) McDaniel, E. W. *Collision Phenomena in Ionized Gases*; Wiley: New York, 1964; Chapter 11.

(7) Spangler, G. E. *Anal. Chem.* **1992**, *64*, 1312.

Table 1. Physical Dimensions and Operating Conditions of IMS Instruments

	IMS instrument			
	A	B	C	D
drift region length (cm)	15.6	11.6	7.0	8.0
drift region diam (cm)	4.9	4.9	2.5	4.3
ionization region length (cm)	8.0	8.0	3.0	6.0
ionization region diam (cm)	3.0	3.0	1.5	1.4
ions measd	$(H_2O)_nH^+$, Cl^-	$(H_2O)_nH^+$	O_2^-	$(H_2O)_nH^+$
temp range (°C)	275	175–325	80–90	240
drift voltage range	2118–4941	1871–4366	1120–2800	1143–1600
t_g range (ms)	0.10–0.50	0.10–0.50	0.10–0.30	0.05–0.50

would have a slope $\beta = 1$ if eq 9 were obeyed exactly, while a larger value could be evidence for broadening by Coulombic repulsion. The first term is the "constant" contribution to pulse width, equal to zero in eq 9, but possibly of nonzero value if factors unaffected by gating or voltage are present. Such factors could include instrumental response times and, possibly, dynamic aspects of ion distributions around opening and closing gates.

To obtain an expression related to resolving power, we divide eq 11 by t_d^2:

$$R^{-2} = \frac{\gamma + \beta t_g^2}{t_d^2} + \frac{\alpha T}{V} = R_p^{-2} + R_d^{-2} \qquad (12)$$

where

$$R_p = \frac{t_d}{(\gamma + \beta t_g^2)^{1/2}} = \frac{L^2}{(\gamma + \beta t_g^2)^{1/2} KV} \qquad (13)$$

is the *pulse-width-only resolving power*, the resolving power that would be observed if diffusion were insignificant, and

$$R_d = (V/\alpha T)^{1/2} \qquad (14)$$

is the *diffusion-only resolving power*, the resolving power that would be obtained with zero initial pulse width and $\gamma = 0$. Note that overall resolving power will be dominated by the *smaller* of R_p and R_d.

In undertaking these studies, we wanted to test whether eq 11 would, in fact, be a good model of peak widths; in addition, we wanted to find α, β, and γ values that would be characteristic of particular IMS instruments over a wide range of operating conditions and that could be used to compare the resolving power of instruments. Finally, we wanted to use these values as a basis for discussing aspects of instrument design that influence resolving power.

EXPERIMENTAL SECTION

Measurements were made using four different IMS instruments, the physical dimensions of which are given in Table 1. Tubes A and B were high-temperature prototypes built at Washington State University, using guard rings fashioned from stainless steel shim stock cemented inside alumina tubing. A schematic diagram of tube B is shown in Figure 1. Tube C was a prototype built by Honeywell CDC, Clearwater, FL, using a traditional stacked ring construction. Tube D was a Phemto-Chem

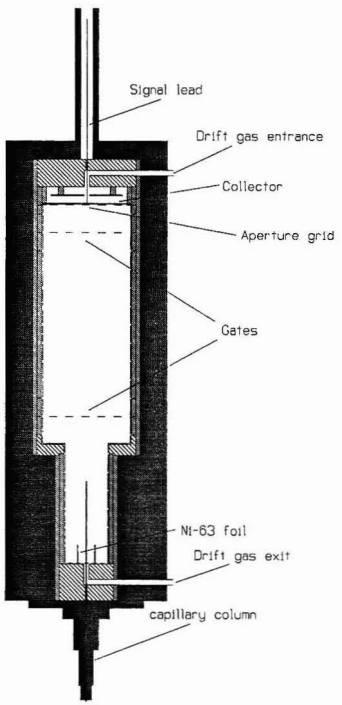


Figure 1. Ion mobility spectrometer.

100 built by PCP Inc. of West Palm Beach, FL, also having a stacked ring design. In all the instruments, guard rings were 0.9 cm wide, separated by 0.1 cm insulators. All used a 10 mCi ^{63}Ni foil as ionization source, except tube A, which used a 25 mCi source. Drift gas flow rate was typically 500 mL/min, and drift tube pressure was typically 700 Torr. Measurements of drift time and peak width were made over ranges of temperature, drift voltage, and initial pulse width for a variety of ions, as summarized in Table 1.

Since the software used with all these instruments has the start of data acquisition coinciding with the rising edge of the gating pulse, drift times were obtained from $t_d = t_{meas} - t_g/2$, where t_{meas} is the time coordinate of the peak maximum. To obtain the most accurate possible measurement of peak widths at half-height, w, from our digitized data, an interpolation procedure was used to locate the time coordinates of the half-height crossings. The data

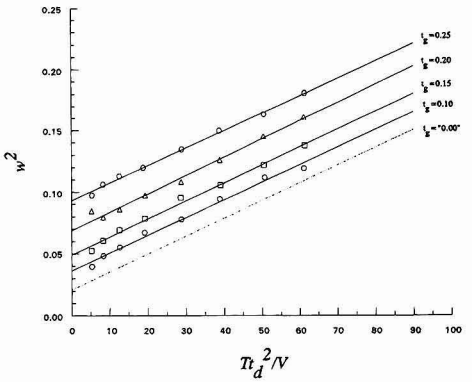


Figure 2. Measured width squared as a function of diffusion parameter for various initial pulse widths. *T*, 275 °C; *L*, 11.6 cm.

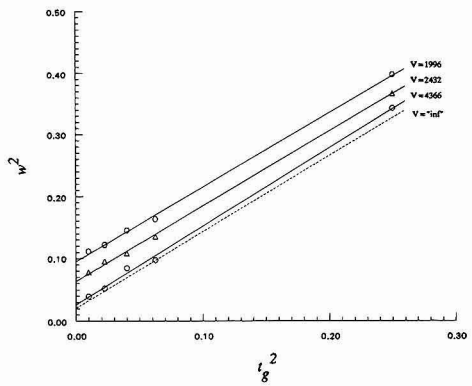


Figure 3. Measured width squared as a function of pulse width squared at various voltages. *T*, 275 °C; *L*, 11.6 cm.

were then subjected to a series of least-squares fitting procedures to determine the α, β, and γ parameters. All the figures to follow pertain to width measurements of the $(H_2O)_nH^+$ reactant ion, although a series of measurements on Cl^-, obtained by chromatographic introduction of CH_2Cl_2 into tube A, was used to confirm that the α, β, and γ parameters for the Cl^- product ion were essentially the same as those for the $(H_2O)_nH^+$ reactant ion. Figure 2 is an example plot of w^2 vs Tt_d^2/V (the slope of which is α), while Figure 3 is an example plot of w^2 vs t_g^2 (the slope of which is β). The solid lines in the two figures show the least-squares fits of the experimental data. In Figure 3, the points at $t_g^2 = 0.25$ are far removed from the other points, have high leverage on the fitted slopes, and thus could raise concerns about the goodness of the linear fit and the values of the slopes. However, other data sets with more evenly spaced points also showed good linearity and similar slope values. The dotted line in Figure 2 was obtained by plotting and performing a least-squares fit of the intercept values of the lines from Figure 3 (thus corresponding to $t_g = 0.00$), while the dotted line in Figure 3 was similarly obtained by plotting and fitting the intercept values of the lines from Figure 2 (corresponding to infinite voltage or zero diffusion). The intercept of the dotted line in either Figure 2 or Figure 3 is an estimate of the γ parameter.

Table 2. Summary of Results from Fitting Peak Width Data

IMS device	$\alpha \times 10^3$ (V/K)	β	$\gamma \times 10^8$ (s^2)	V_{opt}[a]	R_{max}[a]	R_{max}/R_{ideal}[b]
ideal	0.957	1	0	2693	61.4	1
tube A (L = 15.6 cm)	1.40	1.60	0.61	2640	50.2	0.80
tube B (L = 11.6 cm)	1.43	1.24	2.1	1659	39.4	0.80
tube C (L = 7.0 cm)	6.5	1.23	1.5	921	13.8	0.49
tube D (L = 8.0 cm)	1.26	1.13	0.47	1089	34.0	0.88

[a] Calculated for T = 225°C, t_g = 0.20 ms, and K = 4.25 cm^2/Vs. The "ideal" tube is assumed to have a length of 15.6 cm for computing V_{opt} and R_{max}. [b] Calculated for t_g = 0.20 ms.

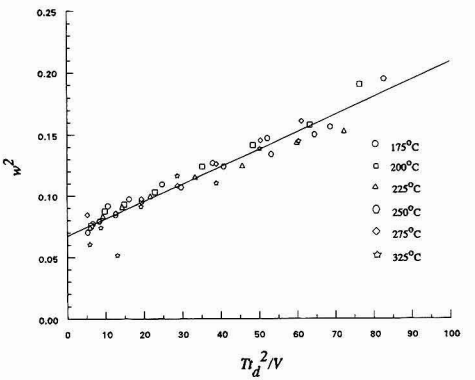


Figure 4. Measured width squared as a function of diffusion parameter at various temperatures. t_g, 0.20 ms; *L*, 11.6 cm.

RESULTS AND DISCUSSION

Quality of the Fit between Model and Experiment. The results of fitting the line width data for the four IMS instruments to eq 11 is summarized in Table 2. The single α, β, and γ parameter values shown in the table for tubes A, C, and D were obtained by averaging all individual values obtained from lines such as those shown in Figures 2 and 3. The data from tube B were treated in an alternate but similar fashion by performing a simultaneous least-squares fit of all experimental data points to eq 11.

The goodness of the fit between eq 11 and experimental width data can be shown with a few example plots. Equation 11 indicates that a plot of w^2 vs Tt_d^2/V for a single t_g and ranging T and V should yield a straight line. Figure 4 shows such a plot for data gathered using tube B, with t_g = 0.20 ms and six temperatures ranging from 175 °C to 325 °C. The solid straight line is a least-squares fit of all the data (slope, 1.41×10^{-3}; intercept, 0.0674). Most of the points lying above the line belong to the lower three temperatures, while most of the points lying below the line belong to the higher three temperatures. The reduced mobility[1] of the $(H_2O)_nH^+$ peak does not change appreciably over the temperature range studied, making it unlikely that changes in cluster size are responsible for the temperature dependence seen in Figure 4. Least-squares fits of data from individual temperature series yield essentially parallel lines. Thus any temperature dependence of

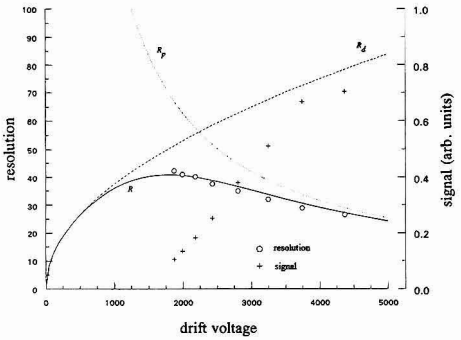


Figure 5. Diffusion and pulse width contributions to resolving power. T, 225 °C; t_g, 0.20 ms; L, 11.6 cm.

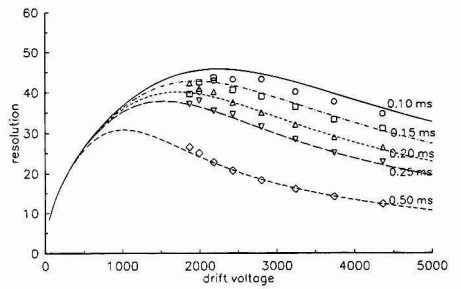


Figure 6. Effect of gate pulse width on resolving power. T, 225 °C; L, 11.6 cm.

α is small. Data for other t_g values show a similar behavior to Figure 4, and all the data taken together are consistent with both β and γ decreasing slightly as temperature increases.

Figure 5 shows measured resolving power values for tube B (T = 225 °C, t_g = 0.20 ms, V ranging) as open circles, together with calculated lines for R, R_p, and R_d as given by eqs 12–14, using the α, β, and γ values from Table 2. At low drift voltage, diffusion is the major factor determining peak width, whereas at high voltage, the initial pulse width becomes dominant. Note how R remains below the R_d and R_p lines, approaching them asymptotically at low and high drift voltage, respectively. Around V = 1500, there is a maximum in the resolving power curve, a situation which will be discussed in the next section. It should be noted that IMS instruments are generally operated at voltages higher than that giving maximum resolving power, as the position of the open circles suggests. The reason for this is that signal levels drop off about linearly with decreasing drift voltage, a manifestation of the usual tradeoff between sensitivity and resolving power. Experimental signal levels are shown as crosses on Figure 5.

Figure 6 shows several sets of measured resolving power values for tube B at T = 225 °C and a range of pulse widths, plus corresponding lines calculated as for Figure 5. The calculated lines do not fit the data for narrow initial pulses as well as they fit the wide pulse data because the least-squares procedure that was used minimizes the magnitude of differences between calculated and experimental widths. A procedure minimizing relative differences would lead to a more uniform-appearing fit. The points in the neighborhood of the maximum resolving power show both

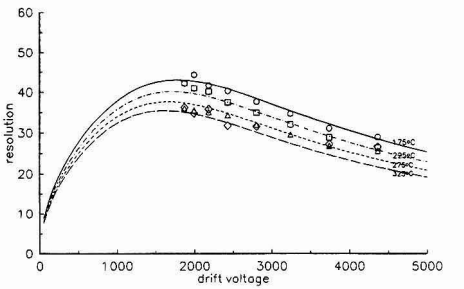


Figure 7. Effect of temperature on resolving power. t_g, 0.20 ms.

Table 3. Functional Dependence of Resolving Power on Operating Parameters

	drift voltage	temp	pulse width	tube length	mobility
$R_d \ll R_p$	$V^{1/2}$	$T^{-1/2}$			
$R_p \ll R_d$	V^{-1}	T^{-1}	t_g^{-1}	L^2	K^{-1}

the most scatter and the least satisfactory correspondence between experimental points and model predictions. From the experimental side, these are the measurements with greatest uncertainty, both because of the high relative uncertainty in measuring the widths of narrow peaks and because the peak intensities are quite low. On the model side, these are the calculated points most affected by small changes in the α, β, and γ parameters.

Figure 7 plots experimental resolving power values for tube B with t_g = 0.20 ms and a range of drift tube temperatures, along with corresponding model predictions shown as solid lines. The scatter in the 325 °C data is the result of thermal noise in the width data. The fit between model and experiment is poorest at high temperature and high voltage. Measured resolving power values are higher than those predicted by the model, because the measured peak widths are narrower than expected. Because diffusion is quite unimportant in these peak widths, the phenomenon must be associated with a small negative temperature dependence in β or γ. This is another manifestation of the effect noted in the discussion of Figure 4 above.

Contributions of V, T, t_g, L, and K to Resolving Power. The effects of the various operating parameters on resolving power are apparent in eqs 12–14 and summarized for the diffusion-dominated and pulse-width-dominated regimes in Table 3.

In the diffusion-dominated low-voltage regime ($R_d \ll R_p$), resolving power is unaffected by an ion's mobility or the length of the drift tube. In this regime, one would simply operate at the highest voltage and lowest temperature possible to achieve the highest resolving power. As we have noted above, however, the weakness of the ion signals in the diffusion-dominated regime requires one to operate where diffusion and initial pulse make comparable contributions to peak width or in the pulse-width-dominated regime.

In the pulse-width-dominated regime ($R_p \ll R_d$), the increases of resolving power with V^{-1}, T^{-1}, L^2, and K^{-1} all arise through the increase of drift time with these parameters. Because IMS signal strength is essentially proportional to Vt_g, using either decreased V or t_g to increase resolving power necessitates striking some

balance between sensitivity and resolving power. Since K is, of course, a property of the ion of interest and not subject to change, only increasing drift tube length offers any possibility of increasing IMS resolving power without loss of signal strength. Our investigations with different tube lengths in this study clearly exhibit the enhancement of resolving power available with a longer tube. Brokenshire[8] has described a tube of 10 cm diameter and $L = 44$ cm, reporting resolving power 5–10 times that of an 8 cm instrument.

Because the dependence of resolving power on voltage changes from $V^{1/2}$ to V^{-1} as one moves from the diffusion-dominated to the pulse-width-dominated regime, resolving power is a maximum at a certain voltage, V_{opt}, an observation first made by Spangler and Collins.[2] Differentiating eq 12 with respect to voltage, setting the result equal to zero, and solving for V yields

$$V_{opt} \left(\frac{\alpha T L^4}{2(\gamma + \beta t_g^2) K^2} \right)^{1/3} \tag{15}$$

Aside from a missing cube root and their inclusion of the η parameter, this is equivalent to Spangler and Collins's eq 24.[2] Substituting eq 15 for V in eq 12 and solving for R yields an expression for the maximum resolving power possible for a particular drift tube and choice of operating conditions:

$$R_{max} = \left(\frac{L^2}{2.598(\gamma + \beta t_g^2)^{1/2} \alpha T K} \right)^{1/3} \tag{16}$$

Values of V_{opt} and R_{max} for the drift tubes used in this study are given in Table 2 for $T = 225$ °C, $t_g = 0.20$ ms, and $K = 4.25$ cm²/V s. On the basis of the $L^{2/3}$ dependence of R_{max}, we would expect Brokenshire's 44 cm instrument to have a maximum resolving power about 3.1 times that of a PCP instrument using the same pulse width and temperature.

One further quantity of interest for a drift tube is its maximum resolving power, expressed as a fraction of the resolving power obtainable with an "ideal" instrument of the same drift length (i.e., an instrument with $\alpha = 0.957 \times 10^{-3}$, $\beta = 1$, and $\gamma = 0$). Equation 16 quickly yields

$$\frac{R_{max}}{R_{ideal}} = \left(\frac{0.957 \times 10^{-3}}{\alpha \left(\frac{\gamma}{t_g^2} + \beta \right)^{1/2}} \right)^{1/3} \tag{17}$$

This ratio is also reported for the drift tubes used in this study in Table 2.

Factors Affecting α, β, and γ. All the measured α, β, and γ parameters in Table 2 exceed the "ideal" values predicted by eq 9, so that the diffusion, pulse width, and constant terms in eq 11 all make peaks wider than expected from the simplest theory.

The α term includes, in addition to actual diffusion, other diffusion-like processes, i.e., broadening processes which depend on the time ions spend in the drift tube. One effect of this sort would be additional diffusion due to ions having higher effective temperature than their surroundings, as in eq 10, from the extra energy being pumped into them by the drift field. However, as mentioned above, this effect is expected to be small for ions of the size studied with IMS.[6] In any event, all drift tubes will be affected about equally by this phenomenon, whatever its magnitude, so this process cannot account for differences observed between IMS instruments in this study.

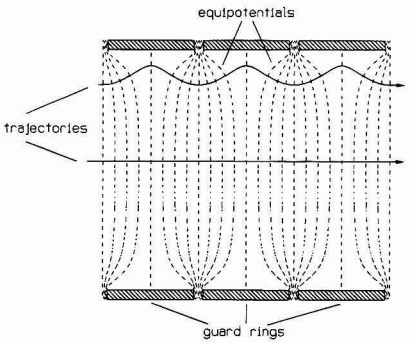


Figure 8. Equipotentials and ion trajectories in a segmented drift tube.

Another factor which can contribute to broadened peaks is radial variation in the electric field. For instruments constructed as stacks of wide rings, as are all the tubes in the present study, the drift field becomes progressively less homogeneous as one moves away from the tube axis, as shown schematically in Figure 8. The closer an ion's path is to the tube wall, the wider the oscillations in electric field it experiences. Any inhomogeneity in the electric field will cause a drift delay relative to an ion which experiences a perfectly uniform field. To see this, suppose that the drift space is divided into two regions of length $L/2$ and that the voltage drop across each region is uniform and equal to $V(1 + \epsilon)/2$ in the first region and $V(1 - \epsilon)/2$ in the second region. Thus the total voltage drop across the drift space is V, and the drift time t_d' of an ion will be equal to the sum of the drift times across the two regions,

$$t_d' = t_{d1} + t_{d2} = \frac{L^2}{KV(1 + \epsilon)(1 - \epsilon)} = \frac{1}{1 - \epsilon^2} t_d > t_d \tag{18}$$

where eq 2 has been used. Note that this same expression would hold for a drift tube divided into a larger number of alternating zones of higher and lower electric field. To accurately compute the effects of field inhomogeneity on drift time in a specific instrument, it would be necessary to map the electric field and to calculate line integrals for an array of ion trajectories. For our present purpose, we merely argue that the greater the inhomogeneity in the electric field, the longer the drift time. We also note that differences in drift time arising from variations in field homogeneity are probably responsible for much of the scatter in tabulated K_0 values.[9] The various IMS instruments used in this study also did not yield identical K_0 values. For example, tube A at 275 °C and tube D at 240 °C yielded 2.52 and 2.76 cm²/sV, respectively, for the K_0 of $(H_2O)_nH^+$.

If every ion experiences exactly the same inhomogeneous electric field, the drift time will be longer and the diffusion

(8) Brokenshire, J. L. FACSS Meeting, Anaheim, CA, October 1991.

(9) Shumate, C.; St. Louis, R. H.; Hill, H. H., Jr. *J. Chromatogr.* **1986**, *373*, 141–173.

contribution to peak width according to eq 8 will correspondingly increase compared to the homogeneous case, but α will be unaffected, since t_d' has exactly the same voltage dependence as t_d. It is differences between the electric fields experienced by different ions that lead to additional peak broadening. An ion pulse leaves the entrance gate as a thin, flat disk, but while in the drift region ions at the outer edge of the disk will lag behind those on the tube axis and lead to a broadened and possibly distorted peak at the collector. If ions in the center of the drift tube experience a homogeneous field while those at the edge of the ion disk find a field varying by about $\pm 1.4\epsilon$, the width due to homogeneity differences, w_{hom}, will be given roughly by

$$w_{hom} \cong t_d' - t_d = \frac{\epsilon^2}{1-\epsilon^2} t_d \qquad (19)$$

Equation 19 is similar to eq 8 in that the width is proportional to the drift time, but different in that w_{hom} lacks the $(T/V)^{1/2}$ dependence of t_{diff}. If eq 9 were modified by the inclusion of the homogeneity effect, the model equation would become

$$w^2 = t_g^2 + \left[\frac{16 \ln 2k}{q} + \frac{\epsilon^4}{(1-\epsilon^2)^2}\frac{V}{T}\right]\frac{T t_d^2}{V} \qquad (20)$$

A term like the second one in the square brackets could account for α values greater than ideal. The functional form indicates that plots of w^2 against Tt_d^2/V should be concave downward, with the slope increasing most notably at low values of Tt_d^2/V. Our plots, such as Figure 2, often seem to show such behavior, but the scatter in the data is such that a firm conclusion is difficult to reach.

The physical dimensions of the four drift tubes in this study tend to confirm these ideas about the effect of field inhomogeneity on peak width. Firstly, the ionization region, where all the primary and secondary ionization processes are presumed to occur, should have a diameter less than the drift region in order to produce a narrow beam of ions that will travel in the most homogeneous portion of the field close to the tube axis. Secondly, a large diameter drift region is desirable, both to increase the field homogeneity along the tube axis and to increase the diameter of the zone where the field is highly homogeneous. Tube C has a much smaller diameter than any of the others, and its much less uniform field presumably gives rise to its large observed α value. While tubes A and B have drift regions slightly greater in diameter than that of tube D, the latter has an ionization region only half as wide as those of A and B. Thus an ion pulse in tube D is more closely confined around the tube axis and should experience a more uniform field than a wider diameter pulse in tubes A or B. This could account for the larger α values for A and B. However, Spangler and Cohen's discussion[10] of electric field modeling by Albritton et al.[11] indicates that tubes A, B, and D should all have less than 1% variation in the electric field experienced by ions in the drift space. In contrast, equating the expression in square brackets in eq 20 with α values from Table 2 and values of V/T representing averages for conditions employed in the experiments with the three tubes, ϵ values of about 0.1 are computed for A, B, and D, indicating an electric field with much more than 1% variation.

Other than tube A, all the IMS instruments had similar values for the pulse width parameter (β = 1.13–1.24). The data of Spangler and Collins[2] are similar, yielding $\beta = 1.15$ when treated as in Figure 3. The ions at the edge of a pulse experience electrostatic repulsion due to all the same-charge ions within the pulse, thus producing broadening of the pulse. The repulsive electric field at the boundary of a pulse is proportional to the pulse duration $t_g^{2.7}$ and would lead to plots of w^2 against t_g^2 having slopes greater than 1 but remaining linear as in the ideal case. Tube A was found to have a construction flaw in its collector region which led to the presence of broad ghost peaks. These in turn confounded our method of measuring peak widths and resulted in an anomolously large β. In fact, it was the large β which originally made us realize the tube was flawed.

The γ parameter comes from broadening processes which remain after processes connected with pulse width and time of residence in the drift space have been removed. These could include amplifier rise time and collector response time. The amplifier rise time in all our experiments was 0.1 ms (10–90%), a value which would be consistent with the observed range of $\gamma^{1/2}$ = 0.07–0.15 ms. Also, the collector begins to respond to an ion cloud before it makes actual contact with the metal surface, in fact as soon as the cloud has passed a horizon in the vicinity of the aperture grid. Aperture grids are typically 0.5 mm away from the collector, so the flight time between grid and collector is on the order of 0.05 ms, large enough to possibly contribute to γ. However, we would also expect this time to be proportional to the drift voltage and thus to be eliminated in the diffusion extrapolation.

While there is thus some justification for associating the α, β, and γ parameters with physical conditions in the drift tube, these remain semiempirical values derived from fitting experimental data. Even with this loose connection to theory, however, the fitting process and the parameters still seem useful as measures of instrument performance and as tools for comparison and prediction.

ACKNOWLEDGMENT

The authors thank David Atkinson for gathering some of the peak width data. Portions of this work were presented at the 47th Northwest Regional Meeting of the American Chemical Society, Missoula, MT, June 17–19, 1992. The work was supported in part by NSF Grant CHE-9021094 to Gonzaga University.

Received for review April 8, 1994. Accepted August 24, 1994.®

® Abstract published in *Advance ACS Abstracts,* October 1, 1994.

(10) Spangler, G. E.; Cohen, M. J. In *Plasma Chromatography*; Carr, T. W., Ed.; Plenum Press: New York, 1984; p 6.

(11) Albritton, D. L.; Martin, D. W.; McDaniel, E. W.; Miller, T. M.; Moseley, J. T. *Measurement of the Low-Energy Transport Parameters of Mass-Identified Ions in Gases*, Appendix IV; Georgia Institute of Technology: Atlanta, 1967.

Anal. Chem. **1994,** *66,* 4202–4209

Liquid–Solid Extraction and Fast Atom Bombardment High-Resolution Mass Spectrometry for the Determination of Hydroxyatrazine in Water at Low–ppt Levels

Zongwei Cai, V. M. Sadagopa Ramanujam, and M. L. Gross*,†

Midwest Center for Mass Spectrometry, Department of Chemistry, University of Nebraska, Lincoln, Nebraska 68588-0304

S. J. Monson, D. A. Cassada, and R. F. Spalding

Water Center, University of Nebraska, Lincoln, Nebraska 68583-0844

Parts-per-trillion levels of hydroxyatrazine (HA) have been quantitatively extracted and eluted from water by liquid–solid extraction with a graphitized carbon-black cartridge. Recoveries of HA (>80%) for this procedure are superior to those obtained when a C-18 cartridge or liquid–liquid extraction with dichloromethane are used. Quantification of HA at picogram levels was accomplished by using isotope dilution and fast atom bombardment high resolution mass spectrometry. No significant interfering spectral background occurs at the masses of interest, those of the $[M + H]^+$ ions of both the analyte and the internal standard, when the liquid matrix is 3:1 dithiothreitol/dithioerythritol. Aqueous samples were fortified with $^{13}C_3$-labeled hydroxyatrazine ($[^{13}C_3]$HA), and sample extracts were analyzed by recording the mass profiles of the target ions. Identification of HA is based on the exact mass of the $[M + H]^+$ ion, and confirmation is by tandem mass spectrometry (FAB-MS/MS) analysis. The method precision in relative standard deviation is 10%, and the accuracy in relative error is <10% for seven standard water samples containing HA at 100 parts per trillion. The method has been used successfully for the first time for the determination of HA and for the simultaneous determination of HA and atrazine, its parent compound, in groundwater.

Understanding the environmental fate of atrazine (ATR) is important because it is used widely as a preemergent herbicide for broadleaf weed and grass control in primarily corn and sorghum productions. Field-applied atrazine is subject to abiotic hydrolysis, leading to dechlorination and formation of hydroxyatrazine (HA). The chemical hydrolysis occurs under a wide range of conditions and is considered to be the predominate degradation pathway of atrazine in the environment.[1–5]

Hydroxyatrazine has been detected at high concentration levels (up to parts per million, ppm) in soils[3–6] and animal tissues.[7,8] Adams and Randtke[9] detected HA in stream and reservoir water but did not report its concentration. In groundwater, HA only exists at low parts-per-trillion (ppt) levels owing to its high sorbitivity to the rock–water matrix and its low solubility in water.[9] Lack of quantitative methods for ultratrace determination of HA has limited research on the fate of atrazine in environmental waters.[10] Therefore, a sensitive analytical method with detection limits of low parts-per-trillion (ppt) levels is needed for HA to support studies of its fate and its degradation pathways in water.[11]

Conventional methods for the determination of atrazine and its degradation products include gas chromatography (GC),[12–14] gas chromatography/mass spectrometry (GC/MS),[11,15–20] and high-performance liquid chromatography (HPLC).[21–32] Gas chromatography/high-resolution mass spectrometry (GC/HRMS) of-

† Present address: Department of Chemistry, Washington University, One Brookings Dr., St. Louis, MO 63130.

(1) Skipper, H. D.; Gilmour, G. M.; Furtick, W. R. *Soil Sci. Am. Proc.* **1967,** *31,* 653.
(2) Best, J. A.; Weber, J. B. *Weed Sci.* **1974,** *22,* 364.
(3) Dao, T. H.; Lavy, T. L.; Sorensen, R. C. *Soil Sci. Soc. Am. J.* **1979,** *43,* 1129.
(4) Wehtje, C.; Leavitt, J. C.; Spalding, R. F. *Sci. Total Environ.* **1981,** *21,* 47.
(5) Rustum, A. M.; Ash, S.; Saxena, A.; Balu, K. *J. Chromatogr.* **1990,** *514,* 209.
(6) Muir. D. C. G.; Baker, B. E. *J. Agric. Food Chem.* **1978,** *26,* 420.
(7) Bakke, J. E.; Larson, J. D.; Price, C. E. *J. Agric. Food Chem.* **1972,** *20,* 602.
(8) Khan, S. U.; Foster, T. S. *J. Agric. Food Chem.* **1976,** *24,* 768.
(9) Adams, C. D.; Randtke, S. T. *Environ. Sci. Technol.* **1992,** *26,* 2218.
(10) Kolpin, D. W.; Kalkhoff, S. J. *Environ. Sci. Technol.* **1993,** *27,* 134.
(11) Cai, Z.; Sadagopa, R. V. M.; Giblin, D. E.; Gross, M. L. *Anal. Chem.* **1993,** *65,* 21.
(12) Popl, M.; Voznakova, Z.; Tatar, V.; Strnadova, J. *J. Chromatogr. Sci.* **1983,** *21,* 39.
(13) Lee, H. B.; Stokker, Y. D. *J.—Assoc. Off. Anal. Chem.* **1986,** *69,* 568.
(14) Junk, G. A.; Richard, J. J. *Anal. Chem.* **1988,** *60,* 451.
(15) Bagnati, R.; Benfenati, D. E.; Fanelli, R. *Chemosphere* **1988,** *17,* 59.
(16) Pereira, W. E.; Rostad, C. E.; Leiker, T. J. *Anal. Chim. Acta* **1990,** *228,* 69.
(17) Shuette, S. A.; Smith, R. G.; Holden, L. R.; Graham, J. A. *Anal. Chim. Acta* **1990,** *236,* 141.
(18) Mills. M. S.; Thurman, E. M. *Anal. Chem.* **1992,** *64,* 1985.
(19) Thurman, E. M.; Meyer, M.; Pomes, M.; Perry, C. A.; Schwab, A. P. *Anal. Chem.* **1990,** *62,* 2043.
(20) Cassada, D. A.; Spalding, R. F.; Cai, Z.; Gross, M. L. *Anal. Chim. Acta* **1994,** *287,* 7.
(21) Eberle, D. O.; Gerber, H. R. *Arch. Environ. Contam. Toxicol.* **1976,** *4,* 101.
(22) Parker, C. E.; Haney, C. A.; Harvan, D. J.; Hass, J. R. *J. Chromatogr.* **1982,** *242,* 77.
(23) Reupert, R.; Ploger, E. *Fresenius J. Anal. Chem.* **1988,** *331,* 503.
(24) Dufek, P.; Pacakova, V. *J. Chromatogr.* **1979,** *187,* 341.
(25) Beilstein, P.; Cook, A. M.; Hutter, R. *J. Agric. Food Chem.* **1981,** *29,* 1132.
(26) Vermeulen, N. M. J.; Apostolides, Z.; Potgieter, D. J. J. *J. Chromatogr.* **1982,** *240,* 247.
(27) Pacakova, V.; Stulik, K.; Prihoda, M. *J. Chromatogr.* **1988,** *442,* 147.
(28) Durand, G.; Barcelo, D. *Toxicol. Environ. Chem.* **1989,** *25,* 1.
(29) Guenter, W. J.; Kettrup, A. *Chromatographia* **1989,** *28,* 209.
(30) Durand, G.; Barcelo, D. *J. Chromatogr.* **1990,** *502,* 275.

0003-2700/94/0366-4202$04.50/0 © 1994 American Chemical Society

fers very high sensitivity and high specificity and has been applied in the trace analysis of atrazine and its dealkylation metabolites in environmental waters.[11] Hydroxyatrazine and other hydroxy-substituted *s*-triazines, however, cannot be determined directly by GC or GC/MS because these analytes are too polar, hydrophilic, and nonvolatile.[5,7,19,29] Furthermore, the derivatization of hydroxy-*s*-triazines via methylating, silylating, or chlorinating agents does not yield quantitative products owing to tautomerization involving the proton of the hydroxy group and the nitrogen of the triazine ring.[7,33,34] HPLC is an attractive alternative to GC or GC/MS because HA absorbs strongly in the UV region.[6,21,26,29–32] The HPLC approach has been successfully used for HA in soil extracts[6,21,26] and laboratory-fortified water[9,29–32] containing HA at parts-per-billion (ppb) to ppm levels. For environmental water, however, no results have been reported because HPLC lacks the required sensitivity and specificity.[28,31,32]

Immunochemical procedures are rapid, inexpensive, enzyme-linked immunosorbent assays (ELISA) that have been applied to the determination of atrazine and its degradation products.[19,35–37] Limitations of haptens and polyclonal antibodies, however, result in uncertain analyte specificity such that some antibodies that are used in the ELISA method do not react significantly with the triazine degradation products.[19] Although a separation of HA from atrazine and some of the dealkylated degradation products is possible by selecting a proper antibody,[37] the selectivity of the method for HA and other hydroxy-substituted *s*-triazines remains unknown. Moreover, the ELISA method has been also limited in determining HA in environmental waters because the method detection limit is higher than the levels of HA in those waters.

Another challenge for determining HA in water is to isolate the compound from water. Extraction efficiencies for HA from water by using the liquid–liquid extraction with dichloromethane and by the liquid–solid extraction using a C-18 bonded silica cartridge are poor.[38] Recoveries of over 85% for HA at ppb levels in fortified water have been reported by using a cyclohexyl silica cartridge[31] and a propylbenzenesulfonic acid cation-exchange cartridge.[32] Adoption of graphitized carbon-black cartridge extraction has provided good recoveries for atrazine and its dealkylation metabolites,[39–41] as well as for other polar compounds,[42,43] but this approach has not bee applied to HA.

Fast atom bombardment (FAB), a soft ionization technique in mass spectrometry, offers several advantages sufficient to meet the challenges in determining hydroxy-*s*-triazines. Recently, fast atom bombardment high resolution mass spectrometry (FAB-HRMS) was shown to be appropriate for the quantitative analysis of aqueous extracts of atrazine at sub-ppt levels.[44] The objective of this study is to develop and apply a FAB-based method for the trace determination of HA in water. The method includes the following steps: (1) liquid–solid extraction with a graphitized carbon-black cartridge for isolating HA from water, (2) FAB-HRMS determination of HA at low-ppt levels, and (3) tandem mass spectrometry (FAB-MS/MS) confirmation of HA.

EXPERIMENTAL SECTION

Reagents. Dichloromethane (pesticide grade), methanol (HPLC grade), and ethyl acetate (pesticide grade) were purchased from Fisher Scientific (Pittsburg, PA). Anhydrous sodium sulfate (analytical grade), from Fisher Scientific, was purified by soxhlet extraction with methanol for 48 h and then heated overnight at 450 °C. Other chemicals were reagent grade and used as received.

The graphitized carbon-black cartridge (3 mL/250 mg) was purchased from Supelco Inc. (Bellefonte, PA). The C-18 bonded silica cartridge (1 g) was obtained from Waters Chromatography (Millipore, MA). Bottled nitrogen gas (dry grade), used for evaporating solvents, was purchased from Air Products and Chemicals Inc. (Allentown, PA), and the gas was transferred through precleaned copper tubing. Purified water was obtained by passing tap water through a Fisher Barnstead 4-Module Nanopure cartridge system.

Native (not isotopically enriched) atrazine (ATR) standard was purchased from AccuStandard Inc (New Haven, CT). Ring-labeled [$^{13}C_3$]atrazine ([$^{13}C_3$]ATR) was synthesized by Merck Frost (Canada). Synthesized native (not isotopically enriched) HA (>99% purity) was obtained from Dr. James Carr of the Department of Chemistry, University of Nebraska–Lincoln. Ring-labeled [$^{13}C_3$]HA was synthesized via hydroxylation of [$^{13}C_3$]ATR according to the protocol provided by Dana Simmons (Ciba Geigy), for synthesizing native HA from ATR.

A mixture of 110 mg of [$^{13}C_3$]ATR, 1.5 mL of concentrated HCl, and 1 mL of H_2O was heated to reflux at 110 °C for 3 h. Upon cooling to room temperature, the reaction solution was diluted with 20 mL of H_2O, and 5 mL of aqueous NH_4OH (4.5 M) was added. A solid precipitate formed. The mixture was stirred for 45 min. After filtration, the solid [$^{13}C_3$]HA was washed with 1 mL of water and 1 mL of acetone and dried in a vacuum desiccator over P_2O_5. The chemical purity of the synthesized [$^{13}C_3$]HA was approximately 95% according to a HPLC determination. An isotope purity of >99% for the synthesized [$^{13}C_3$]HA was measured by both electron ionization (EI) MS and FAB-MS analyses.

Stock standard solutions of native and $^{13}C_3$-labeled HA were prepared separately in methanol. Solutes (2 mg) were weighed accurately and added to 50 mL of methanol. The solution was sonicated and warmed to 50 °C to completely dissolve the compound. The stock solutions of HA and [$^{13}C_3$]HA were further diluted with methanol to obtain the calibration solutions and a fortifying standard solution of 400 pg/μL.

A fortifying standard solution of [$^{13}C_3$]ATR at 100 pg/μL was also prepared for the determination of ATR in water. The details for the calibration and determination of ATR by FAB-HRMS were

(31) Steinheimer, T. R.; Ondrus, M. G. *Water-Resour. Invest. Rep. (U.S. Geol. Surv.)* **1990**, 89–4193.
(32) Lerch, R. N.; Donald, W. W. *J. Agric. Food Chem.* **1994**, *42*, 922.
(33) Cochrane, W. P., *J. Chromatogr. Sci.* **1975**, *13*, 246.
(34) Khan, S. U.; Greenhalgh, R.; Cochrane, W. P. *J. Agric. Food Chem.* **1975**, *23*, 430.
(35) Bushway, R. J.; Perkins, B.; Savage, S. A.; Lekousi, S. J.; Ferguson, B. S. *Bull. Environ. Contam. Toxicol.* **1988**, *40*, 647.
(36) Schlaeppi, J. M.; Werner, F.; Ramsteiner, K. *J. Agric. Food Chem.* **1989**, *37*, 1532.
(37) Thomas, D. H., Beck-Westermeyer, H.; Hage, D. S., submitted for publication in *Anal. Chem.*
(38) Cai, Z.; Spalding, R. F.; Gross, M. L. GC/HRMS and FAB-HRMS Determinations of Atrazine and its Dealkylated and Hydroxylated Products in Ground Water. To be presented at the 42nd ASMS Conference on Mass Spectrometry and Applied Topics, Chicago, IL, May 29, 1994.
(39) Di Corcia, A.; Marchetti, M.; Samperi, R. *J. Chromatogr.* **1987**, *405*, 357.
(40) Di Corcia, A.; Marchetti, M. *Anal. Chem.* **1991**, *63*, 580.
(41) Di Corcia, A.; Samperi, R.; Marcomini, A.; Stelluto, S. *Anal. Chem.* **1993**, *65*, 907.
(42) Borra, C.; Di Corcia, A.; Marchetti, M.; Samperi, R. *Anal. Chem.* **1986**, *58*, 2048.
(43) Andriolini, F.; Borra, C.; Caccamo, F.; Di Corcia, A.; Samperi, R. *Anal. Chem.* **1987**, *59*, 1720.
(44) Caldwell, K. A.; Sadagopa, R. V. M.; Cai, Z.; Gross, M. L. *Anal. Chem.* **1993**, *65*, 2372.

described elsewhere.[44] A standard solution containing 100 pg/μL ATR and [$^{13}C_3$]ATR and 20 pg/μL HA and [$^{13}C_3$]HA in methanol was prepared and used frequently to check the relative response factor (RRF).

The matrix for the FAB-HRMS analysis was a mixture of dithiothreitol (DTT) and dithioerythritol (DTE) (3:1, w/w), both of which were purchased from Aldrich Chemical Co. (Milwaukee, WI). The solid mixture was liquified by heating to 50 °C, and the mixture remained liquid upon cooling to room temperature.

Water Samples. Standard water samples were prepared by fortifying purified water with a native HA standard solution to obtain levels of 5, 100, and 500 ppt. Groundwater was pumped into amber bottles from multilevel samplers installed to depths of 60 ft in a sand and gravel aquifer located near Shelton, NE. The multilevel sampling system is capable of extracting groundwater from discrete levels throughout the 45-ft saturation zone.[45] The samples were stored at 4 °C until analyzed. After addition of the internal standards, the water samples were extracted by the liquid–solid procedure using carbon-black cartridges.

Liquid–Liquid Extraction Using Dichloromethane. Liquid–liquid extraction recoveries of HA with dichloromethane were determined from analyses of water samples fortified with 5 and 500 ppt of native HA. The fortified water samples (200 mL) were each extracted three times with dichloromethane (35 mL each). The extracts were combined and dried with anhydrous sodium sulfate. The [$^{13}C_3$]HA internal standard was added: 2 ng for the samples containing native HA at 5 ppt and 100 ng for those containing HA at 500 ppt. The solution was then concentrated by a slow stream of nitrogen to 20 μL for FAB-HRMS analysis.

Liquid–Solid Extraction Using the C-18 Bonded-Silica Cartridge. The recovery of HA in the procedure using liquid–solid extraction via the C-18 bonded-silica cartridge was determined by analyzing standard water samples (each 200 mL) containing 5 and 500 ppt of HA. The detailed procedures of the C-18 cartridge extraction were reported elsewhere.[11]

Liquid–Solid Extraction Using the Graphitized Carbon-Black Cartridge. The liquid–solid extraction via a graphitized carbon-black cartridge was carried out for samples of standard water and groundwater. The carbon-black cartridge was prewashed sequentially with 2 mL each of dichloromethane, dichloromethane/methanol (80:20, v/v), methanol, and purified water. A sample (200 mL, except as noted in the text) was fortified with [$^{13}C_3$]HA at levels of 10 or 500 ppt for standard water and 100 ppt for groundwater. The sample was drawn through the prewashed carbon-black cartridge at a flow rate of 15–20 mL/min by applying aspirator vacuum. The cartridge was first eluted with 0.5 mL of ethyl acetate to remove residual water. The analyte and the internal standard were then eluted by 5 mL of dichloromethane/methanol (80:20, v/v). Residual water in the ethyl acetate eluant was removed by adding anhydrous sodium sulfate. Both ethyl acetate and dichloromethane/methanol eluants were combined and evaporated to 20–50 μL, depending on the analyte concentrations, by using a slow stream of nitrogen.

For FAB-MS/MS analysis, 1 L of a groundwater sample (1ML4-15) was extracted in order to obtain sufficient HA. The extraction procedure and volume of eluants were same as those described above. Breakthrough in the carbon-black cartridge extraction was determined with 2 L of standard water containing 100 ppt HA.

Method blanks were obtained by passing 0.5 mL of ethyl acetate and 5 mL of dichloromethane/methanol (80:20, v/v) through prewashed carbon-black cartridges. The blank eluant was evaporated to approximately 20 μL and analyzed by FAB-HRMS to test for potential interfering compounds from the cartridge and the solvents.

Safety. Because dichloromethane is a suspected carcinogen, all sample preparations were performed in a hood.

Full Mass Spectra from EI-HRMS. The EI-HRMS analysis of native HA and [$^{13}C_3$]HA standards was conducted on a Kratos MS-50 double-focusing mass spectrometer. Instrument operating conditions were EI at 70 eV, source temperature 250 °C, and resolution 10 000 (10% valley definition). The sample was introduced to the ion source via the direct insertion probe and heated to 150 °C. Spectra of 5–10 scans over the mass range m/z 50–500 were acquired and averaged with a Kratos Mach-3 computer system.

FAB-MS. Positive FAB-MS analyses of native and $^{13}C_3$-labeled HA were performed on a Kratos MS-50 triple-analyzer (EBE configuration) tandem mass spectrometer equipped with a Kratos FAB source, an Iontech FAB gun operated at 6 kV and 1–2 mA emission current, and a Kratos Mach-3 data system. The matrix was the DTT/DTE mixture.

Quantitative determination was conducted on the Kratos MS-50 triple-analyzer instrument. The resolution was 8000–10 000 (10% valley definition). Data were acquired in the mass profile mode[46] by using the selected ion monitoring (SIM) program in the Mach-3 system. Narrow scans (300 ppm sweep width) over the following ions were obtained with the SIM program: [HA + H]$^+$ (m/z 198.1355), [[$^{13}C_3$]HA + H]$^+$ (m/z 201.1456), [ATR + H]$^+$ (m/z 216.1016), and [[$^{13}C_3$]ATR + H]$^+$ (m/z 219.1117). Typically, the first 10 scans were acquired and summed for each mass profile spectrum.

One microliter of the sample extract was placed in 0.5 μL of DTT/DTE matrix that had been loaded onto the FAB probe tip. The mass profile spectrum obtained from a sample analysis was subtracted from the matrix background of 0.5 μL of DTT/DTE. The exact mass and peak intensity were used for qualitative and quantitative analysis, respectively, of ATR and HA. The quantification of ATR was performed by comparing the peak areas of the [ATR + H]$^+$ and [[$^{13}C_3$]ATR + H]$^+$ ions. The peak areas of [HA + H]$^+$ and [[$^{13}C_3$]HA + H]$^+$ ions were used for the determination of HA.

The calibration solutions of HA/[$^{13}C_3$]HA were prepared in methanol at levels of 10–1250 pg/μL HA and 100 pg/μL [$^{13}C_3$]-HA. The solutions were analyzed periodically throughout the method development and sample analysis to establish that data were within the calibration range.

FAB-MS/MS. The collision activated dissociation (CAD) experiments were performed on the same mass spectrometer used for the quantitative FAB-HRMS analyses. The [HA + H]$^+$ ion (m/z 198.1355) was selected and activated in the third field-free region by collisions with helium to give 50% beam reduction. Typically 10–15 scans were signal-averaged for each CAD spectrum.

(45) Spalding, R. F.; Exner, M. E. In *Groundwater Residue Sampling Design*; Nash, R. G., Leslie, A. R., Eds.; ACS Symposium Series 465; American Chemical Society: Washington, DC, 1991; Chapter 15, p 255.

(46) Tong, H. Y.; Giblin, D. L.; Lapp, R. L.; Monson, S. J.; Gross, M. L. *Anal. Chem.* **1991**, *63*, 1772.

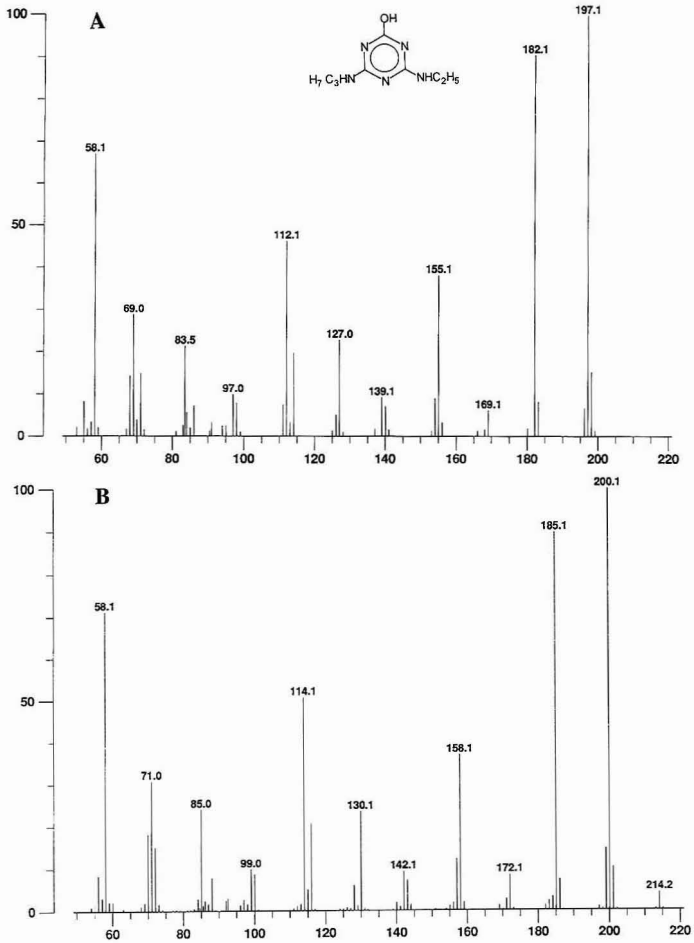


Figure 1. High-resolution EI mass spectra of (A) native hydroxyatrazine and (B) [$^{13}C_3$]hydroxyatrazine. These spectra are low-resolution outputs of high-resolution spectra.

RESULTS AND DISCUSSION

Mass Spectrometry Analyses of HA and [$^{13}C_3$]HA Standards. The EI mass spectra of native HA and [$^{13}C_3$]HA are shown in Figure 1. The fragmentation of HA occurs by elimination of C_2H_4, C_3H_6, and C_2H_4 + C_3H_6 from the molecular ion to give product ions of m/z 169, 155, and 127 via McLafferty rearrangements. The molecular ion also loses CH_3 to give an abundant m/z 182 species that decomposes to m/z 139 by elimination of C_2H_5N. The abundant fragment of m/z 112 may form by loss of CHNO from the m/z 155 ion. This is confirmed by the spectrum of the [$^{13}C_3$]HA; the m/z 112 ion shifts to m/z 114 (the loss is now ^{13}CHNO) and the m/z 155 ion shifts to m/z 158. We expect the homologous m/z 169 ion to give m/z 126 ion, and for the labeled compound, these ions should shift to m/z 172 and 128. This is observed. The above fragmentations, which are in accord with the mass shifts seen for the ^{13}C-labeled compound, were confirmed by measuring the exact masses of the ions to obtain the atom compositions; the mass deviations were less than 6 ppm.

The mass spectra illustrate that the isotope purity of both native and labeled standards is high (>99%). The m/z 214.1542 peak on the mass spectrum of [$^{13}C_3$]HA (Figure 1B) indicates that the labeled standard contains a chemical impurity. The scanning FAB-MS spectrum of [$^{13}C_3$]HA (not shown) further confirms an impurity exists in the standard. The impurity gives an ion of m/z 215 in the positive ion spectrum, indicating that the major contaminant has a molecular weight of 214 and is probably [$^{13}C_3$]hydroxypropazine. The amount of the impurity, however, cannot be determined with high accuracy of either EI-HRMS or FAB-MS analysis because there are likely discrimination effects. The extent of this impurity, which is about 5% according to a HPLC determination, affects the RRF of HA/[$^{13}C_3$]HA but not the accuracy of the HA determination (see the following section).

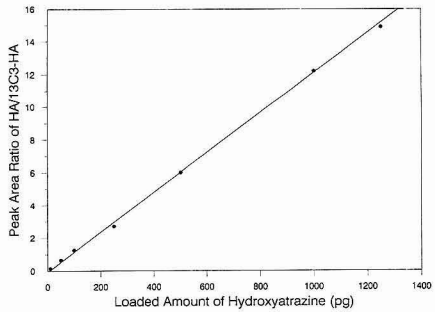


Figure 2. Dynamic ranges for the FAB-HRMS determination of hydroxyatrazine when 100 pg of [$^{13}C_3$]hydroxyatrazine was used as internal standard. Each data point is the average of two runs. The correlation coefficient for the calibration curve is 0.9994.

Calibration and Relative Response Factor of HA/[$^{13}C_3$]-HA. The RRF, the ratio of the intensity of native analyte signal to that of the corresponding internal standard, was obtained from the determination of the calibration standards. The average relative signal response (ratio of signals of native to those of labeled compound) vs concentration of native compound in standard solutions was plotted to obtain a calibration curve over the suitable concentration range. The plot, represented in Figure 2, shows that the method gives a linear dynamic range over 2 orders of magnitude (i.e., 10–1250 pg of native HA, with each solution containing 100 pg of [$^{13}C_3$]HA).

An average RRF of 1.32 was obtained from the analysis of seven standard solutions (RSD = 5.3%). The RRF of HA/[$^{13}C_3$]HA did not vary by more than 10% at any time throughout the method development and sample analysis. Under ideal conditions, the RRF should be equal to 1. The deviation from unity may be due to the presence of the impurity in the internal standard, to errors introduced in the preparation of the standard solutions, and/or to the unresolved background from the matrix and solvent during the FAB-HRMS analysis. Because the chemical impurity in the internal standard does not interfere with the determination of the native HA (see under Potential Interferences), any errors caused by the impurity are nearly eliminated by the use of the relative response factor calibration.

The RRF of ATR/[$^{13}C_3$]ATR obtained from the previous study is 1.07,[44] which was used to measure ATR concentration in the simultaneous determination of HA and ATR. The RRFs were checked periodically throughout the method development and sample analysis stages; the RRFs did not vary by more than 10%.

Recoveries of Hydroxyatrazine with Different Extraction Methods. Three extraction procedures, liquid–liquid extraction with dichloromethane and liquid–solid extractions with either the C-18 bonded-silica cartridge or the graphitized carbon-black cartridge, were tested for the effectiveness in isolating HA from water. The standard water samples containing HA at levels of 5 and 500 ppt were used for determining recoveries (results are listed in Table 1). The data illustrate that HA can be isolated efficiently by the carbon-black extraction, whereas the other two procedures give poor extraction efficiencies.

Two standard water samples (each 2 L) containing 100 ppt of native HA were extracted by using the carbon-black cartridge to test for breakthrough in the extraction. The recoveries of HA were 87% and 81%, respectively. These results indicate that the liquid–solid extraction with the carbon-black cartridge may be used for the efficient isolation of HA from volumes of water as large as 2 L.

Table 1. Recoveries[a] of Hydroxyatrazine in Fortified Water Samples at 5 and 500 ppt Levels

procedure	rec, % (5 ppt soln)	RSD,[b] %	rec, % (500 ppt soln)	RSD,[b] %
liquid–liquid extraction (dichloromethane)	<30		<30	
liquid–solid extraction (C-18 cartridge)	<10		<10	
liquid–solid extraction (carbon-black cartridge)	85	15	94	7

[a] The results (in percent) were obtained from the analysis of three individual samples in duplicate (n = 6). The concentration of HA in the standard water sample is listed in parenthesis. [b] RSD, relative standard deviation.

Potential Interferences. In the FAB-HRMS method, the determination of ATR and HA was based on measurement of the accurate masses for the protonated molecules, $[ATR + H]^+$ and $[HA + H]^+$. This determination may be compromised by interferences and background from the sample extract and/or from the FAB matrix because it does not incorporate on-line chromatographic separation. Although specificity is provided by the use of high mass resolving power (10 000), potential interferences may cause a serious background problem, especially for ultratrace analysis.

Analyses of the standards, both native and $^{13}C_3$-labeled ATR and HA, by scanning EI-HRMS and FAB-MS indicate that these samples do not contain significant interferences. High-resolution mass spectra of ATR and [$^{13}C_3$]ATR,[11] as well as of HA and [$^{13}C_3$]-HA (Figure 1), show that there is no cross interference. Scanning FAB-MS analysis (spectra not shown) also demonstrates that there is no cross interference when this form of ionization is employed. Although an impurity gives an ion of m/z 215 in the FAB spectrum of [$^{13}C_3$]HA, it does not interfere with the determinations of ATR and HA because the ion is resolved from the protonated analytes and internal standards.

A detailed description of matrix-derived background ions from FAB for atrazine determination was given elsewhere.[44] The DTT/DTE was shown to be a suitable matrix for the determination of low-picogram levels of ATR. Although the matrix produces low-intensity background signals in the mass ranges selected for the determinations of ATR and HA, these background ions do not interfere significantly with the determination. Panels A and B of Figure 3 show the background produced from 0.5 μL of DTT/DTE matrix blank and from 0.5 μL of matrix fortified with 10 pg of HA, respectively. The results indicate that when a 0.5 μL of DTT/DTE is used, very low abundance background ions are seen over the mass regions for the four protonated molecules that are monitored. Moreover, the application of the selected ion monitoring program provides the additional benefit that matrix background ion signals may be subtracted. For example, Figure 3C shows the signals obtained for the determination of 10 pg of HA after the background (Figure 3A) was substracted from the spectrum in Figure 3B.

Interferences may be caused by contaminants originating from solvents, glassware, and the carbon-black cartridge. A solvent

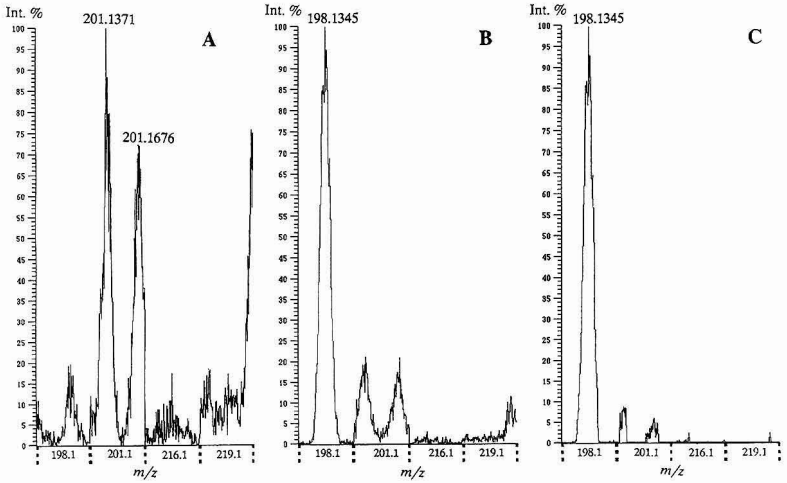


Figure 3. FAB-HRMS spectra of narrow scans (300 ppm sweep width) over four selected ions, $[HA + H]^+$ (m/z 198.1355), $[[^{13}C_3]HA + H]^+$ (m/z 201.1456), $[ATR + H]^+$ (m/z 216.1016), and $[[^{13}C_3]ATR + H]^+$ (m/z 219.1117) of (A) 0.5 μL of DTT/DTE matrix; (B) 10 pg of HA dissolved in 0.5 μL of DTT/DTE, and (C) after the matrix background (A) was subtracted from the spectrum in (B).

Table 2. Results of Determination of HA in Water Samples Fortified at 100 ppt

sample	added, ppt	found, ppt
1	100	120
2	100	115
3	100	115
4	100	90
5	100	110
6	100	110
7	100	95
av result		108
rel error		+8%
RSD[a]		10% (n = 7)[a]

[a] RSD represents relative standard deviation; n is number of samples being analyzed.

cartridge blank was submitted to the quantitative FAB-HRMS method. Narrow scans (300 ppm sweep width) over the mass window for the four ions of m/z 198.1355 and 201.1456 (for native and labeled HA) and of m/z 216.1016 and 219.1117 (for native and labeled ATR) show no significant background signals from the solvents, glassware, or cartridge.

Analysis of Standard Water Samples. Seven fortified standard water samples containing 100 ppt of HA in 200 mL of water were analyzed after adding 500 ppt of $[^{13}C_3]$HA as internal standard. The results in Table 2 demonstrate the accuracy and precision of the method. The relative error for the determination is less than 10%. The method precision given as relative standard deviation (RSD) is 10%.

Analysis of Groundwater Samples. HA levels were determined in 17 groundwater samples. Three method blank samples were randomly inserted into sets of the groundwater samples. The results are listed in Table 3. The number given after the hyphen in the sample identification name represents the depth in feet from which the sample was collected. The data show that the levels of HA in the groundwater samples range from 10 to 30 ppt. A slight decrease in HA concentration with the increase in depth is observed, and this is correlated well with those results obtained for ATR levels (see under Simultaneous Determination of Atrazine and Hydroxyatrazine). The results of three blank samples show there is no detectable cross contamination from one sample loading to another. The detection limit is defined as

Table 3. Levels (ppt) of Hydroxyatrazine and Atrazine in Groundwater Taken at Various Levels from Wells Located Near Shelton, NE

sample ID[a]	HA,[b] ppt	ATR,[c] ppt	HA/ATR[d]
1ML4-15	30	3430	0.009
1ML4-18	30	2870	0.011
1ML4-24	28	2940	0.009
1ML4-34	21	1460	0.015
1ML4-46	10	850	0.012
1ML4-55	11	720	0.015
method blank 1	nd (0.9)[e]	nd (2.5)[e]	
1ML16-17	27	na[f]	
1ML16-20	19	na	
1ML16-26	17	na	
1ML16-34	17	na	
1ML16-46	13	na	
1ML16-55	11	na	
method blank 2	nd (0.7)[e]	na	
1ML27-17	24	na	
1ML27-20	19	na	
1ML27-22	17	na	
1ML27-34	13	na	
1ML27-55	12	na	
method blank 3	nd (1.3)[e]	na	

[a] Sample identification name; ML, multilevel well. The number following ML is the well number (before hyphen) and depth (after hyphen). [b] The level of HA determined in the water sample. $^{13}C_3$-HA (100 ppt) was used as internal standard for the determination of HA. [c] The level of ATR determined in the water sample when simultaneous determination for HA and ATR was conducted. [d] Ratio of the levels of HA and ATR in the groundwater samples. [e] nd, not detected. Detection limit is listed in parenthesis. [f] na, not analyzed.

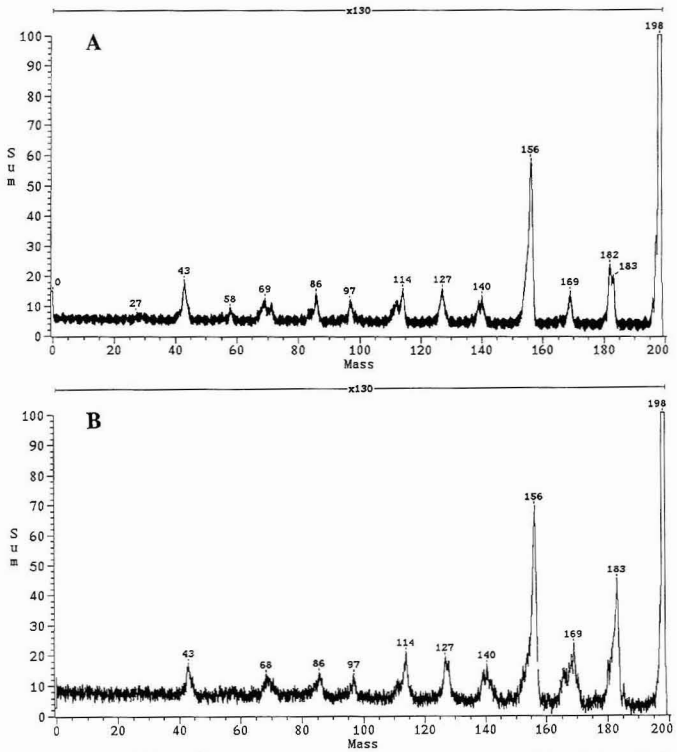


Figure 4. High-energy CAD spectra of $[HA + H]^+$ ion (m/z 198.1355) obtained from the FAB-MS/MS analysis of (A) 10 ng of HA standard and (B) extract of a groundwater sample (1ML4-15). The major fragments of m/z 183, 169, and 156 result from loss CH_3, C_2H_5, and C_3H_6 radicals, respectively.

the concentration of HA required to produce a signal with an intensity of at least 3 times that of the baseline noise. Detection limits of HA for the method blank samples are 0.7−1.3 ppt. Better detection limits should be achievable on newer mass spectrometers equipped with flow FAB; the instrument used here was installed in 1980.

Confirming the Identification of Hydroxyatrazine by FAB-MS/MS. In the quantitative FAB-HRMS analysis, the identification of HA is based on accurate mass measurement for the protonated molecule ($[M + H]^+$) at a mass resolution of 10 000. A compound is identified as HA when the accurate mass of its $[M + H]^+$ ion matches the exact mass of the protonated molecule ion of HA (m/z 198.1355) within ±5 ppm. Because the FAB-HRMS analysis does not contain a chromatographic separation step, confirmation for HA is needed. Tandem mass spectrometry (FAB-MS/MS) was used for this purpose for water samples containing low-ppt levels of HA. The positive FAB-MS/MS analysis provides information regarding fragmentation pathways for the selected ion, the protonated molecule. The high-energy CAD spectrum of the $[M + H]^+$ ion of HA, which was obtained from the FAB-MS/MS determination of 10 ng of HA, is shown in Figure 4A. Figure 4B shows the CAD spectrum for the parent ion of m/z 198.1355 seen in the FAB-MS/MS analysis of a groundwater sample extract. The CAD spectrum is nearly identical to that obtained for 10 ng of HA standard (A), showing major product ions of m/z 183 (loss of CH_3), 182 (loss of CH_4), 169 (loss of C_2H_5), and 156 (loss of C_3H_6). Thus, the FAB-MS/MS analysis serves to confirm the identification of HA, which was assigned on the basis of the accurate mass measurement. The concentration of HA in the sample is 30 ppt, based on the FAB-HRMS analysis (see Table 3).

Simultaneous Determination of Atrazine and Hydroxyatrazine. A standard mixture containing 100 pg/μL ATR and 20 pg/μL HA was analyzed to demonstrate the feasibility of the simultaneous determination of ATR and HA (Figure 5A). The comparison of the peak abundances in the spectra indicates that the method is over 5 times more sensitive for HA than for ATR.

Figure 5B shows the spectra obtained from the simultaneous determination of ATR and HA in a groundwater sample. Prior to the liquid−solid extraction, 100 ng (500 ppt) of $[^{13}C_3]$ATR and 20 ng (100 ppt) of $[^{13}C_3]$HA were added to the 200-mL sample as internal standards for the ATR and HA determinations, respectively. The result indicates that FAB-HRMS may be used for the simultaneous determination of ATR and its hydroxylated degradation product at trace levels in water without employing chromatographic separation.

The concentrations of ATR, HA, and their ratios in groundwater samples are shown in Table 3. The levels of HA in the

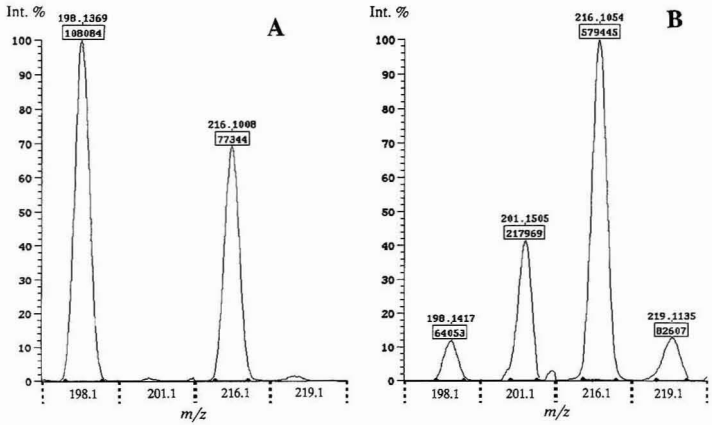


Figure 5. Spectra of narrow scans (300 ppm sweep width) over four selected ions, $[HA + H]^+$ (*m/z* 198.1355), $[[^{13}C_3]HA + H]^+$ (*m/z* 201.1456), $[ATR + H]^+$ (*m/z* 216.1016), and $[[^{13}C_3]ATR + H]^+$ (*m/z* 219.1117) obtained from the simultaneous determination of ATR and HA in (A) a standard mixture containing 100 pg/μL ATR and 20 pg/μL HA and (B) an extract of a groundwater sample (200 mL) in which $[^{13}C_3]$ATR (500 ppt) and $[^{13}C_3]$HA (100 ppt) were added to use as internal standards.

groundwater are about 100 times lower than those for ATR. This is probably because HA is highly sorptive in solid aquifer matrix and less soluble in water than the parent compound. The groundwater data indicate that both ATR and HA levels decrease with decreased depth.

Decreasing amounts of atrazine with depth suggest that increased degradation has occurred in the older, deeper waters. Lower HA levels at lower depths suggests that hydrolysis is not the main degradation pathway of atrazine in groundwater. The hydroxylation of atrazine is probably a zero-order reaction in water where product concentrations are largely controlled by sorption. While the main source of HA in surface water is the desorption of HA from field soil,[9] HA in deep groundwater may result from HA absorption on sediment. ATR in the groundwater comes from nonpoint sources that have infiltrated from surficial soils.

CONCLUSION

The liquid–solid extraction with a graphitized carbon-black cartridge effectively isolates hydroxyatrazine from water. The quantitative FAB-HRMS procedure provides high sensitivity (low-ppt detection limits) for the determination of hydroxyatrazine in groundwater. The method is suitable for the simultaneous determination of atrazine and its hydroxylated degradation product in water. The method was used to analyze environmental water samples to give useful information on the distribution of hydroxyatrazine in groundwater.

ACKNOWLEDGMENT

We thank Professor James Carr, Department of Chemistry, UNL, for the native hydroxyatrazine standard, and Dana Simmons, Ciba Plant Protection, Ciba Geigy, Greensboro, NC, for synthesis procedure for hydroxyatrazine. The research was supported by the UNL Water Center and by the National Science Foundation (Grant DIR 9017262).

Received for review June 2, 1994. Accepted August 11, 1994.[⊗]

[⊗] Abstract published in *Advance ACS Abstracts,* October 1, 1994.

Anal. Chem. **1994,** *66,* 4210–4214

Glycerol-Enhanced Separation of DNA Fragments in Entangled Solution Capillary Electrophoresis

Jing Cheng and Keith R. Mitchelson*

Department of Molecular and Cell Biology, University of Aberdeen, Aberdeen AB9 1AS, U.K.

(Hydroxyalkyl)methylcellulose additives to borate buffers have been used to create physically entangled solutions for fractionation of biological molecules by high-performance capillary electrophoresis, i.e., ESCE. We have observed that addition of glycerol to an entangled solution containing (hydroxypropyl)methylcellulose (HPMC) in Tris–borate buffer markedly improved the separation of double-strand DNA molecules ranging from less than 100 bp to about 1 kb by ESCE. This range of DNA fragment sizes is well suited to many PCR-based studies. We attribute the improved ESCE performance to the borate present in the buffer system. Borate can form dimeric 1:2 borate:didiol complexes with both glycerol and HPMC, acting as a central linkage to allow an entangled solution with different pore size to form chemically.

In the past decade, high-performance capillary electrophoresis (HPCE) has become a hot research and development area in analytical chemistry, especially with regard to capillary coatings, buffer additives, applications, hardware development, and theory. Although HPCE has found applications in many areas of analysis, the separation and examination of biopolymers, especially DNA molecules, is undoubtedly one of the most interesting and quickly advancing fields.[1–3] The examination of double-stranded DNA (dsDNA) fragments such as PCR amplification products and restricted DNA fragments plays an important role in areas of molecular biology such as human disease diagnosis, forensic identification, human genome mapping, etc.

In the separation of dsDNA by HPCE, two kinds of separation medium are employed: gel solution and entangled free solution. In most cases, entangled solution capillary electrophoresis (ESCE) is prefered to gel-filled capillary electrophoresis (GCE) simply because (1) it is difficult to make uniformly gel-filled capillary columns; (2) a gel-filled capillary column has a limited number of operational runs as the matrix is prone to the destruction caused by high current densities and therefore cannot maintain high resolving power constantly; and (3) for polyacrylamide gel-filled columns, the sample can only be injected electrokinetically. DNA species of different lengths are variably loaded during electrokinetic injection. Our laboratory is addressing the application of ESCE for DNA conformational polymorphism studies such as heteroduplex polymorphism assay (HPA)[4] and DNA length polymorphism screening.[5] We have used glycerol as an additive in ESCE to improve the efficiency for distinguishing mismatches in small DNA molecules.[4] This report is a fuller account of the effect of glycerol on the performance of an ESCE system with restriction fragments up to 1353 bp. This size range is suitable for many PCR-based HPCE studies, such as PCR restriction fragment length polymorphism analysis (PCR-RFLP),[6,7] PCR heteroduplex polymorphism assay (PCR-HPA),[4,8] PCR single-stranded conformation polymorphism analysis (PCR-SSCP).[9]

EXPERIMENTAL SECTION

Instrumentation. ESCE was performed on the P/ACE system 5500 (Beckman) in the reversed polarity mode (negative potential at the injection end of the capillary). The temperature was set at 22 °C, and the UV absorbance was monitored at 260 nm. Postrun analysis of data was performed using the Gold Chromatography Data System (Version 8.0). Surface-modified fused silica capillary, DB-17 (J & W Scientific), was used for all analyses. The capillary (57 cm × 100 μm, with effective length of 50 cm) was conditioned with five volumes of the separation buffer mentioned above and then subjected to voltage equilibration for 15 min until a stable base line was achieved. DNA marker was injected into the capillary by electrokinetic injection at negative polarity of 175 V/cm for 15 s. Separations were performed under constant voltage at 228 V/cm for 35 min.

DNA Marker and Buffer System. *Hae*III digested φX 174 DNA was used as the molecular weight marker and was diluted to a concentration of 20 ng/μL with water before injection. The buffer system used for this study consisted of 90 mM Tris–base, 90 mM boric acid, and 2 mM EDTA, pH 8.5, to which 0.5% (w/v) (hydroxypropyl)methylcellulose (HPMC) was added. The viscosity of a 2% aqueous solution for this cellulose derivative (H-7509, Sigma) was 4000 cP at 25 °C. Glycerol was added in different ratios, i.e., 0%, 2.5%, 5.0%, and 7.5% (v/v), before use. The buffers were filtered using a 0.2 μm filter and then degassed for 15 min by sonication before use.

(1) Landers, J. P.; Oda, R. P.; Spelsberg, T. C.; Nolan, J. A.; Ulfelder, K. J. *BioTechniques* **1993**, *14*, 98–111.
(2) Drossman, H.; Luckey, J. A.; Kostichka, A. J.; D'Cunha, J.; Smith, L. M. *Anal. Chem.* **1990**, *62*, 900–903.
(3) Lu, W.; Han, D.-S.; Yuan, J.; Andrieu, J.-M. *Nature* **1994**, *368*, 269–271.
(4) Cheng, J.; Kasuga, T.; Mitchelson, K. R.; Lightly, E. R. T.; Watson, N. D.; Martin, W. J.; Atkinson, D. *J. Chromatogr.* **1994**, *677*, 169–177.
(5) Lightly, E. R. T.; Cheng, J.; Osborne, A.; Miedzybrodzka, Z. H.; Haites, N. E.; Mitchelson, K. R.; Martin, W. J. Separation of the PCR products of the Cellmark cystic fibrosis mutation analysis kit by entangled solution capillary electrophoresis (ESCE). Manuscript in preparation.
(6) Ulfelder, K. J.; Schwartz, H. E.; Hall, J. M.; Sunzeri, F. J. *Anal. Biochem.* **1992**, *200*, 260–267.
(7) Principe, D. D.; Iampieri, M. P.; Germani, D.; Menichelli, A.; Novelli, G.; Dallapiccola, B. *J. Chromatogr.* **1993**, *638*, 277–281.
(8) Khrapko, K.; Hanekamp, J. S.; Thilly, W. G.; Belenkii, A.; Foret, F.; Karger, B. L. *Nucleic Acids Res.* **1994**, 22, 364–369.
(9) Kuypers, A. W. H. M.; Willems, P. M. W.; van der Schans, M. J.; Linssen, P. C. M.; Wessels, M. C.; de Bruijn, C. H. M. M.; Everaerts, F. M.; Mensink, E. J. B. M. *J. Chromatogr.* **1993**, *621*, 149–156.

0003-2700/94/0366-4210$04.50/0 © 1994 American Chemical Society

Table 1. Retention Times (min) of DNA Fragments According to the Ratio of Glycerol (v/v) Added to the Buffer System

	DNA fragment (bp)									
glycerol (v/v, %)	72	118	194	234	276[a]	310	603	872	1078	1353
0.0	12.80	13.40	14.45	15.05	15.77	16.20	19.07	20.27	20.47	20.65
2.5	14.90	15.60	16.90	17.55	18.39	18.91	22.49	24.17	24.60	24.79
5.0	16.80	18.32	19.25	20.00	20.96	21.57	25.81	27.97	28.61	28.88
7.5	18.54	19.51	21.14	22.00	23.10	23.78	28.62	31.12	31.87	32.23

[a] The average value of fragments 271 bp and 282 bp.

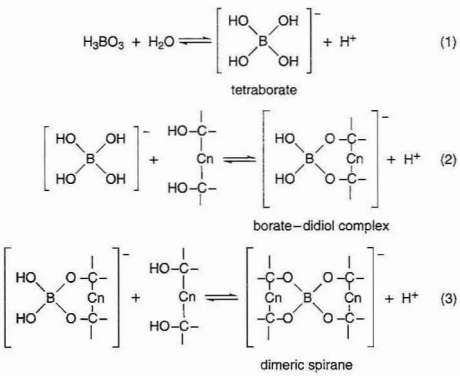
RESULTS AND DISCUSSION

The data for ESCE separation of *Hae*III digested ϕX 174 DNA are shown in Table 1. The basic ESCE system using TBE buffer and containing only HPMC was run at a constant field strength of 228 V/cm at 20 °C. This system achieved base line resolution of fragments in the range from 72 to 872 bp (Figure 1A) except for fragments 271 and 281 bp, which could not be resolved. Only partial separation was achieved among larger DNA fragments of 872, 1078, and 1353 bp. When glycerol was employed as an additive in the ESCE buffer system, resolution for all DNA fragments was improved. The most evident improvement in the separation efficiency is for DNA fragments ranging somewhere from 100 bp to 1 kb. Graphic representation of the effect of increasing the percentage concentration of glycerol from 2.5% to 7.5% is shown in Figures 1B, C, and D. When the percentage concentration of glycerol was lower than 5%, the improvement on the separation is effective for DNA fragments ranging from 100 bp up to 1.3 kb (Figures 1B and C). When the glycerol added is 5% and above, the improvement on the separation occurred mainly from 230 bp to 1.3 kb, which resulted in the separation of 872, 1078, and 1353 bp fragments to base line level (Figures 1C and D). In all cases where glycerol was used as an additive, the separation of fragments 271 bp and 281 bp still cannot be obtained, but separation has been achieved previously when ethidium bromide was also introduced.[4] Figure 2 shows an illustrative presentation of these data where peak to peak migration change is plotted against DNA fragment size. A more conventional representation of these data is given in Figure 3, which shows the relative electrophoretic mobility of DNA fragments (with reference to the 72 bp fragment) plotted against the fragment size. Both Figures 2 and 3 highlight the size range of DNA where the most evident separation improvement has been achieved. When the percentage concentration of glycerol is below 5%, improved separation is achieved for all DNA fragments. Further improvement can be achieved for fragments between 310 bp and about 1 kb by increasing the concentration of glycerol to 7.5%.

The retardation was calculated from migration time of peak of the 1353 bp fragment (data in Table 1). It can be seen from Figure 4 that the increase of glycerol in the separation buffer by steps of 2.5% resulted in the retardation of the DNA migration by about 4 min. The migration time increases linearly with increasing percentage of glycerol. The amount of glycerol added may be therefore optimized depending on the separation requirement of DNA fragments.

As reported in the early pioneering work of Jorgenson and Lukacs,[10] the observed improvement in DNA fragment separation could be explained by the changes in two parameters (i.e., electrophoretic mobility, μ, and molecular diffusion coefficient, D) which directly affect the resolution (R_s) (eq 17 of their work). From Shaw's[11] early work, it was known that the electrophoretic mobility, μ, is inversely proportional to the viscosity of the separation medium. In addition, the molecular diffusion coefficient, D, is also inversely proportional to the viscosity, and, from eq 17 described by Jorgenson and Lukacs,[10] it is clear that the decrease in values of both μ and D would contribute to an increase in the resolution R_s. The addition of glycerol to the HPMC buffer would add to the intrinsic viscosity of the solution, decreasing both electromigration and diffusion of the DNA fragments and improving the separation efficiency.

It is well established in chemical literature that an increase in solution conductivity results from complex formation between borate and polyhydroxy (polyol) compounds.[12-14] In these complexation reactions, tetrahydroxyborate ions $B(OH)_4^-$ react with polyols (where $n = 0$ or 1) with a net release of a proton as shown in equilibria 1–3:



(1)

(2)

(3)

Tetraborate can form either monomeric or dimeric complexes with 1,2-diols or 1,3-diols (equilibria 2 and 3) when the hydroxyl groups are oriented in the appropriate geometry.[15] In the latter case, boric acid forms a dimeric 1:2 borate:diol spirane complex with borate as the central linkage between diols.[12,15] Mono- and dicomplex borate esters can form simultaneously in aqueous

(10) Jorgenson, J. W.; Lukacs, K. D. *Anal. Chem.* **1981**, *53*, 1298–1302.

(11) Shaw, D. J. In *Electrophoresis*; Academic Press: London, 1969.
(12) Zittle, C. A. *Adv. Enzymol.* **1951**, *12*, 493–527.
(13) Böeseken, J. *Adv. Carbohydr. Chem.* **1949**, *4*, 189–210.
(14) Smith, J. T.; Nashabeh, W.; El Rassi, Z. *Anal. Chem.* **1994**, *66*, 1119–1133.
(15) Scouten, W. H. In *Solid Phase Biochemistry*, 1st ed.; John Wiley & Sons: New York, 1983, Chapter 4.

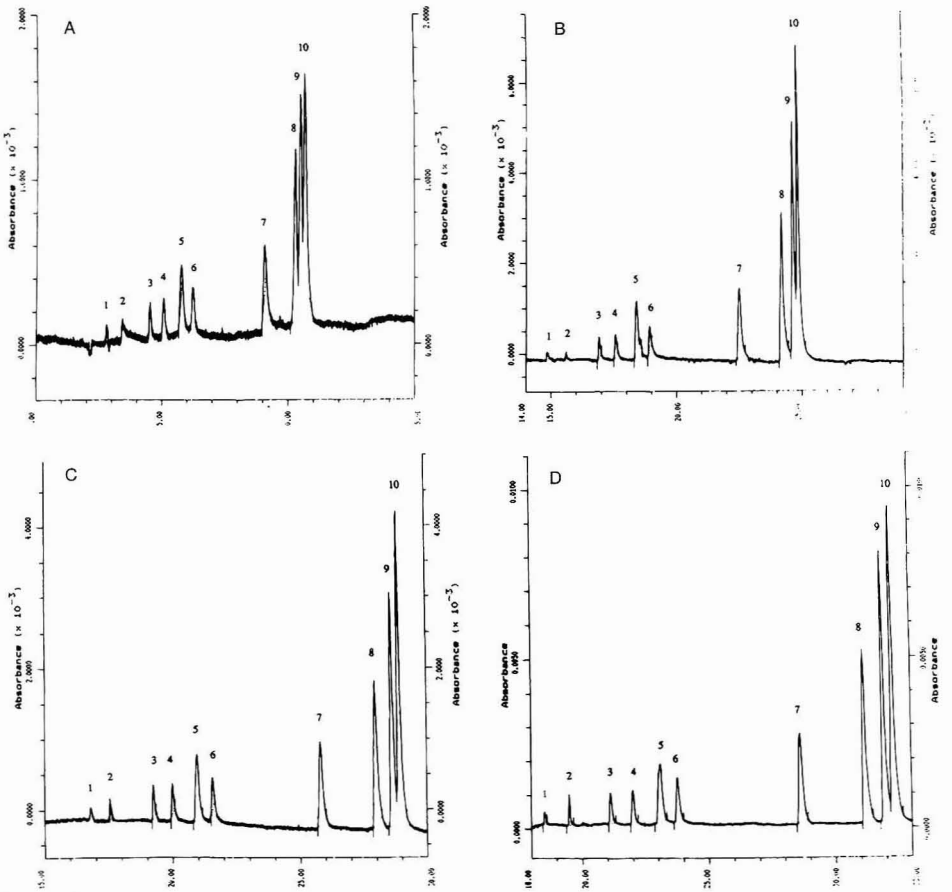


Figure 1. Separation of *Hae*III digested ϕX DNA marker using ESCE with the presence of (A) 0%, (B) 2.5%, (C) 5%, and (D) 7.5% glycerol (v/v). The DNA fragment size for each numbered peak is as follows: 1, 72; 2, 118; 3, 194; 4, 234; 5, 271/281; 6, 310; 7, 603; 8, 872; 9, 1078; and 10, 1353 bp. Conditions: buffer, 90 mM Tris–borate, 2 mM EDTA, pH 8.5, 0.5% (w/v) (hydroxypropyl)methylcellulose (HPMC). Glycerol was added to 0%, 2.5%, 5.0%, and 7.5% (v/v). The efffective length of the column was 50 cm. DNA marker was injected into the capillary by electrokinetic injection at negative polarity of 175 V/cm for 15 s. Separations were performed under constant voltage at 228 V/cm for 35 min.

solution, where their molar ratio is affected by the relative concentration of polyol molecules and borate ions and the presence of substituents on the polyol. (Hydroxyalkyl)methylcelluloses such as HPMC are not completely substituted at all hydroxyl groups, with hydroxypropyl (7–12%) and methoxy (28–30%) substitution of hydroxyl groups.[16] Thus, the formation of the HPMC polymer network may result in part from complexes between boric acid and diol groups on HPMC saccharide units.[12] The entangled polymer network formed in HPMC–borate buffer solutions would therefore be the sum of a looped network[17–19] and a cross-linked polymer network of borate–didiol complexes (Figure 5A).[12] The ability of borate to chemically interact in solution with polysaccharides such as hydroxyethylcellulose[20] and hydroxyethylagarose[21] is evidenced by the reduced effective sieving effect in electrophoresis buffers lacking borate, such as Tris–phosphate buffer or Tris–acetate, respectively. Glycerol may also form monomeric and dimeric complexes with boric acid. We also observed that the current generated during electrophoresis runs increases along with the increase in the amount of glycerol added (Figure 6). It can be seen that, when the percentage of glycerol is smaller that 5%, the increase in current is nearly proportional to the increase of glycerol. The increase in current gradually flattens when the percentage of glycerol is raised above 5%. The probable reason for the nonlinear current increase is that the borate in the buffer was consumed out

(16) Sigma Chemical Corp., Technical Data.
(17) Grossman, P. D.; Soane, D. S. *J. Chromatogr.* **1991**, *559*, 257–266.
(18) Barron, A. E.; Soane, D. S.; Blanch, H. W. *J. Chromatogr.* **1993**, *652*, 3–16.
(19) Bae, Y. C.; Soane, D. *J. Chromatogr.* **1993**, *652*, 17–22.
(20) Nathakarnkitkool, S.; Oefner, P. J.; Bartsch, G.; Chin, M. A.; Bonn, G. K. *Electrophoresis* **1992**, *13*, 18–31.
(21) Peats, S.; Nochumson, S.; Kirkpatrick, F. H. *Biophys. J.* **1986**, *49*, 91a.

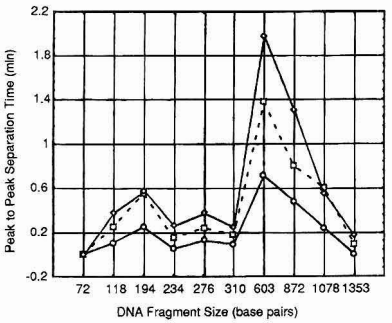


Figure 2. Peak to peak increase in migration time against DNA fragment size (bp). Migration time for each DNA fragment peak in buffer lacking glycerol was substracted from migration times obtained in buffers containing (○) 2.5%, 5.0% (□), and 7.5% (◇) glycerol (v/v).

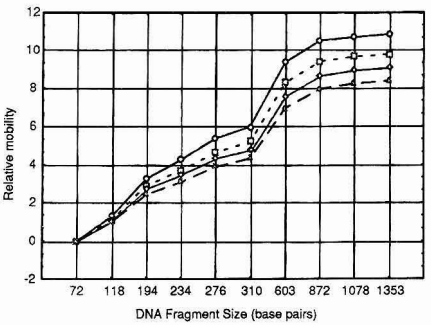


Figure 3. Relative electrophoretic mobility (-10^{-5}·cm^2·s^{-1}·V^{-1}) of each DNA fragment versus DNA fragment size (bp). Relative electrophoretic mobility for each DNA fragment was calculated in relation to the smallest (72 bp) peak for buffers containing 0% (○), 2.5% (□), 5.0% (◇), and 7.5% (△) glycerol (v/v).

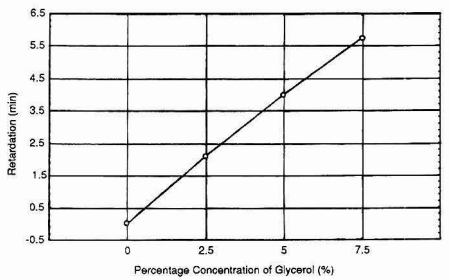


Figure 4. Retardation (min) of the 1353 bp DNA fragment against 0% (v/v) glycerol. Values are the average of two runs.

progressively when more glycerol was added. The investigation stopped when the ratio of glycerol added reached 7.5% (v/v) because higher percentages are too viscous to be driven through the capillary column under pressure. We suggest that this increased current is due to protons released during reaction between glycerol and borate. It is therefore our belief that the improved separation of DNA fragments achieved in this ESCE

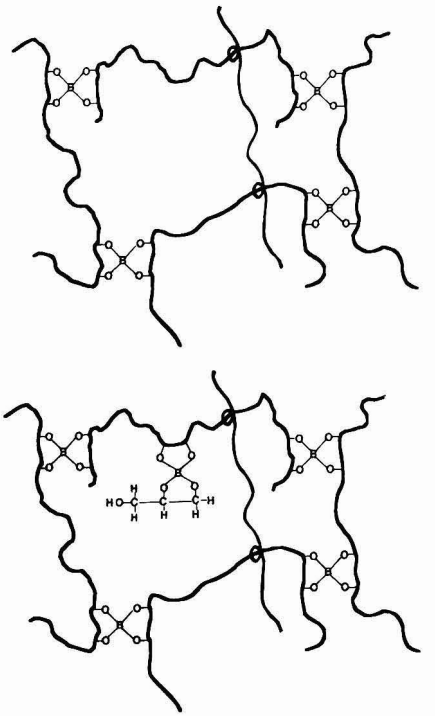


Figure 5. (A, top) 1:2 borate:didiol cross-links between HPMC polymers in an entangled HPMC–borate buffer solution. Entangled (looped) HPMC molecules are also shown. (B, bottom) 1:2 borate: didiol complexes between glycerol:HPMC:borate which may form in an entangled glycerol–HPMC–borate buffer system.

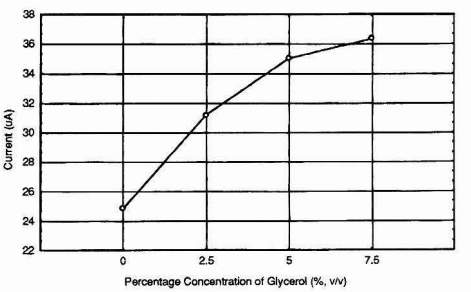


Figure 6. Current (μA) for ESCE runs under constant field of 228 V/cm with separation buffer containing various percentage of glycerol (v/v). Values are the average current for each of two runs.

buffer system is due not only to the intrinsic viscosity effects of glycerol but also to an interaction between the glycerol and other components in the buffer. We envisage that when the glycerol is introduced into the HPMC buffer, dimeric spirane complexation reactions may also occur between glycerol, borate, and HPMC (Figure 5B). We have two models for this interaction. The first model proposes the attachment of glycerol molecules to the HPMC polymers at borate–monodiol intermediates by reaction of glycerol with the free hydroxyl groups of the tetraborate (as

depicted in Figure 5B). The second model proposes the formation of glycerol–borate multimers which may further cross-link HPMC complexes to reduce the effective pore size of the polymer network. We suggest that such a glycerol-containing borate buffer system is chemically entangled in part and should be termed a borate-mediated entangled carbohydrate solution (BMEC). BMEC may have a stronger stability, and increased sieving power in a way similar to the effect observed by using borate buffer to interact with hydroxyethylated agarose causes an increase in the rigidity of the gel, an increase in the agarose bundle radius, and a decrease in the interfiber spacing.[22] The stability of the BMEC formed is dependent upon several factors, such as pH, the concentration of borate, ionic strength, or possibly temperature. We suggest that addition of glycerol to BMEC systems for use in ESCE might be useful for separation of nucleic acid species other than dsDNA. We are currently examining the use of this system for single-stranded conformational polymorphism (SSCP) analysis of PCR-amplified DNA.

The use of glycerol as an additive is different in effect from ethidium bromide. It is known that ethidium bromide preferentially intercalates between GC base pairs, and this results in an increase in the atomic distance between successive base pairs, which distorts the sugar backbone and decreases the pitch of the double helix, thereby changing the charge per unit length and the structure of the molecule.[23,24] When limited amounts of ethidium bromide are added to a DNA mixture, the preferential intercalation of GC-rich fragments results in selectively altered mobility of fragments during electrophoresis. We have previously reported that using both glycerol and ethidium bromide as additives in the TBE buffer containing HPMC results in an overall improvement in the separation of dsDNA.[4]

An application of the phenomenon of borate–polyol complexation for formation of in situ charged micelles with *N*-D-gluco-*N*-methylalkanamide (MEGA) surfactants has been recently reported.[14] The MEGA system gives good separation of various low molecular weight apolar molecules such as herbicides, barbiturates, and polyaromatic compounds by micellar electrokinetic capillary electrophoresis (MECC). A further development of borate complexation for HPCE fractionation allowed the separation of low molecular weight biologically active molecules such as norepinephrine and normetanephrine which react with borate via cis-diols.[25] These molecules differ by only a single hydroxyl group with no change in net charge and were therefore difficult to separate by HPCE in the absence of borate. Consideration of interaction between polyhydroxylated molecules and borate might also be fruitful for HPCE applications (e.g., agarose gel-filled capillary electrophoresis) other than MECC and BMEC.

(22) Dumais, M. M.; Nochumson S. *BioTechniques* **1987**, *5*, 62–67.
(23) Schwartz, H. E.; Ulfelder K. *J. Chromatogr.* **1991**, *559*, 267–283. S.; Foret, F.; Karger, B. L. *J. Chromatogr.* **1993**, *652*, 57–66.
(24) Pariat, Y. F.; Berka, J.; Heiger, D. N.; Schmitt, T.; Vilenchil, M.; Cohen, A. S.; Foret, F.; Karger, B. L. *J. Chromatogr.* **1993**, *652*, 57–66.
(25) Landers, J. P.; Oda, R. P.; Schuchard, M. D. *Anal. Chem.* **1992**, *64*, 2846–2851.

ACKNOWLEDGMENT

The authors would like to thank Beckman Instruments, Inc., for the loan of the P/ACE system 5500 and the capillary column. This work is supported by Scottish Office (SOAFD) and by the UFC Biotechnology Initiative.

Received for review May 9, 1994. Accepted August 26, 1994.[⊗]

[⊗] Abstract published in *Advance ACS Abstracts,* October 1, 1994.

Anal. Chem. **1994,** *66,* 4215–4228

Theory of Field-Programmed Field-Flow Fractionation with Corrections for Steric Effects

P. Stephen Williams and J. Calvin Giddings*

Field-Flow Fractionation Research Center, Department of Chemistry, University of Utah, Salt Lake City, Utah 84112

This paper deals with the principal perturbation to ideal normal-mode elution of particles in field-flow fractionation (FFF). This perturbation is due to the finite size of particles undergoing migration in the FFF channel. The effects of a first-order correction for particle size are examined. Equations are derived for retention time, fractionating power, and steric inversion diameter for operation at constant field strength, as well as under conditions of both exponential and power programmed field decay. Useful limiting equations for fractionating power are derived and their validity is confirmed for typical experimental conditions. The derived equations are necessary for the future development of a systematic optimization strategy for the selection of operating conditions for particle size analysis by FFF. Calculations confirm our previous conclusion that the fractionating power for exponential field programming varies strongly with particle size; this variation is only slightly reduced by steric perturbations. The uniform fractionating power of power programming is slightly disturbed by steric effects although fractionating power remains much more uniform than for exponential programming. It is shown that a higher uniformity in fractionating power can be gained by manipulating the parameters of power programming but that no improvement is possible with exponential programming. Phenomena giving rise to higher order perturbations and to secondary relaxation are discussed and the conditions identified under which these effects are minimized.

The field-flow fractionation (FFF) methods are a family of subtechniques capable of separating particulate or macromolecular materials according to various properties such as mass, size, thermal diffusion, or charge.[1,2] They are elution methods where the components of a sample mixture are swept selectively out of the FFF system by a carrier fluid; they emerge at times governed by one of the physicochemical properties noted above. Usually the system outlet stream is fed to a detector so that quantitative information may be obtained concerning the distribution of material according to the given property. Since the components are physically separated during elution there is the option of taking fractions from the outlet stream for further analysis.

The separation is generally carried out within a thin ($\sim 10^2$ μm) parallel-walled channel with a cross section of high aspect ratio (commonly around 100:1). A field, of gravitational or electrical nature for example, is applied across the thin dimension. Depending on the strength of interaction with this field, each of the sample components approaches some specific equilibrium concentration profile across the channel thickness, with a maximum concentration generally close to one wall—the so-called accumulation wall. The flow of carrier fluid through the channel provides the means of elution, with the different components migrating at velocities determined by the interaction of the fluid velocity profile with their specific concentration profiles. The high aspect ratio of the channel cross section gives rise to a fluid velocity profile that is dominated by the drag effect of the major (parallel) walls. The profile is therefore uniformly parabolic across the thin dimension with small disturbances toward the channel edges where the velocity must also approach zero. The assumption of a simple parabolic fluid velocity profile has allowed the derivation of relatively simple analytical expressions describing sample elution or retention time and system band spreading.

Many different field types have been employed in FFF to drive sample materials toward the accumulation wall. Each field type interacts with sample components on the basis of a different component property. For example, a gravitational or centrifugal field interacts with particles at a level scaled to effective particle mass (particle mass minus the mass of fluid displaced);[3,4] an electrical field interacts according to effective particle or molecular charge;[5,6] a thermal gradient induces migration via the thermal diffusion effect;[7,8] and a cross flow of carrier (through semipermeable channel walls) causes a drag force proportional to the Stokes diameter.[9,10] Each field type is associated with a particular subtechnique of FFF. The examples mentioned correspond to sedimentation, electrical, thermal, and flow FFF, respectively.

Compared to other elution methods, such as size exclusion chromatography, the FFF subtechniques tend to give greater relative differences in retention time for small differences in size

(1) Giddings, J. C. *Science* **1993,** *260,* 1456–1465.
(2) Martin, M.; Williams, P. S. In *Theoretical Advancement in Chromatography and Related Separation Techniques*; Dondi, F., Guiochon, G., Eds. NATO ASI Series C: Mathematical and Physical Sciences 383; Kluwer: Dordrecht, The Netherlands, 1992; pp 513–580.
(3) Giddings, J. C.; Myers, M. N.; Caldwell, K. D.; Fisher, S. R. In *Methods of Biochemical Analysis*; Glick, D., Ed.; John Wiley: New York, 1980; Vol. 26, pp 79–136.
(4) Giddings, J. C.; Caldwell, K. D. In *Physical Methods of Chemistry*; Rossiter, B. W., Hamilton, J. F., Eds.; John Wiley & Sons: New York, 1989; Vol. 3B, Chapter 8, pp 867–938.
(5) Davis, J. M.; Fan, F.-R. F.; Bard, A. J. *Anal. Chem.* **1987,** *59,* 1339–1348.
(6) Giddings, J. C. *J. Chromatogr.* **1989,** *480,* 21–33.
(7) Giddings, J. C.; Caldwell, K. D.; Myers, M. N. *Macromolecules* **1976,** *9,* 106–112.
(8) Schimpf, M. E. *J. Chromatogr.* **1990,** *517,* 405–421.
(9) Giddings, J. C.; Yang, F. J.; Myers, M. N. *Anal. Chem.* **1976,** *48,* 1126–1132.
(10) Ratanathanawongs, S. K.; Giddings, J. C. In *Particle Size Distribution II: Assessment and Characterization*; Provder, T., Ed.; ACS Symposium Series 472; American Chemical Society: Washington, DC, 1991; Chapter 15, pp 229–246.

0003-2700/94/0366-4215$04.50/0 © 1994 American Chemical Society

or in other properties[11] (i.e., they exhibit higher selectivity). While this is desirable for accurate sample characterization,[12] it can lead to difficulties in the analysis of polydisperse materials. Conditions giving adequate retention and resolution of the smaller components result in excessive retention of the larger components. This problem is exacerbated for those subtechniques having the highest selectivity, such as sedimentation FFF (SdFFF). The selectivity of SdFFF is so high that the detectability of larger components is compromised by their elution over extended time intervals and their consequent dilution in the channel outlet stream.[13] These difficulties may be avoided by field programming whereby the field strength is reduced continuously during elution of the sample.[14,15] There are an infinite number of possible field decay programs but two have found most extensive use: the exponential decay of field strength with time[16–18] and the more recently introduced power law decay function known as the power program.[19]

The FFF of submicrometer particles is often approximated (see below) by equations that assume the particles to be point masses. The influence of a first-order correction for finite particle size on both retention time and resolution is examined here. The conditions assumed are not only those of constant field but also of exponential and power programmed field decay. It will be shown that simple limiting equations may be derived for retention and resolution that account for this first-order effect. In a future publication it will be shown how these limiting equations may be used to develop a systematic approach to selection of suitable instrumental conditions for the analysis of given samples.

The conditions for which higher order corrections are expected to become significant are discussed later. The phenomenon of secondary relaxation, associated with programmed field decay, is also considered.

NORMAL-MODE FFF

In the initial conception of FFF,[20] the nonuniformity in concentration across the channel, brought about by the action of the applied field, is countered by Fickian diffusion. If the particles or molecules are vanishingly small compared to the dimensions of the system, and there are no significant particle–particle or particle–wall interactions, then the concentration profile is described by the simple exponential function[1–4]

$$c(x) = c_0 \exp(-x/l) \tag{1}$$

where $c(x)$ is the concentration at distance x from the accumulation wall, c_0 is the concentration at the wall ($x = 0$), and l is a characteristic length parameter approximately equal to the mean thickness of the exponential layer. This exponential concentration profile adjacent to the wall characterizes the so-called *normal mode* of FFF. Since the highest concentration lies in the region next to the accumulation wall, where the fluid velocity approaches zero, the band migrates at a velocity slower than the mean fluid velocity with the result that it is retained relative to the carrier fluid. For the normal mode of elution, the ratio of band velocity $\mathcal{V}$ to mean fluid velocity $\langle v \rangle$, the retention ratio R, has been shown[21] to equal

$$R = \frac{\mathcal{V}}{\langle v \rangle} = 6\lambda(\coth(1/2\lambda) - 2\lambda) \tag{2}$$

where λ is the retention parameter defined as[2–4]

$$\lambda = l/w \tag{3}$$

where w is the thickness of the FFF channel. For strongly retained material, $\lambda \to 0$ and $\coth(1/2\lambda) \to 1$ so that eq 2 reduces to

$$R = 6\lambda(1 - 2\lambda) \tag{4}$$

which deviates from eq 2 by just −0.011% at $\lambda = 0.10$ and −0.36% at $\lambda = 0.15$. The good agreement of eq 4 with eq 2 for strong to quite moderate retention is due to the relatively fast convergence of $\coth(1/2\lambda)$ to unity (for example, $\coth(1/2\lambda) = 1.000\,091$ and $1.002\,549$ for $\lambda = 0.10$ and 0.15, respectively). Thus eq 4 is acceptably accurate for $R \leq 0.5$ or $\lambda \leq 0.1056$.

The field-induced migration toward the accumulation wall, countered by diffusion away from the wall, results in a continuous exchange of material between streamlines within the band thickness. Without this exchange the band would be smeared along the length of the channel by the sheared flow. Equation 1 strictly describes the equilibrium concentration profile, realized only when the carrier fluid is at rest. Channel flow causes the equilibrium to be upset as material at different distances from the wall is displaced at different rates.[22] This departure from equilibrium gives rise to *nonequilibrium band broadening*. In well-designed FFF systems, other contributions to band broadening are comparatively small whereas the nonequilibrium effect is an unavoidable consequence of elution.

Band broadening for FFF is often described in terms of the number N of theoretical plates and the theoretical plate height $H = L/N$, where L is the length of the channel. For normal-mode elution, nonequilibrium effects have been shown[23] to give

$$H = \chi w^2 \langle v \rangle / D \tag{5}$$

where D is the diffusion coefficient of the component and χ is the following function of λ

$$\chi = \frac{2\lambda}{(\coth(1/2\lambda) - 2\lambda)}[(336\lambda^4 + 24\lambda^2 - 1) - (120\lambda^3 - 6\lambda)\coth(1/2\lambda) - (12\lambda^2 - 1)\coth^2(1/2\lambda) - 6\lambda\coth^3(1/2\lambda)] \tag{6}$$

(11) Gunderson, J. J.; Giddings, J. C. *Anal. Chim. Acta* **1986**, *189*, 1–15.
(12) Giddings, J. C.; Williams, P. S. *Am. Lab.* **1993**, *25*, 88–95.
(13) Williams, P. S. In *Field-Flow Fractionation Handbook*; John Wiley: New York; Chapter 9, submitted for publication.
(14) Yang, F. J. F.; Myers, M. N.; Giddings, J. C. *Anal. Chem.* **1974**, *46*, 1924–1930.
(15) Giddings, J. C.; Caldwell, K. D. *Anal. Chem.* **1984**, *56*, 2093–2099.
(16) Yau, W. W.; Kirkland, J. J. *Sep. Sci. Technol.* **1981**, *16*, 577–605.
(17) Kirkland, J. J.; Rementer, S. W.; Yau, W. W. *Anal. Chem.* **1981**, *53*, 1730–1736.
(18) Giddings, J. C.; Williams, P. S.; Beckett, R. *Anal. Chem.* **1987**, *59*, 28–37.
(19) Williams, P. S.; Giddings, J. C. *Anal. Chem.* **1987**, *59*, 2038–2044.
(20) Giddings, J. C. *Sep. Sci.* **1966**, *1*, 123–125.
(21) Hovingh, M. E.; Thompson, G. E.; Giddings, J. C. *Anal. Chem.* **1970**, *42*, 195–203.
(22) Giddings, J. C. *J. Chem. Phys.* **1968**, *49*, 81–85.
(23) Giddings, J. C.; Yoon, Y. H.; Caldwell, K. D.; Myers, M. N.; Hovingh, M. E. *Sep. Sci.* **1975**, *10*, 447–460.

Equation 6 is exactly equivalent to an expression for χ published earlier[23] but is simpler. For small λ values, where $\coth(1/2\lambda) \rightarrow 1$, eq 6 reduces to

$$\chi = \frac{24\lambda^3(1 - 10\lambda + 28\lambda^2)}{(1 - 2\lambda)} \tag{7}$$

which deviates from eq 6 only by -0.11% at $\lambda = 0.10$ and by $+6.1\%$ at $\lambda = 0.15$. Equation 7, like eq 4, is therefore acceptably accurate for $R \leq 0.5$.

The materials studied by FFF are commonly polydisperse, and components are not therefore eluted as discrete peaks with breadths describable in terms of the number of theoretical plates. The resolution R_s of two discrete components, as defined for chromatographic separations, may be predicted, but this is not a useful quantity for describing the overall degree of separation for the continuum of components in a polydisperse material. Consequently a form of "specific resolution" called the *fractionating power* was introduced[18] to describe the separation of continuous size distributions. The particle diameter-based fractionating power F_d is defined by

$$F_d = \frac{R_s}{\delta d/d} = \frac{d}{4\sigma_t}\frac{\delta t_r}{\delta d} \tag{8}$$

where R_s is the resolution, $\delta t_r/4\sigma_t$, for particles differing in diameter by the small relative increment $\delta d/d$ and whose retention times differ by δt_r, and σ_t is the standard deviation in time units for particles of diameter d. In the limit of $\delta d \rightarrow 0$, eq 8 reduces to

$$F_d = \frac{d}{4\sigma_t}\frac{dt_r}{dd} \tag{9}$$

The diameter-based fractionating power is therefore a uniquely defined continuous function of d that is a measure of the relative resolving power of a system for particles of different sizes. Fractionating powers based on relative molecular or particle mass, density, or any other property influencing retention may be similarly defined.

For elution at constant channel flow rate and either a constant or programmed field, the retention time t_r of a component may be obtained by solving the integral equation[14]

$$t^0 = \int_0^{t_r} R\, dt \tag{10}$$

where t^0, the void time, is the time for elution of a nonretained material. The standard deviation in retention time due to nonequilibrium effects is given by[18]

$$\sigma_t = \frac{w}{D^{1/2}R_r}\left(\int_0^{t_r} \chi R\, dt\right)^{1/2} \tag{11}$$

where R_r is the value of the retention ratio at the time of elution (i.e., at time t_r). The determination of F_d, dependent on t_r (in the form of dt_r/dd) and σ_t, therefore requires knowledge of the variation of R and the product χR with time. Combining eqs 2 and 6 we find that

$$\chi R = 12\lambda^2[(336\lambda^4 + 24\lambda^2 - 1) - (120\lambda^3 - 6\lambda)\coth(1/2\lambda) - (12\lambda^2 - 1)\coth^2(1/2\lambda) - 6\lambda\coth^3(1/2\lambda)] \tag{12}$$

which, for $R \leq 0.5$ where $\coth(1/2\lambda) \rightarrow 1$, reduces to

$$\chi R = 144\lambda^4(1 - 10\lambda + 28\lambda^2) \tag{13}$$

Equation 13 deviates from eq 12 by -0.12% at $\lambda = 0.10$ and $+5.8\%$ at $\lambda = 0.15$.

An alternative exact expression for χR that is useful in certain instances, such as for the direct numerical solution of eq 11, is obtained by substituting for $\coth(1/2\lambda)$ in eq 12 using eq 2. The result may be written as

$$\chi R = \frac{(1 - R)R^2}{3} - 4(4R^2 - 5R + 3)\lambda^2 + 480(1 - R)\lambda^4 \tag{14}$$

The retention parameter λ is given by the general equation[2-4]

$$\lambda = D/|U|w \tag{15}$$

where U is the particle velocity induced by interaction with the applied field. Quantity D is given by the Stokes–Einstein equation

$$D = kT/3\pi\eta d \tag{16}$$

where k is the Boltzmann constant, T is the system temperature, η is the carrier fluid viscosity, and d is the hydrodynamic or Stokes particle diameter.

In the case of flow FFF (FlFFF), $|U|$ is simply the cross flow velocity, which is given by $\dot{V}_c/Lb$, where $\dot{V}_c$ is the volumetric cross flow rate, L is the channel length, and b the channel breadth. From eqs 15 and 16 we obtain for FlFFF the equation

$$\lambda = \frac{kTLb}{3\pi\eta w\dot{V}_c d} = \frac{kTV^0}{3\pi\eta w^2\dot{V}_c d} \tag{17}$$

where V^0 is the channel void volume that is equal to Lbw.

In the case of sedimentation FFF (SdFFF), $|U|$ is the sedimentation velocity and we obtain the following equation for λ

$$\lambda = 6kT/\pi|\Delta\varrho G|wd^3 \tag{18}$$

where d is here the equivalent spherical particle diameter. An expression for λ that is general to all field types (i.e., to all subtechniques of FFF) is given by[18]

$$\lambda = \Lambda/Swd^n \tag{19}$$

where Λ is a system constant, S is a quantitative measure of the field strength (always positive by convention), and the exponent n is determined by the field type (e.g., $n = 1$ for FlFFF and $n = 3$ for SdFFF). The dimensions of S are arbitrary; it is simply necessary that the corresponding dimensions of Λ yield a

dimensionless result for λ. Channel thickness w is retained in the denominator of eq 19 (rather than being incorporated within Λ) in order to retain consistency with the forms of eqs 3 and 15. The retention parameter λ is seen to be inversely dependent on field strength and is therefore time dependent during field decay programming.

Using the approximate eqs 4 and 13, expressions have been derived that allow determination of t_r and F_d as functions of d for normal-mode elution under constant field and under various programmed field decay conditions.[18,19,24] Relevant equations for constant field strength, and for the commonly used exponential and power programmed field decays, are given below. In the interests of generality, the solutions are given in terms of n, D, and λ_0, which is the value of λ at the initial field strength S_0 for programmed operation; constant field operation is assumed to be carried out at field strength S_0. The variations of t_r and F_d with d are then readily obtainable for any specific subtechnique.

Constant Field Strength. As mentioned above, we assume for convenience that a field strength equal to S_0 is used so that the retention parameter is equal to λ_0. The following equations will then be equally applicable to the elution of material during the initial constant field periods of the two field programs considered. At constant field strength, R is simply the ratio of void time to retention time, so that to a good approximation (for $R \leq 0.5$)

$$t_r^\dagger = \frac{t^0}{R} = \frac{t^0}{6\lambda_0(1 - 2\lambda_0)} \tag{20}$$

where the superscript † indicates a value predicted for purely normal-mode elution. The diameter-based fractionating power for normal-mode elution with $R \leq 0.5$ is given by[18]

$$F_d^\dagger = \frac{nD^{1/2}}{48w\lambda_0^{\,2}} \frac{\{t^0 - 12t_r^\dagger\lambda_0^{\,2}\}}{\{t_r^\dagger(1 - 10\lambda_0 + 28\lambda_0^{\,2})\}^{1/2}} \tag{21}$$

Because of the analytical solution that exists for $t_r^\dagger$ (given by eq 20), eq 21 may be expressed as

$$F_d^\dagger = \frac{n}{48w}\left(\frac{6Dt^0}{\lambda_0^{\,3}}\right)^{1/2} \frac{(1 - 4\lambda_0)}{(1 - 2\lambda_0)^{1/2}(1 - 10\lambda_0 + 28\lambda_0^{\,2})^{1/2}} \tag{22}$$

We see from eqs 19, 20, and 22 that for elution in the normal mode with $\lambda_0 \to 0$ (i.e., for strongly retained material), retention time increases with d^n and fractionating power increases with $d^{(3n-1)/2}$. It is this rapid increase of $t_r^\dagger$ with d, particularly in the case of SdFFF where $n = 3$, that renders constant field analysis of polydisperse materials impractical.

Exponential Field Decay. In this case, the field is held constant for a time t_1 at the initial strength S_0 after which it is reduced according to

$$S(t) = S_0 \exp(-(t - t_1)/\tau') \tag{23}$$

where $S(t)$ is the field strength at time t and τ' is the exponential decay constant. For material eluting in purely normal-mode conditions during field decay, it may be shown[18] that, based on the approximation of eq 4 for R, retention time is given by

$$t_r^\dagger = \tau' \ln\left(\frac{1}{2\lambda_0}[1 - B^{\dagger 1/2}]\right) + t_1 \tag{24}$$

where

$$B^\dagger = 1 - \frac{2t^0}{3\tau'} + 4\lambda_0\left(\frac{t_1}{\tau'} - 1\right) + 4\lambda_0^{\,2}\left(1 - \frac{2t_1}{\tau'}\right) \tag{25}$$

and, with the approximation of eq 13 for χR, the fractionating power is given by

$$F_d^\dagger = \frac{nD^{1/2}}{48w}\{t^0 - 12t_1\lambda_0^{\,2} - 6\tau'(\lambda_r^{\dagger 2} - \lambda_0^{\,2})\}\{t_1\lambda_0^{\,4}(1 - 10\lambda_0 + 28\lambda_0^{\,2}) + \tau'\lambda_r^{\dagger 4}(3 - 24\lambda_r^\dagger + 56\lambda_r^{\dagger 2})/12 - t_1\lambda_0^{\,4}(3 - 24\lambda_0 + 56\lambda_0^{\,2})/12\}^{-1/2} \tag{26}$$

where $\lambda_r^\dagger$ is the value of λ at time $t_r^\dagger$. Equations 24 and 26 are accurate for elution at $R \leq 0.5$, and since R increases during elution, it is required that $R_r \leq 0.5$.

For the special case of $t_1 = \tau'$, corresponding to the *time-delayed exponential* (TDE) program proposed by Kirkland and Yau,[16,17] and the neglect of the second-order term in λ_0 in $B^\dagger$, eq 24 reduces to

$$t_r^\dagger = \tau' \ln\left(\frac{e}{2\lambda_0}\left[1 - \left\{1 - \frac{2t^0}{3\tau'}\right\}^{1/2}\right]\right) \tag{27}$$

where e is the base for natural logarithms. The log-normal relationship between d and $t_r^\dagger$, characteristic of the TDE program, is apparent in this equation. Whether or not the true TDE program is used, some significant delay time t_1 is commonly employed. If this is so, we may assume that $\lambda_0 \ll 1$ for any material eluting during the field decay; otherwise this material would have eluted during the initial constant field period. Later eluting material will have $\lambda_0 \ll 1$ even if $t_1 = 0$. The assumption that $\lambda_0 \ll 1$ justifies the neglect of second-order terms in λ_0 to obtain eq 27. The same assumption also reduces eq 26 to

$$F_d^\dagger = \frac{nD^{1/2}}{24w\lambda_r^{\dagger 2}} \frac{\{t^0 - 6\tau'\lambda_r^{\dagger 2}\}}{\{\tau'(1 - 8\lambda_r^\dagger + (56/3)\lambda_r^{\dagger 2})\}^{1/2}} \tag{28}$$

For conditions of relatively slow field decay, consistent with high $F_d^\dagger$, all material will elute with $\lambda_r^\dagger \ll 1$, in which case it may be shown that eq 28 reduces to

$$F_d^\dagger = \frac{n(Dt^0)^{1/2}}{6w}\left(\frac{t^0}{\tau'}\right)^{1/2}\left[1 - \left\{1 - \frac{2t^0}{3\tau'}\right\}^{1/2}\right]^{-2} \tag{29}$$

From eq 29 it is seen that, for well-retained material eluting under exponential field decay, $F_d^\dagger \propto d^{-1/2}$ (via the reciprocal dependence of D on d shown by eq 16).

Power Programmed Field Decay. In this case, the field is again held constant for a time t_1 and then reduced according to

(24) Williams, P. S.; Giddings, J. C.; Beckett, R. *J. Liq. Chromatogr.* **1987**, *10*, 1961–1998.

the equation

$$S(t) = S_0\left(\frac{t_1 - t_a}{t - t_a}\right)^p \tag{30}$$

where t_a is a second time parameter that must be less than t_1 and is very commonly negative and p is a real power greater than zero. Unlike for the case of exponential decay, an exact analytical solution for t_r^+ may not be obtained for normal-mode elution under power programmed conditions with R approximated by eq 4. If second-order terms in λ are neglected in carrying out the integration of eq 10, it may be shown however that t_r^+ is given by the approximate equation

$$t_r^+ \approx (t_1 - t_a)\left\{\frac{(p+1)(t^0 - 6t_1\lambda_0)}{6(t_1 - t_a)\lambda_0} + 1\right\}^{1/(p+1)} + t_a \tag{31}$$

For the recommended[19] special relationship between t_1 and t_a given by $t_a = -pt_1$, eq 31 reduces to

$$t_r^+ \approx (p+1)t_1\{t^0/6t_1\lambda_0\}^{1/(p+1)} - pt_1 \tag{32}$$

The fractionating power for normal-mode elution is given by[19]

$$F_d^+ = \frac{nD^{1/2}}{48w}\left\{t^0 - 12t_1\lambda_0^2 - \frac{12}{(2p+1)}[(t_r^+ - t_a)\lambda_r^{+2} - (t_1 - t_a)\lambda_0^2]\right\}\left\{t_1\lambda_0^4[1 - 10\lambda_0 + 28\lambda_0^2] + (t_r^+ - t_a)\lambda_r^{+4}\left[\frac{1}{(4p+1)} - \frac{10\lambda_r^+}{(5p+1)} + \frac{28\lambda_r^{+2}}{(6p+1)}\right] - (t_1 - t_a)\lambda_0^4\left[\frac{1}{(4p+1)} - \frac{10\lambda_0}{(5p+1)} + \frac{28\lambda_0^2}{(6p+1)}\right]\right\}^{-1/2} \tag{33}$$

Again it is required that $R_r \leq 0.5$. If we now assume that $\lambda_0 \ll 1$, which, as discussed above, is a reasonable assumption when a significant constant field period t_1 is employed, and is a good assumption for well-retained material, then eq 33 reduces to

$$F_d^+ = \frac{nD^{1/2}}{48w\lambda_r^{+2}}\left\{t^0 - \frac{12}{(2p+1)}(t_r^+ - t_a)\lambda_r^{+2}\right\} \times \left\{(t_r^+ - t_a)\left[\frac{1}{(4p+1)} - \frac{10\lambda_r^+}{(5p+1)} + \frac{28\lambda_r^{+2}}{(6p+1)}\right]\right\}^{-1/2} \tag{34}$$

Under conditions of slow field decay, where we expect $\lambda_r^+ \ll 1$, eq 34 reduces still further. With substitution for t_r^+ using eq 31, the result may be written in the form

$$F_d^+ = \frac{n}{48w}\left\{\frac{6(4p+1)Dt^0}{(p+1)}\right\}^{1/2}\left[\frac{1}{\lambda_0}\left\{\frac{6(t_1 - t_a)}{(p+1)t^0}\right\}^p\right]^{3/[2(p+1)]} \tag{35}$$

Finally, we note that the term in the second set of parentheses in eq 35 may be reduced yet again for the special case of $t_a = -pt_1$. The desirable feature of the power program is realized when p is set equal to $(3n - 1)$ and F_d^+ consequently becomes independent of d.[19] Fractionating power may be arranged to gradually increase or decrease with the use of p smaller or larger than $(3n - 1)$, respectively. Exponential field decay is incapable of generating a constant F_d^+; it inevitably results in F_d^+ that varies with $d^{-1/2}$.[18,25]

FIRST-ORDER CORRECTIONS FOR FINITE PARTICLE SIZE

When a particle of finite size is driven toward the accumulation wall, the closest possible distance of approach of the particle center to the wall corresponds to its radius. Particles are therefore unable to sample streamlines that are within a radius of the wall—they are sterically excluded from the slowest streamlines. We therefore expect a perturbation of normal-mode elution toward slightly faster migration than predicted by eq 2. We shall see below how fractionating power is affected. This steric exclusion effect corresponds to the first-order correction considered here. Higher order corrections will be necessary under certain conditions, which will be discussed later.

Expressions for both R and χ that include corrections for steric exclusion have been derived by Giddings.[26] The steric corrected retention ratio is given by

$$R = 6\alpha(1 - \alpha) + R_c(1 - 2\alpha)^2 \tag{36}$$

where α is equal to $d/(2w)$ and R_c is a "core channel" retention ratio, applicable to the core region of the channel accessible to the particle center. R_c is given by eq 2 with λ replaced by $\lambda_c = \lambda/(1 - 2\alpha)$. (We use subscript c to denote core values, rather than superscript * as in the original publication,[26] in order to avoid confusion with quasi-equilibrium values of R and λ, which have also been denoted by superscript *.[27,28] It is important to establish this distinguishing symbology for the simultaneous consideration of both steric exclusion and secondary relaxation effects in programmed FFF.[13]) Therefore, substituting for R_c and λ_c in eq 36, we obtain

$$R = 6\alpha(1 - \alpha) + 6\lambda\left\{(1 - 2\alpha)\coth\left(\frac{1 - 2\alpha}{2\lambda}\right) - 2\lambda\right\} \tag{37}$$

When $\coth((1 - 2\alpha)/2\lambda) \rightarrow 1$—this function is close to unity for even quite moderate levels of retention—R reduces to

$$R = 6\alpha(1 - \alpha) + 6\lambda(1 - 2\alpha - 2\lambda) \tag{38}$$

For $R \leq 0.5$, eq 38 is an excellent approximation for eq 37; the approximation is better than that of eq 4 for eq 2 at equivalent levels of retention.

If the particles are small compared to the channel thickness (i.e., $\alpha \ll 1$), then eq 38 reduces to

$$R = 6\alpha + 6\lambda(1 - 2\lambda) \tag{39}$$

(25) Williams, P. S.; Giddings, J. C. *J. Chromatogr.* **1991**, *550*, 787–797.
(26) Giddings, J. C. *Sep. Sci. Technol.* **1978**, *13*, 241–254. Errata *Sep. Sci. Technol.* **1979**, *14*, 869–870.
(27) Giddings, J. C. *Anal. Chem.* **1986**, *58*, 735–740.
(28) Hansen, M. E.; Giddings, J. C.; Schure, M. R.; Beckett, R. *Anal. Chem.* **1988**, *60*, 1434–1442.

It is also apparent from the approach taken by Giddings[26] that

$$\chi R = \chi_c R_c (1 - 2\alpha)^6 \tag{40}$$

where χ_c is given by eq 6 with λ replaced by λ_c. It follows that

$$\chi R = 12\lambda^2\Big[\{336\lambda^4 + 24(1-2\alpha)^2\lambda^2 - (1-2\alpha)^4\} - \{120(1-2\alpha)\lambda^3 - 6(1-2\alpha)^3\lambda\}\coth\Big(\frac{1-2\alpha}{2\lambda}\Big) - \{12(1-2\alpha)^2\lambda^2 - (1-2\alpha)^4\}\coth^2\Big(\frac{1-2\alpha}{2\lambda}\Big) - 6(1-2\alpha)^3\lambda\coth^3\Big(\frac{1-2\alpha}{2\lambda}\Big)\Big] \tag{41}$$

which, for $R \leq 0.5$ (where $\coth((1-2\alpha)/2\lambda) \rightarrow 1$), reduces to

$$\chi R = 144\lambda^4((1-2\alpha)^2 - 10(1-2\alpha)\lambda + 28\lambda^2) \tag{42}$$

For particles that are small compared to channel thickness, this result approaches the normal-mode expression given by eq 13.

For elution under conditions of programmed field decay, a numerical approach is necessary to solve eq 10 for t_r for any given d. In practice, we may substitute eq 38 into eq 10, carry out the integration analytically, and solve numerically for t_r from the resultant expression. Differentiation of the resultant expression with respect to d gives an analytical expression for dt_r/dd, which may be evaluated by using the t_r solution obtained for the particular value of d. Similarly, eq 42 may be substituted into eq 11 and the integration carried out analytically. The value for σ_t may then be obtained for any given d and its retention time t_r. This approach yields accurate results for all particle diameters except those that are very weakly retained and was carried out successfully for our previously reported studies[18,19,24,25,29] where corrections for steric effects were not considered. When $t_1 > 0$, weakly retained material generally elutes under constant field conditions, and t_r and F_d may be obtained analytically via the accurate eqs 37 and 41. This approach was followed where necessary for the production of the computer-generated plots shown below.

Constant Field Strength. For elution at constant field strength S_0, the value for t_r, as mentioned above, may be determined without recourse to numerical methods. An approximate expression for t_r that is good for all but the most weakly retained components is obtained by consideration of eqs 10 and 38, and is given by

$$t_r = \frac{t^0}{R} = \frac{t^0}{6\alpha(1-\alpha) + 6\lambda_0(1-2\alpha-2\lambda_0)} \tag{43}$$

which for $\alpha \ll 1$ reduces to

$$t_r = \frac{t^0}{6\alpha + 6\lambda_0(1-2\lambda_0)} \tag{44}$$

Taking the approach of analytical integration using the approximate expressions 38 and 42, we obtain the following solution for F_d

$$F_d = \frac{nD^{1/2}}{48w}\{t^0 - 12t_r\lambda_0^2 - 6t_r\alpha(1-\alpha) - 6t_r(\alpha/n)(1-2\alpha-2\lambda_0)\}\{t_r\lambda_0^4((1-2\alpha)^2 - 10(1-2\alpha)\lambda_0 + 28\lambda_0^2)\}^{-1/2} \tag{45}$$

The form of eq 45 is directly comparable with the results given later for programmed operation and it is included for this reason. We may, however, substitute for t_r in eq 45 using eq 43 to obtain

$$F_d = \frac{n(6Dt^0)^{1/2}}{48w\lambda_0^2}\{\lambda_0(1-2\alpha-4\lambda_0) - (\alpha/n)\times (1-2\alpha-2\lambda_0)\}\{\alpha(1-\alpha) + \lambda_0(1-2\alpha-2\lambda_0)\}^{-1/2}\times \{(1-2\alpha)^2 - 10(1-2\alpha)\lambda_0 + 28\lambda_0^2\}^{-1/2} \tag{46}$$

When $\alpha \ll 1$, eq 45 reduces to

$$F_d = \frac{nD^{1/2}}{48w\lambda_0^2}\frac{\{t^0 - 12t_r\lambda_0^2 - 6t_r\alpha - 6t_r(\alpha/n)(1-2\lambda_0)\}}{\{t_r(1 - 10\lambda_0 + 28\lambda_0^2)\}^{1/2}} \tag{47}$$

which we may compare to eq 21 to obtain the following expression relating F_d to $F_d^\dagger$

$$F_d = F_d^\dagger\Big(\frac{t_r^\dagger}{t_r}\Big)^{1/2}\frac{\{t^0 - 12t_r\lambda_0^2 - 6t_r\alpha - 6t_r(\alpha/n)(1-2\lambda_0)\}}{\{t^0 - 12t_r^\dagger\lambda_0^2\}} \tag{48}$$

We see from eqs 20 and 44 that for small particles where $\lambda_0^2 \gg \alpha$ we expect $t_r \approx t_r^\dagger$, and eq 48 shows that under these conditions $F_d \approx F_d^\dagger$. If we consider progressively larger particles, α increases in proportion to d, while under constant field strength λ_0 decreases. In fact we would expect that ultimately $\lambda_0^2 \ll \alpha$. In addition, from eqs 20 and 44 it may be shown that

$$t_r/t_r^\dagger = 1 - 6t_r\alpha/t^0 \tag{49}$$

If we substitute for $t_r^\dagger/t_r$ in eq 48 using eq 49, and assume that terms in λ_0^2 and $\alpha\lambda_0$ are relatively small and may be neglected (there will be some cancellation of error in their removal), then the result for significant steric perturbation to isocratic elution is given by

$$F_d \approx F_d^\dagger\frac{\{1 - 6(1+1/n)t_r\alpha/t^0\}}{\{1 - 6t_r\alpha/t^0\}^{1/2}} \tag{50}$$

If we now consider material that elutes well before the steric foldback, then we may assume that $t_r\alpha/t^0$ is small compared to unity. It follows that

$$F_d \approx F_d^\dagger\Big\{1 - 3\frac{t_r\alpha}{t^0}\Big(1 + \frac{2}{n}\Big)\Big\} \tag{51}$$

(29) Williams, P. S.; Kellner, L.; Beckett, R.; Giddings, J. C. *Analyst (London)* **1988**, *113*, 1253–1259.

This equation shows that, for any positive value for n, F_d is reduced by the steric perturbation and furthermore that the degree of reduction increases with d and t_r. We also know that F_d must fall to zero at the point of steric inversion. The fall to zero is better described by eq 50 than by eq 51, although due to higher order perturbations, we cannot expect eq 50 or 43 to yield accurate predictions very close to the inversion point. The latter point will be discussed later.

Exponential Field Decay. Substituting for R in eq 10 using eq 38, and accounting for the time dependence of λ via consideration of eqs 19 and 23, we may carry out the integration and obtain the following equation in t_r

$$t_r = \tau' \ln\left(\frac{1}{2\lambda_0}[1 - 2\alpha - B^{1/2}]\right) + t_1 \tag{52}$$

where

$$B = (1 - 2\alpha)^2 - \frac{2(t^0 - 6t_r\alpha(1 - \alpha))}{3\tau'} + 4\lambda_0(1 - 2\alpha)\left(\frac{t_1}{\tau'} - 1\right) + 4\lambda_0^2\left(1 - \frac{2t_1}{\tau'}\right) \tag{53}$$

A numerical approach is required to solve for t_r because of its occurrence in the B term. If we consider the special case of the TDE program, and assume that $\alpha \ll 1$ and $\lambda_0 \ll 1$, then eq 52 reduces to

$$t_r = \tau' \ln\left(\frac{e}{2\lambda_0}\left[1 - \left\{1 - \frac{2(t^0 - 6t_r\alpha)}{3\tau'}\right\}^{1/2}\right]\right) \tag{54}$$

The fractionating power, based on consideration of eqs 38 and 42, is given by

$$F_d = \frac{nD^{1/2}}{48w}\{t^0 - 12t_1\lambda_0^2 - 6\tau'(\lambda_r^2 - \lambda_0^2) - 6t_r\alpha(1 - \alpha) + 6(\alpha/n)[2\tau'(\lambda_r - \lambda_0) - t_r(1 - 2\alpha) + 2t_1\lambda_0]\}\{t_1\lambda_0^4((1 - 2\alpha)^2 - 10(1 - 2\alpha)\lambda_0 + 28\lambda_0^2) + \tau'\lambda_r^4(3(1 - 2\alpha)^2 - 24(1 - 2\alpha)\lambda_r + 56\lambda_r^2)/12 - \tau'\lambda_0^4(3(1 - 2\alpha)^2 - 24(1 - 2\alpha)\lambda_0 + 56\lambda_0^2)/12\}^{-1/2} \tag{55}$$

where it is assumed that t_r is obtained numerically as explained and λ_r is the retention parameter at time t_r. For the assumptions of $\alpha \ll 1$ and $\lambda_0 \ll 1$, eq 55 reduces to

$$F_d = \frac{nD^{1/2}}{24w\lambda_r^2}\frac{\{t^0 - 6\tau'\lambda_r^2 - 6t_r\alpha(1 + 1/n) + 12\tau'\alpha\lambda_r/n\}}{\{\tau'(1 - 8\lambda_r + (56/3)\lambda_r^2)\}^{1/2}} \tag{56}$$

We may now carry out a comparison with the result for unperturbed normal-mode elution given by eq 28. Again, we would expect a certain amount of error cancellation to obtain the approximate relationship for well-retained material (i.e., $R_r \leq 0.5$)

$$F_d \approx F_d^\dagger(\lambda_r^\dagger/\lambda_r)^2\{1 - 6(1 + 1/n)t_r\alpha/t^0\} \tag{57}$$

From eqs 27 and 54 we see that for TDE programming

$$\frac{\lambda_r^\dagger}{\lambda_r} = \frac{1 - \{1 - 2t^0/3\tau'\}^{1/2}}{1 - \{1 - 2(t^0 - 6t_r\alpha)/3\tau'\}^{1/2}} \approx \frac{1}{1 - 6t_r\alpha/t^0} \tag{58}$$

The approximations of eqs 57 and 58 improve as the rate of field decay is reduced (i.e., as τ' is increased), resulting in smaller λ_r and $\lambda_r^\dagger$. Substituting eq 58 into eq 57 yields the following approximate relationship

$$F_d \approx F_d^\dagger\frac{\{1 - 6(1 + 1/n)t_r\alpha/t^0\}}{\{1 - 6t_r\alpha/t^0\}^2} \tag{59}$$

For material eluting well before the steric foldback we have $t_r\alpha/t^0 \ll 1$ and eq 59 reduces to

$$F_d \approx F_d^\dagger\left\{1 + 6\frac{t_r\alpha}{t^0}\left(1 - \frac{1}{n}\right)\right\} \tag{60}$$

Considering such material eluting well before the steric foldback we see that for FlFFF ($n = 1$) the fractionating power for any particle size is unaffected (at least to a good approximation) by the steric effect, but for SdFFF ($n = 3$) F_d is predicted to increase relative to $F_d^\dagger$. However, irrespective of the value of n, as the foldback is approached then the fractionating power must fall to zero. This trend is indeed predicted by eq 59, which we can expect to be valid for higher $t_r\alpha/t^0$ than the more approximate eq 60.

Power Programmed Field Decay. An approximate expression for t_r may be obtained by carrying out the integration of eq 10 with R given by $6(\alpha + \lambda)$. Second-order terms in λ are thereby neglected and at the same time it is assumed that $\alpha \ll 1$. The result may be rearranged to the form

$$t_r \approx (t_1 - t_a)\left\{\frac{(p + 1)(t^0 - 6t_r\alpha - 6t_1\lambda_0)}{6(t_1 - t_a)\lambda_0} + 1\right\}^{1/(p+1)} + t_a \tag{61}$$

which, for the special case of $t_a = -pt_1$, reduces to

$$t_r \approx (p + 1)t_1\left\{\frac{t^0 - 6t_r\alpha}{6t_1\lambda_0}\right\}^{1/(p+1)} - pt_1 \tag{62}$$

Equations 61 and 62 require numerical solution for retention time t_r.

The fractionating power, based on consideration of eqs 38 and 42, is given by

$$F_d = \frac{nD^{1/2}}{48w}\left\{t^0 - 12t_1\lambda_0^2 - \frac{12}{(2p+1)}[(t_r - t_a)\lambda_r^2 - (t_1 - t_a)\lambda_0^2] - 6t_r\alpha(1-\alpha) + \frac{6\alpha}{n}\left[\frac{2}{(p+1)}((t_r - t_a)\lambda_r - (t_1 - t_a)\lambda_0) - t_r(1-2\alpha) + 2t_1\lambda_0\right]\right\}\left\{t_1\lambda_0^4((1-2\alpha)^2 - 10(1-2\alpha)\lambda_0 + 28\lambda_0^2) + (t_r - t_a)\lambda_r^4\left[\frac{(1-2\alpha)^2}{(4p+1)} - \frac{10(1-2\alpha)\lambda_r}{(5p+1)} + \frac{28\lambda_r^2}{(6p+1)}\right] - (t_1 - t_a)\lambda_0^4\left[\frac{(1-2\alpha)^2}{(4p+1)} - \frac{10(1-2\alpha)\lambda_0}{(5p+1)} + \frac{28\lambda_0^2}{(6p+1)}\right]\right\}^{-1/2} \quad (63)$$

and, for the assumptions of $\alpha \ll 1$ and $\lambda_0 \ll 1$, eq 63 reduces to

$$F_d = \frac{nD^{1/2}}{48w\lambda_r^2}\left\{t^0 - \frac{12}{(2p+1)}(t_r - t_a)\lambda_r^2 - 6(1+1/n)t_r\alpha + \frac{12}{n(p+1)}(t_r - t_a)\alpha\lambda_r\right\}\left\{(t_r - t_a)\left[\frac{1}{(4p+1)} - \frac{10\lambda_r}{(5p+1)} + \frac{28\lambda_r^2}{(6p+1)}\right]\right\}^{-1/2} \quad (64)$$

A comparison of eq 64 with the unperturbed normal-mode result of eq 34 yields the approximate relationship for well-retained material (i.e., $R_r \leq 0.5$)

$$F_d \approx F_d^\dagger\left(\frac{\lambda_r^\dagger}{\lambda_r}\right)^2\left(\frac{t_r^\dagger - t_a}{t_r - t_a}\right)^{1/2}\{1 - 6(1+1/n)t_r\alpha/t^0\} \quad (65)$$

and consideration of eqs 19 and 30 allows us to write eq 65 in the form

$$F_d \approx F_d^\dagger\left(\frac{t_r^\dagger - t_a}{t_r - t_a}\right)^{(4p+1)/2}\{1 - 6(1+1/n)t_r\alpha/t^0\} \quad (66)$$

For the recommended relationship of $t_a = -pt_1$, eqs 32 and 62 show that

$$\left(\frac{t_r^\dagger - t_a}{t_r - t_a}\right) = \{1 - 6t_r\alpha/t^0\}^{-1/(p+1)} \quad (67)$$

It follows that F_d is related to $F_d^\dagger$ by the approximate equation

$$F_d \approx F_d^\dagger\frac{\{1 - 6(1+1/n)t_r\alpha/t^0\}}{\{1 - 6t_r\alpha/t^0\}^{(4p+1)/(2p+2)}} \quad (68)$$

We can restrict consideration once again to material eluting well before foldback to obtain

$$F_d \approx F_d^\dagger\frac{\{1 - 6(1+1/n)t_r\alpha/t^0\}}{\{1 - (3(4p+1)/(p+1))t_r\alpha/t^0\}} \quad (69)$$

If we now consider the special case of $p = (3n - 1)$, which for unperturbed normal-mode elution results in constant F_d, we obtain

$$F_d \approx F_d^\dagger\left\{1 + 6\frac{t_r\alpha}{t^0}\left(1 - \frac{3}{2n}\right)\right\} \quad (70)$$

Comparing this with eq 60, we see that we have a slightly different effect predicted for power programmed field decay than for exponential field decay. SdFFF ($n = 3$) is again predicted to exhibit an increased F_d, but FlFFF ($n = 1$) is predicted to exhibit a reduced F_d compared to unperturbed normal-mode elution. As the steric inversion point is approached then F_d must dip toward zero, and this trend is again correctly predicted by eq 68.

RETENTION TIME IN THE REGION OF STERIC INVERSION

The phenomenon of steric inversion or foldback has been discussed by Giddings and co-workers.[30-33] A qualitative explanation of the effect may be obtained by examination of eqs 38 and 39. We see that the retention ratio is given as the sum of two terms, the first of which increases with particle diameter while the second decreases due to the inverse dependence of λ on d^n. When elution is predominantly in the normal mode, the second term dominates while the first term serves as a steric correction, accounting for the finite size of the particles. For larger particles, the first term increases in significance while the second term becomes smaller. Ultimately, the first term dominates and the retention ratio is predicted to increase with particle size. This behavior corresponds to elution in the steric mode. The point of reversal in the order of elution is known as the steric inversion or steric foldback point. The position d_i of the inversion point on the diameter scale is dependent on experimental conditions. Consideration of eq 39 shows that d_i may be reduced by increasing the field strength. This has the effect of reducing λ and hence reducing the contribution of the second term, thereby allowing the retention behavior described by the first term to dominate sooner. Conversely, the foldback may be shifted to a larger d_i by reducing the field strength.

The retention ratio is not well described by the eqs 37–39 in the region of steric foldback and beyond. In the steric mode where particles are so large that $\lambda \to 0$, the following expression for retention ratio has been used[34,35]

$$R = 6\gamma\alpha \quad (71)$$

where γ is an empirical correction factor that increases with channel flow rate and decreases with increase of field strength.

(30) Myers, M. N.; Giddings, J. C. *Anal. Chem.* **1982**, *54*, 2284–2289.
(31) Lee, S.; Giddings, J. C. *Anal. Chem.* **1988**, *60*, 2328–2333.
(32) Moon, M. H.; Giddings, J. C. *Anal. Chem.* **1992**, *64*, 3029–3037.
(33) Giddings, J. C. *Analyst (London)* **1993**, *118*, 1487–1494.
(34) Giddings, J. C.; Myers, M. N.; Caldwell, K. D.; Pav, J. W. *J. Chromatogr.* **1979**, *185*, 261–271.
(35) Caldwell, K. D.; Nguyen, T. T.; Myers, M. N.; Giddings, J. C. *Sep. Sci. Technol.* **1979**, *14*, 935–946.

This γ factor also has a strong dependence on d. In the case of SdFFF, γ tends to decrease with increase of d, but in flow FFF, the tendency of γ is to first increase with d to some maximum and then to decrease.[36]

There has been some success in explaining these dependencies of γ in terms of the combined effects of hydrodynamic lift forces that act on particles and the expected retardation of particles relative to the confined flow of the carrier fluid.[37-39] While these effects are likely to extend to smaller particles eluting in the normal mode, their influence on mean particle migration velocity for a diffuse layer will be more complicated than for the steric mode. For normal-mode elution, these effects will contribute to higher order perturbations (see later), which will be the subject of a future study. In this work we confine our attention to a first-order size correction, and while we appreciate that under certain experimental conditions there may be significant deviation, this approach allows us to identify the principal effects of field strength, channel flow rate, programming rate, and so on, on retention time, fractionating power, and steric inversion.

In the region of steric inversion, α and λ have comparable magnitude (see below) and when $\alpha \ll 1$ the first order corrected R is given by

$$R = 6\alpha + 6\lambda \tag{72}$$

The steric foldback, by definition, corresponds to the point where $dt_r/dd = 0$. From the definition of F_d (eq 9) we see that at this point fractionating power also falls to zero. When R is assumed to be given by eq 72, it may be shown for both constant field and programmed field operation that

$$t^0/6(n+1) = t_{ri}\alpha_i/n \tag{73}$$

where the subscript i signifies the inversion or foldback point. This simple equation reveals the fundamental relationship between experimental parameters and the foldback point. The requirements for shifting foldback to higher or lower diameter are apparent. For example, if S_0 for a programmed run is held constant but program time constants are increased relative to t^0 (which may be accomplished by simply increasing the time constants and/or increasing $\dot{V}$), then t_r/t^0 will increase for all d. The increase in t_{ri} will not be fully in proportion to the time constants as is the case for pure normal-mode elution, but to satisfy eq 73, α_i must decrease (i.e., foldback would be shifted to smaller d). An increase in field strength for constant field runs would have a similar effect.

The quantitative shift in predicted inversion point brought about by changes in $\dot{V}$, S_0, and program time constants may be derived for each of the considered situations as given below.

Constant Field Strength. From consideration of eq 73 in conjunction with eq 72 at the point of inversion it may be shown that

$$t^0/6(n+1) = t_{ri}\lambda_{0i} \tag{74}$$

where at a constant field strength of S_0, the retention parameter for a particle of inversion diameter d_i is represented as λ_{0i}. From eqs 73 and 74 it follows that

$$\alpha_i = n\lambda_{0i} \tag{75}$$

and if we substitute for λ_{0i} using eq 19, the result may be rearranged to the form

$$d_i = (2n\Lambda/S_0)^{1/(n+1)} \tag{76}$$

The inversion diameter d_i is therefore seen to be inversely dependent on $S_0^{1/(n+1)}$. The known dependence of d_i on channel flow rate[32-35] is due to higher order effects.

Exponential Field Decay. We can substitute for R in eq 10 using eq 39 and carry out the integration for exponential field decay. The result may be differentiated with respect to d and the differential equated to zero for the point of inversion. The final result, with the aid of eq 73, reduces to the following simple form

$$t^0/6(n+1) \approx \tau'\lambda_{ri} + (t_1 - \tau')\lambda_{0i} \tag{77}$$

Terms in λ_0 will tend to be small and, in fact, cancel for the TDE case of $t_1 = \tau'$. From eqs 19, 73, and 77 we obtain

$$d_i \approx \left(\frac{2n\Lambda}{S_0}\frac{\tau'}{t_{ri}}\right)^{1/(n+1)} \exp\left(\frac{t_{ri} - t_1}{(n+1)\tau'}\right) \tag{78}$$

and substituting for t_{ri} using eq 73 and rearranging yields

$$\ln\left(\frac{S_0 w d_i^n}{6(n+1)\Lambda}\frac{t^0}{\tau'}\right) \approx \frac{nw}{3(n+1)d_i}\frac{t^0}{\tau'} - \frac{t_1}{\tau'} \tag{79}$$

For the special case of TDE programming where $t_1 = \tau'$, eq 79 reduces to

$$\ln\left(\frac{eS_0 w d_i^n}{6(n+1)\Lambda}\frac{t^0}{t_1}\right) \approx \frac{nw}{3(n+1)d_i}\frac{t^0}{t_1} \tag{80}$$

Equations 79 and 80 require numerical solution for d_i, given S_0, t_1, τ', and so on. Alternatively, eq 80 may be numerically solved for t_1 (equal to τ'), given S_0 and other parameters, together with some required d_i. Again, we expect a channel flow rate dependence for d_i due to higher order effects, over and above that predicted by eqs 79 and 80.

Power Programmed Decay. The procedure carried out for exponential field decay can be repeated for power programming. The result may be written in the form

$$\frac{t^0}{6(n+1)} \approx \frac{(t_{ri} - t_a)}{(p+1)}\lambda_{ri} + \frac{(pt_1 + t_a)}{(p+1)}\lambda_{0i} \tag{81}$$

(36) Giddings, J. C.; Chen, X.; Wahlund, K.-G.; Myers, M. N. *Anal. Chem.* **1987**, *59*, 1957–1962.
(37) Williams, P. S.; Koch, T.; Giddings, J. C. *Chem. Eng. Commun.* **1992**, *111*, 121–147.
(38) Williams, P. S.; Lee, S.; Giddings, J. C. *Chem. Eng. Commun.*, in press.
(39) Williams, P. S.; Moon, M. H.; Giddings, J. C. In *Particle Size Analysis*; Stanley-Wood, N. G., Lines, R. W., Eds.; Royal Society of Chemistry: Cambridge, UK, 1992; pp 280–289.

In this case terms in λ_0 cancel when at $t_1 = -t_a/p$, but tend to be small in any case. From eqs 19, 73, and 81 we obtain the relationship

$$d_i \approx \left(\frac{2n\Lambda}{S_0}\frac{(t_{ri}-t_a)}{(p+1)t_{ri}}\right)^{1/(n+1)}\left(\frac{t_{ri}-t_a}{t_1-t_a}\right)^{p/(n+1)} \quad (82)$$

Substituting for t_{ri} using eq 73 and rearranging yields

$$\left(\frac{S_0 w d_i^n}{6(n+1)\Lambda}\frac{t^0}{t_1}\right)^{1/(p+1)} \approx \frac{nw}{3(n+1)d_i}\frac{t^0}{(p+1)t_1} + \frac{p}{(p+1)} \quad (83)$$

where the recommended relationship $t_1 = -t_a/p$ is assumed to have been set. This assumption is made here in the interests of brevity. Equation 83 is then directly comparable to eq 80, which holds for the special case of TDE programming. Numerical solution for d_i, given S_0, t_1, and so on, is likewise required here. Alternatively, eq 83 may be solved for t_1 and hence t_a given S_0 and some required d_i.

ILLUSTRATIVE EXAMPLES

The influence of the correction for steric exclusion on retention time and fractionating power may be explained most effectively with the aid of computer-generated plots of predicted values as functions of d for typical experimental conditions. We shall consider typical channel dimensions for SdFFF of $L = 90$ cm, $b = 2$ cm, and $w = 0.025$ cm, giving a void volume $V^0 = 4.5$ mL. For FlFFF the dimensions are $L = 30$ cm, $b = 2$ cm, $w = 0.025$ cm, and $V^0 = 1.5$ mL. We can fix a common inversion point as follows. We set d_i arbitrarily at 1.0 μm. If we consider a channel flow rate $\dot{V}$ of 4.5 mL/min for the SdFFF system so that $t^0 = 1.0$ min, then eq 73 (with $n = 3$) indicates that $t_{ri} = 62.5$ min. To obtain the same d_i and t_{ri} with the FlFFF system (for which $n = 1$), a t^0 of 1.5 min is required, and this indicates a required $\dot{V}$ of 1.0 mL/min. The setting of $\dot{V}$ to 4.5 mL/min for SdFFF and to 1.0 mL/min for FlFFF is not sufficient in itself to fix the inversion point (i.e., both d_i and t_{ri}), but if field conditions (amounting to either the constant field strength or the initial field strength and program time constants) are arranged such that $d_i = 1.0$ μm, then it will follow that $t_{ri} = 62.5$ min.

In addition to these dimensions and channel flow rates, we use a system temperature $T = 298$ K, a carrier fluid viscosity $\eta = 0.01$ P, and in the case of SdFFF, a particle–carrier density difference $\Delta\varrho = 1.5$ g/mL.

Constant Field Strength. Figure 1 shows the results of calculations for constant field SdFFF at a field strength G_0 of 3.20 gravities and $\Delta\varrho = 1.5$ g/mL. This field strength, required to obtain $d_i = 1.0$ μm and therefore $t_{ri} = 62.5$ min, is determined using eq 76. The $t_r^\dagger$ and $F_d^\dagger$ curves are seen to increase with d^3 and d^4, respectively. The steric corrected t_r curve falls below the $t_r^\dagger$ curve, showing the faster elution predicted when steric effects are taken into account (see eq 49). The t_r curve passes through a maximum at $d = 1.0$ μm, at precisely the point where the F_d curve falls to zero. Also included in the figure are plots of the approximate eqs 50 and 51 for F_d. Equation 50 is seen to be an excellent approximation for F_d for the conditions considered, while eq 51 is acceptable only for relatively small steric perturbation.

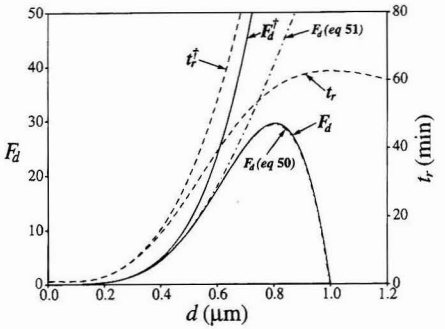


Figure 1. Fractionating power and retention time as functions of d for constant field SdFFF. Channel dimensions: $L = 90$ cm, $b = 2$ cm, $w = 0.025$ cm, and $V^0 = 4.5$ mL. Other parameters: $\dot{V} = 4.5$ mL/min, $G_0 = 3.20$ gravities, $\Delta\varrho = 1.5$ g/mL, $T = 298$ K, and $\eta = 0.01$ P.

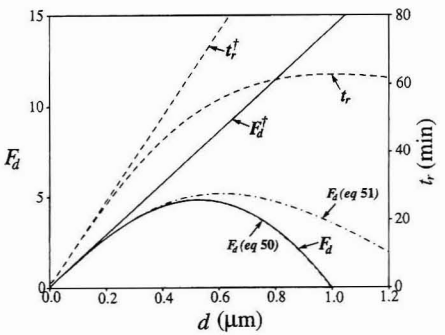


Figure 2. Fractionating power and retention time as functions of d for constant field FlFFF. Channel dimensions: $L = 30$ cm, $b = 2$ cm, $w = 0.025$ cm, and $V^0 = 1.5$ mL. Other parameters: $\dot{V} = 1.0$ mL/min, $\dot{V}_{c0} = 0.314$ mL/min, $T = 298$ K, and $\eta = 0.01$ P.

Results of calculations for constant field FlFFF with $\dot{V}_{c0} = 0.314$ mL/min are shown in Figure 2. The required $\dot{V}_{c0}$ to set d_i at 1.0 μm was obtained using eq 76. For FlFFF, both $t_r^\dagger$ and $F_d^\dagger$ are seen to increase linearly with d. The steric corrected t_r and F_d curves fall below the $t_r^\dagger$ and $F_d^\dagger$ curves, respectively, their deviation increasing with d. The t_r curve passes through a maximum of ~62.5 min at $d = 1.0$ μm as expected, at which point F_d falls to zero. Again the approximate eq 50 for F_d is seen to behave excellently for these conditions, while eq 51 is acceptable only for relatively small steric perturbation. It is interesting to note in comparing Figures 1 and 2 that, for comparable analysis times in isocratic operation, F_d for FlFFF does not rise to such high levels as for SdFFF. However, an acceptable level of F_d is predicted for a wider range of d for FlFFF than for SdFFF.

Exponential Field Decay. Figure 3 shows calculated retention time and fractionating power curves as functions of d for TDE field programmed SdFFF. Channel dimensions and flow rate were assumed to be the same as for Figure 1. A relatively high G_0 of 1000 gravities was arbitrarily assumed, and the delay time t_1 and decay constant τ' were set to 7.00 min in order to set d_i at 1.0 μm in a time of 62.5 min. The appropriate program time constants were obtained by numerical solution of eq 80. Following an initial

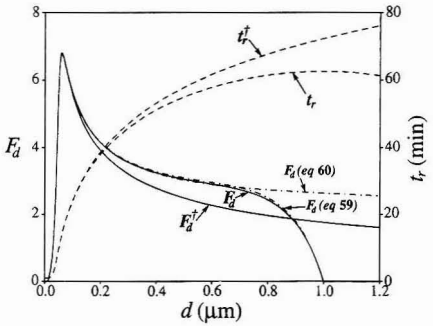


Figure 3. Fractionating power and retention time as functions of d for exponential decay programmed field strength in SdFFF: G_0 = 1000 gravities, t_1 = 7.00 min, and τ' = 7.00 min. Other parameters as for Figure 1.

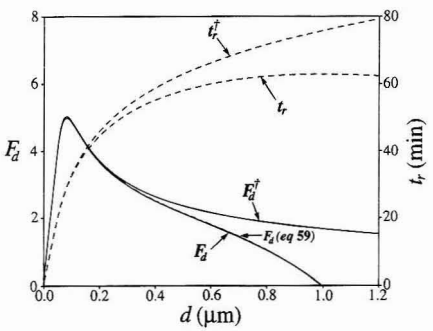


Figure 4. Fractionating power and retention time as functions of d for exponential decay programmed cross flow rate in FlFFF: $\dot{V}_{c0}$ = 1.0 mL/min, t_1 = 18.6 min, and τ' = 18.6 min. Other parameters as for Figure 2.

steep rise, $F_d^\dagger$ decreases according to its dependence on $d^{-1/2}$ (see eq 29). In the case of SdFFF, F_d is at first seen to fall less quickly than $F_d^\dagger$, but ultimately drops to zero at the inversion point. The result is that $F_d > F_d^\dagger$ over a wide range of d, as predicted by eq 60 for $n > 1$. Equation 59 is an excellent approximation for F_d for the conditions considered, and even eq 60 behaves well until the inversion point is quite closely approached. For example, particles corresponding to $d = 0.75$ μm are predicted to elute at ~97% of the projected inversion time, at which point eq 60 overestimates F_d by only 5%.

The results of calculations for TDE programmed cross flow in FlFFF are shown in Figure 4. Channel dimensions and channel flow rate correspond to the values assumed for Figure 2. Initial cross flow rate $\dot{V}_{c0}$ was arbitrarily set at 1.0 mL/min, and t_1 and τ' were set to 18.6 min to again set d_i at 1.0 μm in a time of 62.5 min. These time constants were again obtained by numerical solution of eq 80. In the case of FlFFF, eq 60 does not yield a useful approximation to F_d, the result not differing from $F_d^\dagger$, and it is not therefore included in the figure. Once again, however, eq 59 shows excellent behavior for the considered conditions. Unlike in the case of SdFFF, the fractionating power in TDE programmed FlFFF is seen to be reduced by the steric perturbation for all d eluting before inversion, and F_d tends to fall more rapidly than with $d^{-1/2}$.

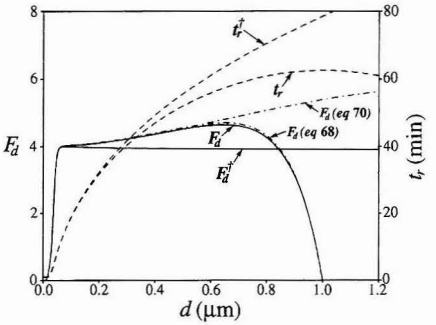


Figure 5. Fractionating power and retention time as functions of d for power programmed field decay in SdFFF: G_0 = 1000 gravities, p = 8, t_1 = 4.16 min, and t_a = −33.28 min. Other parameters as for Figure 1.

The initial rapid rise followed by a decay in both F_d and $F_d^\dagger$ is unavoidable with the use of the exponential field decay program. It has been shown[18] that the initial rise may be attenuated to a certain extent when t_1 is reduced relative to τ'. Nothing may be done to influence the later variation of fractionating power with d however.

Power Programmed Field Decay. Calculated retention times and fractionating powers are shown in Figure 5 for power programmed field decay in SdFFF. Channel dimensions and flow rate correspond to values assumed for Figure 1. An initial field strength G_0 of 1000 gravities was assumed (as for the TDE programming example of Figure 3), together with p = 8, t_1 = 4.16 min, and t_a = −33.28 min in order to set d_i at 1.0 μm in a time of 62.5 min (obtained by numerical solution of eq 83 with n = 3 and p = 8). Following the initial rise, F_d is seen to continue to increase with d. The calculated F_d curve is thus elevated relative to the almost constant $F_d^\dagger$ curve (expected for p = 8 in SdFFF), with the elevation being fairly well described by eq 70 until the inversion is quite closely approached. In this case, particles corresponding to $d = 0.75$ μm are predicted to elute at ~96% of the projected inversion time, at which point eq 70 overestimates F_d by ~10%. Equation 68 is seen to yield an excellent approximation for F_d for the conditions considered.

The corresponding results for power programmed FlFFF are shown in Figure 6. Channel dimensions and channel flow rate were fixed at the values assumed for Figure 2. An initial cross flow rate $\dot{V}_{c0}$ of 1.0 mL/min was assumed (as for the TDE example of Figure 4), together with p = 2, t_1 = 10.37 min, and t_a = −20.74 min to set d_i at 1.0 μm in a time of 62.5 min (obtained by numerical solution of eq 83 with n = 1, and p = 2). The $F_d^\dagger$ curve is seen to approach an almost constant level, as expected for power programming of cross flow with p = 2 in FlFFF. Equation 68 is again seen to yield an excellent approximation for steric-corrected F_d for the conditions considered, while eq 70 is apparently less useful for prediction of F_d in FlFFF than in SdFFF. Finally, the fractionating power is seen to be reduced by steric perturbation for all d eluting before inversion. This behavior is quite different to that predicted for SdFFF. In the case of FlFFF with p = 2, following the initial rise F_d is seen to decrease with increase of d.

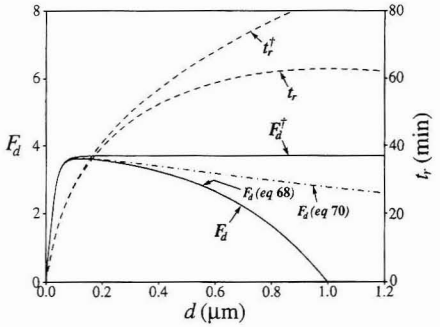


Figure 6. Fractionating power and retention time as functions of d for power programmed cross flow decay in FlFFF: V_{c0} = 1.0 mL/min, p = 2, t_1 = 10.37 min, and t_a = −20.74 min. Other parameters as for Figure 2.

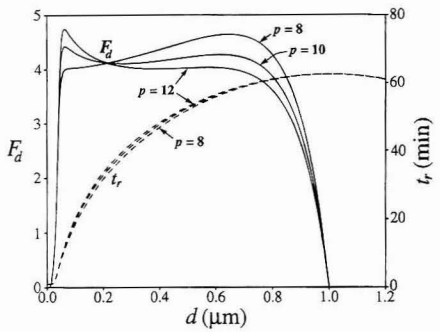


Figure 7. Fractionating power and retention time as functions of d for power programmed field decay in SdFFF. Three examples correspond to the following: p = 8, t_1 = 4.16 min, t_a = −33.28 min; p = 10, t_1 = 4.63 min, t_a = −46.33 min; and p = 12, t_1 = 4.97 min, t_a = −59.68 min. Other parameters as for Figure 5.

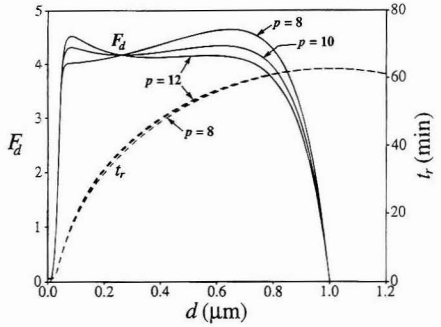


Figure 8. Fractionating power and retention time as functions of d for power programmed field decay in SdFFF. Three examples correspond to the following: p = 8, t_1 = 4.16 min, t_a = −33.28 min; p = 10. t_1 = 4.03 min, t_a = −47.58 min; and p = 12, t_1 = 3.91 min, t_a = −62.17 min. Other parameters as for Figure 5.

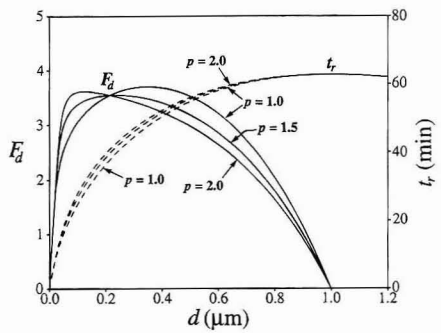


Figure 9. Fractionating power and retention time as functions of d for power programmed cross flow decay in FlFFF. Three examples correspond to the following: p = 2.0, t_1 = 10.37 min, t_a = −20.74 min; p = 1.5, t_1 = 8.56 min, t_a = −12.84 min; and p = 1.0, t_1 = 5.88 min, t_a = −5.88 min. Other parameters as for Figure 6.

It was mentioned above that, in the case of exponential field decay programming, once conditions are arranged for the fractionation of some range of d, little can be done to alter the relative variation of F_d with d over this range. The power program offers an additional degree of freedom, however; the power p influences the relative variation of F_d with d. It has been shown[19] that when $p < 3n - 1$ then $F_d^\dagger$ increases with d and when $p > 3n - 1$ then $F_d^\dagger$ decreases with increase in d. For SdFFF, the use of $p > 8$ might therefore be expected to yield a more uniform F_d over the diameter range of interest. Figure 7 shows the results of calculations of F_d and t_r for p = 8, 10, and 12. In each case, $t_1 = -t_a/p$ and the particular time constants required for use with each p were obtained by solution of eq 83. The parameters for p = 8 are identical to those used for Figure 5. For p = 10, the parameters were t_1 = 4.63 min and t_a = −46.33 min, while for p = 12, they were t_1 = 4.97 min and t_a = −59.68 min. For this example, the predicted F_d is seen to be more uniform when p = 10. A further improvement can be achieved by relaxing the $t_1 = -t_a/p$ relationship. The parameters for the plots shown in Figure 8 were obtained by equating $F_d^\dagger$ for the three programs at d = 0.06 μm (an arbitrary small diameter where $F_d \approx F_d^\dagger$) and hence solving for $(t_1 - t_a)$ via eq 35. Equation 82 was then solved for $(t_{ri} - t_a)$ with d_i = 1.0 μm and hence for t_a in each case. For p = 10, the parameters obtained were t_1 = 4.03 min, t_a = −47.58 min, and for p = 12, the parameters were t_1 = 3.91 min and t_a = −62.17 min.

For the FlFFF case, alternative powers of 1.5 and 1.0 were examined. The results for p = 2, t_1 = 10.37 min, t_a = −20.74 min; p = 1.5, t_1 = 8.56 min, t_a = −12.84 min; and p = 1.0, t_1 = 5.88 min, t_a = −5.88 min are shown in Figure 9. For this particular example, the optimum power appears to be in the region of 1.5.

HIGHER ORDER PERTURBATIONS

Higher order perturbations encompass particle−particle and particle−wall interactions[40-42] as well as various hydrodynamic effects. At low ionic strengths of carrier fluids, both particle−particle and particle−wall interactions tend to be repulsive in nature, causing early elution of material. The repulsion may be confined to shorter range, and the perturbation to retention

(40) Hansen, M. E.; Giddings, J. C.; Beckett, R. *J. Colloid Interface Sci.* **1989**, *132*, 300−312.
(41) Hansen, M. E.; Giddings, J. C. *Anal. Chem.* **1989**, *61*, 811−819.
(42) Mori, Y.; Kimura, K.; Tanigaki, M. *Anal. Chem.* **1990**, *62*, 2668−2672.

reduced, with increase of ionic strength. Too high an ionic strength may induce wall adhesion or particle aggregation, however, which must be avoided. The composition of the wall must be considered along with that of the carrier since the properties of both influence particle–wall interaction.[41] When compositions have been optimized as far as possible, additional advantage may be found in modifying the method used for initial sample relaxation.

During elution, the tendency for wall adhesion is offset to some extent by the hydrodynamic lift forces described below. The risk of adhesion is therefore greatest during a procedure known as stop-flow relaxation. This procedure is often carried out immediately following sample introduction to the channel inlet. Its purpose is to allow the sample components to approach their equilibrium concentration profiles before elution takes place. The stopping of channel flow for a suitable period avoids the excessive band broadening that would occur if particles were allowed to relax across the fast flowing streamlines near the channel center plane. The risk of adhesion would be especially great for programmed runs where a relatively high initial field strength is employed. Methods of non-stop-flow relaxation using reduced thickness (pinched) inlet regions[54,55] or hydrodynamic relaxation[56–58] have been developed to eliminate the inconvenience and time taken for stop-flow relaxation. These methods also have the advantage of retaining hydrodynamic lift during relaxation, which reduces the tendency for wall adhesion.

Particle–particle interaction gives rise to what is essentially a sample overloading effect. The resultant perturbation to retention may often be reduced to insignificant levels simply by decreasing sample concentration and/or size. There are also certain hydrodynamic interactions that occur between particles within concentrated suspensions undergoing sheared flow.[43–45] There is the potential for an overloading phenomenon in these cases too, but their effect has not been observed under typical conditions of FFF elution.

Finally we consider the extension of the hydrodynamic effects that give rise to the mechanism of steric migration into the regime of smaller particles migrating in the normal mode. It is known that a particle of finite size entrained in sheared flow close to a wall migrates at a velocity that is slightly retarded relative to the undisturbed streamline at the position of the particle center.[46] The channel flow is also known to give rise to hydrodynamic lift forces[37,38,47–53] that increase with flow rate and tend to drive particles away from the accumulation wall. Both the retardation effect and, to a lesser extent, the lift forces attenuate quickly as a particle moves from the close vicinity of the wall however. It is apparent that high channel flow rates should be avoided if lift forces are not to greatly disturb the particle concentration profile within the channel. At the same time, if the retardation effect is not to have a significant influence on mean particle migration velocity, then the equilibrium layer thickness must be large relative to particle radius. For material eluting close to the steric inversion point this will not be possible, and in the case of programmed field decay, a significant range of particle sizes eluting before steric inversion may start their migration effectively in the steric mode under the high initial field strength conditions.

SECONDARY RELAXATION EFFECTS

Under conditions of programmed field decay, the effects of secondary relaxation on retention time and fractionating power must be considered. The decay of field strength brings about a continuous change in concentration profile for each sample component. Due to the finite time required for relaxation, the profile for each component tends to lag behind the equilibrium profile corresponding to instantaneous field strength. The process also leads to a distortion of the profile. The change in concentration profile to accommodate a change in field strength during elution is referred to as *secondary relaxation* to distinguish it from the *primary relaxation* that occurs at the inlet of the channel.

A solution for the gradual change in band velocity in response to a step change in field strength has been obtained by Yau and Kirkland,[59] the determination of velocity at arbitrary time following the step change requiring the evaluation of nested sums of infinite series. They applied the approach to exponential field decay and determined the expected perturbation in retention time for certain examples. Such an approach does not lead in an obvious way to a method of predicting those conditions for which secondary relaxation effects will be significant. Based on an approximate perturbation to concentration profile derived by Giddings[27] for small departures from equilibrium, Hansen et al.[28] obtained a relatively simple solution for perturbed retention time under conditions of exponential field decay. Neither approach took steric perturbations into account. The latter approach does however indicate that, for small departures from equilibrium, the relative error in d incurred in data reduction by ignoring secondary relaxation varies with $1/(F_d^*)^2$.[60] This proportionality holds for both power programmed and exponential field decay. It is therefore a simple matter to impose restrictions on conditions consistent with some F_d^* for some relatively small or negligible error in d.

A more thorough treatment of secondary relaxation including its effect on F_d will be the topic of a future publication.

CONCLUSIONS

From the foregoing discussion we conclude that, provided (1) the compositions of the carrier fluid and channel wall are optimized, (2) channel flow rates are not too high, and (3) in the case of programmed field decay, fractionating powers are not too low, then the first-order correction for finite particle size is acceptable for particulate material eluting before, and not close to, steric inversion. The derived equations, in particular the limiting forms for fractionating power, may therefore be used as a basis for the development of a systematic optimization strategy

(43) Eckstein, E. C.; Bailey, D. G.; Shapiro, A. H. *J. Fluid Mech.* **1977**, *79*, 191–208.
(44) Leighton, D.; Acrivos, A. *J. Fluid Mech.* **1987**, *177*, 109–131.
(45) Leighton, D.; Acrivos, A. *J. Fluid Mech.* **1987**, *181*, 415–439.
(46) Goldman, A. J.; Cox, R. G.; Brenner, H. *Chem. Eng. Sci.* **1967**, *22*, 653–660.
(47) Segré, G.; Silberberg, A. *Nature* **1961**, *189*, 209–210.
(48) Segré, G.; Silberberg, A. *J. Fluid Mech.* **1962**, *14*, 115–135.
(49) Segré, G.; Silberberg, A. *J. Fluid Mech.* **1962**, *14*, 136–157.
(50) Cox, R. G.; Brenner, H. *Chem. Eng. Sci.* **1968**, *23*, 147–173.
(51) Ho, B. P.; Leal, L. G. *J. Fluid Mech.* **1974**, *65*, 365–400.
(52) Vasseur, P.; Cox, R. G. *J. Fluid Mech.* **1976**, *78*, 385–413.
(53) Cox, R. G.; Hsu, S. K. *Int. J. Multiphase Flow* **1977**, *3*, 201–222.
(54) Giddings, J. C. *Sep. Sci. Technol.* **1989**, *24*, 755–768.
(55) Moon, M. H.; Myers, M. N.; Giddings, J. C. *J. Chromatogr.* **1990**, *517*, 423–433.
(56) Lee, S.; Myers, M. N.; Giddings, J. C. *Anal. Chem.* **1989**, *61*, 2439–2444.
(57) Giddings, J. C. *Anal. Chem.* **1990**, *62*, 2306–2312.
(58) Liu, M.-K.; Williams, P. S.; Myers, M. N.; Giddings, J. C. *Anal. Chem.* **1991**, *63*, 2115–2122.
(59) Yau, W. W.; Kirkland, J. J. *Anal. Chem.* **1984**, *56*, 1461–1466.
(60) Williams, P. S., unpublished work.

for selection of operating conditions for particle size analysis by FFF. This will be the subject of a future study.

ACKNOWLEDGMENT

This work was supported by Public Health Service Grant GM10851-36 from the National Institutes of Health.

SYMBOLS

b	channel breadth
B	quantity defined by eq 53
$B^\dagger$	quantity defined by eq 25
$c(x)$	concentration as a function of x
c_0	concentration at accumulation wall
d	particle diameter
d_i	inversion particle diameter
D	diffusion coefficient
e	base for natural logarithms
F_d	diameter-based fractionating power defined by eqs 8 and 9
$F_d^\dagger$	fractionating power unperturbed by steric effects
G	sedimentation field strength (acceleration)
G_0	initial sedimentation field strength
H	theoretical plate height
k	Boltzmann's constant
l	mean layer thickness
L	channel length
n	power dependence of λ on d; see eq 19
p	power program parameter; see eq 30
R	retention ratio
R_c	core channel retention ratio
R_r	retention ratio at time t_r
R_s	resolution
S	quantitative measure of field strength
S_d	diameter-based selectivity
S_0	constant or initial field strength
t	time
t_a	time parameter of power program; see eq 30
t_r	retention time
t_{ri}	time to point of inversion
$t_r^\dagger$	retention time if unperturbed by steric effects
t^0	void time
t_1	delay time before onset of field decay; see eqs 23 and 30
T	system temperature
U	field-induced velocity of particle
$\langle v \rangle$	mean carrier fluid velocity
$\mathcal{V}$	band velocity
V^0	channel void volume
$\dot{V}$	channel flow rate
$\dot{V}_c$	cross flow rate
$\dot{V}_{c0}$	initial cross flow rate
w	channel thickness
x	distance from accumulation wall, measured across channel thickness
α	ratio of $d/(2w)$
α_i	ratio of $d_i/(2w)$
γ	steric correction factor; see eq 71
δd	small difference in d
δt_r	small difference in t_r corresponding to δd
$\Delta\varrho$	particle−carrier fluid density difference
η	carrier fluid viscosity
λ	retention parameter $(=l/w)$
λ_c	core channel value of λ $(=\lambda/(1-2\alpha))$
λ_r	value of λ at time t_r
$\lambda_r^\dagger$	value of λ at time $t_r^\dagger$
λ_0	value of λ at field strength S_0
λ_{0i}	value of λ_0 for particle of diameter d_i
Λ	system parameter; see eq 19
σ_t	standard deviation in retention time
τ'	exponential field decay constant; see eq 23
χ	function of λ defined by eq 6
χ_c	core channel value of χ

Received for review June 15, 1994. Accepted September 14, 1994.[⊗]

[⊗] Abstract published in *Advance ACS Abstracts*, October 15, 1994.

Anal. Chem. **1994,** *66,* 4229–4235

Chemometric Optimization of Azide Sensitivity in Reversed-Phase Ion-Interaction HPLC

E. Marengo, M. C. Gennaro,* C. Abrigo, and A. Dinardo

Dipartimento di Chimica Analitica, Università di Torino Via P. Giuria, 5, 10125 Torino, Italy

An optimization study of sensitivity was performed in the determination of azide by reversed-phase ion-interaction HPLC. Sensitivity was optimized as a function of ion-interaction reagent concentration, ion-interaction reagent chain length, and mobile phase flow rate. Different series of experiments were performed in which each new series was planned on the basis of the results of the previous one. The model included square and cubic terms and second-order interactions. An ordinary least-squares (OLS) method was used as the regression method, and the all-model search was applied. The Fisher *F* test and R^2 values were used to estimate the regression model quality. The model proposed contains five parameters and explains 98.21% of the variation in the data about the mean sensitivity. Chromatography under the improved experimental conditions predicted by the model gave a detection limit for sodium azide of 6.0 ppb.

Sodium azide, widely used in the past as a biostatic and antimicrobial agent, has been recently recognized as a cancer-causing agent.[1,2] Some analytical methods for its determination were recently proposed.[1,3–10] An HPLC method recently developed in this laboratory[10] using reversed-phase ion-interaction chromatography made possible the selective determination of azide in the presence of many interferents (such as acetate, carbonate, chloride, fluoride, sulfite, hydrazine, hydroxylamine, nitrate, bromide, iodide, sulfide, thiocyanate, and nitrite). With octylamine orthophosphate (pH 6.4) as the interaction reagent and spectrophotometric detection at 230 nm, detection levels as low as 30 ppb were achieved. During this investigation,[10] it became apparent that the sensitivity depends on several experimental factors: the ion-interaction reagent concentration, the chain length of the alkylammonium ion of the ion-interaction reagent, and the mobile phase flow rate.

The present paper is devoted to an optimization study of the sensitivity of the analysis, as a function of these factors, by the use of chemometric methods.

The literature reports some examples[11–15] of optimization methods in ion-interaction or in ion-pair chromatography. They generally explore the possibility of correlation between capacity factor and the different factors, with predictive aims or for the optimization of resolution.[15] No example has been presented, to our knowledge, concerning optimization of sensitivity for these systems.

In the present study, the factor space was spanned by a grid of experiments. Due to the unpredictable behavior of sensitivity and the possibile existence of multiple sets of locally optimum experimental conditions, different series of experiments in the variable space were performed, in which each new series was planned on the basis of the results previously obtained.

EXPERIMENTAL SECTION

Apparatus. Analyses were carried out with a Merck-Hitachi Lichograph chromatograph Model L-6200 (Tokyo, Japan), equipped with a two-channel Model D-2500 Chromato-integrator, interfaced with a UV/visible detector Model L-4200 and a L-3720 conductivity detector from the same firm.

A Metrohom 654 pH meter equipped with a combined glass–calomel electrode was employed for pH measurements, and a Hitachi (Tokyo, Japan) Model 150-20 spectrophotometer was used for absorbance measurements.

Chemical and Reagents. Ultrapure water from a Millipore Milli-Q purification system (Milford, MA) was used for the preparation of solutions. Hexylamine, heptylamine, octylamine, and sodium azide were Fluka analytical grade chemicals. Orthophosphoric acid and other reagents were Carlo Erba analytical grade chemicals.

Chromatographic Conditions. A 5 μm ODS-2 Spherisorb Phase Separation column fully end-capped and with a carbon load of 12% (0.5 mmol/g) was used, together with a guard precolumn Lichrospher RP-18 (5 μm).

The solutions to be used as the mobile phase were prepared by adding to the weighed amount of the amine (to prepare the prefixed concentration value) the amount of orthophosphoric acid required to obtain the pH value of 6.4 ± 0.2. The chromatographic system was conditioned by passing the eluent through the column

(1) Mackie, H.; Speciale, S. L.; Throop, J.; Yang, T. *J. Chromatogr.* **1982**, *242*, 177–180.
(2) Loprieno, N. In *Mutagenesi Ambientale, Quaderni di Biologia*, 2nd ed.; Piccin, Ed.; Padova-Roma-Milano, Italy, 1987; p 68.
(3) Kubaszewski, E.; Kurzawa, Z.; Lozynski, M. *Anal. Chim. Acta* **1987**, *196*, 267–270.
(4) Vàcha, J.; Tkaczykovà, M.; Rejholcovà, M. *J. Chromatogr.* **1989**, *488*, 506–508.
(5) Hassan, S. S. M.; Ahmed, M. A.; Marzouk, S. A. M.; Elnemma, E. M. *Anal. Chem.* **1991**, *63*, 1547–1552.
(6) Terpinski, E. A. *Analyst* **1985**, *110*, 1403–1404.
(7) Anton, A.; Dodd, J. G.; Harvey, A. E., Jr. *Anal. Chem.* **1960**, *32*, 1209–1210.
(8) Roberson, C. E.; Austin, C. M. *Anal. Chem.* **1957**, *29*, 854–855.
(9) Schilt, A. A.; Sutherland, J. W. *Anal. Chem.* **1964**, *36*, 1805–1807.
(10) Gennaro, M. C.; Abrigo, C.; Marengo, E.; Liberatori, A. *J. Liq. Chromatogr.* **1993**, *16*, 2715–2730.
(11) Shelver, W. L.; Rosenberg, H.; Shelver, W. H. *J. Liq. Chromatogr.* **1991**, *14*, 2119–2129.
(12) Coenegracht, P. M. J.; Van Tuyen, N.; Metting, H. J.; Coene-Gracht-Lamers, P. J. M. *J. Chromatogr.* **1987**, *389*, 351–367.
(13) Bartha, A.; Vigh, G. *J. Chromatogr.* **1989**, *485*, 383–401.
(14) Bartha, A.; Vigh, G.; Stahlberg, J. *J. Chromatogr.* **1989**, *485*, 403–419.
(15) Marengo, E.; Gennaro, M. C.; Abrigo, C. *Anal. Chem.* **1992**, *64*, 1885–1893.

0003-2700/94/0366-4229$04.50/0 © 1994 American Chemical Society

Table 1. Experiments as a Function of (a) Ion-Interaction Reagent Alkylammonium Chain Length (n = 6, 7, 8), (b) Ion-Interaction Reagent Concentration, and (c) Flow Rate[a]

no.	alkyl chain length	concn (mM)	flow rate (mL/min)	sensitivity	retention time (min)
1	6	2.50	0.70	16	6.20
2	6	5.00	0.70	16	7.30
3	6	7.50	0.70	19	7.04
4	6	8.25	0.70	19	6.70
5	6	9.37	0.70	16	6.98
6	6	2.50	1.00	13	4.34
7	6	5.00	1.00	10	5.05
8	6	7.50	1.00	13	4.91
9	6	8.25	1.00	10	4.68
10	6	9.37	1.00	10	4.87
11	6	2.50	1.30	10	3.34
12	6	5.00	1.30	9	3.87
13	6	7.50	1.30	10	3.77
14	6	8.25	1.30	8	3.60
15	6	9.37	1.30	8	3.70
16	7	2.50	0.70	20	12.00
17	7	7.50	0.70	23	12.40
18	7	10.00	0.70	44	13.00
19	7	12.50	0.70	18	12.00
20	7	15.00	0.70	17	9.90
21	7	2.50	1.00	13	8.60
22	7	7.50	1.00	13	8.60
23	7	10.00	1.00	37	9.00
24	7	12.50	1.00	13	8.10
25	7	15.00	1.00	16	7.20
26	7	2.50	1.30	10	6.57
27	7	5.00	1.30	11	6.75
28	7	7.50	1.30	13	6.50
29	7	10.00	1.30	34	6.80
30	7	12.50	1.30	12	6.18
31	7	15.00	1.30	10	5.29
32	8	7.50	0.70	18	13.37
33	8	10.00	0.70	17	15.00
34	8	12.50	0.70	26	14.04
35	8	15.00	0.70	21	12.20
36	8	20.00	0.70	21	11.89
37	8	7.50	1.00	18	9.30
38	8	10.00	1.00	15	9.62
39	8	12.50	1.00	13	9.70
40	8	15.00	1.00	11	8.54
41	8	20.00	1.00	19	8.35
42	8	7.50	1.30	14	7.03
43	8	10.00	1.30	14	8.70
44	8	12.50	1.30	15	7.46
45	8	15.00	1.30	16	6.82
46	8	20.00	1.30	14	6.35

[a] Sensitivity is expressed as peak area integrator units $\times 10^3$.

Table 2. Heptylammonium Orthophosphate: Sensitivity (Integrator Units $\times 10^3$) as a Function of Ion-Interaction Reagent Concentration and Flow Rate

flow rate (mL/min)	ion-interaction concn[a] (mM) 2.50	5.00	7.50	8.75	9.37	10.00	11.25	12.50	15.00
0.70	20		23	27*		44*		18*	17
0.85					33*		55*		
1.00	13		13	17*		37*		13*	16
1.15					25*		46*		
1.30	10	11	13	14*		34*		12*	10

[a] The asterisks indicates the experiments that were in the optimal region.

until a stable baseline signal was obtained; a minimum of 1 h was necessary. Between the uses of different mobile phases and after use, the stationary phase was washed and regenerated by flowing

Table 3. Azide Sensitivity: Comparison of Experimental, Calculated, and Predicted Data[a]

	data responses exptl	calcd	pred
1	27	25	23
2	17	20	21
3	14	14	14
4	44	44	45
5	37	39	40
6	34	34	33
7	18	20	21
8	13	14	15
9	12	9	6
10	33	30	30
11	25	25	25
12	55	53	51
13	46	47	49

[a] Calculated data are the responses predicted by using all data points in the model calculation. Predicted data are the responses calculated in cross-validation by using the model obtained and excluding the particular data point for which prediction is being made.

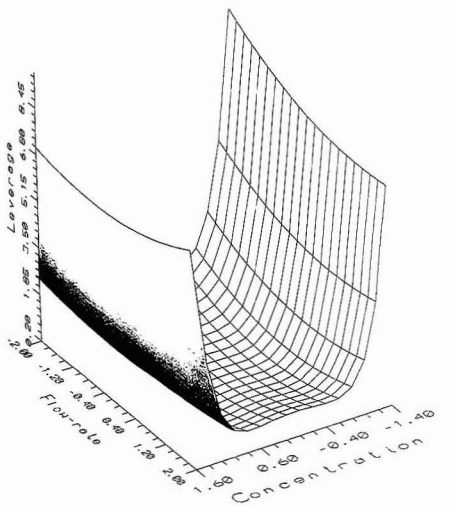


Figure 1. Leverage contour plot in the range-scaled space as a function of concentration and flow rate outside the coded boundary. Heptylammonium orthophosphate as the interaction reagent.

water (1.0 mL/min for 15 min), a 50/50 (v/v) water/methanol mixture (1.0 mL/min for 15 min), and then methanol (1.0 mL/min for 5 min).

RESULTS AND DISCUSSION

Chromatographic Technique. The technique of ion-interaction reversed-phase HPLC already used in this laboratory[10,15,16] for separations of anions and amines makes use of a reversed-phase C-18 stationary phase. The interaction reagent is an alkylammonium salt and represents the only component of the mobile phase which, flowing under isocratic conditions, is assumed to determine a modification of the stationary phase surface. The lipophilic alkylammonium ion and its anion are adsorbed as

(16) Gennaro, M. C.; Bertolo, P. L. *J. Liq. Chromatogr.* **1990**, *13*, 2059–2075.

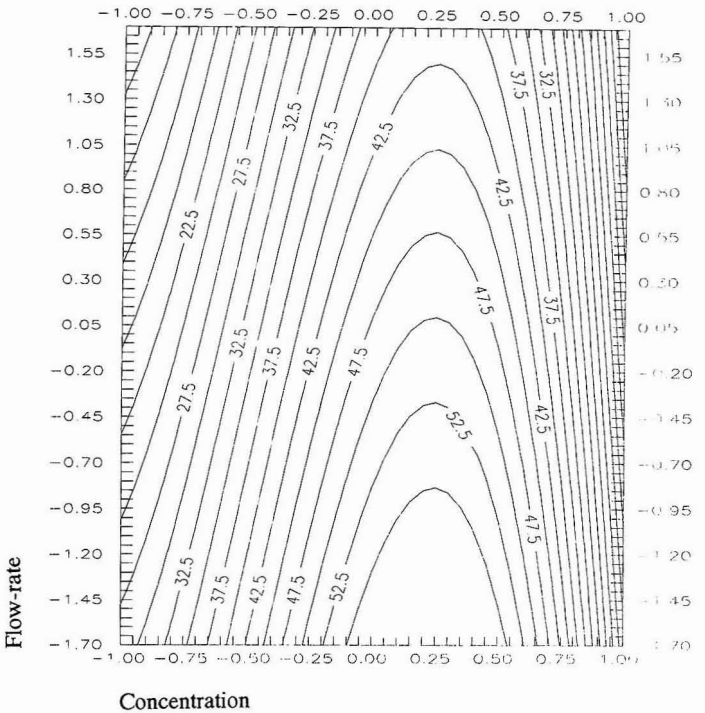


Figure 2. Predicted sensitivity contour plot as a function of flow rate and ion-interaction concentration (range-scaled units). Heptylammonium orthophosphate as the interaction reagent.

ion pairs onto the stationary phase surface, through adsorption and electrostatic forces.[17,18] The original reversed-phase stationary phase is modified into a new stationary phase able to retain both anions and cations through the adsorption onto the stationary-phase surface of new ion pairs, respectively formed with the alkylammonium ion and the anion of the interaction reagent.

The quantitative determination of sodium azide was performed in the previous work by the use of 5.0 mM octylammonium orthophosphate as the interaction reagent at pH 6.4, at which azide is predominantly present as hydrazoate anion N_3^- ($pK_a = 4.74$). Through spectrophotometric detection at 230 nm ($\epsilon = 1190 \pm 6$ L mol^{-1} cm^{-1}), a detection level of 30 ppb was obtained through experimental optimization.

In the present paper, the dependence of sensitivity on the ion-interaction reagent concentration, alkyl chain length, and mobile-phase flow rate was investigated. Sensitivity was measured as the area of the chromatographic peak (as calculated by the integrator) which corresponds to the standardized concentration of 1.0 ppm.

Planning of the Experiments. Hexyl-, heptyl-, and octylammonium ($n = 6$, 7, and 8) orthophosphate were used as the interaction reagents. The mobile-phase flow rates (ranging between 0.7 and 1.3) were sampled in order to guarantee acceptable analysis times.

The variable space was spanned by a grid of experiments. The starting configuration of experiments for each chain length of the interaction reagent was chosen on the basis of the already published results.[10] Each successive series of proofs was selected on the basis of the previous results by extrapolating in the direction of increasing sensitivity until no further improvement was achieved.

All the experimental data obtained for sensitivity and retention time during this explorative phase are listed in Table 1, which shows that a change in sensitivity is taking place along the different ion-interaction reagents as a function of chain length. It can be observed that the best sensitivities are achieved in a narrow region of flow rate and concentration for the heptylammonium salt as the interaction reagent. This result confirms our previous findings in ion-interaction chromatographic studies, in which with heptylammonium orthophosphate highest sensitivities were obtained[19,20] with respect to both hexylammonium and octylammonium orthophosphate.

While the increased sensitivity correlated to flow rate decrease can be considered an expected result,[21] it is difficult to explain the observed strong change of sensitivity correlated with a narrow change of concentration.

(17) Stahlberg, J. *J. Chromatogr.* **1986**, *356*, 231–245.
(18) Bidlingmeyer, B. A. *J. Chromatogr. Sci.* **1980**, *18*, 525–539.
(19) Gennaro, M. C.; Bertolo, P. L. *J. Chromatog.* **1989**, *472*, 433–440.
(20) Gennaro, M. C.; Bertolo, P. L.; Baldo, M. A.; Daniele, S.; Mazzocchin, G. A. *J. Liq. Chromatogr.* **1991**, *472*, 115–138.
(21) Synder, L. R.; Kirkland, J. J. *Introduction to Modern Liquid Chromatography*, 2nd ed.; Wiley-Interscience: New York, 1979.

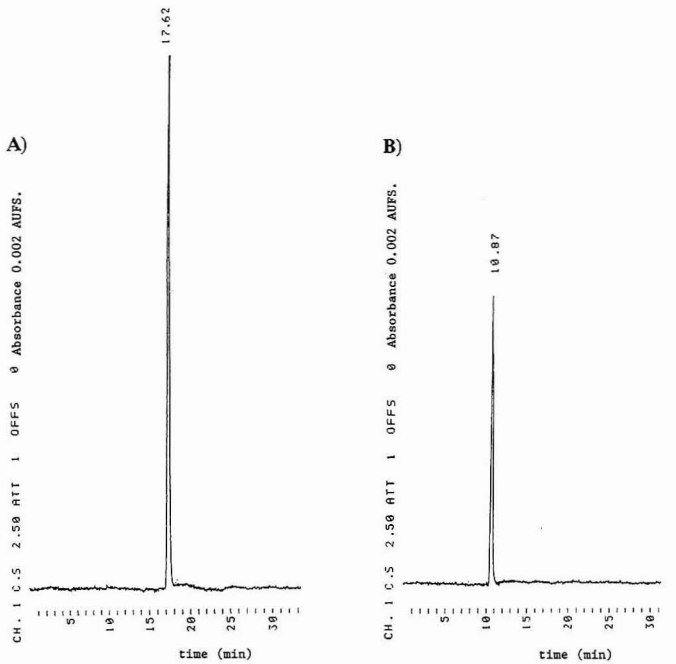


Figure 3. Comparison between the sensitivity obtained in the optimized conditions (A) and the best sensitivity (B) obtained before optimization. Chromatographic conditions: stationary phase, phase separation ODS-2, 250 × 4.6 mm, 5 μm, end-capped; spectrophotometric detection, 230 nm; 100 μL injected. Ion-interaction reagent: (A) 11.075 mM heptylammonium orthophosphate; flow rate 0.49 mL/min. (B) 11.250 mM heptylammonium orthophosphate; flow rate 0.85 mL/min.

Also when hexylammonium and octylammonium orthophosphate are used as the interaction reagents, narrow regions of concentration can be envisaged in which sensitivity increases. The variations are not as large as for heptylammonium salt, and moreover, the maximum of sensitivity is much smaller.

A series of measurements were therefore performed with heptylammonium orthophosphate, which provided the maximum sensitivity.

The starting set of experiments was executed, for three different flow rates (0.7, 1.0, and 1.3 mL/min), at varying concentrations of the ion-interaction reagent (2.5, 5.0, 7.5, 10.0, 12.5, and 15.0 mM; Table 2), in order to explore the concentration range and to define the region of interest. The values of sensitivity at concentrations of 7.5, 10.0, and 12.5 mM suggest that the optimum could be achieved between 7.5 and 10.0 mM; therefore, experiments at concentrations of 8.75 an 9.37 mM (Table 2) were performed to investigate this experimental region.

These experiments, however, did not provide any sensitivity improvement. Further experiments at an ion-interaction reagent concentration of 11.25 mM (Table 2) were performed to verify whether the optimum could be in the direction of increased ion-interaction reagent concentration, i.e., between 10.0 and 12.5 mM. This region proved to be optimal.

Calculations of the Regression Model for Sensitivity Optimization. In order to determine the experimental settings able to give the most sensitive determination of NaN_3 with heptylammonium orthophosphate as the interaction reagent, a regression model was calculated which correlates sensitivity with the experimental variables of concentration and flow rate.

An ordinary least-squares (OLS)[22] method was used as the regression method and the all-model search; i.e., the exhaustive search for the best regression model was applied. Before calculating the regression model, the independent variables were range-scaled within the range ±1 so that the regression coefficients represented half the change of the response caused by

Table 4. Model Equations Correlating Retention (*Y*) to Ion-Interaction Reagent Concentration (*C*) and Flow Rate (*F*)

Hexylammonium Orthophosphate
$Y = 4.990 + 0.1674C - 1.594F - 0.454C^2 + 0.480F^2$
$R^2 = 0.9840$
$R^2_{CV} = 0.9634$
Heptylammonium Orthophosphate
$Y = 8.959 - 0.674C - 2.808F - 1.185C^2 + 0.751F^2$
$R^2 = 0.9805$
$R^2_{CV} = 0.9568$
Octylammonium Orthophosphate
$Y = 9.000 - 0.848C - 3.014F + 1.184F^2$
$R^2 = 0.9414$
$R^2_{CV} = 0.8935$

(22) Davis J. C. *Statistical and Data Analysis in Geology*, 2nd ed.; John & Sons: New York, 1986.

each variable along its range.[23] The regression coefficients can be easily interpreted on this basis and they can be compared one to each other, when the relative importance of the factors is discussed.

Only the 13 experiments (marked by asterisks in Table 2) lying in the neighborhood of the optimal region were used.

In an attempt to find the better model, the effect of including quadratic, cubic, and two-factor interaction parameters was investigated. In the all-model search, all possible models with 1, 2, ..., n parameters (where n is the number of variables) are compared and the best is selected. The algorithm applied searches for the best model with one variable, with two variables, and so on, on the basis of the F test for the significance of the regression. The selection of the final model among the best ones is performed by an F test, where the best regression model with i parameters is compared with the best regression model with $i - 1$ parameters, i.e.

$$F = \frac{(\mathrm{SSE}_{\mathrm{reduced}} - \mathrm{SSE}_{\mathrm{complete}})/r}{\mathrm{SSE}_{\mathrm{complete}}/(N - p)} \quad (1)$$

where $\mathrm{SSE}_{\mathrm{reduced}}$ and $\mathrm{SSE}_{\mathrm{complete}}$ are the residual sums of squares associated with the models with $i - 1$ and i parameters, respectively, r is the difference in the number of parameters of the compared models ($r = 1$ in our case), N is the number of experiments, and p is the number of parameters in the complete model.[24] The regression model significant to the F test and characterized by the highest coefficient of multiple determination R^2 (i.e., the variance explained in the response) is retained. R^2 is defined as usual:

$$R^2 = 1 - (\mathrm{SSE}/\mathrm{SST}) \quad (2)$$

where SST is the total sum of squares.

The final model obtained (where S the sensitivity, C the molar concentration of ion-interaction reagent, and F the mobile phase flow rate) is a five-parameter model:

$$S = 48.045 + 19.060C - 31.068C^2 - 21.656C^3 - 5.357F \quad (3)$$

which explains 98.21% of the variation in the data about the mean sensitivity. Comparison between the best five-parameter model (four independent variables plus the intercept) and the best four-parameter one performed by the above-mentioned F-test provides a value of 38.1, which is significant ($F_{1,8} = 11.26$ at the 99% confidence level), while the best six-parameter model with respect to the best five-parameter one shows an F value of 2.63 ($F_{1,7} = 12.25$ at the 99% confidence level).

The leave-one-out cross-validated predicted sensitivity values obtained by using the selected model are listed in Table 3, with respect to the experimental data. The predictive ability of the obtained regression model was evaluated by the coefficient of multiple determination in prediction (leave-one-out cross-validation) defined as

$$R^2_{\mathrm{CV}} = 1 - \mathrm{SSE}_{\mathrm{CV}}/\mathrm{SST} \quad (4)$$

where $\mathrm{SSE}_{\mathrm{CV}}$ is the residual sum of squares calculated by using the predicted responses in leave-one-out cross-validation. The value obtained ($R^2_{\mathrm{CV}} = 0.9480$) is very satisfactory and suggests that the model can be used for prediction and optimization purposes.

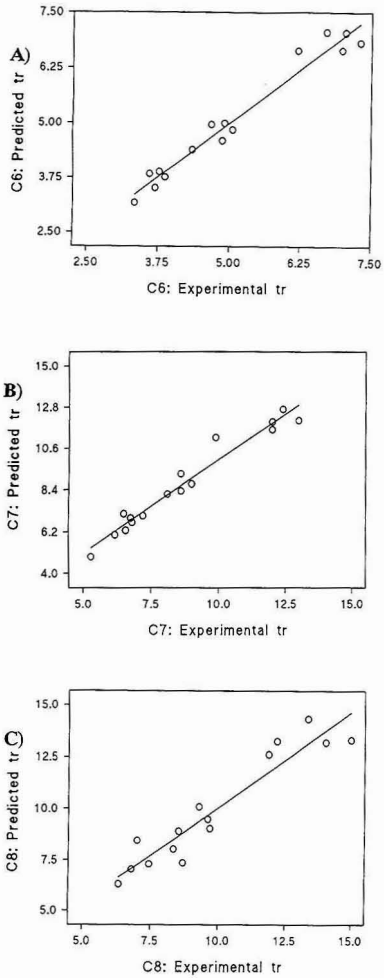


Figure 4. Predicted (Y) vs experimental (X) retention times (min): (A) hexylammonium orthophosphate as the ion-interaction reagent, $Y = (0.9968 \pm 0.0131)\ X$, $R^2 = 0.9637$; (B) heptylammonium orthophosphate as the ion-interaction reagent, $Y = (0.9990 \pm 0.0144)\ X$, $R^2 = 0.9574$; (C) octylammonium orthophosphate as the ion-interaction reagent, $Y = (0.9977 \pm 0.0227)\ X$, $R^2 = 0.8948$.

In order to select the region where the model is statistically reliable for optimization, *leverage* analysis around the sampled region was performed.[25,26] Leverage is a measure of the uncertainty introduced on the predicted responses by the particular

(23) Carlson, R. *Design and Optimization in Organic Synthesis*; Elsevier: Amsterdam, 1992; p 51.

(24) Cornell, J. A. *Experiments with Mixtures*; Wiley Series in Probability and Mathemetical Statistics; Wiley and Sons: New York, 1990.

(25) Brereton, R. G. *Chemometrics Applications of Mathematics and Statistics to Laboratory Systems*; E. Horwood: New York, 1990.

(26) Deming, S. N.; Morgan, S. L. *Experimental Design: a Chemometric Approach*; Elsevier: Amsterdam, 1987.

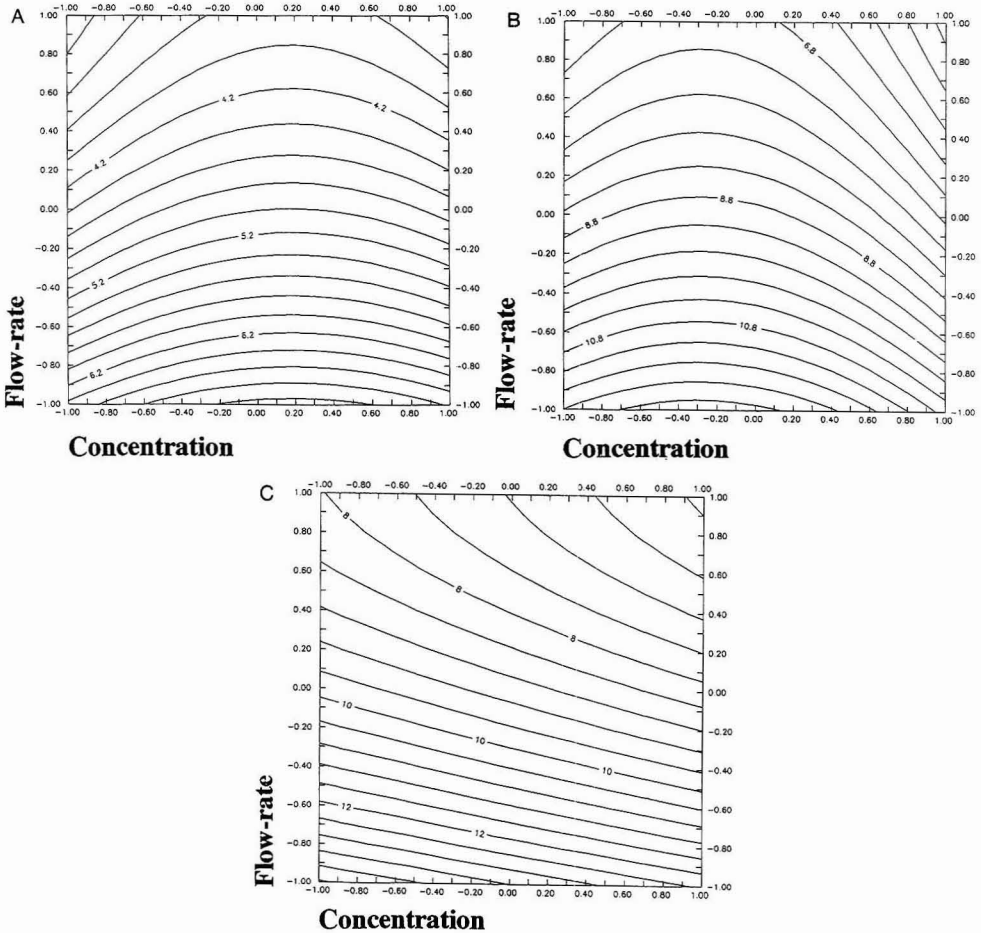


Figure 5. Contour plots of retention times (min) as a function of the experimental parameters of concentration and flow rate: (A) hexyl-, (B) heptyl-, and (C) octylammonium orthophosphate as the interaction reagent.

experimental design selected and also depends on the model matrix, i.e., on the functional dependence of the model from the original variables. The leverage can be calculated by the equation:

$$l = \mathbf{x}(\mathbf{X}'\mathbf{X})^{-1}\mathbf{x}' \qquad (5)$$

where $\mathbf{X}$ is the model matrix containing the experimental data; $\mathbf{X}'$ is its transpose, $\mathbf{x}$ is a vector containing the coordinates of the experimental point for which the leverage is to be calculated, $\mathbf{x}'$ is the transpose of $\mathbf{x}$. A leverage smaller than 1 indicates that the prediction uncertainty introduced by the experimental design is smaller than the experimental error.

Usually the uncertainty on the predicted response values increases very rapidly for predictions outside the sampled region (extrapolations). A mesh contour plot of the leverage in a region outside the ±1 coded boundary was built (Figure 1) in order to find out the proper area where the calculated model can be used for optimization purposes.

As it can be noted from Figure 1, the leverage, calculated with eq 5, behaves very differently for flow rate and concentration. It increases very rapidly outside the sampled region with concentration while its variation with flow rate is much lower. This produces a different acceptable range for flow rate (linear dependence) and concentration (third-order polynomial). Moreover, the leverage behavior is not completely symmetric, corresponding to the asymmetry of the experimental design. The search region selected was between ±1.7 for the flow rate and ±1 for the alkylammonium salt concentration.

The contour plot of the predicted sensitivities in the selected region is shown in Figure 2. The range of factor levels plotted corresponds to uncoded ranges of 0.49−1.51 mL/min for the flow rate and to the original boundaries for the ion-interaction reagent concentration.

In order to determine the best experimental conditions, a grid search algorithm was applied to the regression model previously

calculated within the plotted region. The search step was 0.01 in range-scaled units.

The best sensitivity was predicted as a peak area of 59.640 for the interaction reagent concentration 11.075 mM and for the flow rate of 0.49 mL/min. Experiments were performed in these conditions, and Figure 3 shows, as an example, the comparison between the best chromatogram obtained before optimization and the chromatogram obtained in the optimized conditions for the same azide concentration (0.50 ppm).

For azide concentrations ranging between 10 and 50 ppb, a calibration plot of peak area (y) vs azide concentration showed a coefficient of determination $R^2 = 0.9883$ and a slope (which corresponds to sensitivity) equal to 62.500, which can be well compared with the predicted value 59.640. By considering in the chromatogram a signal-to-noise ratio of 3, a detection limit of 6.0 ppb was evaluated. The validity of the chemometric treatment and its predictive ability is here clearly evidenced by the remarkable increase of sensitivity achieved with respect to the results previously obtained.[10]

Since a large number of experimental data corresponding to the retention times of NaN_3 in different conditions of flow rate, concentration, and chain length of the ion-interaction reagent were available (Table 1), a regression model was also calculated to correlate these variables to the retention times with the aim of rationalizing the effect of the experimental factors on the retention times. The same regression procedure previously applied for the sensitivity optimization was used. The models reported in Table 4 were obtained for the different ion-interaction reagents. They fit the experimental responses very well, and their predictive ability is very good, as can be observed from the plot reporting the leave-one-out cross-validated predictions vs the experimental data (Figure 4) and from the coefficient of multiple determination in prediction R^2_{CV} reported in Table 4.

The contour plots of retention times against the experimental factors are represented in Figure 5. The dependence on the flow rate is as expected: a flow rate increase causes an approximately linear increase of retention times. There is also a dependence of retention time on the chain length, which can be studied by comparing the average retention times for the different ion-interaction reagents. Generally, in the separation of anionic species, an increase of the number of carbon atoms in the ion-interaction reagent causes an increase of retention times. This could be ascribed, at least in the range of chain length considered, to a higher percentage coverage of the surface of the stationary phase obtained with more lipophilic alkylammonium salts.

The concentration seems to exert a slight negative effect on retention times, at least in the range considered, for octylammonium phosphate as the interaction reagent. In the case of hexyl- and heptylammonium salts, a parabolic dependence has been found.

The application of chemometric techniques allowed the optimization of sensitivity and rationalized the effect of the experimental factors on retention.

Sensitivity optimization provided a detection limit of 6 ppb, which is quite a good result, because it is worth remarking that the whole determination does not require any pretreatment or derivatization of the sample and, as mentioned above, is interferent-free from many species.

ACKNOWLEDGMENT

This investigation has been supported by the Italian National Research Council (CNR, Rome, Italy).

Received for review August 25, 1993. Accepted July 27, 1994.[⊗]

[⊗] Abstract published in *Advance ACS Abstracts*, September 15, 1994.

Anal. Chem. **1994,** *66,* 4236–4242

Modeling Flow Profiles and Dispersion in Capillary Electrophoresis with Nonuniform ζ Potential

Catherine A. Keely,* Tom A. A. M. van de Goor, and Douglass McManigill

Hewlett Packard Laboratories, 3500 Deer Creek Road, P.O. Box 10350, Palo Alto, California 94303-0867

We have reported earlier that in capillary electrophoresis experiments at low pH values, broadening of the sample peak can be unusually high—higher than can be accounted for by diffusion alone. In this paper, theoretical flow profiles inside the capillary have been examined as contributing to band broadening and raising the plate height. The theory is based on the expectation that the ζ potential changes along the length of the capillary, *z*, due to electrical fields that exist across the wall of the capillary. This paper discusses the particular case in which the radial voltage across the capillary wall is constrained to be a linear function of *z*. This case applies to the configuration in which the capillary is covered by a conductive shield. The configuration is of special interest because it can allow control of electroosmotic flow under specific conditions. Given that the radial voltage is a linear function of *z*, it is reasoned that *ζ(z)* can also be assumed to be linear. The theory is developed for the resulting velocity profile as a function of *z*, and the effect on dispersion and plate height is presented. The theory includes addition of pressure and the corresponding influence on plate height.

In capillary electrophoresis (CE), high voltage is applied between the ends of the capillary, generating an axial electric field. Due to the electrical environment near the inside wall of the capillary, which is dependent on parameters such as the capillary surface and the buffer, the axial field will generate electroosmotic flow (EOF) through the capillary. The ζ potential is the parameter representing the electrical condition at the wall which relates the axial field to the electroosmotic flow.

In recent years, a number of papers have been published discussing the existence and effect of fields acting not along the length of the capillary but across the wall.[1-9] These radially directed electric fields are induced by the high axial electric fields required in CE. Their magnitude has been shown to have an effect on the electroosmotic (EO) velocity when using low pH buffers (typically pH 2–5) are used.[1,5] Thus, researchers have designed capillary configurations which constrain the radial electric fields to take advantage of this phenomenon.

To understand the effect of the radial fields on the EO velocity, several papers have proposed models in which the ζ potential on the inside surface of the capillary is modified by the radial field.[4,8] These models treat the capillary wall as a combination of capacitors and resistors which allow the external electrical environment to have an effect on the internal electrical environment. These models provide some insight on the mechanisms by which radial fields affect electroosmotic flow, but they do not address the increased plate height.

It is normally expected that the efficiency of the CE system or the number of theoretical plates follows the relation $N = \mu El/2D$[10] (see Glossary for definition of all terms). This has been verified when the buffer pH is above about 5. We have previously reported that at low pH conditions there is increased dispersion (or decreased efficiency) in the sample peaks in conventional CE, and the above equation does not hold. In capillary configurations where radial fields are constrained, there remains this extra dispersion, resulting in a lower efficiency N or a higher plate height H, where $H = L_{det}/N$.[1]

This paper combines several theoretical models and examines the flow profile in the capillary and the plate height obtained. In this theory, the radial field changes along the length of the capillary, affecting the ζ potential, flow profile, and dispersion which must also change along the length. The effect of a pressure differential on the flow profile is also included in the theory.

THEORY

In standard CE, the electroosmotic velocity u is given by the Helmhotz–Smoluchowski equation,[11]

$$u = \mu_{eo}E = -\frac{\epsilon_w}{\eta}\zeta E \qquad (1)$$

In this equation, the ζ potential is normally assumed to be constant. In the theory developed below, it is shown that this is not always the case, and changing ζ impacts the flow profile and plate height.

ζ Potential. Several models exist describing the ζ potential for a system. For CE, the ζ potential is defined as the electrical potential at the shear plane of the liquid, and it is an experimentally determined quantity. While models may differ in their description

(1) Keely, C. A.; Holloway, R. R.; van de Goor, A. A. A. M.; McManigill, D. *J. Chromatogr. A* **1993**, *652*, 283–289.
(2) Lee, C. S.; Blanchard, W. C.; Wu, C.-T. *Anal. Chem.* **1990**, *62*, 1550–1552.
(3) Lee, C. S.; McManigill, D.; Patel, B. *Anal. Chem.* **1991**, *63*, 1519–1523.
(4) Wu, C.-T.; Huang, T.-L.; Lee, C. S. *Anal. Chem.* **1993**, *65*, 568–571.
(5) Huang, T.-L.; Tsai, P.; Wu, C.-T.; Lee, C. S. *Anal. Chem.* **1993**, *65*, 2887–2893.
(6) Ghowski, K.; Gale, R. J. In *Proceedings of the International Symposium on Biosensor Technology 1989*; Buck, R. P., Ed.; Marcel Dekker: New York, 1990; pp 55–62.
(7) Holloway, R. R.; Keely, C. A.; Lux, J. A.; Mcmanigill, D.; Young, J. E. 4th International Symposium on High Performance Capillary Electrophoresis, Amsterdam, February 9–13, 1992; Poster PT-27.
(8) Hayes, M. A.; Ewing, A. G. *Anal. Chem.* **1992**, *64*, 512–516.
(9) Hayes, M. A.; Kheterpal, I.; Ewing, A. G. *Anal. Chem.* **1993**, *65*, 2010–2013.
(10) Jorgenson, J. W.; Lukacs, K. D. *Anal. Chem.* **1981**, *53*, 1298–1302.
(11) Hunter, R. J. *Zeta Potential in Colloid Science*; Academic Press: London, 1981.

0003-2700/94/0366-4236$04.50/0 © 1994 American Chemical Society

of the potential in the region between the shear plane and the capillary wall, there is typically an exponential drop from the double layer to the center of the capillary.[11]

Based on the Debye–Hückel theory, for electrophoresis in bare fused silica, it is reasonable to assume the following relation between ζ and the wall potential Ψ_0:[8,11,12]

$$\zeta = \Psi_0 \exp[-\kappa x] \tag{2}$$

The double layer thickness is κ^{-1}, where

$$\kappa = \left(\frac{1000e^2 N_A}{\epsilon_w kT}\sum_i z_i^2 M_i\right)^{1/2} \tag{3}$$

which, as is shown, is dependent on the electrolyte composition and concentration.[13] The value of x represents the distance from the wall to the shear layer and is estimated to be between 3 and 10 nm.[13] Since this quantity is not well defined, the value of ζ is correspondingly uncertain.

From the Gouy–Chapman model, the wall potential in volts for a 1:1 electrolyte at 298 K is dependent on the buffer concentration c and the surface charge density σ_t and is given by[13]

$$\Psi_0 = 0.0514 \sinh^{-1}\frac{\sigma_t 8.513}{\sqrt{c}} \tag{4}$$

Hayes and Ewing[8] have developed an expression for σ_t when a radial field is present as the sum of a pH-dependent fused silica surface charge term, σ_{Si}, and a radial voltage-dependent surface charge term, σ_v:

$$\sigma_t = \epsilon_{Si} + \sigma_V \tag{5}$$

$$\epsilon_{Si} = \frac{-e\gamma}{1 + ([H^+]/K_a)}$$

$$\sigma_V = \epsilon_{Si}\frac{V_R}{r_i}\left(\frac{1}{\ln r_o/r_i}\right)$$

The term σ_{Si} is a simplification of the equilibrium conditions at the inside surface of the capillary, and a more elaborate model may include other variables. The term σ_V is derived by treating the capillary as a cylindrical capacitor. Combining the above relations for ζ, Ψ_0, and σ_t, one obtains the ζ potential (and hence the EO mobility μ_{eo} through eq 1) as a function of several variable parameters: pH, radial voltage, inside and outside radius, inside surface material (through K_a and γ), capillary wall material (through ϵ_{Si}), buffer composition and concentration (through κ and c), and shear layer location (through x).

ζ Potential Dependencies. The relationship between the ζ potential and the radial voltage is of primary interest here, because of the observed effect of radial voltage on EO velocity. Thus, this relation as predicted by eqs 1–5 is now examined by plotting the electroosmotic mobility as a function of a few important variables.

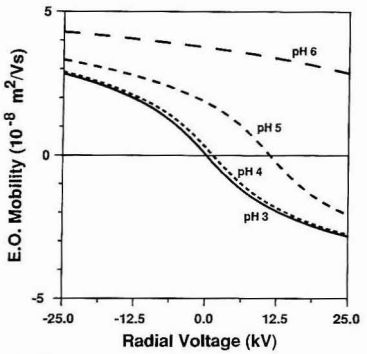


Figure 1. Electroosmotic mobility vs radial voltage as predicted by eqs 1–5 with four different pH values (pK_a = 5.8, 10 mM buffer concentration).

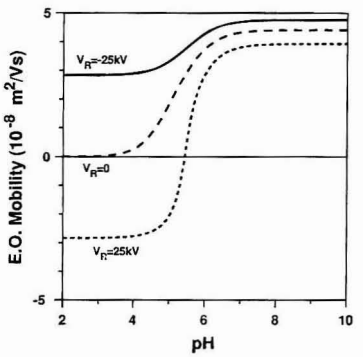


Figure 2. Electroosmotic mobility vs pH as predicted by eqs 1–5 with three different settings for the radial voltage (pK_a = 5.8, 10 mM buffer concentration).

Figures 1–4 illustrate the EO mobility dependence. In the equations, the capillary dimensions are assumed to be r_o = 0.050 mm and r_i = 0.0125 mm. Figure 1 graphs the theoretical curve for the EO mobility vs the radial voltage for four pH values, where the radial voltage is the potential drop measured across the wall from outside to inside. At pH 3, changing the radial voltage causes a large change in EO mobility, but this effect is reduced at high pH values and is nearly gone by pH 6. Figure 2 shows this effect in a different way; the EO mobility is plotted as a function of pH for three values of radial voltage. The mobility range between the lines for $V_R = -25$ kV and $V_R = 25$ kV (voltages chosen strictly for comparison purposes) is a measure of the range over which the mobility may be controlled. Given the fused silica surface in this model, the range is severely reduced above pH 5. In this model, the pH value can only be shifted by changing the silanol surface equilibrium constant, K_a. This is shown in Figure 3, where the EO mobility vs pH is given for three equilibrium constants. The center curve uses the value taken from Scales,[14] where the

(12) Davies, J. T.; Rideal, E. K. *Interfacial Phenomena*; Academic Press: New York, 1963.

(13) Hiemenz, P. C. *Principles of Colloid and Surface Chemistry*; Marcel Dekker: New York, 1986.

(14) Scales, P. J.; Grieser, F.; Healy, T. W. *Langmuir* **1992**, *8*, 965–974.

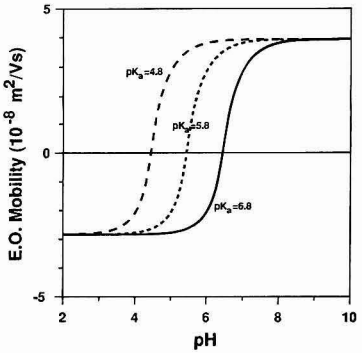


Figure 3. Electroosmotic mobility vs pH as predicted by eqs 1–5 with three different settings for the equilibrium constant (V_R = 25 kV, 10 mM buffer concentration).

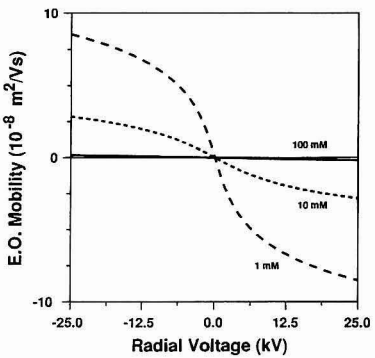


Figure 4. Electroosmotic mobility vs radial voltage as predicted by eqs 1–5 with three different buffer concentrations (pK_a = 5.8, pH = 3.0).

pK_a is 5.8. To increase the pH value where the curve rises, a pK_a of 6.8 is used, and to shift the curve to the left, a pK_a of 4.8 is used. Possible factors influencing this value in an actual capillary may be capillary pretreatment, manufacturing conditions, or contamination. Finally, the effect of buffer concentration is shown in Figure 4, where the mobility is plotted against the radial voltage for three values of concentration c. The graph indicates that a lower concentration buffer would produce a greater change in mobility as the radial voltage is changed.

Velocity Profile. The theory development above determines ζ as a function of many parameters, including the radial voltage across the capillary wall. In a CE system, it can be expected that the radial voltage will be different in different parts of the capillary or will change as a function of distance along the capillary length, z. Anderson and Idol[15] developed a theory for the velocity profile in a capillary given that ζ is an arbitrary function of z. The theory produces a stream function, and from the stream function the flow is calculated and expressed as the sum of a primary flow and a secondary flow. The primary flow is constant, is only in the z direction, and is equivalent to the average bulk flow. Anderson and Idol's secondary flow has radial and axial direction components, is a function of both radius r and distance z, and averages to zero over any capillary cross section. The flow components in the z-direction, $v_{zp}(z)$ and $v_{zs}(r,z)$, are of interest here and are given in the Appendix along with their reduced forms,

$$v_{zp} = \hat{u} \tag{6}$$

$$\bar{v}_{zs}(r,z) = -[u(z) - \hat{u}](1 - 2r^2) \tag{7}$$

which are justified later by the simplified model. This represents a constant bulk velocity $\hat{u}$ and a superimposed parabolic profile $\bar{v}_{zs}$.

If the capillary is subjected to pressure-driven flow in addition to the EOF, pressure flow terms must be added to the profiles. The primary velocity profile is then

$$v_{zp}(p) = \hat{u} + \frac{pr_i^2}{8\eta l} \tag{8}$$

and the contribution to the secondary velocity profile is the familiar parabolic laminar flow profile,

$$v_{zsp}(r,p) = \frac{pr_i^2}{8\eta l}(1 - 2r^2) \tag{9}$$

so that the complete secondary profile is

$$\bar{v}_{zs}(r,z,p) = \left(-[u(z) - \hat{u}] + \frac{pr_i^2}{8\eta l}\right)(1 - 2r^2) \tag{10}$$

Dispersion. In capillary electrophoresis, a sample boundary traveling through the system experiences various forces which cause the boundary to become less sharp and the flow front less pluglike. Thermal diffusion and velocity profile are two of the main dispersive forces that cause broadened peaks in an electropherogram. Their combined effects are measured by calculating the plate height or efficiency (plate numbers) of the system.

For a capillary electrophoresis system, plate height is defined as

$$H = \frac{\sigma_L^2}{L_{det}} \tag{11}$$

Neglecting the injection variance and the variance due to the finite detection window, the sample peak variance is the sum of the dispersion effects over the time,[16]

$$\sigma_L^2 = 2\int_0^t K_d \, dt$$

where K_d is the dispersion due to diffusion and the velocity profile. The dispersion due to the profile can be calculated according to the method of Datta and Kotamarthi,[17] adapting for the z-dependent profile, giving a dispersion that is a function of z,

(15) Anderson, J. L.; Idol, W. K. *Chem. Eng. Commun.* **1985**, *38*, 93–106.

(16) Aris, R. *Proc. R. Soc. London* **1956**, *A235*, 67–77.

(17) Datta, R.; Kotamarthi, V. R. *AIChE J.* **1990**, *36*, 916–926.

$$K_d(z) = D - \frac{2r_i^2}{D}\int_0^1\left[\int_0^{r}\frac{1}{r'}\left[\int_0^{r'} v_{zs}(r'',z)r''\,dr''\right]dr'\right] \times v_{zs}(r,z)r\,dr \quad (12)$$

which is the diffusion effect added to the effect of concentration changes resulting from the velocity profile perturbations. Since K_d is a function of z, the time integral in the variance equation above must be changed to reflect the z dependence. The appropriate peak variance expression is then the integral of the dispersion effects over the distance z traveled in the capillary,

$$\sigma_L^2 = \frac{2}{\hat{u}}\int_0^z K_d(z)\,dz \quad (13)$$

Using the equations for H, σ_L^2, $K_d(z)$, $v_{zs}(r,z)$, $u(z)$, and $\zeta(z)$, the plate height can be calculated as a function of z. This can be done with relative ease using a symbolic math computer program such as Mathematica (Wolfram Research, Champaign, IL), which was used for all calculations in this paper.

SIMPLIFIED MODEL FOR CE

In most capillary electrophoresis systems, there is no intentional radial voltage applied across the wall. However, due to the axial electric field used in the separation, the voltage inside the capillary changes along the length, normally in a linear fashion. Since the voltage far outside the capillary eventually returns to ground (i.e., at the instrument chassis), a radial field must exist across the wall. This field is presumed to be very small unless there is an electrically constrained section close to the capillary, for example, the detector which is usually held at ground or crossed coils in a coiled capillary configuration. At that point, there would be a locally stronger radial field.

In order to take advantage of the EOF control phenomenon mentioned earlier, capillaries have been electrically constrained over much of their length. The remaining sections of this paper examine how the electrical constraints affect the velocity profile and the resulting plate height based on the theory developed above.

To represent the electrical environment, the capillary is modeled as being unconstrained over the first 25% of its length and grounded over the last 75% and at the outlet end. Electrical finite element models designed for static field analysis have shown that when the constrained region ends abruptly, the radial field drops to the new level within a few capillary diameters.[18] Therefore, the function $V_R(z)$ may be taken as zero in the unconstrained region and as the difference between the outside and inside voltage in the grounded region. If it is further assumed that the voltage inside the capillary changes linearly along the length, then the resulting $V_R(z)$ is as shown in Figure 5a.

Approximation of ζ Potential and Flow Profile. In the earlier Theory section, eqs 2–5 provided a specific expression for $\zeta(V_R)$. This function has a sigmoidal shape over the radial voltage region of interest, proportional to the curves given in Figures 1 and 4. Assuming the piecewise linear relation for $V_R(z)$ given in Figure 5a, one obtains the function $\zeta(z)$ which would have the same shape as $\zeta(V_r)$. Substituting this expression into Anderson and Idol's secondary velocity profile expression and then integrating to obtain the dispersion and plate height would be quite difficult. However, by approximating $\zeta(z)$ as linear in any given section as shown in Figure 5b, that is,

$$\zeta(z) = (\zeta_2 - \zeta_1)\frac{z}{l} + \zeta_1 \quad (14)$$

Anderson and Idol's expression for $v_{zs}(r,z)$ predicts a secondary profile that is parabolic in r and linear in z in the given section. As shown in the Appendix, without pressure it reduces to eq 7, where $u(z)$ is given by eq 1 with linear $\zeta(z)$, and $\hat{u}$ is the average bulk flow. This profile can be substituted and processed through the dispersion and plate height equations, and thus the plate height can be examined as a function of $\zeta(z)$. The equations needed to generate results are eq 1 and eqs 7–14, and again they are easily processed by Mathematica.

In eq 14, ζ_1 and ζ_2 are chosen by trial and error using the Mathematica program to calculate the velocity and plate height generated by given ζ_1 and ζ_2 and adjusting their values until the velocity and plate height match the reference experimental value for the chosen experimental configuration. Once ζ_1 and ζ_2 are chosen, they are used in all calculations for that experiment.

It has been proposed by Hayes et al.[9] that the presence of a radial voltage may cause the ζ potential to spread out along the inside surface of the capillary by surface conductance. If this is the case, the appropriate model for $\zeta(z)$ may not have the sharp drop indicated in Figure 5 but instead a more gentle slope from the inlet potential to the extreme low potential. $\zeta(z)$ could still be modeled with linear sections, and the simplified flow profile equation could still be used. The results of this paper, however, use $\zeta(z)$ as shown in Figure 5.

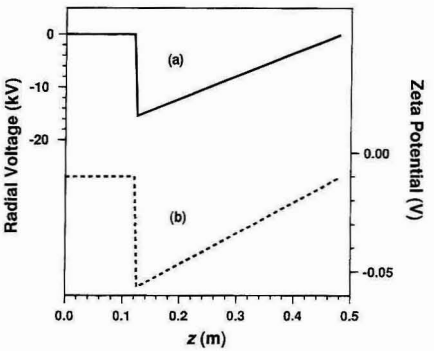


Figure 5. (a) Radial voltage V_R and (b) ζ potential as a function of distance along the capillary z for the given 75% grounded capillary.

RESULTS AND DISCUSSION

Assumptions. In using eq 14 above, assumptions must be made for the ζ_1 and ζ_2 terms. In principle, these could be determined using eqs 2–5, but due to uncertainties in those expressions, the resulting ζ value would be reliable only to within a factor of 5 or so, whereas the plate height results are sensitive to as little as a 1% change in ζ_1 and ζ_2. Thus, appropriate initial values were selected by matching experimental data. Experimen-

(18) Cole, W. D. 6th International Symposium on High Performance Capillary Electrophoresis, San Diego, CA, Jan 31–Feb 3, 1994; Poster P-326.

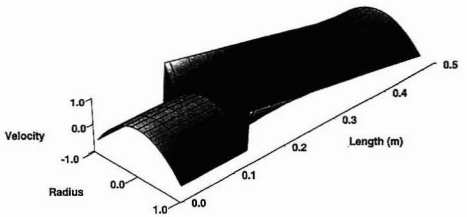


Figure 6. Surface plot of the secondary velocity as a function of the capillary radius and length as given by eq 7. Secondary velocity is normalized to the bulk velocity, and radius is normalized to the capillary inside radius. Results are for the capillary configuration given in the text.

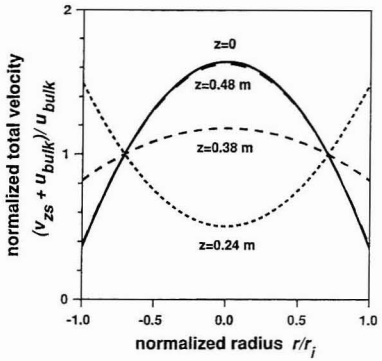


Figure 7. Total velocity profiles for four locations along the capillary length as given by eqs 6 and 7. Velocity is normalized to the bulk velocity (thus average across radius is 1), and radius is normalized to the capillary inside radius.

tal parameters used in the theory: bare fused silica capillary dimensions of 0.050 mm i.d. and 0.365 mm o.d., 0.48 m long; detector at 0.4 m from inlet; outlet end held at ground; inlet end held at 25 kV; resulting bulk EO velocity of 1.0 mm/s; grounded sheath covering the last 75% of the capillary; running buffer 10 mM phosphate buffer with 0.5% dimethyl sulfoxide (DMSO) at pH 2.7; sample front 10 mM phosphate buffer with 1% DMSO at pH 2.7.

The reference experiment was performed on a Hewlett Packard 3D CE (Palo Alto, CA) using capillaries from Polymicro Technologies (Phoenix, AZ) with a ground sheath produced in-house by titanium and gold sputtering, and chemical sources were Alltech (Deerfield, IL) and J. T. Baker (Jackson, TN). The experiment produced a plate height of 9.6 μm and a bulk velocity of 1.0 mm/s for the DMSO front, and with values of $\zeta_1 = 10$ mV and $\zeta_2 = -57$ mV, eqs 7–14 generate the same plate height and velocity values. The theory developed is valid for other conditions, but the values of ζ_1 and ζ_2 must be chosen to match each case.

Velocity Profile. Based on the discussion in the Simplified Model section above, the function $\zeta(z)$ will follow the function V_R. Thus the ζ potential along the length of the capillary was chosen as shown in Figure 5b, which is proportional to the V_R function.

The resulting secondary flow profiles $\bar{v}_{zs}(r,z)$ are given in the surface plot in Figure 6 and at distances along the capillary in Figure 7. Several important points are illustrated by these profiles. Note how the profile changes significantly over the length of the capillary. At the capillary entrance ($z = 0$), the secondary velocity along the wall ($r/r_i = 1$) is negative with respect to the bulk velocity, resulting in a normalized velocity of less than 1, while at the center ($r/r_i = 0$), the secondary velocity is nearly equal to the bulk velocity, producing a normalized velocity of nearly 2. This gives a forward pointing parabolic profile. At about $z = 0.12$ m, the profile abruptly reverses; the secondary velocity at the wall is nearly equal to the bulk velocity, and at the center it is opposite of the bulk velocity, giving a backward pointing parabolic profile. Farther along the length it gradually changes back to a forward pointing parabolic profile. Note also that the magnitude of this secondary profile is of the same order of magnitude as the bulk flow; thus, near the entrance, the total velocity at the wall is reduced to only 20% of the bulk velocity and at the center it is increased to 160% of the bulk velocity. With such large deviations from a pluglike flow, it is expected that plate height would increase.

Plate Height. In fact, Figure 8 shows the theoretical plate height prediction, which is a function of the detector position along the length (indicated by the z axis). The configuration assumptions are as stated earlier except the inlet voltage is 15 kV, the buffer is 5 mM, the bulk EO velocity is 0.4 mm/s, and the capillary length is 78 cm, with the grounded sheath over the center 62 cm. To match the experimental bulk EO velocity and plate height of 10.0 μm at $z = 0.165$ m, the appropriate values of ζ_1 and ζ_2 are -11 and -57 mV, respectively. Here, the plate height can be thought of as representing the sum of the dispersive profiles that a sample front must pass through, divided by the length over which the sample front has traveled. Given the current configuration, a detector placed at about $z = 0.165$ m would reguster a high plate height because the sample must pass through highly dispersive regions to get to the detector, but a detector placed at $z = 0.555$ m would register a much lower plate height because the sample passes through additional profiles which are flatter and less dispersive.

Preliminary experiments support this theory. To test the theory, an experimental setup was built in which the capillary was looped to pass by a single detector (Linear Instruments, Reno, NV) twice. A metal braid was used to provide the ground sheath, and 15 kV (Spellman High Voltage, Plainview, NY) was applied to the inlet end while the outlet end was held at ground. The first pass was at 0.165 m from the inlet, the second pass at 0.555 m, and other conditions were as described above. The DMSO front was detected as a step up in the absorption signal on the first pass and than another step up on the second pass. The resulting measured plate heights are shown in Figure 8. Since the theoretical curve is forced to pass through the data point at $z = 0.165$ m, the usefulness of this data is only to indicate that the theory and experiment are in agreement on the reduction of plate height at $z = 0.555$ m relative to $z = 0.165$ m.

When a constant pressure is held across the capillary during electrophoresis, the theoretical secondary velocity profile must include the laminar flow contribution term as in eq 10. The predictions for the resulting plate height for the 75% grounded configuration and conditions given in the Assumptions section are somewhat surprising. Figure 9 gives the theoretical curve, where by definition the plate height with 0 mbar of pressure is 9.6 μm.

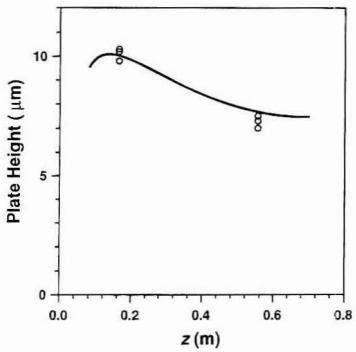


Figure 8. Theoretical plate height as a function of distance along the capillary. The shape of the curve is generated by eqs 10–13, but the offset is obtained by selecting values in eq 14 such that the curve runs through the point at $z = 0.165$ m. Data points are for three repeated experiments with detectors at $z = 0.165$ m and $z = 0.555$ m.

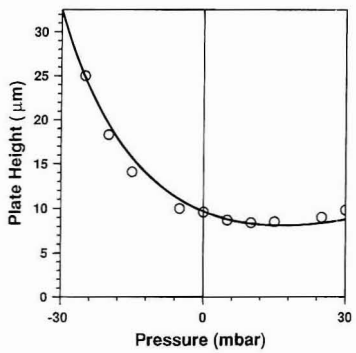


Figure 9. Theoretical plate height as a function of applied pressure. The shape of the curve is generated by eqs 10–13, but the offset is obtained by selecting values in eq 14 such that the curve runs through the point at $p = 0$. Data points are for experiments with constant pressure applied during CE run.

The curve indicates that adding forward pressure up to above 30 mbar does not increase the plate height, and in fact the minimum plate height is achieved with about 15 mbar of forward pressure. On the other hand, negative pressure greatly increases the plate height. This can be understood by analyzing the effect of constant pressure on the profiles everywhere along the capillary. Referring to Figure 6, forward pressure would further degrade the profile near the inlet but would help flatten the profile near the middle of the capillary. Conversely, negative pressure would flatten the profile in the entrance section but would further elongate it in the middle. It then follows that programming the pressure to flatten the profile as a particular sample front reaches a particular position would keep the selected sample front pluglike at all times and would theoretically reduce the plate height to the level at which diffusion is the only significant dispersing factor.

The theoretical results shown in Figure 9 were experimentally verified by applying a constant pressure during electrophoresis under the given conditions. The results for various pressures match the curve extremely well, as shown by Figure 9. This indicates that the theory is in fact able to predict how a pressure profile superimposed on electroosmotic flow affects the plate height.

CONCLUSIONS

Anderson and Idol developed a theoretical expression describing the velocity profile in a capillary as a function of the distance along the capillary z, given an arbitrary function $\zeta(z)$. In this paper we have assumed that $\zeta(z)$ is a piecewise linear function, which we have shown approximates the case when there is a constant potential (or grounded) sheath outside the capillary. Given $\zeta(z)$ as linear in z, Anderson and Idol's expression predicts that the velocity profile in the capillary will consist of a primary constant bulk flow component and a secondary component of comparable magnitude. The secondary component is parabolic across the capillary radius and linear along the capillary length (following the linear $\zeta(z)$ function). The velocity profile thus changes along the length of the capillary due to the changing ζ potential. Since the flow front is not pluglike, it will cause an increase in plate height. The theoretical plate height caused by this profile is analyzed as a function of the distance along the capillary. A pressure profile superimposed on the capillary can in some cases compensate for the disturbed profile, and the theory as well as experiments show that the plate height is reduced when a small amount of constant forward pressure is applied. Programming the pressure to change as a particular sample front enters a particular section of the capillary would theoretically allow one to maintain a flat flow front for that sample everywhere along the capillary.

Preliminary experiments have been performed to confirm the theory. For the specific conditions tested measuring plate height at two points along the capillary length, the data points and theory are in agreement. The predicted and measured plate heights are also in agreement when a constant pressure is applied along with electroosmosis.

The theory developed in this paper allows one to predict the velocity profile everywhere in the capillary and the resulting plate height given a known ζ potential function $\zeta(z)$ that is piecewise linear. Its validity is thus completely dependent on how well the ζ potential is known. This emphasizes the importance of understanding the ζ potential in order to understand the larger observations such as plate height and resolution in a CE system. Although this paper has concentrated on the development and implications of the theory, the experiments showing the effect of constant pressure and the change in plate height for two points along the capillary length are in accordance with the theory's predictions.

ACKNOWLEDGMENT

The authors wish to sincerely thank Robert Holloway, Wesley Cole, James Young, and Joel Myerson for their contribution to the chemistry development, electrical models, and mechanical configuration and for their helpful discussions.

APPENDIX

Anderson and Idol[15] determined that for an arbitrary $\zeta(z)$, giving an arbitrary $u(z)$, the primary and secondary velocity profiles (without additional pressure) in the z-direction are given respectively by

$$v_{zp}(z) = \frac{1}{l}\int_0^l u(z)\,dz$$

$$\equiv \hat{u} \tag{15}$$

$$v_{zs}(r,z) = -(1-2r^2)\sum_{n=1}^{\infty}\left(a_n \cos\frac{n\pi z}{l} + b_n \sin\frac{n\pi z}{l}\right) \tag{16}$$

where

$$a_n = \frac{2}{l}\int_0^l u(z)\cos\frac{n\pi z}{l}\,dz$$

$$b_n = \frac{2}{l}\int_0^l u(z)\sin\frac{n\pi z}{l}\,dz$$

The summation term in eq 16 is the Fourier series for $u(z)$ less the $n = 0$ term, which here is equal to $\hat{u}$. Assuming that $u(z)$ is a linear function, the summation converges to $u(z) - \hat{u}$. Thus, $v_{zs}(r,z)$ reduces to eq 7.

GLOSSARY

c	buffer concentration, M
D	diffusion coefficient, m^2/s
E	axial electric field, V/m
e	electronic charge, 1.6×10^{-19} C/charge
H	plate height, m
$[H^+]$	absolute concentration of H^+ ions, dimensionless
K_a	acid dissociation constant of silanol groups at inside capillary wall, dimensionless
K_d	total dispersion, m^2/s
k	Boltzmann constant, 1.38×10^{-23} J/K
L_{det}	length of capillary from inlet to detector, m
l	total length of capillary, m
M_i	molar concentration of ions for species i, M
N	plate numbers, or efficiency, dimensionless
N_A	Avogadro's number, 6.02×10^{23} mol^{-1}
p	pressure, N/m^2
pK_a	$-\log K_a$, dimensionless
r	normalized radius variable, dimensionless
r'	integration variable representing r
r''	integration variable representing r
r_i	capillary inside radius, m
r_o	capillary outside radius, m
T	temperature, K
t	time variable, s
u	electroosmotic velocity, i.e., at inside wall, m/s
$\hat{u}$	u_{bulk}, average bulk velocity, m/s
V_R	radial voltage across capillary wall, outside to inside, V
v_{zp}	primary velocity in the z-direction, m/s
v_{zpp}	primary velocity in the z-direction due to pressure, m/s
v_{zs}	secondary velocity in the z-direction, m/s
$\bar{v}_{zs}$	secondary velocity in the z-direction assuming $\zeta(z)$ linear, m/s
v_{zsp}	secondary velocity in the z-direction due to pressure, m/s
x	distance from capillary wall to shear layer, m
z	distance along capillary axis variable, m
z_i	valence number for species i, dimensionless
γ	concentration of hydroxyl groups at capillary surface, charge/m^2
ϵ_{Si}	permittivity of capillary wall material, here 3.36×10^{-11} C^2/Nm^2
ϵ_w	permittivity of buffer, here 6.93×10^{-10} C^2/Nm^2
ζ	ζ potential, V
ζ_1	boundary of $\zeta(z)$, V
ζ_2	boundary of $\zeta(z)$, V
η	viscosity of buffer, here 0.001 Ns/m^2
κ^{-1}	double layer thickness, m
μ	overall mobility, m^2/V s
μ_{eo}	electroosmotic mobility, m^2/V s
Ψ_0	potential at the capillary wall, V
σ_L^2	length-based variance, m^2
σ_t	total surface charge, C/m^2
σ_{Si}	dissociation-dependent surface charge term, C/m^2
σ_V	radial voltage-dependent surface charge term, C/m^2

Received for review May 27, 1994. Accepted September 1, 1994.[⊗]

[⊗] Abstract published in *Advance ACS Abstracts*, October 15, 1994.

Anal. Chem. **1994,** *66,* 4243–4252

Effects of Linear Polyacrylamide Concentrations and Applied Voltages on the Separation of Oligonucleotides and DNA Sequencing Fragments by Capillary Electrophoresis

Takashi Manabe,*,† Nong Chen,‡ and Shigeru Terabe

Department of Material Sciences, Faculty of Science, Himeji Institute of Technology, Hyogo 678-12, Japan

Masafumi Yohda and Isao Endo

Chemical Engineering Laboratory, The Institute of Physical and Chemical Research, Saitama 351-01, Japan

Oligonucleotides and DNA sequencing fragments have been separated by capillary electrophoresis employing linear polyacrylamide (LPA) as a sieving matrix. A commercially available apparatus equipped with a laser-induced fluorescence (LIF) detection system has been utilized, but the capillary cartridge has been modified to position the capillaries without coiling. The performance of the separation, the relationship between resolution and analysis time, has been examined using poly(dT)$_{16-500}$ by changing LPA concentration, capillary length, and electric field strength. It was found that, for large DNA fragments, the migration time interval between bands decreases linearly as DNA fragment size increases. This implies that there exists a maximum base number to be resolved, irrespective of the band width (we named the maximum base number N_{max}). The higher value of N_{max} is obtained when the applied field strength is lower, but this accompanies longer analysis time with a concomitant increase in band width. Simple experimental equations have been proposed to calculate resolution and migration times of DNA fragments separated in our system at given electrophoretic conditions. Using 9% *T* LPA and an electric field strength of 100 V/cm, single-base resolution of M13mp10 DNA fragments up to 520 nucleotides has been obtained.

The determination of the total DNA sequence of a gene is the key process to understanding the structure and the concerted function of the gene products in cells and organs. Aiming to improve the performance of DNA sequencing, capillary gel electrophoresis has been utilized for the separation of DNA sequencing fragments.[1-9] In capillaries, the efficiency of heat dissipation is much higher than in slab gels; thus, much higher electric fields can be applied during electrophoresis, which speeds up the separation process. However, the high electric fields also lead to a loss of separation of large DNA fragments. The loss of resolution of large DNA fragments in small-pore gels and/or strong electric fields has been observed in agarose gel electrophoresis in a slab format,[10,11] and the biased reptation model has been proposed to quantitatively predict the experimental parameters necessary for the resolution of these molecules.[12,13] The model was also applied to explain the mobility behavior of DNA fragments separated by capillary electrophoresis in cross-linked polyacrylamide gels.[14] Although linear polyacrylamide is one of the promising matrices in capillary electrophoretic separation of DNA fragments, and several reports of successful application in DNA sequencing have appeared,[4-7] the mobility behavior of DNA fragments in linear polyacrylamide has not been fully analyzed.

In this paper, we report on the separation and laser-induced fluorescence detection of FITC-labeled oligonucleotides and DNA sequencing reaction products by capillary electrophoresis employing linear polyacrylamide as a sieving matrix. The mobility behavior of DNA fragments is analyzed, and the electrophoretic conditions that optimize the performance of DNA sequencing by capillary electrophoresis with linear polyacrylamide are presented.

EXPERIMENTAL SECTION

Apparatus. In all of the experiments, a P/ACE System 2100 capillary electrophoresis instrument equipped with an argon ion laser module and a fluorescence detector (Beckman Instruments,

† Present address: Department of Chemistry, Faculty of Science, Ehime University, 2-5 Bunkyo-Cho, Matsuyama City, Japan 790.

‡ On leave from National Chromatographic R. & A. Center, Dailian Institute of Chemical Physics, Chinese Academy of Sciences, Dailian 116011, China.

(1) Luckey, J. A.; Drossman, H.; Kostichka, A. J.; Mead, D. A.; D'Cunha, J.; Norris, T. B.; Smith, L. M. *Nucleic Acids Res.* **1990**, *18*, 4417–4421.
(2) Guttman, A.; Cohen, A. S.; Heiger, D. N.; Karger, B. L. *Anal. Chem.* **1990**, *62*, 137–141.
(3) Swerdlow, H.; Zhang, J. Z.; Chen, D. Y.; Harke, H. R.; Grey, R.; Wu, S.; Dovichi, N. J.; Fuller, C. *Anal. Chem.* **1991**, *63*, 2835–2841.
(4) Huang, X. C.; Quesada, M. A.; Mathies, R. A. *Anal. Chem.* **1992**, *64*, 967–972.
(5) Huang, X. C.; Quesada, M. A.; Mathies, R. A. *Anal. Chem.* **1992**, *64*, 2149–2154.
(6) Pentoney, S. L., Jr.; Konrad, K. D.; Kaye, W. *Electrophoresis* **1992**, *13*, 467–474.
(7) Ruiz-Martinez, M. C.; Berka, J.; Belenkii, A.; Foret, F.; Miller, A. W.; Karger, B. L. *Anal. Chem.* **1993**, *65*, 2851–2858.
(8) Luckey, J. A.; Smith, L. M. *Anal. Chem.* **1993**, *65*, 2841–2850.
(9) Nishikawa, T.; Kambara, H. *Electrophoresis* **1994**, *15*, 215–220.
(10) McDonell, M. W.; Simon, M. N.; Studier, F. W. *J. Mol. Biol.* **1978**, *110*, 119–146.
(11) Fangman, W. L. *Nucleic Acids Res.* **1978**, *5*, 653–665. Brumley, R. L., Jr.; Smith, L. M. *Nucleic Acids Res.* **1991**, *19*, 4121–4126.
(12) Lumpkin, O. J.; DéJardin, P.; Zimm, B. H. *Biopolymers* **1985**, *24*, 1573–1593.
(13) Slater, G. W.; Rousseau, J.; Noolandi, J.; Turmel, C.; Lalande, M. *Biopolymers* **1988**, *27*, 509–524.
(14) Luckey, J. A.; Norris, T. B.; Smith, L. M. *J. Phys. Chem.* **1993**, *97*, 3067–3075.

0003-2700/94/0366-4243$04.50/0 © 1994 American Chemical Society

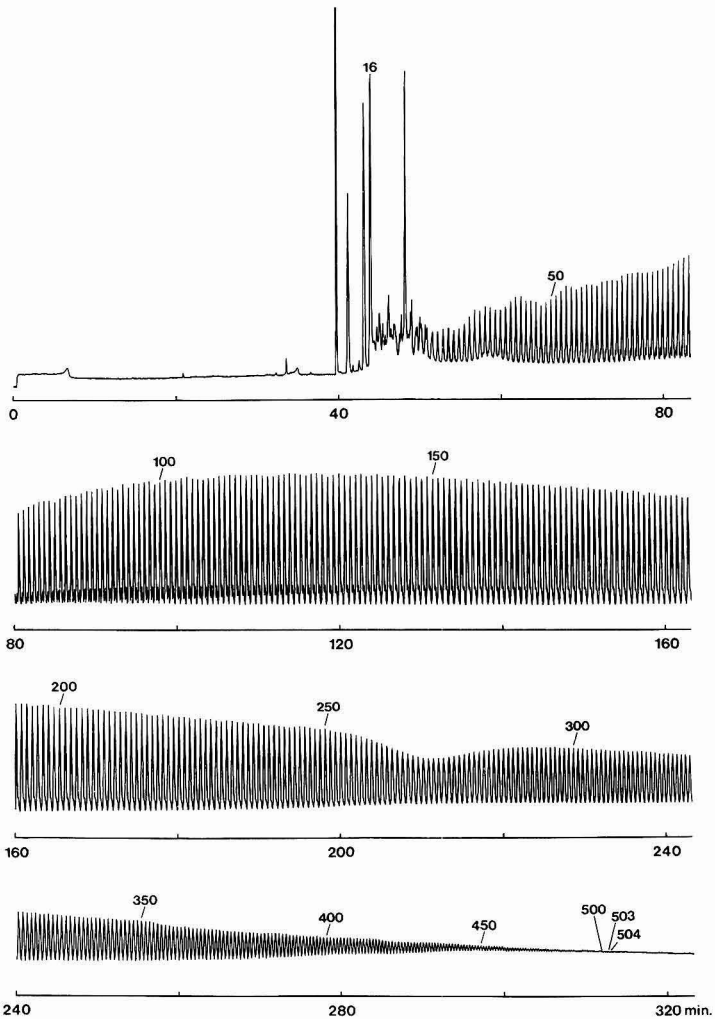


Figure 1. Separation of poly(deoxythymidylic acid(s)) (p(dT)). A mixture of FITC-labeled poly(deoxythymidylic acid(s)) (FITC-p$(dT)_{16-500}$) was subjected to capillary electrophoresis in 9% LPA, at an electric field of 200 V/cm and an effective capillary length of 50 cm. Fluorescence intensity was monitored on column with excitation at 488 nm and emission at 520 nm. Capillary inner diameter was 75 μm, and sample injection was at 175 V/cm for 40 s. The buffer was 0.1 M Tris–borate buffer containing 7 M urea (pH 8.3).

Inc., Fullerton, CA) was used with the cathode on the injection side and the anode on the detection side. All of the electropherograms presented in this paper were obtained by employing a Beckman capillary cartridge which had been modified in our laboratory in order to position a fused-silica capillary without coiling. The separations were monitored on column with excitation at 488 nm and emission at 520 nm. Data points were taken every 500 ms and stored on an IBM PS/2 50Z computer.

Capillaries Filled with Non-Cross-Linked Polyacrylamide. Capillary columns filled with non-cross-linked polyacrylamide were prepared as follows. Fused-silica capillary tubing (375-μm o.d., 75-μm i.d., Polymicro Technologies, Phoenix, AZ) was cut into 55–115-cm segments with detection windows located 11 cm from one end. The capillaries were cleaned by successively filling with 0.1 M NaOH, deionized water, and methanol. The inner surface of the capillaries was then derivatized with (3-methacryloxypropyl)-trimethoxysilane[15,16] in a 1:1 methanol solution and left at room temperature overnight. The derivatizing solution was removed by passing methanol through the capillaries. A layer of non-cross-linked polyacrylamide was then bonded to the inner surface of

(15) Hjerten, S. *J. Chromatogr.* **1985**, *347*, 191–198.
(16) Cohen, A. S.; Karger, B. L. *J. Chromatogr.* **1987**, *397*, 409–417.

the capillaries by filling them with a degassed solution of 3% acrylamide−0.06% ammonium persulfate (APS)−0.006% *N,N,N′,N′*-tetramethylethylenediamine (TEMED) and leaving them overnight. The 3% polyacrylamide in the capillary was extruded by water pressure with a gas-tight microsyringe. Non-cross-linked polyacrylamide was then polymerized in the capillaries by filling them with a degassed solution of 5%, 7%, or 9% acrylamide−0.1 M Tris−borate buffer (pH 8.3) containing 7 M urea, 0.06% APS, and 0.006% TEMED. The capillaries were left overnight at room temperature.

Samples. A mixture of poly(deoxyadenylic acid(s)) from 40 to 60 bases long ($p(dA)_{40-60}$) was purchased from Pharmacia LKB Biotechnology AB (Bromma). A sample of poly(deoxythymidylic acid), which is a mixture of FITC-labeled poly(dT)s from 16 to ~500 bases long (FITC-$p(dT)_{16-500}$), was provided by Dr. S. Hata and Dr. T. Osumi (Himeji Institute of Technology). Briefly, FITC-$p(dT)_{16-500}$ was prepared using poly(deoxyadenylic acid) [p(dA), average 539 nucleotides, Pharmacia LKB] as a template, FITC-labeled $p(dT)_{16}$ as a primer, and the sequencing reagent kit (Sequenase Version 2.0, United States Biochemical, Cleveland, OH). FITC-labeled M13mp10 sequencing fragments were provided by Dr. H. Kambara (Central Research Laboratory, Hitachi Ltd., Tokyo). The samples were mixed with formamide (80% v/v) and stored at −20 °C in the dark. Prior to injection, a 6-μL aliquot was heated to 90 °C for 2 min and then quickly placed on ice.

Electrophoresis. The capillaries were preelectrophoresed in 0.1 M Tris−borate buffer−7 M urea (pH 8.3) for 20 min at 100 V/cm and then for 20 min at 200 V/cm. Samples were injected electrokinetically at 10 kV for 40 s, irrespective of the electric field strength of the separation run. Since the modified capillary cartridge was employed, the temperature control system of the electrophoresis apparatus was not used.

RESULTS AND DISCUSSION

Capillary Coating and Modification of Capillary Cartridge. In preliminary experiments of oligonucleotide analysis, we used capillary cartridges which were supplied with the electrophoresis instrument. Linear polyacrylamide (LPA, 9% *T* and 0% *C* or 12% *T* and 0% *C*) was prepared in uncoated straight capillaries, then the capillaries were coiled in a 32-mm-diameter mandrel, and set in the cartridge. Employing these capillaries, we could obtain reasonable resolution for purified $p(dA)_{40-60}$ or for double-stranded DNA fragments, PBR322 *Hae*III digests.[17] However, when samples such as FITC-$p(dT)_{16-500}$ or FITC-M13mp10 sequencing fragments were subjected to electrophoresis, single-base resolution could not be achieved for oligonucleotides longer than ~200 bases. Further, the resolution rapidly deteriorated within 2−3 runs. Since these results suggested weak bonding of LPA on the untreated surface of fused silica capillaries, we employed LPA coating.[15,18] The coating of the capillary inner surface with 3% *T* LPA improved the resolution, and oligonucleotides up to ~350 bases could be resolved by one base difference. The influence of column shape alteration on performance in capillary electrophoresis has been examined in detail by Wicar et al.,[19] and it has been demonstrated that the coiling changes the polymer network structure, resulting in the loss of column efficiency. In order to minimize the effect of column shape alteration, we modified the capillary cartridge so that capillaries of any lengths can be positioned without coiling. This modification further improved the resolution, as shown in the next section.

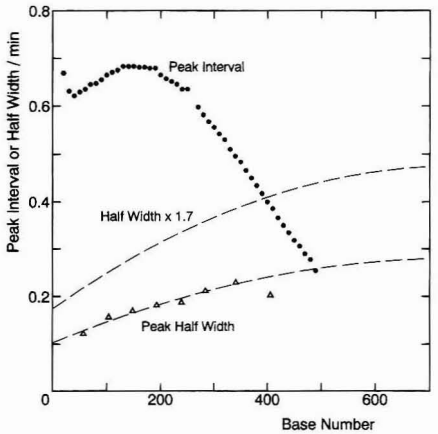


Figure 2. Peak interval and peak half-width vs base number of p(dT). The pattern shown in Figure 1 was analyzed. The symbols ● and △ indicate the calculated peak intervals (pi) and peak half-widths (hw), respectively. The dotted curve on the symbol △ is the second-order best-fit curve (r = 0.984) for the values of hw. In order to estimate the range of p(dT) base number separated in a resolution (R) higher than 1.0, the curve for the values of hw multiplied by 1.7 was also shown.

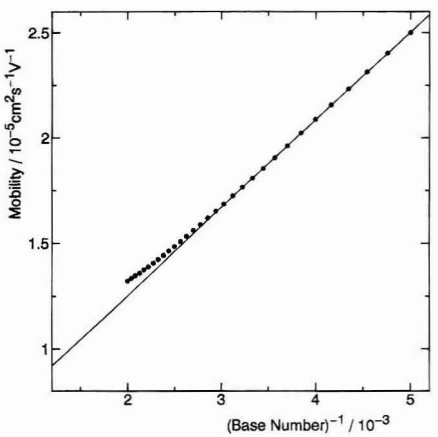


Figure 3. Mobility (μ) vs reciprocal base number ($1/N$). The data were obtained from the pattern shown in Figure 1 for peaks of p(dT) longer than 200 bases.

Analysis of the Resolution of FITC-p(dT). Figure 1 shows one of the separation patterns of FITC-$p(dT)_{16-500}$ in 9% *T* LPA, where the electric field was 200 V/cm and the effective capillary length was 50 cm. Assigning the peak position of the primer FITC-$p(dT)_{16}$, the base number was counted for each peak on the pattern and oligodeoxythymidic acids up to 500 bases were found

(17) Manabe, T.; Terabe, S. *Jpn. J. Electrophor.* **1993**, *37*, 123−128.
(18) Yin, H.-F.; Lux, J. A.; Schomburg, G. *J. High Resolut. Chromatogr.* **1990**, *13*, 624−627.
(19) Wicar, S.; Vilenchik, M.; Belenkii, A.; Cohen, A. S.; Karger, B. L. *J. Microcolumn Sep.* **1992**, *4*, 339−348.

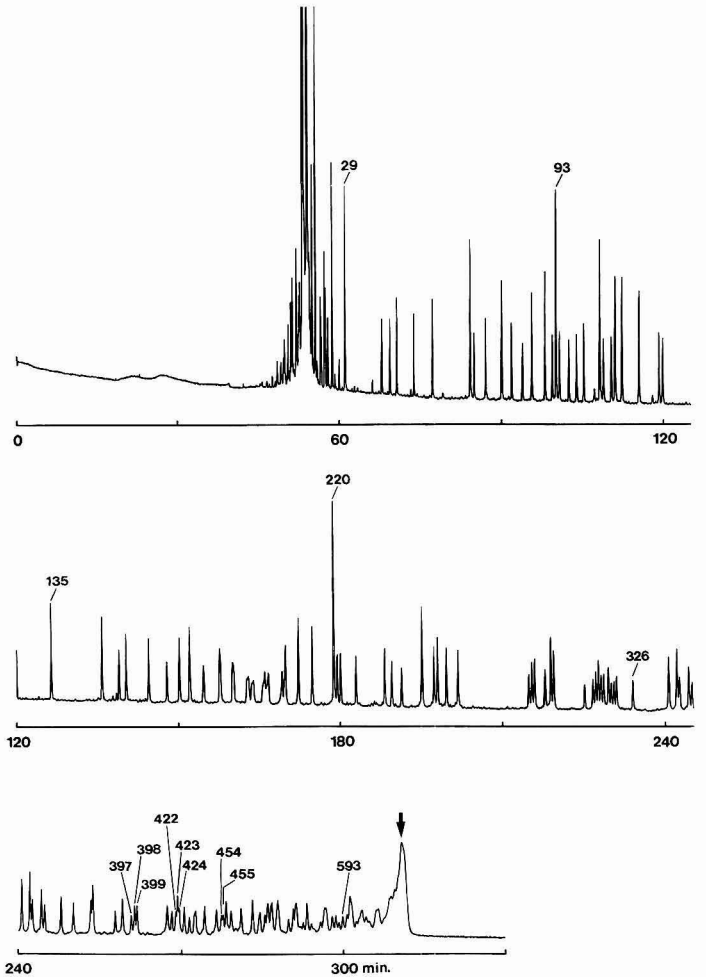


Figure 4. Separation of FITC-labeled M13mp10 DNA fragments (thymidine reaction products). Electrophoretic conditions were the same as shown in Figure 1.

to be resolved under these electrophoretic conditions. For the p(dT) peaks corresponding to base numbers 50–260, each peak was accompanied by a small peak or a shoulder, suggesting the presence of minor derivatives of FITC-p(dT). The minor peaks merged into the main peaks around base number 270 and then the peak widths and the peak spacings changed irregularly around this point. If we assume the peak shapes are Gaussian, the resolution of two adjacent p(dT) peaks can be expressed by the following equation:

$$R = (2 \ln 2)^{1/2} \frac{t_2 - t_1}{\mathrm{hw}_1 + \mathrm{hw}_2} \quad (1)$$

where t_1 and t_2 are the peak migration times and hw_1 and hw_2 are the full widths at half-maximum. Then the peak intervals and half-widths obtained from Figure 1 were plotted against base numbers of p(dT) (Figure 2). From the point of intersection of the plot of peak interval and the extrapolated plot of peak half-width, it is calculated that p(dT)s having base numbers up to 490 have been separated at a resolution (R) greater than 0.59. Likewise, in order to calculate the range of base number separated in R higher than 1.0, the values of half-width are multiplied by 1.7 and plotted in the figure. p(dT)s up to 390 bases were calculated to be separated in R higher than 1.0, in the electrophoretic conditions employed. Therefore, the plot of peak interval is very important to practically predict the separable base number. The data shown in Figure 2 suggest that the plot of p(dT) peak interval can be linearly extrapolated to base number axis, ~650 bases being the maximum

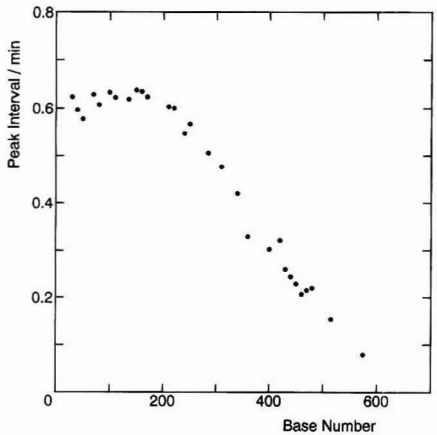


Figure 5. Averaged peak interval vs fragment size. The pattern shown in Figure 4 was analyzed. Averaged peak intervals were calculated by dividing the adjacent peak intervals by the difference of the base numbers.

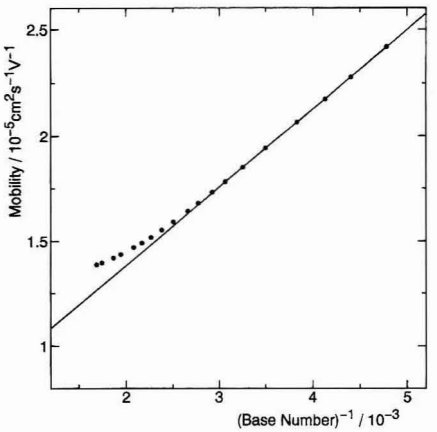


Figure 6. Mobility vs reciprocal base number for the pattern shown in Figure 4. Calculation was done for the DNA peaks longer than 200 bases.

base number separable (N_{max}) under these electrophoretic conditions.

Separation Regimes of FITC-p(dT). The plot of peak interval shown in Figure 2 also suggests that the p(dT) separation regime changes as the p(dT) base number changes; the increase of peak interval at base numbers ~40–100 can be interpreted by the Ogston sieving model,[20,21] and the decrease of peak interval at base numbers larger than ~200 by the reptation model.[22,23] When the DNA fragment is too large to fit into a single pore of the polymer network, it is assumed that it moves through the pore in a snakelike fashion (reptation). It has been established that in the reptation regime (without stretching), the mobility of DNA fragment μ is given by the following form:[23,24]

$$\mu = \mu_0(a/N) \tag{2}$$

where μ_0 is the free-solution mobility of a DNA fragment, N is the length of the DNA chain in nucleotide units, a is a constant that depends on the pore size of the polymer network, and both μ_0 and a are independent of the DNA length N or the electric field E. However, for a long fragment under a high electric field, the electric field forces the molecule to be stretched and oriented and eq 2 has to be modified to take this into account:[25,26]

$$\mu = \mu_0(a/N) + bE^2 \tag{3}$$

where b is the expansion coefficient that depends on the pore size of the polymer network as well as the DNA length. Equation 3 predicts that long fragments will have size-independent mobilities, which has been found experimentally.[10,11] This regime of reptation is termed the biased reptation regime or the reptation regime with stretching. Comparing eq 2 and eq 3, it is clear that the onset of the biased reptation regime can be detected when the electrophoretic mobilities of DNA fragments (μ) are plotted against the reciprocal of the DNA chain lengths ($1/N$). Figure 3 shows a μ vs $1/N$ plot for p(dT) fragments, as calculated from the data shown in Figure 1 for DNA fragments between 200 and 490 bases long. The deviation from linearity appears at ~320 bases, suggesting that the biased reptation regime starts even at these relatively short DNA chain lengths when the sieving matrix is 9% LPA and the electric field is 200 V/cm.

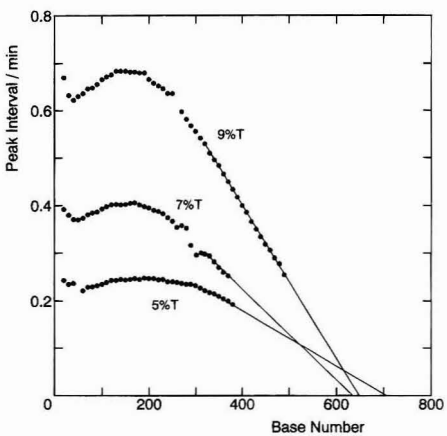


Figure 7. Peak interval vs base number at three LPA concentrations. FITC-p(dT)$_{16-500}$ was subjected to capillary electrophoresis at 5%, 7%, or 9% LPA concentration. Other electrophoretic conditions are the same as in Figure 1. The lines are the best-fit lines for the points of p(dT)s longer than 320 bases.

(20) Ogston, A. G. *Trans. Faraday Soc.* **1958**, *54*, 1754–1757.
(21) Rodbard, D.; Chrambach, A. *Proc. Natl. Acad. Sci. U.S.A.* **1970**, *65*, 970–977.
(22) deGennes, P. G. *J. Chem. Phys.* **1971**, *55*, 572–579.
(23) Lerman, L. S.; Frisch, H. L. *Biopolymers* **1982**, *21*, 995–997.
(24) Lumpkin, O. J.; Zimm, B. H. *Biopolymers* **1982**, *21*, 2315–2316.
(25) Slater, G. W.; Noolandi, J. *Biopolymers* **1986**, *25*, 431–454.
(26) Slater, G. W.; Rousseau, J.; Noolandi, J. *Biopolymers* **1987**, *26*, 863–872.

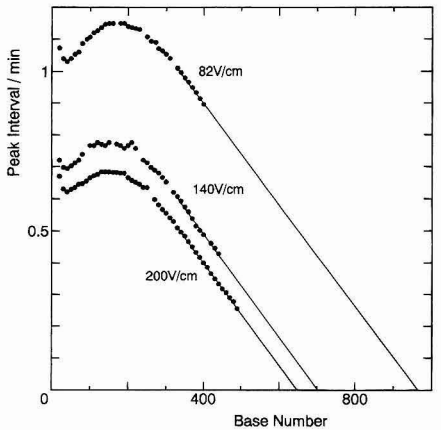


Figure 8. Peak interval vs base number at three field strengths. FITC-p(dT)$_{16-500}$ was subjected to capillary electrophoresis at 9% LPA concentration and at 200, 140, and 82 V/cm. Other conditions are the same as in Figures 1 and 7.

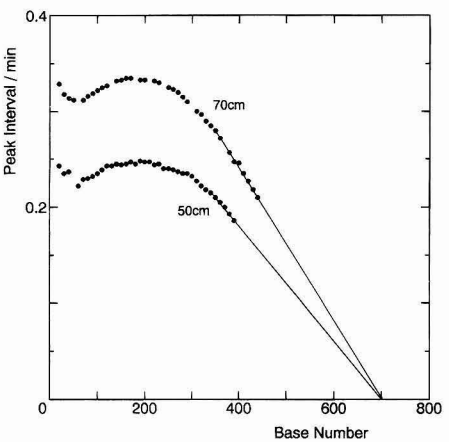


Figure 9. Peak interval vs base number at different capillary lengths. FITC-p(dT)$_{16-500}$ was subjected to capillary electrophoresis at 5% LPA concentration. Other electrophoretic conditions are the same as in Figure 1. The lines are the best-fit lines for the points of p(dT)s longer than 350 bases.

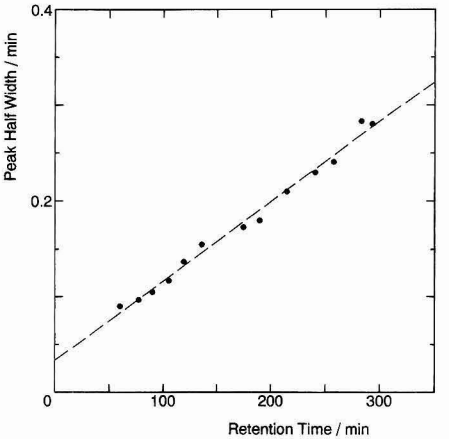


Figure 10. Peak half-width vs migration time plot. The data were obtained from the pattern shown in Figure 4. The line is the best-fit line ($r = 0.995$) for the 13 peaks.

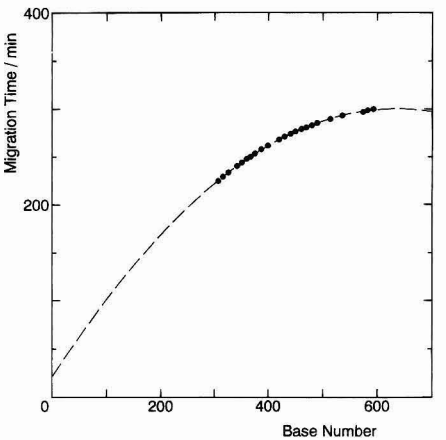


Figure 11. Migration time vs base number. The data were obtained from the pattern in Figure 4, and a second-order best-fit curve (r = 0.999 89) was traced for the 23 peaks of DNA fragments longer than 320 bases.

Analysis of the Resolution of FITC-M13mp10 Sequencing Fragments. The estimation of N_{max} is quite important to predict the performance of capillary electrophoresis in DNA sequencing. To obtain another estimate of N_{max}, the resolution of FITC-M13mp10 sequencing reaction products was examined under the same electrophoretic conditions as those employed in the analysis of p(dT)$_{16-500}$. Figure 4 shows one of the electropherograms of the sequencing reaction products (thymidine reaction products) separated in 9% LPA, the capillary effective length being 50 cm and the electric field 200 V/cm. The mobility differences between single-base adjacent peaks can be clearly detected up to the peaks corresponding to 454 and 455 bases. However, the resolution gradually deteriorated, and after the appearance of the large peak at migration time 311 min, no fluorescent peak was detected. From the base number of each DNA peak calculated from the known sequence of M13 DNA, averaged peak intervals, i.e., peak intervals of adjacent peaks divided by the differences of base number, were calculated from the data shown in Figure 4. Figure 5 shows a plot of the averaged peak intervals vs the DNA chain lengths in base number. It is clear that the plot can be linearly extrapolated to ~640 bases ($N_{max} = 640$), which is in accordance with the value of N_{max} (650 bases) predicted for p(dT) fragments.

Separation Regimes of M13mp10 Sequencing Fragments. The plot of mobility (μ) vs reciprocal base number ($1/N$) (Figure 6) for the data shown in Figure 4 confirmed that the onset of the biased reptation regime occurs at ~320 bases. Furthermore, since the mobilities of DNA fragments longer than 500 bases could be

plotted, the tendency to have a size-independent mobility is more apparent in the case of the M13 DNA fragments than in the case of p(dT). Therefore, the large fluorescent peak marked by an arrow in Figure 4 is likely to represent a mixed peak of DNA fragments longer than 650 bases. The results shown in Figures 1–6 clearly demonstrate that, at 9% T LPA concentration and at 200 V/cm electric field, DNA fragments longer than ~650 bases cannot be separated. The tendency of long DNA fragments to have a size-independent mobility has been attributed to the stretching of the molecules, caused by the forced movement through small pores under high electric fields.[25,26] Next, the effect of LPA concentration (pore size) and the effect of electric field on N_{max} were examined separately.

Effect of LPA Concentration on Peak Interval and N_{max}. Figure 7 shows a plot of peak interval vs the base number of $p(dT)_{16-500}$ at three LPA concentrations, where the electric field (200 V/cm) and the capillary length (50 cm) were unchanged. The higher LPA concentration is preferable for better resolution because of the larger values of peak interval. However, the pore size of the polyacrylamide network does not obviously affect the value of N_{max}, except that in 5% LPA the N_{max} value (~700 bases) is somewhat larger than in 7% or 9% LPA (~650 bases).

Effect of Electric Field on Peak Interval and N_{max}. Figure 8 shows a plot of peak interval vs the base number of $p(dT)_{16-500}$ at three different electric fields, where the LPA concentration (9%) and the capillary length (50 cm) were unchanged. Higher values of peak interval and N_{max} are obtained at lower electric fields. The estimated values of N_{max}, obtained by extrapolating the plots, were ~650 bases at 200 V/cm, ~700 bases at 140 V/cm, and ~970 bases at 82 V/cm. In separate experiments employing a 40-cm capillary, the N_{max} value was estimated to be 930 bases at 100 V/cm. These results indicate that lower field strengths are preferable for the resolution of long DNA fragments. However, the migration time of DNA fragments increases proportionally as the electric field decreases.

Effect of Capillary Length on N_{max}. Since the N_{max} value is obtained by linear extrapolation of the peak interval vs base number plot, the value must be independent of the capillary length employed. In fact, the increase of capillary length from 50 to 70 cm (at 5% LPA concentration and 200 V/cm electric field) proportionally increases the peak intervals as shown in Figure 9, giving the same value of N_{max} of 700 bases.

Prediction of Resolution at Various Capillary Lengths. Once we obtained the values of peak interval at a certain capillary length, the values in any capillary lengths could be calculated proportionally, as shown in Figure 9. Therefore, the resolution of DNA fragments at any capillary length can be predicted if the relationship between the capillary length and the values of peak half-width is analyzed, as has been illustrated in Figure 2. Luckey et al.[14] assumed that all sources of band broadening are independent of one another and expressed the net effect of the band broadening mechanisms in the following equation;

$$\sigma^2_T = \sigma^2_{Inj} + \sigma^2_{Det} + \sigma^2_{\Delta T} + \sigma^2_{Diff} \quad (4)$$

where σ_T is the total peak variance, and σ_{Inj} is the variance arising from the electrokinetic injection, σ_{Det} from the finite detection volume, $\sigma_{\Delta T}$ from the thermal gradients across the capillary, and σ_{Diff} from the diffusion of bands in the polymer network. The half-width is then given by

Table 1. Predicted Values of Resolution and Migration Time for Long DNA Fragments Separated in 9% LPA and at 200 V/cm

base no.	resolution (R)	migration time (min)
	L = 20 cm	
350	0.83	98
400	0.65	105
450	0.49	111
500	0.35	115
550	0.21	118
600	0.09	120
	L = 40 cm	
350	0.97	195
400	0.75	210
450	0.56	221
500	0.40	230
550	0.25	236
600	0.10	240
	L = 60 cm	
350	1.03	293
400	0.79	314
450	0.59	332
500	0.42	345
550	0.26	354
600	0.11	359

$$hw = 2(2 \ln 2)^{1/2}\sigma_T/\mu E \quad (5)$$

where μE is the velocity of the measured band. For our practical purpose to estimate the maximum base number separable in our electrophoretic conditions, we can employ the values of hw measured at a certain capillary length. Figure 10 shows a plot of peak half-width vs migration time, obtained from the data shown in Figure 4. The plots clearly show that the observed values of hw_{obs} are the sum of the migration time-dependent part and the migration time-independent part;

$$hw_{obs} = k_1(c,E)t + k_2(c,E) \quad (6)$$

where k_1 and k_2 are constants at a given LPA concentration (c) and field strength (E) and t is the migration times of the peaks. The term $k_1(c,E)t$ might include the variances of σ_{Det}, $\sigma_{\Delta T}$, and σ_{Diff}, and the term $k_2(c,E)$ might include the variance of σ_{Inj}. The constants k_1 and k_2 were calculated from the best-fit line (r = 0.995):

$$hw_{obs} = 8.33 \times 10^{-4}t + 0.0332 \quad (7)$$

at 9% LPA and 200 V/cm. In this equation, hw_{obs} and t are expressed in time (min). When the migration times of the DNA peaks in Figure 4 were plotted against the DNA fragment lengths (base number, N) for 23 peaks in the range from 320 to 590 bases (Figure 11), the plot almost perfectly fitted (r = 0.999 89) the following quadratic equation:

$$T = -6.92 \times 10^{-4}N^2 + 0.88N + 20.7 \quad (8)$$

The formula for peak interval (pi) vs base number (N) relationship can be obtained by differentiating eq 8:

$$pi = -1.384 \times 10^{-3}\,(N - 636)\,(L/50) \quad (9)$$

Table 2. Predicted Values of Resolution and Migration Time for Long DNA Fragments Separated in 9% LPA and at 100 V/cm

base no.	resolution (R)	migration time (min)
	$L = 20$ cm	
350	0.78	161
400	0.67	178
450	0.57	194
500	0.49	209
550	0.42	222
600	0.35	233
650	0.29	243
700	0.23	251
750	0.18	257
800	0.12	262
850	0.08	266
900	0.03	267
	$L = 40$ cm	
350	0.99	322
400	0.83	357
450	0.70	389
500	0.59	418
550	0.50	443
600	0.42	466
650	0.34	485
700	0.27	501
750	0.21	514
800	0.15	524
850	0.09	531
900	0.03	535
	$L = 100$ cm	
350	1.16	804
400	0.97	892
450	0.81	972
500	0.68	1044
550	0.57	1108
600	0.47	1165
650	0.38	1213
700	0.30	1254
750	0.23	1286
800	0.16	1311
850	0.10	1328
900	0.03	1337

Table 3. Predicted Values of Resolution and Migration Time for Long DNA Fragments Separated in 5% LPA and at 100 V/cm

base no.	resolution (R)	migration time (min)
	$L = 40$ cm	
350	0.58	152
400	0.51	169
450	0.46	186
500	0.41	201
550	0.36	216
600	0.33	230
650	0.29	243
700	0.26	255
750	0.23	266
800	0.21	277
850	0.19	286
900	0.16	295
950	0.14	302
1000	0.12	309
	$L = 60$ cm	
350	0.66	227
400	0.58	254
450	0.51	278
500	0.45	302
550	0.40	324
600	0.36	345
650	0.32	365
700	0.29	383
750	0.26	400
800	0.23	415
850	0.20	429
900	0.18	442
950	0.15	454
1000	0.13	464
	$L = 100$ cm	
350	0.75	379
400	0.65	423
450	0.57	464
500	0.50	503
550	0.44	540
600	0.39	575
650	0.35	608
700	0.31	638
750	0.28	666
800	0.25	692
850	0.22	715
900	0.19	737
950	0.17	756
1000	0.14	773

where 50 cm is the actual capillary length employed to obtain the results shown in Figure 4, L is the capillary length (cm) to be employed, and 636 is the N_{max} value that corresponds to the intersection of the peak interval plot with the base number axis in Figure 5. We used this equation instead of that obtained by actually fitting the plot in Figure 5. From eqs 7–9 and give the values of L, the resolution ($R = 0.59 \times$ pi/hw) and the migration times of long DNA fragments have been calculated and some of the calculation results are shown in Table 1. The DNA length separable at a resolution of 0.50 in 9% LPA, at 200 V/cm, and using a 20 cm capillary is calculated to be 446 bases, and this number might only increase to 476 when a 60-cm capillary is employed, whereas the analysis time would increase 3-fold. Similar calculations were performed from one electropherogram obtained in 9% LPA and at 100 V/cm (Table 2) and another in 5% LPA and at 100 V/cm (Table 3). As shown in Tables 1–3, if the efficiency is the most important factor in DNA sequencing, the use of high electric fields and short capillaries filled with LPA in a relatively high concentration is recommended. However, if the sequencing of long DNA fragments in one electrophoretic run is the major aim, low LPA concentrations and low electric fields must be employed, with long capillaries and subsequently with long analysis time.[9] It is also obvious from the tables that the improvement of the peak recognition software is very important in order to determine the sequence of long DNA fragments in single electrophoretic run.

Analysis of M13mp10 Sequencing Fragments at 100 V/cm. Examining the calculated results in Tables 1–3, the conditions of 9% LPA and 100 V/cm were expected to give good performance both in separable base number and in analysis time. Figure 12 shows one of the separation patterns of FITC-labeled M13mp10 fragments (thymidine reaction products) in 9% LPA, at 100 V/cm, and with capillary effective length 40 cm. Although the capillary length is shorter than in the case shown in Figure 4, single-base resolution was obtained up to 521 and 522 bases. Moreover, fluorescent peaks for DNA fragments longer than 700 bases could be detected, as expected from the calculation.

Further Improvement of Resolution. Concerning the further improvement of the resolution of DNA fragments, minimizing the contribution of the injection variance σ_{Inj} (we employed a 40-s injection time) and that of the finite detection volume σ_{Det} (our laser detection system had a 120-μm beam width) would be the simplest way. For example, if the contributions of σ_{Det} and

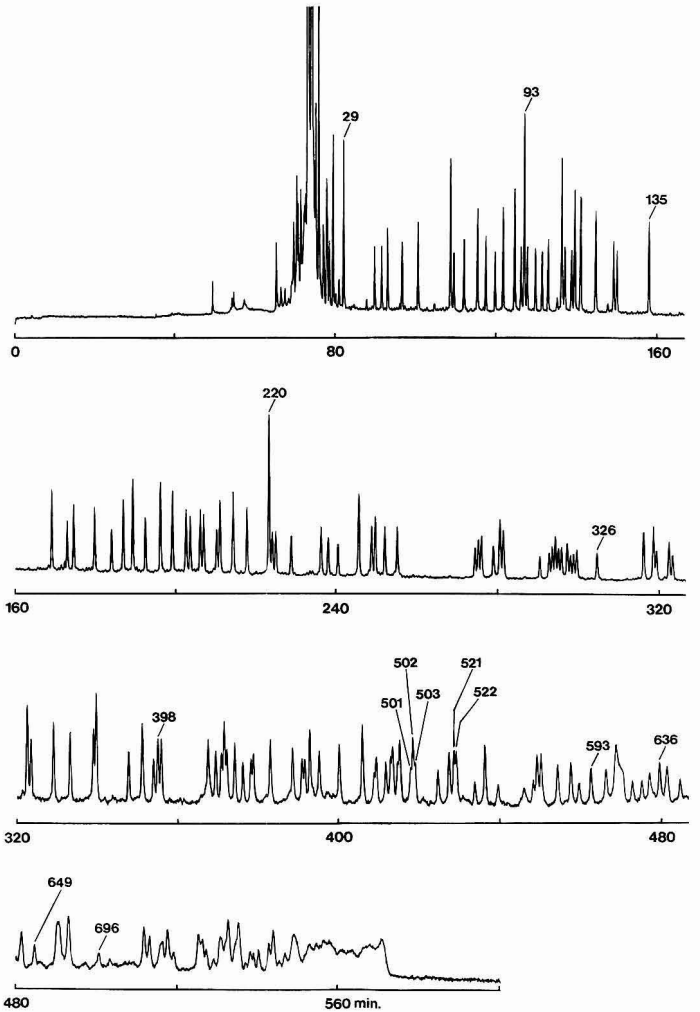


Figure 12. Separation of FITC-labeled M13mp10 DNA fragments (thymidine reaction products). Electric field was 100 V/cm, and capillary length was 40 cm. Other electrophoretic conditions were the same as shown in Figure 1, except the injection was at 213 V/cm for 40 s.

σ_{Inj} were both negligible, the equation for the observed half-width at 9% LPA and 200 V/cm (eq 7) can be written in the following form:

$$hw_{obs} = (8.33 \times 10^{-4} - 0.012/L)T \qquad (10)$$

Then the base number separable with a resolution of 0.5 was calculated to increase from 476 to 523 at 9% LPA, with 200 V/cm field strength and using a 60-cm capillary.

Another point to be improved is to minimize the deformation of capillary shape;[19] although we modified the cartridge, we still have to bend the capillary to position it. This is inevitable if we are to use any of the commercial instruments. The effect of capillary deformation on the resolution is reported to be time-dependent[19] and seems to be difficult to evaluate quantitatively. Improvement of resolution from this point of view awaits further investigation.

Performance of Capillary Electrophoresis in DNA Sequencing. High-performance DNA sequencing by capillary electrophoresis has been reported by Ruiz-Martinez et al.,[7] employing replaceable linear polyacrylamide. They employed 6% LPA and modified the denaturing agent of the running buffer from the typical 7 M urea to 3.5 M urea plus 30% (v/v) formamide[7] aiming to reduce the viscosity of the medium and to enhance the

denaturing ability[27] with the addition of formamide. As shown in Table 3, it is predicted that capillaries filled with 5% LPA with 7 M urea can separate DNA fragments up to 500 bases in resolution higher than 0.5. Therefore, the technique of LPA replacement should be applicable for the separation of long DNA fragments. High-performance DNA sequencing by capillary electrophoresis has also been reported by Luckey and Smith,[8] employing cross-linked polyacrylamide gel. They systematically examined the effect of electric field strength on the separation of DNA fragments and indicated that, at an electric field strength of roughly 200 V/cm, capillary gel electrophoresis is most efficient in their experimental conditions (Tris–phosphate–EDTA buffer, 50-μm-i.d. capillaries, 4% *T*/5% *C* polyacrylamide gel). These results coincides with our results in LPA capillaries, shown in Table 1, that the combination of high electric field (200 V/cm) and short capillaries provides aim high efficiency in the separation of DNA fragments shorter than ~450 bases. Examination of the N_{max} values in capillaries filled with cross-linked polyacrylamide gel, at various gel compositions and electric field strengths, will provide general understanding of the performance of capillary electrophoresis in DNA sequence analysis.

CONCLUSIONS

Our capillary electrophoretic analysis of oligonucleotides and DNA sequencing reaction products in linear polyacrylamide shed light on the separation behavior of long DNA fragments at high electric fields. The prediction of maximum separable base number (N_{max}) enabled us to predict the performance of capillary electrophoretic separation of long DNA fragments at any capillary length. Although the values of predicted resolution given in Tables 1–3 are specific for our apparatus, the trends should be generally applicable for analysis in linear polyacrylamide. Similar analysis of the resolution of long DNA sequencing fragments in cross-linked polyacrylamide, in various acrylamide concentrations and cross-linker concentrations, will provide a general understanding of the performance that can be expected for capillary electrophoresis in DNA sequencing.

(27) Rocheleau, M. J.; Grey, R. J.; Chen, R. Y.; Harke, H. R.; Dovichi, N. J. *Electrophoresis* **1992**, *13*, 484–486.

ACKNOWLEDGMENT

The authors thank Dr. S. Hata, Dr. T. Osumi, and Dr. H. Kambara for kindly providing DNA samples and Dr. H. Yamamoto for helpful discussions. N.C. is grateful to Prof. T. Nakagawa of Kyoto University for his kind invitation to Japan. This work was supported by a grant from the Institute of Physical and Chemical Research (RIKEN).

Received July 19, 1994. Accepted September 1, 1994.[⊗]

[⊗] Abstract published in *Advance ACS Abstracts,* October 1, 1994.

Anal. Chem. **1994,** *66,* 4253–4257

Retention Prediction Based on Molecular Interactions in Packed-Column Supercritical Fluid Chromatography

Darren M. Heaton,* Keith D. Bartle, and Anthony A. Clifford

School of Chemistry, University of Leeds, Leeds LS2 9JT, UK

Matthew S. Klee and Terry A. Berger

Hewlett Packard Company, Wilmington, Delaware 19808

A model for retention prediction in packed-column supercritical fluid chromatography based upon multicomponent solubility parameters, δ_d, δ_o, δ_{in}, δ_a, and δ_b, is proposed. These parameters are direct measures of a solute's ability to partake in dispersive, dipole–dipole, dipole–induced dipole, and hydrogen-bonding acidic and basic interactions, respectively. Retention data for a series of aromatic molecules of form Ph–X was obtained on ODS, phenyl, nitrile, and amino bonded phases and bare silica. Carbon dioxide at a pressure of 114–135 bar modified with up to 20% methanol at a temperature of 60 °C was used as mobile phase. Retention is described by an equation of the form $\ln k' = V_m(a\delta_d + b\delta_o + c\delta_{in} + d\delta_a + e\delta_b + f)$, where V_m represents molar volume, k' represents capacity factor, and a–f are weighting coefficients. The model is used to derive δ values for new compounds and is extended to retention prediction for disubstituted aromatics.

The development of a chromatographic method for a new analyte is often a process of trial and error coupled with experience of similar or closely related compounds. This often includes the selection of stationary and mobile phase compositions that give the required resolution of the sample's components within a reasonable time span.

Many methods have been proposed for retention prediction in both GC and HPLC. Examples include structure/retention relationships for alkylbenzenes,[1] alkylbiphenyls, disubstituted aromatics,[2] monosubstituted aliphatics,[3] and linear solvation energy (LSE) approaches[4,5] in HPLC, and statistical,[6] retention index,[7] phase constant,[8] and LSE[9] methods in GC. Such methods potentially allow the determination of optimum chromatographic conditions before any analyses are performed. Although no such methods as yet, however, exist for SFC, correlations between solute structure and solubility in supercritical fluids have been proposed.[10]

SFC has several advantages over GC and HPLC. One of the more important is the ability to fine tune the fluid properties and retention mechanism by adjusting temperature and pressure. The high diffusion coefficients of gases are achieved at higher temperatures and lower fluid densities (and therefore pressures), giving rise to a volatility-based mechanism, whereas the solvation power of liquids is approached at lower temperatures and higher pressures, resulting in a predominantly solvation-based mechanism.

Recently, there has been a good deal of renewed interest in SFC using packed columns. Advantages of packed-column SFC include generally shorter analysis times compared to HPLC, since the van Deemter minimum is shifted toward higher flow rates for supercritical fluids. In addition, the higher phase ratio of packed columns compared to capillary means that the transition to semipreparative SFC is relatively easy.

In the present study, a retention model for packed-column SFC is proposed based on molecular properties of the solute such as polarizability, polarity, and acidity/basicity. Potential for such interactions can be expressed by multicomponent solubility parameters,[11–15] which are derived by resolving into components the total solubility parameter[16] (eq 1), where ΔE_v represents molar

$$\delta = (\Delta E_v / V_m)^{1/2} \quad (1)$$

vaporization energy of a compound and V_m its molar volume.

Initially,[17] δ was resolved into dispersive, polar, and hydrogen-bonding parameters, δ_d, δ_p, and δ_h, respectively, where the polar parameter accounted for dipole–dipole and dipole–induced dipole interactions and the hydrogen-bonding parameter accounted for

(1) Kriz, J.; Puncochararova, J.; Vodicka, L.; Vareka, J. *J. Chromatogr.* **1988,** *437,* 177.
(2) Smith, R. M.; Burr, C. M. *J. Chromatogr.* **1991,** *559,* 335–356.
(3) Smith, R. M.; Burr, C. M. *J. Chromatogr.* **1989,** *481,* 71–84.
(4) Kamlet, M. J.; Abraham, M. H.; Carr, P. W.; Doherty, R. M.; Taft, R. W. *J. Chem. Soc., Perkin Trans. 2* **1988,** 2087–2092.
(5) Taft, R. W.; Abboud, J.-L. M.; Kamlet, M. J.; Abraham, M. H. *J. Solution Chem.* **1985,** *14* (3), 153–186.
(6) Heberger, K. *Chromatographia* **1990.** *29* (7/8), 375–384.
(7) Hanai, T.; Hong, C. *J. High Resolut. Chromatogr.* **1989,** *12,* 327–332.
(8) Rohrschneider, L. *LC-GC Int.* **1993,** *6* (9), 553–561.
(9) Li, J.; Zhang, Y.; Carr, P. W. *Anal. Chem.* **1993,** *65,* 1969–1979.
(10) King, J. W.; Friedrich, J. P. *J. Chromatogr.* **1990,** *517,* 449–458.
(11) Karger, B. L.; Snyder, L. R.; Eon, C. *J. Chromatogr.* **1976,** *125,* 71–88.
(12) Karger, B. L.; Snyder, L. R.; Eon, C. *Anal. Chem.* **1978,** *50,* 2126–2136.
(13) Barton, A. F. M. *Chem. Rev.* **1975,** *75,* 731–753.
(14) Hanson, C.; Beerbower, A. *Kirk–Othmer Encyclopedia of Chemical Technology,* 2nd ed.; Standen, A., Ed.: Interscience Publishers (John Wiley & Sons): New York, 1971; Suppl. Vol., pp 889–910.
(15) Barton, A. F. M. *Handbook of Solubility Parameters and Other Cohesion Parameters;* CRC Press, Inc.: Boca Raton, FL, 1983.
(16) Hildebrand, J. H.; Prausnitz, J. M.; Scott, R. L. *Regular and Related Solutions;* Van Nostrand-Reinhold: Princeton, NJ, 1970.
(17) Hansen, C. *Ind. Eng. Chem. Prod. Res. Dev.* **1969,** *8,* 2.

0003-2700/94/0366-4253$04.50/0 © 1994 American Chemical Society

both acidic and basic interactions. This treatment was later expanded,[18] the total solubility parameter, δ, being resolved into five components, δ_d, δ_o, δ_{in}, δ_a, and δ_b, representing dispersive, dipole–dipole, dipole–induced dipole, and hydrogen-bonding acidity and basicity, respectively.

Such parameters for a solute, solvent, or stationary phase in a chromatographic system can readily be related to internal energy. This allows the derivation[12,18] of expressions representing transfer energies (from the gas phase) of adsorption ΔE^A and of solution ΔE^S for a solute. In SFC, we are concerned with adsorption and solution of a solute, and it can be shown that an expression in the form of eq 2 describes the energy of partition for this process,

$$\Delta E_{\text{partition}} = -n(\Delta E^A)_{j,a} - (\Delta E^S)_{i,j} + (\Delta E^A)_{i,j} + (\Delta E^A)_{i,a} \quad (2)$$

where i, j, and a represent solute, solvent, and adsorbent, respectively, and n is the molar volume ratio (V_i/V_j).

By substituting for the ΔE values, and using $\Delta G = -RT \ln(k'/\beta)$,[12] where k' is the chromatographic capacity factor and β the phase ratio, it can be shown that eq 3 can be used to describe

$$\ln k'_i = V_{m,i}(a\delta_{d,i} + b\delta_{o,i} + c\delta_{in,i} + d\delta_{a,i} + e\delta_{b,i} + f) \quad (3)$$

retention, where a–f are constants for a given stationary and mobile phase at a given temperature and V_m is molar volume.

The coefficients a–f for each temperature and mobile/stationary phase combination can be deduced by measuring retentions of probe solutes for which solubility parameters and molar volumes are known. These coefficients then allow the prediction of retention for other solutes whose solubility parameters have been calculated.

The five component solubility parameters can be calculated using a series of semiempirical equations.[18] The dispersive parameter, δ_d, is best calculated by use of an equation based upon the Lorentz–Lorenz expression.[19] This relates the refractive index, n, to δ_d (eq 4). Dipole–dipole and dipole–induced dipole

$$\delta_d = -2.24 + 53x - 58x^2 + 22x^3 \quad \text{where} \quad x = (n^2 - 1)/(n^2 + 2) \quad (4)$$

parameters can be calculated directly given the dipole moment using eqs 5 and 6, where C_o and C_{in} are constants obtained from

$$\delta_o = C_o\mu/V_m \quad (5)$$

$$\delta_{in} = C_{in}\mu^2/V_m \quad (6)$$

calibration with compounds whose solubility parameters and dipole moments are known.

Hydrogen-bonding solubility parameters are calculated by assuming that the energy of hydrogen bond interaction is the product of some function of the donor acidity (A) and acceptor basicity (B).[20] This leads to expressions in the form of eqs 7 and 8. C_{hb} is once again obtained by calibration using compounds

$$\delta_a = C_{hb}A/V_m \quad (7)$$

$$\delta_b = C_{hb}B/V_m \quad (8)$$

for which data are known.

Therefore, having obtained values for the coefficients a–f, and calculated the solubility parameters for a compound, the capacity factor for a given mobile and stationary phase is readily obtained from eq 3.

EXPERIMENTAL SECTION

1. Reagents and Materials. Reagents and materials used were obtained from various suppliers and were of analytical grade or better.

2. Supercritical Fluid Chromatography. A Hewlett Packard G1205A SFC system was employed for the chromatography. Carbon dioxide modified with small quantities of methanol at 60 °C was used as mobile phase. A multiple wavelength ultraviolet detector (MWD) was used at appropriate wavelengths. Sample introduction was via a Rheodyne 7410 injection valve fitted with a 0.5 μL sample loop. Standard HPLC packed columns (25 cm × 4.6 mm) were obtained from Phase Separations Ltd., Deeside, UK, and contained 5 μm diameter particles of octadecylsilyl (ODS2), phenyl-, nitrile-, and amino-bonded phases, and bare silica.

Retention times for series of probe molecules of general formulas Ph–X and C_6H_4XY, where X and Y represent substituents, were analyzed using methanol-modified (0%, 1%, 3%, 5%, 10%, 20% vol) carbon dioxide mobile phases. Solutions (1–5% w/w) were injected in HPLC grade dichloromethane, methanol, or hexane, depending on their solubility.

RESULTS AND DISCUSSION

1. Calculation of Void Time. Void times for the columns employed were calculated by considering column and packing dimensions, applying conservation of mass flow,[21] and assuming that the pressure drop across the column is linear.[22] This lead to a general expression for the total flow rate in the column, F_c, (eq 9), where $\varrho_p^{CO_2}$ and ϱ_p^{MeOH} represent the densities of carbon

$$F_c = (\varrho_p^{CO_2}F_p^{CO_2} + \varrho_p^{MeOH}F_p^{MeOH})/\varrho_c \quad (9)$$

dioxide and methanol in the pumps and ϱ_c is the mean density of the fluid mixture in the column obtained by calculating the mean column pressure from the column inlet and outlet pressures and then calculating the corresponding density. $F_p^{CO_2}$, F_p^{MeOH} represent the flow rates of carbon dioxide and methanol in the pumps. All fluid densities were obtained using standard PC software[23] except densities of liquid methanol in the pump, which were

(18) Keller, R. A.; Karger, B. L.; Snyder, L. R. *Gas Chromatography, 1970 Proceedings of the 8th International Symposium on Gas Chromatography*; Institute of Petroleum: London, 1971; pp 125–140.

(19) Smyth, C. P. *Dielectric Behavior and Structure*; McGraw-Hill: New York, 1955.

(20) Taft. R. W.; Gurka, D.; Joris, L.; Schleyer, P. von R.; Rakshys, J. W. *J. Am. Chem. Soc.* **1969**, *91*, 4801.

(21) Osonubu, M. O.; Martire, D. E. *5th International Symposium on Supercritical Fluid Chromatography and Extraction*; Baltimore, MD, January 10–14, 1994; Poster B-10.

(22) Schoenmakers, P. J.; Rothfusz, P. E.; Verhoeven, F. C. C. J. G. *J. Chromatogr.* **1987**, *395*, 91–110.

(23) *SF Solver Software for Supercritical Fluid Analysis*, version 2.5.1; Isco, Inc.: Lincoln, NE, 1991.

Table 1. Comparison of Calculated Void Times and "Nonretained" Solvent Front Times on an ODS2 Bonded Phase Packed HPLC Column[a]

% MeOH	calc void time, min	solvent retention time, min						
		C_6H_{14}	MeOH	ether	acetone	CCl_4	$CHCl_3$	CH_2Cl_2
0	0.464	0.947	1.070	0.953	0.958	1.244	1.120	1.003
1	0.490	0.994	1.037	0.944	0.925	1.230	1.128	1.011
3	0.556	1.038	1.001	0.938	0.952	1.204	1.107	1.058
5	0.613	1.079	0.946	0.925	0.978	1.199	1.096	1.068
10	0.732	1.153	0.818	0.974	1.013	1.198	1.120	1.134
20	0.853	1.162	0.876	1.051	1.042	1.181	1.116	1.099

[a] Conditions: temp, 60 °C; flow, 2 mL/min; column outlet pressure, 114–117 bar; fluid, CO_2 + x% methanol.

obtained from a database[24] incorporating the Lee–Kesler–Plocker equation of state. Column inlet and outlet pressures were measured to be 125–135 and 114–117 bar, respectively, depending on column type and modifier proportion. Flow rates were the values set by the SFC control software and gave rise to a total premixed flow rate of 2 mL/min in the pumps.

The value of F_c together with the column dimensions and the manufacturer's value for the void volume of the packing (both assumed to be constant for all five columns) readily allowed the calculation of void time for each column/mobile phase combination. The small variation in pressure drop across the different columns resulted in slight differences in calculated void time for a given mobile phase. These calculated values were compared with solvent front times for several solvents obtained by use of each column/mobile phase combination. Such solvent front times are often assumed to be nonretained and are frequently used in calculating capacity factors and retention indexes. Table 1 compares calculated void times with solvent front times obtained using the ODS2 column. For all five stationary phases, the calculated void times were found to be less than that shown by the solvents, indicating that solvents are in fact retained to a certain extent. This difference also illustrates the large variation in void times calculated by different methods,[25] highlights the difficulty that is often encountered when attempts to estimate such quantities are made, and can introduce the largest systematic error in the development of models for retention in chromatography.

2. Calculation of Capacity Factor. Capacity factors were calculated using eq 10, where M_1 represents the first statistical

$$k' = \frac{M_1 - c_0 - t_0}{t_0} \tag{10}$$

moment[26–30] (peak centroid), t_0 is the void time, and c_0 is a correction for extracolumn tubing. First statistical moment was used instead of the peak maximum because it is a more fundamental measure of retention (being independent of peak shape). The correction, c_0, was deduced by replacing the column with a zero dead volume connector and measuring the delay between injection and detection for a range of solvents under the conditions used for the probe compounds. Example capacity factor values for the ODS2 column are shown in Table 2.

Table 2. Predicted and Experimental Capacity Factors for a Series of Monosubstituted Benzene Probe Molecules with Various Mobile Phases (CO_2 + x% MeOH Modifier)[a]

compd substituent X	% MeOH modifier	ODS2 Column k′	
		expt	pred
H	0	1.906	2.161
Me	0	2.441	2.220
CO_2H	0	ne[b]	ne
COMe	0	24.310	24.347
NO_2	0	5.628	5.597
OH	0	ne	ne
Cl	0	3.112	3.323
Br	0	4.163	3.882
H	1	1.696	1.553
Me	1	2.151	2.176
CO_2H	1	43.483	30.955
COMe	1	4.291	3.201
NO_2	1	4.227	4.541
OH	1	5.614	8.279
Cl	1	2.708	4.636
Br	1	3.585	2.931
H	3	1.267	1.371
Me	3	1.596	1.476
CO_2H	3	6.938	6.211
COMe	3	2.734	2.488
NO_2	3	2.816	2.869
OH	3	3.302	3.747
Cl	3	1.968	2.480
Br	3	2.583	2.278
H	5	1.029	1.153
Me	5	1.261	1.146
CO_2H	5	3.718	3.510
COMe	5	2.053	1.956
NO_2	5	2.115	2.128
OH	5	2.477	2.645
Cl	5	1.547	1.812
Br	5	1.989	1.789
H	10	0.653	0.763
Me	10	0.796	0.703
CO_2H	10	1.729	1.660
COMe	10	1.133	1.096
NO_2	10	1.192	1.193
OH	10	1.322	1.384
Cl	10	0.955	1.111
Br	10	1.216	1.083
H	20	0.411	0.480
Me	20	0.486	0.428
CO_2H	20	0.512	0.484
COMe	20	0.464	0.443
NO_2	20	0.484	0.486
OH	20	0.372	0.397
Cl	20	0.537	0.642
Br	20	0.664	0.584

[a] Conditions: column outlet pressure, 114–117 bar; flow, 2 mL/min; Oven temp, 60 °C. [b] ne, not eluted in 60 min.

3. Retention Modeling. Capacity factors and solubility parameters[11,15] for each monosubstituted probe molecule, stationary, and mobile phase were incorporated into expressions in the form of eq 3. These were solved simultaneously for each stationary/mobile phase combination using matrices.[31] This gave values of a–f for each stationary/mobile phase combination. These coefficients for the ODS2 column are tabulated in Table 3.

(24) National Engineering Laboratories, Glasgow, UK.
(25) Wainwright, M. S.; Haken, J. K. *J. Chromatogr., Chromatogr. Rev.* **1980**, *184*, 1–20.
(26) Grushka, E.; Myers, M. N.; Giddings, J. C. *Anal. Chem.* **1970**, *42*, 21–26.
(27) Yau, W. W.; Kirkland, J. J. *J. Chromatogr.* **1991**, *556*, 111–118.
(28) Grushka, E. *Anal. Chem.* **1972**, *44*, 1733–1738.
(29) Jeansonne, M. S.; Foley, J. P. *J. Chromatogr.* **1989**, *461*, 149–163.
(30) Cai, C. P.; Wu, N. S. *Chromatographia* **1991**, *31* (11/12), 595–599.
(31) *MathCAD* Student Edition Software, version 2.06; MathSoft Inc., Addison Wesley: Reading, MA, 1988.

Table 3. $a-f$ Values for ODS2 Column Obtained by Use of a Series of Monosubstituted Benzene Probes[a]

	weighting coefficients $a-f$					
% MeOH	10^4a	10^4b	10^4c	10^4d	10^4e	10^4f
0	19.2	−0.868	24.5		25.2	−306
1	−39.2	36.9	−63.8	5.98	−5.78	793
3	−1.98	19.2	−30.7	3.31	−3.30	76.4
5	5.32	14.9	−23.5	2.55	−2.15	−81.5
10	4.57	15.1	−28.7	1.15	−1.53	−114
20	−4.26	18.4	−52.2	−3.06	−2.15	0.588

[a] Conditions: column outlet pressure, 114−117 bar; flow, 2 mL/min; oven temp, 60 °C; fluid, CO_2 + x% methanol.

Coefficients are seen to vary a large amount on moving from pure carbon dioxide mobile phase to 1% methanol modifier, thereafter showing a much more gradual variation with increasing modifier proportion. This is consistent with the formation of a thin layer of methanol on the stationary phase, thereby changing the nature of the surface. The coefficients $a-f$ are *related* to the five-component δ values for the stationary phase[12] and so are a crude measure of the stationary phase's ability to partake in the five different types of molecular interaction. Although these coefficients do not always vary smoothly, as might be expected, they do give us an insight into the behavior of the stationary phase in addition to that of the solutes. The fluctuations in these values can be attributed to inadequacies in the present retention model, which does not describe behavior perfectly. In addition, the shortage of available literature data means that the coefficients are derived by using the minimum amount of data, thereby increasing the potential for errors. This obviously leaves scope for future improvement in the model, which might allow both stationary phase trends and solute behavior in SFC to be better understood in terms of individual molecular interactions.

Resulting $a-f$ coefficients, solubility parameters, and molar volumes were substituted into eq 3, and predicted k' values (Table 2) plotted against experimental k' values. Plots were linear about the line $y = x$, thus indicating eq 3 to be a promising model for the prediction of retention in packed-column SFC. To confirm the validity of the model, several probe compounds were eliminated from the data set used to calculate the coefficients and the resulting coefficients used to predict the capacity factor of the eliminated probes. The predicted values showed some scatter, but usually predicted the retention to within a factor of 2. This prediction, however, since several probes were omitted from the simultaneous equations, meant that coefficients were being derived from the minimum amount of data (i.e., six unknowns from six simultaneous equations). This eliminates any cancellation of errors in the values of the coefficients, thus making predicted k' values more error prone. Due to the limited availability of five-component solubility parameters in the literature, it was not possible to use a much larger data set in the derivation of coefficients $a-f$.

4. Prediction of Solubility Parameters. Sets of equations in the form of eq 3 together with $a-f$ values (Table 3), V_m, and k' values can be solved simultaneously, allowing the determination of unknown five-component solubility parameters. Hence, by measuring retention for new compounds, δ values can be determined.

Solubility parameters for several monosubstituted aromatics were determined in this way. Resulting values are contained in Table 4. The values obtained were somewhat dependent on the data sets used to form the equations. Best results were obtained when equations from the $a-f$ values at 3%, 5%, and 10% methanol-modified mobile phases for all five stationary phases were used together. This could be because the definition of capacity factor means that for values obtained at high modifier concentrations, t_r is close to t_0 and so errors are more evident. For lower modifier concentrations t_0 is smaller, resulting once again in a larger capacity factor error. The addition of methanol to carbon dioxide mobile phase causes an increase in density and therefore an increase in void time for a given column void volume. Hence, by using data at 3%, 5%, and 10%, the best estimates for solubility parameters were obtained.

Table 4. Predicted Five-Component Solubility Parameters Calculated by Using eq 3 with $a-f$ Values (Table 3), Retention Data, and Molar Volumes

	parameters				
	δ_d	δ_o	δ_{in}	δ_a	δ_b
octylbenzene	17.7	0.0	0.0	0.0	5.7
octanophenone	19.9	5.6	0.8	0.0	5.6
methylbenzoate	19.2	4.5	0.8	0.4	6.2
aniline	19.6	6.3	1.3	7.9	10.2

Table 5. Predicted Five-Component Solubility Parameters for a Series of Disubstituted Aromatics

(a) Predicted (Incremental) δ Values for Disubstituted Aromatics

compound	δ_d	δ_o	δ_{in}	δ_a	δ_d
o,m,p-$C_6H_4(NO_2)$(Me)	18.8	7.4	2.3	0.0	2.0
o,m,p-C_6H_4(Br)(Me)	19.0	3.1	0.4	0.0	2.0
o,m,p-$C_6H_4(NO_2)$(Br)	20.2	10.5	2.7	0.0	2.8

(b) Predicted (eqs 4, 11, and 12) δ Values for Disubstituted Aromatics

substituents/position	δ_d	δ_o	δ_{in}	δ_a	δ_b
o-$C_6H_4(NO_2)$(Me)	19.3	7.2	2.1	0.0	2.0
m-$C_6H_4(NO_2)$(Me)	19.3	7.2	2.1	0.0	2.0
p-$C_6H_4(NO_2)$(Me)	19.3[a]	6.9	2.0	0.0	2.0
o-C_6H_4(Br)(Me)	19.5	3.2	0.4	0.0	2.0
m-C_6H_4(Br)(Me)	19.4	3.2	0.3	0.0	2.0
p-C_6H_4(Br)(Me)	19.3	3.1	0.3	0.0	2.0
o-$C_6H_4(NO_2)$(Br)	20.4[a]	8.9	2.3	0.0	2.8
m-$C_6H_4(NO_2)$(Br)	20.4	9.3	2.4	0.0	2.8
p-$C_6H_4(NO_2)$(Br)	20.4[a]	10.6	2.8	0.0	2.8

[a] Values for these solids assumed to equal the values for the liquid isomers as no refractive index available.

Resulting values were consistent with homologues and related molecules. For example, with octylbenzene the dispersive value of 17.7 $MPa^{1/2}$ illustrates the continuing decrease expected for the homologous series Ph−R, in which benzene has a value of 18.8 $MPa^{1/2}$ and toluene 18.2 $MPa^{1/2}$. The hydrogen-bonding basicity value of 5.7 $MPa^{1/2}$ for octylbenzene, although too large, reflects the increased aliphatic proportion (positive inductive effect) of the molecule compared to benzene and toluene for which $\delta_b = 1.2$ $MPa^{1/2}$.

Similar reasoning can be applied to the other compounds whose solubility parameters were derived in this way.

5. Application to Disubstituted Benzenes. The model was extended to several disubstituted benzenes in two different ways. Initially a group incremental approach was used. This took the

Table 6. Experimental and Predicted Capacity Factor Values Obtained for Disubstituted Benzenes on an ODS2 Column with a Variety of Mobile Phases (CO_2 + x% methanol)[a]

substituents/ arrangement	% MeOH	k′ expt	k′ pred[b]	k′ pred[c]
Me/NO_2 ortho	0	6.118	6.242	6.611
Me/NO_2 meta	0	6.883	6.299	6.674
Me/NO_2 para	0	7.511	6.885	7.118
Me/Br ortho	0	5.736	4.046	4.536
Me/Br meta	0	5.419	4.100	4.364
Me/Br para	0	5.451	4.143	4.315
NO_2/Br ortho	0	10.461	13.522	12.775
NO_2/Br meta	0	10.288	11.983	11.637
NO_2/Br para	0	10.016	8.775	9.358
Me/NO_2 ortho	1	4.703	7.495	6.338
Me/NO_2 meta	1	5.178	7.571	6.397
Me/NO_2 para	1	5.532	8.348	6.600
Me/Br ortho	1	4.869	4.519	3.733
Me/Br meta	1	4.600	4.584	4.282
Me/Br para	1	4.628	4.637	4.342
NO_2/Br ortho	1	8.353	12.050	7.205
NO_2/Br meta	1	8.363	10.736	7.261
NO_2/Br para	1	7.938	7.970	7.146
Me/NO_2 ortho	3	3.174	3.411	3.464
Me/NO_2 meta	3	3.460	3.432	3.486
Me/NO_2 para	3	3.614	3.642	3.581
Me/Br ortho	3	3.454	2.597	2.626
Me/Br meta	3	3.262	2.621	2.758
Me/Br para	3	3.269	2.640	2.721
NO_2/Br ortho	3	5.236	6.135	4.854
NO_2/Br meta	3	5.304	5.639	4.764
NO_2/Br para	3	5.061	4.539	4.467
Me/NO_2 ortho	5	2.348	2.295	2.416
Me/NO_2 meta	5	2.532	2.304	2.427
Me/NO_2 para	5	2.642	2.399	2.467
Me/Br ortho	5	2.603	1.870	1.965
Me/Br meta	5	2.467	1.881	2.022
Me/Br para	5	2.475	1.890	1.983
NO_2/Br ortho	5	3.693	4.073	3.449
NO_2/Br meta	5	3.748	3.816	3.399
NO_2/Br para	5	3.605	3.226	3.233
Me/NO_2 ortho	10	1.277	1.188	1.260
Me/NO_2 meta	10	1.352	1.189	1.261
Me/NO_2 para	10	1.408	1.199	1.250
Me/Br ortho	10	1.539	1.063	1.113
Me/Br meta	10	1.446	1.064	1.147
Me/Br para	10	1.456	1.064	1.121
NO_2/Br ortho	10	1.870	1.984	1.714
NO_2/Br meta	10	1.902	1.922	1.736
NO_2/Br para	10	1.846	1.771	1.762
Me/NO_2 ortho	20	0.533	0.450	0.475
Me/NO_2 meta	20	0.554	0.448	0.474
Me/NO_2 para	20	0.562	0.431	0.455
Me/Br ortho	20	0.821	0.558	0.556
Me/Br meta	20	0.772	0.555	0.593
Me/Br para	20	0.767	0.553	0.580
NO_2/Br ortho	20	0.692	0.614	0.546
NO_2/Br meta	20	0.765	0.628	0.576
NO_2/Br para	20	0.736	0.666	0.637

[a] Conditions: column outlet pressure, 114–117 bar; flow, 2 mL/min; oven, 60 °C. [b] Predicted using incremental solubility parameters (Table 5a). [c] Predicted using Solubility parameters obtained by use of eqs 4, 11, and 12 (Table 5b).

five-component solubility parameters for the probes (Ph–X) and subtracted the corresponding parameters for benzene, yielding solubility parameter increments for substituents X. These individual increments were then added as appropriate to the solubility parameters for benzene, giving estimates of the solubility parameters for disubstituted benzenes (Table 5a).

Experimental capacity factors were deduced from measured retentions for the disubstituted compounds in the same way as for the monosubstituted compounds. Example values of predicted and experimental capacity factors using the ODS2 column are shown in Table 6. These were then plotted against the predicted capacity factors obtained by substituting into eq 3 values for molar volume, a–f coefficients, and the incrementally derived solubility parameters. Elution order of the ortho, meta, and para isomers was often correctly predicted. Some values often fell just above the $y = x$ line, indicating that the model was tending to overestimate the capacity factors. This is possibly due to steric effects which inhibit interactions of each group with the stationary phase thus decreasing retention. This steric effect will be different for ortho, meta, and para isomers.

Alternatively, solubility parameters can be calculated by using modified forms of eqs 4–8. The calculation of the dispersive solubility parameter can be performed by using eq 4 in its present form. Equations 5 and 6 for dipole–dipole and dipole–induced dipole parameters require modification[11] for species with n substituents (eqs 11 and 12), where i represents the ith substituent,

$$\delta_{in} = (C_{in}/V_m)\sum_{i}^{n}(\mu_i)^2 \qquad (11)$$

$$\delta_o = (C_o/V_m)\sum_{i}^{n}\mu_i \qquad (12)$$

and μ_i the dipole moment for the functional group. μ_i was taken as the dipole moment of the monosubstituted benzene with appropriate substituent X.

The hydrogen-bonding parameters were estimated by the group incremental approach as described above.

These resulting solubility parameters (Table 5b) were substituted into eq 3 together with molar volumes and a–f coefficients yielding capacity factors. These predicted values were once again plotted against the experimental values resulting in approximately straight line plots. Predicted values were now generally closer to the experimental values. This method of prediction did not, however, predict the correct elution order of the ortho, meta, and para isomers as often as the group incremental method. This can be attributed to the partial cancellation of the molar volume term in eq 3 with the volume terms in eqs 11 and 12, often resulting in values for the different isomers that are closer together. Variations in the magnitudes and signs of the remaining terms in eq 3 are frequently sufficient to affect the predicted elution order of the different isomers.

ACKNOWLEDGMENT

The authors thank Hewlett Packard for supplying equipment and software, and the University of Leeds Henry Ellison Scholarship Fund for supporting this work. Thanks also are due to B. Frere, D. Fogarty, and D. Mills for practical help and useful discussions.

Received for review June 29, 1994. Accepted August 26, 1994.[⊗]

[⊗] Abstract published in *Advance ACS Abstracts,* October 1, 1994.

Anal. Chem. **1994,** *66,* 4258–4264

Determination of Chloride, Nitrate, Sulfate, Nitrite, Fluoride, and Phosphate by On-Line Coupled Capillary Isotachophoresis–Capillary Zone Electrophoresis with Conductivity Detection

Dušan Kaniansky,*,† Imrich Zelenský,† Anna Hybenová,† and Francis I. Onuska‡

Department of Analytical Chemistry, Faculty of Natural Sciences, Comenius University, Mlynská Dolina CH-2, 842 15 Bratislava, Slovak Republic, and Aquatic Ecosystem Protection Branch, National Water Research Institute, Environment Canada, 867 Lakeshore Road, P.O. Box 5050, Burlington, Ontario L7R 4A6, Canada

Capillary zone electrophoresis (CZE) on-line coupled with capillary isotachophoresis (ITP) in the column-coupling configuration of the separation unit was studied for determination of nitrite, fluoride, and phosphate persent in a large excess of chloride, nitrate, and sulfate. Such distributions of these anions are typical for many environmental matrices, and it is shown that the ITP–CZE tandem enables the ITP determination of the macroconstituents, while ITP-preconcentrated microconstituents cleaned up from the macroconstituents can be determined by CZE with a conductivity detector. This approach was effective when the concentration ratio of macro-microconstituents was less than (2–3) × 10^4. The limits of detection achieved for the microconstituents (200, 300, and 600 pptr for nitrite, fluoride, and phosphate, respectively) enabled their determinations at low parts per billion concentrations in instances when the concentrations of sulfate or chloride in the samples were higher than 1000 ppm. Although in such situations the load capacity of the ITP column was not sufficient to provide the quantitations of the macroconstituents, the ITP sample cleanup enabled the CZE determinations of the microconstituents present in the samples at 10^5–10^6-fold lower concentrations. Experiments with samples of such extreme compositions showed that anionic impurities from the ITP electrolyte solutions transferred together with the analytes into the CZE column are probably the main hindrances in extending this dynamic concentration range by decreasing the limits of the detection to a level associated with the noise characteristics of the conductivity detector.

At present, ion chromatography (IC) has a dominant position among the separation methods used for the analysis of inorganic anions (see, e.g., refs 1–4). However, when the separation efficiencies typically achieved by IC are compared to those characterizing capillary zone electrophoresis (CZE) for the same group of analytes,[5] it is apparent that the latter technique has advantages. As the effective mobilities of inorganic anions differ sufficiently due to differences in their ionic mobilities[5,6] and/or can be influenced in a desired way via appropriately chosen pH (differences in pK_a values) and/or via the use of suitable nonionic additives,[7,8] the selectivity factors[9] are also favorable in achieving rapid resolutions of the analytes by CZE.

Although in some instances it is possible to determine very low concentrations of inorganic anions by CZE,[10,11] problems occur when the concentrations of the sample constituents differ considerably. This is due to the fact that the determination of microconstituents may require the sample load to have a negative impact on both the migration velocities and the resolutions of the analytes.[12] The use of indirect detection, as preferred in CZE of inorganic anions (see, e.g., refs 5, 10, 11), is also less favorable in achieving adequate load capacities since low detection limits are met through a low concentration of the carrier constituent.[13] In this context, it is to be noted that the load capacity limits may hinder the CZE determination of inorganic anions also in instances when the analytes are detected by the detection techniques having no prior restrictions with respect to the concentration of the carrier electrolyte.[14]

Of the inorganic anions which are currently monitored in water, chloride, sulfate, and in many instances also nitrate can be considered anionic macroconstituents. These are typically accompanied by nitrite, fluoride, and phosphate present in water samples at 10^2–10^5-fold lower concentrations. Such a wide concentration span probably cannot be covered by CZE, especially when restrictions of the detection in the indirect mode are taken

† Comenius University.

‡ National Water Research Institute, Environment Canada.

(1) MacCarthy, P.; Klusman, R. W.; Rice, J. A. *Anal. Chem.* **1989**, *61*, 269R.
(2) Frankenberger, W. T., Jr.; Mehra, H. C.; Gjerde, D. T. *J. Chromatogr.* **1990**, *504*, 211.
(3) MacCarthy, P.; Klusman, R. W.; Cowling, S. W.; Rice, J. A. *Anal. Chem.* **1991**, *63*, 301R.
(4) Tarter, J. G., Ed. *Ion Chromatography*; M. Dekker; New York and Basel, 1987.
(5) Jones, W. R.; Jandik, P. *J. Chromatogr.* **1991**, *546*, 445.
(6) Hirokawa, T.; Nishino, M.; Aoki, N.; Kiso, Y.; Sawamoto, Y.; Yagi, T.; Akiyama, J. I. *J. Chromatogr.* **1983**, *271*, D1.
(7) Fukushi, K.; Hiiro, K. *J. Chromatogr.* **1990**, *518*, 189.
(8) Madajová, V.; Turcelová, E.; Kaniansky, D. *J. Chromatogr.* **1992**, *589*, 329.
(9) Foret, F.; Boček, P. *Adv. Electrophor.* **1989**, *3*, 271.
(10) Bandoux, G.; Jandik, P.; Jones, W. R. *J. Chromatogr.* **1992**, *602*, 79.
(11) Jackson, P. E.; Haddad, P. R. *J. Chromatogr.* **1993**, *640*, 481.
(12) Beckers, J. L.; Everaerts, F. M. *J. Chromatogr.* **1990**, *508*, 3.
(13) Yeung, E. S. *Acc. Chem. Res.* **1989**, *22*, 125.
(14) Amran, M. B.; Lakkis, M. D.; Lagarde, F.; Leroy, M. J. F.; Lopez-Sanchez, J. F.; Rauret, G. *Fresenius J. Anal. Chem.* **1993**, *345*, 420.

0003-2700/94/0366-4258$04.50/0 © 1994 American Chemical Society

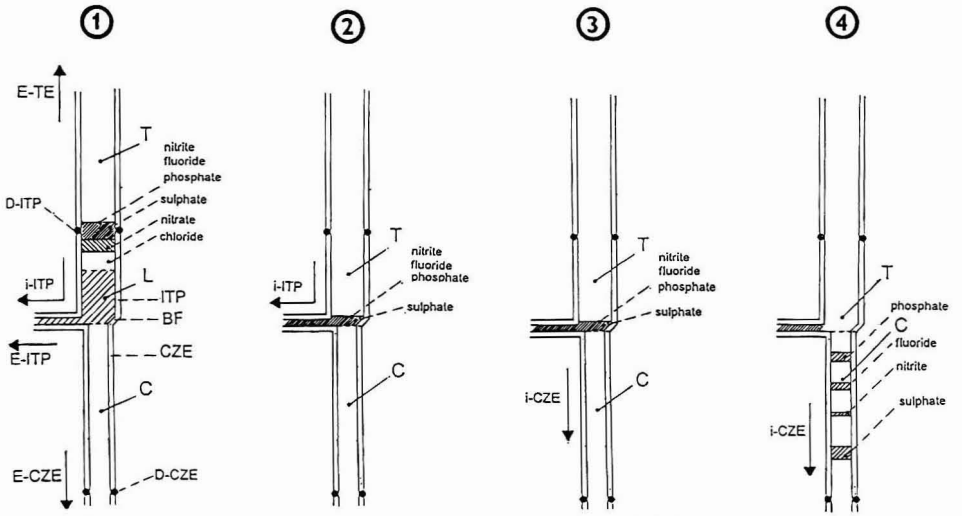


Figure 1. Schematic illustration of the ITP determination of chloride, nitrate, and sulfate and the CZE determination of nitrite, fluoride, and phosphate in column-coupling CE instrument. 1, ITP separation of the anions in the ITP column (ITP stage); 2, removal of the macroconstituents (chloride, nitrate, sulfate) from the separation compartment; 3, transfer of the sample microconstituents (nitrite, fluoride, phosphate) into the CZE column (after the microconstituents, focused in the boundary layer between the sulfate and terminating zones, reach the position as shown in step 2, a high-voltage relay is switching the columns so that the driving current flows through the column); 4, CZE separation of the microconstituents (CZE stage). L, T, C refer to leading, terminating, and carrier electrolytes, respectively; D-ITP, D-CZE are detectors for the ITP and CZE columns, respectively; ITP is the ITP column; CZE is the CZE column; BF is the bifurcation block; E-TE is the direction to the terminating electrode; E-ITP is the direction to the counter electrode of the ITP column; E-CZE is the direction to the counter electrode of the CZE column; i-ITP is the direction of the driving current in the ITP stage; and i-CZE is the direction of the driving current in the CZE stage.

into account.[15] It appears that at present CZE offers for this analytical problem only a moderate improvement over the early days of this technique.[16]

Capillary isotachophoresis (ITP) in the column-coupling configuration of the separation unit provides a two-step procedure (integrated into one electrophoretic run) for a simultaneous determination of the anionic macro- and microconstituents in water.[17] However, its use is limited when the concentrations of the macroconstituents are ca. 10^3-fold higher than those of the microconstituents. Two independent ITP runs provide a way to perform these measurements when the concentration ratio of macro-/microconstituents is in the range 10^3–10^4.[18] For higher values of this ratio, the determination of the microconstituents is possible only when a suitable sample preparation procedure is employed. For fluoride and phosphate, such procedures which are compatible with the ITP determinations are described in the literature.[19,20] However, their use is both time and labor intensive.

It was shown recently that an on-line combination of ITP with CZE in the column-coupling capillary electrophoresis instrument is a convenient capillary electrophoresis (CE) alternative to the analysis of trace ionogenic constituents present in a large excess of matrix ions.[21–29] Analytical capabilities of such a combination are apparent from the following facts.

(i) In the ITP column (capable of accommodating sample volumes up to several hundred microliters), the sample constituents are separated into a stack of the zones with trace analytes focused into a narrow band(s).

(ii) As matrix constituents are forced to migrate out of the separation compartment at the end of the ITP column, the sample is cleaned up before its injection onto the CZE column. This removal of the matrix is well defined and very reproducible when it is based on the signal from the detector used to monitor the ITP separation (see, e.g., ref 28).

(iii) The trace analytes present in the injected sample, concentrated and cleaned up from the matrix in the ITP stage (column), are completely transferred onto the CZE column as a narrow sample pulse.

(iv) An overall selectivity of the analysis can be enhanced when

(15) Foret, F.; Fanali, S.; Ossicini, L.; Boček, P. *J. Chromatogr.* **1989**, *470*, 299.
(16) Gebauer, P.; Deml, M.; Boček, P.; Janák, J. *J. Chromatogr.* **1983**, *267*, 455.
(17) Zelenský, I.; Zelenská, V.; Kaniansky, D.; Havaši, P.; Lednárová, V. *J. Chromatogr.* **1984**, *294*, 317.
(18) Tkáčová, J.; Zelenský, I.; Kaniansky, D. In *Hydrochémia* 85; Bilíková, A., Hucko, P., Lehocký, J., Stankovič, V., Eds.; Water Research Institute: Bratislava, Slovakia, 1985; p 421.
(19) Fukushi, K.; Hiiro, K. *Bunseki Kagaku* **1985**, *34*, 21.
(20) Fukushi, K.; Hiiro, K. *Bunseki Kagaku* **1985**, *34*, 205.
(21) Kaniansky, D.; Marák, J. *J. Chromatogr.* **1990**, *498*, 191.
(22) Stegehuis, D. S.; Irth, H.; Tjaden, U. R.; van der Greef, J. *J. Chromatogr.* **1991**, *538*, 393.
(23) Křivánková, L.; Foret, F.; Boček, P. *J. Chromatogr.* **1991**, *545*, 307.
(24) Stegehuis, D. S.; Tjaden, U. R.; van der Greef, J. *J. Chromatogr.* **1992**, *591*, 341.
(25) Foret, F.; Szoko, E.; Karger, B. L. *J. Chromatogr.* **1992**, *608*, 3.
(26) Reinhoud, N. J.; Tinke, A. P.; Tjaden, U. R.; Niesen, W. M. A.; van der Greef, J. *J. Chromatogr.* **1992**, *627*, 263.
(27) Hirokawa, T.; Okushi, A.; Kiso, Y. *J. Chromatogr.* **1993**, *634*, 101.
(28) Kaniansky, D.; Marák, J.; Madajová, V.; Šimuničová, E. *J. Chromatogr.* **1993**, *638*, 137.
(29) Kaniansky, D.; Iványi, F.; Onuska, F. I. *Anal. Chem.* **1994**, *66*, 1817.

Table 1. Electrolyte Systems[a]

	electrolyte				
	ITP-1		ITP-2		
parameter	L	T	L	T	C
solvent	H_2O	H_2O	H_2O	H_2O	H_2O
anion	Cl^-	Asp	Cl^-	Asp	Asp
concentration (mM)	8	4	8	4	10
counterion	BALA	BALA	BALA	BALA	BALA
co-counterion	BTP				
concentration (mM)	3				
pH	3.4	4	3,4	4	3,4
additive	MHEC		MHEC		MHEC
concentration (%, w/v)	0.2		0,2		0,2

[a] Abbreviations used: MHEC, methylhydroxyethylcellulose; BALA, β-alanine; Asp, aspartic acid; BTP, bis-tris propane, 1,3-bis[tris(hydroxymethyl)methylamino]propane; L, leading; T, terminating; C, carrier.

Table 2. Parameters of the Regression Equations for the Calibration Lines, Limits of Detection, and Reproducibilities of the ITP Determinations of Chloride, Nitrate, and Sulfate[a]

	regression equation[b]				
anion	*a* (s)	*b* (s/ppm)	CC	LOD (ppm)	RSD (%)
chloride	0.56	0.4279	0.9984	5	4.2
nitrate	−0.11	0.2635	0.9998	2	1
sulfate	0.49	0.319	0.9999	1	0.5

[a] Abbreviations used: a, intercept; b, slope; CC, correlation coefficient; LOD, limit of detection; RSD, median of the relative standard deviations for five samples (each sample analyzed five times). [b] The calibration data were obtained from 60 runs for calibration mixtures containing chloride in the range 20–90 ppm, nitrate in the range 5–40 ppm, and sulfate in the range 25–125 ppm.

the separations in the ITP and CZE columns are based on different separation mechanisms.[28]

The aim of this work was to study analytical capabilities of the ITP–CZE tandem to determine chloride, nitrate, sulfate, nitrite, fluoride, and phosphate in the concentration range within which these anions are found in water samples. In previous work, the ITP stage was used merely for the cleanup of the samples and/or for the preconcentration of the trace analytes. Here, we extend the use of this stage to the determination of sample macroconstituents (chloride, nitrate, sulfate) while maintaining the cleanup and preconcentration capabilities. The CZE stage is intended to perform final separation of the trace anions (nitrite, fluoride, phosphate) with their detection by a conductivity detector.

EXPERIMENTAL SECTION

Instrumentation. A CS isotachophoretic analyzer (Villa-Labeco, Spišská Nová Ves, Slovak Republic) that enables CE separations in the column-coupling mode was used. This analyzer is provided with two conductivity detectors (to monitor the separations in both columns) and with a UV absorbance detector. The separation unit of the analyzer was assembled from components provided by the manufacturer and also from those developed in this laboratory.

The ITP column (Villa-Labeco) was provided with a 0.85 mm i.d. capillary tube (o.d. ~ 1.15 mm) made of fluorinated ethylene–propylene (FEP) copolymer. The length of the capillary tube to the conductivity cell was 150 mm. The CZE columns (Villa-Labeco) used a 0.30 mm i.d. (o.d. ~ 0.65 mm) capillary tube made of FEP (the length from the inlet to the conductivity cell was 150 mm) and a 0.35 mm i.d. (o.d. ~ 0.70 mm) capillary tube made of the same material (the length from the inlet to the detection cell was 150 mm). The capillary tubes were placed in compartments made of Plexiglas that allowed efficient dissipation of heat produced on the passage of current.

Table 3. Maximum Tolerable Concentrations (ppm) of Chloride and Sulfate for Varying Concentrations of Nitrate (ppm) in the ITP Determination

	maximum concn[a]	
nitrate concn	chloride	sulfate
5	100	125
10	75	125
20	75	125
30	75	100
40	50	125

[a] When both anions are present in the sample.

The samples were injected with the aid of a sampling valve with a 30 μL internal sampling loop.

The data from the detectors were acquired and processed by an ITP.SOFT program (KasComp, Bratislava, Slovak Republic) which runs on a 386 PC computer.

Chemicals. Chemicals used for the preparation of the electrolyte solutions were obtained from Serva (Heidelberg, Germany), Sigma (St. Louis, MO), Reanal (Budapest, Hungary), and Lachema (Brno, Czech Republic). Some of them were purified by conventional methods, and analytical grade chemicals were used as delivered. Methylhydroxyethylcellulose 30 000 (MHEC) served as an anticonvective additive in the electrolyte solutions. A stock aqueous solution containing 1% (w/v) of the derivative was purified on a mixed-bed ion exchanger (Amberlite MB-1; Serva).

Water from an Aqualabo two-stage demineralization unit (Aqualabo, Brno, Czech Republic) was further purified by circulation in a laboratory-made demineralization system made of poly(tetrafluoroethylene) and packed with Amberlite MB-1 mixed-bed ion exchanger (Serva). At the outlet, water of ca. 0.06 $\mu S \cdot cm^{-1}$ specfic conductivity was filtered through a 0.45 μm filter (Gelman, Ann Arbor, MI).

RESULTS AND DISCUSSION

Separating Conditions. As mentioned above, in our approach the ITP determination of chloride, nitrate, and sulfate was combined with the CZE determination of nitrite, fluoride, and phosphate using the ITP–CZE tandem in the column-coupling system. This tandem offers several working modes,[21,28] and the one preferred in this work consists of the following steps (see also Figure 1).

(1) Chloride, nitrate, and sulfate are separated by ITP into their zones, while nitrite, fluoride, and phosphate are focused as a group into a narrow band migrating in the ITP stack behind the zones of macroconstituents. This is a favorable migration configuration as far as an efficient use of the ITP column is concerned.[31] The

(30) Křivánková, L.; Gebauer, P.; Thorman, W.; Mosher, R. A.; Boček, P. *J. Chromatogr.* **1993**, *638*, 119.

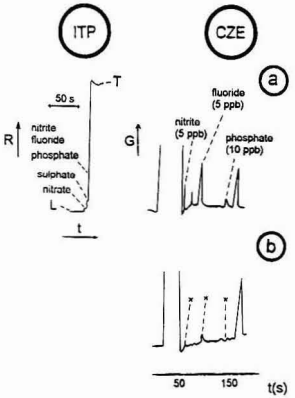


Figure 2. Electropherograms from the separations of a model mixture of inorganic anions (nitrate, 6 ppm; sulfate, 2.5 ppm; nitrite, 5 ppb; fluoride, 5 ppb; phosphate, 10 ppb; chloride present in the sample coincided with the leading electrolyte zone (L)). The ITP separation (lasting 8 min) was carried out in the electrolyte system ITP-1 (Table 1), and the carrier electrolyte CZE (Table 1) was used in the separation of microconstituents. The migration positions of the microconstituents as obtained in a blank run (b) are marked with asterisks (compare the run with the sample (a)). The driving currents were 250 and 75 μA in the ITP and CZE stages, respectively. R, G, t refer to the increasing resistance, conductance, and time, respectively; L, T are the leading and terminating zones, respectively. An isotachopherogram from the blank run (omitted) showed only the boundary between the leading and terminating anions (impurities were not detectable).

Table 4. Separation Efficiencies for Nitrite, Fluoride, and Phosphate at Various Concentrations[a]

	separation efficiency (N/m)[b]		
concn (ppb)	nitrite	fluoride	phosphate
5	224 000	84 000	
10	150 000	56 000	174 000
15	120 000	58 000	
20	88 000	55 000	160 000
30			121 000
40			84 000
50	68 000	27 000	
100	68 000	15 000	79 000

[a] Sample volumes were 30 μL. [b] Number of theoretical plates per meter.

signal from the conductivity detector employed in this stage provides data used in the quantitations of the macroconstituents.

(2) Chloride, nitrate, and sulfate are removed from the separation compartment by migrating in the direction to the counter electrode of the ITP column. Timing of this removal is based on the signal from the conductivity detector as obtained in step 1. This cleanup step is stopped after the band of the microconstituents reaches a position close to the start of the CZE column in the bifurcation block (Figure 1).

(3) The sample fraction containing the microconstituents and the rear part of the zone of the macroconstituent with the lowest effective mobility is transferred onto the CZE column.

(31) Mikkers, F. E. P.; Everaers, F. M.; Peek, J. A. F. *J. Chromatogr.* **1979**, *168*, 293.

Table 5. Regression Equations of Calibration Lines and Reproducibilities of CZE Determinations of Nitrite, Fluoride, and Phosphate[a]

	regression equation			RSD (%)	
anion	a (mV·s)	b (mV·s/ppb)	CC	A	B
nitrite	1.38	0.153	0.9994	0.87	0.95
fluoride	2.71	0.597	0.9999	0.7	1.11
phosphate	0.86	0.0987	0.9999	2.21	2.36

[a] Abbreviations used: a, intercept; b, slope; CC, correlation coefficient; RSD, relative standard deviation; A, model sample containing 15 ppb of nitrite, 15 ppb of fluoride, and 30 ppb of phosphate; B, model sample containing 20 ppb of nitrite, 20 ppb of fluoride, and 40 ppb of phosphate. The calibration solutions contained 5–375 ppb of nitrite, 5–375 ppb of fluoride, ane 10–750 ppb of phosphate, and the regression equations were calculated from 14 data points.

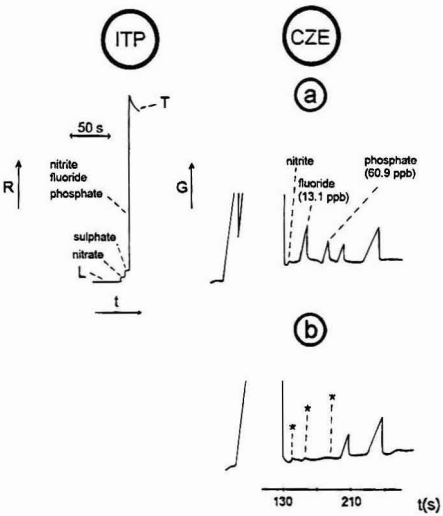


Figure 3. ITP and CZE determinations of macro- and microconstituents in a river water sample (Yamaska River, Quebec, Canada). The sample directly injected into the analyzer was found to contain 15.0 ppm, (RSD = 2.6%) of chloride, 7.3 ppm (RSD = 0.5%) of nitrate, 5.9 ppm (RSD = 0.9%) of sulfate, 13.1 ppb (RSD = 0.9%) of fluoride, and 60.9 ppb (RSD = 3.4%) of phosphate. Nitrite was below the limit of detection (200 pptr). The quantitations were based on five parallel runs. The time for the ITP separation was 8 min. An isotachopherogram from the blank run (omitted) showed only the boundary between the leading the terminating anions (impurities were not detectable). The separation conditions, the driving currents, and the meanings of the symbols are the same as in Figure 1.

(4) The microconstituents are resolved under the separating conditions employed in the CZE column, and their detection is performed by the conductivity detector.

There are three basic alternatives in selecting the electrolyte systems for the ITP and CZE stages in the ITP–CZE tandem.[30] Of these, the one using identical terminating and carrier constituents was preferred in this work because it does not require replenishment of the electrolyte solution in the ITP column after the sample fraction of analytical interest is transferred onto the CZE column. An actual choice of the constituents of the electrolyte solutions followed the above separation and sample

Table 6. Influence of a Varying Excess of Macroconstituents on CZE Determinations[a] of Trace Concentrations of Nitrite, Fluoride, and Phosphate

	microconstituents						macroconstituents	
	nitrite (ppb)		fluoride (ppb)		phosphate (ppb)			
sample no.	taken	CZE	taken	CZE	taken	CZE	sulfate (ppm)	chloride (ppm)
1	5	5.6	5	4.8	10	11.3	250	
2	5	4.7	5	5.3	10	11.3	500	
3	5	5.1	5	6.1	10	12.3	750	
4	5	5.4	5	4.6	10	10	1250	
5	5	4.5	5	4.7	10	10		1000
7	5	4.9	5	5.1	10	10.4		2000
8	5	0	5	2.8	10	12.2		2500

[a] Mean values from two parallel runs.

cleanup scheme. From this scheme it is apparent that the leading electrolyte has to meet the following requirements.

(i) To provide the ITP separation of the macroconstituents and at the same time a group separation and concentration of the microconstituents into a narrow band. It is also required that the migration configuration as given in (1) (Figure 1) is achieved.

(ii) To reduce the number of anionically migrating constituents, i.e., to reduce the number of potentially interfering anionic constituents, a low pH of the leading electrolyte is mandatory.

There are several leading electrolytes proposed for the ITP separation of the anions of our interest.[17,32-35] The one fulfilling the requirements stated above for this type of samples is described in Table 1 under ITP-1.

Besides the microconstituents, a small part of the macroconstituents is transferred onto the CZE column. A part of this material is transferred with the microconstituents to guarantee their high recoveries on the column transfer (see Figure 1), and the rest is due to diffusion of the leading electrolyte constituents into the CZE column during the ITP separation (the solutions in the columns are in direct contact in the bifurcation block; see Figure 1). Therefore, the separating conditions in the CZE stage were chosen not only to provide the resolutions of nitrite, fluoride, and phosphate but also to speed up their defocusing from the macroconstituents.[36] From the ionic mobilities of the anions involved and from pK_a values of the corresponding acids,[6] it is clear that a low pH of the carrier electrolyte is an optimum. Further, in the choice of the carrier constituent (serving also as a terminating anion in the ITP stage), it was necessary to take into consideration also the requirements related to the use of the conductivity detector in the CZE stage to get favorable molar responses of the detector to the analytes[37] while the electromigration dispersion is kept to a minimum. The composition of the carrier electrolyte used in this work (system CZE in Table 1) was a reasonable compromise considering all the above requirements.

ITP Determination of Chloride Nitrate, and Sulfate. Working conditions (leading electrolyte, sample injection volume, i.d. of the capillary tube, driving current) employed in the ITP determination of chloride, nirtate, and sulfate were in fact identical to those used for the same purpose in the ITP–ITP tandem.[17,18] Therefore, analytical performance data describing the ITP determination in this work (Table 2) were close to those reported in the quoted references.

A series of model mixtures containing chloride, nitrate, and sulfate at varying concentrations were analyzed to find maximum concentrations of these anions that can be determined simultaneously with the microconstituents in one run. It is apparent (Table 3) that the concentration of nitrate in the sample (having the intermediate effective mobility between those of chloride and sulfate) limited an overall sample load. This is what was expected from a theoretical treatment of the ITP separation process.[31,38] From a practical point of view, it means that such a load capacity of the ITP stage enables the determination of the anions in a wide variety of water samples.

CZE Determination of Nitrite, Fluoride, and Phosphate. As is clear from electropherograms in Figure 2 nitrite, fluoride, and phosphate were baseline resolved under the separating conditions employed in the CZE stage. It is also apparent that the transferred macroconstituents (a large peak migrating in front of nitrite in Figure 2) did not interfere with their determination. The reproducibilities of the migration times of the CZE analytes were 1% or less when their concentration in the samples were below 40–50 ppb. At higher concentrations, they were systematically biased by the electromigration dispersion.[37] This dispersive phenomenon had a negative effect on the separation efficiencies of the analyte, as is clear from the data in Table 4. Nevertheless, parameters of the regression equations describing the calibration lines show that reliable quantitations of the microconstituents were possible under such conditions (Table 5).

Besides the separation and concentration of the analytes of interest, ITP also concentrates ionic impurities present in the leading and terminating electrolytes (originating from the components of which the solutions of the electrolytes were prepared) when they migrate isotachophoretically. For example, in the CZE separations shown in Figure 2, peak areas of the impurities in the migration positions of the analytes corresponded to ca. 2 ppb of nitrate and 1 ppb of fluoride. An impurity peak migrating in the neighborhood of phosphate (see the blank run in Figure 2b) was equivalent to ca. 3 ppb of this analyte. Fluctuations in the peak areas of these impurities (background noise) were in fact determinating the limits of detection (LODs) for our analytes.

(32) Kaniansky, D.; Zelenský, Í.; Havaši, P.; Cerovský, M. *J. Chromatogr.* **1986**, *367*, 274.
(33) Vacik, J.; Muselasová, I. *J. Chromatogr.* **1985**, *320*, 199.
(34) Zelenský, I.; Šimuničová, E.; Zelenská, V.; Kaniansky, D.; Havaši, P.; Chaláni, P. *J. Chromatogr.* **1985**, *325*, 161.
(35) Křivánková, L.; Boček, P. *Chem. Prùmysl* **1988**, *38*, 97.
(36) Gebauer, P.; Thormann, W.; Boček, P. *J. Chromatogr.* **1992**, *608*, 47.
(37) Mikkers, F. E. P.; Everaerts, F. M.; Verheggen, Th.P.E.M. *J. Chromatogr.* **1979**, *169*, 1.
(38) Boček, P.; Deml, M.; Kaplanová, B.; Janák, J. *J. Chromatogr.* **1978**, *160*, 1.

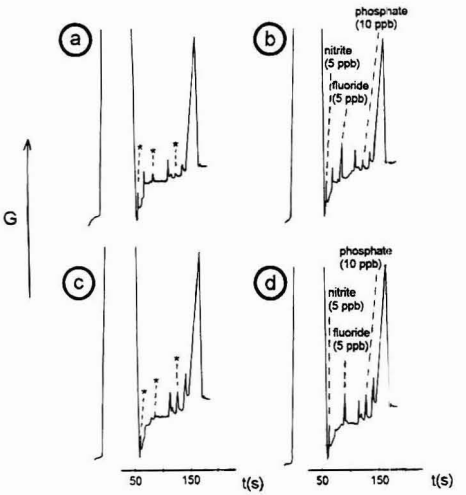


Figure 4. Electropherograms from the CZE determination of parts per billion concentrations of microconstituents present in a model mixture containing 1250 ppm of sulfate. (a) Blank run (the terminating electrolyte was injected); (b) sample containing microconstituents and sulfate at a 10 ppm concentration; (c) sample containing 1250 ppm of sulfate; (d) the same as (c) only the sample also contained 5 ppb of each nitrite and fluoride and 10 ppb of phosphate. Asterisks in runs a and c mark the migration positions of the microconstituents. The ITP separation was carried out in the system ITP-2 (Table 1), and the carrier electrolyte CZE (Table 1) was used in the CZE column. The driving currents were 250 and 75 μA in the ITP and CZE stages, respectively. G refers to increasing conductance.

Estimates of the relative standard deviations of the peak areas of the impurities as obtained in repeated blank runs (six runs related to the experiments in Figure 2) served as a measure of these fluctuations. From the signal-to-noise ratio of three, we obtained the LOD values of 200, 300, and 600 pptr (parts per trillion) for nitrite, fluoride, and phosphate, respectively. These values are ca. 5–10 times greater than those which were expected from the noise characteristics of the conductivity detector. As no special attention was paid to the purity of the chemicals used in the preparation of the leading and terminating electrolyte solutions, it is reasonable to expect that the appropriate measures taken in this respect could reduce the LOD values, making them comparable to those associated with the performance of the conductivity detector.

Analytical Potentialities of the ITP–CZE Tandem. Electropherograms given in Figure 3 illustrate the use of the ITP–CZE tandem with the conductivity detectors for the analysis of a practical sample. In this instance the CZE column of a larger i.d. (0.35 mm) was employed to test a column of a higher load capacity. Relevant data (see figure legend) show that, also under such conditions, very reproducible CZE determinations were possible.

In some instances (see, e.g., refs 18–20 and 39) it is necessary to analyze samples containing chloride, sulfate, and nitrate in a very large excess relative to nitrite, fluoride, and phosphate. The potential of ITP–CZE tandem for the analysis of such sample types was evaluated with a series of model mixtures containing constant concentrations of the microconstituents, while the concentrations of chloride and sulfate varied (See Table 6). As is apparent from the data in Table 3, the concentrations of chloride and sulfate were in some of the model samples several times above the load capacity of the ITP column for these anions. The data in Table 6 show that microconstituents were fully recovered by the ITP pretreatment when the concentration of chloride was 2000 ppm or less or the concentration of sulfate was 1250 ppm or less. As low parts per billion concentrations of the microconstituents could also be determined at such concentrations of sulfate and/or chloride, we can state that the ITP–CZE tandem enables the CZE determination of nitrite, fluoride, and phosphate in a 10^5–10^6-fold excess of the macroconstituents. The main problems in these experiments were associated with the purities of the chemicals from which the model mixtures were prepared. For example, from the electropherograms in Figure 4, we can see that the injection of sulfate at a 1250 ppm concentration was responsible for an increase of the peak area of phosphate equivalent to ca. 10 ppb concentration of this anion in the sample (see the electropherograms in Figure 4a and 4c). The origin of this peak was confirmed in a run with a chloride sample (containing chloride at a concentration leading to the same prolongation of the ITP separation, while the background signal in the migration position of phosphate was identical to that in the blank run; Figure 4a). Therefore, on spiking the sample with a 10 ppb concentration of phosphate, it was necessary to make a correction for a significantly higher blank value and thus introduce a higher random error into the determination. Similarly, the nitrate spikes, even considerably higher nitrite concentrations were detected. A prolongation of the ITP pretreatment by injecting the samples containing 1250 ppm of sulfate (12 min longer ITP separation to comparison to the blank run in Figure 4a) led to an increase of the peak areas of some of the unidentified constituents (see, e.g., a peak migrating immediately behind phosphate in Figure 4). In this instance, the origin of these peaks was associated with impurities in the ITP electrolyte solutions.

CONCLUSIONS

From the results presented in this work, it seems appropriate to state that the on-line coupling of ITP with CZE in the column-coupling configuration of the separation unit offers a very promising alternative to the determination of the studied anions in situations when their concentrations differ considerably. It is also apparent that the load capacity of the ITP column sets a limit for a simultaneous determination of both macro- (sulfate, nitrate, and chloride) and microconstituents (nitrite, fluoride, and phosphate). Thus, when the concentration ratio of macro-/microconstituents was higher than $(2–3) \times 10^4$, the analysis had to be divided into two runs (separate determinations of both groups of anions). In this way, e.g., the ITP cleanup provided a way to determine the microconstituents present in samples with a 10^5–10^6-fold excess of macroconstituents.

The anionic impurities from the electrolyte solutions accumulated in the ITP stage between the leading and terminating zones were main disturbances in the CZE analysis of microconstituents. In this respect, only the use of high purity chemicals in the preparation of the electrolyte solutions for the ITP stage can define limits of the ITP–CZE tandem. The use of conductivity

(39) Shotyk, W. *J. Chromatogr.* **1993**, *640*, 309.

detector in CZE has some limitations.[37] Nevertheless, this work showed that its performance was not limiting in achieving subparts per billion detection limits for the studied analytes. In this context, it can also be concluded that only advances related to the purities of the electrolyte solutions in the ITP stage will define its limitations and, eventually, initiate further research related to the detection.

ACKNOWLEDGMENT

This work was supported by a grant provided by Slovak Grant Agency for Science.

Received for review June 29, 1994. Accepted September 8, 1994.[⊗]

[⊗] Abstract published in *Advance ACS Abstracts,* October 15, 1994.

Anal. Chem. **1994,** *66,* 4265–4271

Determination of Urinary Albumin Using High-Performance Immunoaffinity Chromatography and Flow Injection Analysis

Peggy F. Ruhn, Jay D. Taylor, and David S. Hage*

Department of Chemistry, University of Nebraska, Lincoln, Nebraska 68588–0304

The detection of low levels of albumin in urine can be an important aid in the early diagnosis of kidney disease. In this study, an automated system for urine analysis was developed that could simultaneously measure both albumin and creatinine, an indicator of urine output and volume. Albumin was determined by use of a column that contained immobilized anti-albumin antibodies. An on-line flow injection analysis system was used to measure creatinine as this solute eluted nonretained from the antibody column. The total analysis time of the system was 5 min per injection. Limits of detection for albumin and creatinine in a 20 μL sample (at S/N = 2) were 3 and 5 mg/L, respectively. The response for these compounds covered the range of clinical interest. Within-run precision for both analytes was ±1–2% at normal urine concentrations. The results of this method showed good agreement with those obtained by reference techniques. This approach can be adapted for the detection of other urine components by changing the type of antibody column used in the system.

High-performance immunoaffinity chromatography (HPIAC) is a separation technique that uses immobilized antibodies to form a selective stationary phase for sample analysis.[1] In HPIAC, antibodies with the ability to bind the compound of interest are immobilized or adsorbed onto a rigid, high-performance support and placed into a column. When samples are applied to this column, the analyte of interest binds to the immobilized antibodies while other components elute nonretained. By changing the column conditions, the analyte can later be eluted for quantitation or collected for further use. In previous work, it has been shown that separations based on this approach generally take only a few minutes to perform and are easy to automate.[2–7] The specificity of this method makes it appealing for use with a variety of complex biological samples, including serum,[3,5] plasma,[6] and cerebrospinal fluid.[8]

One disadvantage of HPIAC is that any information regarding nonretained sample components is generally lost once these components have passed through the antibody column. Some of this information could be recovered if these nonretained components were later measured by a second analytical method. One technique that might be used for this purpose is flow injection analysis (FIA). This work will examine the combination of HPIAC and FIA, using the determination of albumin in urine as an example.

The measurement of urinary albumin is currently being promoted as a means for the early detection of kidney disease in individuals with diabetes, hypertension, and a number of other disorders.[9–16] Albumin, which is the major protein in serum, is normally prevented by the kidneys from entering urine. However, in certain disease states (e.g., diabetes mellitus), damage can occur to the filtering ability of the kidneys, thus resulting in leakage and an increase in urinary albumin levels. Normal levels of urinary albumin occur at approximately 5–30 mg/L for a 1 L daily urine output. For the same urine volume, the presence of increased albumin levels (i.e., microalbuminuria) is generally said to occur when concentrations of 30–300 mg/L are detected.[9]

A problem that is commonly associated with the quantitative measurement of albumin, or any other solute, in urine is that some correction must be made for the daily variations that occur in urine output and volume. One way this problem can be minimized is by collecting samples over long time periods (e.g., 24 h). For short-term samples, an alternative approach is to divide the measured concentration of an analyte by the concentration of some reference compound present in the same matrix. Creatinine is one solute that is typically used for this purpose.[9,17] This compound is formed by the nonenzymatic cyclization of creatine in muscle tissue.[18] Because the production and release of creatinine into urine occurs at a relatively constant rate, creatinine levels in urine can be used as a correction factor for fluctuations in urine volume.[17] Creatinine levels are often measured by a

(1) Phillips, T. M. *LC Mag.* **1985**, *3*, 962–972.
(2) De Alwis, W. U.; Wilson, G. S. *Anal. Chem.* **1985**, *57*, 2754–2756.
(3) Hage, D. S.; Walters, R. R. *J. Chromatogr.* **1987**, *386*, 37–49.
(4) De Alwis, U.; Wilson, G. S. *Anal. Chem.* **1987**, *59*, 2786–2789.
(5) Ohlson, S.; Gudmundsson, B.-M.; Wikstrom, P.; Larsson, P.-O. *Clin. Chem.* **1988**, *34*, 2039–2043.
(6) Hage, D. S.; Kao, P. C. *Anal. Chem.* **1991**, *63*, 586–595.
(7) Hage, D. S.; Thomas, D. H.; Beck, M. S. *Anal. Chem.* **1993**, *65*, 1622–1630.
(8) Phillips, T. M.; More, N. S.; Queen, W. D.; Holohan, T. V.; Kramer, N. C.; Thompson, A. M. *J. Chromatogr.* **1984**, *317*, 173–179.
(9) Shihabi, Z. K.; Konen, J. C.; O'Connor, M. L. *Clin. Chem.* **1991**, *37*, 621–624.
(10) Bakker, A. J. *Clin. Chem.* **1988**, *34*, 82–86.
(11) Medcalf, E. A.; Newman, D. J.; Gorman, E. G.; Price, C. P. *Clin. Chem.* **1990**, *36*, 446–449.
(12) Harmoinen, A.; Vuorinen, P.; Jokela, H. *Clin. Chim. Acta* **1987**, *166*, 85–89.
(13) Niwa, T.; Katsuzaki, T.; Tatemichi, N.; Kato, K.; Yazawa, T.; Maeda, K. *Clin. Chim. Acta* **1989**, *186*, 391–396.
(14) Kramer, B. K.; Jesse, U.; Ress, K. M.; Schmulling, R. M.; Risler, T. *Clin. Chem.* **1987**, *33*, 609–611.
(15) Frost, S. J.; Firth, G. B.; Chakraborty, J. *J. Immunol. Methods* **1990**, *134*, 207–213.
(16) Woo, J.; Floyd, M.; Cannon, D. L.; Kahan, B. *Clin. Chem.* **1978**, *24*, 1464–1467.
(17) Lemann, J., Jr.; Doumas, B. T. *Clin. Chem.* **1987**, *33*, 297–299.
(18) Tietz, N. W., Ed. *Textbook of Clinical Chemistry*; W. B. Saunders Co.: Philadelphia, 1986.

0003-2700/94/0366-4265$04.50/0 © 1994 American Chemical Society

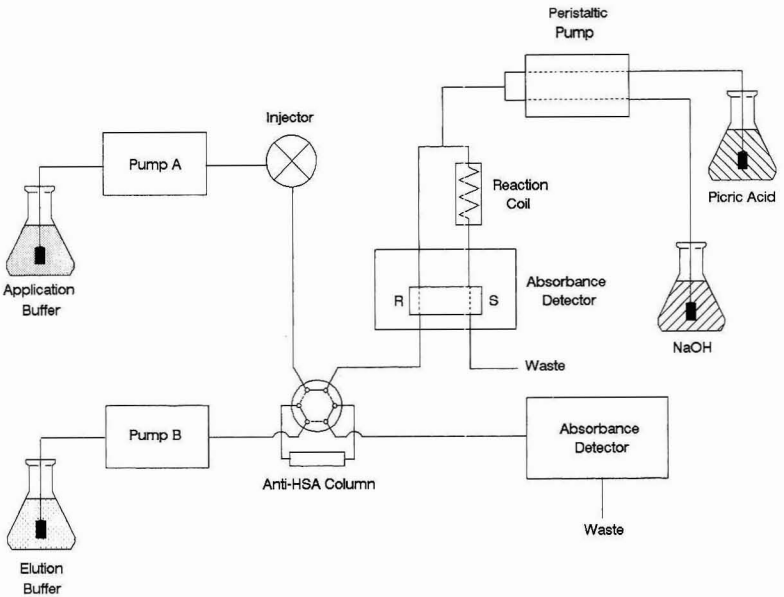


Figure 1. Schematic of the HPIAC/FIA system.

colorimetric technique known as the Jaffe method. In this method, creatinine is combined with an alkaline picrate solution to form an orange-red complex. This technique can be performed either manually or as part of an automated flow-through system.[18]

This work will examine the combination of HPIAC with FIA to form an automated method for the simultaneous analysis of albumin and creatinine in urine. Items to be considered in the development of this technique will include the adsorption and elution properties of the HPIAC column and the optimum reaction conditions required for the FIA system. The precision, limits of detection, and speed of the overall method will then be evaluated. The effects of potential interferences in both the HPIAC and FIA systems will also be examined. Finally, the performance of this technique versus current methods for urinary albumin will be discussed and the extension of this approach to other analytes will be considered.

EXPERIMENTAL SECTION

Reagents. The human serum albumin (HSA), anti-HSA antibodies (goat, fractionated), human immunoglobulin G, periodic acid, pyruvate, oxaloacetate, α-ketoglutarate, acetoacetate, human transferrin, urea, human hemoglobin, and 2,4,6-trinitrobenzenesulfonic acid (TNBS) were obtained from Sigma Chemical Co. (St. Louis, MO). The Nucleosil Si-1000 (7 μm particle diameter, 1000 Å pore size) was from Alltech (Deerfield, IL). Reagents for the bicinchoninic acid (BCA) protein assay were purchased from Pierce (Rockford, IL). The oxalic dihydrazide, picric acid, and creatinine were from Aldrich (Milwaukee, WI). Commercial urine controls were purchased from Curtin Matheson Scientific (Houston, TX). Reagents for the sodium dodecyl sulfate–polyacrylamide gel electrophoresis (SDS–PAGE) were obtained from USB (Cleveland, OH) and Amresco (Solon, OH). All other chemicals used were of the purest grades available. All solutions were prepared with water from a NANOpure water system (Barnstead, Dubuque, IA).

Instrumentation. The final system used in this study for the analysis of albumin and creatinine is shown in Figure 1. The chromatographic portion consisted of one CM3000 isocratic pump, one CM4000 gradient pump, and one SM3100 UV/visible variable-wavelength absorbance detector from LDC/Milton Roy (Riviera Beach, FL). The FIA system consisted of one peristaltic pump (Scientific Industries, Bohemia, NY) and one Lambda-Max 481 UV/visible variable-wavelength absorbance detector (Waters/Millipore, Milford, MA). The reactor used in the FIA system was a serpentine type II reaction chamber made from 1.5 m × 0.5 mm i.d. PTFE tubing.[19] Samples were injected onto the HPIAC/FIA system by using an LDC Analytical 713 autosampler equipped with a Rheodyne 7012 valve (Cotati, CA) and a 20 μL injection loop. A Rheodyne 7010 switching valve was used to change the HPIAC column from the application buffer to elution buffer. All columns were packed by using an HPLC column slurry packer from Alltech. A Hoefer SE 600 vertical slab gel electrophoresis unit (San Francisco, CA) and Molecular Dynamics scanning densitometer (Sunnyvale, CA) were used in the SDS–PAGE studies.

Antibody Column Preparation. Diol-bonded Nucleosil Si-1000 silica was prepared as described previously.[20] The diol coverage of the Nucleosil prior to activation was 53 ± 2 μmol/g of silica (±1 SD), as determined in triplicate by the periodate oxidation method.[21,22] Oxalic dihydrazide-activated silica was prepared from the diol-bonded silica as described earlier.[20] The

(19) Curtis, M. A.; Shahwan, G. J. *LC-GC* **1988**, *6*, 158–164.
(20) Ruhn, P. F.; Garver, S.; Hage, D. S. *J. Chromatogr. A* **1994**, *669*, 9–19.

amount of active hydrazide groups on the resulting support was 4.1 ± 0.5 μmol/g of silica (±1 SD), as measured in duplicate by a TNBS assay.[20]

Anti-HSA antibodies were oxidized in their carbohydrate regions with periodic acid, as described previously.[23,24] The oxidized antibodies were then purified[24] and reacted with the oxalic dihydrazide-activated silica, resulting in the formation of a stable hydrazone bond between the antibodies and the activated support.[20] After immobilization, the silica was centrifuged and washed three times with 0.10 M phosphate buffer (pH 7.0) containing 2.0 M sodium chloride, followed by three rinses with 0.10 M phosphate buffer (pH 7.0). This support was stored at 4 °C in the pH 7.0 phosphate buffer until further use. A portion of the anti-HSA silica was further washed with deionized water and dried under reduced pressure for use in a BCA protein assay.[25] This assay was performed by using nonimmobilized anti-HSA antibodies as the standard and diol-bonded silica as the blank. The protein content of the anti-HSA support, as determined in triplicate measurements by the BCA method, was 65 ± 7 mg/g of silica (±1 SD).

Chromatography. The HPIAC column was prepared by packing the anti-HSA silica support into a 6.35 mm × 2.1 mm i.d. stainless steel column at 3700 psi. The packing solvent and application buffer for this column was 0.10 M phosphate buffer (pH 7.0). The elution buffer was 0.10 M phosphate buffer (pH 2.5). Before use on the column, all mobile phases were degassed under vacuum for 10 min and filtered through a 0.45 μm cellulose acetate filter. All HSA standards were prepared in the pH 7.0 application buffer. All chromatographic studies were performed at room temperature. In-house controls were prepared by pooling urine collected from several healthy, college-age subjects. As with any biological specimen, appropriate biohazard precautions should be observed in the handling and disposal of these types of samples.

The flow rates used for the HPIAC application and elution buffers were 0.5 and 1.0 mL/min, respectively. The following sequence of events was used for the injection and elution of compounds on the chromatographic system: 0.0 min, sample was injected and nonretained solutes were washed through to the FIA system; 2.5 min, retained HSA was eluted from the antibody column by changing the position of the switching valve so that pH 2.5 buffer flowed through this column; 4.5 min, the antibody column was switched back to the application buffer and allowed to regenerate; 5.0 min, the analysis sequence was completed and the next sample was injected. HSA eluting from the HPIAC column was detected by monitoring the absorbance of the pH 2.5 buffer at 280 nm.

The binding capacity of the HPIAC column was determined by frontal analysis, using an application buffer that contained 55 mg/L HSA. This solution was applied to the column at flow rates of 0.10–0.2 mL/min. A consistent capacity was obtained throughout this range of flow rates, indicating that the results were not subject to any significant kinetic effects under these conditions.[6,7] The analyte solution was applied to the column by using the same valve configuration as reported previously.[26] The amount of HSA required to saturate the anti-HSA column was determined by integrating the resulting breakthrough curves.[27] HSA that was retained by the column was removed at the end of each experiment by applying the pH 2.5 elution buffer. Corrections for the system void volume and nonspecific binding were made by performing similar experiments on blank columns containing only diol-bonded silica or the oxalic dihydrazide-activated support.

The linear and dynamic ranges of the anti-HSA antibody column were determined by making triplicate injections of 0–5 g/L HSA samples. Samples for the interference studies were prepared by injecting 1:1 mixtures of a normal urine control combined with a solution of the desired test compound dissolved in the pH 7.0 application buffer. The compounds and final spiked concentrations examined in the interferences studies included 0.25–5 mg/L hemoglobin, 0.75–15 mg/L immunoglobulin G, 2–20 mg/L transferrin, 0.7–7 g/L creatinine, 0.06–2.50 g/L glucose, or 6–60 g/L urea.

The protein content of peaks eluting from the anti-HSA column were examined by using SDS–PAGE. This was performed by injecting a 0.1 g/L HSA standard or normal urine control onto the antibody column at a flow rate of 0.5 mL/min while collecting fractions of the nonretained and retained peaks. These fractions were adjusted to pH 6.0 and applied in 25 μL aliquots to a 14 mm × 16 mm polyacrylamide gel containing 7.5% cross-linking agent in the resolving gel and 4% cross-linking agent in the stacking gel.[28] Other samples applied to the gel included 2–40 mg/L HSA standards and a series of molecular weight markers ranging in size from 20 100 to 116 400. The samples and standards were separated for 3 h at a constant current of 25 mA. Protein bands in the final gel were detected by a silver stain.[29]

Flow Injection Analysis. In the final FIA system, application buffer that was leaving the HPIAC column was first passed through the reference side of an absorbance detector to measure the initial response at 510 nm due to creatinine and other sample components (see Figure 1). The application buffer stream was then combined in a mixing tee with separate solutions containing 1.6 M sodium hydroxide and 0.06 M picric acid, each applied at a flow rate of approximately 0.6 mL/min. The resulting mixture was passed through the reaction coil of the FIA system and back into the sample cell of the FIA detector. By comparing the detector responses measured for the sample before and after reaction, the signal due to only the picrate–creatinine complex was obtained. All picric acid solutions used in this work were prepared from a slurry containing about 35% (w/w) water, as obtained from the supplier. Care must be taken in the handling and use of this reagent since solid picric acid can be explosive on impact.

The linear and dynamic ranges of the FIA system were determined by making triplicate injections of 0–10 g/L creatinine standards prepared in the pH 7.0 application buffer. Samples for the FIA interference studies were made in the same fashion as described for the HPIAC column. The compounds and final spiked concentrations tested in these studies included 3–30 mg/L acetone, 0.25–2.50 g/L acetoacetate, 8–400 mg/L albumin (HSA),

(21) Siggia, S.; Hanna, J. G. *Quantitative Organic Analysis*; Wiley: New York, 1979; pp 42–43.
(22) Woolf, A. A. *Anal. Chem.* **1982**, *54*, 2134–2136.
(23) O'Shannessy, D. J.; Quarles, R. H. *J. Immunol. Methods* **1987**, *99*, 153–161.
(24) Keener, C. R.; Wolfe, C. A. C.; Hage, D. S. *Biotechniques* **1994**, *16*, 894–897.
(25) Smith, P. K.; Krohn, R. I.; Hermanson, G. T.; Mallia, A. K.; Gartner, F. H.; Provenzano, M. D.; Fujimoto, E. K.; Goeke, N. M.; Olson, B. J.; Klenk, D. C. *Anal. Biochem.* **1985**, *150*, 76–85.
(26) Loun, B.; Hage, D. S. *J. Chromatogr.* **1992**, *579*, 225–235.
(27) Lund, U. *J. Liq. Chromatogr.* **1981**, *4*, 1933–1945.
(28) Laemmli, U. K. *Nature* **1970**, *227*, 680–685.
(29) Merril, C. R.; Goldman, D.; Sedman, S. A.; Ebert, M. H. *Science* **1981**, *211*, 1437–1438.

0.25–2.50 g/L glucose, 0.25–2.50 g/L α-ketoglutarate, 0.25–2.50 g/L oxaloacetate, or 8.8–88 mg/L pyruvate.

RESULTS AND DISCUSSION

Optimization of Chromatographic System. One important factor to consider in the design of an HPIAC method is the binding capacity of the immobilized antibody column. In this work, the column binding capacity was determined by frontal analysis to be 0.49 ± 0.05 nmol of HSA (±1 SD). At this level of binding, a 20 μL injection of normal urine containing 5–30 mg/L albumin would use up approximately 0.3–1.8% of the total antibody binding sites. Even samples containing albumin levels of 300 mg/L would require less than 20% of the column capacity. Thus, the amount of active antibody in the column was considered to be sufficient for work with these types of albumin levels.

Besides the binding capacity of the column, another item that must be considered is the rate at which the immobilized antibodies will bind to the analyte.[3] This can be evaluated by using expressions derived for the "split-peak" effect, as described earlier.[3,7] For example, if it is assumed that adsorption is the rate-limiting step in analyte retention and that analyte–antibody binding is essentially irreversible on the time scale of the experiment, then the relative amount of analyte that elutes in the nonretained or free fraction of the column (f) can be estimated by the following formula:[7]

$$f = (S_o/\text{load A}) \ln[1 + (e^{\text{loadA}/S_o} - 1)e^{-1/s_o}] \qquad (1)$$

In eq 1, the term load A represents the relative moles of injected analyte versus the moles of active antibody sites present in the column. The term S_o is a system constant that is a combination of several terms, including the moles of antibody binding sites (m_L), the injection flow rate (F), and the apparent second-order adsorption rate constant for analyte–antibody binding (k_3), where $S_o = F/(k_3 m_L)$.[7]

It has been demonstrated earlier that the type of anti-HSA support used in this work has adsorption-limited kinetics.[7] It has also been shown that eq 1 gives a good fit to data obtained with this matrix. Using expressions derived from eq 1, it has been further determined that the value of k_3 for the immobilized antibodies on this support is roughly 4.8×10^4 M^{-1} s^{-1}.[7]

By using this value for k_3 and the measured binding capacity of the immobilized antibody column, it was possible to determine the value of S_o for the HPIAC system. This S_o value was calculated to be 0.35 when an injection flow rate of 0.5 mL/min was used. Under these conditions, eq 1 predicts that the albumin present in a sample load of 1.8% (i.e., a 20 μL injection of 30 mg/L HSA) will have about 94% binding to the HPIAC column. For a 20 μL injection of 300 mg/L HSA (i.e., an 18% column load), eq 1 predicts that 92% of the injected albumin will bind. This result was confirmed by SDS–PAGE, which revealed that greater than 90% of the albumin in a 100 mg/L sample was retained by the HPIAC column at a flow rate of 0.5 mL/min. Even higher degrees of binding could be obtained on this system by increasing the column length or by decreasing the injection flow rate.[3,30]

After the adsorption characteristics of the anti-HSA column were examined, the elution properties of this column were also considered. An elution pH of 2.5 was chosen because it has been shown in previous work to give quantitative desorption of albumin from this type of immobilized antibody support.[3,7] It is also desirable for an elution buffer to have the ability to rapidly release analyte from the column and to allow for fast regeneration of the immobilized antibodies when they are brought back to the initial application conditions. The rate at which analyte was released by the elution buffer was examined through carry-over studies in which alternate samples of pH 7.0 phosphate buffer and 0.1 g/L HSA were injected and eluted from the column. It was found in these studies that over 95% of the retained analyte was removed from the HPIAC column within 2.0 min when a pH 2.5 elution buffer flowing at 1.0 mL/min was used. Column regeneration was studied by making injections of similar albumin standards at various time intervals following the application of pH 7.0 phosphate buffer to the HPIAC support. A comparison of the retained and nonretained areas of these samples indicated that a time of only 1 min was required for the quantitative recovery of column activity.

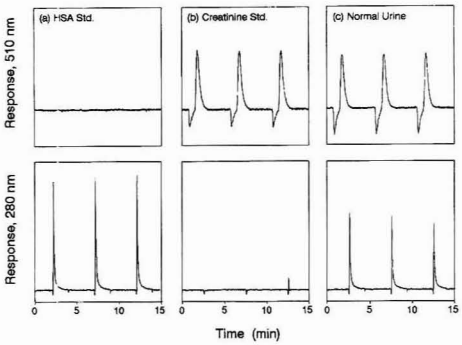


Figure 2. Typical responses obtained on the HPIAC/FIA system for albumin and creatinine. The results have been corrected for the presence of background peaks produced when the HPIAC column is switched between the pH 7.0 and pH 2.5 phosphate buffers.

The last item considered in the optimization of the HPIAC system was the amount of time required for washing nonretained components from the antibody column. This was examined by switching the HPIAC column from the application buffer to the elution buffer at different time intervals following the injection of a normal urine sample. Wash times of 1.3–5 min produced analyte peaks with consistent heights and areas. However, wash times of 1 min or less gave an apparent peak height for HSA that was at least 20% larger than expected. This increase in peak size indicated that some nonretained components, which had not been fully removed from the column, were coeluting with the bound albumin fraction. This problem was avoided in all later studies by using a wash time of 2 min for all samples and standards.

Based on the results of these optimization studies, a scheme with a total analysis time of 5 min per injection was developed for the HPIAC system. This included 2 min for sample injection and column washing, 2 min for elution of the retained HSA, and 1 min for column regeneration. Figure 2 shows typical chromatograms obtained with this scheme for 20 μL injections of standards and urine samples. The 5 min cycle time used in this technique is comparable to that reported for several previous HPIAC methods.[3,5,6]

(30) Hage, D. S.; Walters, R. R.; Hethcote, H. W. *Anal. Chem.* **1986**, *58*, 274–279.

Optimization of FIA System. Several items were considered in coupling the HPIAC system with an FIA method for creatinine. For example, an attempt was made to produce an optimized FIA system that could give a reasonable response for creatinine in less than 5 min. This restriction was used in order to avoid adding any extra time to that already required for the albumin measurements. The goal of a 5 min analysis was partially met by using a flow rate of 0.6 mL/min per line for the FIA reagents and a reaction coil volume of approximately 3 mL. Under these conditions, the total time that solute spent in the reaction coil was less than 1.8 min.

Because urine contains some components that absorb at 510 nm, it was necessary to include in the FIA system some means of determining this background response. As shown in Figure 1, this was accomplished by passing the nonretained fraction of each sample through the reference side of the FIA detector before reagent addition. This gave a negative peak following injection that was related to the background absorbance of the sample components. After these components were washed through the FIA detector, they were combined with the sodium hydroxide and picric acid reagents, allowed to react, and passed through the sample side of the same absorbance detector. This gave a second, positive peak related to the sample background plus the absorbance of the newly formed picrate–creatinine complex. By comparing the signals measured before and after reagent addition, the signal due to only the picrate–creatinine complex was obtained. Both the positive and negative peaks produced by this approach could be measured at baseline resolution within the 5 min time limit set for the FIA method (see Figure 2).

After the initial design of the FIA system had been established, the concentrations of the picric acid and sodium hydroxide reagents were adjusted to optimize the response of this system. The effect of picric acid concentration on the FIA signal was examined by injecting a 2.0 g/L creatinine standard into the pH 7.0 application buffer and combining this with 1.0 M sodium hydroxide and solutions containing 0–0.06 M picric acid. The response increased linearly with the concentration of picric acid that was used. The maximum signal was obtained at a concentration of 0.06 M picric acid. This was the level of picric acid that was used in all later studies. Higher concentrations of this reagent could not be examined easily because this level approached that of a saturated picric acid solution.

The effect of sodium hydroxide concentration on the response of the FIA system was examined next. This was studied in the same manner as used in the picric acid studies, but with the picric acid now being held at 0.06 M and sodium hydroxide concentration being varied. Figure 3 shows the results obtained. At low to intermediate levels of sodium hydroxide (i.e., 0–1.0 M), an increase in response with concentration was noted. This was expected since hydroxide is known to have a large effect on the rate of picrate–creatinine complexation.[18] At higher concentrations of sodium hydroxide (i.e., 1.6–2.5 M), a decrease in response was observed as an insoluble precipitate began to form in the reaction mixture. As a compromise between obtaining a large response and minimizing the extent of precipitation, a concentration of 1.6 M sodium hydroxide was used in all further work.

For convenience, the majority of FIA analyses described in this work were performed at room temperature. The effect of small temperature variations on the response of this method was examined by injecting a 2.0 g/L creatinine standard onto the FIA system while the temperature of the reaction coil was varied between 20 and 35 °C. A linear increase in signal with temperature was observed, with a change in the response of 2%/°C. This change is small compared to the range of levels observed for creatinine in normal urine samples[18] and was considered acceptable for use in this study.

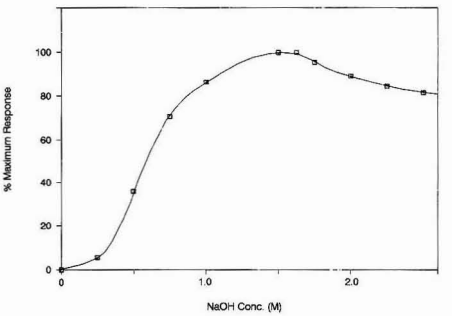


Figure 3. Effect of sodium hydroxide optimization on the response of the FIA system. The experimental conditions are given in the text.

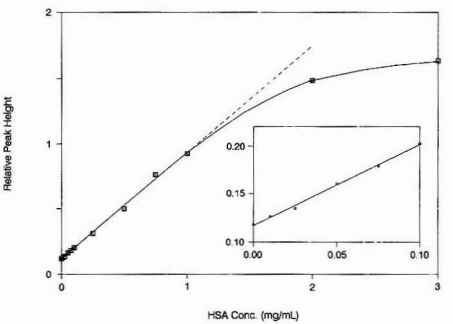


Figure 4. Calibration curve for HSA on the HPIAC system. Parameters for the best-fit line are given in the text. The inset shows an enlarged view of the lower six points in the graph.

System Performance. Figure 2 shows examples of the responses obtained on the HPIAC/FIA system for urine and standards containing albumin or creatinine. As already stated, the total analysis time for the entire system was set at 5 min per 20 μL sample injection. This gives the system a potential throughput of 12 samples/h, or approximately 290 samples/day. A closer examination of the results in Figure 2 shows that there is no detectable response at 510 nm from the albumin standard or at 280 nm when only the creatinine standard was injected. However, the response from a normal urine control produced a signal at both detectors, indicating that both albumin and creatinine were present in this sample. In further studies, it was found that the size of the creatinine signal was the same whether or not the HPIAC column was present in the system. This indicated that no significant interactions were occurring between creatinine and the immobilized antibody support.

Figure 4 shows a typical calibration curve obtained for albumin on the HPIAC/FIA system. The best-fit line for this graph has a slope of 0.84 (±0.02) L/g HSA, an intercept of 0.117 (±0.001), and a correlation coefficient of 0.9984 for the lower six points in

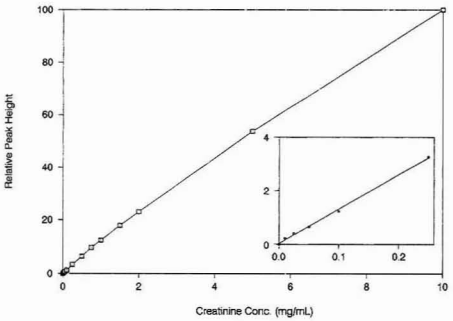


Figure 5. Calibration curve for creatinine on the FIA system. Parameters for the best-fit line are given in the text. The inset shows an enlarged view of the lower six points in the graph.

the graph. The limit of detection for albumin was determined to be 3 mg/L at a signal-to-noise ratio of two (i.e., S/N = 2). The linear range (i.e., those concentrations giving a result within ±5% of the best-fit line) extended up to approximately 1.0 g/L HSA. The limit of detection and linear region of this curve covered the entire range of interest for the detection of microalbuminuria, or from 5 to 300 mg/L.[9]

The upper end of the linear range for the HPIAC column occurred at approximately a 1:1 load of albumin versus the available antibody binding sites. However, because there is a decrease in binding efficiency at high sample loads (see eq 1), even samples in excess of the column binding capacity could produce a change in response when injected. With this particular column, kinetic effects allowed the dynamic range to extend to approximately 3 g/L HSA. A similar extension of the dynamic range beyond the known column binding capacity has been reported previously for other HPIAC systems.[7,31]

A typical calibration curve obtained for creatinine on the FIA system is shown in Figure 5. A nearly linear response was seen over the entire concentration range studied. The best-fit line shown in Figure 5 has a slope of 12.8 (±0.3) L/g, an intercept of 0.03 (±0.03), and a correlation coefficient of 0.9988 for the lower six points in the graph. The limit of detection for creatinine was determined to be 5 mg/L (S/N = 2), and the dynamic range was found to extend up to at least 10 g/L. This response brackets the levels of creatinine seen in normal urine samples, which are generally said to occur between 0.5 and 2.1 g/L.[32]

Within-day precision of the HPIAC system was determined by making 20 sequential injections of albumin standards containing either 15 or 35 mg/L HSA. The relative standard deviations determined for these samples were ±0.7% and ±0.8%, respectively. Within-day precision of the FIA system was determined in a similar manner by making 24 sequential injections of a normal urine control containing 0.82 g/L creatinine. The relative standard deviation obtained for this sample was ±1.7%.

A commercial urine control containing known levels of albumin and creatinine was used to determine the accuracy of the HPIAC/FIA system. The results obtained by this system for three measurements of the control sample were 25 ± 2 mg/L albumin (±1 SD) and 0.82 ± 0.08 g/L creatinine. These results showed good agreement with the values provided by the manufacturer (i.e., 20–30 mg/L albumin and 0.89 ± 0.09 g/L creatinine).

Table 1. Potential Interferences Examined on the HPIAC/FIA System

test compound	normal range[a]	interference range
	HPIAC System	
creatinine	0.6–1.6 g/L	>7 g/L
glucose	10–150 mg/L	>2.5 g/L
hemoglobin	<0.3 mg/L	>5 mg/L
immunoglobulin G	0.6–9.1 mg/L	>15 mg/L
transferrin	0–1.9 mg/L	>20 mg/L
urea	12–20 g/L	>60 g/L
	FIA System	
acetone	0–3 mg/L	>30 mg/L
acetoacetate	<0.05 g/L	>0.1 g/L
albumin	5–30 mg/L	>0.4 g/L
glucose	10–150 mg/L	>2.5 g/L
α-ketoglutarate		>0.5 g/L
oxaloacetate	8–40 mg/L	>0.2 g/L
pyruvate	88 mg/L	>88 mg/L

[a] All values are based on a 1 L output of urine per day (range, 0.4–25 L per day).[18] The reference ranges for acetoacetate and pyruvate are from ref 18, the normal range for albumin is from ref 9, and all other normal ranges are from ref 32.

The HPIAC column described in this study was used for over 650 sample and standard injections before any signs of apparent degradation were noted (e.g., a sudden increase in column back pressure or a significant decrease in the size of retained peaks). This type of stability has been reported in earlier work with other immobilized antibody columns operated under similar elution conditions.[2,6,31] When stored in pH 7.0 phosphate buffer at 4 °C, the unpacked anti-HSA silica had no apparent loss of activity over the course of at least 6 months. This result also agrees with observations made in previous studies using silica-based immobilized antibody supports.[2,6,31]

Interference Studies. Besides albumin, a number of other proteins can be found in urine. Table 1 lists some common examples of these proteins and gives their normal urine levels. The effect of these proteins and other urine components on the response of the HPIAC system was examined by injecting a normal urine sample spiked with various amounts of these solutes. The original concentration of albumin in the urine sample was 17 mg/L. The levels of each test solute that was added to this sample are summarized in the Experimental Section. The height of the retained peak obtained for each spiked sample was compared to that obtained with the same urine mixed with only pH 7.0 application buffer. The results showed that there was less than a 7% change in peak size for all of the compounds and concentrations studied. This indicated that none of these solutes had any significant effects on the HPIAC system under the conditions tested. The results of this study agreed with SDS–PAGE experiments that examined the protein content of the retained HPIAC fraction for normal control urine. Only one protein band was observed in this retained fraction. This band comigrated with known albumin standards, thus confirming the identity of this species.

A number of potential interferences were also examined for the FIA system. In serum or plasma there are several non-creatinine solutes that can give a response in the Jaffe reaction,[18] but urine usually has fairly low concentrations for most of these

(31) Thomas, D. H.; Beck-Westermeyer, M. S.; Hage, D. S. *Anal. Chem.*, in press.
(32) Tietz, N. W., Ed. *Clinical Guide to Laboratory Tests*, 2nd ed.; W. B. Saunders Co.: Philadelphia, 1990.

compounds.[18,32] Table 1 lists a number of these compounds and gives their normal urine levels. The effects of these solutes on the FIA method were examined by spiking each compound into a control urine sample which contained an initial creatinine concentration of 0.82 g/L. The levels of the test solutes that were added are given in the Experimental Section. Most of the compounds tested did not cause any detectable change in the creatinine response, but greater than 10% deviations were noted for acetoacetate, oxaloacetate, and α-ketoglutarate at levels above the cutoffs listed in Table 1. However, in all cases the concentrations of the potential interferences at which these deviations began to occur were much higher than those seen in typical urine samples.

CONCLUSION

In this study, we examined the use of high-performance immunoaffinity chromatography and flow injection analysis for the determination of albumin and creatinine in urine. The final system had an analysis time of 5 min for both analytes and required only 20 μL of sample per injection. This sample size is comparable to that used in many previous methods for urinary albumin.[10,11,14,15] However, the overall analysis time is much shorter than the periods of 1–16 h reported for earlier manual methods[13–16] and is slightly shorter than the time required by automated techniques based on immunoturbidimetry.[10,11]

Calibration curves obtained on the HPIAC/FIA system cover the range of clinical interest for both albumin and creatinine. The within-day precision of this method for albumin in normal urine samples (±0.7–0.8% at 15–35 mg/L HSA) is smaller than that reported for either manual methods (5–9%)[14,15] or previous automated techniques for this analyte (2.3–4.8%).[10,11] In addition, the results of the HPIAC/FIA technique show no major interferences from many common solutes and proteins found in urine samples.

Like HPIAC, many current techniques for urinary albumin require the use of antibodies for the selective determination of HSA in samples. Examples include methods based on immunoturbidimetry,[10–12] enzyme immunoassays,[13,14] and radioimmunoassays.[15,16] One general advantage of HPIAC over these other techniques is that the same antibody population can be reused for multiple analyses. In this particular experiment, the same antibody column was used for over 650 sample and standard injections. This factor, along with the high precision of most HPLC systems, is probably what helps to produce the small within-run variation noted for the HPIAC method.

One advantage of the HPIAC/FIA system is its ability to provide a direct measurement of albumin in samples. This type of measurement does not require the use of any labeled compounds for detection, such as those used in radioimmunoassays or enzyme immunoassays. Besides reducing the number of required reagents, this approach helps to decrease the analysis time because fewer steps are needed for reagent addition, sample washing, and signal production. Problems associated with label stability and handling, especially when radioisotopes are used, are also eliminated by this approach.

The ability to use HPIAC along with an FIA assay for creatinine simplifies the measurement of urinary albumin because it allows the albumin results to be automatically normalized for changes in urine volume. This means that short-term urine samples, as well as 12 or 24 h specimens, can be processed and used to obtain quantitative results. By using different types of HPIAC columns, this same approach could be adapted for use in the measurement of other solutes in urine. Possible applications include the determination of other urinary proteins (e.g., hemoglobin and transferrin) or the measurement of excreted drugs and their metabolites.

ACKNOWLEDGMENT

This work was supported by the National Institutes of Health under Grant GM44931. P.F.R. was supported by a fellowship from the University of Nebraska Center for Biotechnology. The authors thank John Swart and Teresa Urlacher for their assistance in the SDS–PAGE studies.

Received for review July 18, 1994. Accepted September 2, 1994.

® Abstract published in *Advance ACS Abstracts,* October 1, 1994.

Anal. Chem. **1994,** *66,* 4272–4277

Separation of Carrier-Free Holmium-166 from Neutron-Irradiated Dysprosium Targets

Ekaterina Dadachova,[†] Saed Mirzadeh,[*,‡] Richard M. Lambrecht,[†] Eric L. Hetherington,[†] and F. F. Knapp, Jr.[‡]

Biomedicine and Health Program, Australian Nuclear Science and Technology Organisation (ANSTO), PMB 1, Menai 2234, New South Wales, Australia, and Nuclear Medicine Group, Oak Ridge National Laboratory (ORNL), P.O. Box 2008, Oak Ridge, Tennessee 37831–6229

Holmium-166 (^{166}Ho, $t_{1/2}$ = 26.4 h) is utilized in radiotherapeutic applications such as radioimmunospecific pharmaceuticals, bone marrow ablation, and radiation synovectomy. High specific activity ^{166}Ho can be obtained from the decay of dysprosium-166 (^{166}Dy, $t_{1/2}$ = 81.5 h). Dysprosium-166 is produced by the ^{164}Dy[n,γ]^{165}Dy-[n,γ]^{166}Dy reaction in a nuclear reactor. The applicability of reversed phase ion-exchange chromatographic methods was demonstrated for the separation of carrier-free ^{166}Ho from milligram quantities of $^{164}Dy_2O_3$ irradiated targets. An efficient and quantitative separation was achieved utilizing a metal-free HPLC system with Dowex AG 50WX12 or Aminex-A5 cation exchangers and α-hydroxyisobutyric acid (α-HIBA) as the eluent (0.085 M, pH = 4.3 adjusted with NH_4OH). The Aminex-A5 column gave a separation factor of ~10^3 between Ho and Dy. Subsequent to the acidic destruction of the Ho–HIBA complex, Ho^{3+} was further purified on a small cation-exchange column from acidic chloride solutions. The separation was achieved within 2 h, with a 95% overall radiochemical yield for carrier-free ^{166}Ho with a Dy breakthrough of <0.1%.

Holmium-166 (^{166}Ho) is utilized in medical radiotherapeutic applications[1–7] because of its physical properties, which include high-energy β radiation [$E_{\beta 1}$ = 1855 keV (51%), $E_{\beta 2}$ = 1776 keV (48%), and $E_{\beta av}$ = 666 keV], a 26.4-h half-life, and decay to a stable daughter. In addition, ^{166}Ho has chemical characteristics suitable for protein labeling with bifunctional chelates. Holmium-166 also emits low-intensity and low-energy γ-rays (80.5 keV, 6%) which are suitable for imaging. Due to the absence of high-energy γ-rays in its decay, ^{166}Ho may be used for outpatient therapy without significant external radiation to other individuals.

Although ^{166}Ho with moderate specific activity can be produced by the ^{165}Ho[n,γ]^{166}Ho reaction, its radionuclidic parent, ^{166}Dy ($t_{1/2}$ = 81.5 h), can serve as a source of high specific activity ^{166}Ho. Dysprosium-166 is produced by double neutron capture reaction on ^{164}Dy. In certain applications, such as protein labeling, the use of a high specific activity radioisotope is essential. In addition, generator-produced ^{166}Ho is free from 1200-y ^{166m}Ho, which is unavoidably coproduced with ^{166}Ho by the ^{165}Ho[n,γ] reaction.

Successful separation of rare earths has been achieved by reversed phase ion-exchange chromatography with cation-exchange resins such as Dowex AG 50W and Aminex-A5 and sodium or ammonium salts of α-hydroxyisobutyric acid (α-HIBA) as complexing agents.[8–10] Yoshida and Haraguchi[11] used a strong cation-exchange resin IEX-210SC for the separation of several rare earths with ammonium lactate as the mobile phase. Elbanovski et al.[12] purified yttrium from heavy lanthanides (mainly Dy and Ho) by use of Wofatit KPS cation exchanger and Tiron (disodium salt of pyrocatechol-3,5-disulfonic acid) as eluent. Dynamic ion-exchange chromatography was recently used for rapid separations of rare earths.[13–15] Separation of nanogram amounts of the rare earths Y, Th, and U was performed on the HPLC 5-mC_{18} reversed phase column with mobile phase consisting of ammonium *n*-octylsulfonate (as dynamic exchanger), α-HIBA, and methanol.[13] On-column formation of nitrilotriacetato complexes of rare earths in a reversed phase ODS column in the presence of 1-octanesulfonate provided a high-resolution chromatographic system for the separation of individual rare earth elements at room temperature.[16] Purification of Y concentrate from heavy lanthanides on various types of anion exchangers in iminodiacetate form has been studied.[17] Separations without complexing agents (e.g., mixtures of methanol and nitric acid) were also reported.[18,19]

Partition chromatography offers a possibility for separating small amounts of both light or heavy rare earths using tributyl phosphate (TBP) as the stationary phase and 11–15 M HNO_3 or

[†] ANSTO.
[‡] ORNL.

(1) Mumper, R. J.; Ryo, U. Y.; Jay, M. *J. Nucl. Med.* **1991**, *32*, 2139.
(2) Turner, J. H.; Claringbold, P. G.; Klemp, P. F. B.; Normann, P. E.; Glancy, R. J.; Hetherington, E. L.; Najdovski, L.; Lambrecht, R. M. *Nucl. Med. Commun.*, in press.
(3) Turner, J. H.; Claringbold, P. G. Australian Patent PJ9726,20, April 1990.
(4) Pak. K. B.; Kim, J. R.; Lambrecht, R. M. Korean Patent Application 93-30600,29, December 1993.
(5) Kasi, L. P.; Macey D.; Imam, S.; Bayouth, M.; Dimopoulos, M.; Podoloff, D.; Bhadkamkar, V.; Garlich, J.; McMillan, K; Simson, J.; Champlin, R. *J. Nucl. Med.* **1993**, *34*, 33p (abstract).
(6) Parks, N. J.; Kawakami, T. G.; Avila, M. J.; White, R.; Cain, G. R.; Rakka, S. D.; Hornoff, W.; Fisher, P.; Moore, P. *Blood* **1993**, *83*, 318.
(7) Lieberman, E.; Bordoni, M.; Thorenton, K. U.S. Patent 4,849,209, 18 July 1989.
(8) Smith, H. L.; Hoffman, D. C. *J. Inorg. Chem.* **1956**, *3*, 243.
(9) Choppin, G. R.; Chopoorian, J. A. *J. Inorg. Chem.* **1961**, *22*, 97.
(10) Hohlein, G. von; Voller, H.; Weinlander, W. *Radiochim. Acta* **1969**, *11*, 172.
(11) Yoshida, K.; Haraguchi, H. *Anal. Chem.* **1984**, *56*, 2580.
(12) Elbanovski, M.; Makowska, B.; Hoppe, K.; Paetz, M.; Ludwiczak, E. *Pol. J. Appl Chem.* 1991, *35*, 23.
(13) Barkley, D. J.; Blanchette, M. *Anal. Chem.* **1986**, *58*, 2222.
(14) Cassidy, R. M.; Elchuk, S.; Elliot, N. L.; Green, L. W.; Knight, C. H. *Anal. Chem.* **1986**, *58*, 1181.
(15) Knight, C. H.; Cassidy, R. M.; Recoskie, B. M.; Green, L. W. *Anal. Chem.* **1984**, *54*, 474.
(16) Kuroda, R.; Wada, T.; Kokubo, Y.; Oguma, K. *Talanta* **1993**, *40*, 237.
(17) Hubicka, H. *Hung. J. Ind. Chem.* **1987**, *15*, 349.
(18) Larsen, N. R.; Pedersen, W. B. *J. Radioanal. Chem.* **1978**, *45*, 135.
(19) Cha, K. W.; Pakk, Y. K. *Anal. Sci. Technol.* **1989**, *2*, 23.

0003-2700/94/0366-4272$04.50/0 © 1994 American Chemical Society

HCl as the mobile phase[20,21] or bis(2-ethylhexyl) hydrogen phosphate (HDEHP) as an extracting agent from 0.2 to 5 M HNO_3.[22,23] Partial separation of mixtures of rare earths with electrophoresis on paper and acetylcellulose films in a medium of α-HIBA,[24,25] and with high-voltage capillary electrophoresis,[26,27] has also been reported. Solvent extraction techniques have been used extensively for separation and preconcentration of rare earths.[28,29]

In spite of the rather large number of publications on rare earth separations, only a few address the separation in a micro–macrocomponent system, where microscopic amounts (≤1 μg) of one member of the lanthanide series are separated from macroscopic amounts (≥1 mg) of another member. Because of the uniform chemistry exhibited throughout the lanthanide series, the separation factors between the adjacent members are very small. For example, separation of 1 μg of Tb from 110 mg of Er was studied by partition chromatography using a HDEHP/Kieselguhr column.[23] In this case, the separation factor between the two rare earths was ~17. Under similar conditions, the separation factor for the Dy–Ho pair was only 2.2.[23] Yasumi et al.[30] reported separation of carrier-free ^{163}Ho produced by the ^{164}Dy[p,2n] reaction from milligram amounts of a Dy–metal target. An initial separation of a ^{163}Ho fraction from the dissolved target material was carried out on the AG 50Wx8 cation exchanger using 0.48 M α-HIBA as eluent. Further purification of the ^{163}Ho fraction from various radioactive impurities required ~20 h. Separation of carrier-free ^{166}Ho from Dy_2O_3 targets with partition chromatography using HDEHP or TBP as stationary phase and 3–12 M HNO_3 as mobile phase was unsatisfactory for biomedical applications of ^{166}Ho.[31]

This paper demonstrates the applicability of reversed phase LC and HPLC ion-exchange chromatography for separation of carrier-free ^{166}Ho from neutron-irradiated $^{164}Dy_2O_3$ targets. In addition, the method described herein defines a selective and convenient means to prepare ^{166}Ho in high radionuclidic purity and in a solvent suitable for radiolabeling of pharmaceuticals.

EXPERIMENTAL SECTION

Reagents and Materials. Isotopically enriched ^{164}Dy (97%) as Dy_2O_3 was obtained from ORNL and Medgenix Diagnostics GmbH. The cation-exchange resins Dowex AG 50Wx4 (H^+ form, 100–200 mesh, 106–250 μm, 1.1 mequiv/mL), AG 50Wx8 (H^+ form, 100–200 mesh, 106–250 μm, 1.7 mequiv/mL), and AG 50WX12 (H^+ form, 200–400 mesh, 53–106 μm, 2.1 mequiv/mL) and Aminex-A5 (Na^+ form, cross-linkage 8%, 132 μm) were purchased from Bio-Rad Labs. The resins were stored in H_2O, and AG 50W resins were converted to the Na^+ form before use. The α-HIBA (98%), Arsenazo III [2,7-bis(o-arsenophenolazo)-1,6-dihydroxynaphthalene-3,6-disulfonic acid, 99.99%], and Dy_2O_3 (99.9%) were supplied from Aldrich. All other inorganic chemicals were of reagent grade.

Radiochemical Reagents and Radioactivity Measurements. Targets consisting of 5–10 mg of $^{164}Dy_2O_3$, encapsulated either in a quartz ampule or in a titanium can, were irradiated in the hydraulic tube of the ORNL high-flux isotope reactor (HFIR) at a thermal neutron flux of 2.0×10^{15} n·s^{-1}·cm^{-2} for 1 or 8 days or in the pneumatic tube of the ANSTO high-flux Australian reactor (HIFAR) at 5×10^{13} n·s^{-1}·cm^{-2} for 12 h. Following irradiation, the target was allowed to cool for 2 days, then was dissolved in 5 mL of 9 M HCl, and evaporated to dryness and the residue was dissolved in 1 mL of 0.01 M HNO_3. Dy–carrier solution of 58 mg/mL was prepared using the same procedure. Mixtures of active and inactive solutions were prepared as needed for the separations.

γ-Spectrometry was performed using a Ge(Li) detector coupled to a PC-based MCA. The 80.5-keV (6%) γ-rays of ^{166}Ho and 82.4-keV (13%) γ-rays of ^{166}Dy were used for detection. Our detection limit for ^{166}Dy was estimated to be 70 pCi. All radioactive samples and standards were counted in 10-mL vials in a constant liquid geometry. Percent activities were calculated relative to the external standards.

Apparatus. The ^{166}Ho/^{166}Dy separation was performed using a metal-free Isco Model 2350 HPLC pump, Rheodyne Model 9125 syringe injector, and Isco Retriever-500 fraction collector. The determination of Dy was performed on a DMS 100 UV/visible spectrophotometer.

Column Preparation. The following columns were prepared for separation of ^{166}Ho from Dy mixtures:

Column A. A 0.8 × 20 cm glass column was packed with 100–200 mesh AG 50W resin of varying cross-linkage (Na^+ form) and operated at 87 °C (melting point of α-HIBA).

Column B. A 1.8 × 50 cm glass column was packed with 200–400 mesh of AG 50WX12 resin and was operated at room temperature except as noted.

Column C. A 0.4 × 15 cm HPLC metal-free column was packed with the same type of resin as column B.

Column D. A 0.4 × 25 cm HPLC metal-free column was packed with Aminex-A5 cation-exchange resin. Columns C and D were always operated at room temperature.

Column E. A 1.3 × 2.1 cm glass column was packed with the same type of resin as column B. Column E was used for purification of ^{166}Ho from the complexing agent after separation from Dy.

Separation of ^{166}Ho from Dy. All columns were preequilibrated with the appropriate eluent before injection of the Ho/Dy samples. Column A was eluted at a flow rate of 0.6–1.0 mL/min with 0.2–0.3 M aqueous solution of α-HIBA at pH = 4.28–4.63 adjusted with NH_4OH. The column loads were typically 1 mL in volume in which the contents of ^{164}Dy varied between 0.2 and 3 mg in 0.01 M HNO_3. Column B was eluted at a rate 0.8 mL/min (once at 1.6 mL/min) with 0.132–0.2 M α-HIBA at pH = 4.2–4.3 adjusted with NaOH, except for 0.132 M samples, where the pH was adjusted with NH_4OH. In this case, the sample volume was 150 μL with Dy contents of 200–400 μg in 0.01 M HNO_3. Columns C and D were eluted with 0.066–0.132 M α-HIBA at pH

(20) Siekierski, S.; Fidelis, I. *J. Chromatogr.* **1960**, *4*, 60.
(21) Fidelis, I.; Siekierski, S. *J. Chromatogr.* **1961**, *5*, 161.
(22) Mirzadeh, S.; et al. Oak Ridge Nat. Lab., [*Rep.*] **1992**, (June), *ORNL/TM-12159*.
(23) Sochacka, R. J.; Siekierski, S. *J. Chromatogr.* **1964**, *16*, 376.
(24) Aizetmuller, K.; Buchtela, K.; Grass, F.; Hecht, F. *Mikrochim. Acta* **1964**, *6*, 1089.
(25) Buchtela, K.; Aitzetmuller, K.; Grass, F. *Atomkernenergie* **1965**, *10*, 264.
(26) Foret, F.; Fanali, S.; Nardi, A.; Bocek, P. *Electrophoresis* **1990**, *11*, 780.
(27) Chen, M.; Cassidy, R. M. *J. Chromatogr.* **1992**, *602*, 227.
(28) Tang, J.; Wai, C. M. *Anal. Chem.*, **1986**, *58*, 3235.
(29) Stevenson, P. C.; Nervik, W. E. *The Radiochemistry of the Rare Earths, Sc, Y, and Ac*; Natl. Acad. Sci., Natl. Res. Council, Nuclear Science Series NAS-NS-3020; National Academy of Science, National Research Council: Washington, DC, 1961; pp 86–150.
(30) Yasumi, S.; Rajasekaran, G.; Ando, M. *Proceedings of the International Conference on Neutrino-82*, Hungary; 1982; p 59.
(31) Dadachova, E.; Mirzadeh, S; Lambrecht, R. M.; Kanpp, F. F. *Radiochem. Radioanal. Lett.*, in press.

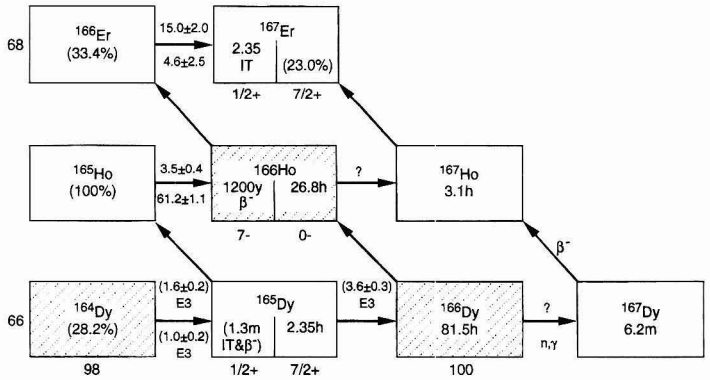


Figure 1. Scheme for production of ^{166}Ho and ^{166}Dy in a nuclear reactor.

Table 1. Reactor Productions of ^{166}Dy[a]

reactor/irradiation position	neutron flux ($n \cdot s^{-1} \cdot cm^{-2}$)	T_{irr} (days)	^{166}Dy Yield (mCi/mg of ^{164}Dy)
HFIR-HT[b]	2.0×10^{15}	8	3.5×10^3
		1	2.2×10^3
HIFAR-PT[c]	5×10^{13}	0.5	~2

[a] Targets were 97% isotopically enriched $^{164}Dy_2O_3$. [b] HFIR-HT, ORNL high-flux isotope reactor, hydraulic tube. [c] HIFAR-PT, ANSTO high-flux australian reactor, pneumatic tube.

= 4.2–4.3 adjusted with NH_4OH. In certain experiments, ^{166}Ho was eluted with 0.085 M α-HIBA and Dy with 0.132 M. Volume of samples were 150 μL in which the contents of ^{164}Dy varied between 200 μg and 2.5 mg in 0.01 M HNO_3.

Purification of ^{166}Ho from α-HIBA after Separation from Dy. The combined fraction containing ^{166}Ho (usually 25–30 mL) was acidified with 1 M HCl to pH = 2 and loaded on column E preequilibrated with 1 M HCl. The column was washed with 6 × 10 mL portions of 1 M HCl to remove α-HIBA. These fractions were evaporated to dryness for further analysis. Purified ^{166}Ho was eluted from the column at a rate 2 mL/min with 12 × 2 mL portions of 6 M HCl.

Spectrophotometric Determination of Stable Dy. For calibrations, solutions of $DyCl_3$ and Arsenazo III were buffered at pH = 4.0 with 0.01 M acetate buffer at an ionic strength of 0.1 (NaCl) and mixed in the Dy:Arsenazo III ratio of 1:1. The absorbance was monitored at 660 nm. Free Arsenazo III absorbs only slightly at this wavelength and pH ($\epsilon = 650\ cm^{-1} \cdot M^{-1}$) while the 1:1 and 1:2 lanthanide complexes of Arsenazo III have extinction coefficients of 3.5×10^4 and $5.0 \times 10^4\ cm^{-1} \cdot M^{-1}$, respectively.[32] The detection limit of Dy was estimated to be ~2 μg/mL. For determination of Dy contents in carrier-free ^{166}Ho fraction, solutions containing ^{166}Ho (6 M HCl) were evaporated to near dryness. The residue was dissolved in 1 mL of 0.01 M acetate buffer at ionic strength of 0.1, and Dy concentration was determined.

RESULTS

Production of ^{166}Dy. Dysprosium-166 is produced by double neutron-capture on ^{164}Dy in a nuclear reactor (see Figure 1). Table 1 summarizes the experimental yields of ^{166}Dy. The yields of ^{166}Dy, produced in the hydraulic tube of the ORNL HFIR was 2.2 and 3.5 Ci/mg of ^{164}Dy (the initial mass of ^{164}Dy) for 1 and 8 days of irradiation, respectively. The relative reduction of the yield for the 8-day irradiation is due to the very large effective decay constant ($\lambda + \phi_n\sigma$) of the short-lived intermediate nuclei, ^{165}Dy, which results in substantial target depletion. The low yield from

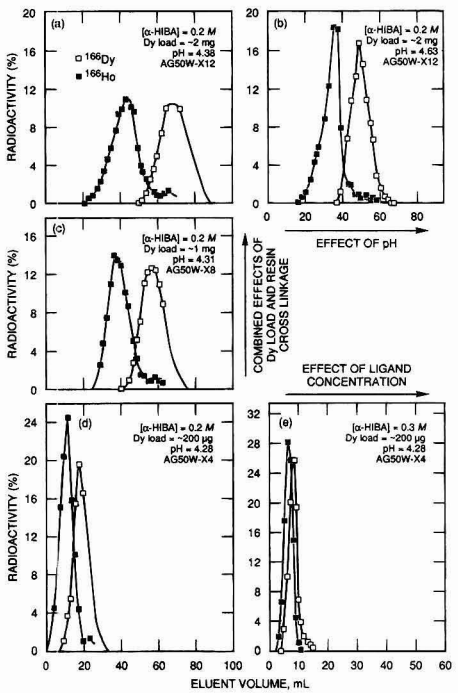


Figure 2. Separation of ^{166}Ho/Dy mixtures using column A (AG50W, 100–200 mesh, 0.8 × 20 cm at 87 °C): influence of pH (a, b), combined effects of Dy load and degree of resin cross-linkage (a, c, d), and effect of ligand concentration (d, e).

(32) Cacheris, W. P.; Nickle, S. K.; Sherry, A. D. *Inorg. Chem.* **1987**, *26*, 958.

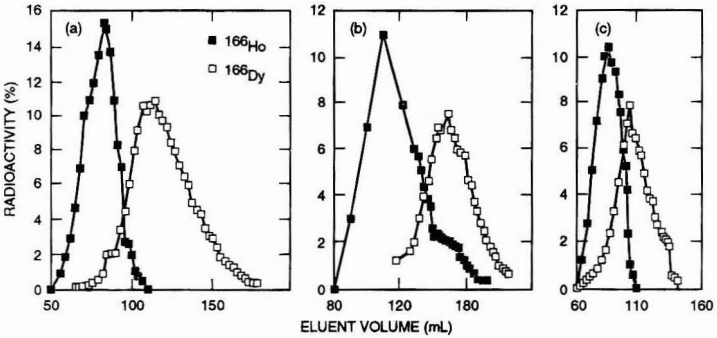


Figure 3. Effect of temperature on separation of ^{166}Ho/Dy mixtures using column B (AG 50WX12, 200–400 mesh, 1.8 × 50 cm): [α-HIBA] = 0.2 M; Dy load, 400 μg); T (°C) = (a) 25, (b) 37, and (c) 57.

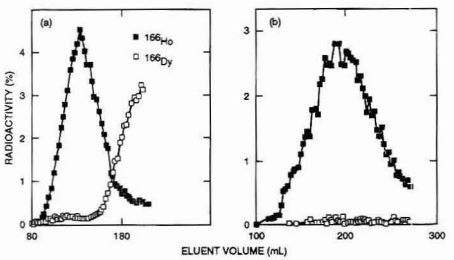


figure 4. Combined effects of [α-HIBA] and Dy load on separation of ^{166}Ho/Dy mixtures (column B): Dy load, (a) 200 (b) 400 μg; [α-HIBA] = (a) 0.145 and (b) 0.132 M.

the ANSTO HIFAR simply reflects the 40-fold reduction in the neutron flux (in the double-neutron-capture process, yield is proportional to the square of the neutron flux).

^{166}Ho/Dy Separation. The results from the first series of experiments employing column A, depicted in Figure 2, define the following general conditions for the separation of ^{166}Ho from Dy on AG 50W resins: [α-HIBA] < 0.2 M; pH in the range from 4.3 to 4.6; resin cross-linkage 8 and 12. Separations were performed at 87 °C and a flow rate of 0.6–1.0 mL/min.

Variables studied with the larger column B include flow rate, temperature, and concentration of α-HIBA (see Figures 3 and 4). The optimal flow rate for column B was found to be 0.8 mL/min. The separation was not quantitative at higher flow rates. The retention time and full width at half-maximum (fwhm) of peaks decreased at higher temperature (Figure 3), but it appears that under similar conditions, better separation was achieved at lower temperature. Figure 4 illustrates the combined effects of α-HIBA concentration and Dy load. At pH = 4.3 and T = 25 °C, reducing the concentration of α-HIBA from 0.145 to 0.132 M improved the separation, even though the Dy load increased from 200 to 400 μg. The substitution of NH_4OH for NaOH, which was used for pH adjustment, may have also contributed to improvement of separation. Figure 4b shows that a quantitative separation between carrier-free ^{166}Ho and 400 μg of Dy was achieved when the concentration of α-HIBA was decreased to 0.132 M. The fraction of Dy in ^{166}Ho, in this case, was estimated to be <4%, or 3 μg by UV measurement. Due to the large size of column B, however, complete separation of ^{166}Ho fraction took ~6 h.

The results obtained from column C are shown in Figure 5. In this case, the column was eluted at p_{sys} = 200 psi at a flow rate of 0.8 mL/min. Optimization of the elution parameters was carried out in the range of α-HIBA concentrations from 0.066 to 0.132 M at pH = 4.27. As shown in Figure 5, 0.085 M α-HIBA provides almost complete separation of ^{166}Ho from 1.5, 2.0, and 2.5 mg of Dy (panels a–c of Figure 5, respectively). The fractions of Dy in ^{166}Ho fractions were 1.7% when Dy load on the column was 1.5 mg and 2.7% for Dy loads of 2.0 and 2.5 mg. In all three cases, complete elution of ^{166}Ho required ~1 h. In the cases of 2.0- and 2.5-mg Dy loads, after elution of ~96% of ^{166}Ho activity, Dy was stripped off the column with 0.132 M α-HIBA (Figure 5b,c).

The results obtained from column D (Aminex-A5) are shown in Figure 6. Separations of ^{166}Ho from 1.5–2.5 mg of Dy were performed via elution with 0.085 M α-HIBA. As shown, an increase in system pressure from 700 to 1400 psi resulted in significant improvement of the separation efficiency of the column. The back pressure in column D increased slightly in each pass as a result of improving the packing conditions. Similar to column C, complete elution of ^{166}Ho fraction required ~1 h followed by Dy elution with 0.132 M α-HIBA.

Preparation of ^{166}Ho in Ionic Form after Separation from Dy. The results of separation of ^{166}Ho in ionic form from the α-HIBA complexing agent on column E are shown in Figure 7. As seen, ^{166}Ho was strongly retained by the resin when the column was washed with 6 × 10 mL of 1 M HCl and then was stripped off the column with 24 mL of 6 M HCl. Upon evaporation, the column washes 1–4 showed decreasing amounts of α-HIBA, while washes 5 and 6 were visibly clear. Spectrophotometric analysis of $^{166}Ho^{3+}$ in 1 mL of 0.01 M acetate buffer at 0.1 ionic strength detected ~35 μg of Dy after separation from 2.5 mg of Dy on an AG 50W column (column C) and ≤2 μg after separation on Aminex-A5 (column D).

DISCUSSION

The separation scheme described here is based on reversed phase ion-exchange chromatography, where Ho and Dy are partitioned between the cation-exchange resin (AG 50W and Aminex-A5) and the mobile phase containing the weakly complexing ligand α-HIBA at pH = 4.3–4.6. As a consequence of "lanthanide contraction" and smaller ionic radii, the complex of α-HIBA with Ho has slightly higher thermodynamic stability than

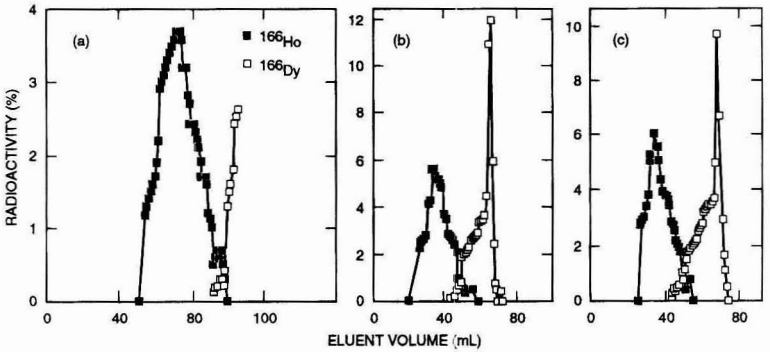


Figure 5. Separation of ^{166}Ho from 1.5–2.5 mg of Dy on a metal-free HPLC using column C (AG 50WX12, 200–400 mesh, 0.4 × 15 cm) via elution with 0.085 M α-HIBA at pH = 4.27 and p = 200 psi: Dy load (mg), (a) 1.5, (b) 2.0, and (c) 2.5. Dy was stripped off the column with 0.132 M α-HIBA from (a) 0, (b) 59, and (c) 63 mL.

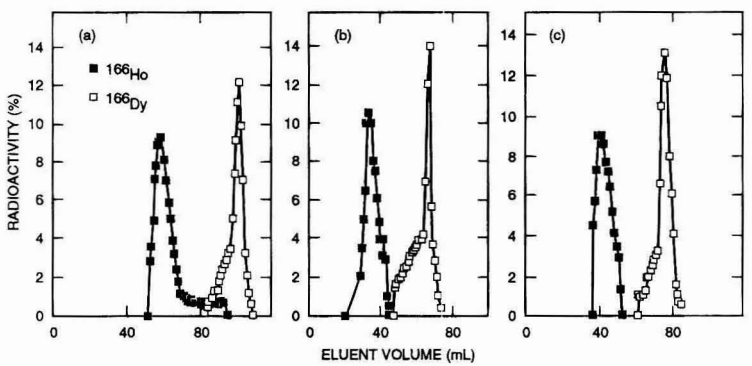


Figure 6. Separation of ^{166}Ho from 1.5–2.5 mg of Dy on a metal-free HPLC using column D (Aminex-A5, 0.4 × 25 cm) via elution with 0.085 M α-HIBA at pH = 4.27: Dy load, (a) 1.5, (b) 2.0, and (c) 2.5 mg; system pressure, (a) 750, (b) 1000, and (c) 1400 psi. Dy was stripped off the column with 0.132 M α-HIBA from (a) 92, (b) 62, and (c) 70 mL.

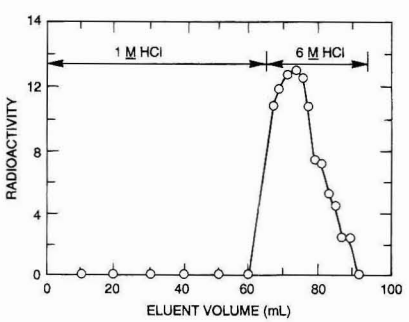


Figure 7. Elution profile of carrier-free ^{166}Ho from column E (AG 50WX12, 200–400 mesh, 1.3 × 2.1 cm) with HCl solutions.

that with Dy, and the elution pattern is reversed with Ho being eluted first. The log β (overall stability constant) of Ho and Dy complexes with α-HIBA are 7.67 and 7.24 at 0.1 ionic strength, respectively.[9] The technique has been used extensively for separation of various members of lanthanides, but it is believed that the present study is the first demonstration of the applicability of this technique for the separation of carrier-free ^{166}Ho from milligram quantities of Dy, where carrier-free ^{166}Ho is produced from β^- decay of ^{166}Dy. Under optimum conditions of [α-HIBA] = 0.085 M, pH = 4.27 (adjusted with NH_4OH), T = 25 °C, and flow rate of 0.8 mL/min, quantitative separation between Ho and Dy was achieved in a metal-free HPLC column containing AG 50WX12 resin (0.4 × 15 cm, 200–400 mesh) operated at 200 psi. In this case, the separation factor between Ho and Dy, calculated as the ratio of (% recovery of Ho)/(% recovery of Dy), was ~60. At higher column pressure, better separation was obtained at lower α-HIBA concentration. A much larger column (1.8 × 50 cm), containing the same resin and operating just above the atmospheric pressure, was not as effective as the above noted smaller HPLC column. Under similar experimental conditions as above, Aminex-A5 owing to its smaller particle size (~13 μm) provided the best resolution. A separation factor of ~950 between Ho and Dy was obtained with an Aminex-A5 column operated at 1400 psi. Further separation of the purified ^{166}Ho from α-HIBA was achieved with a small column of AG 50WX12 (200–400 mesh) from 1 M HCl solution followed by elution of the ionic Ho^{3+} from the column with 6 M HCl.

In conclusion, the possibility of obtaining carrier-free ^{166}Ho from decay of ^{166}Dy was demonstrated. It was shown that, within a narrow pH range and ligand concentration, it is possible to separate carrier-free ^{166}Ho with high yield (95%) from milligram quantities of neutron-irradiated Dy target by use of a HPLC system. The entire separation process was achieved within 2 h and the separation factor between Ho and Dy was ~950 (corresponding to a Dy breakthrough of ~0.1%) in a single pass. These results provided a basis for development of a ^{166}Dy → ^{166}Ho biomedical generator system, which is currently under evaluation.

ACKNOWLEDGMENT

Research at ANSTO was supported by the Commonwealth of Australia. Research at ORNL was supported by the OHER, U.S. Department of Energy, under Contract DE-AC5−840R214 with Martin Marietta Energy Systems, Inc.

Received for review May 25, 1994. Accepted August 24, 1994.[⊗]

[⊗] Abstract published in *Advance ACS Abstracts,* October 1, 1994.

Anal. Chem. **1994,** *66,* 4278–4282

Foam Flotation Enrichment of Enantiomers

Daniel W. Armstrong,* Eve Y. Zhou, Shushi Chen, Kang Le, and Yubing Tang

Department of Chemistry, University of Missouri–Rolla, Rolla Missouri 65401

Adsorptive bubble separation methods are known to be useful for processing large amounts of material at a relatively low cost. These techniques have been used to enrich components from both heterogeneous and homogeneous solutions. There is a need for economical process-scale enantiomeric separations. Thus far there has been little evidence to support the feasibility of using an adsorptive bubble process to enrich enantiomers. We demonstrate that foam-forming chiral collectors can be used in conjunction with an inexpensive glass device to enantiomerically enrich some pharmaceutically important compounds as well as derivatized and underivatized amino acids. Factors that appeared to affect this water-based separation include the following: (a) column length, (b) column geometry and packing, (c) gas flow rate, (d) concentration of the collector and the racemate, (e) nature of the collector, (f) temperature, (g) pH, (h) reflux time, (i) foam dryness, and (j) the presence of other materials in the sample (e.g., miscible organic solvents, salts, etc.). The chiral collectors used in this study are known to be able to associate with analytes via ligand exchange interactions, hydrophobic inclusion complexation, and hydrogen-bonding interactions among others.

Separations via "adsorptive bubble techniques" (e.g., flotation, foam flotation, froth flotation, floc flotation, floc–foam flotation, etc.) have been used for many years.[1] These methods often are used to process large amounts of material (high volume) at a relatively low cost. The separations can be accomplished in either batch or continuous processes. Flotation is an important technique for concentrating sulfide ores.[2] Most of the flotation methods used by the mining industry involve treating slurries of finely ground material with a *collector* (i.e., a surfactant that adsorbs or binds to the component of interest thereby giving it a hydrophobic surface). The hydrophobic particles tend to adhere to and be carried by gas bubbles, thereby separating them from other material that does not adhere to the bubbles.[2–4]

More recently flotation methods have been used in conjunction with homogeneous solutions, that is, to enrich certain dissolved solutes. The species most often enriched by this method are metal cations or chelates.[5–10] This process is often referred to as ion flotation and has been reviewed previously.[11–14]

Theoretically, bubble flotation methods could separate or enrich any dissolved substance, provided an appropriate collector with adequate selectivity can be found. During the course of our studies on chiral recognition, it was noticed that aqueous solutions of some molecules used as chiral selectors produced foam upon agitation. This raised the possibility of enantiomerically enriching compounds via an absorptive bubble process. Some chiral selectors were used in previous water-based enantioseparation methods.[15–24] To our knowledge, these are the first reported enantiomeric enrichments achieved with an adsorptive bubble type of separation technique.

EXPERIMENTAL SECTION

Materials. Heptakis(2,6-di-*O*-methyl)-β-cyclodextrin was purchased from Sigma (St. Louis, MO), permethyl-β-cyclodextrin was obtained from Cyclolab R&D Laboratory (Budapest, Hungary), and hydroxypropyl-β-cyclodextrin was obtained from Consortium Fur Elektrochemische Industrie GMBH. As has been noted before, no commerical derivatized cyclodextrins are pure; they are composed of mixtures of homologues and isomers.[25] Warfarin, D- and L-*N*-*t*-BOC-phenylalanine, D- and L-*N*-*t*-BOC-chlorophenylalanine, dansyl-D,L-tryptophan, dansyl-D,L-phenylalanine, *N*-heptyl-L-hydroxyproline, vancomycin, and digitonin were purchased from Sigma. SQ 30,840 and SQ 31,236 were obtained from Squibb (New Brunswick, NJ). All solvents were obtained from Fisher Scientific (Fair Lawn, NJ). The silica cartridges for solid phase extraction were purchased from Alltech (Deerfield, IL). All HPLC columns were obtained from Advanced Separation Technology Inc. (Whippany, NJ). Pyrex gas dispersion tubes and other glassware were obtained from Fisher Scientific.

(1) Gaudin, A. M. *Flotation*; McGraw Hill: New York, 1932.
(2) Rossberg, K. S. E., Ed. *Flotation of Sulfide Minerals*; Elsevier: Amsterdam, 1985.
(3) Castro, S. H., Alvared, J. Froth Flotation. In *Developments in Mineral Processing*; Fuerstenau, D. W., Ed.; Elsevier: Amsterdam, 1988.
(4) Ramey, M. W., Ed. *Flotation Agents and Processes, Technology and Applications*; Noyes Data Corp., Park Ridge, NJ, 1980.
(5) Walling, C.; Ruff, E. E.; Thornton, J. L. *J. Chem. Phys.* **1957**, *67*, 486.
(6) Wace, P. E.; Banfield, D. C. *Chem. Process Eng.* **1966**, *47*, 70.
(7) Jorne, J.; Rubin, E. *Sep. Sci.* **1969**, *4*, 313.
(8) Huang, R. C. H.; Talbot, F. D. *Can. J. Chem. Eng.* **1973**, *51*, 709.
(9) Kubota, K.; Hayashi, S. *Can. J. Chem. Eng.* **1977**, *55*, 286.
(10) Walkowiak, W. *Sep. Sci. Technol.* **1991**, *26*, 559.
(11) Rusanov, A. I.; Levicer, S. A.; Zarov, V. T. *Poverchnostnage Radelene Vercestv*, Ezd. Chimija: Leningrad, 1981.
(12) Golman, A. M. *Ionnaja Flotacija*; Nedra: Moscow, 1982.
(13) Grieves, R. B. In *Treatise on Analytical Chemistry*; 2nd ed.; Elving, P. F., Ed.; Wiley-Interscience: New York, 1982; Vol. 5.
(14) Wilson, D. J.; Clarke, A. N. *Topics in Foam Flotation*; Dekker: New York, 1983.
(15) Davankov, V. A.; Kurganov, A. A.; Bocklov, A. S. *Advances in Chromatography*; Giddings, J. C., Grushka, E., Cazes, J., Brown, P. R., Eds.; Marcel Dekker: New York, 1983; Vol. 22, p 71.
(16) Hare, P. E.; Gil-Av, E. *J. Chromatogr.* **1976**, *122*, 205.
(17) Lepage, J.; Lindner, W.; Davies, G.; Karger, B. *Anal. Chem.* **1979**, *51*, 433.
(18) Armstrong, D. W.; DeMond, W. *J. Chromatogr. Sci.* **1984**, *22*, 411.
(19) Armstrong, D. W.; Faulkner, J. R., Jr.; Han, S. M. *J. Chromatogr.* **1988**, *452*, 323.
(20) Snopek, J.; Jelinek, I.; Smolkova–Keulemansova, E. *J. Chromatogr.* **1988**, *452*, 571.
(21) Otsuka, K.; Terabe, S. *J. Chromatogr.* **1990**, *515*, 221.
(22) Pawlowska, M. *Chirality* **1991**, *3*, 136.
(23) Armstrong, D. W.; Rundlett, K.; Reid, G. L., III *Anal. Chem.* **1994**, *66*, 1990.
(24) Armstrong, D. W.; Rundlett, K.; Chen, J. R. *Chirality* **1994**, *6*, 496.
(25) Armstrong, D. W.; Li, W.; Chang, C.-D., Pitha, J. *Anal. Chem.* **1990**, *62*, 914.

0003-2700/94/0366-4278$04.50/0 © 1994 American Chemical Society

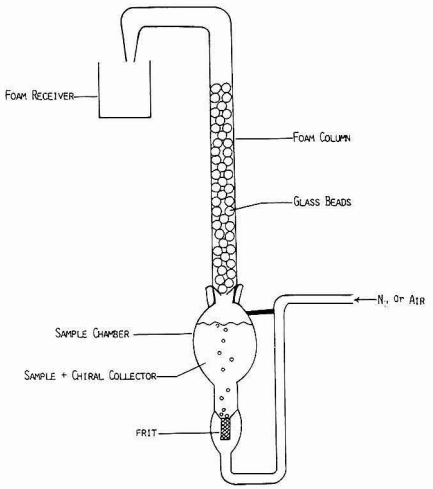


Figure 1. Schematic showing the glass foaming device used in this work. The detachable column fits into the sample chamber. Air or nitrogen gas enters the bottom of the sample chamber through a fine glass frit. The foam produced in the sample chamber passes into the column. The velocity with which the foam travels up the column is controlled by the gas flow rate and also is affected by any packing material in the column. Many of the bubbles that make up the foam break, thereby forming a thin layer of liquid that flows down the inner surfaces of the column toward the sample chamber.

The foaming device used in this study is shown in Figure 1. This was constructed (along with others) by our glass blower according to our instructions. It consists of three basic parts: (1) a sample chamber, which holds an aqueous or buffer solution containing the racemate and the chiral collector, (2) the gas introduction section, which is separated from the sample chamber by a fine porous frit, and (3) a detachable foam column (25 cm or 40 cm × 1.6 cm i.d.) that may contain 7 mm diameter glass bead packing material. Several of these devices can be operated in series if desired.

Methods. Stock solutions of compounds studied were made into stock solutions in ethanol (or in acetonitrile for those analytes analyzed using vancomycin) at a concentration of 12 mg/mL). Solutions of the chiral collector were made in distilled water or buffer at concentrations ranging from 0.01% to 1%. One milliliter of the racemic mixture solution and 19 mL of chiral collector solution were placed into the foaming chamber, and the foaming column was attached to the sample chamber via a ground-glass joint. Air was used to generate bubbles from the bottom of the chamber. The height of the foam in the column was controlled by adjusting the air flow rate with a fine control valve. In general, dry foam formed after a period of controlled reflux gives the best results. The glass beads also seem to help produce a finer, slower rising foam. The foam bubbles tend to break on the way up the column thereby producing a thin film of liquid that flows down the column (i.e., opposite to the foam migration). The airflow rate was adjusted so that a steady countercurrent condition was produced (somewhat analogous to that of a fractional distillation column). At this point no foam passes to the receiver (Figure 1). A foam fraction was collected either by slightly increasing the flow rate to force some foam into the receiver or by using a syringe connected to a long thin Teflon tube on the needle to reach the top layer of the foam in the column. In some experiments, 3 mL of a foam fraction and 12 mL of fresh collector solution were used for a series of consecutive runs. Most enantiomeric ratios in the foam fractions were determined by HPLC. A Shimadzu LC 6A liquid chromatography with a variable-wavelength detector and a C-R3A Chromatopac data system were used for all data analysis. The chromatographic conditions for the separation of all compounds studied are listed in Table 1. The UV detection wavelength was 254 nm for all analytes except for the *N*-*t*-BOC amino acids, which was 225 nm. The warfarin peaks overlapped with the collector, thus solid phase extraction on a silica cartridge was employed to remove the collector before HPLC injection. The silica cartridge was washed with 3–5 mL of diethyl ether before the warfarin fraction was loaded, and then warfarin was eluted from the cartridge with diethyl ether and collected for analysis. Foam fractions of other compounds were injected directly on the chiral stationary phase containing LC column. The enantiomeric purity of dansyl-tryptophan and dansyl-phenylalanine were determined directly on a Waters Quanta 4000 CE apparatus equipped with a 254 nm lamp and a 50 μm (i.d.) × 32 cm (24 cm to detector) fused silica capillary. The run buffer contained 0.1 M, pH 6 phosphate buffer plus 2 mM vancomycin as the chiral selector.[24]

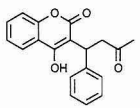
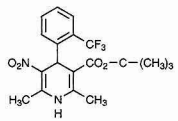
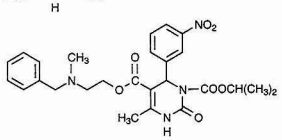
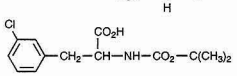
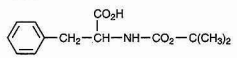
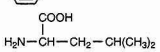
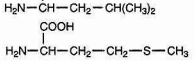
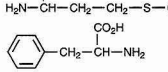
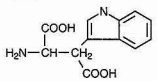
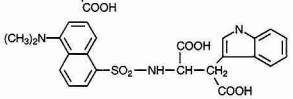
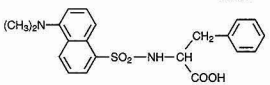
General conditions for the alkylhydroxyproline and digitonin chiral collector experiments were as follows: 5 mL of 0.02% (unless indicated otherwise) surfactant solution (*n*-heptyl-L-hydroxyproline, for example) in water was mixed with 0.25 mL of stock solutions of leucine (2 mg/mL), methionine (2.32 mg/mL), phenylalanine (2.6 mg/mL), and tryptophan (2.8 mg/mL). Approximately 4.4 mg of cupric acetate was added to the solution. When foaming was completed, the residual solution was analyzed as outlined below. All amino acids were derivatized with (6-aminoquinolyl)-*N*-hydroxysuccinimidyl carbamate (AQC) and separated via HPLC as indicated in Table I. This achiral derivatization procedure for amino acids and the enantioselective separation method has been described previously.[25]

RESULTS AND DISCUSSION

The enrichment of enantiomers using foaming agents (collectors) that also are chiral selectors is examined in this work. It is understood that there are other possible approaches that could produce enantiomeric enrichments as well. For example, an adsorptive bubble method might be feasible if the racemate itself was surface active and a nonfoaming chiral selector was employed. In the former case (which is the focus of this paper), the physicochemical properties of the chiral collector are all important. It must be (a) at least partially water soluble, (b) able to create a foam, (c) able to enantioselectively bind the analyte, and (d) able to maintain some surface activity when associating with at least one of the two enantiomers. Enantioselectivity could result either from a difference in the association energy between the chiral collector and the two enantiomers, from a difference in the surface adsorption of the two diastereomeric (collector plus enantiomer) complexes, or from some combination of these two factors.

Examples of chiral collectors that meet the aforementioned physicochemical criteria include some derivatized cyclodextrins, alkylated amino acids, digitonin, and some antibiotics. Enantiomeric enrichment conditions and results using these collectors are given in Tables 2 and 3. Table 2 summarizes the data for

Table 1. Analytical Separation Conditions for Enantiomeric Excess Determinations

racemate	structure	column	mobile phase[f] or run buffer
warfarin		Cyclobond I[b]	acetonitrile/methanol/acetic acid/triethylamine (90/10/0.004/0.004)
SQ 30,840		Cyclobond I RSP[c]	aqueous buffer[g]/acetonitrile (80/20)
SQ 31,236		Cyclobond I SP[d]	aqueous buffer[g]/acetonitrile (85/15)
N-t-Boc-chlorophenylalanine		Cyclobond I RSP[c]	aqueous buffer[h]/acetonitrile (95/5)
N-t-Boc-phenylalanine		Cyclobond I RSP[c]	aqueous buffer[h]/acetonitrile (93/7)
leucine[a]		Cyclobond I[b]	acetonitrile/methanol/acetic acid/triethylamine (90/10/0.4/2)
methionine[a]		Cyclobond I[b]	acetonitrile/methanol/acetic acid/triethylamine (96/4/0.6/1)
phenylalanine[a]		Cyclobond I[b]	acetonitrile/methanol/acetic acid/triethylamine (90/10/0.4/1.2)
tryptophan[a]		Cyclobond I[b]	acetonitrile/methanol/acetic acid/triethylamine (96/4/0.6/1.2)
dansyl-tryptophan		fused silica[e]	0.1 M phosphate buffer (pH 6) containing 3 mM vancomycin[24]
dansyl-phenylalanine		fused silica[e]	0.1 M phosphate buffer (pH 6) containing 3 mM vancomycin[24]

[a] Before analysis these amino acids were derivatized with AQC; fluorescent tagging agent. See ref 25 for the complete procedure. [b] Cyclobond I refers to a 25 cm (4.6 cm i.d.) native β-cyclodextrin HPLC column. [c] Cyclobond I RSP refers to a 25 cm (4.6 cm i.d.) *rac*-hydroxypropyl-β-cyclodextrin HPLC column. [d] Cyclobond I SP refers to a 25 cm (4.6 cm i.d.) (*S*)-hydroxypropyl-β-cyclodextrin HPLC column. [e] This column is a 50 μm (i.d.) $\times$ 32 cm (24 cm to detector) fused silica capillary used in capillary electrophoresis. [f] Mobile phase compositions are given as volume ratios. [g] The buffer consisted of 1% triethylammonium acetate (aq), pH 4.1. [h] The buffer consisted of 1% triethylammonium acetate (aq), pH 7.1.

different derivatized cyclodextrin collectors while Table 3 does the same for all other chiral collectors. Note that the alkylproline collectors (Table 3) were used in a "ligand exchange" format.[15-17] Hence, copper(II) salts were dissolved in solution before foaming (see Experimental Section).

A number of things are evident from the data (Tables 2 and 3). First and foremost, it is clearly demonstrated that enantiomeric enrichments are possible using adsorptive bubble processes. While enantiomeric enrichments after a single pass through the column at room temperature (ee's = 4–30) are not extraordinary, they are easily enhanced by modifying certain experimental conditions. As can be seen in Table 2 for *N-t*-BOC-chlorophenylalanine and *N-t*-BOC-phenylalanine, lowering the temperature of the foam flotation column and sample reservoir to 4 °C results in a significant increase in the enantiomeric excess. Increasing the length of the foam column from 25 to 40 cm also appeared to enhance the effectiveness of the separation (Table 2 and Figure 2). The results for warfarin were particularly interesting. This was because enrichments were produced with two different cyclodextrin derivatives but they gave opposite enantiomeric selectivity (Figure 3 and Table 2). This was the only case where an enantioselective reversal was observed. Enantiomeric enrichments also can be enhanced by repeating the foam fractionation process with a series of identical devices (see Experimental Section for details). Results for two different compounds (when hydroxypropyl-β-cyclodextrin was used as the chiral collector) are shown in Tables 4 and 5. It appears that there are some similarities between the operation of a foam fractionation

Table 2. Foam Flotation Conditions and Enantiomeric Enrichments Using Derivatized Cyclodextrin Collectors

racemates	collectors[a]	collector conc (g/100 mL)	temp (°C)	foaming column ht (cm)	no. of passes through column	enantiomeric ratio[b]	ee[c] (%)
warfarin	PM-β-CD	1	23	25	1	60/40	20
	DM-β-CD	1	23	25	1	44/56	12
SQ 30,840	Oct-β-CD	1	23	25	1	56/44	12
	HP-β-CD	1	23	25	1	66/34	32
SQ 31,236	HP-β-CD	1	23	25	1	46/54	8
N-*t*-BOC-chlorophenylalanine	PM-β-CD	0.05	23	25	1	47/53	6
	PM-β-CD	0.05	4	25	1	37/63	26
N-*t*-BOC-phenylalanine	PM-β-CD	0.05	23	25	1	41/59	18
	PM-β-CD	0.05	4	25	1	18/82	64
	PM-β-CD	0.05	4	40	1	12/88	76
	DM-β-CD	0.05	4	25	1	48/52	4

[a] Abbreviations: PM-β-CD = heptakis-2,3,6-tri-*O*-methyl-β-cyclodextrin; DM-β-CD = heptakis-2,6-di-*O*-methyl-β-cyclodextrin; Oct-β-CD = a mixture of β-cyclodextrin monooctyl and dioctyl esters; HP-β-CD = hydroxypropyl-β-cyclodextrin. [b] This is the peak area ratio of first peak/second peak. [c] Enantiomeric excess (ee) is defined as follows: $ee = [(E_1 - E_2)/(E_1 + E_2)] \times 100\%$, where E_1 is the amount of the enantiomer present in higher concentration and E_2 is the amount of the enantiomer present in lower concentration.

Table 3. Foam Flotation Conditions and Enantiomeric Enrichments Using Chiral Collectors Not Related to Cyclodextrin

racemates	collectors[a]	collector conc (g/100 mL)	temp (°C)	foaming column ht (cm)	no. of passes through column	enantiomeric ratio[b]	ee[c] (%)
leucine	Hep-HProl	0.4	23	25	1	35/65	30
	Dodec-HProl	satd soln	23	25	1	46/54	8
methionine	Hep-Hprol	0.2	23	25	1	42/58	16
phenylalanine	Hep-HProl	0.2	23	25	1	41/59	18
tryptophan	digitonin	satd soln	23	25	1	47/53	6
dansyl-tryptophan	vancomycin	0.06	4	25	1	41/59	18
dansyl-phenylalanine	vancomycin	0.06	4	25	1	47/53	6

[a] Abbreviations: Hep-HProl = *n*-heptyl-L-hydroxyproline; Dodec-Hprol = *n*-dodecyl-L-hydroxyproline. [b] This is the peak area ratio of first peak/second peak. [c] Enantiomeric excess (ee) is defined as follows: $ee = [(E_1 - E_2)/(E_1 + E_2)] \times 100\%$, where E_1 is the amount of the enantiomer present in higher concentration and E_2 is the amount of the enantiomer present in lower concentration.

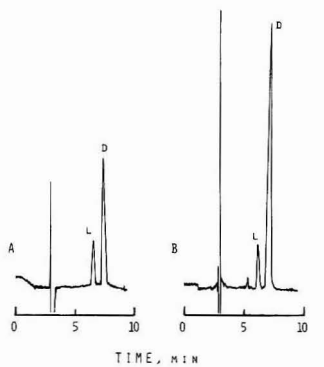


Figure 2. LC chromatograms showing the enantiomeric enrichment of D-*N*-*t*-BOC-phenylalanine (i.e., the second peak in both chromatograms) using (A) a 25 or (B) a 40 cm long foam column. The experiment was carried out at 4 °C using permethyl-β-cyclodextrin as the chiral collector, under total reflux conditions (see Experimental Section). The analytical LC chiral separations were done on a Cyclobond I-RSP column (see Table 1 for exact conditions).

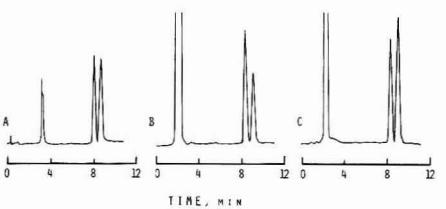


Figure 3. LC chromatograms: (A) separation of racemic warfarin starting material, (B) foam-enriched product using permethyl-β-cyclodextrin as a chiral collector, and (C) foam-enriched product using heptakis(2,6-di-*O*-methyl)-β-cyclodextrin as a chiral collector. Experiments B and C were done at room temperature using a 25 cm long packed foam column (see Experimental Section). The analytical separations were done on a Cyclobond I HPLC column (see Table 1 for exact conditions).

column and a fractional distillation column. For example, longer columns (Table 2) and additional fractionation cycles (Tables 4 and 5) give a more highly enriched product. The best results are obtained in both systems when the columns are operated under "reflux" conditions (where there is a countercurrent flow in the column). As shown in Figure 4, allowing the foam system to equilibrate or reflux for a period of time (before sample removal) enhances the enrichment process. However, after this particular system has equilibrated for a period of time (~25–90 min), there is no benefit (i.e., no further enrichments) in extending the process.

Figure 4 also shows that the concentration of the chiral collector affects the enantiomeric enrichment. There appears to be an optimum concentration of collector and racemate for every system. The enantiomeric excess decreases if the system is operated with too much or too little collector. The optimum concentrations of collector and racemate must be determined empirically. As yet we have found no recognizible trend or theory

Table 4. Effect of Repeated Passes through a Foam Flotation Column on the Enantiomeric Enrichment of SQ 30,840[a]

	cycle number							
peak area	1	2	3	4	5	6	7	8
first peak	2.31	2.44	1.39	1.22	1.18	1.23	0.82	0.68
second peak	2.08	1.55	0.76	0.56	0.55	0.44	0.24	0.16
peak ratio	1.11	1.61	1.83	2.18	2.15	2.80	3.42	4.25

[a] Hydroxypropyl-β-cyclodextrin was used as the chiral collector (See Experimental Section and Table II for further experimental details.

Table 5. Effect of Repeated Passes through a Foam Flotation Column on the Enantiomeric Enrichment of SQ 31,236[a]

	cycle number					
peak area	1	2	3	4	5	6
first peak	3.61	2.66	1.97	1.48	1.22	0.64
second peak	4.26	3.42	2.66	2.16	2.55	1.43
peak ratio	1.18	1.28	1.35	1.46	2.09	2.23

[a] Hydroxypropyl-β-cyclodextrin was used as the chiral collector (See Experimental Section and Table II for further experimental details.

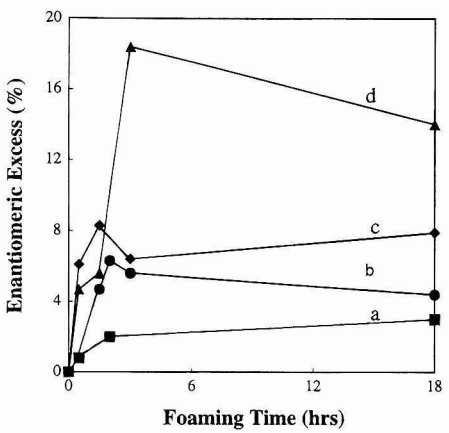


Figure 4. Effect of reflux equilibration time and concentration of the chiral collector on the enantiomeric enrichment of D-*N*-*t*-BOC-phenylalanine. Each curve represents a different concentration of the permethyl-β-cyclodextrin chiral collector: (a) 1%, (b) 0.1%, (c) 0.01%, and (d) 0.05%. Experiments were done at room temperature using a 25 cm long packed foam column. The chiral collector was permethyl-β-cyclodextrin. See the Experimental Section and Tables 1 and 2 for further details.

that allows a prediction of the best absolute and/or relative concentrations. Another factor that affects the enantiomeric excess is the pH of the sample solution. Figure 5 indicates that L-*N*-*t*-BOC-phenylalanine is more highly enriched at pH's near 3 than at more basic pH's. This is not surprising in view of past enantioseparation results in reversed phase HPLC.[26,27] The pH

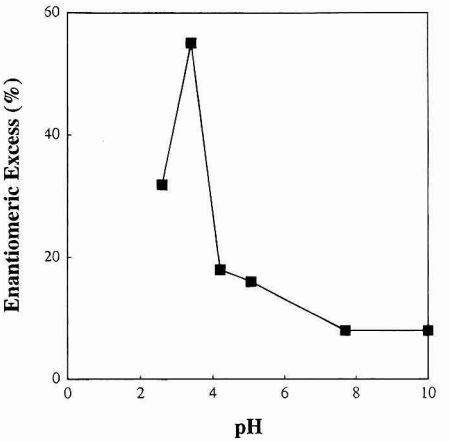


Figure 5. pH dependance for the enantiomeric enrichment of *N*-*t*-BOC-phenylalanine. See Experimental Section for all conditions. The buffer was 0.01% triethylammonium acetate.

controls the ionization state of the analyte and in some cases of the chiral selector. Consequently, enantioselective interactions are strongly pH dependent. It is not unusual in HPLC and capillary electrophoresis for an enantiomeric separation to occur at one pH and not at another.[23,24,27,28] Clearly, optimization of the pH can be as important in foam flotation as in most other water-based enantioseparation techniques.

CONCLUSIONS

A variety of different chiral collectors were used in this work. This indicates that the foam flotation of enantiomers is not narrowly applicable. When associating with an analyte, the chiral collector can make use of a variety of interactions including the following: inclusion complex formation and hydrogen bonding (as in the case of the derivatized cyclodextrins in Table 2); ligand exchange interactions (Table 3); steric interactions (which are important for all of the chiral collectors tested); and combinations thereof. The relatively low cost, the ease with which the separations are performed, and the ability to enrich large samples on a continuous basis are all important factors for large-scale enantiomeric separations. It should be noted that a complete economic analysis of this technique (which was not the focus of this work) must take in to account the ease with which the chiral collector can be separated from the product and recycled. Also, it is possible to design chiral collectors for specific separations. This would not only enhance the enantioselectivity but would also allow optimization of the surface-active properties. It is hoped that the data presented here will stimulate an increase in interest in this area of separations.

ACKNOWLEDGMENT

Support of this work by the Department of Energy, Offices of Basic Science (DE FG02 88ER13819), and the Biotechnology Research and Development Corp. are gratefully acknowledged.

Received for review July 25, 1994. Accepted September 17, 1994.

[⊗] Abstract published in *Advance ACS Abstracts,* October 15, 1994.

(26) Pawlowska, M.; Chen, S.; Armstrong, D. W. *J. Chromatogr.* **1993**, *641*, 2257.
(27) Armstrong, D. W.; Li, W. *Chromatogr. Forum* **1987**, *2*, 43.
(28) Han, S. M.; Armstrong, D. W. *J. Chromatogr.* **1987**, *389*, 256.

Anal. Chem. **1994,** *66,* 4283–4287

Determination of the Active Hydrogen Content in Pyridine–Borane Complex by Schiff Base Reduction and High-Performance Liquid Chromatography

James A. Morley,* Lee Elrod, Jr., and John F. Bauer

PPD Physical Analytical Chemistry Department, Abbott Laboratories, 1401 Sheridan Road, North Chicago, Illinois 60064

Borohydrides and borane complexes have been widely used as selective reducing agents in many chemical applications. In particular, the pyridine–borane complex (PBC, C_5H_5N–BH_3) is very stable to hydrolysis and is an attractive reagent for large-scale reductions that are common in the pharmaceutical industry. This report describes a simple, rapid, and reproducible method for quantitating the active hydrogen content in PBC. The method exploits the ease with which Schiff bases are reduced by amine–boranes and uses high-performance liquid chromatography to quantitate the reduction product. The method is not affected by small amounts of extraneous moisture and can be carried out in common glassware. The potential application of the analytical procedure to other amine–borane complexes is also discussed.

The leukotrienes have been associated with the mediation of allergic and inflammatory responses in humans.[1] The 5-lipoxygenase enzyme is a crucial component in the biosynthesis of leukotrienes via the metabolism of arachidonic acid.[2] Therefore, the inhibition of 5-lipoxygenase is considered a potential approach for the treatment of inflammation and allergy. Zileuton (*N*-(1-benzo[*b*]thien-2-ylethyl)-*N*-hydroxyurea or ABT-077) is a potent inhibitor of 5-lipoxygenase[3] and is currently in clinical trials for treatment of allergic asthma and inflammation. An intermediate step in the current synthesis of zileuton employs the pyridine–borane complex (PBC) on a production scale to reduce an oxime to a hydroxylamine. This necessitates the storage of PBC in large quantities for extended periods. The reduction is carried out with an excess of the complex and results in good yields. Our interests were twofold: to develop a rapid and reliable method for the measurement of active hydrogen to support the synthesis and to develop a stability indicating procedure to assure the quality of warehoused PBC. We report here a simple, rapid, and reproducible method for the quantitation of active hydrogen in PBC via the reduction of *N*-benzylideneaniline and high-performance liquid chromatographic quantitation (HPLC) of the product, *N*-phenylbenzylamine. The procedure does not require specialized equipment.

Diborane and borane complexes have been used extensively as selective reducing agents in organic synthesis.[4] The amine–borane complexes have a broad range of physical properties, solubilities, and reactivities that depend on the nature of the amine.[5,6] For example, the N-arylamine–borane complexes are hydrolyzed by water and alcohols, whereas the complexes of several *N*-alkylamines are water soluble and exhibit moderate to remarkable stabilities to acid hydrolysis.[5] Weakly basic or hindered amines give complexes wherein boron is more electrophilic, whereas stronger bases form stronger complexes that are more stable to hydrolytic conditions and behave more like borohydrides.[6] For example, at 25 °C, the morpholine–borane complex is slowly hydrolyzed (120 min) in 50% 1 N HCl/50% ethylene glycol, while the *N*-phenylmorpholine–borane complex rapidly hydrolyzes (2 min).[5] Many amine–borane complexes including PBC are commercially available and, unlike diborane or tetrahydrofuran–borane complex, can be easily handled in the laboratory. Alternately, PBC can be prepared in high yield by the treatment of pyridine hydrochloride with sodium borohydride.[7] The active hydrogen, reducing power, boron content, and pyridine content of material prepared in this manner is consistent with the proposed complex.

Typical reductions with boranes use an excess of reagent and generally do not require a precise knowledge of the active hydrogen content. The vendors' label claims are sufficient in these instances. Nonetheless, there are several accounts in the literature of methods to determine the analytical concentration of hydride in borohydride and amine–borane compounds. The classical method is the hydrogen evolution or gasometric measurement which quantitates the active hydrogen as evolved hydrogen after hydrolysis of the boron compound.[8] This approach has also been used to quantitate amines by complexation with excess diborane and subsequent determination of the remaining diborane.[9] Other methods include volumetric determination of active hydrogen by the oxidation of the borohydride or amine–borane complex with iodine,[10] hypochlorite,[11] silver nitrate,[12] and

(1) Samuelson, S. *Science* **1983**, *220*, 565.
(2) Borgeat, P. *J. Med. Chem.* **1981**, *24*, 121. Cashman, J. R.; Oliva, S. L. *Drugs Today* **1988**, *24*, 723.
(3) Bell, R. L.; Young, P. R.; Albert, D.; Lanni, C.; Summers, J. B.; Brooks, D. W.; Rubin, P.; Carter, G. W. *Int. J. Immunopharmacol.* **1992**, *14*(3), 505.
(4) Brown, H. C. *Boranes in Organic Chemistry*; Cornell University Press: Ithaca, NY, 1972.
(5) Lane, C. F. *Aldrichim. Acta* **1973**, *6*(3), 51.
(6) Pelter, A.; Rosser, R. M. *J. Chem. Soc., Perkin Trans. 1* **1984**, 717.
(7) Taylor, M. D.; Grant, L. R.; Sands, C. A. *J. Am. Chem. Soc.* **1955**, *77*, 1506.
(8) Chaikin, S. W.; Brown, W. G. *J. Am. Chem. Soc.* **1949**, *71*, 122. Schlesinger, H. I. *Ibid.* **1953**, *75*, 215.
(9) Lyle, R. E.; Southwick, E. W. *Anal. Chem.* **1968**, *40*, 2201.
(10) Mathews, M. B. *J. Biol. Chem.* **1948**, *176*, 229.

0003-2700/94/0366-4283$04.50/0 © 1994 American Chemical Society

iodate.[13] A voltammetric procedure has also been recently described for sodium borohydride.[14] The hydrogen evolution method, though accurate, is not a practical procedure for the routine determination of the active hydrogen content in PBC in a quality control environment. This procedure is time consuming and requires specialized equipment. Of the remaining methods, the oxidation with iodate (iodometric titration) has generally been considered the most accurate alternative to the gasometric determination. However, this titration cannot be readily automated; the samples must be titrated immediately, or low results are obtained due to the atmospheric oxidation of iodide to iodine. The iodometric titration also cannot distinguish between hydride and other species capable of iodate reduction. Therefore, titrating a sample of PBC does not indicate directly the reagent's potency for carrying out a synthetic organic reduction. In a laboratory-scale synthesis, this may not be a critical parameter, but in those cases where strict stoichiometric addition of active hydrogen is mandatory, the potency of the reagent must be known with accuracy. This is espically critical when many resources are expended to produce a compound in large batches for pharmaceutical or industrial use. Preliminary efforts aimed at directly chromatographing PBC either destroyed the phase (gas chromarography on a poly(ethylene glycol) phase) or gave results significantly lower than iodometric titration values (HPLC on a polystyrene resin). Both approaches are severely limited by the lack of a readily available reference standard and the potentially high reactivity of the compound.

EXPERIMENTAL SECTION

Chromatographic Conditions and Instrumentation. The HPLC system used in this work consisted of a ternary pump, Model SP-8800 (Thermo Separation Products, Santa Clara, CA); an autosampler, Model SIL-6B (Shimadzu Corp., Kyoto, Japan); and a UV detector, Spectra Physics Model SP-100 (Thermo Separation Products). Chromatograms were processed using a Model C-R4A Chromatopac (Shimadzu Corp.).

A Nucleosil C_{18} chromatographic column (5 μm, 4 mm × 12.5 cm, 100-Å pore size; Machery-Nagel, Duren, Germany) was used in this method. The HPLC buffer consisted of a 0.05 M phosphate buffer (13.6 g of monobasic potassium phosphate in 2 L of distilled water) adjusted to pH 2.7 (±0.1) with phosphoric acid. Isocratic elution was carried out with a mobile phase of 60% buffer/40% acetonitrile. The flow rate was 1.0 mL/min with UV detection at 254 nm (0.1 AUFS). All chromatography was performed at ambient temperature.

Materials. ***Caution***! Although PBC is normally a very stable compound, care should be taken in storing or handling any hydride- or hydrogen-producing reagent. PBC is a liquid and can easily be transferred by syringe or glass pipet.

All solvents used in this study were reagent grade or HPLC grade (EM Science, Gibbstown, NJ). Commercial PBC was used in all experiments. The *N*-benzylideneaniline, *N*-phenylbenzylamine (free base), acetic anhydride, and other amine–borane complexes were used as received (Aldrich Chemical Co., Milwaukee, WI).

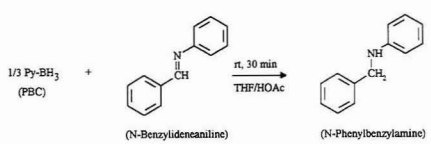
The *N*-phenylbenzylamine hydrochloride used as a reference standard was prepared by bubbling gaseous hydrochloric acid through a hexane/THF (92/8) solution of the free base. The resulting off-white solid was collected by vacuum filtration and washed with hexane. The hydrochloride salt gave satisfactory ^{1}H NMR, MS, and IR spectra. The purity (>99.5%) of the salt was determined by titration ($AgNO_3$ and $HClO_4$), HPLC, and Karl Fischer moisture. The following data were also obtained: mp (uncorrected) = 203–205 °C; molar absorptivity (246 nm) = 12 174 M^{-1} cm^{-1} (c = 0.01, CH_3CN/H_2O(1:1)). Elemental analysis (theory): C, 71.06 (71.07); H, 6.14 (6.42); N, 6.36 (6.38); Cl, 16.0 (16.1). The hydrochloride salt turns slightly green on exposure to light and air. This does not significantly affect the potency of the material.

Procedure for the Determination of Active Hydrogen Content. Stock solutions of PBC and *N*-benzylideneaniline in tetrahydrofuran were prepared by dissolving 250 mg of PBC and 2 g of *N*-benzylideneaniline in separate 50-mL volumetric flasks. Five milliliter aliquots of each stock solution were combined in a 100-mL volumetric flask, and 10 mL of glacial acetic acid was added. The resulting solution was mechanically shaken for 30 min followed by dilution to volume with diluent (HPLC buffer/acetonitrile, 1:1). After being further diluted 4.0 mL to 100.0 mL with diluent, the sample preparation was assayed versus a standard preparation of approximately 60 μg/mL *N*-phenylbenzylamine (free base concentration). The identity of the product of *N*-benzylideneaniline reduction was confirmed by isolating the material from a sample preparation run at twice the above scale. The crude *N*-phenylbenzylamine was converted to the hydrochloride salt with HCl gas and recrystallized from ethanol/hexane to give material with spectral properties (^{1}H NMR, IR) consistent with *N*-phenylbenzylamine hydrochloride. The isolated material coeluted with the standard preparation when spiked into the assay standard, further confirming the identity of the reduction product.

The iodometric titrations used for comparison were carried out according to an established procedure[13] with the slight modification that PBC was dissolved in methanol prior to the determination.

RESULTS AND DISCUSSION

Active hydrogen in PBC is determined using the following reaction:



This reaction is a modification of a literature procedure where the reduction of Schiff bases to secondary amines was observed with the dimethylamine–borane complex.[15] The room temperature reduction of the Schiff base *N*-benzylideneaniline by PBC in a mixed solvent of tetrahydrofuran (THF)/glacial acetic acid (1:1) proceeds smoothly to give *N*-phenylbenzylamine in quantitative yields. The imine is used in a large excess to insure the complete

(11) Chaikin, S. W. *Anal. Chem.* **1953**, *25*, 831. Pecsok, R. L. *J. Am. Chem. Soc.* **1953**, *75*, 2862.
(12) Brown, H. C.; Boyd, A. C., Jr. *Anal. Chem.* **1955**, *27*, 150.
(13) Lyttle, D. A.; Jensen, E. H.; Struck, W. A. *Anal. Chem.* **1952**, *24*, 1843.
(14) Mirkin, M. V.; Bard, A. J. *Anal. Chem.* **1991**, *63*, 532.
(15) Billman, J. H.; McDowell, J. W. *J. Org. Chem.* **1961**, *26*, 1437.

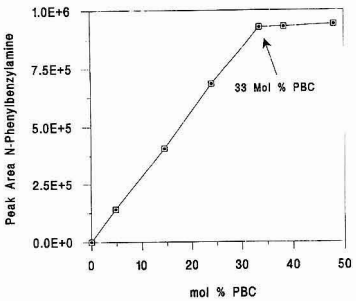


Figure 1. Peak area response of *N*-phenylbenzylamine versus mol % of added PBC.

consumption of PBC. The reduction does not occur in the absence of PBC, and no significant hydrolysis of the imine to benzaldehyde was observed (no benzyl alcohol produced). The presence of insoluble boric acid, a PBC hydrolysis product, did not significantly affect the assay. It was not necessary to heat the reaction, as was previously noted in the reduction of several Schiff bases by dimethyl- and trimethylamine–borane complexes.[15,16] The lower temperature used here also avoided any formation of side products such as acylated material that was observed in the reductions with trimethylamine–borane complex.[16] Furthermore, stressing the reaction mixture by heating on a steam bath gave only a 6% lower yield of *N*-phenylbenzylamine with no significant amount of acylated material present.[17] The stability of PBC to hydrolysis in acetic acid has previously been investigated.[6] These investigators found that the complex does not appreciably decompose after 1 h in acetic acid. The THF in the solvent mixture was originally present to insure complete solubility of the reactants. However, the role of this solvent may be much more than solubility related. The partial conversion of the PBC to a more reactive THF–borane moiety may be possible in an acidic media.

The stoichiometry of the reaction was examined by carrying out the reduction at varying mole ratios (PBC/imine) and plotting the resulting *N*-phenylbenzylamine peak area versus the mole ratio of PBC. As shown in Figure 1, the peak area for the product amine plateaus after the addition of 33 mol % of PBC. This finding is consistent with the 1:3 mole ratio of borane:imine found previously for Schiff base reduction by dimethylamine–borane complex[15] ((acyloxy)borohydride species have been implicated as likely intermediates in the reduction of imines, iminium salts, and enamines with sodium borohydride or amine–borane complexes in carboxylic acid solvents[18] and have also been suggested in the reductive alkylations of indoles,[19] quinolines,[20] and secondary amines[21] by sodium borohydride in carboxylic acid solvents). However, the data presented here suggest that no intermediate (acyloxy)borohydride species is formed with the acetic acid prior to reduction. This would have resulted in a lower than expected

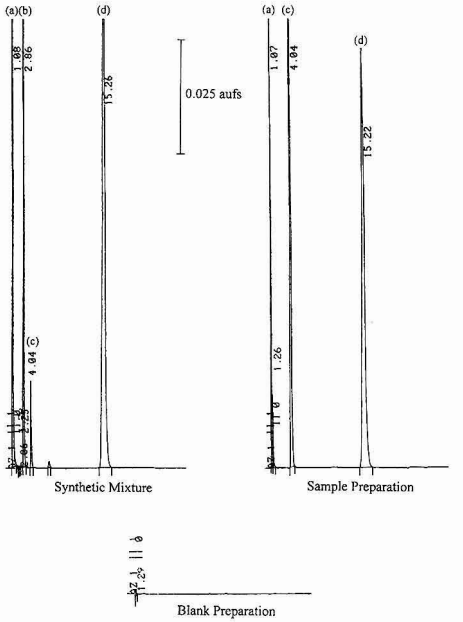


Figure 2. Representative chromatograms of a synthetic mixture, sample preparation, and a blank preparation (20-μL injections; the sample preparation is described in the text; blank, HPLC buffer/acetonitrile, 1:1). Peak identities: (a) pyridine; (b) PBC; (c) *N*-benzylideneaniline; (d) *N*-phenylbenzylamine.

borane:imine ratio. No further investigation into the mechanism of the reduction was done.

The *N*-phenylbenzylamine produced by the reduction of *N*-benzylideneaniline is quantitated versus an authentic standard of *N*-phenylbenzylamine hydrochloride. Although the free base is commercially available, the hydrochloride salt of N-phenylbenzylamine provides a more stable and easily purified reference standard. The active hydrogen content (mmol of hydrogen/g of sample) in the sample is determined from the stoichiometry of the reaction (theory = 32.3 mmol of hydrogen/g of PBC). Shown in Figure 2 are representative chromatograms of a synthetic mixture, a typical assay solution, and a blank preparation.

The effect of variations in the HPLC eluent on the chromatographic behavior of *N*-phenylbenzylamine was studied. The *N*-phenylbenzylamine standard preparation was chromatographed using eluents which contained 30–50% acetonitrile and using eluents containing buffers at pH 2.1–3.1. Our system suitability requirements (i.e., capacity factors of 10–20 and tailing factors $\leq$1.4) were satisfied when the pH was $\geq$2.6 and the acetonitrile concentration was $\leq$40%. The experiments indicated that small variations in the eluent composition would have negligible consequences on the chromatographic finish of the method.

(16) Billman, J. H.; McDowell, J. W. *J. Org. Chem.* **1962**, *27*, 2640.
(17) Crude N-acylated phenylbenzylamine was prepared according to a general procedure: Morley, J. A.; Elrod, L. E., Jr. *Chromatographia* **1993**, *37*(5/6), 295.
(18) Hutchins, R. O.; Su, W.-Y.; Sivakumar, R.; Cistone, F.; Stercho, Y. P. *J. Org. Chem.* **1983**, *48*, 3412.
(19) Gribble, G. W.; Lord, P. D.; Skotnicki, J.; Dietz, S. E.; Eaton, J. T.; Johnson, J. L. *J. Am. Chem. Soc.* **1974**, *96*, 7812.
(20) Gribble, G. W.; Heald, P. W. *Synthesis* **1975**, 650.
(21) Gribble, G. W.; Jasinski, J. M.; Pellicone, J. T.; Panetta, J. A. *Synthesis* **1978**, 766.

Table 1. Precision Data for the Determination of Active Hydrogen in PBC

	active hydrogen (mmol/g of sample)		
analyst	A	B	C
1	30.4	29.7	19.1
1	30.1	29.9	19.2
1	30.2	29.7	18.8
2	30.3	30.2	19.7
2	30.8	30.2	19.6
2	31.6	30.2	19.2
mean[a]	30.6 (30.5)	30.0 (29.8)	19.3 (22.2)
SD	0.56	0.25	0.33
RSD	±1.8	±0.83	±1.7

[a] The value in parentheses is by iodometric titration (average of two determinations by a single analyst).

Table 2. Solution Stability Data (in μg/mL) for Standard and Sample Preparations[a]

time (h)	standard[b]	time (h)	sample[c]
0		0	59.1
9	60.7	10	59.1
11	61.1	12	58.3
13	60.1	14	58.4
15	62.5	16	62.5
17	62.0	18	58.8
19	61.6	20	59.6
mean	61.3		59.4
SD	0.878		1.44
RSD	±1.43		±2.42

[a] Standard and sample preparations quantitated versus an initial standard preparation. [b] 60.7 μg/mL theory. [c] 59.1 μg/mL theory.

The detector response for the reduction product, *N*-phenylbenzylamine, is linear from 30.2 to 90.5 μg/mL (free base concentration corresponding to 50–150% of the standard preparation). The equation of the line (four data points) was found to be $y = (11\,140 \pm 186)x + 451\ (\pm 11\,915)$ with a correlation coefficient (r) of 0.9996. Similar results were obtained for peak height response. The reduction reaction was found to be linear from 5.1 to 35.6 mg of PBC (corresponding to 20–142% of the described sample preparation). The plot of *N*-phenylbenzylamine versus PBC added (five data points) gave a correlation coefficient of 0.9997 with the equation $y = (25\,926 \pm 426)x + 11\,863\ (\pm 9948)$.

The precision of the analytical method was determined by two analysts on different instruments using three lots of PBC. The results are shown in Table 1. Lots A and B were typical incoming bulk material, whereas lot C was material that had decomposed to an orange-red, viscous liquid on storage. Also included in the table are data generated by the iodometric titration.[13] The data indicate that there is good agreement between the two methods for typical lots of PBC (lots A and B). These lots were clear and colorless samples that contained no precipitate indicative of hydrolysis. However, examination of an atypical lot, lot C, gave significantly higher values with the iodometric titration. The THF stock solution of lot C contained copious amounts of precipitate (presumably boric acid). We subsequently determined that boric acid did not interfere in the reduction of *N*-benzylideneaniline. In contrast, lot C was completely soluble under the iodometric titration conditions (essentially alkaline methanol), and boric acid did not interfere in this assay, either. The results suggest that some other reducing agent has formed on decomposition that does not contain active hydrogen but is capable of reducing iodate to iodide. This would account for higher values with the titration procedure. The source of the assay bias for lot C was not investigated any further.

Several of the parameters of the reduction reaction were investigated. The effect of extraneous water present in the reaction mixture was examined by performing the reaction in the presence of small amounts of added water. Samples were prepared as described in the Experimental Section with 0, 0.05, 0.1, and 1 mL of water added to the 5-mL aliquots of *N*-benzylideneaniline used for the sample reduction. After the usual workup, the amount of *N*-phenylbenzylamine was quantitated versus a standard preparation. At these addition levels, residual water had no effect on the amount of reduction product formed. The results indicate that the rigorous drying of solvent and glassware sometimes necessary in reductive chemistry is not necessary for this method. The effect of reaction time was demonstrated by shaking the reaction mixtures up to 60 min at room temperature. Integrated peak areas of *N*-phenylbenzylamine did not increase after 10 min. The chromatograms also showed complete consumption of PBC at this time (10 min), indicating complete reduction.

The amount of acetic acid used in the sample preparation was varied from 1 to 15 mL (10–150% of the assay levels), and the reaction mixtures were worked-up as described in the Experimental Section. Examination of the integrated peak areas of *N*-phenylbenzylamine revealed no difference for the 5-, 10-, and 15-mL acetic acid reactions (corresponding to 50, 100, and 150% of the assay preparation). However, the reaction containing 1 mL of acetic acid (10% assay preparation) gave a significantly lower (~30%) peak area for *N*-phenylbenzylamine. Since no significant byproducts or impurities were observed using the stated conditions, no further optimization of the acetic acid content was pursued. Similarly, the amount of *N*-benzylideneaniline was found to have essentially no effect on the amount of *N*-phenylbenzylamine formed when compared at 50, 100, and 150% of the assay levels.

Solution stability data were obtained to determine the feasibility of using an automated HPLC finish in the method. A sample preparation and a standard preparation were made using the described procedure for solutions containing 59.1 and 60.7 μg/mL of *N*-phenylbenzylamine, respectively. Repetitive injections of these preparations demonstrated solution stability for both solutions to at least 19–20 h at room temperature. The data are summarized in Table 2 and demonstrate that automated HPLC runs are acceptable.

Attempts were made to apply this methodology, along with some variations, to other amine–borane complexes. The complexes were chosen such that a wide range of hydrolytic stability was surveyed (Table 3). The experiments in Table 3 were not optimized and represent an initial trial of developing a general procedure for active hydrogen determination in amine–borane complexes. It was found that the complexes of 2,6-lutidine, morpholine, and *tert*-butylamine were less soluble in THF than previously reported[5] and therefore gave low yields of *N*-phenylbenzylamine under the conditions described in the Experimental Section. Although soluble in THF, the trimethylamine complex required an extended reaction (shake) time to go to completion. This result is consistent with reports that this complex is highly

Table 3. Determination of Active Hydrogen in Amine–Borane Complexes[a]

amine	theory	method A[b]	method B[c]	method C[d]
trimethylamine	41.1	39.3[e]	20.2	37.9
2,6-lutidine	24.8	14.1	15.1	15.6
morpholine	29.7	24.0	15.9	27.6
tert-butylamine	34.5	26.3	16.4	27.3
N-phenylmorpholine	16.9	*f*	*f*	*f*

[a] The values are presented as mmol of active hydrogen/g of sample. [b] The determination as described in the Experimental Section, except where noted. [c] The amine–borane complexes were dissolved in pyridine. The remainder of the determination was as described in the Experimental Section. [d] The amine–borane complexes were dissolved in glacial acetic acid. The determinations were performed as in the Experimental Section, except that 10 mL of THF/acetic acid (1:1) was used in place of 10 mL of neat acetic acid and the reaction was heated for 1 h on a steam bath. [e] The reaction (shake) time was extended to 3 h. [f] No *N*-phenylbenzylamine was detected.

stable to hydrolysis[5] and should therefore be less reactive under the described conditions. The complexes were found to be soluble in pyridine (method B, Table 3) and glacial acetic acid (method C, Table 3) at active hydrogen concentrations similar to that described for PBC in the Experimental Section. The results for the trimethylamine and morpholine complexes (method C, Table 3) are promising and suggest that a general procedure may require only the fine-tuning of the reaction conditions. The *N*-phenylmorpholine complex gave no indication of imine reduction and was apparently rapidly hydrolyzed. A slight bubbling indicative of hydrogen evolution was observed when this complex was added to acetic acid. This finding is consistent with the known hydrolytic instability of *N*-arylamine–borane complexes.

CONCLUSIONS

A simple, rapid, and quantitative method for the determination of the active hydrogen content of PBC has been described. The gasometric procedure, under the proper conditions and attention by the analyst, is the most direct way of quantitating active hydrogen but is not a practical method for rapid analysis. The method described herein is also a direct means for determining the organic reducing power of PBC because the reduction of the Schiff base, *N*-benzylideneaniline, will not take place in the absence of a source of active hydrogen. Volumetric methods, such as the iodometric titration, quantitate the overall reducing power of a compound and do not differentiate between reducing species. The method described here uses an automated HPLC finish which allows for a high throughput of samples with little analyst time. Neither the gasometric nor the volumetric procedure can be readily automated.

Preliminary experiments for applying this procedure to other amine–borane complexes gave promising results with the trimethylamine complex. Development of a general assay for the amine–borane complexes was outside of the scope of this method; however, this work has laid the foundation on which a more universal assay may be built for determining the active hydrogen in borohydrides and borane complexes.

ACKNOWLEDGMENT

The authors thank Diane Horgen for her assistance in the preparation of the manuscript.

Received for review May 20, 1994. Accepted August 24, 1994.[®]

[®] Abstract published in *Advance ACS Abstracts,* October 1, 1994.

Anal. Chem. **1994,** *66,* 4288–4294

Prediction of Temperature-Programmed Retention Indexes for Polynuclear Aromatic Hydrocarbons in Gas Chromatography

Agneta Bemgård,* Anders Colmsjö, and Kent Wrangskog

Department of Analytical Chemistry, National Institute of Occupational Health, S-171 84 Solna, Sweden

The objective of this study was to relate temperature-programmed GC retention indexes of nonsubstituted PAHs with calculated molecular properties. Prediction of retention was made by use of a partial least squares regression equation using five descriptors, i.e., first-order valence molecular connectivity, ionization potential, length, height, and quadrupole moment. Retention index predictability was studied with respect to individual molecular weight ranges. Pericondensed PAHs were more accurately predicted (RMS = 1.6 index units (iu) or coefficient of variation of 0.31%) than catacondensed PAHs (RMS = 5.8 iu or coefficient of variation of 1.1%) with the descriptor set employed.

Polycyclic aromatic hydrocarbons (PAHs) comprise a large group of environmentally interesting and hazardous compounds. The complexity and the comparatively low amounts of these compounds in the environment make it necessary to develop suitable cleanup and separation methods for analysis. However, identification of many of these substances is difficult due to a lack of pure reference compounds. An attempt to solve this problem would be to find the relationship between gas chromatographic retention and molecular properties.

Retention in gas chromatography is a result of interactions between the solutes and the stationary phase and is determined primarily by dispersion, induction, and orientation forces.[1,2] For nonpolar stationary phases, the dispersion, or London forces, is considered to be of upmost importance; i.e., the chromatographic retention is related to the solute vapor pressure or the solute boiling point, which has been demonstrated by, for example, Borwitzky and Schomburg,[3] Bartle et al.,[4] and White.[5] Unfortunately, boiling point data of PAHs are very limited,[4] especially for the higher molecular weight PAHs. However, boiling points have been found to correlate with molecular structure (topology), and in 1947 Wiener[6] had already determined boiling points of paraffins by use of two topological indexes. After this report, many authors followed and introduced new topological indexes for a wide range of compounds.[7–12] As has been pointed out in several studies, a major disadvantage of the topological indexes is their degeneracy; i.e., isomers tend, in many cases, to obtain identical numerical values. The above-mentioned structural indexes are all possible to calculate only by knowledge of the chemical structure of the molecule. The availability of computer programs makes it possible to energy-minimize molecules in three dimensions, which provides the values for bond lengths, bond angles, planarity, energy, and charge on each atom in the molecule. Thereafter, geometrical and electrical descriptors can be derived as well. Recently, rather rigorous works have been permitted by use of statistical methods to correlate retention indexes (or boiling points) to a variety of descriptors. By use of linear combinations of quantitative structure–property relationship (QSPR), more or less accurate relations to retention have been derived for different types of compound groups such as alcohols and olefins,[13–15] PCBs, PCDDs, and PCDFs,[16–22] hydrocarbons,[6,23–26] and PAHs and nitro-PAHs.[3–5,20,27–33] The results in these studies show good correlation of topological, geometrical, and electrical descriptors vs retention on chromatographic columns. However, the physicochemical meaning with a special computer choice of descriptors is often hard to evaluate. As mentioned by Ong and Hites,[20] there may be risks with this type of linear combinations, such as random correlation when to many descriptors are used in the correlation data set.

(1) Keulemans, A. I. M.; Kwantes, A.; Zaal, P. *Anal. Chim. Acta* **1955**, *13*, 357.
(2) Vernon, F. *Dev. Chromatogr.* **1978**, *1*, 1.
(3) Borwitzky, H.; Schomburg, G. *J. Chromatogr.* **1979**, *170*, 99.
(4) Bartle, K. D.; Lee, M. L.; Wise, S. A. *Chromatographia* **1981**, *14*, 69.
(5) White, C. M. *J. Chem. Eng. Data* **1986**, *31*, 198.
(6) Wiener, H. *J. Am. Chem. Soc.* **1947**, *69*, 17.
(7) Hosoya, H. *Bull. Chem. Soc. Jpn.* **1971**, *44*, 2332.
(8) Randic, M. *J. Am. Chem. Soc.* **1975**, *97*, 6609.
(9) Kier, L. B.; Murray, W. J.; Randic, M.; Hall, L. H. *J. Pharm. Sci.* **1976**, *65*, 1226.
(10) Balaban, A. T. *Chem. Phys. Lett.* **1982**, *89*, 399.
(11) Randic, M. *J. Chem. Inf. Comput. Sci.* **1984**, *24*, 164.
(12) Kier, L. B. *Quant. Struct.-Act. Relat. Pharmacol. Chem. Biol.* **1985**, *4*, 109.
(13) Hansen, P. J.; Jurs, P. C. *Anal. Chem.* **1987**, *59*, 2322.
(14) Smeeks, F. C.; Jurs, P. C. *Anal. Chim. Acta* **1990**, *233*, 111.
(15) Arruda, A. C.; Heinzen, V. E. F.; Yunes, R. A. *J. Chromatogr.* **1993**, *630*, 251.
(16) Hale, M. D.; Hileman, F. D.; Mazer, T.; Shell, T. L.; Noble, R. W.; Brooks, J. J. *Anal. Chem.* **1985**, *57*, 640.
(17) Donnelly, J. R.; Munslow, W. D.; Mitchum, R. K.; Sovocool, G. W. *J. Chromatogr.* **1987**, *392*, 51.
(18) Hasan, M. N.; Jurs, P. C. *Anal. Chem.* **1988**, *60*, 978.
(19) Robbat, A., Jr.; Xyrafas, G.; Marshall, D. *Anal. Chem.* **1988**, *60*, 982.
(20) Ong, V. S.; Hites, R. A. *Anal. Chem.* **1991**, *63*, 2829.
(21) Makino, M.; Kamiya, M.; Matsushita, H. *Chemosphere* **1992**, *25*, 1839.
(22) Seybold, P. G.; Bertrand, J. *Anal. Chem.* **1993**, *65*, 1631.
(23) Stanton, D. T.; Jurs, P. C. *Anal. Chem.* **1990**, *62*, 2323.
(24) Stanton, D. T.; Jurs, P. C.; Hicks, M. G. *J. Chem. Inf. Comput. Sci.* **1991**, *31*, 301.
(25) Woloszyn, T. F.; Jurs, P. C. *Anal. Chem.* **1992**, *64*, 3059.
(26) Woloszyn, T. F.; Jurs, P. C. *Anal. Chem.* **1993**, *65*, 582.
(27) Lamparczyk, H.; Wilczynska, D.; Radecki, A. *Chromatographia* **1983**, *17*, 300.
(28) Kaliszan. R.; Lamparczyk, H. *J. Chromatogr. Sci.* **1978**, *16*, 246.
(29) Whalen-Pedersen, E. K.; Jurs, P. C. *Anal. Chem.* **1981**, *53*, 2184.
(30) White, C. M.; Robbat, A., Jr.; Hoes, R. M. *Chromatographia* **1983**, *17*, 605.
(31) Doherty, P. J.; Hoes, R. M.; Robbat, A., Jr.; White, C. M. *Anal. Chem.* **1984**, *56*, 2697.
(32) Robbat, A., Jr.; Corso, N. P.; Doherty, P. J.; Marshall, D. *Anal. Chem.* **1986**, *58*, 2072.
(33) Rohrbaugh, R. H.; Jurs, P. C. *Anal. Chem.* **1986**, *58*, 1210.

0003-2700/94/0366-4288$04.50/0 © 1994 American Chemical Society

In this work, focus has been maintained on finding a relation between different descriptors and retention indexes for nonsubstituted PAHs with molecular range 178–350. Temperature-programmed retention indexes, with PAHs as bracketing compounds,[34] were correlated to a set of physical descriptors by means of multiple linear regression (MLR) and partial linear regression (PLS). The two statistical methods were further compared. As purely statistical methods are used in this process, the quality of the result can only be interpreted by means of predictability. Obviously, a good prediction model is of outermost interest for qualitative chemical analysis. Unknown compounds might thus be identified despite the lack of reference compounds. This technique is especially useful for the identification of polynuclear aromatic compounds (PACs), polychlorinated PACs and other types of compounds where great efforts are being made in order to distinguish between isomeric forms or congeners. Due to a large number of similar compounds in such groups, synthesis is often a very time consuming and difficult way to approach the identification process.

EXPERIMENTAL SECTION

Chromatography. Temperature-programmed retention indexes (RI) for 70 compounds with molecular weight ranging from 178 to 350 (Table 1) were taken from either ref 34 or ref 35 or obtained according to Lee et al. and Vassilaros et al.,[34,36] on a Carlo-Erba Mega HRGC (Milan, Italy) equipped with a flame ionization detector and a 15 m × 0.28 mm i.d. XTI-5 column, having a film thickness of 0.25 μm (Restek Corp., Bellefonte, PA). This column can be considered equivalent to the homemade SE-52 column used in ref 34. As bracketing compounds, phenanthrene, chrysene, picene, benzo[*c*]picene, and dinaphtho[2,1-*a*:2,1-*h*]anthracene were used. On-column injections were performed at an oven temperature of 70 °C, and after 2 min the oven temperature was programmed at 5 °C/min to 350 °C. Hydrogen was used as carrier gas. The 70 PAHs, Table 1, were either purchased from Promchem (Wessel, Germany) or obtained from other laboratories (see Acknowledgment). The retention indexes were recalculated and linearized by the use of two index determinators before further calculations. Phenanthrene was given RI = 300 and picene RI = 500. Thus, for the GC system used, chrysene was adjusted to 407.50 and benzo[*c*]picene to 582.50 in order to achieve linearity between elution time and retention index. Only interpolated index values were used; i.e., a bracketing standard must elute on each side of the compound to be determined.

Descriptor Generation. The molecular structures were initially created by use of MacMimic (InStar Software, Lund, Sweden), and the molecular geometrical structures were transferred to a molecular mechanics MM2(91) computer program for self-consistent field calculations to obtain geometrically optimized structures by energy minimization. The optimized structural geometries obtained for aromatic C–C bond lengths were 1.378–1.462 Å; C–H bond lengths were 1.099–1.103 Å. Bond angels of C–C–C were between 117.6 and 124.3°, and for H–C–C, the angles varied between 116.1and 122.4°. The variations in bond lengths and dihedral angels were dependent on the planarity or nonplanarity of the molecules, i.e., fjord and bay regions as

(34) Lee, M. L.; Vassilaros, D. L.; White, C. M.; Novotny, M. *Anal. Chem.* **1979**, *51*, 768.
(35) Bemgård, A.; Colmsjö, A.; Lundmark, B. O. *J. Chromatogr.* **1992**, *595*, 247.
(36) Vassilaros, D. L.; Kong, R. C.; Later D. W.; Lee M. L. *J. Chromatogr.* **1982**, *252*, 1.

Table 1. Compound Names, Molecular Weights (MW), and References from Where the Retention Indexes Were Obtained

no.	compound	MW	ref
1	phenanthrene	178	34
2	anthracene	178	34
3	pyrene	202	34
4	fluoranthene	202	34
5	triphenylene	228	34
6	chrysene	228	34
7	benz[*a*]anthracene	228	34
8	benzo[*c*]phenanthrene	228	34
9	naphthacene	228	34
10	benzo[*e*]pyrene	252	34
11	benzo[*a*]pyrene	252	34
12	perylene	252	34
13	benzo[*a*]fluoranthene	252	*a*
14	benzo[*b*]fluoranthene	252	34
15	benzo[*j*]fluoranthene	252	*a*
16	benzo[*k*]fluoranthene	252	34
17	dibenzo[*ghi,k*]fluoranthene	276	*a*
18	indeno[1,2,3-*cd*]fluoranthene	276	*a*
19	benzo[*ghi*]perylene	276	*a*
20	indeno[1,2,3-*cd*]pyrene	276	*a*
21	dibenzo[*c,g*]phenanthrene	278	*a*
22	dibenz[*a,c*]anthracene	278	34
23	benzo[*g*]chrysene	278	*a*
24	dibenzo[*b,g*]phenanthrene	278	*a*
25	benzo[*c*]chrysene	278	*a*
26	dibenz[*a,j*]anthracene	278	*a*
27	pentaphene	278	*a*
28	benzo[*a*]naphthacene	278	*a*
29	dibenz[*a,h*]anthracene	278	34
30	benzo[*b*]chrysene	278	34
31	picene	278	34
32	pentacene	278	34
33	coronene	300	35
34	dibenzo[*a,e*]pyrene	302	*a*
35	dibenzo[*a,h*]pyrene	302	*a*
36	dibenzo[*a,l*]pyrene	302	*a*
37	naphtho[2,3-*a*]pyrene	302	*a*
38	naphtho[2,3-*e*]pyrene	302	*a*
39	dibenzo[*a,e*]fluoranthene	302	*a*
40	dibenzo[*a,f*]fluoranthene	302	*a*
41	dibenzo[*a,k*]fluoranthene	302	*a*
42	dibenzo[*b,e*]fluoranthene	302	*a*
43	dibenzo[*b,k*]fluoranthene	302	*a*
44	dibenzo[*j,l*]fluoranthene	302	*a*
45	naphtho[1,2-*k*]fluoranthene	302	*a*
46	naphtho[2,3-*b*]fluoranthene	302	*a*
47	naphtho[2,3-*j*]fluoranthene	302	*a*
48	naphtho[2,3-*k*]fluoranthene	302	*a*
49	benzo[*a*]perylene	302	*a*
50	benzo[*b*]perylene	302	*a*
51	rubicene	326	*a*
52	peropyrene	326	*a*
53	naphtho[8,1,2-*bcd*]perylene	326	*a*
54	dibenzo[*e,ghi*]perylene	326	*a*
55	phenanthro[3,4-*c*]phenanthrene	328	35
56	dibenzo[*g,p*]chrysene	328	35
57	naphtho[2,3-*g*]chrysene	328	35
58	naphtho[1,2-*b*]triphenylene	328	35
59	benzo[*k*]pentaphene	328	35
60	benzo[*c*]pentaphene	328	35
61	naphtho[1,2-*b*]chrysene	328	35
62	dibenzo[*b,k*]chrysene	328	35
63	benzo[*b*]picene	328	35
64	benzo[*c*]picene	328	35
65	naphtho[1,2-*a*]naphthacene	328	35
66	dibenzo[*a,c*]naphthacene	328	35
67	hexaphene	328	35
68	naphtho[2,1-*a*]naphthacene	328	35
69	benzo[*a*]pentacene	328	35
70	benzo[*a*]coronene	350	35

[a] Retention indexes measured in this work according to the Experimental Section.

well as the five-membered ring content influencing the dihedral angels. The angel of C−C−C in the five-membered ring varied between 104.6 and 135.7°.

The geometrically optimized molecular structures, defined by the three-dimensional Cartesian coordinates, were entered as input files for the calculation of the physicochemical descriptors. The calculations were made by use of a semiempirical molecular orbital package of MOPAC 6.00, QCPE 455 (F. J. Seiler Research Laboratory, U.S. Air Force Academy) on a VAX-11/750 (DEC) computer running under a VMS 5.4-3 operating system. The semiempirical modified neglect of diatomic differential overlap (MNDO) Hamiltonian was used in the electronic part of the calculations to obtain data for molecular orbitals, heat of formation, polarizabilities, ionization potential, dipole moment, highest occupied molecular orbital (HOMO), and lowest unoccupied molecular orbital (LUMO). Multipole moments and topological indexes were calculated by structure and charge data from MNDO on a homemade program for IBM-PC.

Molecular dimensions were calculated from the three-dimensional Cartesian coordinates after addition of the van der Waals radii of the carbon and the hydrogen atoms, respectively. The dimensions (in Å) were obtained by fitting the molecule into a box of maximum length to breadth dimensions, yielding a height value as a measure of planarity. Two types of boxes were created: one based only on hydrogen atoms (r = 1.20 Å) and one based on all atoms (radii of aromatic carbon = 1.85 Å). The difference in the boxes will be found mainly in heights, where the box based on hydrogen atoms detects small nonplanarities otherwise concealed by the larger carbon atoms.

Computer Programs Used for Regression. All statistics were run on STATED,[37] an IBM-PC program that handles PLS statistics[38] with optimization of number of factors and prediction statistics according to predicted error sum of squares (PRESS) statistics. All data were extracted from a matrix containing 25 descriptor values for 70 compounds.

Retention Index Models. Physicochemical variables or descriptors were linearly correlated to the linearized retention indexes by use of MLR or PLS. The validity of a correlation was performed by PRESS statistics, where each retention index is predicted by a model based on the others[16] and the root-mean-square errors (RMS) of the residuals give the root-mean-square errors from prediction (RMSP). The results from PRESS statistics give an idea of the prediction strength of the model.

As a final test of prediction strength, isomeric groups were withdrawn from the data set during modeling. The obtained model was then used for prediction of the withheld group.

Outlier Analysis. Outliers were excluded from the calculations based on their individual deviations from experimental data. The level of rejection was determined by how much a particular compound constitutes of the group to be calculated. I.e a large group of compounds demands a lower level of rejection than does a smaller group. Outliers were rejected at the 5% level.

Units. In all the proceeding calculations, ionization potential was measured in eV, physical dimensions in Å and quadrupole moment in $C \cdot m^2 \cdot 10^{-40}$.

(37) STATED. Multivariate Statistic Software for IBM-PC; Arbetsmiljöinstitutet/IKA, Solna, Sweden, 1994.

(38) Martens, H.; Naes, T. *Multivariate Calibration*; John Wiley & Sons: New York, 1992.

RESULTS AND DISCUSSION

Choice of Descriptors. Recently, Ong and Hites[20] presented a reasonable equation relating the retention of PAHs to polarizability, and ionization potential and the square of the dipole moment, of which polarizability was shown previously to correlate linearly to retention.[27] All these descriptors can further be explained by chromatographic theories, although dipole moments are very small for all compounds in this study, yielding an error of calculation in the same range as the calculated dipole moment. The model presented by Ong and Hites was also applied to the 70 PAHs in our work and compared with a similar model, but instead with the square of the dipole moment replaced by the quadrupole moment.[39] This exchange resulted in approximately 15% reduction of the RMS and the RMSP. The predictability of the model was in the same range as reported earlier,[20] i.e., a standard error of the mean of approximately 2.4%. From this the conclusion was drawn that the quadrupole moment could be a possible descriptor in the assessment of gas chromatographic retention of PAHs.

Molecular connectivity indexes (χ) have previously been correlated to retention and boiling points of PAHs and nitrated PAHs.[5,28,29,31,32] First-, second-, and third-order valence molecular connectivities were thus added to our descriptor set. Finally, the molecular shape, mostly described by length to breadth ratio (L/B or η), has been shown to correlate linearly to retention in both gas[40] and reversed-phase liquid chromatography.[41] The molecular shape was taken into consideration by inclusion of the length, breadth, and height (in Å) in the descriptor set as well as the maximum length to breadth ratio. Molecular weight can be used as a descriptor, but because of correlation with the first-order valence molecular connectivity and absence of discrepancy for isomers, this descriptor was not included in the data set. Apart from the above-mentioned descriptors, heat of formation, LUMO, number of fjord regions, and number of five-membered rings were included in the data set. Based on negligible or small prediction properties of individual descriptors or collinearity between descriptors, five were chosen for the final model, i.e., Ionization potential (IP), first-order valence molecular connectivity ($^1\chi$), length (L), height (H), and quadrupole moment (Q). The molecular length and height were obtained from the box based on the carbon atom radii. Neither polarizability nor the squared dipole moment fell out as useful descriptors from this descriptor set.

Modeling Process. The PLS method is supposed to determine the trends in a material with few data points but many descriptors and should thus be superior to MLR. The number of factors that have to be included in the model is a measure of how fast the trend is located. If the maximum number of factors is used, the PLS method is equivalent to MLR. The number of factors used in this work was determined by the first local minimum obtained by PRESS statistics, i.e., when the addition of an extra factor to the model resulted in decreased predictability. If, on the other hand, no such minimum was obtained, the maximum number of factors was used (five in this work), making MLR and PLS equivalent. The latter can also indicate that no simple linear relation can be found with the descriptors used.

(39) Buckingham, A. D. *Quat. Rev.* **1958**, 183.

(40) Kaliszan, R.; Lamparczyk, H.; Radecki, A. *Biochem. Pharmacol.* **1979**, *28*, 123.

(41) Wise, S. A.; Bonnett, W. J.; Guenther, F. R.; May, W. E. *J. Chromatogr. Sci.* **1981**, *19*, 457.

Table 2. Regression Equations for Isomeric Groups: $I = I_0 + k_1IP + k_2{}^1\chi + k_3L + k_4H + k_5Q$[a,b]

MW[c]	252[d]	278	302	328
n	7	12	17	15
outliers	0	3[e]	0	1[f]
factors in PLS	4	2	3	1
I_0	−2612.4	−957.18	−1256.8	5193.9
k_1 (IP)	−15.65	9.717	−12.00	−15.36
	(3.60)	(5.33)	(4.12)	(2.62)
k_2 ($^1\chi$)	470.6	156.85	244.24	−468.67
	(93.18)	(80.43)	(88.58)	(90.79)
k_3 (L)	0.849	2.190	0.370	1.625
	(0.31)	(2.20)	(0.23)	(0.59)
k_4 (H)		−4.579	−7.157	−4.207
		(1.27)	(1.20)	(0.38)
k_5 (Q)	−0.957	1.427	−1.042	−1.947
	(2.91)	(10.77)	(5.86)	(5.62)
RMS (iu)	0.60	1.36	0.86	5.20
RMSP (iu)	1.73	2.65	1.27	6.01
RMS (%)	0.13	0.28	0.16	0.89
RMSP (%)	0.38	0.54	0.24	1.03

[a] Abbreviations: IP, ionization potential; $^1\chi$, first-order valence molecular connectivity; L, length; H, height; Q, quadrupole moment. [b] In parentheses are the relative contributions in percent from the descriptors to the retention model of PAHs. [c] For compound identity see Table 1. [d] The height (H) was not included in the regression. [e] Outlier compounds 21, 28, and 32 (Table 1). [f] Outlier compound 55 (Table 1).

Table 3. Regression Equations for Molecular Intervals: $I = I_0 + k_1IP + k_2{}^1\chi + k_3L + k_4H + k_5Q$[a,b]

MW	178−350	178−300	300−350
n	70	33	38
outliers	3[c]	3[d]	1[e]
factors in PLS	5	5	5
I_0	180.63	80.457	226.96
k_1 (IP)	−17.631	−9.693	−20.319
	(15.21)	(10.01)	(15.16)
k_2 ($^1\chi$)	77.344	82.354	78.429
	(66.20)	(72.42)	(64.54)
k_3 (L)	1.041	0.497	0.822
	(1.63)	(0.84)	(1.19)
k_4 (H)	−9.116	−7.389	−9.069
	(3.87)	(3.60)	(3.39)
k_5 (Q)	−1.009	−0.994	−1.246
	(13.10)	(13.12)	(15.72)
RMS (iu)	5.09	3.77	4.40
RMSP (iu)	5.70	5.05	5.16
RMS (%)	0.99	0.84	0.78
RMSP (%)	1.11	1.13	0.92

[a] Abbreviations: as in Table 2. [b] In parentheses are the relative contributions in percent from the descriptors to the retention model of PAHs. [c] Outlier compounds 2, 32, and 55 (Table 1). [d] Outlier compounds 21, 28, and 32 (Table 1). [e] Outlier compound 55 (Table 1).

Predictability, expressed as PRESS statistics, was always better for the PLS model than for the MLR model in all calculations where less than the maximum number of factors was needed. Thus, only the results for the PLS models are presented.

Prediction of Retention Indexes for Isomeric Groups. The obtained relationships between retention indexes of PAHs and the five descriptors for four isomeric groups are shown in Table 2. For all groups the first-order valence molecular connectivity turned out to be the most important factor, contributing by more than 80% to the regression. The physical dimensions, length and height, only contributed to a small extent to the regression equations. However, removal of L and H from the model resulted in significantly increased RMS and RMSP. In general, the contribution of different descriptors to the regression model apart from the connectivity is difficult to interpret. RMS derived from the difference of the actual measured values and the values given by the regression equation was comparatively small. Even the RMS values derived from the prediction models (RMSP) were in some cases small even though the data points are few. For examples, the RMSP for isomers with molecular weight (MW) 302 (n = 17) was 1.27 index units (iu). The best predicted individual residual value was 0.11 iu, and the least accurate was 3.4 iu. Expressed as retention time for the GC system employed in this study, this means that the retention of a PAH with MW 302 can be expected to be predicted with an error of less than 6.5 s in a 40 min chromatogram (RMSP). This can also be expressed as a 0.24% standard error of the mean.

Outliers were found in the groups with MW 278 and 328. In MW group 328 compound 55 (Table 1), phenanthro[3,4-c]phenanthrene was erroneously predicted to be a higher value by more than 40 iu compared with the experimental value. This is the most nonplanar compound within the data set. Nonplanar compounds are known to elute earlier than planar, and the descriptor expected to take this property into account, the height, did not to a full extent explain this deviation. In MW group 278, three outliers were found; i.e., compounds 21, 28, and 32, whereas compound 21, dibenzo[c,g]phenanthrene is strongly nonplanar and also predicted to be a higher value, probably due to insufficient information in the height descriptor. No simple explanation for the deviation of the two other compounds can be given.

A maximum number of factors was needed for the isomers with MW 252, i.e., four factors. Due to zero information content in the height descriptor, this was excluded. Only seven data points were available, which were too few compared to the number of descriptors (four in that regression), indicating that no conclusions could be drawn from the results. Apart from the MW 252, optimum was achieved with less than maximum number of factors for all other groups, indicating more reliable results, particularly for the isomers with MW 302.

Prediction of Retention Indexes in Molecular Weight Ranges. Regarding molecular weight intervals in Table 3, the accuracy was somewhat lower but the trends were more significant. Different outliers were found when regression was made for the whole interval (MW 178−350), i.e., anthracene, pentacene, and phenanthro[3,4-c]phenanthrene (compounds 2, 32, and 55, Table 1). The maximum number of factors was required in the PLS algorithm in order to obtain optimal predictability. This yielded equivalent regression equations for PLS and MLR. The connectivity index is still the most significant factor although slightly less important when compared to the isomeric groups. Thus, the connectivity descriptor may replace the molecular weight in all models discussed in this paper due to strong correlation to molecular weight and a good linear regression between connectivity and retention within isomeric groups. Figure 1a shows the correlation between experimental and predicted (by PRESS statistics) retention indexes according to the equation for the total molecular weight interval, shown in Table 3, row 1; and Figure 1b shows the corresponding residual plot. Only minor changes in the adapted model was achieved upon

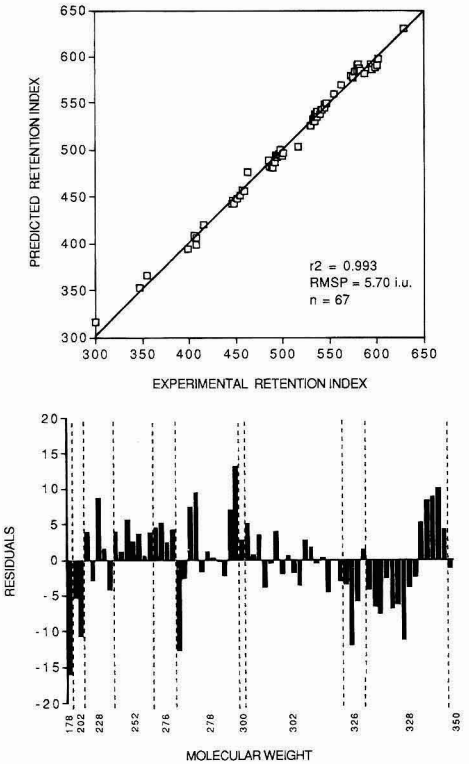


Figure 1. (a, top) Predicted (by press statistics) vs experimental retention indexes for the total molecular weight interval 178–350 and (b, bottom) the corresponding residual plot.

division of the data set into low (178–300) and high (300–350) molecular weight intervals, suggesting similar chromatographic behavior for low- and high-boiling compounds.

Prediction of Retention Indexes for Cata- and Pericondensed PAHs, Respectively. From the residual plot in Figure 1b, it was observed that the equation fitted better for some isomers than for others; e.g., compounds with molecular weights of 252, 276, and 302 were predicted with higher accuracy than the rest. Due to the relatively good predictability of the pericondensed PAHs, an assumption was made that different models should be applied for peri- and catacondensed PAHs or that the latter group requires a more complex approach. The data were thus divided into a catacondensed group consisting of PAHs having molecular weights of 228, 278, and 328 and a pericondensed group including molecular weights of 202, 252, 276, 300, 302, 326, and 350. Subsequent outlier analysis resulted in the same compounds as earlier being assessed as outliers in the catacondensed group, i.e., compounds 2, 32, and 55. In the pericondensed, group, three new outliers appeared (compounds 3, 4, and 53 in Table 1). The results obtained from the PLS calculations are presented in Table 4. From the RMS and RMSP values, it is obvious that the model is good for prediction of retention of pericondensed PAHs. Overall predictability determined by PRESS statistics was 2 iu. In Figure

Table 4. Regression Equations for Cata- and Pericondensed PAHs: $I = I_0 + k_1\mathrm{IP} + k_2{}^1\chi + k_3L + k_4H + k_5Q$[a,b]

MW	cata	peri
n	34	36
outliers	3[c]	3[d]
factors	5	5
I_0	114.42	166.49
k_1 (IP)	−14.038	−14.080
	(7.38)	(13.25)
k_2 ($^1\chi$)	118.193	73.924
	(61.08)	(70.61)
k_3 (L)	1.873	0.146
	(1.87)	(0.24)
k_4 (H)	−9.032	−6.750
	(2.43)	(3.02)
k_5 (Q)	−3.576	−0.867
	(27.24)	(12.88)
RMS (iu)	5.80	1.62
RMSP (iu)	7.45	1.98
RMS (%)	1.13	0.31
RMSP (%)	1.45	0.38

[a] Abbreviations: as in Table 2. [b] In parentheses are the relative contributions in percent from the descriptors to the retention model of PAHs. [c] Outlier compounds 2, 32, and 55 (Table 1). [d] Outlier compounds 3, 4, and 53 (Table 1).

2a experimentally determined vs predicted retention indexes for the pericondensed PAHs are plotted. The residual plot in Figure 2b, derived from PRESS statistics, implicated a nondistorted model with quite a homogenous spreading of the residuals around zero. For the pericondensed compounds with molecular weights of 252, 276, and 302, the equation is useful, although predictability for MW 326 is lower. The results obtained by the model derived from the catacondensed group indicated decreased accuracy of predictability compared to the total regression equation in Table 3.

Evaluation of the Models by Prediction of Isomeric Group Retention Indexes. From the discussion above, it can be concluded that, among the presented models, the equation obtained by relating retention indexes of pericondensed PAHs to the five descriptors gave the most accurate predictability for PAHs. The predictability has been assessed, this far, by a jack-knifing procedure and expressed by PRESS statistics. In order to evaluate the models for different isomers, all isomeric groups were excluded, one by one, from the data set and predicted by the model determined from the remaining PAHs (except outliers). This was performed by the equation of all 70 (67 after removal of outliers) PAHs (similar to Table 3, row 1), and of all pericondensed and catacondensed PAHs from Table 4. For the compounds with molecular weights of 202 ($n = 2$), 228 ($n = 5$), 252 ($n = 7$), 276 ($n = 4$), 278 ($n = 11$), and 326 ($n = 3$ or $n = 4$), all compounds in the groups were withdrawn for the model processing whereas the groups having molecular weights of 302 ($n = 17$) and 328 ($n = 14$) were divided into two. However, when all compounds were used for regression ($n = 67$), all isomers with MW 302 and 328 were withdrawn for prediction, respectively. The residual plots from prediction are presented in Figure 3a–c. Comparing these plots with the residual plots in Figures 1b and 2b, no pronounced changes can be observed. RMSP for all predicted isomers indexes (Figure 3a) was 6.2 iu, RMSP for all predicted catacondensed isomers (Figure 3b) was 6.88 iu, and RMSP for the predicted

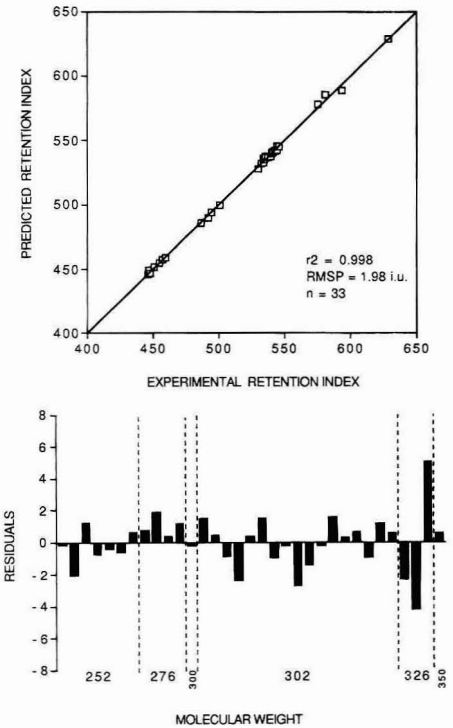


Figure 2. (a, top) Predicted (by press statistics) vs experimental retention indexes for the pericondensed PAHs and (b, bottom) the corresponding residual plot.

pericondensed isomers (Figure 3c) was 2.5 iu, thus indicating that the models were stable for these types of compounds.

Practical Remarks. In practice, the RMSP of the retention data must be compared to the retention data of the entire isomeric group. That is, a small elution time interval demands a very good model of prediction if individual compounds are to be discerned from other unknown isomers. On the other hand, a more or less inaccurate model can be useful if the compounds to be distinguished are spread out in a large elution time interval. As an example, the GC/MS analysis of the commercially available rubicene (MW = 326) showed two compounds with the same molecular weight in the product. Fluorescence analysis indicated that the minor compound was rubicene. If so, rubicene must be considered as an outlier in the models calculated in this paper (the error of prediction was 19 index units). Further analysis proved that previously recorded fluorescence data had been based on the impurity of the product. The inclusion of the other compound in the model described here yielded an error of only 2.3 index units. This is an example which demonstrates that the purpose of the model must be considered together with the evaluation of RMSP values.

Comparing predictability of this work with results presented by other authors is not simple. In general, the standard error of the mean is used in order to describe the overall predictability of a model. In Table 5, an attempt was made to compare the

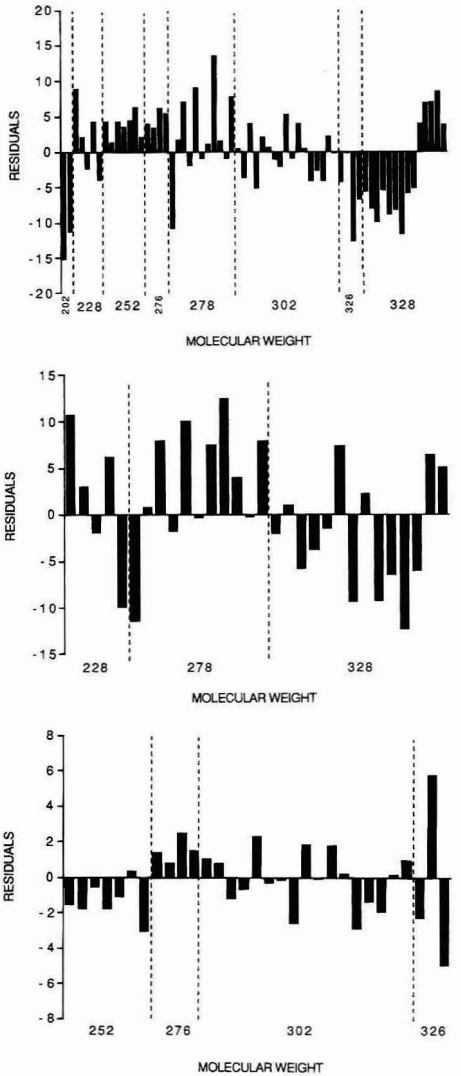


Figure 3. Residual plots when each isomeric group was withdrawn from the modeling process and predicted by the rest of the compounds using a model including (a, top) all PAHs for the regression, (b, middle) the catacondensed PAHs for regression, and (c, bottom) the pericondensed PAHs for regression.

accuracy of the predicted values obtained by the models presented in this work with the predictability of a number of other models, calculated for PAHs, PCBs, etc. Comparably successful results concerning the prediction accuracy have been achieved by the selection of the presented five descriptors.

Descriptors that are important but not yet used are probably missing in the models presented. The interaction of solutes with different phases in a chromatographic column may not be

Table 5. Comparison of Coefficient of Variation Data Described as Standard Error of the Mean with Literature Data

compd types	std error of the mean (CV %)	ref
PCB	2.5	20
PCB	1.7	18
PCB	<1	19
NO-PAH	0.76	32
PAH	2.7	28
PAH	2.6	20
PAH	0.99	this work
PAH (pericondensed)	0.31	this work

calculated accurately due to lack of exact knowledge of the interaction processes and due to inaccurate calculations of physical properties. Additional descriptors and more accurately calculated values, together with non-linear regression models, will probably be a useful future approach in order to increase the accuracy of prediction of retention of unknown compounds.

ACKNOWLEDGMENT

The authors thank Dr. J. Fetzer, Dr. S. Wise, Dr. M. Lee, and Dr. C. White for the donation of PAH standard compounds. Dr. B. Roos is acknowledged for helpful comments in the initial stage of this work. Finally, thanks are due to Mrs. M. Reuterdahl for linguistic review of the manuscript.

Received for review June 2, 1994. Accepted August 24, 1994.[⊗]

[⊗] Abstract published in *Advance ACS Abstracts*, October 1, 1994.

Anal. Chem. **1994,** *66,* 4295–4301

On-Line Coupling of Liquid Chromatography to Biochemical Assays Based on Fluorescent-Labeled Ligands

A. J. Oosterkamp, H. Irth,* U. R. Tjaden, and J. van der Greef

Leiden/Amsterdam Center for Drug Research, Division of Analytical Chemistry, University of Leiden, P.O. Box 9502, 2300 RA Leiden, The Netherlands

The on-line coupling of liquid chromatography (LC) to a biochemical detection (BCD) technique based fluorescein-labeled ligands as reporter molecules is described. In a first step, affinity proteins such as antibodies or avidin are added to the LC effluent to react with ligands (analytes) eluting from the LC column. Unbound affinity proteins react, in a second step, with an excess of fluorescein-labeled ligand to titrate the remaining free binding sites. Prior to detection of the labeled ligand/protein complex, free and bound label are separated on the basis of the considerable difference in molecular weight. A short (10 × 4.0 mm i.d.) column packed with a restricted-access support is used to trap the free labeled ligand at the hydrophobic inner surface of the pores. The high molecular weight labeled ligand/protein complex passes this column unretained and is detected by means of fluorescence detection. The interaction between biotin and avidin was chosen as a model system. A detection limit of 160 fmol was obtained for biotin using reversed-phase LC–BCD. An equilibrium and kinetic model is described which relates the detector response to the concentration of affinity protein, fluorescent label, and reaction time.

The combination of liquid chromatography (LC) with biochemical detection (BCD) methods greatly enhances the performance of both techniques and provides analytical methods which are characterized by high selectivity and sensitivity.[1] LC has been successfully coupled to catalytic[2] or affinity-based biological detection techniques[3,4] using enzymes and antibodies, respectively, for analyte recognition. The separation power of LC systems, particular in combination with automated sample cleanup techniques, can solve the problem of cross-reactivity which is characteristic for most biological assays. On the other hand, the inherent selectivity and sensitivity of bioassays extends the applicability of LC in, for example, environmental analysis, clinical analysis, or bioanalysis.

Catalytic and affinity-based detection techniques differ fundamentally in the way the binding of analytes to the target protein is monitored. Catalytic systems involving enzyme–substrate reactions are mainly detected by electrochemical detection[5,6] monitoring electron transfers which occur during the breakdown of the substrate. Affinity-based detection techniques generally rely on reporter molecules such as radioactive and luminescent labels or enzymes to detect the binding of analytes to, for example, antibodies or receptors.[7]

Both catalytic and affinity-based detection techniques can be carried out in continuous-flow systems and can principally be implemented in flow injection (FI) and LC systems. However, the dynamic nature of these techniques restricts the type of suitable assays to those detection principles which (i) provide short reaction times, i.e., less than 5 min, and (ii) are able to generate a continuous signal without the need of regeneration. If coupling to LC is intended, the bioassay has to be compatible with the LC mobile phase constituents, particularly with organic modifiers such as acetonitrile or methanol. Various detection principles based on both competitive[8,9] and noncompetitive[3,10–13] assays which principally meet these requirements were reported. Kusterbeck et al.[8,9] described an FI assay based on the displacement of labeled antibodies bound to an immobilized antigen support. A noncompetitive FI enzyme immunoassay has been reported by Kronkvist et al.[10] that uses a protein G column to separate free and antibody-bound enzyme labels. Recently we described an immunochemical detection (ICD) system coupled to LC in which fluorescein-labeled antibodies were added to the LC effluent to monitor the presence of antigenic analytes.[3,4] Optimum reaction times of 1–2 min were obtained, which are of the same order of magnitude as those characteristic for chemical postcolumn derivatization techniques. Moreover, organic modifiers such as acetonitrile and methanol were tolerated up to 10 and 35%, respectively.

The immunoreagent used for this assay consisted of fluorescein-labeled Fab fragments of anti-digoxigenin antibodies which were immunopurified and commercially available. We realized, however, that the commercial availability of purified, labeled antibodies

(1) De Frutos, M.; Regnier, F. E. *Anal. Chem.* **1993**, *65*, 17A.
(2) Marko-Varga, G. *Electroanalysis* **1992**, *4*, 403.
(3) Irth, H.; Oosterkamp, A. J.; van der Welle, W.; Tjaden, U. R.; van der Greef, J. *J. Chromatogr.* **1994**, *633*, 65.
(4) Oosterkamp, A. J.; Irth, H.; Beth, M.; Unger, K. K.; Tjaden, U. R.; Van der Greef, J. *J. Chromatogr.* **1993**, *653*, 55.
(5) Turner, A. P. F.; Karube, I.; Wilson, G. S., Eds. *Biosensors*; Proceedings of a Royal Society Discussion Meeting held on 28 and 29 May 1986; The Royal Society: London, 1987.
(6) Scheller, F.; Schubert, F. *Biosensoren*; Akademie-Verlag: Berlin, 1989.
(7) Hammilä, I. A. *Applications of Fluorescence in Immunoassays*; Chemical Analysis 117; Wiley-Interscience: New York, 1991.
(8) Kusterbeck, A. W.; Wemhoff, G. A.; Charles, P. T.; Yeager, D. A.; Bredehorst, R.; Vogel, C-W.; Ligler, F. S. *J. Immunol. Methods* **1990**, *135*, 191.
(9) Whelan, J. P.; Kusterbeck, A. W.; Wemhoff, G. A.; Bredehorst, R.; Ligler, F. S. *Anal. Chem.* **1993**, *65*, 3561.
(10) Kronkvist, K. Ph.D. Dissertation, Lund, Sweden, 1993 part V.
(11) Gunaratna, P. C.; Wilson, G. C. *Anal. Chem.* **1993**, *65*, 1152.
(12) Freytag, J. W.; Lau, H. P.; Wadsley, J. *Clin. Chem.* **1984**, *30*, 1494.
(13) Nilsson, M.; Hakanson, H.; Mattiason, B. *J. Chromatogr.* **1992**, *597*, 383.

0003-2700/94/0366-4295$04.50/0 © 1994 American Chemical Society

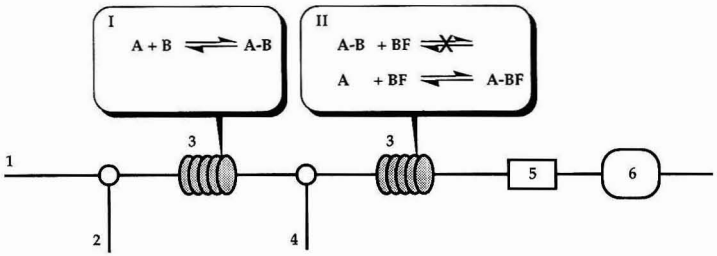


Figure 1. Scheme of the BCD system. Key: 1, eluate of the HPLC column; 2, reagent pump for avidin solution; 3, reaction coil; 4, reagent pump for fluorescein–biotin solution; 5, column packed with C_{18}-silica restricted-access support; 6, fluorescence detector. A, avidin; B, biotin; BF, fluorescein–biotin.

is the exception rather than the rule. In most cases, antibodies against drugs, for example, are available as unlabeled, only crudely purified antiserum. Although labeling and purification schemes for antibodies and other affinity proteins are well documented, the use of commercially available antisera without any pretreatment should be considered as well.

In the present paper we describe an on-line LC–BCD system which uses labeled ligands instead of labeled proteins as reporter molecules. A theoretical model was developed to determine the influence of reaction time, affinity protein and label concentration, and association rate constant on the detector response. The interaction between biotin and avidin was chosen as a model system. Avidin is a well-characterized protein of 75 kDa which consists of four subunits, each possessing one binding site for biotin. The interaction of biotin and avidin is extremely strong (affinity constant, $K_a = 0.6 \times 10^{15}$ L/mol), with a fast association rate and a slow dissociation rate, i.e., $k_{+1} = 2.4 \times 10^7$ L·mol^{-1} s^{-1} and $k_{-1} = 0.4 \times 10^{-7}$ s^{-1}, respectively.[14]

EXPERIMENTAL SECTION

Materials. Avidin, fluorescein-labeled avidin, biotin, and fluorescein-labeled biotin were purchased from Sigma (St. Louis, MO). Sodium chloride and sodium phosphate were from Merck (Darmstadt, Germany). Acetonitrile was obtained from Rathburn Chemicals (Walkerburn, U.K.). All other organic solvents were purchased from Baker (Deventer, The Netherlands) and were of analytical grade. Restricted-access precolumns were a gift of Prof. Boos (University of Munich, Germany). Binding buffer consisted of sodium phosphate (10 mmol/L, pH 8.0) containing 0.5 mol/L sodium chloride. Blocking reagent (Boehringer Mannheim, Mannheim, Germany) was prepared according to the manufacturer's specifications.

Apparatus. The FI– and LC–BCD system (see Figure 1) consisted of two Kratos-ABI (Ramsey, NJ) Spectroflow 400 pumps and a Pharmacia (Uppsala, Sweden) P3500 pump used to deliver the mobile phase, the labeled biotin, and the avidin solution, respectively, a Gilson 231 autosampler equipped with a Rheodyne six-port injection valve (injection loop, 20 μL), and a Merck (Darmstadt, Germany) 1080 fluorescence detector (excitation wavelength, 486 nm; emission wavelength, 520 nm). The FI carrier solution consisted of binding buffer and was pumped at a flow rate of 0.4 mL/min. LC separations were carried out on a 100- × 3.0-mm i.d. stainless-steel column packed with Nucleosil C_{18} (5 μm particles, Macherey-Nagel, Düren, Germany) using methanol/aqueous triethylammonium acetate (10 mmol/L, pH 7.0) 10:90 v/v, as mobile phase. The avidin (34 nmol/L) and fluorescein–biotin (200 nmol/L) solutions were prepared in binding buffer and added to the LC or FI carrier solution via inverted Y-type mixing unions. The avidin solution was pumped at a flow rate of 0.4 mL/min for both LC– and FI–BCD systems. The fluorescein–biotin solution was delivered at a flow rate of 0.4 mL/min using FI–BCD and 0.8 mL/min using LC–BCD. Knitted 0.5 mm i.d. poly(tetrafluoroethylene) reaction coils with an internal volume of 800 and 400 μL for reactions I and II, respectively, were used. The reaction was performed at 20 °C. Separation of free and avidin-bound fluorescein–biotin was performed using a 10- × 4.0-mm i.d. column packed with C_{18} alkanediol silica[15] donated by Prof. Boos (University of Munich, Germany). The analytical system was controlled by Gilson 605 GSIOC driver software connected to a personal computer.

Batch Experiments. The performance of the BCD system under equilibrium conditions was tested in the FI mode by incubating 0.4 mL of avidin (34 nmol/L) in batch for 15 min with 0.4 mL of different biotin concentrations. To this was added 0.4 mL of fluorescein–biotin (200 nmol/L), and the sample was incubated for another 15 min. The amount of avidin/fluorescein–biotin complex formed was measured by injecting the reaction mixture into an FI system in which the injection valve was connected directly to the restricted-access reversed-phase (RA-RP) column and the fluorescence detector.

Stopped-Flow Experiments. The influence of the reaction time on detection sensitivity was measured in the stopped-flow mode by connecting coil 3 of reaction I (see Figure 1) to a Must (Spark Holland, Emmen, The Netherlands) switching unit equipped with a six-port Rheodyne injection valve. After injection of biotin, reaction coil 3 was switched off-line to achieve reaction times of 30, 60, 120, and 180 s.

Calculation of Theoretical Detection Limits. The computer simulation was performed on a personal computer using Turbo-Pascal (Borland, Scotts Valley, CA). The detector noise (N) was calculated using eq 9 (see Results and Discussion) with $n_f = 0.005$ and $n_s = 10^{-10}$ mol/L. The signal (S) was calculated according to eq 8 (see Theory). The LOD was determined by an iteration procedure in which the biotin concentration was varied in increments of 10^{-10} mol/L until a signal-to-noise ratio of 3 was

(14) Green, N. M. *Methods Enzymol.* **1990**, *184*, 51.

(15) Boos, K.-S.; Walfort, A.; Lubda, D.; Eisenbeiss, F. German Patent DE41 30 475 A1, 1991.

obtained for a given avidin concentration. The procedure was repeated for avidin concentration ranging from 10^{-10} to 10^{-7} mol/L at increments of 10^{-11} mol/L.

THEORY

The LC–BCD system using labeled ligands as reporter molecules is based on a two-step affinity reaction (see Figure 1). The performance of the BCD system has been investigated using avidin as affinity protein, biotin as ligand, and fluorescein-labeled biotin (fluorescein–biotin) as labeled ligand. In the following, the four binding sites of avidin are considered as individual, independent subunits. Avidin concentrations are calculated as concentration of free binding sites.

In the first step of the BCD system, avidin (A) is added to the LC effluent to react with biotin (B) or biotinylated compounds eluting from the LC column to form avidin–biotin complexes (A–B) in concentrations proportional to the biotin concentration, provided that [A] ≥ [B]:

$$A + B \underset{k_{-1}}{\overset{k_{+1}}{\rightleftharpoons}} A\text{–}B \qquad \text{(I)}$$

In the second step, an excess of fluorescein-labeled biotin (BF) is added to the reaction mixture to saturate the binding sites of unbound avidin molecules:

$$A + BF \underset{k_{-1}}{\overset{k_{+1}}{\rightleftharpoons}} A\text{–}BF \qquad \text{(II)}$$

The avidin/fluorescein–biotin complex (A–BF) formed is separated from free fluorescein–biotin prior to fluorescence detection on the basis of the difference in molecular size (separation principle; see below). The detection response decreases with increasing biotin concentrations.

Similar to the immunochemical detection system reported earlier, which employed fluorescein-labeled antibodies,[3] the present BCD technique is solely based on fast association reactions of biotin or fluorescein–biotin with an avidin binding site. An equilibrium model describing the relationship between detector response, i.e., the concentration of the avidin/fluorescein–biotin complex, and the concentration of biotin is derived from the two sequential biochemical reactions. In this model, band broadening due to dispersion is not considered.

The amount of avidin/biotin complex formed in reaction I is calculated

$$K_D = \frac{([A]_0 - [A\text{–}B])([B]_0 - [A\text{–}B])}{[A\text{–}B]} \qquad (1)$$

with K_D being the binding constant, $[A]_0$ the avidin concentration added, and [A–B] the concentration of avidin–biotin complex formed.

The concentration of free avidin ($[A]_B$) after this reaction is

$$[A]_B = [A]_0 - [A\text{–}B] \qquad (2)$$

The concentration of avidin/fluorescein–biotin ([A–BF]) formed can be calculated by

$$K_D = \frac{([A]_B - [A\text{–}BF])([BF]_0 - [A\text{–}BF])}{[A\text{–}BF]} \qquad (3)$$

where $[BF]_0$ is the fluorescein–biotin concentration added.

Substituting eq 2 in eq 3 provides a relationship between the biotin concentration ([B]) and the avidin/fluorescein–biotin concentration ([A–BF]) as a function of the avidin and fluorescein–biotin concentration and the binding constant, K_D, assuming that the total system is in equilibrium.

Preliminary experiments (see below) have shown that the biochemical reaction between biotin and avidin does not reach equilibrium under the reaction conditions chosen (reaction time, avidin concentration) despite the high association rate constant. This resulted in a lower detection response than predicted by the equilibrium model. We therefore developed a kinetic model which relates the detector response to the biotin concentration under nonequilibrium conditions. The model is based on the assumption that dissociation of the avidin/biotin and avidin/fluorescein–biotin complexes is negligible within the time range of the postcolumn reaction (1–2 min). This assumption is true for most bioaffinity interaction systems with dissociation constants on the order of 10^{-2}–10^{-3} s^{-1}.

The model developed does not consider band broadening introduced by the reaction coil, although this may play a role at longer reaction times.

The association of biotin with the avidin is described by second-order kinetics:

$$d[A\text{–}B] = [A][B]k_{+1}t \qquad (4)$$

Assuming that $[A\text{–}B]_{t=0} = 0$, $[A]_{t=0} = [A]_0$, and $[B]_{t=0} = [B]_0$, integration of eq 4 results in[16]

$$k_{+1}t = \frac{1}{[B]_0 - [A]_0}\left(\ln\frac{[A\text{–}B] - [B]_0}{[A\text{–}B] - [A]_0} - \ln\frac{[B]_0}{[A]_0}\right) \qquad (5)$$

From eq 5, the concentration of avidin/biotin complex after reaction I can be derived:

$$[A\text{–}B] = [A]_0[B]_0\frac{\exp^{-([B]_0 - [A]_0)k_{+1}t} - 1}{[A]_0 \exp^{-([B]_0 - [A]_0)k_{+1}t} - [B]_0} \qquad (6)$$

The concentration of free avidin after reaction I can be calculated according to eq 2. Equation 6 is used to calculate the concentration of avidin/fluorescein–biotin complex formed in reaction II by replacing $[A]_0$ with $[A]_B$ and $[B]_0$ with $[BF]_0$:

$$[A\text{–}BF] = [A]_B[BF]_0\frac{\exp^{-([BF]_0 - [A]_B)k_{+1}t} - 1}{[A]_B \exp^{-([BF]_0 - [A]_B)k_{+1}t} - [BF]_0} \qquad (7)$$

Combining eqs 6 and 7 provides a formula which relates the detector response to the most important parameters of the BCD system, i.e., the reaction time, the concentrations of analyte and avidin, and the dissociation rate constant. The signal obtained

(16) Weiland, G. A.; Molinoff, P. B. *Life Sci.* **1981**, *29*, 313.

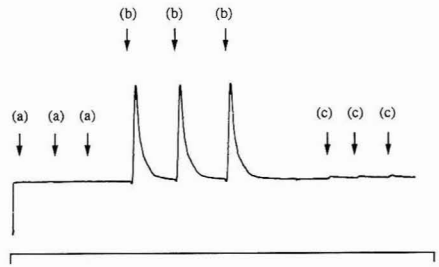


Figure 2. Direct injection of (a) fluorescein–biotin (10 nmol/L), (b) fluorescein–biotin (10 nmol/L) incubated with avidin (10 nmol/L), and (c) fluorescein–biotin (10 nmol/L) incubated with avidin (10 nmol/L) which was preincubated with biotin (1 μmol/L).

by indirect fluorescence detection corresponding to a certain ligand concentration ($[B]_0$) is then described as

$$S = r([A-BF]_0 - [A-BF]_B) \quad (8)$$

where r is the response factor of A–BF for a given fluorescence detector, $[A-BF]_0$ and $[A-BF]_B$ are calculated according to the combined formula of eqs 6 and 7 at $B = 0$ and $B = B_0$, respectively.

RESULTS AND DISCUSSION

Separation of Bound and Free Label. Similar to all heterogeneous batch-type biological assays, free and avidin-bound fluorescein–biotin must be separated prior to detection. Separation can be achieved in a continuous-flow system by exploiting the difference in biochemical activity or molecular mass. This separation should introduce only a minimum of extracolumn band broadening and allow the overall system to be operated continuously without the need of regeneration. In the present system, we chose a separation technique which exploits the considerable difference in molecular mass between free fluorescein–biotin (<1 kDa) and avidin/fluorescein–biotin (>50 kDa). For this purpose, a short column (10 × 4 mm i.d., 5 in Figure 1) packed with a restricted-access reversed-phase (RA-RP) support was placed in the carrier stream prior to the detector. The RA-RP support consists of C_{18}-bonded porous silica.[15] The pores of the particles are shielded by a hydrophilic, polymerous alkane diol layer which efficiently excludes proteins with a molecular mass above 15 kDa. The free fluorescein–biotin is retained at the hydrophobic inner surface of the pores. The avidin/fluorescein–biotin complex is excluded from the pores and passes unretained to the fluorescence detector.

The separation of free and avidin-bound fluorescein–biotin is demonstrated in Figure 2. In Figure 2a and b, repeated injections of fluorescein–biotin and fluorescein–biotin incubated with avidin are shown. While free fluorescein–biotin is completely retained by the RA-RP column, avidin-bound fluorescein–biotin passes the RA-RP column unretained and without appreciable peak broadening. The specificity of the binding between fluorescein–biotin and avidin is demonstrated in Figure 2c, representing the same experiment as in figure 2b but using avidin preincubated with an excess of unlabeled biotin (1 μmol/L). The degree of nonspecific binding of avidin/fluorescein–biotin complex to the RA-RP support was derived from the measurements shown in Figure 2c.

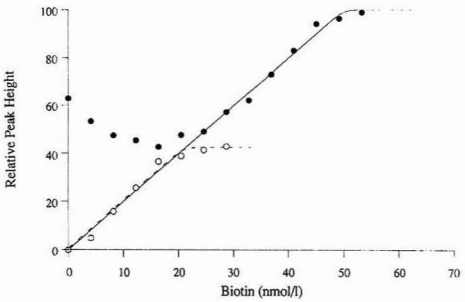


Figure 3. Detector signal *vs.* biotin concentration. (—) Predicted by the equilibrium model using 17 nmol/L avidin; (●) values measured with the BCD system using 17 nmol/L avidin; (– –) predicted by the equilibrium model using 17 nmol/L avidin which was preincubated with 34 nmol/L biotin; (○) values measured with the BCD system using 17 nmol/L avidin which was preincubated with 34 nmol/L biotin.

At the very low concentrations of protein used, the untreated RA-RP support exhibited a very high degree of nonspecific binding (>95%) in the particular case of avidin and avidin/fluorescein–biotin. This is in contrast to the earlier experiments,[4] where the RA-RP was used in sample pretreatment for direct plasma injections. Nonspecific binding of avidin/fluorescein–biotin was drastically reduced by equilibrating the RA-RP column with 2 mL of blocking reagent consisting of a casein hydrolysate with an average protein concentration of 70 mg/mL. Moreover, 0.5 mol/L sodium chloride was added to the avidin and fluorescein–biotin solutions. In this way, the nonspecific binding was reduced to 0.5%. Nonionic surfactants, e.g., Tween-10 or Brij-35, which are currently used to efficiently reduce nonspecific binding of immunocomplexes to affinity supports,[3,4] appeared to be not compatible with the RA-RP support.

Free fluorescein–biotin was retained efficiently on the C_{18}-bonded inner surface or the RA-RP support. The breakthrough volume of fluorescein–biotin dissolved in binding buffer was larger than 300 mL. Due to the high breakthrough volume, the BCD system could be used for at least 24 h. The column was easily regenerated by rinsing with acetonitrile:water (40:60 v/v).

Influence of Multivalency. Initial experiments to test the performance of the BCD system were carried out under equilibrium conditions and in the FI mode. Avidin was incubated for 15 min with different concentrations of biotin. Next fluorescein–biotin was added, and the sample was incubated for 15 min prior to injection in the FI system. Figure 3 shows a graph representing the theoretical response, derived from the equilibrium model, and the fluorescence response measured as a function of the biotin concentration. Both curves are similar at biotin concentrations higher than 10 nmol/L. However, at biotin concentrations lower than 10 nmol/L, they differ significantly. Instead of an increasing indirect fluorescence signal, a decrease was observed. A possible explanation for this observation can be derived from the tetravalency of avidin, assuming that the fully occupied 4:1 fluorescein–biotin/avidin complex has a lower fluorescence quantum yield than the 3:1 complex due to internal quenching. On the other hand, the 2:1 and 1:1 complexes have a lower quantum yield than the 4:1 complex because of the lower number of fluorescein molecules bound per molecule of avidin. We tested this hypothesis by preincubating avidin with a 2-fold molar excess of biotin

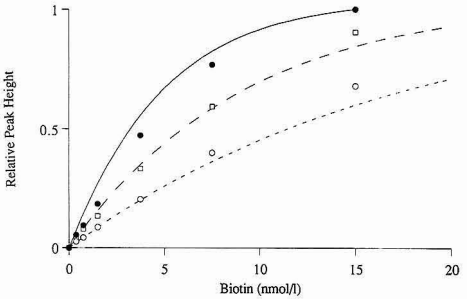


Figure 4. Detector signal vs biotin concentration at different reaction times for reaction I predicted by the kinetic model at (—) 120 s, (— —) 60 s, and (- - -) 30 s and values measured with the BCD system at (●) 120 s, (○) 60 s, and (□) 30 s. Avidin concentration, 17 nmol/L; fluorescein–biotin concentration, 200 nmol/L; reaction time for reaction II, 60 s; other conditions, see Experimental Section.

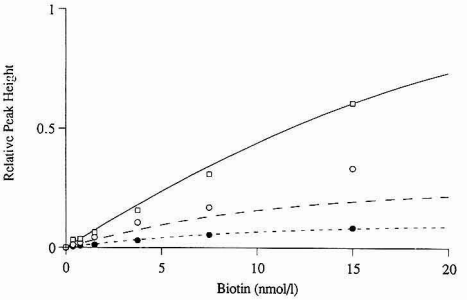


Figure 5. Detector signal vs biotin concentration at avidin concentrations predicted by the kinetic model at (—) 17 nmol/L, (— —) 4.3 nmol/L, and (- - -) 1.7 nmol/L and values measured with the BCD system at (□) 17 nmol/L, (○) 4.3 nmol/L, and (●) 1.7 nmol/L. Fluorescein–biotin concentration, 200 nmol/L; reaction time for reaction I, 60 s; reaction time for reaction II, 60 s; other conditions, see Experimental Section.

and using the 2:1 biotin/avidin complex formed as reagent. The dashed line in Figure 3 shows that preincubation with biotin resulted in a shift of the calibration line and a linear increase of the indirect fluorescent signal with increasing analyte concentrations at concentrations down to 1 nmol/L. In all subsequent experiments, avidin was therefore preincubated with a 2-fold molar excess of biotin prior to its use as reagent.

Optimization of Reaction Conditions. From eqs 6 and 7 it can be derived that for a given bioaffinity system, that is, for constant association and dissociation rate constants, the reaction time and the concentration of avidin are the most relevant parameters to be optimized. The influence of the reaction time on the detector response is demonstrated in Figure 4. The curves are derived from eqs 6 and 7, assuming an association rate constant of 2×10^6 L mol^{-1} s^{-1}, an avidin concentration corresponding to 17 nmol/L of free binding sites, and a label concentration of 200 nmol/L. The reaction time for reaction II was 60 s. The theoretical curves closely match the values measured ($n = 3$) under stopped flow conditions. Both theoretical curves and experimental data indicate that the system has not reached equilibrium at the longest reaction time of 120 s. A further increase of the reaction time did not result in larger peak heights since the gain in sensitivity due to a more complete reaction is counteracted by band broadening caused by dispersion in the open-tubular postcolumn reactor. No attempts were made to use segmented reaction detection systems which are recommended if reaction times longer than 5 min are needed.[17]

When the BCD is operated at a maximum reaction time, the concentration of avidin is the most important parameter to be optimized. Increasing avidin concentrations results in higher concentrations of both ligand–protein and label–protein complexes as predicted by eqs 6 and 7. Higher label–protein concentrations cause an increase of the background signal and baseline noise, which finally will counteract the gain in sensitivity due to increased ligand–protein concentrations.

Quantitative Aspects. In Figure 5, theoretical and experimental ($n = 3$) calibration values for biotin are shown at three

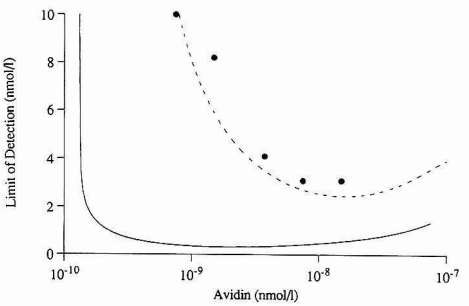


Figure 6. Limit of detection vs avidin concentration predicted by the kinetic model for (- - -) $k_{+1} = 2 \times 10^6$ s^{-1} and (—) $k_{+1} = 2 \times 10^7$ s-1; (●) values measured with the BCD system. Fluorescein–biotin concentration, 200 nmol/L; reaction time for reaction I, 60 s; reaction time for reaction II, 60 s; other conditions, see Experimental Section.

different avidin concentrations. In the concentration range between 1 and 20 nmol/L biotin, the indirect fluorescence signal increases linearly with the avidin concentration. To predict the limit of detection (LOD) as a function of the avidin concentration, an iterative simulation model was developed. In this model, the detector signal, S, at a certain avidin concentration was calculated according to eq 8. The detector noise, N, was calculated (see eq 9) by a function consisting of a constant part, n_s, i.e., the instrument noise in absence of A–BF (shot noise) and a variable part, n_f, which depends linearly on the concentration of label–protein complex (flicker noise):[18]

$$N = r(n_f[A\text{–}BF] + n_s) \tag{9}$$

In Figure 6, the theoretical LOD calculated as S/N = 3 is depicted as a function of the avidin concentration for two different BCD systems with association rate constants of 2×10^6 and 2×10^7 L mol^{-1} s^{-1}, respectively. The simulation assumes that [BF] $\gg$ [A]$_B$ to assure near equilibrium conditions for reaction II (reaction time, 60 s). The LODs measured were divided by a factor of 4 to correct for dilution due to band broadening. The

(17) Lillig, B.; Engelhardt, H. In *Reaction Detection in Liquid Chromatography*; Krull, I. S., Ed.; Marcel Dekker, Inc.: New York, 1986; p 1.
(18) Mho, S.-I.; Yeung, E. S. *Anal. Chem.* **1985**, *57*, 2253.

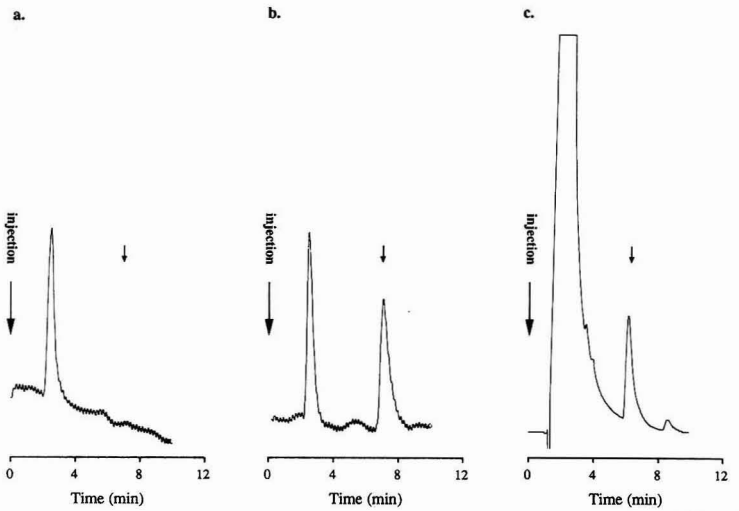


Figure 7. (a) LC–BCD of a blank sample; (b) LC–BCD of biotin (40 nmol/L); (c) LC–UV detection at 210 nm of biotin (400 μmol/L). Conditions, see Experimental Section.

avidin concentration providing the lowest LOD depends strongly on the association rate constant. Of particular interest are the different shapes of the curves at different rate constants. At a low association rate constant, a rather narrow optimum is obtained, and changes of the protein concentration in either direction cause a significant increase of the LOD. At a higher association rate constant (curve 2), the optimum range is much broader, and changes in the avidin concentration are less critical. The optimal avidin concentration of the present system was 17 nmol/L.

On-Line Coupling to Liquid Chromatography. The BCD system was coupled on-line to reversed-phase LC using C_{18}-bonded silica as stationary phase. Compared to the FI, the flow rate of the label pump (3 in Figure 1) was increased from 0.4 to 0.8 mL/min, and reaction coil 2 was shortened to provide a reaction time of 15 s. Chromatograms representing LC–BCD of a blank sample, a sample spiked with 40 nmol/L biotin, and LC–UV detection of a sample spiked with 400 μmol/L biotin omitting the postcolumn reaction detection system are shown in Figure 7. The extracolumn band broadening of the BCD system amounts to σ_{BCD} = 9.9 s at a total peak width, σ_{tot}, of 15.0 s, which is acceptable if the increase in selectivity provided by the BCD system is considered.

Compared to the FI–BCD system, which is operated with a purely aqueous carrier solvent, the LC mobile phase may contain organic modifiers such as methanol or acetonitrile. We showed earlier[3,4] that we could operate a postcolumn immunochemical detection system at an acetonitrile content (after mixing) up to 15%. In the present system, the presence of organic modifier did not hamper significantly the interaction between biotin and avidin. However, a methanol content of 2.5% in the LC mobile phase resulted in an increased background signal, which is possibly caused by the breakthough of polar impurities due to the weaker retention on the RA-RP support. After equilibration for 30 min, a stable baseline was obtained, and the BCD system could be operated for 24 h at a total flow rate of 1.6 mL/min before regeneration of the RA-RP was required.

Table 1

	FI		LC	
concn (ng/mL)	precision (%)	accuracy (%)	precision (%)	accuracy (%)
2	0.8	95.5	16.8	92.5
5	0.8	99.7	11.0	98.9
20	0.8	99.5	6.5	107.2
LOD (fmol)	40		160	

Table 1 summarizes the data on accuracy, precision, and limit of detection obtained with both FI– and LC–BCD. An avidin concentration corresponding to 17 nmol/L free binding sites was used throughout these experiments. The detection limit (signal-to-noise ratio, 3:1) using LC–BCD was a factor of 1000 lower than the LOD obtained for LC–UV. The indirect detector signal was linear in the concentration range of 8–200 nmol/L (20 μL injections, r^2 = 0.998). The low avidin concentration chosen to obtain the highest sensitivity inherently leads to a rather small linear range of the present method.

CONCLUSIONS

We are currently adapting the present method to be used in combination with labeled antigens and antisera for LC–ICD of pesticides and their metabolites. Compared to the LC–ICD system reported earlier,[3,4] the present system has the considerable advantage that it principally permits the use of unlabeled, unpurified affinity proteins. The preparation of labeled antigens is based on the same chemistry which has been used for the coupling of the hapten to the carrier protein used for immobilization. The detection limit of the present indirect detection technique is of the same order of magnitude, i.e., in the femtomole range, which was obtained with LC–ICD using labeled antibodies.

(19) Tyssen, P. In *Practise and Theory of Enzyme Immunoassay*; Burdon, R. H., Knippenberg, P. H., Eds.; Elsevier: Amsterdam, 1985; p 130.

Separation of free and protein-bound label using a restricted-access reversed-phase support requires rather hydrophobic label for efficient retention. Future research is devoted to alternative separation techniques to achieve the same goal for rather polar labels. The use of short columns, however, is advantageous with respect to band broadening, and the availability of restricted-access supports with different internal surface, e.g., ion-exchange functionalities, should extend the range of suitable labels.

From a theoretical point of view, the present method is applicable to all those bioaffinity interactions that are characterized by high binding constants and high association and small dissociation rate constants. Particularly the magnitude of the dissociation rate constant plays a crucial role. If the dissociation rate contant is too high, it is likely that the excess of label added in the second step will displace ligand molecules bound to the affinity protein in the first step, rendering detection impossible. From the kinetic model described above, it can be derived that, for example, at a dissociation rate constant of 10^{-2} s^{-1} and a reaction time of 60 s for reaction 2, the signal is reduced by 50% compared to bioaffinity interaction systems with dissociation rates lower than 10^{-4} s^{-1}. Most dissociation rate constants for antibody–antigen interactions are well below 10^{-2} s^{-1},[19] allowing the design of ICD methods on the basis of the present detection principle.

ACKNOWLEDGMENT

We thank Prof. Dr. Karl-Siegfried Boos (University of Munich, Germany) for providing us with restricted-access support precolumns.

Received for review July 6, 1994. Accepted August 25, 1994.[⊗]

[⊗] Abstract published in *Advance ACS Abstracts,* October 1, 1994.

Anal. Chem. **1994,** *66,* 4302–4307

Time-Resolved Immunofluorometric Determination of Specific mRNA Sequences Amplified by the Polymerase Chain Reaction

Susan Bortolin and Theodore K. Christopoulos*

Department of Chemistry and Biochemistry, University of Windsor, 401 Sunset Avenue, Windsor, Ontario, N9B 3P4, Canada

We report a highly sensitive time-resolved immunofluorometric method for quantification of polymerase chain reaction (PCR)-amplified mRNA sequences. The PCR primers are labeled at their 5′ ends, one with biotin and the other with a hapten. The modified primers are incorporated, during PCR, in the amplified product. The PCR product is captured, through its biotin moiety, to a streptavidin-coated solid phase and subsequently is detected with an alkaline phosphatase-labeled antibody. The phosphate ester of fluorosalicylic acid is used as a substrate. The fluorosalicylate produced forms a highly fluorescent ternary complex with Tb^{3+}–EDTA, which is measured by time-resolved fluorometry. We chose the determination of PCR-amplified chronic myelogenous leukemia-specific mRNA as a model system. mRNA molecules corresponding to 0.1 leukemic cell in the presence of 0.5 million normal cells may be detected (signal-to-background ratio of 1.5). The method provides a sensitive and rapid nonisotopic alternative to Southern blot and hybridization with radioactive probes.

The polymerase chain reaction[1,2] (PCR) is a unique analytical concept with enormous impact because it enhances (amplifies) exponentially the mass of the analyte of interest (a specific DNA fragment from a complex biological sample) before its detection.

DNA serves as the initial target for amplification. RNA amplification can be accomplished by first generating a complementary copy of DNA with reverse transcriptase.[3,4]

The advent of the polymerase chain reaction has facilitated the identification of point mutations, deletions, and insertions responsible for inherited disorders. Furthermore, it has made possible the detection of viral and bacterial nucleic acids present in very low concentrations in human body fluids and other biological specimens. As well, a challenging analytical problem in the diagnosis and monitoring of neoplastic disorders is the detection and quantification of a single or a few cancer cells in the presence of a vast excess of normal cells. This, in several cases, can be accomplished by amplifying DNA or RNA sequences that are specific and characteristic of the abnormal cells and subsequently analyzing the amplified fragments.

The most commonly used methods for analysis of PCR products are qualitative and involve ethidium bromide staining of the DNA fragments after their separation by agarose gel electrophoresis. Polyacrylamide is also used and provides better detectability by ethidium staining because the gels are thinner. Dot blot or Southern blot followed by hybridization with specific radioactive oligonucleotide probes is also widely used. Both are sensitive but qualitative and time-consuming techniques. For several applications quantitative analysis of PCR products is desirable. Recently, a time-resolved fluorometric method for quantitation of PCR products in agarose gels was described.[5] The method uses a PCR primer labeled with the Eu^{3+} chelator 4,7-bis(chlorosulfophenyl)-1,10-phenanthroline-2,9-dicarboxylic acid. The PCR products are analyzed by agarose gel electrophoresis, stained with Eu^{3+}, and measured by scanning with a time-resolved fluorometer. High-performance liquid chromatography has also been used to separate and quantify the PCR products.[6]

Other nonisotopic methods for analyzing PCR products involve incorporation of primers that are labeled with an "affinity molecule" (such as biotin) and a "detection molecule". Thus, the double-labeled products can be captured on a solid phase (microtitration wells, beads, etc.) and then linked to a nonisotopic detection system.[7] Biotin may be used either as an affinity molecule (with an avidin-coated solid phase) or as a detection molecule in combination with (strept)avidin, labeled with an enzyme[7,9,10] or a fluorescent Eu^{3+} chelate.[8] Immobilized oligonucleotide probes may be used alternatively to capture the labeled amplified product.[9] Sandwich hybridization assays have also been reported[10] where an unlabeled PCR product is allowed to hybridize, simultaneously, with an immobilized probe and a detection probe.

In this paper, a new method is presented for the quantitative analysis of PCR products. The PCR primers are first labeled at their 5′ ends, one with biotin and the other with a hapten (digoxigenin). Both primers are incorporated in the amplified product during PCR. The double-labeled amplified product is added directly (without prior purification) to microtitration wells coated with streptavidin. The amplified fragment is captured on

(1) Mullis, K. B.; Faloona, F. A. *Methods Enzymol.* **1987,** *155,* 335–350.
(2) Gibbs, R. A. *Anal. Chem.* **1990,** *62,* 1202–1214.
(3) Wang, A. M.; Doyle, M. V.; Mark, D. F. *Proc. Natl. Acad. Sci. U.S.A.* **1989,** *86,* 9717–9721.
(4) Noonan, K. E.; Beck, C.; Holzmayer, T. A.; Chin, J. E.; Wunder, J. S.; Andrulis, I. L.; Gazdar, A. F.; Willman, C. L.; Griffith, B.; Von Hoff, D. D.; Robinson, I. B. *Proc. Natl. Acad. Sci. U.S.A.* **1990,** *87,* 7160–7164.
(5) Chan, A.; Diamandis, E. P.; Krajden, M. *Anal. Chem.* **1993,** *65,* 158–163.
(6) Zeillinger, R.; Schneeberger, C.; Speiser, P.; Kury, F. *BioTechniques* **1993,** *15,* 89–95.
(7) Kemp. D. J.; Smith, D. B.; Foote, S. J.; Samaras, N.; Peterson. M. G. *Proc. Natl. Acad. Sci. U.S.A.* **1989,** *86,* 2423–2427.
(8) Dahlen, P. *Anal. Biochem.* **1987,** *164,* 78–83.
(9) Loeffelholz, M. J.; Lewinski, C. A.; Silver, S. R.; Purohit, A. P.; Herman, S. A.; Buonagurio, D. A.; Dragon, E. A. *J. Clin. Microbiol.* **1992,** *30,* 2847–2851.
(10) Keller. G. H.; Huang, D. P.; Manak, M. M. *Anal. Biochem.* **1989,** *177,* 27–32.

0003-2700/94/0366-4302$04.50/0 © 1994 American Chemical Society

the solid phase through its biotin moiety and subsequently is detected with an alkaline phosphatase-labeled antibody. The phosphate ester of fluorosalicylate (FSAP) is used as the substrate. Fluorosalicylate, produced by alkaline phosphatase-catalyzed hydrolysis of FSAP, forms a highly fluorescent complex with Tb^{3+}–EDTA[11–13] at a pH of 12.5. The complexes are measured by time-resolved fluorometry. The method has been applied to the determination of PCR-amplified chronic myelogenous leukemia-specific mRNA. The proposed methodology successfully combines the advantages of the polymerase chain reaction and time-resolved fluorometry.[14]

MATERIALS AND METHODS

Instrumentation. The CyberFluor 615 immunoanalyzer (CyberFluor Inc., Toronto, ON, Canada), a time-resolved fluorometer, was used for measuring the fluorescence of Tb^{3+} solutions. PCR experiments were performed with the Perkin-Elmer Cetus DNA thermal cycler (Perkin-Elmer, Norwalk, CT).

Materials. All media and cell culture reagents were obtained from Gibco Laboratories Life Technologies Inc. (Gaithersburg, MD). Cells were grown in 25-mL polystyrene culture flasks obtained from Corning (Corning, NY).

K562 cells, a Philadelphia chromosome positive cell line, were obtained from the American Type Culture Collection (ATCC No. CCL 243, Rockville, MD) and were cultured in suspension in media consisting of 90% RPMI 1640 with L-glutamine, 10% fetal bovine serum (FBS), 50 KU/L penicillin, and 50 mg/L streptomycin. HL-60, a human promyelocytic leukemia cell line negative for the Philadelphia chromosome, was also obtained from ATCC (No. CCL 240). HL-60 cells were grown in suspension, in media consisting of 80% RPMI 1640 with L-glutamine, 20% FBS, 50 KU/L penicillin, and 50 mg/L streptomycin. Magnetic polystyrene beads (2.8 μm in diameter) with oligo$(dT)_{25}$ covalently attached to their surface as well as the magnetic particle concentrator (MPC-E), used in the isolation of mRNA, were purchased from Dynal (Oslo, Norway). Digoxigenin-3-*O*-methylcarbonyl-ϵ-aminocaproic acid *N*-hydroxysuccinimide ester (NHS-DIG), polyclonal anti-digoxigenin antibody (from sheep) Fab fragments conjugated to alkaline phosphatase (750 units/mL of conjugate), human placental ribonuclease inhibitor, "blocking reagent" (catalog No. 1096 176), and bovine serum albumin (BSA) were obtained through Boehringer (Laval, Quebec, PQ, Canada). Sulfosuccinimidyl 6-(biotinamido)-hexanoate (NHS-LC-Biotin) was from Pierce (Rockford, IL). Deoxyribonucleotides (dNTP) and Sephadex G-25 columns (NAP-5) were from Pharmacia-LKB (Montreal, Quebec, PQ, Canada). Moloney murine leukemia virus reverse transcriptase was from Gibco. Terbium chloride hexahydrate was obtained from Aldrich Chemical Co. (Milwaukee, WI). Streptavidin, diethyl pyrocarbonate, and mineral oil were from Sigma (St. Louis, MO). The phosphate ester of 5-fluorosalicylic acid (FSAP) was from CyberFluor Inc. The Bio-ladder DNA markers used in agarose gel electrophoresis of PCR products were from Biosynthesis Inc. (Lewisville, TX). Opaque, flat-bottom polystyrene microtitration wells, Microlite 2, were obtained from Dynatech Laboratories Inc. (Chantilly, VI).

Four oligonucleotide sequences were used in this work as PCR primers (synthesized by Biosynthesis Inc.): (a) 5′-CAGTGCAACGAAAAGGTTGGGGTC-3′, a 24-mer complementary to ABL exon II, which serves as the 3′ primer for PCR I; (b) 5′-TTTCAGAAGCTTCTCCCTGAC-3′, a 21-mer homologous to BCR exon 2, which serves as the 5′ primer of the first PCR (PCR I); (c) 5′-NH_2-GGAGCTGCAGATGCTGACCAAC-3′, a 22-mer homologous to BCR exon 2, as previously described;[15] (d) 5′-NH_2-TCAGACCCTGAGGCTCAAAGTC-3′, a 22-mer complementary to ABL exon II (from ref 15). Oligonucleotides c and d serve as primers for the second PCR (PCR II) and carry at their 5′ end a free amino group to allow for subsequent labeling reactions.

Solutions. A stock 10^{-2} mol/L 5-fluorosalicylic acid phosphate ester solution was prepared by dissolving 4.7 mg of the compound in 2 mL of a 0.1 mol/L NaOH solution. This solution was stored at 4 °C. Fresh FSAP substrate solutions were prepared just before use by diluting 10-fold the stock in the substrate buffer. The substrate buffer contained 1 mmol/L $MgCl_2$, 0.1 mol/L NaCl, and 0.1 mol/L tris(hydroxymethyl)aminomethane (Tris), pH 9.5. The "developing solution" contained 2 mmol/L $TbCl_3$, 3 mmol/L EDTA, 1 mol/L Tris, and 0.4 mol/L NaOH. The phosphate-buffered saline (PBS) was a 10 mmol/L sodium phosphate, 1.76 mmol/L potassium phosphate, 0.14 mol/L NaCl and 2.7 mmol/L KCl solution, pH 7.4. The transcription buffer contained 250 mmol/L Tris-HCl, 375 mmol/L KCl, and 15 mmol/L $MgCl_2$, pH 8.3. The wash solution contained 50 mmol/L Tris, pH 7.4, 0.15 mol/L NaCl, and 0.1% (v/v) Tween 20.

All solutions used in mRNA purification and cDNA synthesis were prepared with diethylpyrocarbonate-treated water[16] and all containers, pipets and pipet tips were autoclaved to eliminate ribonuclease activity.

mRNA Isolation and cDNA Synthesis. mRNA was isolated from 1 million cells using 200 μg of magnetic beads.[17] The beads were pipeted in a microcentrifuge tube and washed twice with 400 μL of PBS and once with 400 μL of binding buffer consisting of 1 mol/L LiCl, 20 mmol/L Tris, pH 7.5, 2 mmol/L EDTA, and 0.4% sodium dodecyl sulfate. Finally, they were resuspended in 100 μL of binding buffer. The cells were washed three times with PBS in a microcentrifuge tube and then centrifuged at 12000*g* for 2 min. The supernatant was removed, and 100 μL of lysis buffer (0.14 mol/L NaCl, 1.5 mmol/L $MgCl_2$, 10 mmol/L Tris, pH 8.6, 0.5% Nonidet P-40, 1 mmol/L dithiothreitol) and 25 units of ribonuclease inhibitor were added to the pellet and mixed thoroughly. The mixture was left on ice for 1 minute and then centrifuged at 12000*g* for 2 min to remove the nuclei and cell debris. The supernatant was then transferred into the microcentrifuge tube containing the magnetic beads. The cell extract–magnetic bead mixture was incubated at room temperature for 5 min to allow the mRNA to hybridize with the immobilized oligo$(dT)_{25}$. The beads were then separated from the solution using the MPC-E magnetic concentrator. The supernatant was discarded, and the beads were washed at least three times with 400 μL of a buffer containing 0.15 mol/L LiCl, 10 mmol/L Tris, pH 7.5 and 2 mmol/L EDTA in order to completely remove any other

(11) Evangelista, R. A.; Pollak, A.; Gudgin-Templeton, E. F. *Anal. Biochem.* **1991,** *197,* 213–224.
(12) Christopoulos, T. K.; Diamandis, E. P. *Anal. Chem.* **1992,** *64,* 342–346.
(13) Papanastasiou-Diamandi, A.; Christopoulos, T. K.; Diamandis, E. P. *Clin. Chem.* **1992,** *38,* 545–548.
(14) Diamandis, E. P.; Christopoulos, T. K. *Anal. Chem.* **1990,** *62,* 1149A–1157A.
(15) Kawasaki, E. S.; Clark, S. S.; Coyne, M. Y.; Smith, S. D.; Champlin, R.; Witte, N. O.; McCormick, F. P. *Proc. Natl. Acad. Sci. U.S.A.* **1988,** *85,* 5698–5702.
(16) Sambrook, J.; Fritsch, E. F.; Maniatis, T. *Molecular Cloning. A Laboratory Manual,* 2nd ed.; Cold Spring Harbor Laboratory Press: Cold Spring Harbor, NY, 1989.
(17) Spurkland, A. *Trends Genet.* **1992,** *8,* 225–226.

cellular RNA and protein. Finally, the beads were resuspended in 10 μL of 2 mmol/L EDTA and incubated at 65 °C for 2 min. The beads were again separated from solution, and the supernatant was quickly removed and added to the reverse transcription reaction mixture consisting of 4 μL of transcription buffer, 2 μL (400 units) of reverse transcriptase, 2 μL of 0.1 mol/L dithiothreitol, 1 μL of 20 mmol/L dNTP, 0.7 μL (40 units/μL) of ribonucleasease inhibitor, and 1 μL of 10 μmol/L PCR I 3′ primer (primer a). The mixture was incubated at 37 °C for 1 h. Upon completion of the reaction and prior to PCR amplification, the cDNA-containing tubes were incubated at 95 °C for 4 min to inactivate the reverse transcriptase.

Labeling of PCR II Primers. The PCR II 5′ primer (primer c) was labeled with a 500 molar excess of NHS-LC-biotin at pH 9.1. NHS-LC-biotin contains a six-carbon-atom spacer between the *N*-hydroxysuccinimidyl group and the biotin moiety. This allows the binding of the biotinylated oligonucleotide to streptavidin without steric hindrance.[18] To 0.1 mL of a 0.1 mmol/L solution of the primer in water we added 20 μL of 0.5 mol/L carbonate buffer, pH 9.1. Sixty microliters of an 84 mmol/L solution of NHS-LC-biotin in water was then added to the primer solution, and the reaction was allowed to proceed for 2 h at room temperature. The labeled primer was diluted to 0.5 mL with water and purified by size exclusion chromatography on Sephadex G-25 disposable columns (NAP-5). The column was equilibrated with 10 mL of a 10 mmol/L sodium phosphate buffer, pH 6.8. The labeled primer solution was diluted to 0.5 mL with water, loaded onto the column, and eluted with 1 mL of the same buffer. The purification step was repeated once more to remove any free biotin. The final concentration of the purified biotinylated primer was 6.7 μmol/L.

The PCR II 3′ primer (primer d) was labeled with a 500 molar excess of NHS-DIG at pH 9.1. To 0.1 mL of a 0.1 mmol/L solution of the primer in water we added 20 μL of 0.5 mol/L carbonate buffer, pH 9.1, and 33 μL of a 0.15 mol/L solution of NHS-DIG in dimethyl sulfoxide. The solution was incubated for 2 h at room temperature. The volume was then brought to 0.5 mL with water, and the labeled primer was purified only once by using the NAP-5 column as described above. The final concentration of the purified DIG-labeled primer was 10 μmol/L.

Polymerase Chain Reaction. Prior to the PCR experiments, the pipets, pipet tips, PCR buffer, and mineral oil (in glass containers) were irradiated with ultraviolet light in a laminar hood for at least 1 h, to destroy traces of contaminating DNA.[19] Furthermore, the PCR experiment and the analysis of PCR products were performed in separate rooms to avoid contamination. PCR I was carried out in a total volume of 100 μL consisting of 40 mmol/L KCl, 2 mmol/L $MgCl_2$, 40 mmol/L Tris, pH 8.3, 80 mg/L BSA, 0.5 μmol/L of each of the 5′ and 3′ PCR I primers, and 40 μmol/L of each deoxyribonucleotide. The sample volume was 10 or 20 μL. Mineral oil was layered over the reaction mixture to prevent evaporation. PCR was initiated using the "hot start" protocol.[20] The reaction mixture was first heated to 95 °C for 5 min and then 2.5 units of Taq polymerase was added. The reaction was carried out for 25 cycles, the conditions of each cycle being denaturation at 95 °C for 20 s, primer annealing at 60 °C for 15 s, and primer extension at 72 °C for 1 min. Upon completion of all 25 cycles, the reaction mixture was held at 72 °C for 10 min to allow the final products to reanneal and then was cooled at 4 °C. The PCR I product was diluted 50-fold in water, and 5 μL was pipeted into the PCR II mixture. PCR II was also performed in a total volume of 100 μL for 30 cycles. The biotinylated 5′ primer (0.5 μmol/L) and the DIG-labeled 3′ primer (0.5 μmol/L) were employed. All other reagents and conditions were as in PCR I.

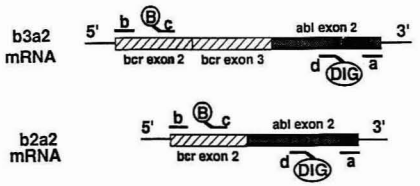


Figure 1. Structure of chronic myelogenous leukemia-specific mRNAs (b_3a_2 and b_2a_2) and the location of PCR I and PCR II primers used throughout this work. Primer a is used for the reverse transcription reaction. Primers a and b are used in PCR I. Primers c (biotinylated) and d (labeled with the hapten digoxigenin) are used in PCR II.

Preparation of Streptavidin-Coated Microtitration Wells. The coating solution was a 1.4 mg/L solution of streptavidin in PBS, pH 7.4. Opaque polystyrene microtitration wells were coated, by physical adsorption, overnight at room temperature with 100 μL of coating solution, then sealed with clear tape, and stored at 4 °C. Coated wells are stable for at least 1 month.

Determination of PCR Products by Time-Resolved Fluorescence Immunoassay. Streptavidin-coated wells were washed four times with wash buffer (see under Solutions) and blocked for 30 min with 200 μL of a 1% (w/v) solution of blocking reagent in 0.1 mol/L maleate, 0.15 mol/L NaCl, pH 7.5. The wells were again washed four times, and 100 μL of PCR II product, diluted 25-fold in PBS containing 0.1% Tween 20, was pipeted into each well in duplicate. After 30-min incubation (shaking at room temperature), the wells were washed four times. Then, 100 μL of 0.3 unit/mL alkaline phosphatase-labeled anti-DIG antibody, diluted in the wash buffer, was added and incubated for 30 min. Following this incubation, the wells were washed four times and 100 μL of 1 mmol/L FSAP, diluted in substrate buffer, was added to each well and incubated for 30 min at room temperature. Subsequently, 100 μL of developing solution was added to each well and shaken for 1 min. The fluorescence was measured with the time-resolved fluorometer. Excitation and emission wavelengths were set at 337 and 615 nm, respectively.

RESULTS AND DISCUSSION

Chronic myelogenous leukemia (CML) is characterized by the presence of the Philadelphia chromosome, a translocated chromosome 22. The abnormality involves the movement of most of the abl protooncogene from chromosome 9 to the bcr gene of chromosome 22. Expression of the fused genes results in a specific 8.5-Kb mRNA, characteristic of the disease.[21]

The mRNA structure at the bcr–abl gene fusion region,[15] as well as the location of PCR I primers (a and b) and PCR II primers (c and d) used in this work, are shown in Figure 1.

(18) Diamandis, E. P.; Christopoulos, T. K. *Clin. Chem.* **1991,** *37,* 625–636.
(19) Kwok, S.; Higuchi, R. *Nature* **1989,** *339,* 237–238.
(20) D'Aquila, R. T.; Bechtel, L. J.; Videler, J. A.; Eron, J. J.; Gorczyca, P.; Kaplan, J. C. *Nucleic Acids Res.* **1991,** *19,* 3749.
(21) Freireich, E. J.; Kantarjian, H. *Leukemia: Advances in Research and Treatment;* Kluwer Academic Publishers: Boston, MA, 1993.

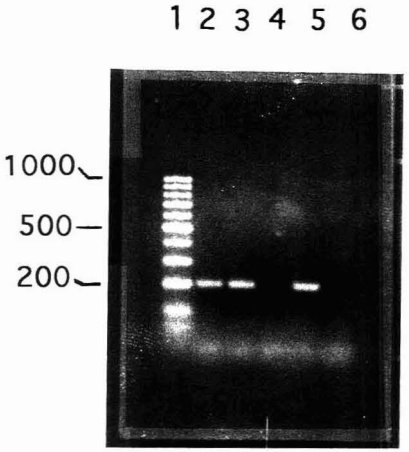


Figure 2. Agarose gel (2%) electrophoresis and ethidium bromide staining of 10 μL of PCR II product generated from 10 000 K562 cells as described in the text: (lane 1) molecular weight markers. The length in base pairs is shown on the left side. Bands are every 100 bp starting from 1000 bp; (lane 2) PCR II product with PCR I annealing temperature at 65 °C; (lane 3) PCR II product with PCR I annealing temperature of 60 °C; (lane 4) negative control without PCR template; (lane 5) PCR II with PCR I annealing temperature of 55 °C; (lane 6) same as in lane 4. A single band is always observed after PCR II at the expected size (200 bp).

Two types of mRNA can be formed as a result of the Philadelphia translocation.[22-24] Either the bcr exon 3 is joined to abl exon II (b_3a_2 mRNA) or the bcr exon 2 is joined to abl exon II (b_2a_2 mRNA). Because the two pairs of PCR primers are located on bcr exon 2 and abl exon II, the present method is applicable to both types of mRNA. Typically, mRNA from 1 million cells is isolated directly by using oligo$(dT)_{25}$-coated magnetic beads (a 20-min protocol). The cell lysis buffer employed disrupts only the cell membrane whereas the nuclei (containing DNA, protein, and small nuclear RNA) remain intact. The nuclei are removed by centrifugation, and the cytoplasm is mixed with the magnetic beads. At a high ionic strength, the poly(A) tail at the 3′ end of mRNA hybridizes with the oligo$(dT)_{25}$ whereas protein, rRNA, and tRNA are washed out. Subsequently, the mRNA is recovered with a low ionic strength buffer at 65 °C and is transcribed immediately. Alternatively, the total RNA could be used as a template but its isolation is more tedious and lengthy.[16]

The isolated mRNA is first converted to single-stranded cDNA, which can then be amplified by PCR. The reverse transcription reaction is carried out by using the 3′ PCR primer (complementary to abl exon II) instead of an oligo(dT) primer commonly employed. This enhances the specificity of the reaction since only the useful mRNA fragment is transcribed as opposed to total mRNA in the latter case.

The PCR I is performed with unlabeled primers a and b and produces a 308-bp DNA fragment when b_3a_2 mRNA from K562 cells serves as the template. Subsequently, the PCR II is performed with a biotinylated primer c and a DIG-labeled primer d. PCR II generates a 200-bp double-labeled product for the K562 mRNA. The PCR II amplified product is captured through its biotin moiety on a streptavidin-coated solid phase and is detected with an ALP-labeled antibody directed against the digoxigenin moiety. Unincorporated biotinylated primer is also captured on the solid phase but is not detected. Unincorporated DIG-labeled primer is washed out before detection.

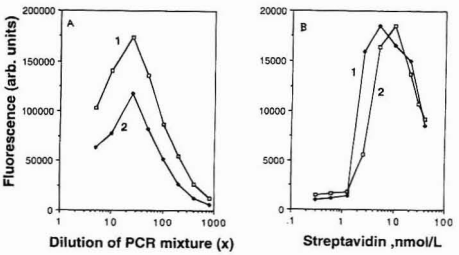


Figure 3. (A) Optimization of the dilution of the double-labeled PCR II product prior to its addition to microtitration wells coated with 0.14 μg of streptavidin. PCR II product representative of (1) 10 000 and (2) 100 cells. (B) Optimization of streptavidin concentration in experiments intending to enhance the capacity of the solid phase. (1) Streptavidin, at various concentrations, is first incubated with the PCR II product and then added to wells coated with 0.1 μg of biotinylated albumin. (2) Streptavidin, at various concentrations, is first incubated with the same solid phase as in (1) and then the PCR II product is added. For details,see text.

The specificity of the proposed system is mainly based on the selection of appropriate PCR conditions such that only the expected amplification product is obtained. Nonspecific, double-labeled DNA fragments, if present, would also be measured by our assay, whereas single-labeled nonspecific DNA fragments give no signal. For these reasons, the nested PCR approach, as opposed to a single PCR, was chosen. When only one round of PCR was performed, some nonspecific DNA fragments (in particular at 400 bp) were present along with the expected product. With nested PCR, a single DNA fragment is always obtained (Figure 2). The PCR I product is diluted 50-fold prior to its addition to the PCR II to ensure that the concentration of the PCR I primers is sufficiently reduced to allow PCR II to proceed with the labeled primers. The "hot start" protocol used, in which the Taq polymerase is not added until the reaction mixture reaches a temperature of 95 °C, serves to reduce the nonspecific amplification due to mispriming events occuring at lower temperatures.

The effect of the annealing temperature on the purity and yield of the PCR product was studied at 55, 60, 65, and 72 °C. Amplified DNA was analyzed by both agarose gel electrophoresis and immunofluorometry. It was found that an annealing temperature of 60 °C held for 15 s is optimal. Higher annealing temperatures resulted in a significant decrease of the fluorescence because of a reduced reaction yield. Similar studies were performed for the primer, deoxynucleotide, and Mg^{2+} concentrations. Concentrations of 0.5 μmol/L of each primer, 40 μmol/L of each dNTP, and 2 mmol/L Mg^{2+} appeared to yield the most specific PCR product. A typical electrophoretogram of the final amplified product (after PCR II) is shown in Figure 2.

The dilution of the PCR product prior to its addition to the streptavidin-coated microtitration wells was optimized, and the

(22) Heisterkamp, N.; Stam, K.; Groffen, J.; de Klein, A.; Grosveld, G. *Nature (London)* **1985,** *315,* 758–761.
(23) Grosveld, G.; Verwwoerd, T.; van Agthoven, T.; de Klein, A.; Ramchandran, K. L.; Heisterkamp, N.; Stam, K.; Groffen, J. *Mol. Cell Biol.* **1986,** *6,* 607–616.
(24) Shtivelman, E.; Lifshitz, B.; Gale, R. P.; Roe, B. A.; Canaani, E. *Cell* **1986,** *47,* 277–284.

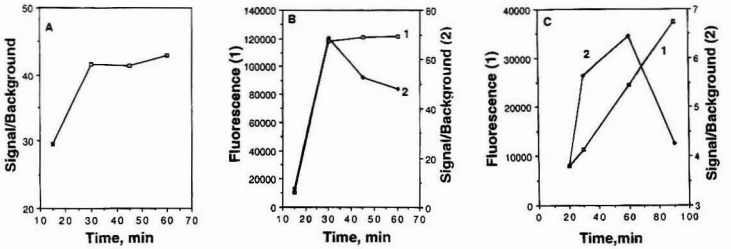


Figure 4. Optimization of the proposed immunofluorometric assay. The signal-to-background ratio is the ratio of the fluorescence obtained with PCR II product present and not present. (A) Optimization of the incubation time for the capture of the double-labeled PCR II product on streptavidin-coated solid phase. The product is captured through its biotin moiety and then is detected by using an anti-digoxigenin antibody labeled with alkaline phosphatase. Fluorosalicyl phosphate serves as the substrate. Concentrations and incubation conditions for all reagents are given in the text. (B) Optimization of the incubation time for the binding of the alkaline phosphatase-labeled anti-digoxigenin antibody. Line 1 represents the fluorescence vs time and line 2 represents the signal-to-background ratio vs time. (C) Optimization of the substrate incubation time. Lines 1 and 2 are defined as in B).

results are presented in Figure 3A. As the amount of PCR product added per well increases the signal also increases. However, when the binding capacity of the solid phase is exceeded, the fluorescence decreases due to competition between the excess biotinylated primer and the double-labeled PCR product. Because of its smaller size, the free primer is able to diffuse faster, thereby reducing the available streptavidin sites for the product. The optimal dilution of the PCR mixture is 25-fold (4 μL of the original PCR mixture per well), which corresponds to a binding capacity of 2 pmol of biotinylated DNA (i.e., primer and product) per well. Various buffers were tested as diluents for the PCR product. It was found that there is no significant difference in the observed fluorescence when the "DNA capture" step is carried out in the pH range of 5.5–8.0.

We investigated various ways of enhancing the binding capacity of the solid phase. Human serum albumin (HSA) and BSA were exhaustively biotinylated by reacting with a 250 molar excess of NHS-LC-Biotin in 0.1 mol/L carbonate buffer, pH 9.1. The excess biotin was then removed by dialysis. Microtitration wells were coated with 100 μL of a 1 mg/L solution of the biotinylated albumin. The PCR product was first incubated with an appropriate concentration of streptavidin for 30 min. Then, 100 μL of the mixture was pipeted per well. Streptavidin has four binding sites for biotin. Careful optimization of streptavidin concentration was required because, if the biotinylated DNA is in excess, then there are no available sites on streptavidin for binding to the solid phase and the complex is washed out. In Figure 3B(1), the effect of streptavidin concentration on the fluorescence is shown. Alternatively, streptavidin and PCR product were added simultaneously to biotinylated albumin-coated solid phase and incubated for 30 min. The optimization of streptavidin concentration is shown in Figure 3B(2). Experiments were also performed where streptavidin was polymerized with glutaraldehyde before coating. All these experiments gave no significant improvement of the signal over the direct coating of the solid phase with streptavidin.

The effect of incubation time of the diluted PCR product with the streptavidin-coated solid phase was studied in the range of 15–60 min (see Figure 4A). It was found that a plateau in the signal-to-background ratio is obtained after a 30-min incubation. Furthermore, the incubation time for the alkaline phosphatase-labeled anti-DIG antibody was studied in the range of 15–60 min (Figure 4B). The signal (Figure 4B(1)) remains constant after a 30-min incubation. However, longer incubation times result in an increased nonspecific binding of the antibody to the solid phase thereby decreasing the signal-to-background ratio (Figure 4B(2)). We kept a 30-min incubation time as the optimum. The incubation time for the alkaline phosphatase reaction was studied in the range of 20–90 min (see Figure 4C). A continuous increase of the signal (Figure 4C(1)) with time is observed. However, after 60 min of incubation, the increase in the background is such that the signal-to-background ratio decreases (Figure 4C(2)).

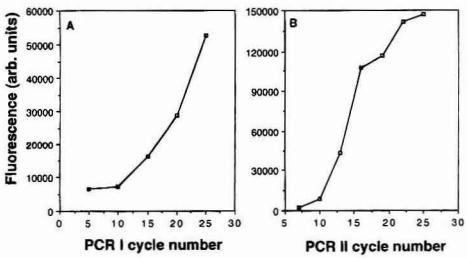


Figure 5. Study of the variation of the fluorescence with the number of PCR I and PCR II cycles. (A) mRNA corresponding to 1000 K562 cells was amplified with varying number of PCR I cycles. The PCR I products were diluted 50 times in water and 5 μL were applied to PCR II for 25 cycles. PCR II products were captured on streptavidin coated wells and detected with alkaline phosphatase-labeled anti-digoxigenin antibody. FSAP was used as substrate. (B) mRNA produced from 10000 K562 cells was amplified with 25 cycles of PCR I. The PCR I product was diluted as above and 5 μL were reamplified with varying number of PCR II cycles. PCR II products were detected as above.

Figure 5 shows the effect of the number of PCR I cycles (Figure 5A) and PCR II cycles (Figure 5B) on the fluorescence. The fluorescence increases with the number of cycles for both PCR I and PCR II. PCR II began to plateau at 25 cycles. The plateau is mainly due to competition between primer–template complex formation and template reannealing as well as to saturation of the Taq polymerase by the excessive amount of product.

The sensitivity and specificity of the optimized protocol was investigated as follows. We prepared mixtures of mRNA–cDNA from K562 cells (Philadelphia chromosome positive) and HL-60 cells (negative for the Philadelphia chromosome). Samples

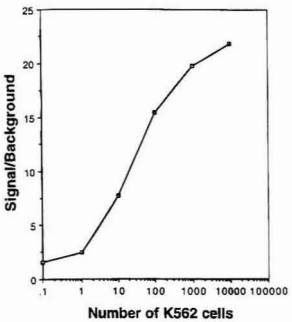


Figure 6. Mixtures containing mRNA from 0.1 to 10 000 K562 cells in the presence of 500 000 HL-60 cells analyzed with the proposed assay (i.e., PCR I, PCR II and time-resolved immunofluorometric detection of the amplified product). The signal-to-background ratio was then plotted vs the number of K562 cells. It can be seen that a sample containing mRNA corresponding to 0.1 cell gives a signal-to-background ratio of 1.50.

containing mRNA corresponding to 0, 0.1, 1.0, 10, 100, 1000, and 10 000 K562 cells in the presence of 500 000 HL-60 cells were analyzed with the proposed system. The results are presented in Figure 6. mRNA corresponding to 0.1 leukemic cell in the presence of 0.5 million "normal" cells can be detected (signal-to-background ratio of 1.5). Since only $^1/_{25}$th of the original PCR mixture was used for analysis, the fluorescence signal represents amplified product from less than 0.1 cell. The quantitative nature of the proposed method can be deduced by the increase in fluorescence with the number of leukemic cells in the sample.

A highly sensitive, PCR-based method for detecting bcr–abl mRNA hybrids has already been reported.[15] The method involves separation of the amplified fragments by electrophoresis, followed by Southern blotting and hybridization with ^{32}P-labeled oligonucleotide probes that are complementary to bcr–abl junction sequences. The sensitivity reported is "less than one cell" in the presence of 1 million HL-60 cells. The method proposed here avoids all these post-PCR steps and uses nonisotopic detection without compromising the sensitivity.

Recently an assay for p210, the 210-kDa protein product of the bcr–abl fused gene, was reported as an additional test for diagnosis and monitoring of CML patients.[25] The method is based on polyacrylamide gel electrophoresis of cell lysates, followed by Western blotting, reaction with a monoclonal anti-abl antibody, and detection of the immunocomplexes with horseradish peroxidase-labeled goat anti-mouse antibody. The method can detect about 2000 K562 cells in the presence of 1 million normal cells.

In conclusion, combination of the polymerase chain reaction with time-resolved immunofluorometric determination of the amplified products provides a powerful quantitative analytical system which could replace procedures such as gel electrophoresis, Southern blot, and hybridization for the analysis of PCR products. Due to its sensitivity, the proposed system can be used to monitor expression levels of specific mRNA molecules in a very small number of cells and from small amounts of tissue samples, which may be valuable in the diagnosis of cancer, metabolic disorders, and infectious diseases.

ACKNOWLEDGMENT

This work was supported by grants to T.K.C. from the National Science and Engineering Research Council of Canada (NSERC), The Van Slyke Society of the American Association for Clinical Chemistry (AACC), and the Research Board of the University of Windsor.

Received for review July 8, 1994. Accepted September 15, 1994.[⊗]

[⊗] Abstract published in *Advance ACS Abstracts,* October 15, 1994.

(25) Guo, J. Q.; Lian, J. Y.; Xian, Y. M.; Lee, M. S.; Deisseroth, A. B.; Stass, S. A.; Champlin, R. E.; Talpaz, M.; Wang, J. Y. J.; Arlinghaus R. B. *Blood* **1994,** *83,* 3629–3637.

Anal. Chem. **1994,** *66,* 4308–4315

Two-Dimensional High-Performance Liquid Chromatography Using Monodisperse Polymer Beads Containing Segregated Chemistries Prepared by Pore Size Specific Functionalization. Single-Column Combinations of Size Exclusion or Ion Exchange with Reversed-Phase Chromatography

Vladimir Smigol, Frantisek Svec, and Jean M. J. Fréchet*

Baker Laboratory, Department of Chemistry, Cornell University, Ithaca, New York 14853-1301

Separation media for the complete separation of complex samples that require a combination of size exclusion or ion-exchange with reversed-phase chromatographic modes in a single column have been prepared from size monodisperse 10 μm poly(glycidyl methacrylate-*co*-ethylene dimethacrylate) beads using a pore size specific functionalization process. To achieve the first combination of chromatographic modes, the large pores of the beads were selectively hydrolyzed to diols using aqueous poly(styrenesulfonic acid), while highly hydrophobic octadecyl groups were introduced into the small pores by reaction of the remaining epoxide groups with octadecylamine. These beads provide excellent protein recoveries and may be used for the direct injection separation of samples containing both hydrophilic proteins and hydrophobic drugs. Beads containing diethylamino groups in the large pores and octadecyl functionalities in the small pores were also prepared by size-selective modification. A plot of log *k'* against ionic strength of the mobile phase for these beads shows the absence of hydrophobic interactions and documents the clean ion-exchange mechanism of protein separation. Examination of the small pores in both types of separation media confirmed that their hydrophobicity was sufficient to allow the separations of small molecules in reversed-phase mode. Column packed with these dual-chemistry beads exhibited high efficiencies and were used successfully for the separations of proteins and alkylbenzenes or drugs.

Multidimensional chromatography provides access to dramatic improvements in peak capacity since capacity in a two-dimensional separation is equal to the product of peak capacities in both dimensions.[1] In addition, much better resolution is expected in the separation of complex mixtures.[2,3] Major fields of application for two-dimensional techniques are thin-layer chromatography and electrophoretic separations.[4] While two-dimensional separation is readily achieved with the planar medium of thin-layer chromatography by simply rotating the medium 90° after the first separation and proceeding with further elution, this approach cannot be used with a HPLC column. Therefore, chromatographic methods that involve column switching have been developed. A peak containing a class of compounds separated from the rest of the sample in the first column is directed into a second column where it is separated into its individual components.[4] For example, coupled size exclusion and reversed-phase columns have been used for the separation and detection of components in plant extracts[5,6] and in rubber stock.[6] Several columns may also be used to separate different families of compounds, but in this case the instrumentation becomes rather complex.

Stationary phases based on modified porous silica with both hydrophilic outer surface and hydrophobic pores (internal surface reversed-phase media, ISRP) have been developed by Pinkerton.[7] These columns allow the direct injection of complex matrices such as plasma, serum, saliva, or urine into a column for the determination of drugs and metabolites without any pretreatment, while also preventing the accumulation of proteins and the resultant clogging of the column. ISRP phases are prepared in a multistage process that begins with a complete hydrophobization of the entire surface of small-pore silica beads. In the next step, an enzyme that is totally excluded from the inner pores cleaves the hydrophobic moieties only at the *outer* surface of beads rendering it hydrophilic. The hydrophobic groups within the pores remain unchanged. In separation processes involving the ISRP packings, *all* proteins are eluted as one peak at V_i followed by the other separated analytes. Following this initial work, several varieties of these *restricted access media* have been developed.[8–10] The main advantage of these packings is that fouling of the beads by accumulation of

(1) Giddings, J. C. *J. High. Resolut. Chromatogr., Chromatogr. Commun.* **1987,** *10,* 319.
(2) Giddings, J. C. *Anal. Chem.* **1984,** *56,* 1258A.
(3) Little, E. L.; Jeansonne, M. S.; Foley, J. P. *Anal. Chem.* **1992,** *63,* 33.
(4) *Multidimensional Chromatography: Techniques and Applications.* Cortes, H. J., Ed.; M. Dekker: New York, 1990.
(5) Erni, F.; Frei, R. W. *J. Chromatogr.* **1978,** *149,* 561.
(6) Johnson, E. L.; Gloor, R; Majors, R. E. *J. Chromatogr.* **1978,** *149,* 571.
(7) Hagestam, I. H.; Pinkerton, T. C. *Anal. Chem.* **1985,** *57,* 1757.
(8) Pinkerton, T. C. *J. Chromatogr.* **1991,** *544,* 13.
(9) Haginaka, J. *Trends Anal. Chem.* **1991,** *10* (1), 17.

0003-2700/94/0366-4308$04.50/0 © 1994 American Chemical Society

proteins on their surface is prevented while small molecules penetrate the beads and are separated in normal fashion.

We have recently introduced the concept of pore size specific functionalization to prepare porous media in which pores within different size ranges may be endowed with different chemistries.[11-13] This concept relies on the use of catalysts with defined molecular volumes that are able to perform a chemical modification process only in those pores large enough to allow their access. Overall, control of the modification process relies on control of the hydrodynamic volume of the catalyst as opposed to the usual modification process for which kinetics factors are the sole consideration. The method is well suited for the preparation of separation media with pores modified according to their size and allows the preparation of beads with different chemistries segregated in different size pores.

This concept also adds a new perspective to chromatographic separation of complex samples. Its feasibility was first documented with the preparation of a separation medium for the direct-injection HPLC determination of drugs in biological fluids.[14] The concept of pore size specific modification was then extended with the preparation and use of a single packing in which hydrophobic interaction chromatography of proteins and reversed-phase chromatography of small molecules could proceed consecutively.[15]

While our earlier communication was focused on a medium with only phenyl surface chemistry that had different coverage levels segregated in different size pores (gradient of coverage density),[15] this report concerns separation media, in which totally different chemistries are localized separately in small and large pores, respectively (gradient of chemistries), and their application in HPLC separations of complex samples.

EXPERIMENTAL SECTION

Materials. A narrow molecular weight distribution sodium poly(styrenesulfonate) ($M_w = 5000$, $M_w/M_n = 1.09$) was obtained from Scientific Polymer Products, Inc. (Ontario, NY). Prior to its use, the sodium salt was converted to the free acid by an ion-exchange process using a AG 50W-X strong acid cation exchanger (Bio-Rad, Richmond, CA). Vitamin B_{12} (cyanocobalamin, MW 1356), cytochrome *c* (from bovine heart, MW 13 400), ribonuclease A (from bovine pancreas, MW 13 600), lysozyme (MW 14 100), myoglobin (from horse heart, MW 17 000), soya bean trypsin inhibitor (MW 22 500), carbonic anhydrase (from bovine erythrocytes, MW 29 000), chicken egg albumin (ovalbumin, Grade V, MW 45 000), bovine serum albumin (98–99%, MW 66 700), human serum albumin (essentially fat free, MW 69 000), conalbumin (from chicken egg white, Type I, MW 75 500), alcohol dehydrogenase (from yeast, MW 150 000), β-amylase (from sweet potatoes, MW 200 000), apoferritin (from horse spleen, MW 443 000), bovine thyroglobulin (MW 669 000), hemocyanin (from limulus polyphemus hemolymph, MW 3 750 000), bovine dried plasma, and the anticonvulsant drugs (procainamide, lidocain, carbamazepine, phenytoin, desipramine, phenobarbital) were purchased from Sigma. The hydrocarbon standards were obtained from Aldrich. All solvents were HPLC grade.

Polymer Beads. Uniformly sized 10-μm porous 60:40 vol % glycidyl methacrylate–ethylene dimethacrylate copolymer beads (resin **I**) were prepared by a modified shape template swelling and polymerization method described in detail elsewhere.[16,17] Cyclohexanol (60 vol %) was used as the porogenic solvent. The specific surface area was calculated from nitrogen sorption using the BET method (combined BET sorptometer and mercury porosimeter, Porous Materials Inc., Ithaca, NY). The pore size distribution, pore volume, and median pore diameter were calculated from the retention volume of polystyrene standards (Polymer Laboratories, Church Stretton, UK) in THF.[18] The content of epoxide groups was determined by volumetric titration.[14]

Preparation of the Separation Media. The beads containing multiple functionalities were prepared by the modification process shown in Scheme 1.

Pore Size Specific Hydrolysis of Epoxide Groups. The hydrolysis of resin **I** containing epoxide groups (Scheme 1, modification step a) was catalyzed with 1 wt.% aqueous solution of poly(styrenesulfonic acid) (MW 5000) containing 0.054 mol/L sulfonic groups. The epoxide resin (1.6 g) was placed in a 50 mL beaker, 10 mL of aqueous catalyst solution was added, and the beaker was sealed with Parafilm. The dispersion was stirred magnetically at ambient temperature for 48 h. The resulting, partly modified, beads A containing functionalities **II** were then filtered off on a fritted glass filter and washed with water until neutral, washed with acetone, and dried in vacuo at room temperature.

Aminolysis of Residual Epoxide Groups with Octadecylamine. Beads A (1.5 g) containing both vicinal hydroxyl groups **II** in large pores and residual epoxide groups in small pores were admixed to 5 g of molten octadecylamine in a 50-mL round-bottom flask at 70 °C, and the mixture was stirred for 16 h (modification step b). The reaction mixture was then diluted with 20 mL of 1,4–dioxane, stirred for 30 min, and filtered. The resulting beads B containing groups **III** were washed with dioxane and water. Any unreacted epoxide groups remaining due to steric constrains were hydrolyzed in 20 mL of 0.1 mol/L sulfuric acid at 60 °C for 4 h. The beads were filtered, washed with water and then with methanol, and dried.

The amino group content of the beads was 0.35 mmol/g as determined by elemental analysis of nitrogen as well as by an acid–base titration.

Reaction with Epichlorohydrin. Dry beads B from the previous reaction step were dispersed in 20 mL of water and stirred magnetically for 16 h. The excess water was removed on a fritted glass filter, and the beads were redispersed in 20 mL of 50 wt.% aqueous KOH and stirred for 1 h. After removal of the liquid, the beads were added to 40 mL of an epichlorohydrin–water (1:1) mixture and stirred at room temperature for 3 h (modification step c). The product was washed with water and acetone and dried to afford epoxidized beads C containing functionalities **IV** (1.12 mmol/g epoxide groups determined by volumetric titration).

Aminolysis of Epoxide Groups with Diethylamine. The epoxidized beads C (1.5 g) were placed in a 50-mL round bottom flask and 20 mL of diethylamine was added. After heating at reflux

(10) Anderson, D. J. *Anal. Chem.* **1993**, *65*, 434R.
(11) Fréchet, J. M. J. *Macromol. Chem., Macromol. Symp.* **1993**, *70/71*, 289.
(12) Smigol, V.; Svec, F.; Fréchet, J. M. J. *Macromolecules* **1993**, *26*, 5615.
(13) Svec, F.; Fréchet, J. M. J. *Adv. Mater.* **1994**, *6*, 342.
(14) Smigol, V.; Svec, F.; Fréchet, J. M. J. *J. Liquid Chromatogr.* **1994**, *17*, 891.
(15) Smigol, V.; Svec, F.; Fréchet, J. M. J. *Anal. Chem.* **1994**, *66*, 2129.
(16) Smigol, V.; Svec, F. *J. Appl. Polym. Sci.* **1992**, *46*, 1439.
(17) Smigol, V.; Svec, F. *J. Appl. Polym. Sci.* **1993**, *48*, 2033.
(18) Halasz, I.; Martin, K. *Angew. Chem., Int. Ed. Eng.* **1978**, *17*, 901.

(55 °C) for 6 h, the resin was filtered and washed with water (modification step d). Any remaining unreacted epoxide groups were again hydrolyzed in 20 mL of 0.1 mol/L sulfuric acid at 60 °C for 4 h to afford beads D containing functionalities **V**. Finally, the beads were filtered, washed with water and then with methanol, and dried. The beads contained 0.62 mmol/g groups **V**, as determined by elemental analysis of nitrogen after subtraction of the nitrogen introduced with octadecylamino groups.

High-Performance Liquid Chromatography. The properties of the beads prepared in this study were determined by chromatography carried out in a 300-mm × 7.8-mm i.d. or 50-mm × 8-mm i.d. stainless steel columns using a commercial HPLC chromatograph (IBM-Nicolet ternary gradient liquid chromatograph LC 9560) equipped with a Rheodyne 7125 loop injector and a Hewlett-Packard 1050 UV detector.

Protein Recovery. The protein recovery from the beads packed in a 100-mm × 8-mm i.d. column was measured upon isocratic elution at ambient temperature. Recovery was calculated as the percentage of the peak area of protein leaving the column with respect to the peak area of the same amount of the protein injected into a system from which the column was removed and the inlet and outlet capillaries were connected. The mobile phase was 0.15 mol/L sodium chloride in 0.15 mol/L phosphate buffer (pH 7) for the size exclusion mode, while 0.5 mol/L sodium chloride in 0.01 mol/L TRIS-HCl buffer solution (pH 7.6) was used for the ion-exchange mode . All other chromatographic conditions were identical for both modes: flow rate 1 mL/min, 10 mg/mL protein solution in buffer, injection 20 μL, detection 280 nm. The experimental error is less than 10%.

RESULTS AND DISCUSSION

Direct HPLC separations of complex biological samples either require a quite elaborate equipment that involves several columns, pumps, and valves or a less important part of the mixture is eluted as a single peak without any separation of its components. The dual-column two-dimensional HPLC technique falls in the first category[4] while the single-column separations that use the restricted access media represent the other group.[8–10] Obviously, the second approach that involves only a single column is simpler, and therefore, it is preferred in the separation of biological samples. However, this technique only provides limited information as the proteins are simply eluted in a single peak. The recently introduced[11–15] approach involving a single column packed with a separation medium that combines two segregated chemistries overcomes this limitation, separates all of the components of the mixture, and provides a more complete analysis.

Reversed-phase chromatography is the most frequently used separation mode for small hydrophobic compounds while biological macromolecules such as proteins are typically separated by size exclusion, ion-exchange, or hydrophobic interaction chromatography.[19] Therefore, a combination of reversed-phase chromatography with one of the other modes would be ideally suited for the separation of complex mixtures that contain both small molecules and proteins. In order to avoid contact of the proteins with the highly hydrophobic surface that is required for reversed phase, the pores that are readily accessible to the proteins must not contain any such groups. The highly hydrophobic functionalities must be "hidden" in pores that are smaller than the hydrodynamic size of the protein molecules. The restricted access media solve this problem by using porous silica beads in which essentially *all* pores are smaller than the proteins. Once the external surface of the beads has been made hydrophilic, the proteins have no tendency to adhere to it and they leave the column without being separated since they cannot penetrate the beads.[7] In our approach, we use beads with a relatively broad pore size distribution; therefore, the proteins penetrate those pores that are large enough to accommodate them but they encounter a surface chemistry that has been optimized for their separation. This is because only the pores smaller than the proteins are functionalized with the hydrophobic chemistry. Therefore no proteins can stick to the column, yet the reversed-phase separation of small molecules is still possible. In order to document the feasibility of the pore size specific modification process for the preparation of such a dual-chemistry medium, we prepared beads containing C18 groups in small pores and either hydroxyl or diethylamino groups in the large pores. These materials can be used for the separation of mixtures of proteins and small hydrophobic molecules using *consecutive* reversed-phase and either size exclusion or ion-exchange chromatographic modes.

Design of the Separation Medium with Bimodal Chemistry. The concept of the pore size specific modification has been described in detail previously.[11–13,15] Briefly, the concept relies on the restricted access of molecules to porous structure as a function of their hydrodynamic volume, a phenomenon that is also the basis of the technique of size exclusion chromatography. Therefore only large pores are modified when a polymer catalyst is used. For example, the epoxide groups of the poly(glycidyl methacrylate-*co*-ethylene dimethacrylate) are modified in a pore size specific fashion by a hydrolysis reaction that is catalyzed by poly(styrenesulfonic acid). The small pores remain completely unchanged during this reaction but they can be modified later by reaction with a low molecular weight reagent that is small enough to penetrate them, such as octadecylamine. Since the large pores are already "deactivated", the later reaction takes place exclusively in the small pores and both chemistries are segregated. The process used for the preparation of the media with bimodal distribution involves only a few steps shown in Scheme 1.

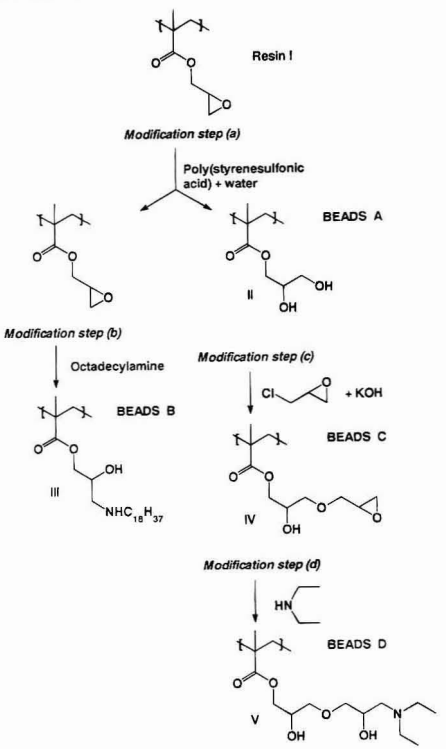
Hydrolysis of poly(glycidyl methacrylate-*co*-ethylene dimethacrylate) beads catalyzed by poly(styrenesulfonic acid) (MW 5000; modification step a) introduces vicinal hydroxyl groups in pores large enough to accommodate the polymeric acid. The molecular weight of the polymeric catalyst chosen was lower than the typical molecular weight of proteins to be separated ($>10^4$) in order to be on the safe side and avoid any contact of the proteins with the highly hydrophobic functionalities contained in the smaller pores. In the second reaction step (modification step b, Scheme 1), the remaining epoxide groups react with octadecylamine in dioxane to afford beads B. The content of the hydrophobic octadecyl groups is 0.35 mmol/g according to N analysis. These beads can be immediately used for the separation of mixtures using a combination of size exclusion and reversed-phase chromatography.

Two additional steps are required for the preparation of a different separation medium that combines the characteristics needed for both ion-exchange and reversed-phase chromatography. First, the hydroxyl groups are "activated" again[20] by a base-

(19) *HPLC of Biological Molecules, Methods and Applications*; Gooding, K. M., Regnier, F. E., Eds.; M. Dekker: New York, 1990.

(20) Turkova, J.; Blaha, K.; Horacek, J.; Vajcner, J.; Frydrychova, A.; Coupek, J. *J. Chromatogr.* **1981**, *215*, 165.

Scheme 1



catalyzed reaction with epichlorohydrin (modification step c, Scheme 1). The epoxide content determined by volumetric titration was 1.12 mmol/g. Though there are some hydroxyl groups present even in the small pores, their reaction is unlikely both because of the shielding effect of the bulky substituent and because of their hydrophobic environment that impairs reaction in the aqueous medium. The final reaction step is the aminolysis of the epoxy-activated beads with diethylamine (modification step d, Scheme 1) to afford beads D containing *N,N*-diethylamino groups (0.62 mmol/g). As a final precaution, the beads are treated again with dilute sulfuric acid to ensure that no epoxide groups remain because these might react with the proteins and interfere with their separation. At this stage, the beads contain segregated hydrophobic and ionizable groups useful for a combination of ion-exchange and reversed-phase chromatography.

Because all the above modification reactions proceed under relatively mild conditions, the appearance of the products monitored by optical microscopy does not change.

Chromatographic Evaluation of Beads with Bimodal Chemistry. The dual-chemistry beads can be used not only to separate complex mixtures but also for the simple separation of either family of compounds. Therefore, their chromatographic properties were evaluated first in a single mode.

Reversed-Phase Chromatography of Small Molecules. A characteristic of reversed-phase chromatography is the linearity

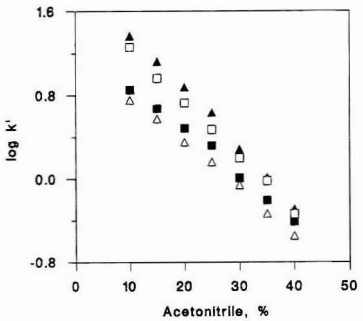


Figure 1. Retention factor k' of a 50-mm × 8-mm i.d. column packed with beads D (open points) and a 300-mm × 7.8-mm i.d. column packed with beads B (closed points) as a function of acetonitrile concentration in the mobile phase: mobile phase, acetonitrile–water; flow rate, 1 mL/min; analytes, benzene (squares) and ethylbenzene (triangles).

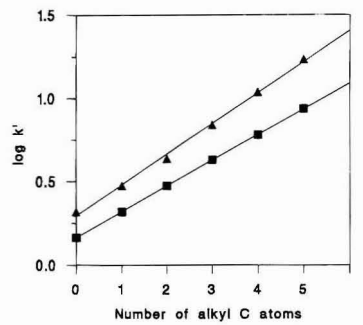


Figure 2. Variation of retention factor k' with the number of carbon atoms in a homologous series of substituted aromatic hydrocarbons (benzene to amylbenzene): columns, 50-mm × 8-mm i.d., beads D (▲) and 300-mm × 7.8-mm i.d., beads B (■); mobile phase, acetonitrile–water (25:75); flow rate, 1 mL/min.

of the plot of retention factor k' vs volume fraction of acetonitrile in the mobile phase. This provides for a simple test of the retention mechanism. Indeed, the dependency was found to be linear for various compounds including alkylbenzenes and anticonvulsant drugs. Figure 1 shows the effect of mobile-phase composition on the retention factors of benzene and ethylbenzene for the columns packed with beads B and D and documents the linearity of the dependency. Retention factors in a 25:75 vol % acetonitrile–water mixture were plotted against the number of carbon atoms in the alkyl chain of the alkylbenzenes. Figure 2 shows that these plots are also linear with a slope of 0.155 and 0.185 for the beads having 1,2-diol and diethylamino chemistry in their large pores, respectively. The slopes represents the retention increase caused by one methylene group in the alkyl chain of alkylbenzenes (selectivity α) and compare favorably to those of C18-alkylated silica and alkylated polymer gels.[21] Surprisingly, since both beads have the same chemistry in their small pores, the selectivity of beads D with the diethylamino chemistry in the large pores is higher than that of the hydrolyzed 1,2-diol

(21) Tanaka, N.; Araki, M. *Adv. Chromatogr.* **1989**, *30*, 81.

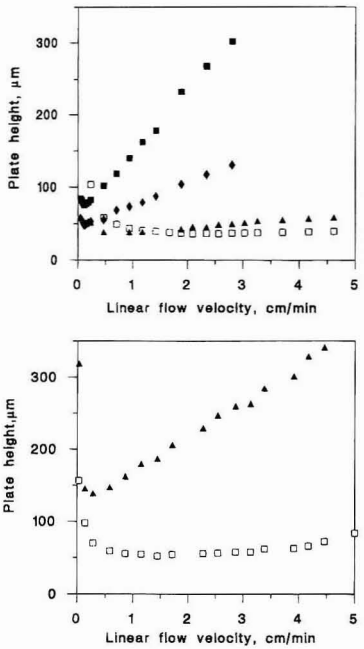


Figure 3. Effect of flow rate on efficiency and back pressure of a column packed with beads containing segregated chemistries: (a, top) column, 300-mm × 7.8−mm i.d., beads B; mobile phase, acetonitrile; analyte, toluene (□); mobile phase, 0.15 mol/L NaCl in 0.1 mol/L phosphate buffer (pH 7); analytes, uracil (▲), cytochrome *c* (◆), and conalbumin (■). (b, bottom) Column, 50-mm × 8-mm i.d., beads D; mobile phase, acetonitrile; analyte, toluene (□); mobile phase, 0.15 mol/L NaCl in 0.01 mol/L TRIS-HCl buffer (pH 7.6); analyte, myoglobin (▲).

beads B. This suggests that the ethyl substituents in the large pores also make a small contribution to the overall hydrophobicity of the separation medium.

A Van Demteer plot obtained for the column packed with the 10-μm beads B (Figure 3a) shows the effect of flow rate on column efficiency. The maximum plate number of 28 000 corresponding to a reduced plate height of 3.6 particle diameters is achieved with toluene in acetonitrile at a flow rate of 1 mL/min.

The efficiency obtained for the column packed with beads D is lower than that for beads B. A maximum of about 20 000 plates that corresponds to a reduced plate height of $5.2d_p$ is obtained for toluene at a flow rate of 0.5 mL/min (Figure 3b).

Size Exclusion Chromatography of Proteins. Because the molecular weights of proteins range from thousands to millions, it is possible to separate some of them according to their hydrodynamic volumes by size exclusion chromatography. Typically, the separation is achieved in an aqueous medium. The surface of pores in which the separation takes place must be hydrophilic, otherwise recovery of the proteins is poor and the stationary phase quickly loses its separation ability. The vicinal hydroxyl groups in the large pores of beads A obtained by hydrolysis of the epoxide groups should endow the surface with sufficient hydrophilicity. Indeed, Table 2 documents the almost

Table 1. Properties of Uniformly Sized Poly(Glycidyl Methacrylate-*co*-Ethylene Dimethacrylate) Beads

particle size, μm	10.0
epoxide groups, mmol/g	2.7
specific pore volume,[a] mL/g	1.1
median pore diameter,[a] nm	13.8
median pore diameter,[b] nm	10.9
polystyrene exclusion limit,[a] MW	3.4×10^5
specific surface area,[b] m^2/g	114

[a] Calculated from size exclusion chromatography data. [b] Calculated from BET measurement.

Table 2. Protein Recoveries from Columns Packed with Beads Containing Bimodal Chemistries

	protein recovery, %	
protein	SE-RP[a]	IE-RP[b]
cytochrome *c*	108	103
myoglobin	93	98
ribonuclease A	105	102
ovalbumin	107	104
bovine serum albumin	91	96
human serum albumin	93	98
conalbumine	101	101
lysozyme	107	100
chymotrypsinogen	105	99
trypsin inhibitor	89	94
bovine plasma	92	

[a] Column SE-RP was packed with beads containing vicinal diol groups in the large pores and octadecylamino groups in the small pores. [b] Column IE-RP was packed with beads containing diethylamino groups in the large pores and octadecylamino groups in the small pores.

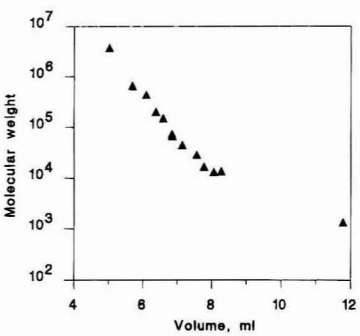


Figure 4. Size exclusion calibration curve for column 300-mm × 7.8-mm i.d. packed with beads B: mobile phase, 0.15 mol/L NaCl in 0.1 mol/L phosphate buffer (pH 7); flow rate, 1 mL/min; analytes, (down from the upper left corner) hemocyanine, thyroglobulin, apoferritin, β-amylase, alcohol dehydrogenase, conalbumine, bovine serum albumin, carbonic anhydrase, myoglobin, cytochrome *c*, ribonuclease A, and vitamin B_{12}.

complete recovery of all the proteins tested. Figure 4 shows a calibration curve obtained for the series of proteins. Though the beads were not specifically designed for separation by size exclusion, the calibration curve is rather linear in the range of molecular weights from about 13 000 to almost 2×10^6. In contrast, the polystyrene exclusion limit observed for the original unmodified epoxide beads was only 3.4×10^5. This apparent discrepancy is actually not a concern since the comparison should

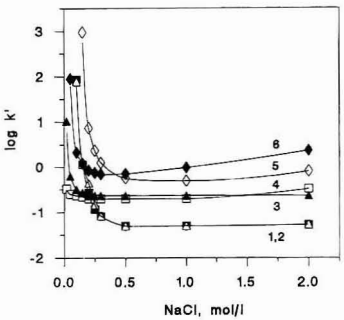


Figure 5. Effect of sodium chloride concentration on the retention factor k' for various proteins in columns packed with beads D containing segregated chemistries: column, 50-mm × 8-mm i.d.; mobile phase, 0.01 mol/L TRIS-HCl buffer solution (pH 7.6); flow rate, 1 mL/min; UV detection; analytes, bovine serum albumin (1), human serum albumin (2), soya bean trypsin inhibitor (3), myoglobin (4), cytochrome *c* (5), and lysozyme (6).

be based on molecular volumes rather than on molecular weights.

The efficiency of the column packed with beads B in the size exclusion mode is rather high. The plate number of 24 000 (reduced plate height $3.8d_p$) measured for uracil in an aqueous mobile phase is very high at a flow rate of 0.2 mL/min. The plate number for proteins is 21 000 and 13 500 plates/m for cytochrome *c* and conalbumin, respectively, at a flow rate of 0.05 mL/min (Figure 3a). However, this flow rate is unrealistic because the separation would take too long to be achieved. Though the efficiency decreases with increasing flow rate, the column still provides remarkable values of 14 000 and 10 000 plates/m for cytochrome and conalbumin, respectively, at a more acceptable flow rate of 0.5 mL/min. Myoglobin is not retained in beads D (Figure 5, curve 4) and can be used for the determination of the efficiency of a column packed with these beads operating in the size exclusion mode. The maximum plate number is about 7200 plates/m at a flow rate of 0.1 mL/min.

Ion-Exchange Chromatography of Proteins. The separation of proteins by ion-exchange chromatography results from the interaction of the charged surface of the separation medium with charged groups of the protein. Here again, hydrophobicity of the surface would have a very detrimental effect on both recovery and column stability. Table 2 shows that beads D with the diethylamino chemistry in the large pores also afford very good recoveries for all proteins tested. Figure 5 shows the plot of retention factor against concentration of salt in the mobile phase. The curves have a shape typical for the ion-exchange chromatography of proteins[19] and clearly document the absence of hydrophobic interactions that would be characterized by retention curves with a concave shape.[22,23]

Separations of Complex Mixtures. The hydrophobic groups in the media described above are completely hidden in the small pores and are therefore inaccessible to large protein molecules. Therefore, a column packed with beads B can be used for the

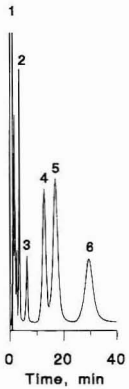


Figure 6. Direct-injection separation of bovine serum plasma and anticonvulsant drugs in a column packed with beads B: column, 150-mm × 4.6-mm i.d.; mobile phase, 0.15 mol/L NaCl in 0.1 mol/L phosphate buffer (pH 7)–acetonitrile 80:20; injected volume, 20 mL; UV detection, 254 nm; peaks (1) bovine serum plasma (70 mg/mL), (2) procainamide (10 μg/mL), (3) lidocain (20 μg/mL), (4) carbamazepine (8 μg/mL), (5) phenytoin (40 μg/mL), (6) desipramine (10 μg/mL).

direct-injection separation of hydrophobic drugs in blood plasma. Figure 6 shows an excellent separation of five drugs from a sample containing a large excess of plasma proteins. This separation is actually quite comparable to one achieved with a typical restricted access medium.

However, the great advantage of the beads modified in pore size specific fashion is seen in processes where each of two entirely different families of compounds present in a sample have to be completely separated. The chromatograms of Figure 7 illustrate separations of mixtures consisting of proteins and alkylbenzenes or drugs in a column packed with beads B. After injection, the hydrophobic part of the sample is adsorbed at the top of the column in the small hydrophobic pores while the other part, the proteins, remains in solution. Elution of the proteins proceeds in size exclusion mode at a flow rate suitable for a good separation. This flow rate is a tradeoff between column efficiency and retention time of the smallest nonadsorbed molecule. We have chosen a flow rate of 0.2 mL/min for which the separation of four proteins (thyroglobulin MW 669 000, human serum albumin MW 69 000, bovine carbonic anhydrase MW 29 000, ribonuclease A MW 13 600) and vitamin B_{12} (MW 1356) occurs within 60 min while column efficiency remains sufficiently high. After 65 min in size exclusion mode, the elution mode is changed (this point is shown as a vertical line in the chromatograms). Acetonitrile is admixed to the original mobile phase, and the hydrophobic compounds initially adsorbed at the top of the column are separated in the isocratic reversed-phase mode. The separations of both families of compounds shown in Figure 7 are sufficient even for a quantitative analysis and document the feasibility of the concept.

The other set of chromatograms shown in Figure 8 illustrates separations obtained for a column packed with beads D operating first in the ion-exchange mode for the separation of proteins and then followed by reversed-phase mode for the separation of small hydrophobic molecules. The sample is injected into a flow of a

(22) Kennedy, L. A.; Kopaciewicz, W.; Regnier, F. E. *J. Chromatogr.* **1986**, *359*, 73.
(23) Heinitz, M. L.; Kennedy, L. A.; Kopaciewicz, W.; Regnier, F. E. *J. Chromatogr.* **1988**, *443*, 173.

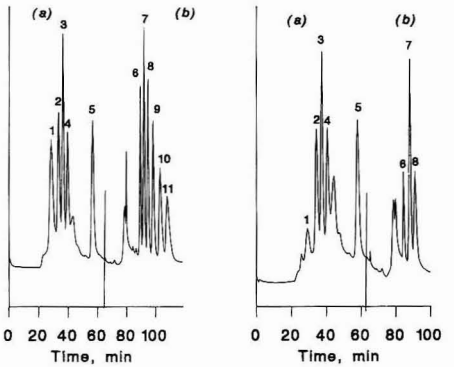


Figure 7. Separation of proteins and alkylbenzenes or anticonvulsant drugs in consecutive size exclusion (a) and reversed-phase (b) chromatographic modes in a column packed with beads B containing segregated chemistries: column, 300-mm × 7.8-mm i.d.; mobile phase, 0.15 mol/L NaCl in 0.1 mol/L phosphate buffer solution (pH 7) for 65 min at a flow rate of 0.2 mL/min followed by buffer–acetonitrile mixture (65:35 v/v); flow rate, 1 mL/min; UV detection, 254 nm; peaks (left-hand panel) thyroglobulin (1), human serum albumin (2), carbonic anhydrase (3), ribonuclease A (4), vitamin B_{12} (5), benzene (6), toluene (7), ethylbenzene (8), propylbenzene (9), butylbenzene (10), and amylbenzene (11); peaks (right-hand panel) thyroglobulin (1), human serum albumin (2), carbonic anhydrase (3), ribonuclease A (4), vitamin B_{12} (5), phenobarbital (6), carbazepamine (7), and phenytoin (8).

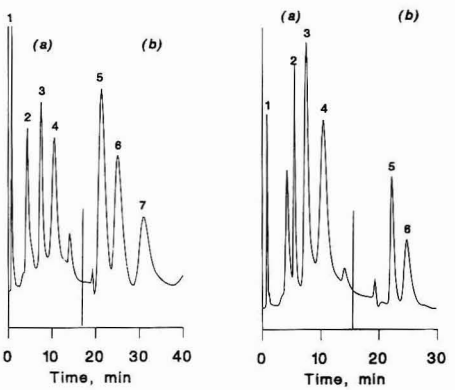


Figure 8. Separation of proteins and alkylbenzenes or anticonvulsant drugs in consecutive ion-exchange a and reversed-phase b chromatographic modes in a column packed with beads D containing segregated chemistries: column, 50-mm × 8-mm i.d.; mobile phase, gradient from 0 to 0.5 mol/L NaCl in 0.01 mol/L TRIS-HCl buffer (pH 7.6) within 30 min followed by buffer–acetonitrile mixture (80:20 v/v); flow rate 1 mL/min; UV detection, 254 nm; peaks (left-hand panel) myoglobin (1), cytochrome *c* (2), bovine serum albumin (3), soya bean trypsin inhibitor (4), toluene (5), ethylbenzene (6), and propylbenzene (7); peaks (right-hand panel) myoglobin (1), cytochrome *c* (2), bovine serum albumin (3), soya bean trypsin inhibitor (4), carbazepamine (5), and phenytoin (6).

low ionic strength buffer solution (0.01 mol/L TRIS-HCl). In contrast to the combined size exclusion and reversed-phase chromatography described above, *all* of the components of the sample are initially adsorbed at the top of the column in this case. The adsorption is size selective, and the components are separated into two groups according to their hydrodynamic size and their affinity toward the functionalities of the pore surface. The proteins are adsorbed by ion exchange in large pores while the small molecules are retained within small pores by hydrophobic interactions. The pore size selective, chemistry-driven adsorption represents the first step of the separation. Both parts of the original sample are then separated independently in two different chromatographic modes. The proteins are eluted in ion-exchange mode using an increasing sodium chloride gradient while the small molecules remain adsorbed at the top of the column during this separation and are not eluted until the mobile phase containing the organic modifier (acetonitrile) is applied and isocratic reversed-phase mode is used.

The separation of proteins shown in Figure 8 also confirms that the ion-exchange mechanism must be operative. The proteins (myoglobin MW 17 000, cytochrome A MW 13 400, bovine serum albumin MW 66 700, soya bean trypsin inhibitor MW 22 500) are eluted regardless of their molecular weight according to their net charges. This documents the absence of size exclusion effects in the protein separation. Clearly, the flow rate of 1 mL/min is too high and the length of the column (150 mm) is too short for an efficient separation by size exclusion. The higher flow rate together with the mobile-phase gradient results in an acceleration of the protein separation compared to the size exclusion chromatography with beads B and decrease in the total time required for analysis. However, the separation of hydrophobic small molecules that follows the ion-exchange chromatography is poorer than that observed with beads B. The peaks are broader because the efficiency of the shorter column is lower.

One might wonder whether or not single-column separations of complex mixtures such as those shown in Figures 7 and 8 would be feasible with other separation media. It is likely that some of the restricted access media with optimized pore size distribution would indeed be able to separate a sample using consecutive size exclusion and reversed-phase modes. However, the combination of ion-exchange with reversed-phase chromatography is not easily matched. The mixed-mode phases with nonsegregated chemistries as well as the blended phases do not provide for the first step separation into component families, one of which is held into the column while the other is separated, and the elution is not specific for each of these families. We believe our media are unique in their ability to separate a complex sample in consecutive ion-exchange and reversed modes.

The experimental results also demonstrate that the separations shown in Figures 7 and 8 have all the attributes of a two-dimensional separation.[1,2] The first step separates the components of the sample into two classes that are stored separately in different pores. Both classes of compounds are then subjected to a separation into individual components. This is particularly true for the combination of ion-exchange and reversed-phase chromatography as both families of compounds separated in the first step remain at the top of column until they are separated in the second step.

CONCLUSION

Separations of different families of compounds in two different chromatographic modes confirms that the pore size specific functionalization provides separation media with two segregated chemistries. The chromatographic results clearly document that

the separation of complex samples in two consecutive modes is feasible. Though this report describes media with only two different surface chemistries located in the large pores and used for the separation of proteins contained in the sample, the concept of the pore size specific modification of porous materials allows the design of many other chemistries exclusively within the large pores without compromising the properties of the small pores and vice versa. The use of a reaction path involving modifications controlled by polymeric reagents or catalysts with different molecular sizes can result in separation media accommodating more than two segregated chemistries. These media are currently under investigation.

ACKNOWLEDGMENT

Financial support of this research by the National Institutes of Health (GM 44885-05) is gratefully acknowledged. This work also made use of Cornell Material Science Center MLR Central Facilities (Polymer Research Facility) supported by the National Science Foundation under Award DMR-9121654.

Received for review June 30, 1994. Accepted September 17, 1994.[⊗]

[⊗] Abstract published in *Advance ACS Abstracts,* October 15, 1994.

Anal. Chem. **1994,** *66,* 4316–4323

Organic Gas Sorption Characteristics of Plasma-Deposited Amino Acid Films

Iwao Sugimoto,* Masayuki Nakamura, and Hiroki Kuwano

NTT Interdisciplinary Research Laboratories, Midori-cho, Musashino-shi, Tokyo 180, Japan

Plasma-deposited organic films prepared by radio frequency sputtering of amino acids, such as D-phenylalanine and D-glutamic acid, are basically composed of unit structures of the original amino acids. Moreover, static secondary ion mass spectroscopy suggests the formation of peptide bonds due to plasma reactions. These films have a hydrophilic structure that gives them a high affinity for polar solvent gases. Alcohols with a small volume and a linear structure are preferentially sorbed, suggesting that the steric effects and apolar solvation effects of alkyl groups of alcohols are crucial for organic gas sorption of these films.

Biological chemosensory materials, such as receptor proteins and lipids, are so fragile that they are likely to lose their sensing ability when they are embedded in artificial transduction systems or used in nonbiological media. The intriguing aspects of biomimetic chemical sensing are the selective, sensitive, and reproducible detection of nonreactive organic molecules through weak intermolecular interactions and steric effects. The goal of these studies is to establish olfactory and taste sensory systems. Besides transduction and data-processing systems, the probing films play significant roles in the detection and determination of organic molecules and have been investigated on the basis of supramolecular chemistry.[1-13] However, biomimetic films composed of artificial host and lipid molecules may lack sensitivity and durability. Moreover, the film–substrate interface science, including the immobilization of these films on transduction systems, is a crucial issue in the transduction of sensory information.

While the structure of plasma-deposited organic films is likely to be undefinable and uncontrollable, the main advantages of these films are high durability and adhesive strength to the substrates. These characteristics of plasma organic films are due to energetic film components that are likely to form interpenetrating film networks that induce high atomic density. These features of plasma-deposited organic films are remarkable, especially for sputtering deposition, and are effective in such organic film technologies as chemical sensing and gas separation. The usefulness of plasma organic films for gas sensing has been reported by several groups.[14-17]

Among several nonionic interactions, intermolecular interactions for physisorption strongly depend on the dispersive force, which is primarily due to polar groups. Protein molecules composed of amino acids play significant roles in this type of interaction in biological systems. This work reports the preparation, characterization, and organic gas sorption properties of plasma films produced by sputtering of amino acids.

Supplying amino acids, which have low vapor pressure, into a vacuum reaction chamber is a crucial problem in plasma preparation of organic films. We used the sputtering method, which can directly feed solid source material into the plasmas. Even though it is difficult to control the plasma reactions, we can prepare films that preserve the basic structures of amino acids well enough that the expected film characteristics are generated under moderate plasma conditions.

EXPERIMENTAL SECTION

D-Phenylalanine and D-glutamic acid were used as the raw materials for the radio frequency (rf) sputtering reactions. These two amino acids (>98%) were obtained from Tokyo Kasei and Kanto Chemical, respectively, and used without further purification. Each amino acid was dissolved and dispersed in deionized water at 70 °C and then spread on a polyethylene (PE) disk (135 mm in diameter, 10 mm thick). After the solvent water had completely evaporated, the PE disk coated with amino acid was used as a sputtering target. Plasma organic films were deposited on a nondoped ⟨100⟩ silicon wafer and a polished ⟨100⟩ MgO plate for film characterization and on a 9-MHz AT-cut quartz crystal microbalance (QCM) plate (8.5 mm in diameter and 0.1 mm thick) for gas sorption analysis by using 13.56-MHz rf sputtering in a sputter-up configuration. A QCM is a precise mass-measuring device that can detect nanogram mass changes. Half of each side of the QCM plate was coated with a gold electrode (4 mm in diameter) before deposition. The gas pressure during sputtering was 0.15 Torr, using helium as the plasma working gas (3.8 mL/min). The interelectrode distance was 50 mm, and the rf power density was 0.42 W/cm^2. The mean film thickness deposited on each side of the QCM plate was 0.3 μm.

(1) Lai, C. S. L.; Moody, G. J.; Thomas, J. D. R.; Mulligan, D. C.; Stoddart, J. F.; Zarzycki, R. *J. Chem. Soc., Perkin Trans. 2* **1988**, 319.
(2) Ueno, A.; Suzuki, I.; Osa, T. *Chem. Lett.* **1989**, 1059.
(3) Rebek, J., Jr. *Angew. Chem., Int. Ed. Engl.* **1990**, *29*, 245.
(4) Lehn, J.-M. *Angew. Chem., Int. Ed. Engl.* **1990**, *29*, 1304.
(5) Okahata, Y.; En-na, G.; Ebato, H. *Anal. Chem.* **1990**, *62*, 1431.
(6) Foster, R. J.; Cadogan, R. J.; Telting, M. T.; Diamond, D.; Harris, S. J.; McKervey, M. A. *Sensors Actuators B* **1991**, *4*, 325.
(7) Dickert, F. L.; Bauer, P. A. *Adv. Mater.* **1991**, *3*, 436.
(8) Brodbelt, J.; Maleknia, S.; Liou, C.-C.; Lagow, R. *J. Am. Chem. Soc.* **1991**, *113*, 5913.
(9) Maleknia S.; Brodbelt, J. *J. Am. Chem. Soc.* **1992**, *114*, 4295.
(10) Dickert, F. L.; Haunschild, A.; Maune, V. *Sensors Actuators B* **1993**, *12*, 169.
(11) Izatt, R. M.; Bradshow, J. S.; Pawlak, K.; Bruening, R. L.;Tarbet, B. J. *Chem. Rev.* **1992**, *92*, 1261.
(12) Cram, D. J. *Nature* **1992**, *356*, 29.
(13) Vögtle, F. *Supramolecular Chemistry*; John Wiley & Sons: Chichester, West Sussex, 1991.
(14) Kurosawa, S.; Kamo, N.; Matsui, D.; Kobatake, Y. *Anal. Chem.* **1990**, *62*, 353.
(15) Butler, M. A.; Buss, R. J.; Galuska, J. *Appl. Phys.* **1991**, *70*, 2326.
(16) Sugimoto, I. J. *Appl. Phys.* **1991**, *70*, 2887.
(17) Inagaki, N.; Tasaka, S.; Nozue, Y. *J. Appl. Polym. Sci.* **1992**, *45*, 1041.

0003-2700/94/0366-4316$04.50/0 © 1994 American Chemical Society

The contact angle of water was measured by placing drops of pure water on the sample films and observing the angle with a cathetometer equipped with a goniometer eyepiece (Kyowa Face contact angle meter). A 0.01 mL drops of pure water was dropped with a syringe that incorporated a plunger driven by a micrometer.

The plasma organic films deposited on the gold electrodes on the QCM plate were analyzed by using micro-infrared (IR) spectroscopy (JASCO FTIR-5M/MICRO-10). The wavenumber resolution was 4 cm^{-1}, measured with a Hg–Cd–Te detector by the reflection method. The films deposited on the ⟨100⟩ MgO substrate were analyzed by using ultraviolet–visible (UV–vis) spectroscopy (Shimadzu, UV-160A) with a wavelength resolution of 2 nm.

X-ray photoelectron spectroscopy (XPS, VG MicroLab-MK2) was performed at low power (100 W) using Mg Kα radiation as the excitation source. The prepared samples were stored in a vacuum chamber at $<10^{-1}$ Torr to prevent aging and contamination. The chamber pressure during analysis was kept at $<3.5 \times 10^{-10}$ Torr, and ion etching to remove surface contamination was not carried out to avoid any structural changes. The incident angle of the x-ray beam and the photoelectron takeoff angle with respect to the film surface were 40° and 90°, respectively. Each binding energy was calibrated to compensate for charging by setting the strongest C_{1s} peak to 284.6 eV, which is representative for CH_x systems. The raw material spectrum of each amino acid was obtained from pressed pellets.

To reinforce the structural analysis, we performed time-of-flight secondary ion mass spectrometry (TOF-SIMS, Charles Evans & Associates TFS surface analyzer). To satisfy static SIMS conditions, the pulsed 8.5-keV Cs^+ primary ion beam current was reduced to 1 nA/cm^2. The focused Cs^+ ion beam spot was 60 μm in diameter, and the total ion dose was about 10^{12} ion/cm^2. The focused secondary ions were accelerated to 4.45 keV and detected by a TOF mass spectrometer which contained three sector electrostatic energy analyzers. The pressure in the sample chamber was kept below 10^{-9} Torr during analysis. Original amino acids were analyzed using pressed pellets, as was the case with XPS.

The plasma-film-coated QCM was connected to an oscillator circuit, and the downward shift in resonance frequency induced by mass loading was estimated to be 1.05 ng/Hz by Sauerbrey's equation.[18] The gas sorption measuring system was basically the same as in our previous study.[19] The analyte gas was generated by a flow system comprised of an organic solvent diffusion tube immersed in a temperature bath. Pure air (99.9999%) was used as a carrier gas for the analyte as well as for a standard gas. The concentration of analyte was controlled at 20 ppm by adjusting the tube temperature (from 30 to 50 °C) and the carrier gas flow rate (from 0.2 to 0.6 L/min). The typical gas flow rate was 0.2 L/min. The QCM was placed in a 30-mL sorption cell, which was kept in an incubator at 25 °C. The organic vapor, diluted with pure air, was introduced into the sorption cell after a baseline fluctuation below 0.1 Hz/min was established. Switching between the background- and gas sorption-measuring modes was done quickly by using a four-port housing valve, which produced a step response and kept the gas pressure constant. The gas sorption characteristics of each film were measured for 3 h.

(18) Sauerbrey, G. Z. *Z. Phys.* **1959**, *155*, 206.
(19) Sugimoto, I.; Nakamura, M.; Kuwano, H. *Sensors Actuators B* **1993**, *10*, 117.

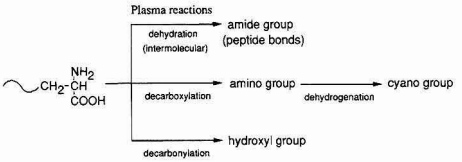


Figure 1. Plasma reaction schemes of primary amino acids.

RESULTS AND DISCUSSION

The most effective plasma reaction source is the excited electrons that are ubiquitous in plasma and can induce reductive reactions. The reduced species can induce intramolecular elimination and/or intermolecular polymerization reactions.[20] In addition, ultraviolet photoreactions by plasma emission may be significant for photosensitive species. The most probable plasma reactions for primary amino acids are summarized in Figure 1. The behaviors of amino acids in plasmas are interesting from the viewpoint of protein chemistry.[21–23]

We evaluated the deposition rates of amino acid films by analyzing the resonance frequency shift of the QCM substrates. The mean values were 13.0 Å/min for phenylalanine and 20.5 Å/min for glutamic acid. These amino acid plasmas could be sustained without feeding helium gas once the plasma was initiated. Both of the amino acids' deposition rates on the heliumless plasma are comparable to those on helium plasma. The higher deposition rate for glutamic acid may be due to its sublimation characteristic (subl. 200 °C).[24] The deposition rate decreased when Ar, Kr, or Xe was used as the plasma working gas. These results suggest that massive bombardment effects are not crucial for sputtering deposition. The contact angles of pure water (at 54% humidity and 22 °C) on the phenylalanine and glutamic acid films deposited on silicon wafers were 67° and 57°, respectively. The smaller angle for the glutamic acid film is probably attributable to the binary carboxyl system of glutamic acid.

The IR spectra of both films show substantially the same pattern (Figure 2). The strong band around 3400 cm^{-1} can be assigned to the N–H stretching mode of the amine group and the O–H stretching mode for the carboxyl group. The other strong band around 1680 cm^{-1} originates from the carbonyl stretching mode. In plasmas which contain a considerable number of activated electrons, the saturated carbon systems are likely to be changed into unsaturated systems by elimination reactions. The strong band tail at the lower wavenumber side may reflect the stretching vibration mode of the C=C bonds, including the benzene ring skeleton for the phenylalanine film. We cannot unambiguously determine whether the carbonyl bonds belong to the carboxyl, ketone, or amide groups. The C–H stretching mode around 2950 cm^{-1} is also clearly observed in both spectra, and the relative intensity ratio of this C–H band to the C=O band for phenylalanine film is somewhat stronger than that for glutamic acid film, reflecting the molecular structure of the raw materials.

(20) Hollahan, J. R.; Bell, A. T. *Techniques and Applications of Plasma Chemistry*; John Wiley & Sons: New York, 1974.
(21) Miller, S. L. *Science* **1953**, *177*, 528.
(22) Oró, J. *Nature* **1963**, *197*, 862.
(23) Hollahan, J. R.; Emanuel, C. F. *Biochim. Biophys. Acta* **1970**, *208*, 317.
(24) Windholz, M., Ed. *The Merck Index*; Merck: Rahway, NJ, 1983.

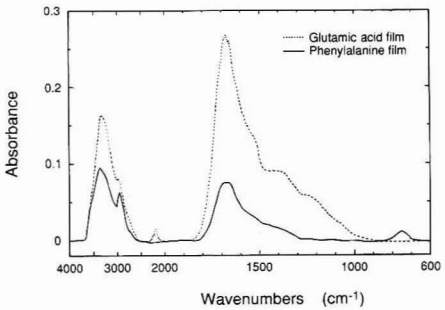


Figure 2. Infrared spectra of the plasma organic films of amino acids.

In the phenylalanine film spectrum, a band due to the C–H wagging motion outside the benzene ring is observed at around 770 cm^{-1}. This preservation of the benzene skeleton suggests high stability for plasma reactions. The weak peak at around 2200 cm^{-1}, which is observable only for glutamic acid, can be assigned to the cyano groups. The formation of the cyano groups probably derives from the decarboxylation and full dehydrogenation of α-amino acid moiety. Compared to the phenylalanine film, the area ratio of the 3400 cm^{-1} band to the 1680 cm^{-1} band for the glutamic acid film is smaller. This reduction in relative intensity of the former band suggests that the amino groups are likely to change into cyano groups due to dehydrogenation reactions. The production of cyano groups has also been reported in the plasma polymerization of allylamine derivatives.[25–27] The absence of cyano groups in the phenylalanine film is the main difference from the glutamic acid film.

The UV–vis spectra of the plasma-deposited amino acid films are featureless, with absorption peaks at about 280 nm. Compared to that of the glutamic acid film, the absorption coefficient of the phenylalanine film is large over the full range of measured wavelengths, and the absorption edge is at a higher wavelength. The UV–vis absorption characteristics of the phenylalanine film suggest that the film has a higher atomic density and/or a highly unsaturated framework.

The atomic ratios we obtained from XPS using sensitivity factors[28] (with an accuracy of about 2%) are shown in Table 1, including those for the unsputtered raw materials. Even though these analytical results do not include hydrogen, it is noteworthy that in the phenylalanine film, the atomic ratios are basically the same for the sputtered and unsputtered films, suggesting almost stoichiometric values. However, the concentration of oxygen increased to approximately 10%, and the concentrations of carbon and nitrogen were reduced for the unsputtered glutamic acid, relative to its stoichiometry. This oxygen enrichment may derive from the high affinity for water (oxygen source) due to the molecular structure of the binary carboxylic system. Compared with unsputtered glutamic acid, the sputtered film is apparently deficient in oxygen atoms, which belong to carboxylic groups.

(25) Hollahan, J. R.; Wydeven, T. *Science* **1973**, *179*, 500.
(26) Hozumi, K.; Kitamura, K.; Hashimoto, H.; Hamaoka, T.; Fujisawa, H.; Ishikawa, T. J. *Appl. Polym. Sci.* **1983**, *28*, 1651.
(27) Ko, Tze-M.; Cooper, S. L. *J. Appl. Polym. Sci.* **1993**, *47*, 1601.
(28) Warner, C. D.; Rigg, W. M.; Davis, L. E.; Moulder, J. E.; Muilenberg, G. E. *Handbook of X-ray Photoelectron Spectroscopy*; Perkin-Elmer: Minnesota, 1979.

Table 1. Atomic Concentrations (%) of Amino Acids Estimated from XPS Analysis

	C	O	N
	Phenylalanine		
stoichiometry	75.0	16.7	8.3
unsputtered	75.5	16.2	8.4
sputtered film	77.6	13.2	9.2
	Glutamic Acid		
stoichiometry	62.5	25.0	12.5
unsputtered	55.9	34.5	9.6
sputtered film	64.0	19.4	16.6

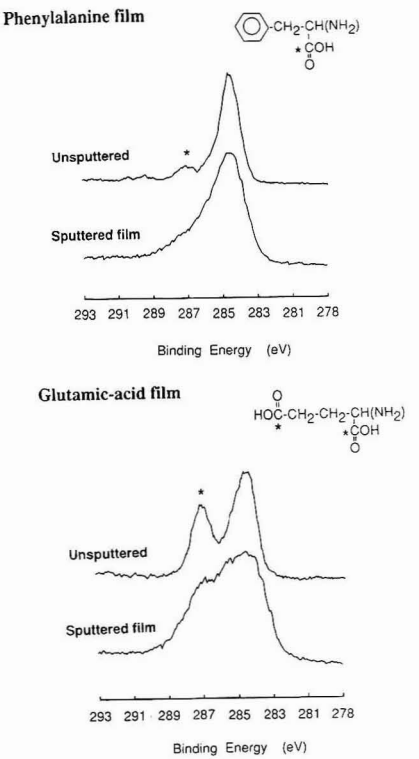


Figure 3. C_{1s} XPS spectra of the amino acids.

The oxygen is presumably eliminated in the form of carbon dioxide, carbon monoxide, and water molecules, leaving behind amino, hydroxyl, and amide groups.[20] The presence of cyano groups observed by IR spectroscopy (Figure 2) is indicative of the promoted plasma reactions through the formation of amino groups by decarboxylation (Figure 1). These plasma reaction characteristics of glutamic acid may be attributed to its structure being less stable than that of phenylalanine during plasma reactions.

The X-ray photoelectron spectra of the C_{1s} region for both films are shown in Figure 3. In the spectra for both raw materials, the conspicuous band observed on the higher binding energy side (~287 eV) of the main bands (284.6 eV) is likely to be due to carboxylic carbons. The area ratios of these carbonyl carbons to

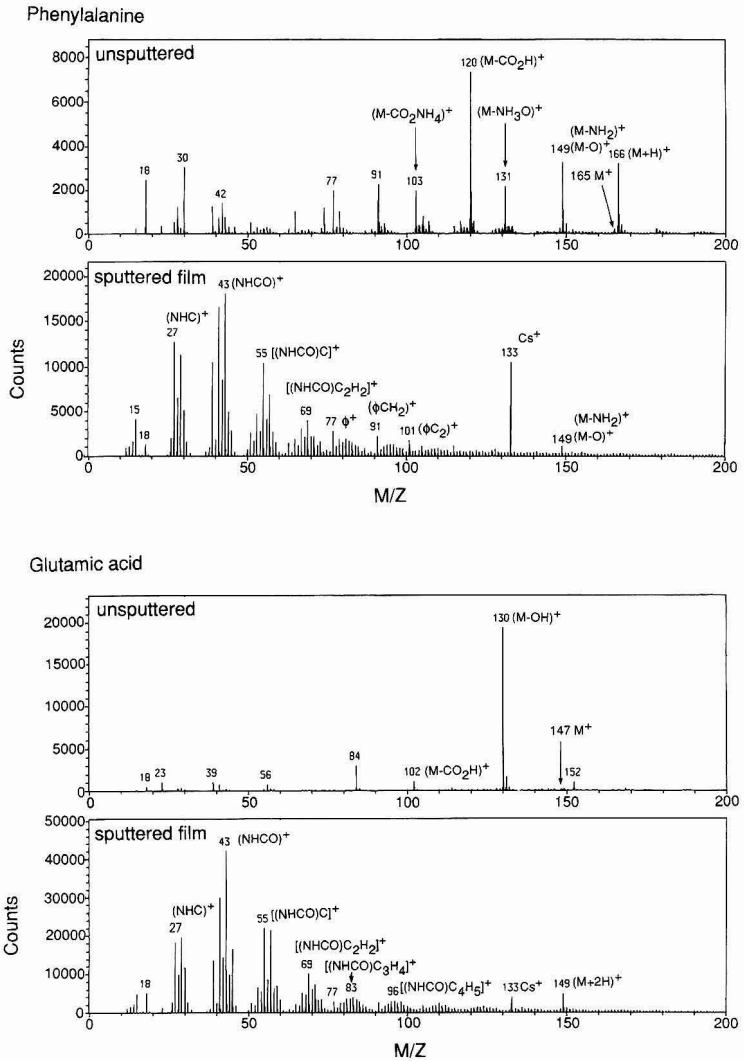


Figure 4. TOF-SIMS positive ion spectra: (a) phenylalanine film and (b) glutamic acid film.

the other carbons are estimated to be 2:3 for glutamic acid and 1:8 for phenylalanine. These XPS analyses satisfactorily reflect their stoichiometric molecular structures. However, the two characteristic peaks of the C_{1s} XPS spectrum observed in the unsputtered raw materials are altered in both sputtered films. The valley between the two main peaks located at about 286–287 eV is enhanced. There are many possible candidates for these signals, such as the carbonyl and amide groups, which are generated by plasma reactions. However, these spectra may mostly reflect the raw materials, which are in the form of physically vapor-deposited films. The O_{1s} and N_{1s} spectra for all of the raw and sputtered amino acids are identical without showing fine structures.

We obtained fragmentation patterns of the positive and negative ions by using TOF-SIMS (Figures 4 and 5). Both of the original amino acids are better characterized by the positive ion spectra than by the negative ion spectra. Each of the positive and negative ion spectra of both sputtered films differ from the spectra of their raw materials; however, the fragmentation patterns of both sputtered films significantly resemble each other, suggesting that these film frameworks contain the same components. In the positive ion spectra, both of the sputtered films exhibit

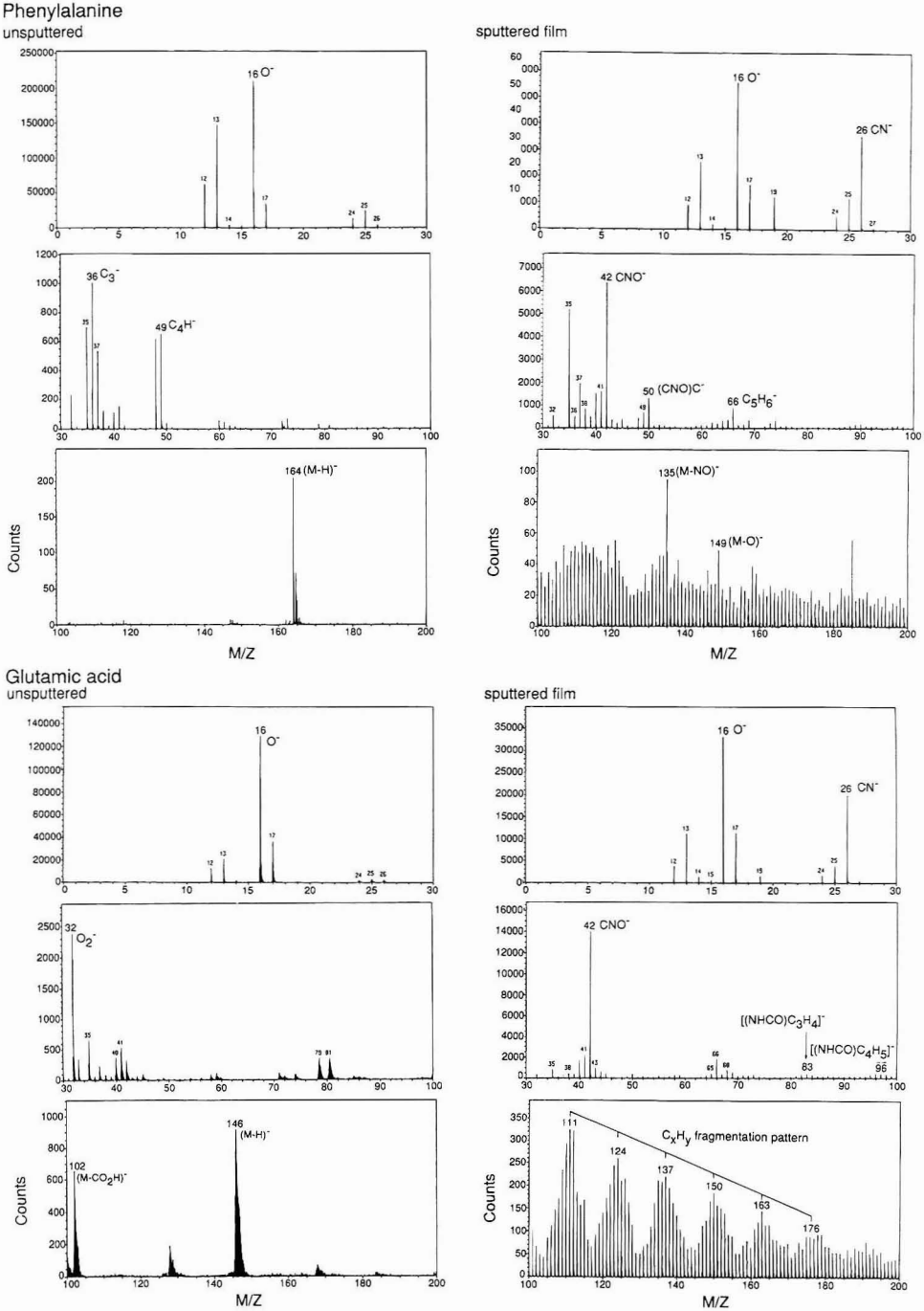


Figure 5. TOF-SIMS negative ion spectra: (a) phenylalanine film and (b) glutamic acid film.

Table 2. Sorption Characteristics of 20-ppm Organic Solvent Vapors

solvent	concentration of sorbed molecules (mmol/L)		time constant (s)[a]	
	glutamic acid film	phenylalanine film	glutamic acid film	phenylalanine film
n-pentane	0.75	1.54	21.5	15.8
n-hexane	2.08	3.44	28.6	23.8
n-heptane	1.40	2.60	21.5	15.8
n-octane	0.54	2.26	62.2	45.8
cyclohexane	2.04	3.16	100.0	47.0
benzene	1.84	6.59	34.0	27.4
toluene	1.14	4.91	41.5	128.7
o-xylene	1.84	6.59	35.8	66.9
m-xylene	1.28	12.36	31.1	217.1
p-xylene	2.45	8.19	31.8	53.0
chlorobenzene	2.57	6.48	44.8	57.6
acetone	2.04	60.49	40.0	1281.0
2-butanone	1.06	22.61	29.3	602.7
2-hexanone	10.48	42.39	28.6	23.8
methyl acetate	1.64	3.24	23.7	75.2
ethyl acetate	3.79	22.54	42.3	370.4
N,N-dimethyl-formamide	5.34	214.67	42.3	1006.5

[a] Time constant (τ), a measure of equilibration time, is derived from the curve fitting of the dynamic sorption curve, which is represented as a Langmuir-type equation: $m(t) = a[1 - \exp(-t/\tau)]$, where m is the amount of sorption, a is the saturation mass, and t is the measurement time.

patterns based on the amide group [m/z 15 (HN), 27 (HNC), 43 (HNCO), 55 ((HNCO)C), 69 ((HNCO)C_2H_2)]. Both also have the fragments of the amide group [m/z 16 (O), 26 (CN), 42 (CNO)] exclusively in the negative ion spectra. Taking into account these analytical results, we can expect that the peptide bonds (amide group) are formed through plasma reactions of the amino acids. This expectation is also supported by the inertness of both of the sputtered films to ninhydrin reaction, which detects the existence of free primary amino acids.[29]

Both of the sputtered films generally contain the hydrocarbon fragmentation patterns in both ion spectra. Besides the amide group, the fragmentation pattern based on the phenyl group [m/z 77 (Ph), 91 (Ph)CH_2), 101 (PhC_2)] is observable in the phenylalanine film spectrum (Figure 4a). The glutamic acid film has signals originating from the methylene groups attached to the amide group [m/z 83 ((HNCO)C_3H_4), 96 ((HNCO)C_4H_5)] (Figure 4b). The carbon frameworks constructing the original amino acids should therefore be partially preserved in the sputtered films.

Spectroscopic analysis revealed that the plasma-deposited amino acid films contain a number of hydrophilic groups originating from the raw materials. The key feature suggesting hydrophilic film characteristics is attributed to those functional groups possessing a high affinity for polar molecules. We reviewed current efforts to obtain preferential sorption for polar solvent vapors by using QCM devices coated with plasma organic films. Sorption study of primary alcohols offers valuable insights into the scope and nature of plasma organic films as chemical sensing probes.

The gas sorption ability of several organic solvents was examined by using 0.3-μm plasma-deposited amino acid films (Table 2). The amount of sorbed gas is defined as the maximum concentration in the film during a 3-h measurement. In general, the phenylalanine film has a higher affinity for organic vapors than does the glutamic acid film, and both of the amino acid films exhibit selective affinity for polar solvents, such as ketones, esters, and amides. It is noteworthy that acetone and *N,N*-dimethyformamide have extremely high solubility for phenylalanine film and do not show such a selective sorption for glutamic acid film. Among the hydrocarbons, aromatic solvents are likely to be sorbed in larger quantities than saturated solvents for the phenylalanine film. The benzene moiety in the phenylalanine film may contribute to the slight affinity for aromatic solvents. However, we cannot conceive of any meaningful features in the methylated benzene group or of any significant correlation between the concentration of sorbed molecules and the time constant of the sorption curves. However, the polar solvents with an extremely large sorption concentration seem to show a large time constant in phenylalanine film.

We used normal alcohols (C_1–C_7) with various carbon numbers as simplified systems for analyzing the effects of carbon chains on the sorption characteristics of the polar solvent gases. Table 3 shows the concentration of sorbed molecules and time constants, together with the molecular volume, and tracks activity of the solvates. It compares the results for hydrophobic fluoropolymer film, which was produced by rf sputtering of poly(chlorotrifluoroethylene) (PCTFE) in He plasma,[15] with those for hydrophilic amino acid films. The amino acid films, especially the phenylalanine film, have a high affinity for all of the alcohols, suggesting a basically preferential characteristic of the lower-carbon-number alcohols. The amount of sorbed alcohols on the glutamic acid film decreases as the carbon number of the alcohols increases. The variation in the concentration of sorbed alcohols with an increasing carbon number, however, tends to become U-shaped for the phenylalanine film. The slight enhancement of affinity for alcohols with a higher volume may be attributed to the small lipophilicity of the phenylalanine film, which is composed of a larger number of hydrocarbon moieties than the glutamic acid film. These structures induce a somewhat amphiphilic characteristic in the phenylalanine film. In addition, the large tracks activity of heptanol may be responsible for increasing its sorption concentration. In contrast, the PCTFE film shows a low affinity for all of the alcohols and the opposite dependence of sorption concentration on the carbon number of alcohols. It is noteworthy that this film has extremely low affinity for alcohols with lower carbon numbers, suggesting that the molecular volume is not a decisive factor for the sorption of alcohols in this PCTFE film. Apolar complexation between the PCTFE film networks and the hydrocarbon moieties of alcohols plays a significant role in the sorption of alcohols.

The alcohol sorption by hydrophilic amino acid films is primarily attributed to the dipole interactions by the hydroxyl group. The remaining alkyl groups can behave freely. Therefore, we examined the steric effects of alkyl groups on the sorption of butyl alcohols for the glutamic acid film, which showed a simple variation in the sorption of normal alcohols depending on the carbon number (Table 3). The film showed an extremely high affinity for the *n*-butyl group (Table 4). The more branched the structure of the alkyl groups becomes, the less likely butyl alcohols are to be sorbed. That is, this order of decreasing sorption matches the decrease in the flexibility of alkyl groups. This remarkable steric effect, therefore, strongly reflects the solvation availability of alkyl groups. The flexible *n*-butyl alcohols

(29) Conn, E. E.; Stumph, P. K. *Outlines of Biochemistry, 4th ed.*; John Wiley & Sons: New York, 1976.

Table 3. Sorption Characteristics of Normal Alcohols (20 ppm)

	molecular volume (Å^3)	tracks activity[a] (p/p_0, $\times 10^{-5}$)	concentration of sorbed molecules (mmol/L) glutamic acid film	phenylalanine film	PCTFE film	time constant (s) glutamic acid film	phenylalanine film	PCTFE film
methanol	20	12	23.59	103.98	0.00	48.6	105.2	
ethanol	30	26	10.48	69.23	0.81	39.9	1019.7	57.4
propanol	40	74	5.42	25.50	2.28	27.7	181.7	1793.4
butanol	50	235	3.89	15.24	2.71	31.1	81.5	2650.0
pentanol	60	697	3.37	17.15	4.04	39.8	43.5	3242.0
heptanol	80	6609	2.42	27.48	10.30	17.6	156.8	1677.6

[a] Tracks activity represents the ability for condensation and the resulting loss of a free vapor state; p is the partial pressure and p_0 is the saturation vapor pressure at measuring temperature (25 °C).

Table 4. Sorption Characteristics of Butanols for Glutamic Acid Film

	tracks activity (p/p_0, $\times 10^{-5}$)	concentration of sorbed molecules (mmol/L)
n-butyl alcohol	235	3.89
sec-butyl alcohol	86	2.18
isobutyl alcohol	132	0.75
tert-butyl alcohol	37	0.57

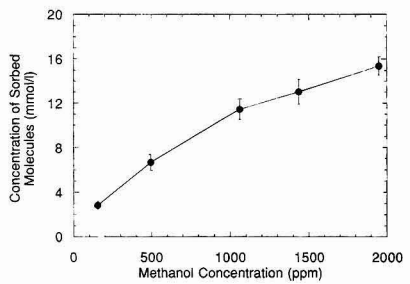


Figure 6. Sorption isotherms of PCTFE film for methanol vapors at 25 °C.

must be highly solvated by film molecules and become thermodynamically stable adducts, which closely corresponds to the entropy effect of liquid solvation.[30] In addition, these steric effects may also rely on the minimum cross-sectional area of butyl alcohols. The more the branching, the more film sections become inaccessible, because a molecule cannot fit through cross-linked chains. These experimental results suggest that organic gas sorption is governed by the solvation of solute gas molecules by solvent plasma-deposited amino acid films.

We examined the sorption isotherms of amino acid films and PCTFE film for benzene and methanol vapors ranging from 20 to 2000 ppm at 25 °C (Figures 6–9). For both vapors, the PCTFE film shows an almost linear correlation, suggesting that its partition coefficient is constant (obeying Henry's law). However, the hydrophilic amino acid films exhibit complicated features. For methanol, both amino acid films have a large sorption concentration due to the dipole–dipole interactions, and the sorption concentrations tend to increase with an increasing vapor concentration. The sorption is suppressed at vapor concentrations above 1000 ppm. This saturation phenomenon is probably due to the

(30) Israelachvili, J. N. *Intermolecular and Surface Forces*; Academic Press: London, 1985.

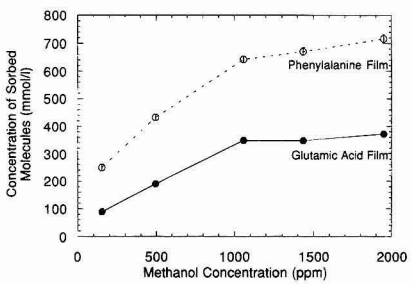


Figure 7. Sorption isotherms of amino acid films for methanol vapors at 25 °C.

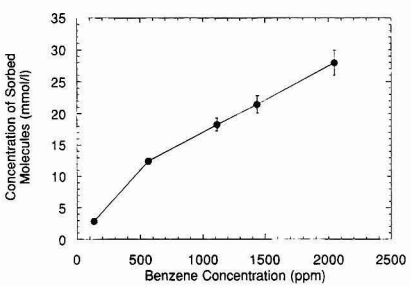


Figure 8. Sorption isotherms of PCTFE film for benzene vapors at 25 °C.

reduction of the thermodynamically stable energy of dissolvation, resulting from the dissipation of the interactive sites in the solvent film. For benzene, the amino acid films do not have a meaningful correlation between the sorption concentration and the vapor concentration. This lack of dependence suggests that the dipole-driven sorption characteristics of the amino acid films do not govern the sorption of a benzene π-system without dipolarity.

CONCLUSIONS

Plasma-deposited organic films prepared by rf sputtering of amino acids generally preserve the basic structure of the raw materials. Micro-infrared and X-ray photoelectron spectroscopies revealed that the phenylalanine film is probably composed of the same units as a phenylalanine molecule. Glutamic acid, however, is likely to undergo plasma reactions, resulting in the deficiency of oxygen in the deposited film containing cyano groups. These

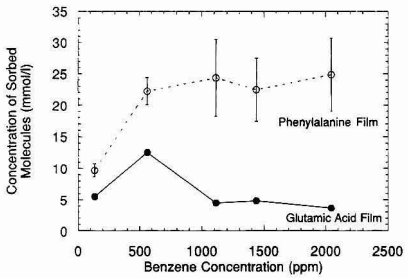


Figure 9. Sorption isotherms of amino acid films for benzene vapors at 25 °C.

results suggest that deoxygenation and dehydrogenation are characteristic plasma reactions of saturated amino acids and that these reactions can be suppressed by a stable moiety, such as a benzene ring. These plasma organic films, especially phenylalanine film, have a high affinity for polar organic solvent vapors. The affinity for normal alcohols of these hydrophilic amino acid films is stronger for the lower-molecular-weight alcohols. This sorption dependence on the carbon number of normal alcohols is opposite to that of the hydrophobic fluoropolymer film produced by rf sputtering of poly(chlorotrifluoroethylene). The glutamic acid film shows extremely high affinity for a *n*-butyl alcohol, suggesting steric effects. These findings show the great potential of using moderate plasmas for preparing organic films with amino acids, which are useful for chemical-sensing probes that utilize solvation effects.

Received for review April 21, 1994. Accepted August 25, 1994.[⊗]

[⊗] Abstract published in *Advance ACS Abstracts,* October 15, 1994.

Anal. Chem. **1994,** *66,* 4324–4331

Influence of Vapor Deposition Parameters on SERS Active Ag Film Morphology and Optical Properties

David J. Semin and Kathy L. Rowlen*

Department of Chemistry and Biochemistry, Boulder, Colorado 80309

The magnitude of surface enhancement from thin metal films is known to be critically dependent on film morphology. In order to establish the best methodology for generating reproducible vapor-deposited thin metal films, the influence of a wide range of experimental deposition variables on Ag film morphology and optical properties was investigated by use of a combination of optical absorption, atomic force microscopy, and surface-enhanced Raman spectroscopy (SERS). The specific variables examined include quality of glass substrate, glass pretreatment, deposition rate, deposition temperature, deposition geometry, and postdeposition annealing. The type of glass substrate ("white" glass vs "float" glass) was found to be an important factor for producing high-quality Ag films. However, glass pretreatment appeared to be relatively unimportant. Deposition rate and geometry are critical parameters in generating reproducible films. In addition, mild elevation of substrate temperature (Δ20 °C) strongly affects film characteristics. A detailed analysis of SERS reproducibility, based on these variables, is reported.

Thin metal films are employed as substrates in a broad range of fields due to their unique optical and electronic properties. Perhaps the most widespread application of thin metal films is as the active surface for surface-enhanced Raman scattering (SERS). Although other rough metal substrates provide surface enhancement, such as electrodes, colloids, and metal-coated nanospheres, vapor-deposited thin metal films are widely used because of their stability and the ease with which they are prepared and characterized.[1-6] While the morphology and optical characteristics of vapor-deposited thin metal films have been studied as a function of deposition parameters, film reproducibility, especially in the context of SERS, remains an issue. SERS active metal films are prepared differently in every laboratory, resulting in a unique morphology and therefore unique optical properties. The goal of this work is to establish which of the many experimental variables of vapor deposition are most important in generating reproducible SERS active Ag films.

Schlegel and Cotton conducted a detailed study of the effect of deposition rate on the morphology and optical properties of thin Ag films.[4] They found that as the deposition rate is increased the optical density of 5 nm thick films decreases and the wavelength maximum red shifts. In addition, the magnitude of SERS from an adsorbate is reduced for films deposited at faster rates. These optical trends were explained by changes observed in the morphology of the films, determined by transmission electron microscopy (TEM), as a function of deposition rate; faster rates resulting in less separated Ag islands. While these results are in agreement with a qualitative study published by Sennett and Scott in 1950,[5] a recent atomic force microscopic (AFM) study by Roark and Rowlen demonstrated that the morphology of Ag films on the TEM substrate (Formvar) is not the same as the morphology of Ag films on glass.[7,8] In a recent study by Van Duyne et al.,[6] in which AFM was employed for surface characterization of Ag films, no changes were observed in morphology, optical absorbance, or SERS activity as a function of deposition rate. Van Duyne and co-workers noted two possible reasons for the discrepancy between the two studies: (1) differences in pretreatment (i.e., cleaning) of the glass substrates prior to deposition and (2) potential differences in the degree of radiative heating during the deposition. In the study presented here, the influence of quality of glass substrate, substrate pretreatment, deposition rate, deposition temperature, deposition geometry, and postdeposition annealing on the optical and morphological characteristics of thin Ag films is quantitatively investigated. In addition, a detailed analysis of SERS reproducibility is reported.

EXPERIMENTAL SECTION

Reagents. Ag powder, 5–8 μm, was used for preparation of Ag films (Aldrich, 99.9+%). Two nonresonantly enhanced adsorbates, 4,4′-dipyridyl (BP, 98%) and *trans*-1,2-bis(4-pyridyl)ethylene (BPE, 97%), were used as purchased (Aldrich). A resonantly enhanced adsorbate, zinc tetraphenylporphine (ZnTPP, synthetic), was used as purchased (Aldrich). Spectroscopic grade methanol (Burdick & Jackson) and analytical grade acetone (Mallinckrodt) were used as received. Concentrations of BP, BPE, and ZnTPP solutions were 1×10^{-3}, 4×10^{-4}, and 1×10^{-4} M in acetone, respectively. Application of analytes on the Ag films was achieved either by dipping for 1 min or by dropping 20 μL of analyte solution on the films.

Microscope Slide Pretreatment. Precleaned glass microscope slides were obtained from both Fisher Scientific and VWR Scientific Inc. The quality of the precleaned microscope slides varied considerably and will be discussed later in the text. Three

(1) Davis, C. A.; McKenzie, D. R.; McPhedran, R. C. *Opt. Commun.* **1991**, *85*, 70–82.
(2) Royer, P.; Goudonnet, J. P.; Warmack, R. J.; Ferrell, T. L. *Phys. Rev. B* **1987**, *35*, 3753–3759.
(3) Yoshida, S.; Yamaguchi, T.; Kinbara, A. *J. Opt. Soc. Am.* **1971**, *61*, 463–469.
(4) Schlegel, V. L.; Cotton, T. M. *Anal. Chem.* **1991**, *63*, 241–247.
(5) Sennett, R. S.; Scott, G. D. *J. Opt. Soc. Am.* **1950**, *40*, 203–211.
(6) Van Duyne, R. P.; Hulteen, J. C.; Treichel, D. A. *J. Chem. Phys.* **1993**, *99*, 2101–2115.
(7) Roark, S. E.; Rowlen, K. L. *Anal. Chem.* **1994**, *66*, 261–270.
(8) Roark, S. E.; Rowlen, K. L. *Chem. Phys. Lett.* **1993**, *212*, 50–56.

0003-2700/94/0366-4324$04.50/0 © 1994 American Chemical Society

different cleaning procedures were compared by simultaneous deposition on the three substrates. The cleaning procedure reported by Schlegel and Cotton involved washing in 3 M KOH/methanol solution for a minimum of 1 h, followed by sonicating three times in doubly distilled water.[4] The glass slides were dried at 110 °C for a minimum of 20 min prior to deposition. The slides were cooled to room temperature before introduction into the vacuum chamber. The cleaning procedure reported by Van Duyne et al.[6] involved soaking the slides in 1 M NaOH for 1 h, followed by successive sonications in deionized water, methanol, and acetone. No heat was used to dry the slides before deposition. A third cleaning procedure, one often used in our laboratory, involved washing in 3 M NaOH for 1 h, followed by rinsing and sonicating four times in doubly deionized water. The slides were then dried at 110 °C for a minimum of 20 min prior to deposition. In order to further compare various pretreatments, experiments were also conducted with a drastic pretreatment of 10 M NaOH soak for 1 h, followed by successive sonications in doubly deionized water.

Deposition Apparatus. Thin Ag films were deposited with a Denton Vacuum DV-502 vapor-phase depositor. Over the several months required for this study, the pressure inside the deposition chamber ranged from 5×10^{-6} to 1×10^{-5} Torr. The film thickness and the deposition rate were monitored with a factory calibrated, temperature-controlled, quartz crystal microbalance (QCM; Syncon Instruments STM-100). The QCM was interfaced to a personal computer (486-DX) in order to obtain the mean deposition rate as well as the variation in rate as a function of time. The QCM was placed adjacent to and in the same plane as the substrate. The distance between the source and substrate could be varied between 22 and 12 cm and is specified for each experiment. A custom-built temperature-controlled aluminum block served as the substrate holder for thermal experiments. A Neslab RTE-110 liquid circulation bath served as the temperature controller. The substrate temperatures were measured with a calibrated K-type CO1 thermocouple (Omega) that was placed in direct contact with the substrate. A second K-type thermocouple was positioned in the same plane and adjacent to the substrate to measure radiative heating changes during a deposition. For postdeposition annealing experiments, industrial laboratory grade nitrogen (>95%) flowed continuously across the surface of the films.

Silver Film Deposition. Unless otherwise stated, all film thicknesses reported herein are 50 Å. The deposition rate was controlled by the current passed through either a molybdenum (99.9+%, Aldrich) or tantulum (99.9+%, Ted Pella Inc.) boat. Typically, a constant deposition rate was established prior to exposing the substrate to the source. However, results were similar when the predetermined deposition rate was obtained during the deposition. It should be recognized that this may be a significant source of error when interlaboratory comparisons are made, particularly for fast deposition rates (i.e., ≥5 Å/s). For angle-resolved depositions, the glass substrate was mounted on a angle calibrated rotation stage, such that the substrate could be rotated out of the deposition plane. The deposition rate was ~0.2 Å/s, and the thickness was ~50 Å. The films were deposited at angles ranging, in 10° intervals, from 0° to 40°. Three absorbance spectra were taken over the length of the slide.

Characterization of Silver Films. Optical absorption data were obtained on a Hewlett-Packard 8452A diode array spectrometer. Both the Raman and AFM instruments and operating conditions were described previously.[7] As in all AFM studies, deconvolution of the tip function represents a challenging problem due to uncertainty in the geometry of the scanning tip.[9]

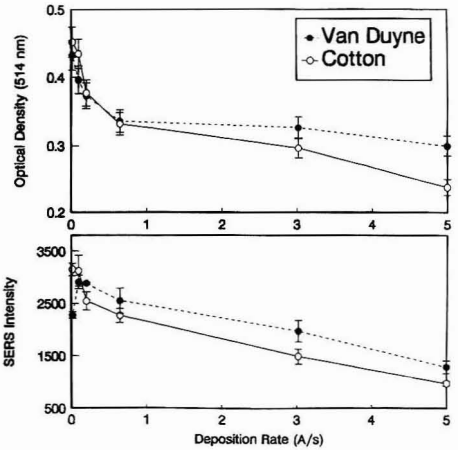


Figure 1. Optical and SERS comparison for the two pretreatments (see text) as a function of deposition rate. The individual deposition rates from low to high were 0.02, 0.10, 0.20, 0.65, 3.02, and 5.00 Å/s, respectively. The relative error in optical density is 5%, based on separate study of 10 Ag films. SERS intensity measurements are based on the 1293 cm^{-1} band of BP. The error bars represent the range from two experiments. The source to substrate distance was 21 cm.

RESULTS AND DISCUSSION

Deposition Rate. In order to investigate the influence of substrate (typically glass) cleaning procedures, a single glass slide was divided into two separate halves. One half was cleaned with the procedure reported by Schlegel and Cotton[4] (refer to Experimental Section for details), and the other half was cleaned with the procedure reported by Van Duyne et al.[6] The slides were placed side by side in the deposition chamber, and 5 nm of Ag was deposited simultaneously onto both. This procedure was followed for six deposition rates, ranging from 0.02 to 5.0 Å/s. Figure 1 shows the trend in optical density at 514 nm and SERS intensity from BP for both substrate pretreatments. Comparable intensity trends were observed for the resonantly enhanced ZnTPP. For both pretreatments, as the deposition rate is increased the wavelength maximum red shifts, optical density decreases, and SERS intensity decreases. The optical density at 514 nm is most highly correlated with the SERS intensity. Within error, the two substrates (which differ only in how they were cleaned) exhibit the same general trend. Likewise, comparisons of 3 M NaOH and 10 M NaOH as cleaning procedures yield, within error, identical film properties. Thus, the observed differences in deposition rate dependence between the two laboratories cannot be ascribed to substrate pretreatment.

Atomic force micrographs (see Figure 2) of the films show the same qualitative trends in particle size and shape as those

(9) *Artifacts in SPM*; technical note; Topometrix Corp., 1991.

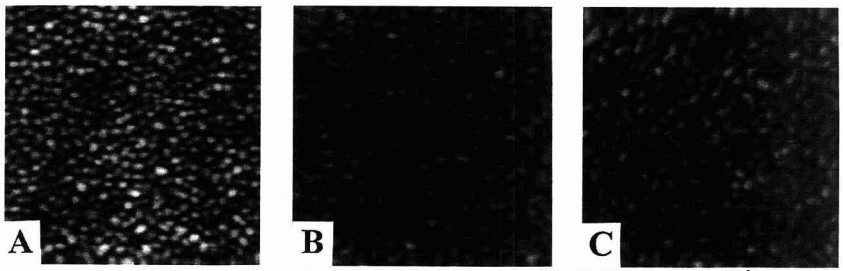


Figure 2. Representative AFM images of 5 nm Ag films deposited with varying rates: (A) 0.02, (B) 0.20, and (C) 2.5 Å/s. Image sizes are 500 nm × 500 nm. All of the AFM images in this work are unfiltered.

reported by Schlegel and Cotton; as the rate increases the particles become less separated with a corresponding decrease in aspect ratio. Referring again to Figure 1, note that, within error, there is little change in optical characteristics over the range of deposition rates investigated by Van Duyne et al. (0.5–20 Å/s). This is also in qualitative agreement with the deposition rate study of Schlegel and Cotton; the most dramatic influence of deposition rate is observed for deposition rates below 0.5 Å/s. It is therefore possible that the observed differences in deposition rate dependence are due to the relatively fast deposition rates employed by Van Duyne et al. Another possible explanation to be addressed, as noted by Van Duyne, is a difference in radiative heating during deposition.

Elevated Deposition Temperature. Sennett and Scott[5] qualitatively investigated the effect of substrate temperature on thin metal film morphology and found little difference in morphology for temperatures below 70 °C. A more recent study of thicker Ag films (>10 nm) found little temperature dependence over the range of 20–150 °C.[10] While Schlegel and Cotton did not measure the temperature of the substrate during deposition, they reasoned that because of the distance between the source and substrate (12 cm), as well as minimal changes in the pressure during deposition, any changes in substrate temperature were probably slight. In our laboratory, under conditions matched to those reported by Schlegel and Cotton, the increase in temperature ranges from ~5 to 15 °C for a 5 nm film deposited at 0.2 Å/s. In the deposition system utilized by Van Duyne et al.,[6] in which multiple substrates are mounted on a rotating stage,[11] the substrate temperature was found to remain fairly constant at 22 °C for a deposition rate of 3.0 Å/s. In order to determine whether or not a small increase in temperature (e.g., 10–20 °C) could account for the observed differences in the two systems (Cotton vs Van Duyne), a temperature study was conducted by mounting the glass substrates on a temperature-controlled aluminum block. Figure 3 summarizes the trend in optical density and wavelength maximum for a series of films deposited at the same rate (0.20 Å/s), but at different temperatures (20, 30, 40, and 80 °C). The increase in substrate temperature during deposition results in blue-shifted spectra with a narrower bandwidth and higher optical density at 514 nm. Over the range of deposition temperatures given above, the optical density at wavelength maximum remains, within error, unchanged. Atomic force micrographs of the films indicate that as the substrate temperature is increased, larger Ag particles are formed with greater interparticle separation (Figure 4). The particle height histograms from a computer-aided manual sampling of 30 Ag particles are shown in Figure 4. From this analysis, the mean particle height increases from 5.0 ± 1 to 6.7 ± 1 nm for films deposited at 20 and 40 °C, respectively. The mean aspect ratio for Ag deposited at 20 and 40 °C increases from 0.5 to 0.6. The trend in particle height, as a function of temperature, has also been investigated by a more comprehensive statistical evaluation of the micrographs (the details of which will be published at a later date). By sampling ~1500 particles on

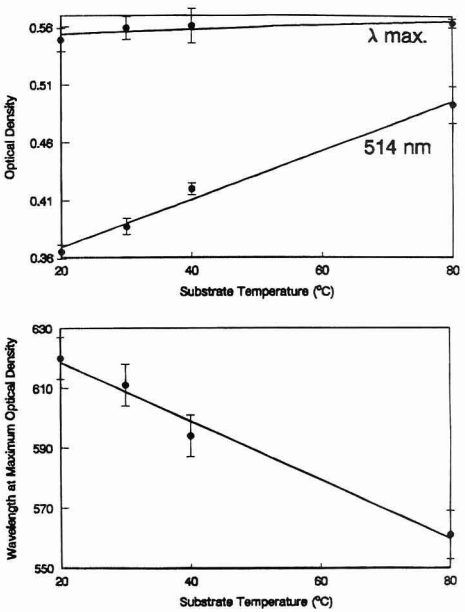


Figure 3. Relationship between optical data and substrate deposition temperatures. Error bars ($\pm\sigma$) derive from three measurements across the length of the slide. The source-to-substrate distance was 12 cm for the 20, 30, and 40 °C films. The source-to-substrate distance was 21 cm for the 80 °C film. Deposition rates were 0.19, 0.19, 0.18, and 0.18 Å/s for the 20, 30, 40, and 80 °C Ag films, respectively.

(10) Dutta, P. K.; Wilman, H. *J. Phys. D: Appl. Phys.* **1970**, *3*, 839–853.
(11) Hulteen, J., Northwestern U., Evanston, IL, personal communication.

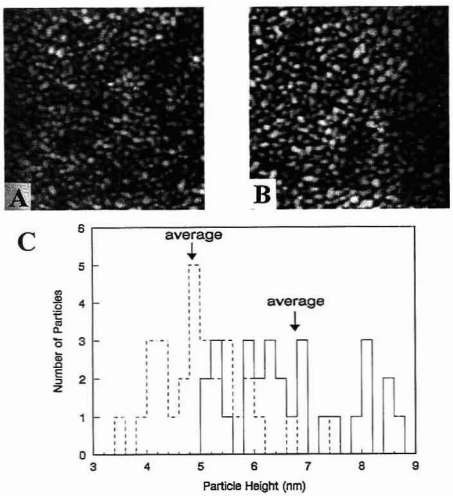


Figure 4. AFM images for the (A) 20 °C as-deposited film and (B) 40 °C as-deposited film. Image sizes are 500 nm × 500 nm. (C) is a histogram of particle heights (nm) as measured from a random sampling of 30 particles. The dashed line represents the height distribution for the film deposited at 20 °C, and the solid line represents the height distribution for the film deposited at 40 °C.

each micrograph (1 μm × 1 μm), the distribution in particle height was found to be Gaussian and the mean particle heights were ~6.5 and 9.5 nm, for the 20 and 40 °C films, respectively. While the absolute magnitude in particle heights is different for the two sampling methods, the trend is the same. Correlated with these changes in morphology and the increase in optical density at 514 nm, as the deposition temperature is increased, is an increase in SERS activity (~15% over 25 °C range). Similar trends in film characteristics were observed for quartz substrates. In summary, this study indicates that even small changes in the substrate temperature during deposition can affect Ag film morphology and optical characteristics.

Since, in most systems the temperature of the substrate is not controlled, temperature rises of 15–20 °C over the period of the deposition (~4 min for 0.2 Å/s deposition of a 5 nm film) may not result in the same order of magnitude changes observed under controlled conditions, but could account for some of the variability in film characteristics. For experiments in which the temperature is not controlled, within experimental error, the change in temperature appears to be independent of deposition rate. Thus, the observed deposition rate dependence is real and not a simple function of temperature. If an increase in deposition rate (red shift in λ_{max}) were accompanied by increased temperatures (blue shift in λ_{max}), the two opposed trends may account for no overall dependence on deposition rate.

Postdeposition Annealing. It is well documented that the film characteristics of thin Ag films on glass and quartz are strongly affected by high-temperature annealing.[6,12–15] Typically, the films are heated above 200 °C for 20 min to 1 h (e.g., ref 6). The absorbance spectrum of an annealed film is generally blue-shifted, has a lower optical density, and has a narrower bandwidth. A study by Aussenegg et al.[12] indicates that mild heating (<80 °C for 20 min) also results in drastic changes in film optical characteristics; a 70 nm blue shift, a decrease in optical density, and narrowing of the absorption band. In order to quantify the effects of low annealing temperatures on film properties, a series of experiments were conducted in which the temperature of the film was elevated a maximum of only 60 °C above room temperature.

A single microscope slide was cleaned with the procedure outlined by Schlegel and Cotton[4] and divided into halves. One half of the slide was mounted on the temperature-controlled aluminum block within the vacuum deposition chamber (~7 × 10^{-6} Torr). As a control, the other half of the slide was positioned on the block in the same geometry with respect to the vapor source but was thermally insulated. A 5.0 nm film was simultaneously deposited onto both slides at a rate of 0.18 Å/s. The temperature of both halves was continuously monitored throughout the deposition and during postdeposition annealing. After the deposition, the films were allowed to cool for ~15 min resulting in final substrate temperatures of ~23 °C. The temperature block (and therefore the uninsulated slide) was then heated to 80 °C and maintained at that temperature for 45 min. The temperature of the insulated slide rose only ~5 °C over this period. After 45 min the system was allowed to cool to room temperature before the vacuum was broken. The annealed (uninsulated) slide was blue-shifted with respect to the "as-deposited" sample, 602 and 620 nm for the wavelength maxima, respectively. An increase in optical density at 514 nm and decrease in optical density at the wavelength maximum was observed. Atomic force micrographs of the two films show that annealing results in larger Ag particles with greater interparticle separation. Our results are comparable to an experiment by Aussenegg et al.,[12] which involved postdeposition annealing of a 4 nm Ag film by thermal radiation from the source (800 °C under vacuum for 20 min) located 30 cm from the film. Surprisingly, our results are also similar to the postdeposition annealing study conducted by Van Duyne et al.[6] in which 5 nm films were heated to 600 K for 1 h.

In order to address the effect of these mild annealing conditions on SERS intensity, a temperature study was conducted under nitrogen. A 5.0 nm Ag film was deposited at 0.20 Å/s. The slide was then cut into three sections. Two sections of the slide were dipped into a BPE solution for 1 min. Since it has been shown that solvent exposure can affect Ag film properties,[7] optical absorption spectra were taken 1 h after sample application. Two sections were then positioned on another custom-built temperature-controlled block that served as a substrate holder for SERS experiments. One section was positioned in the laser excitation beam path and was not moved throughout the experiment. The second section was periodically removed from the block in order to obtain an absorbance spectrum. The temperature of both substrates was raised in 10° increments and maintained at a given temperature for 15 min. Both sections were continuously purged with nitrogen during the entire experiment. The third section, the blank, was not exposed to adsorbate or elevated temperatures. Figure 5 shows the optical characteristics for this in situ SERS

(12) Aussenegg, F. R.; Leitner, A.; Lippitsch, M. E.; Reinisch, H.; Riegler, M. *Surf. Sci.* **1987**, *189/190*, 935–945.
(13) McCarthy, S. L. *J. Vac. Sci. Technol.* **1976**, *13*, 135–138.
(14) Bennett, J. M.; Hurt, H. H.; Rahn, J. P.; Elson, J. M.; Guenther, K. H.; Rasigni, M.; Varnier, F. *Appl. Opt.* **1985**, *24*, 2701–2711.
(15) Hurt, H. H.; Bennett, J. M. *Appl. Opt.* **1985**, *24*, 2712–2720.

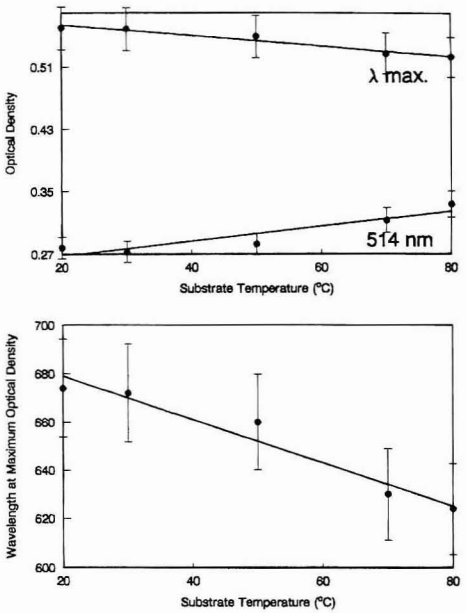


Figure 5. Relationship between optical characteristics and postdeposition substrate temperatures. The 5 nm Ag film was deposited at 0.19 Å/s at a source to substrate distance of 21 cm. Throughout the experiment, nitrogen flowed across the surface of the film. Absorbance spectra were acquired immediately after removal from the temperature block. Relative error was estimated to be 5% for the optical density and 3% for the wavelength at maximum optical density (from a separate study of 10 films). The spectra are red-shifted with respect to those shown in Figure 3 due to application of the sample (BPE).[4]

annealing experiment. As the substrate temperature was elevated, a blue shift in the absorbance spectra occurred. Optical density decreased at the wavelength maximum and increased at 514 nm. Highly correlated with the optical density at 514 nm is the SERS intensity of BPE. As shown in Figure 6, the SERS intensity increases by a factor of 7 from 30 to 80 °C. While all of the bands in the BPE spectrum increased in intensity, the slope of the increase varied. This behavior may be due to molecular reorientation at the Ag surface.[16,17] After 80 °C was reached, the film was cooled back to 30 °C in 10° increments. As is clearly evident in Figure 6, the final SERS intensity is still significantly greater than the initial "as-deposited" film, suggesting a permanent morphological change.

As can be observed by comparing Figures 3 and 5, "annealing" during the deposition leads to little or no change in optical density at the wavelength maximum, whereas postdeposition annealing results in a decrease in optical density. The reason for such differences in optical density (at wavelength maximum) are not clear at this time, but may be associated with differences in particle size *distributions*. A quantitative comparison of particle size distributions for both annealing experiments is in progress.

(16) Fujii, S.; Misono, Y.; Itoh, K. *Surf. Sci.* **1992**, *277*, 220–228.
(17) Itoh, K.; Yaita, M.; Hasegawa, T.; Fujii, S.; Misono, Y. *J. Electron Spectrosc. Relat. Phenom.* **1990**, *54/55*, 923–932.

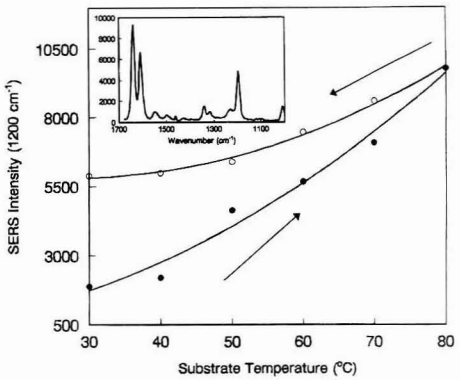


Figure 6. Relationship between SERS intensity of the 1200 cm^{-1} band in BPE and postdeposition substrate temperature. Spectra were acquired with 514.5 nm excitation and a 10 s integration time. The sample was equilibrated 15 min at each temperature prior to obtaining the spectrum. Arrows represent the direction of the temperature increase or decrease. The inset graph shows the SERS spectrum of BPE acquired with 514.5 nm (~50 mW) excitation and a 15 s integration time.

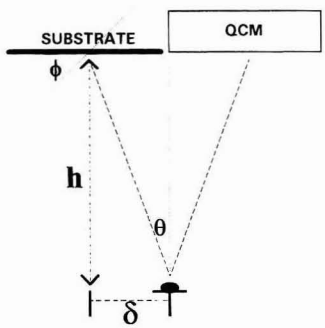


Figure 7. Diagram of vapor deposition arrangement. The angle θ is defined as the angle between the point source normal and the middle of both the substrate and the QCM. The linear distance δ is defined as the distance between the point source and the middle of the substrate. The linear distance h is defined as the source to substrate height, with the QCM positioned in the plane of the substrate. Angle ϕ is the angular rotation of the substrate out of the plane of the QCM.

Deposition Geometry. Another variable in vapor deposition of thin metal films is the geometry between the source and substrate. It is well-known that the rate of flux, and therefore deposition rate, from a point source can vary as a function of angle away from the source. The angular dependence is cos θ, where θ is the angle from normal (see Figure 7). In order to emphasize this variable as a potential source of error for interlaboratory comparisons, a detailed study was conducted. Figure 7 shows a typical configuration for the vapor source, the substrate, and a thickness monitor (e.g., QCM). Although the QCM is relatively easy to calibrate,[18] if the angle between the vapor source and the

(18) Fornari, B.; Mattei, G.; Pagannone, M. *J. Vac. Sci. Technol. A* **1988**, *6*, 167–168.

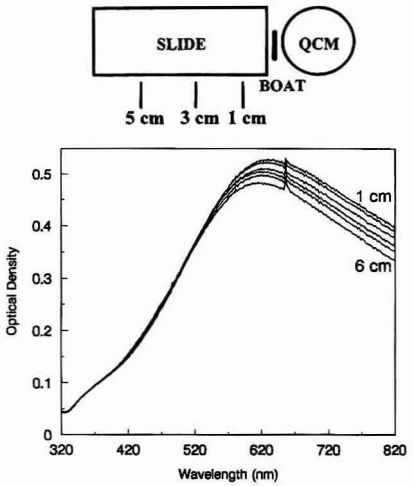


Figure 8. Optical data across the length of a slide positioned in the same plane as the QCM. The 5 nm Ag film was deposited at 0.19 Å/s with a source-to-substrate distance of 21 cm.

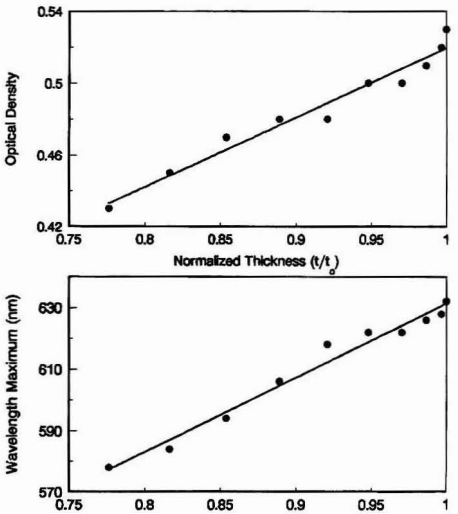


Figure 9. relationships for normalized film thickness (see text for details).

substrate is different from that between the source and the QCM, both the rate and thickness measured at the QCM will be different from the rate and thickness at the substrate. To demonstrate this, a glass microscope slide was positioned adjacent to the QCM in the manner shown in Figure 8. The QCM and slide were in the same plane 21 cm above the source. The optical density of the slide was probed at 1 cm intervals over the length of the slide (7 cm). As observed in Figure 8, the absorbance spectra blue shift and decrease in optical density as the angle between the source and substrate increases. Since, below 9 nm film thickness, both optical density and the wavelength maximum are reasonably linear with thickness,[19] the spectral data indicate a decrease in film thickness with increasing angle. Vapor deposition of metal in the system described in Figure 7 should obey Knudsen's cosine law. Specifically, our instrumental configuration should follow the relationship for a point source and a plane receiver:[20]

$$t = \frac{m}{4\pi\varrho}\frac{\cos\theta}{r^2} = \frac{mh}{4\pi\varrho(h^2+\delta^2)^{3/2}} \qquad t_o = \frac{m}{4\pi\varrho}\frac{1}{h^2}\frac{t}{t_o} = \frac{h}{(1+(\delta/h)^2)^{3/2}} \xrightarrow{\text{normalized}} \frac{1}{(1+(\delta/h)^2)^{3/2}}$$

where t is thickness (cm) deposited at an angle (θ) with respect to the source, t_o is the thickness deposited directly above the source ($\theta = 0$), t/t_o is normalized thickness, m is mass (g), ϱ is density (g/cm^3), and h and δ are distances defined in Figure 7. As shown in Figure 9, a plot of optical density vs t/t_o is linear ($R = 0.98$, $m = 0.39 \pm 0.03$), as is a plot of wavelength maximum vs t/t_o ($R = 0.99$, $m = 242 \pm 13$). Deposition in our system does indeed obey the cosine law.

The angle between the source and the substrate can also be varied by rotating the substrate out of the "deposition plane", as designated by ϕ in Figure 7. Sennett and Scott[5] noted that the structure and optical characteristics of thin metal films was fairly independent of deposition angle (ϕ). However, others have noted a strong correlation between deposition angle and thin film morphology.[21] In this study, the planar deposition angle was varied between 0° and 40°. The optical density decreases, and therefore thickness decreases linearly with cos ϕ; the slope of the regression line is 0.65 ± 0.01 with a R value of 1.0. In summary, these studies highlight the importance of deposition geometry. For interlaboratory comparisons, care must be taken to specify the exact geometry (in at least two coordinates) with respect to both the source and the thickness monitor.

Reproducibility: Substrate. One of the first things to consider in generating reproducible SERS signals is the substrate. Perhaps the most common substrates for SERS active metal films are glass microscope slides. While the choice of cleaning procedure does not appear to have a measurable influence on film characteristics, the choice of glass is crucial. Glass slides are typically prepared either by mechanically drawing malleable glass or by floating molten glass on liquid Sn.[22] The surface characteristics of glass slides that are drawn, often referred to as "water white" glass, can vary substantially from batch to batch and are generally microscopically rough. "White" glass can be distinguished from float glass by the color observed when the slides are viewed along an edge; white glass is clear and float glass is a light green. The float glass has the important advantage of being very flat; however, the two sides of the slide can be quite different. The side of the slide that is not in contact with Sn is typically exposed to a mixture of 5% H_2 and 95% N_2 during preparation.

(19) Roark, S. E.; Rowlen, K. L. *Appl. Spectrosc.* **1992**, *46*, 1759–1761.
(20) Holland, L. *Vacuum Deposition of Thin Films*; Wiley & Sons: New York, 1956; p 146.
(21) Cocks, F. H.; Peterson, M. J.; Jones, P. L. *Thin Solid Films* **1980**, *70*, 297–301.
(22) Sanford, P., Erie Scientific Co., Portsmouth, NH, personal communication.

The Sn side can be easily identified by its yellow fluorescence (due to Sn impurities) when exposed to 254 nm light.[22] The effect of the two chemically distinct sides of float glass on Ag film characteristics was investigated by depositing a 5 nm film simultaneously onto two halves of a slide; both the Sn side and the non-Sn side were exposed to the source. From five separate experiments, the wavelength at maximum optical density is consistently (33 ± 13 nm) red-shifted for Ag on the Sn side of the glass. In addition, the optical density is significantly reduced (~20%) for Ag on the Sn side. Although, micrographs were not obtained for these samples, the trend in optical characteristics implies a more oblate Ag particle shape on the Sn side of the glass substrate.

Normally, the preparation for glass microscope slides is not specified by the distributor; thus, the quality of the slides can vary significantly from package to package. For example, Figure 10 shows atomic force micrographs of two different microscope slides. Note that deep pits (~6–10 nm) can be found on some slides. Also shown in Figure 10 is a micrograph of a Ag film on the pitted glass. It is clear that these pits strongly affect morphology. The optical spectra of Ag films prepared on pitted slides are blue-shifted with respect to films on smooth slides. In order to obtain reproducible SERS active surfaces, the non-Sn side of float glass should be used as the substrate.

Sample Application. Two methods for applying a sample to the Ag film were evaluated; dip-coating a 20 μL drop of the respective analyte in a volatile solvent and a 1 min immersion into the analyte solution.[4] Based on the evaluation of the relative error in SERS intensity for 67 films over a period of 3 months, the immersion technique exhibited a factor of ~2 larger relative error than the dip-coating technique. On the basis of this analysis, drop coating was employed as the application technique for all further studies.

Deposition Rate and Cooling Period. The rate at which a given vapor deposition proceeds, as determined by the QCM, can vary substantially. For example, the average relative error in deposition rate for a total of eight depositions over a 3 day period was ~19% (for ~0.2 Å/s). On the basis of the previously outlined influence of deposition rate on film optical characteristics, in order to compare one deposition to another, the average rate should be reported along with the variation in rate. Another important variable for obtaining reproducible optical characteristics for thin Ag films is the "cooling period", or the time the film is allowed to remain under vacuum after deposition.[3,12] When the Ag film is removed immediately after deposition (1 min), the optical density is significantly lower (~10%) and the wavelength at maximum optical density is 30 nm red-shifted with respect to films left in the chamber 15 min after deposition. Correspondingly, films removed immediately from vacuum exhibit much lower SERS activity (~40% lower).

SERS Measurements. A detailed comparison of the variation in SERS intensity was conducted for (1) multiple measurements on a single slide (5 nm film on a glass microscope slide), (2) slides prepared from separate depositions on a given day, and (3) slides prepared from depositions on different days. A total of 63 measurements on seven films deposited over a period of 3 days were evaluated. For multiple measurements on a single film the relative error is ~15%. Film-to-film relative error is ~20%. This study suggests that a large portion of the error in SERS measurements arises from the process of making a SERS measurement

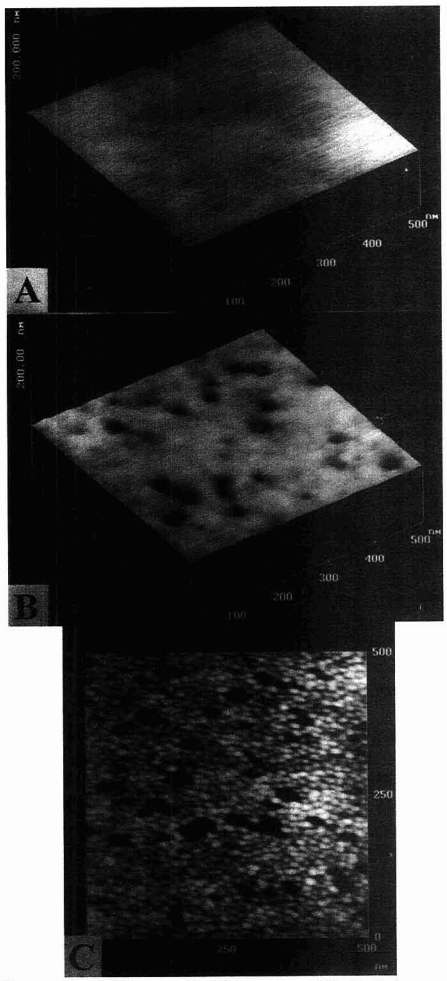


Figure 10. AFM images for (A) bare glass, (B) pitted glass, and (C) a 5 nm (0.01 Å/s) Ag film on the pitted glass. Image sizes are 500 nm × 500 nm. The images are shown in real space; i.e., the *z*-axis is not exaggerated.

(i.e., sample coverage, sample alignment, laser intensity, instrument alignment, etc.), rather than the deposition process. Under conditions optimized for generating reproducible Ag films, SERS intensity from individual films deposited on the same day exhibits only slightly greater relative error than multiple measurements on a single film. Day-to-day reproducibility can be quite good (~20% relative error) if no instrumental changes are necessary.

In summary, it appears that the difference in deposition rate dependence observed between the Cotton and Van Duyne laboratories can be explained by the higher deposition rates utilized by Van Duyne et al.[6] Based on this study, in order to obtain reproducible SERS active Ag films the following steps should be taken: (1) select the appropriate substrate, if glass is to be used, the non-Sn side of float glass should be used; (2) the

substrate should be cleaned, but for glass the cleaning procedures investigated here do not appear to result in observable differences in surface characteristics; (3) for accurate measurement of deposition rate and final thickness, as well as interlaboratory comparison, the deposition geometry should be carefully considered; (4) slower deposition rates (≤0.2 Å/s) have inherently less error and result in greater SERS active films; (5) the films should remain under vacuum for a minimum of 15 min after deposition; and (6) since even mild temperature elevation (Δ20 °C) results in changes in film characteristics, the temperature of the substrate should be controlled, or at least monitored, during deposition. However, as concluded by Schlegel and Cotton,[4] as long as the temperature change is reproducible, the resulting morphological and optical properties of each film should be reproducible.

ACKNOWLEDGMENT

The authors thank K. A. Douglas for use of the atomic force microscope and S. George for helpful discussions. K.L.R. thanks the Beckman Foundation for a Young Investigator Award and the Society of Analytical Chemists of Pittsburgh for a fellowship. This work was supported by a grant from the National Science Foundation (CHE-9311638).

Received for review May 9, 1994. Accepted September 9, 1994.[⊗]

[⊗] Abstract published in *Advance ACS Abstracts,* October 15, 1994.

Anal. Chem. **1994,** *66,* 4332–4336

Alkali Metal, Alkaline Earth Metal, and Ammonium Ion Selectivities of Dibenzo-16-Crown-5 Compounds with Functional Side Arms in Ion-Selective Electrodes

Akira Ohki,† Jian Ping Lu, Xiaowu Huang, and Richard A. Bartsch*

Department of Chemistry and Biochemistry, Texas Tech University, Lubbock, Texas 79409-1061

Potentiometric selectivities of 11 dibenzo-16-crown-5 compounds for alkali metal, alkaline earth metal, and ammonium ions have been determined in solvent polymeric membrane electrodes. The ionophores bear one or two pendent groups on the central carbon of the three-carbon bridge in the polyether ring. Side-arm variation includes OCH_3, $OCH_2CH_2OCH_3$, $OCH_2CO_2C_2H_5$, $OCH_2C(O)N(C_2H_5)_2$, and $OCH_2C(O)N(C_5H_{11})_2$ units. Attachment of a propyl group to the ring carbon that bears an extended, oxygen-containing side arm increases the selectivity for Na^+ relative to larger alkali metal and alkaline earth metal cations. For a given side arm, a linear relationship is obtained when the enhancement in Na^+ selectivity produced by attachment of a geminal propyl group is plotted against the diameter of the interference ion. Potentiometric responses of the dibenzo-16-crown-5 compounds are rationalized in terms of the crown ether ring size and the oxygen basicity, conformational positioning, and rigidity of the side arm.

In earlier work, we prepared lariat ether[1] derivatives of dibenzo-16-crown-5, such as *sym*-(R)-dibenzo-16-crown-5-oxyacetic acid (**1** with R = H or alkyl) in which an oxyacetic acid group (OCH_2CO_2H) is attached to the central carbon of the three-carbon bridge in the polyether ring. Such proton-ionizable lariat ethers in their ionized forms are efficient and selective agents for the solvent extraction of alkali metal, alkaline earth metal, and lanthanide ions and their transport through liquid membranes.[2-11] We have also investigated the influence of nonionizable side arms, such as OCH_2CO_2H (unionized),[12] $OCH_2CO_2C_2H_5$,[12] and $OCH_2C(O)NRR'$ with R = H or alkyl (C_2–C_6) and R' = alkyl (C_2–C_6),[12,13] upon the complexation of Li^+, Na^+, and K^+ by dibenzo-16-crown-5 compounds in solvent polymeric membrane electrodes.

In the present study, we have determined the potentiometric selectivities of solvent polymeric membrane electrodes containing dibenzo-16-crown-5 compounds **2**–**12** (Figure 1) as ionophores for five alkali metal, four alkaline earth metal, and ammonium ions. Within the series of compounds **3**–**7**, the side-arm variation on the central carbon of the three-carbon bridge in the polyether ring includes OCH_3, $OCH_2CH_2OCH_3$, $OCH_2CO_2C_2H_5$, $OCH_2C(O)N(C_2H_5)_2$, and $OCH_2C(O)N(C_5H_{11})_2$ units; while in **8**–**12**, a geminal propyl group is attached to the central carbon in addition to the oxygen-containing side arm.

EXPERIMENTAL SECTION

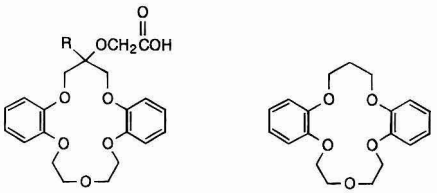
Chemicals. Poly(vinyl chloride) (PVC) with an average polymerization degree of 1100 was purchased from Wako Pure Chemical Industries (Osaka, Japan). *o*-Nitrophenyl octyl ether (NPOE) and potassium tetrakis(*p*-chlorophenyl)borate (KTpClPB) were obtained from Dojindo Laboratories (Kumamoto, Japan). Alkali metal and alkaline earth metal chlorides, ammonium chloride, and tetrahydrofuran (THF) were reagent-grade chemicals. Deionized water was prepared by passing distilled water through three Barnstead D8922 combination cartridges in series. Dibenzo-16-crown-5 compounds **3**, **5**–**8**, and **10**–**12** are known compounds.[12,13]

The new lariat ethers, *sym*-(1,4-dioxapentyl)dibenzo-16-crown-5 (**4**) and *sym*-(1,4-dioxapentyl)(propyl)dibenzo-16-crown-5 (**9**), were prepared as follows. After removal of the protecting mineral oil from 1.02 g of potassium hydride (35% dispersion in mineral oil, 9.0 mmol) by washing with pentane under nitrogen, 3.0 mmol of *sym*-(hydroxy)dibenzo-16-crown-5[14] or *sym*-(hydroxy)(propyl)-dibenzo-16-crown-5[15] in 100 mL of dry THF was added. The mixture was stirred for 30 min at room temperarture and 0.56 mL (6.0 mmol) of 1-bromo-2-methoxyethane was added dropwise.

† Permanent address: Department of Applied Chemistry and Chemical Engineering, Faculty of Engineering, Kagoshima University, Kagoshima 890, Japan.

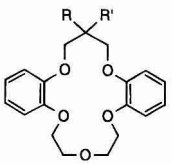
(1) Gokel, G. W.; Dishong, D. M.; Diamond, C. J. *J. Chem. Soc., Chem. Commun.* **1980**, 1053–1054.
(2) Strzelbicki, J.; Bartsch, R. A. *Anal. Chem.* **1981**, *53*, 1894–1899.
(3) Bartsch, R. A.; Heo, G. S.; Kang, S. I.; Liu, Y.; Strzelbicki, J. *J. Org. Chem.* **1982**, *47*, 457–460.
(4) Charewicz, W. A.; Heo, G. S.; Bartsch, R. A. *Anal. Chem.* **1982**, *54*, 2094–2097.
(5) Bartsch, R. A.; Liu, Y.; Kang, S. I.; Son, B.; Heo, G. S.; Hipes, P. G.; Bills, L. *J. Org. Chem.* **1983**, *48*, 4864–4869.
(6) Tang, J.; Wai, C. M. *Anal. Chem.* **1986**, *58*, 3233–3235.
(7) Charewicz, W. A.; Walkowiak, W.; Bartsch, R. A. *Anal. Chem.* **1987**, *59*, 494–496.
(8) Tang, J.; Wai, C. M. *J. Membr. Sci.*, **1988**, *35*, 339–345.
(9) Bartsch, R. A. *Solvent Extr. Ion Exch.* **1989**, *7*, 829–854.
(10) Walkowiak, W.; Charewicz, W. A.; Kang, S. I.; Yang, I. W.; Pugia, M. J.; Bartsch, R. A. *Anal. Chem.* **1990**, *62*, 2018–2021.
(11) Wai, C. M.; Du, H. S. *Anal. Chem.* **1990**, *62*, 2412–2414.
(12) Ohki, A; Lu, J. P.; Bartsch, R. A. *Anal. Chem.* **1994**, *66*, 651–654.
(13) Ohki, A; Maeda, S.; Lu, J. P.; Bartsch, R. A. *Anal. Chem.* **1994**, *66*, 1743–1746.
(14) Heo, G. S.; Bartsch, R. A.; Schlobohm, L. L.; Lee, J. G. *J. Org. Chem.* **1981**, *46*, 3574–3575.
(15) Hayashita, T.: Goo, M.-J.; Lee, J.-C.; Kim, J. S.; Kryzkawski, J.; Bartsch, R. A. *Anal. Chem.* **1990**, *62*, 2283–2287.

0003-2700/94/0366-4332$04.50/0 © 1994 American Chemical Society



1

2



When R = H	R'	When R = C_3H_7
3	$-OCH_3$	8
4	$-OCH_2CH_2OCH_3$	9
5	$-OCH_2CO_2C_2H_5$	10
6	$-OCH_2C(O)N(C_2H_5)_2$	11
7	$-OCH_2C(O)N(C_5H_{11})_2$	12

Figure 1. Structures of dibenzo-16-crown-5 and related lariat ether derivatives.

The mixture was refluxed for 4 h, and water was carefully added to destroy the unreacted potassium hydride. The THF was evaporated in vacuo, and dichloromethane (150 mL) and water (100 mL) were added to the residue. The mixture was shaken, and the dichloromethane layer was separated, washed with water (2 × 50 mL), dried over magnesium sulfate, and evaporated in vacuo to give the crude product. For **4**, the crude product was recrystallized from hexanes (50 mL) to give a 77% yield of white crystals: mp 62–63 °C; IR (deposit from $CDCl_3$ solution on a NaCl plate), 1256 (C–O) cm^{-1}; ^1H NMR ($CDCl_3$), δ 3.40–3.55 (s, 3 H); 3.62–4.40 (m, 17 H); 6.83–7.05 (m, 8 H). Anal. Calcd for $C_{22}H_{28}O_7$: C, 65.35; H, 6.93. Found: C, 65.56; H, 6.96. For **9**, the crude product was chromatographed on alumina with dichloromethane as eluent to give a colorless oil in 83% yield: IR (neat), 1257 (C–O) cm^{-1}; ^1H NMR ($CDCl_3$), δ 0.94–1.01 (t, 3 H), 1.40–1.55 (m, 2 H), 1.88–2.00 (m, 2 H), 3.40 (s, 3 H), 3.55–3.62 (t, 2 H), 3.90–4.35 (m, 14 H), 6.81–6.96 (m, 8 H). Anal. Calcd for $C_{25}H_{34}O_7$: C, 67.24; H, 7.67. Found: C, 67.46; H, 7.77.

Preparation of PVC Membranes. PVC (50 mg), NPOE (100 mg), the lariat ether (5.0 mg), and KTpClPB (1.0 mg) were dissolved in 1.5 mL of THF. An aliquot of the THF solution was poured onto a porous poly(tetrafluoroethylene) (PTFE) membrane attached to a PVC tube, and the solvent was allowed to evaporate for 15–20 min. Addition of the THF solution and evaporation were repeated eight or nine times. The resulting PVC tube with the coated PTFE membrane was fixed on a Denki Kagaku Keiki (DKK, Musashino, Tokyo, Japan) No. 7900 electrode body. An internal filling solution of 0.10 M NaCl was added to the electrode. The electrode was conditioned by soaking in 0.10 M NaCl solution for 12 h before use.

Measurements. Potentiometric measurements with a membrane electrode were carried out at 24–25 °C with a voltage meter (Fisher Scientific Accumet 50 pH meter), a double-junction Ag–AgCl reference electrode (DKK No. 4083), and a magnetic stirrer to agitate the sample solution. The electrode cell was Ag–AgCl/0.10 M NaCl/PVC membrane/sample solution/0.10 M NH_4NO_3/3.0 M KCl/Ag–AgCl. Single ion activities were obtained as described previously.[12] The selectivity coefficients ($K_{Na,M}^{Pot}$) were determined by the fixed interference method.[16] The constant background concentrations of interfering ions were 0.10 or 0.50 M for Li^+, 1.0×10^{-2} or 5.0×10^{-2} M for K^+, 2.0×10^{-2} or 0.10 M for Rb^+ and Cs^+, 0.10 or 0.50 M for NH_4^+, 1.0 M for Mg^{2+}, and 0.50 M for Ca^{2+}, Sr^{2+}, and Ba^{2+}. For a given solvent polymeric membrane electrode system, the potentiometric selectivity was determined twice for each of two independently prepared membranes. The average value for the potentiometric selectivity was calculated from the values obtained for the four measurements. The standard deviation from the average value for log K^{Pot} was less than 0.05.

RESULTS AND DISCUSSION

Potentiometric Selectivities of Ionophores 2–12. Ionophores **2–12** were incorporated into solvent polymeric membranes in which PVC was the polymer and NPOE was the membrane solvent. For the ion-selective electrodes (ISEs) prepared from these membranes, potentiometric selectivities for Na^+ relative to other alkali metal cations, to alkaline earth metal cations and to NH_4^+ were determined by the fixed interference method.[16] Nernstian responses (59 mV/decade) were obtained for these solvent polymeric membrane electrodes. In Table 1 are recorded the selectivities (log $K_{Na,M}^{Pot}$) for the ISEs based on ionophores **2–12**.

When dibenzo-16-crown-5 (**2**) was utilized as the ionophore in the solvent polymeric membrane, positive log $K_{Na,M}^{Pot}$ values were observed for M = K^+ and Rb^+. Thus the ISE exhibits a greater potentiometric response to K^+ and Rb^+ than to Na^+. The response to monovalent cations decreases in the order $K^+ > Rb^+ > Na^+ > Cs^+ > NH_4^+ > Li^+$.

From comparison of the cavity diameter of dibenzo-16-crown-5 and the ionic diameters of the alkali metal ions and NH_4^+,[17,18] both Na^+ and Li^+ are expected to form inclusion or nesting complexes,[19] with Na^+ fitting the polyether cavity much better than Li^+. On the other hand, K^+, Rb^+, Cs^+, and NH_4^+ are too large to fit within the cavity and should form perching complexes,[19] which are anticipated to be less stable than nesting complexes. Although selective response to Na^+ is expected for the ISE containing ionophore **2**, it does not exhibit such selectivity. This is ascribed to a higher hydration energy of Na^+ compared with K^+ and Rb^+.[12,20]

Lariat ethers **3–7** are substituted dibenzo-16-crown-5 compounds which have one or more oxygen atoms in their side arms. These oxygen atoms are potential ligation sites for cationic species.

(16) Recommendation for Nomenclature of Ion-Selective Electrodes. *Pure Appl. Chem.* **1976**, *48*, 127–132.

(17) Lamb, J. D.; Izatt, R. M.; Christensen, J. J. In *Progress in Macrocyclic Chemistry*; Izatt, R. M., Christensen, J. J., Eds.; Wiley: New York, 1981; Vol. 2, pp 41–90.

(18) Izatt, R. M.; Bradshaw, J. S.; Nielsen, S. A.; Lamb, J. D.; Christensen, J. J.; Sen, D. *Chem. Rev.* **1985**, *85*, 271–339.

(19) Cram, D. J.; Trueblood, K. N. In *Host Guest Complex Chemistry. Macrocycles*; Vögtle, F., Weber, E., Eds.; Springer-Verlag: New York, 1985; pp 135–188.

(20) Burgess, J. *Metal Ions in Solution*; Wiley: New York, 1978; p 186.

Table 1. Potentiometric Selectivities of Lariat Ethers 2–12 for Na^+ over Alkali Metal, Alkaline Earth Metal, and Ammonium Ions

lariat ether[a]			$-\log K_{Na,M}^{Pot}$								
cmpd	R	R′	Li^+	K^+	Rb^+	Cs^+	Mg^{2+}	Ca^{2+}	Sr^{2+}	Ba^{2+}	NH_4^+
2	H	H	2.48[b]	−0.42[b]	−0.06	0.48	3.36	2.49	2.22	2.62	0.94
3	H	OCH_3	3.08[b]	−0.07[b]	0.29	0.88	3.53	2.88	2.50	2.59	1.48
4	H	$OCH_2CH_2OCH_3$	3.23	0.46	0.81	1.49	3.67	3.20	2.62	3.08	1.93
5	H	$OCH_2CO_2C_2H_5$	3.87[b]	0.45[b]	0.88	1.46	3.81	3.40	2.63	2.56	1.97
6	H	$OCH_2C(O)N(C_2H_5)_2$	3.02[b]	0.79[b]	1.42	2.05	3.76	2.90	2.31	1.40	2.11
7	H	$OCH_2C(O)N(C_5H_{11})_2$	3.14[c]	0.98[c]	1.48	2.18	3.88	3.19	2.41	1.56	2.13
8	C_3H_7	OCH_3	2.99[b]	0.34[b]	0.35	1.08	3.73	3.25	2.53	3.09	1.68
9	C_3H_7	$OCH_2CH_2OCH_3$	3.49	1.34	1.96	2.53	3.81	3.78	2.62	3.63	3.03
10	C_3H_7	$OCH_2CO_2C_2H_5$	3.73[b]	1.49[b]	2.16	2.61	3.80	3.84	2.70	3.18	3.20
11	C_3H_7	$OCH_2C(O)N(C_2H_5)_2$	2.84[b]	1.98[b]	2.62	3.07	3.83	3.55	2.66	2.76	3.02
12	C_3H_7	$OCH_2C(O)N(C_5H_{11})_2$	2.91[c]	2.13[c]	2.77	3.18	3.85	3.63	2.71	2.68	3.12

[a] Structures of the lariat ethers are shown in Figure 1. [b] Data from ref 12. [c] Data from ref 13.

Compared with **2**, the log $K_{Na,M}^{Pot}$ values for *sym*-(methoxy)-dibenzo-16-crown-5 (**3**), which has a methoxy group for the side arm, are more negative by 0.35–0.60 for M = Li^+, K^+, Rb^+, Cs^+, and NH_4^+. This is attributed to an increase in the Na^+ complexation by **3** relative to **2** due to coordination of Na^+ by the oxygen atoms in the crown ether ring and in the side arm. When a second ether oxygen is introduced into the side arm to give **4**, the log $K_{Na,M}^{Pot}$ values become more negative by 0.15 when M = Li^+ and by 0.45–0.61 when M = K^+, Rb^+, Cs^+, and NH_4^+ compared with the values for **3**. This demonstrates coordination of the complexed Na^+ by the second oxygen in the side arm as well. The enhancement in Na^+ selectivity for the ISE containing **4** relative to **3** is larger when the competing ion forms a perching complex (with K^+, Rb^+, Cs^+, or NH_4^+) rather than a nesting complex (with Li^+).

Lariat ethers **5**–**7** have side arms of $OCH_2CO_2C_2H_5$, $OCH_2C(O)N(C_2H_5)_2$, and $OCH_2C(O)N(C_5H_{11})_2$, respectively. Compared with **3**, for which the side arm is OCH_3, the log $K_{Na,M}^{Pot}$ values noted for **5**–**7** when M = K^+, Rb^+, Cs^+, and NH_4^+ are more negative by 0.49–0.59, 0.63–1.17, and 0.65–1.30, respectively. This is consistent with interaction of both the ether and the carbonyl oxygens in the side arm with the polyether cavity-complexed Na^+. Examination of CPK (Corey–Pauling–Kortum) space-filling models reveals that when the side arm is oriented over the crown ether cavity, the carboxyl oxygen can occupy an apical coordination site for the complexed Na^+. The Na^+ selectivity increases as the pendent side-arm function is changed from ester to amide, which is in agreement with the enhanced basicity of the carbonyl oxygen in the latter.[21] Also the trend for slightly higher Na^+ selectivity for the *N,N*-dipentyloxyacetamide side arm in **7** compared with the corresponding *N,N*-diethyloxyacetamide side arm in **6** may be rationalized in terms of an anticipated slightly higher carbonyl oxygen basicity of the former.

Effect of Preorganization. Lariat ethers **8**–**12** have a geminal propyl group attached to the central carbon of the three-carbon bridge in the polyether ring, as well as an oxygen-containing side arm. The presence of the geminal propyl group is postulated to orient the functional side arm over the cyclic polyether cavity in a conformation that requires minimal structural reorganization for metal ion complexation.[12] Such preorganization of the binding site enhances selectivity.[19,22]

To probe the effect of preorganization on Na^+ selectivity, the difference in log $K_{Na,M}^{Pot}$ values between lariat ethers with and

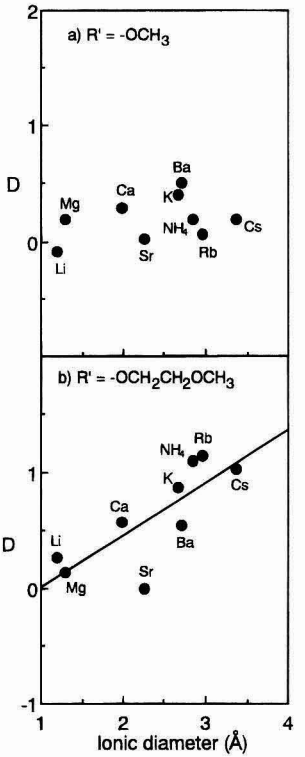


Figure 2. Differences in log $K_{Na,M}^{Pot}$ between lariat ethers with and without a geminal propyl group [$-D$ = (log $K_{Na,M}^{Pot}$ for the lariat ether with a geminal propyl group) − (log $K_{Na,M}^{Pot}$ for the corresponding lariat ether with a geminal hydrogen atom)] for dibenzo-16-crown-5 lariat ethers with (a) OCH_3 and (b) $OCH_2CH_2OCH_3$ side arms versus the diameter of the interference ion M^+.

(21) March, J. *Advanced Organic Chemistry*; Wiley: New York, 1985; pp 220–221.

(22) Cram, D. J. *Angew. Chem., Int. Ed. Engl.* **1986**, *25*, 1039–1057.

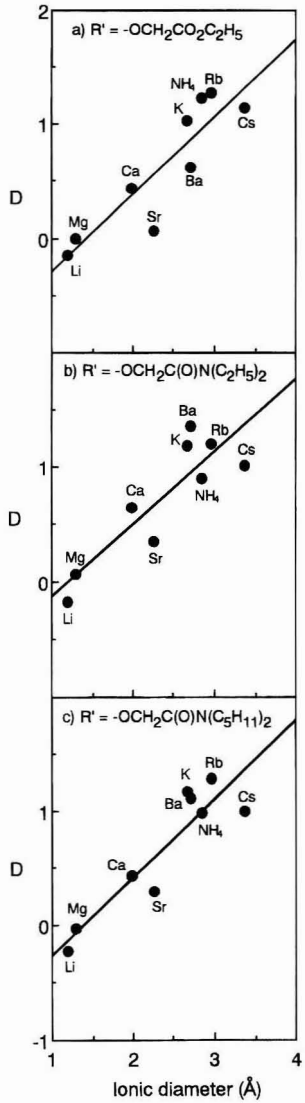


Figure 3. Differences in log $K_{Na,M}^{Pot}$ between lariat ethers with and without a geminal propyl group [$-D$ = (log $K_{Na,M}^{Pot}$ for the lariat ether with a geminal propyl group) − (log $K_{Na,M}^{Pot}$ for the corresponding lariat ether with a geminal hydrogen atom)] for dibenzo-16-crown-5 lariat ethers with (a) $OCH_2CO_2C_2H_5$, (b) $OCH_2C(O)N(C_2H_5)_2$, and (c) $OCH_2C(O)N(C_5H_{11})_2$ side arms versus the diameter of the interference ion M^+.

without the geminal propyl group [$-D$ = (log $K_{Na,M}^{Pot}$ for the lariat ether with a geminal propyl group) − (log $K_{Na,M}^{Pot}$ for the corresponding lariat ether with a geminal hydrogen atom)] is plotted against the ionic diameter of the interference cations (M^+ and M^{2+}). Such plots are shown for dibenzo-16-crown-5 lariat ethers with OCH_3 and $OCH_2CH_2OCH_3$ side arms in Figure 2 and for corresponding compounds with $OCH_2CO_2C_2H_5$, $OCH_2C(O)N(C_2H_5)_2$, and $OCH_2C(O)N(C_5H_{11})_2$ side arms in Figure 3.

Table 2. Slopes and Correlation Coefficients for the Plots in Figures 2b and 3a–c

R′	slope	corr coeff
$OCH_2C(O)N(C_5H_{11})_2$	0.69	0.91
$OCH_2CO_2C_2H_5$	0.68	0.89
$OCH_2C(O)N(C_2H_5)_2$	0.64	0.87
$OCH_2CH_2OCH_3$	0.46	0.79

When the oxygen-containing side arm is OCH_3, only slight variation in the magniture of D is noted as the diameter of the interference ion is increased (Figure 2a). Thus this side arm is judged to be too short to undergo better positioning over the binding site when the geminal propyl group is introduced.

Linear relationships between the D values and the ionic diameters are evident for lariat ethers with $OCH_2CH_2OCH_3$, $OCH_2CO_2C_2H_5$, $OCH_2C(O)N(C_2H_5)_2$, and $OCH_2C(O)N(C_5H_{11})_2$ side arms (see Figures 2b and 3a–c, respectively). As the size of the interference cations is enhanced, the difference in Na^+ selectivity between lariat ethers with and without the geminal propyl group becomes larger. The correlations include data points for monovalent alkali metal and ammonium ions, as well as divalent alkaline earth metal ions. Thus the D value is found to depend on the size of interference ion, but not its charge. It appears that a preorganized ionophore structure disfavors formation of the perching complexes[19] that are anticipated for metal cations larger than Na^+ by a steric effect. As the size of the interference ion is enhanced, conformational preorganization of the side arm becomes increasingly detrimental to the stability of a perching complex for the interference ion.

Slopes and correlation coefficients for the plots shown in Figures 2b and 3a–c are presented in Table 2. The slopes are appreciably greater when the side arm of the lariat ether terminates with an amide or ester group compared with a terminal ether function, even though an ether oxygen is more basic than a carbonyl oxygen.[21] For the ester and amide groups, the carbonyl carbon is sp^2 hybridized, which requires coplanarity of the carbon atom α to the carbonyl group, the carbonyl carbon, the carbonyl oxygen, and the second oxygen atom of the ester (or the nitrogen atom of the amide). Thus the presence of a carbonyl group introduces considerable rigidity into the side arm. For the current series of lariat ether amides and esters, this helps position the carbonyl oxygen over the crown ether cavity and preorganize the binding site. On the other hand, the $OCH_2CH_2OCH_3$ side arm is more flexible, which provides a lower level of conformational preorganization. It is proposed that a greater preorganization of the binding sites in the lariat ether amides and esters makes them more sensitive to the size of the interference ion in a perching complex. This increases the slope of the correlation lines shown in Figures 2 and 3 for the lariat ethers with amide and ester-containing side arms.

In conclusion, we have probed the influence of side-arm variation in dibenzo-16-crown-5 lariat ethers upon their potentiometric responses to alkali metal, alkaline earth metal, and ammonium ions by incorporation of these ionophores into ISE systems. Attachment of a propyl group to the ring carbon that bears an extended oxygen-containing side arm increases the

selectivity for Na^+ relative to larger alkali metal and alkaline earth metal ions and to ammonium ions. When the enhancement in Na^+ selectivity arising from attachment of a geminal propyl group is plotted against the size of the interference ions, a linear relationship is obtained. The potentiometric responses of dibenzo-16-crown-5 lariat ethers can be rationalized in terms of the crown ether ring size and the oxygen basicity, conformational positioning, and rigidity of the side arm.

ACKNOWLEDGMENT

This research was supported by the Division of Chemical Sciences of the Office of Basic Energy Sciences of the U.S. Department of Energy (Grant DE-FG03094ER14416).

Received for review July 11, 1994. Accepted August 31, 1993.[⊗]

[⊗] Abstract published in *Advance ACS Abstracts,* October 1, 1994.

Anal. Chem. **1994,** *66,* 4337–4344

This Research Contribution is in Commemoration of the Life and Science of I. M. Kolthoff (1894–1993).

Electrocatalysis of NADH Oxidation with Electropolymerized Films of 3,4-Dihydroxybenzaldehyde

F. Pariente,[†] E. Lorenzo,*[,†] and H. D. Abruña*[,‡]

Departamento de Química Analítica y Análisis Instrumental, Universidad Autónoma de Madrid, Canto Blanco 28049, Madrid, Spain, and Department of Chemistry, Baker Laboratory, Cornell University, Ithaca, New York 14853-1301

The oxidation of 3,4-dihydroxybenzaldehyde (3,4-DHB) on glassy carbon electrodes gives rise to stable redox-active electropolymerized films containing a quinone moiety. The redox response of the films is that anticipated for a surface-immobilized redox couple, and the pH dependence of the redox activity of these films is 60 mV/pH unit, which is very close to the anticipated Nernstian dependence of 59 mV/pH unit. We have characterized the dependence of the growth of these films on the solution concentration of 3,4-DHB, the potential for deposition, the time of deposition, and the pH. In addition, we have measured their permeability and apparent diffusion coefficient (D_{app}) of these films. These films exhibit potent and persistent electrocatalytic behavior toward NADH oxidation. In a flow injection analysis determination, the limit of detection is estimated to be in the submicromolar regime.

Because of their ubiquitous use as coenzymes by over 300 dehydrogenases, β-nicotinamide adenine dinucleotide (NADH) and its oxidized form (NAD^+) have been the subjects of numerous studies geared at understanding the factors that may control their redox activity. In particular, much effort has been devoted to identifying materials that may exhibit electrocatalytic oxidation of NADH. Of particular interest have been materials that may be attached to electrode surfaces[1–8] because of their potential utility in a wide range of sensor applications. The major difficulty arises as a result of the high overpotential that is typically encountered for NADH oxidation at bare electrode surfaces.[9] Although the reversible potential for NADH oxidation is estimated to be −0.32 vs NHE,[10] there is typically a very high overpotential, which can be as high as 1.0 V.[11]

A number of approaches have been employed in an effort to accelerate the kinetics of NADH oxidation. In one of the earlier attempts, Blaedel and Jenkins[12] employed an electrochemical pretreatment of carbon electrodes. They believed that the oxidative pretreatment produced surface hydroxyl, quinones, and other groups which were responsible for the improved performance.

It is generally accepted that *o*-quinones can be quite active in the electrocatalytic oxidation of NADH, and as a result numerous derivatives incorporating such a group have been employed. For example, Kuwana and Tse were able to obtain electrodes with catalytic activity by covalent attachment of 1,2-hydroquinones to the surface of pyrolytic graphite.[13] In addition, a number of investigators have employed graphite electrodes modified with adsorbed aromatics containing catechol functionalities.[14–16] This approach was recently extended to the use of self-assembling monolayers on gold and platinum electrodes.[17] In addition, Miller and co-workers prepared polymeric materials derived from poly(methacrolyl chloride) and dopamine which, when adsorbed, also exhibited electrocatalytic activity toward NADH oxidation.[18]

Porter et al. very recently reported that electrooxidation of amines on glassy carbon electrodes resulted in the formation of a C–N covalent bond, giving rise to electrodes modified with the amine-containing material. In this way they were able to immobilize dopamine (which has an *o*-quinone moiety) onto glassy carbon electrodes. Such modified electrodes exhibited electrocatalytic activity toward NADH oxidation.[19]

[†] Universidad Autónoma de Madrid.
[‡] Cornell University.

(1) Murray, R. W. In *Electroanalytical Chemistry*; Bard, A. J., Ed.; Marcel Dekker: New York, 1984; Vol. 13, p 191.
(2) Murray, R. W. *Annu. Rev. Mater. Sci.* **1984**, *14*, 145.
(3) Murray, R. W. *Accts. Chem. Res.* **1980**, *13*, 135.
(4) Faulkner, L. R. *Chem. Eng. News* **1982**, *60* (Feb 27), 28.
(5) Abruña, H. D. *Coord. Chem. Rev.* **1988**, *86*, 135.
(6) Abruña, H. D. In *Electroresponsive Molecular and Polymeric Systems*; Skotheim, T. A. Ed.; Marcel Dekker: New York, 1988; p 92.
(7) Fujihira, M. In *Topics in Organic Chemistry*; Fry, A. J., Britton, W. R., Eds.; Plenum: New York, 1986; p 255.
(8) Gorton, L. *J. Chem. Soc., Faraday Trans. 1* **1986**, *82*, 1245.
(9) Elving, P. J.; Schmakel, C. O.; Santhanam, K. S. V. *Crit. Rev. Anal. Chem.* **1976**, *6*, 1.
(10) Clark, W. M. Oxidation Reduction Potentials of Organic Compounds; The Williams and Wilkins Co.: Baltimore, MD, 1960.
(11) (a) Aizawa, M.; Coughlin, R. W.; Charles, M. *Biochim. Biophys. Acta* **1975**, *385*, 382. (b) Leduc, P.; Thevenot, D. *Bioelectrochem. Bioeng.* **1974**, *1*, 1.
(12) Blaedel, W. J.; Jenkins, R. A. *Anal. Chem.* **1976**, *48*, 1240.
(13) Tse, D. C. S.; Kuwana, T. *Anal. Chem.* **1978**, *50*, 1315.
(14) Jaegefeldt, H.; Torstensson, Gorton, L. G. O.; Johansson, G. *Anal. Chem.* **1981**, *53*, 1979.
(15) Ueda, C.; Tse, D. C. S.; Kuwana, T. *Anal. Chem.* **1982**, *54*, 850.
(16) Jaegefeldt, H.; Kuwana, T.; Johansson, G. *J. Am. Chem. Soc.* **1983**, *105*, 1805.
(17) (a) Kunitake, M.; Akiyoshi, K.; Kawatana, K.; Nakashima, N.; Manabe, O. *J. Electroanal. Chem.* **1990**, *292*, 277. (b) Lorenzo, E.; Pariente, F.; Sánchez, L.; Tirado, J.; Abruña, H. D., manuscript in preparation.
(18) (a) Degrand, C.; Miller, L. L. *J. Am. Chem. Soc.* **1980**, *102*, 5728. (b) Fukui, M.; Kitani, A.; Degrand, C.; Miller, L. L. *J. Am. Chem. Soc.* **1982**, *104*, 28.

0003-2700/94/0366-4337$04.50/0 © 1994 American Chemical Society

In addition to quinone moieties, a number of dyes[20-23] have been employed. These are typically employed in carbon paste electrodes or as electropolymerized films. Moreover, Albery and co-workers have employed conducting salts derived from TCNQ for the catalytic oxidation of NADH.[24,25]

One of the major difficulties with virtually all of the approaches described above relates to the lifetime of the modified electrodes and in some cases the difficulty of modification. Thus, there is still a great deal of interest in the development of new or alternative approaches for the electrocatalytic oxidation of NADH, especially for materials immobilized on electrode surfaces.

We have recently found that the electrooxidation of 3,4-dihydroxybenzaldehyde on glassy carbon electrodes gives rise to stable redox-active electropolymerized films. These films exhibit very high and persistent electrocatalytic activity for the oxidation of NADH. We describe the preparation and characterization of such modified electrodes and their electrocatalytic activity for NADH oxidation.

EXPERIMENTAL SECTION

Materials. 3,4-Dihydroxybenzaldhyde (3,4-DHB; 97% purity) from Aldrich Chemical Co. was recrystallized twice from water using activated charcoal. Methylviologen dichloride hydrate (Aldrich) was used as received. NADH (grade III) was obtained from Sigma Chemical Co. and was used as received. Tris and acetate buffers (0.10 M) containing 0.10 M $NaNO_3$ were used. Water was purified with a Millipore Milli-Q system. All solutions were prepared just prior to use.

Apparatus. Cyclic voltammetric studies were carried out with a BAS CV-27 potentiostat and a Linseys X-Y recorder. Teflon-shrouded glassy carbon electrodes (area, 0.071 cm^2) and platinum disk electrodes sealed in glass (area, 0.01 cm^2) were used as working electrodes. A coiled platinum wire served as the auxiliary electrode. Except as described below for FIA measurements, all potentials are reported against a sodium saturated calomel electrode (SSCE) without regard for the liquid junction. A Pine Instruments rotating disk electrode system with a glassy carbon disk electrode (area, 0.23 cm^2) was employed in rotating disk electrode experiments.

Double potential step chronocoulometry experiments were carried out using a BAS 100 voltammetric analyzer with pulse widths from 5 to 100 ms.

For the FIA measurements, a Metrohm 656 detector with a Metrohm EA-1096 flow-through wall-jet cell, equipped with a glassy carbon working electrode and a silver−silver chloride (3 M KCl) reference electrode, was used. The electrode was modified at a constant potential of +0.30 V for 3 min in 0.5 mM 3,4-DHB solution in pH 7 Tris/nitrate buffer. The potential of the modified electrode was held at +0.30 V (vs Ag/AgCl), and the currents were monitored with a Metrohm 641 VA potentiostat and recorded on a Linseys L-6512 Y-t recorder. The carrier stream was pumped by a Watson Marlow 202 U/1 peristaltic pump, and the sample was injected into the carrier stream by a six-way injection Rheodyne Type 50 valve.

Procedures. (a) Electrode Pretreatment and Activation. Prior to each experiment, glassy carbon electrodes were polished with 1 μm diamond paste (Buehler) and rinsed with water and acetone. In the cases where activated electrodes were employed, the polished electrodes were placed in 1.0 M NaOH solution and the potential held at +1.20 V for 5 min, followed by potential cycling from −0.20 to +1.0 V in buffer solution for 5 min. The electrode was rinsed with water, and the modification with 3,4-DHB was carried out as described below.

SnO_2 electrodes (NESA glass from PPG Industries) were cleaned with methanol and acetone prior to use.

(b) Electrode Modification with 3,4-DHB. Two different methods were used in the modification of the electrodes with 3,4-DHB. In the first case, the activated electrode was placed in a solution containing 0.05−2.0 mM 3,4-DHB in Tris/nitrate buffer (pH 7.0 or 8.0) and the potential held at about +0.20 V (depending on pH, vide infra) for 3 min. In the second case, the activated electrode was modified by cycling the potential between −0.20 and +0.30 V (at 25 or 100 mV) in a 0.5 mM solution of 3,4-DHB in Tris/nitrate buffer (pH 7.0 or 8.0).

(c) FIA Analysis. The carrier stream, Tris/nitrate buffer (pH 7.0), was pumped through the electrochemical cell at a flow rate of 0.7 $mL \cdot min^{-1}$. After a steady background current was obtained (typically 1 min), 75 μL of increasing concentrations of NADH were introduced, and the change in current at an applied potential of +0.30 V was recorded.

RESULTS AND DISCUSSION

1. Electrochemical Response of 3,4-DHB in Solution and Its Electropolymerization. Cyclic voltammograms of 1 mM 3,4-DHB (see Figure 1 for structure) in Tris/nitrate buffer (pH 8.0) were carried out over the potential range of −0.30 to +0.80 V with glassy carbon electrodes that were either polished or polished and activated as described in the Experimental Section.

On the first voltammetric scan at an activated electrode (Figure 1A) (initial potential of −0.30 V), a sharp anodic peak is observed at a peak potential value of +0.25 V. No further anodic processes were observed up to potentials of +0.80 V. Upon scan reversal at +0.80 V, a small cathodic wave was observed at a peak potential value of +0.04 V. On further potential scanning, an additional anodic peak was observed at a peak potential value of +0.13 V. This wave could be due to hydroxylation of the immobilized material to the triol. Such behavior has been previously reported by Kuwana and co-workers.[26]

In addition, the initial sharp anodic peak was broadened significantly, and the peak potential value shifted to +0.42 V. Upon continuous scanning, this peak continued to broaden and shift. In addition, all of the voltammetric processes decreased in intensity with continued potential cycling (Figure 1A).

On the other hand, if the potential is cycled within the limits of −0.20 and +0.30 V, there is a continuous decrease in the amplitude of the initial sharp anodic peak (Figure 1B). Concomitant with this process is the emergence of a new reversible peak with a formal potential of +0.15 V and whose peak intensity increases with cycling. The shape of this new voltammetric feature is that of a surface-immobilized redox couple, suggesting

(19) Deinhammer, R. S.; Ho, M.; Anderegg, J. W.; Porter, M. D. *Langmuir* **1994**, *10*, 1306.
(20) Torstensson, A.; Gorton, L. *J. Electroanal. Chem.* **1981**, *130*, 199.
(21) Gorton, L.; Csöregi, E.; Domínguez, E.; Emnéus, J.; Jönsson-Pettersson, G.; Marko-Varga, G.; Persson, B. *Anal. Chim. Acta* **1991**, *250*, 203.
(22) Tanaka, K.; Tokuda, K.; Ohsaka, T. *J. Chem. Soc., Chem. Commun.* **1993**, 1770.
(23) Kulys, J.; Gleixner, G.; Schuhmann, W.; Schmidt, H.-L. *Electroanalysis* **1993**, *5*, 201.
(24) Albery, W. J.; Bartlett, P. N. *J. Chem. Soc., Chem. Commun.* **1984**, 234.
(25) Albery, W. J.; Bartlett, P. N.; Cass, A. E. G. *Phil. Trans. R. Soc. London, B* **1987**, *316*, 107.
(26) Gui, J. Y.; Hance, G. W.; Kuwana, T. *J. Electroanal. Chem.* **1991**, *309*, 73.

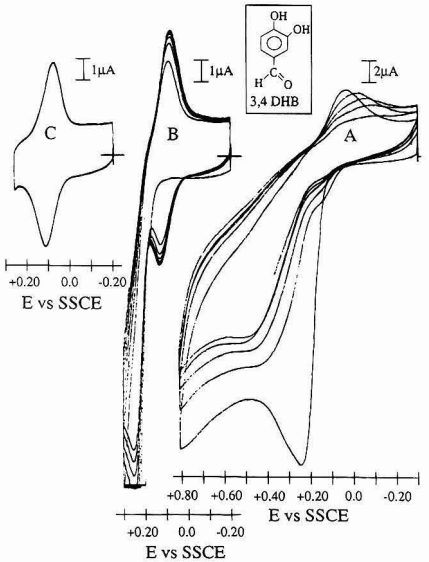


Figure 1. Cyclic voltammograms at 100 mV/s of 1.0 mM 3,4-DHB in Tris/nitrate buffer (pH 7.0) at an activated glassy carbon electrode. Scan limits, −0.30 to +0.80 V (A) and -0.20 to +0.30 V (B). (C) Cyclic voltammogram of the modified electrode obtained in Figure 1B in Tris/nitrate buffer solution (pH 7.0). Scan rate, 100 mV/s. Inset: structure of 3,4-DHB.

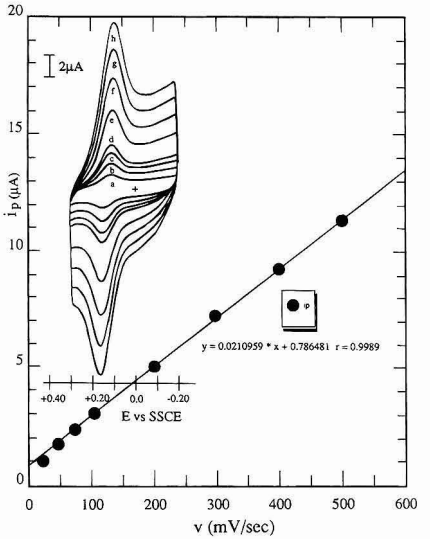


Figure 2. Sweep rate dependence of the cyclic voltammetric response of a glassy carbon electrode modified with 3,4-DHB in Tris/nitrate buffer (pH 7.0). Scan rates, 25(a); 50 (b); 75 (c); 100 (d); 200 (e); 300 (f); 400 (g); and 500 mV/s (h). Inset: plot of anodic peak current vs sweep rate.

the formation of a redox-active polymeric (or oligomeric) film on the electrode surface.

If the electrode is subsequently removed from the cell, rinsed with water, and placed in Tris/nitrate buffer (pH 7.0) containing no 3,4-DHB, a voltammetric peak typical of a surface-immobilized redox couple is observed with a formal potential value of +0.15 V (Figure 1C). Although there is some loss (typically about 10%) of material during the first 4−5 scans, further loss of the surface-immobilized material takes place at a much slower rate as described below. On the other hand, if the potential is cycled to values more positive than +0.40 V, there is a very rapid and complete loss of the surface-immobilized material. Although this implies that care must be exercised in terms of what potentials are applied, it also provides for a very easy and convenient way to regenerate the electrode.

Similar results, except with higher, more stable, and more reproducible coverages, are obtained if the electropolymerization is carried out at constant potential during a prescribed amount of time, with the potential being dependent on the pH of the electrolyte (vide infra). In general, best results were obtained when the applied potential was 50 mV beyond the peak for the oxidation of 3,4-DHB.

Although qualitatively similar results were obtained for electrodes that were only polished, consistently superior results were obtained with electrodes that had been polished and activated in base as described in the Experimental Section. Thus, all further studies were carried out with activated glassy carbon electrodes.

The electropolymerized films exhibited the behavior anticipated for a surface-immobilized redox couple. As shown in Figure 2, the wave had the expected wave shape for a surface-confined redox center with a small (although not zero) ΔE_p value. In addition, the current was directly proportional to the rate of potential sweep over the range of 25 to 500 mV/s, suggesting facile charge transfer kinetics (Figure 2).

Experiments identical to those described above for glassy carbon electrodes were carried out on polished platinum electrodes (platinum electrodes were not activated, but rather prior to use, the potential was cycled in supporting electrolyte until a stable background response was obtained). However, in this case, no evidence of electropolymerization was apparent in the potential range used above.

In an attempt to identify the species responsible for the observed polymerization reaction, the voltammetric response of benzaldehyde at an activated glassy carbon electrode was obtained. Benzaldehyde exhibited a totally irreversible wave with a peak potential value of +1.80 V. However, there was no evidence of polymerization. In fact, when the electrode was removed from the benzaldehyde solution and placed in Tris/nitrate buffer (pH 7.0), there were no redox processes over the range of +0.50 to −0.20 V other than background currents.

Although the 3,4-DHB did not polymerize at a platinum electrode surface, we observed polymerization at a SnO_2 electrode, suggesting that the presence of oxygen containing surface species is likely to play a role. In addition, the fact that activated electrodes gave rise to more stable deposits and higher coverages is also consistent with this.

In the work by Porter et al. mentioned earlier,[19] they found that, whereas deposition took place on glassy carbon electrodes, such was not the case on HOPG. This difference in reactivity

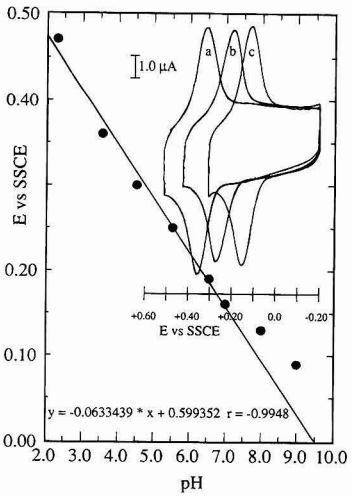


Figure 3. pH dependence of the cyclic voltammetric response (at 100 mV/s) of a glassy carbon electrode modified with 3,4-DHB. pH values are (a) 3.6; (b) 5.5, and c. 7.0. Inset: plot of formal potential vs pH.

was ascribed to the presence of oxygen functionalities in the former and their absence in the latter.

It is well known that phenol and related derivatives undergo electrooxidative polymerization to give rise to conducting polymer films of poly(phenylene oxide). Such a process occurs at a variety of electrode surfaces including platinum. The fact that no detectable electropolymerization of 3,4-DHB was observed at a platinum electrode would suggest that a phenol-type polymerization process is not operative under our experimental conditions. Hapiot[27] and co-workers very recently reported on an electrochemical and pulsed radiolytic study of the oxidative dimerization (and oligomerization) of phenolic aldehydes. These investigators propose a mechanism based on the dimerization of phenoxy radicals. We believe that a similar mechanism might be operative in our case, although we have no direct experimental evidence in support of this assertion.

2. pH Dependence Studies of the Electropolymerized Films. Since the 3,4-DHB has an *o*-quinone moiety, we anticipated that the redox response for the electropolymerized material would be pH dependent. In order to ascertain this, the voltammetric response of a modified electrode was obtained in solutions of varying pH from 2 to 10. As can be seen in Figure 3, the formal potential of the surface redox couple was pH dependent, with a slope of 60 mV/pH unit which is very close to the anticipated Nernstian value of 59 mV for a two-electron, two-proton process. There is also a change in slope for pH values above 7, which we ascribe to deprotonation of the deposited material, since the first pK_a of 3,4-DHB is reported to be 7.21.[28] Thus, the slope of 60 mV/pH unit quoted above was for pH values below 7. Another point that should also be mentioned is that there was no detectable change in the surface coverage over pH values from 2 to 10, pointing to the stability of the film over a very broad pH range.

(27) Hapiot, P.; Pinson, J.; Francesch, C.; Mhamdi, F.; Rolando, C.; Neta, P. *J. Phys. Chem.* **1994**, *98*, 2641.
(28) Slabbert, N. P. *Tetrahedron* **1977**, *33*, 821.

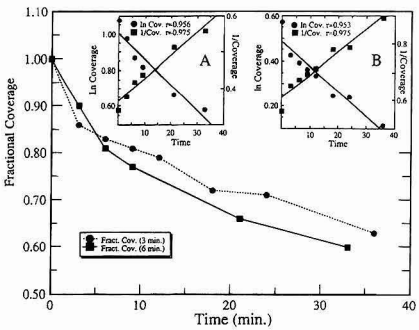


Figure 4. (Main panel) Variations in fractional coverage as a function of time of continuous scanning (scan rate, 100 mV/s) for a glassy carbon electrode modified with an electropolymerized film of 3,4-DHB. Deposition was carried out from 0.5 mM 3,4-DHB in Tris/nitrate buffer (pH 7.0) at a fixed potential of +0.20 V for 3 (●) or 6 min (■). Insets: first- and second-order plots for the variation in fractional coverage as a function of time for electrodes modified for (A) 6 and (B) 3 min.

3. Mode of Deposition. As described in the Experimental Section, two different deposition methods were employed, and these involved cycling the potential or holding the potential constant during the electropolymerization process, respectively. In order to determine the most effective method for electrode modification, comparisons were made in terms of the stability of the resulting films. This involved measuring the decay of the redox activity of the electropolymerized film.

In the case where electropolymerization was at constant potential, the applied potential was +0.20 V, since this was determined to be the optimal value (vide infra). The electrodes were modified for 3 and 6 min. After modification, the electrodes were rinsed with water and placed in pH 7.0 Tris/nitrate buffer, and the decay of the surface wave with time was determined. Whereas there was a significant decay in both cases, it was somewhat higher for electrodes that had been modified for 6 min relative to those modified for 3 min, as can be seen in the main panel of Figure 4. For both sets of experiments, plots of ln coverage vs time as well as 1/coverage vs time were constructed. As can be seen in insets A and B in Figure 4, better agreement (correlation) was obtained when the data were plotted as 1/coverage vs time, suggesting that the decay process is second order.

Similar experiments were carried out for electropolymerization effected by cycling of the potential. In this case, two different sweep rates were employed: 25 and 100 mV/s, respectively. As can be seen in the main panel of Figure 5, there was again a rather significant loss of electroactivity, with the effect being somewhat higher for electrodes where the sweep rate was 100 mV/s. As was done for the case of electrodes modified by holding the potential, plots of ln coverage vs time as well as 1/coverage vs time were constructed. As in the previous case, better fits were obtained for plots of 1/coverage vs time, again suggesting that the decay process was second order.

It should also be mentioned that after about 30 min of continuous cycling, the rate of decay slows down significantly for electrodes prepared by either method. In fact, the additional loss is less than about 5% for cycling of up to 8 continuous hours. This suggests that the initial decay observed in Figures 4 and 5 might

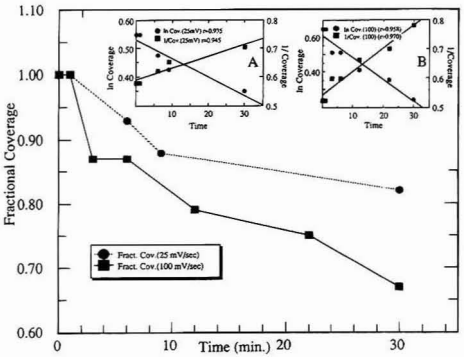


Figure 5. Variations in fractional coverage as a function of time of continuous scanning (scan rate, 100 mV/s) for a glassy carbon electrode modified with an electropolymerized film of 3,4-DHB. Deposition was carried out from 0.5 mM 3,4-DHB in Tris/nitrate buffer (pH 7.0) cycling the potential between −0.2 and 0.3 V at 25 (●) or 100 mV/s (■). Insets: first- and second-order plots for the variation in fractional coverage as a function of time for electrodes modified at (A) 25 and (B) 100 mV/s.

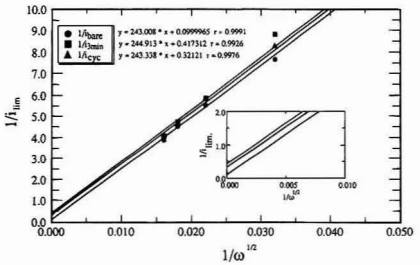


Figure 6. Reciprocal Levich plots ($1/i_l$ vs $1/\omega^{1/2}$) for the reduction of methyl viologen (1 mM) in 0.10 M $NaNO_3$ at a bare glassy carbon electrode as well as at electrodes modified with 3,4-DHB at constant potential or by cycling the potential for 3 min. Inset: expanded region near the intercept.

be due to material that is weakly bound to the surface or to short-length polymer chains that can desorb from the electrode surface with relative ease. The remaining material, however, is quite persistent, as mentioned above.

We also studied the permeability and the apparent diffusion coefficient, D_{app}, of films prepared by both methods. In the permeability studies, the limiting current, i_l for the electrochemical reaction of a solute (methyl viologen (MV) in this case) that partitions (with partition coefficient P) and diffuses into a rotated disk electrode through a film barrier with diffusion constant $D_{s,pol}$ (which is different from the value in solution) is described by eq 1:[29]

$$\frac{1}{i_l} = \frac{1}{nFAD_{s,pol}PC_s/d} + \frac{1}{0.62nFAD_s^{2/3}\nu^{-1/6}\omega^{1/2}C_s} \quad (1)$$

where d is the film thickness and ω is in rad/s.

The two terms on the right-hand side of eq 1 represent the rates of solute diffusion through the film and through the Levich depletion layer in solution, respectively. If diffusion through the film is slower than diffusion through the Levich layer, a plot of i_l vs $\omega^{1/2}$ (a Levich plot) will not be linear. However, a plot of i_l^{-1} vs $\omega^{-1/2}$ (an inverse Levich plot) will be linear, and from the intercept, the value of ($D_{s,pol}P/d$) can be obtained.

We have carried out such an analysis at both bare and 3,4-DHB-modified electrodes (modified by cycling the potential as well as by electropolymerization at constant potential) using methyl viologen in solution. From values of the limiting current we constructed inverse Levich plots (Figure 6), and from their intercepts we calculated $PD_{s,pol}/d$ values for MV permeation. We obtain values of 0.13 and 0.20 cm·s^{-1} for polymerization at constant potential and by potential cycling, respectively. From the slope of the inverse Levich plot, the diffusion coefficient for MV in solution was determined to be (8.7 ± 0.1) × 10^{-6} cm^2 s^{-1}, in agreement with values obtained at an unmodified glassy carbon electrode as well as literature values.[30]

Thus, it is clear that permeation rates through electropolymerized films of 3,4-DHB are rapid, so one would not anticipate kinetic limitations.

In general, it was found that more stable and reproducible deposits were obtained when the electropolymerization was carried out at constant potential, and subsequent studies were carried out with electrodes modified in this fashion.

Using double potential step chronocoulometry, we determined the apparent diffusion coefficients (D_{app}) for electropolymerized films of 3,4-DHB deposited at constant potential (+0.20 V, 0.5 mM concentration of 3,4-DHB, pH 7) for 1, 6, 12, and 24 min. Values for both reduction and oxidation processes were determined. In all cases we found that the slopes of the resulting Anson plots were virtually identical, indicating the same value of D_{app} (1.6 × 10^{-10} cm^2/s) for all polymerization times as well as for both oxidation and reduction processes.

4. Properties of the Electropolymerized Films Prepared at Constant Applied Potential as a Function of pH, Concentration of 3,4-DHB, and Time of Deposition. The dependence of the properties of the electropolymerized films prepared at constant applied potential for 3 min was studied as a function of pH during deposition. In these studies the potential applied during electropolymerization was chosen to be 50 mV beyond the peak potential for the oxidation of 3,4-DHB. (Recall that this process is pH dependent.) The results are presented in Table 1. In general, it was found that the best results were obtained at slightly acidic pH values, although variations in the pH range from 4.5 to 6.5 were not dramatic. However, for pH values above 7, a significant decrease in the surface coverage is observed which could be due to deprotonation.[28] Nonetheless, in studying the electrocatalytic oxidation of NADH, it was found that a higher catalytic activity was obtained for electrodes prepared at pH 7−8 (vide infra). Thus, as a compromise, electrodes were modified at pH 7 and at a potential of +0.20 V.

We also studied the effect of solution concentration of 3,4-DHB on the properties of the resulting films. In these studies, the films were prepared at pH 7.0 at a constant applied potential of +0.20 V for 3 min. The effect was ascertained by plotting the surface

(29) Ikeda, T.; Schmehl, R.; Denisevich, P.; Willman, K.; Murray, R. W. *J. Am. Chem. Soc.* **1982**, *104*, 2683.

(30) Steckhan, E.; Kuwana, T. *Ber. Bunseges. Phys. Chem.* **1974**, *78*, 253.

Table 1. Variations in the Properties of Electropolymerized Films of 3,4 DHB as a Function of Deposition Potential and pH

pH	E_{dep}[a] (V)	$I_{p,a}$[b] (μA)	$I_{p,c}$[b] (μA)	$E_{p,a}$[c] (V)	$E_{p,c}$[c] (V)	ΔE_p[d] (mV)	$E^{o'}$[e] (V)	Γ_a[f]	Γ_c[f]
3.5	+0.45	5.8	5.7	+0.360	+0.300	60	+0.330	3.74	3.83
4.5	+0.40	6.6	6.2	+0.305	+0.255	50	+0.280	4.99	4.98
5.5	+0.35	4.7	4.5	+0.250	+0.190	60	+0.220	3.23	3.47
6.5	+0.25	4.5	4.3	+0.170	+0.100	70	+0.135	3.72	3.90
7.0	+0.20	4.2	4.1	+0.150	+0.100	40	+0.130	3.21	3.06
8.0	+0.17	4.1	4.0	+0.120	+0.080	40	+0.100	2.53	2.67
9.0	+0.15	2.9	3.1	+0.050	+0.020	30	+0.035	1.87	2.20
10.2	+0.10	2.9	2.7	−0.030	−0.060	30	−0.045	1.70	1.70

[a] Deposition potential vs SSCE. [b] Anodic and cathodic peak currents. [c] Anodic and cathodic peak potentials vs SSCE. [d] Defined as $E_{p,a} - E_{p,c}$. [e] Formal potential defined as $(E_{p,a} + E_{p,c})/2$ vs SSCE. [f] Coverages in mol/cm^2 × 10^{10}.

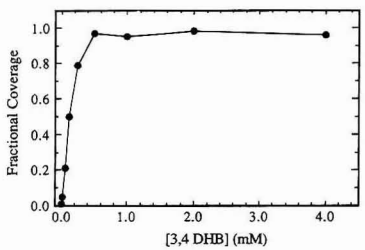


Figure 7. Dependence of fractional coverage on solution concentration of 3,4-DHB in Tris/nitrate buffer (pH 7.0) for electrodes modified by electropolymerization at a fixed potential of +0.20 V for 3 min. The fractional coverage is defined as Γ/Γ_{max}, where $\Gamma_{max} = 3 \times 10^{-10}$ mol/cm^2. The data presented are the averages of three determinations.

coverage normalized to the solution concentration of 3,4-DHB. As can be seen in Figure 7, there is a sharp rise in the normalized coverage with the solution concentration of 3,4-DHB which levels off for solution concentrations above 0.50 mM.

Finally, the effect of time of deposition was determined. In this case, the resulting coverage of material on the electrode surface was monitored as function of time of deposition using a solution concentration of 0.50 mM at a pH of 7.0 and a potential of +0.20 V. We observe that for deposition times below 60 s, the surface coverage increases with time. For deposition times over 120 s and up to 10 min, there is no further increase in the surface coverage. However, when deposition is carried out for extensive time periods (25 min), the measured coverage actually decreases. We believe that this might be due, at least in part, to transport limitations through an ostensibly thicker polymer film so that only a fraction of it is electrochemically active. Such behavior has been previously documented for other polymer films on electrodes.[1-7]

With the intent of ascertaining this effect, a transparent SnO_2 electrode was modified by cycling the potential between −0.20 and +0.30 V for 4 h. Afterward, the spectrum of the modified electrode was compared to that obtained prior to deposition. From an analysis of the interference peaks, we estimate the thickness of the film to be of the order of 1000 Å. However, from integration of the area under the voltammetric wave, a much lower coverage (about 5 × 10^{-10} mol/cm^2) was obtained, consistent with our earlier statement that only a very small fraction of the deposited polymer is electroactive.

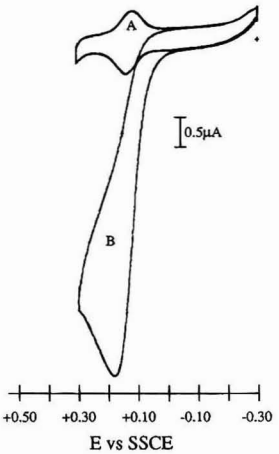


Figure 8. Voltammetric behavior at 10 mV/s in Tris/nitrate buffer (pH 8.0) of a glassy carbon electrode modified with 3,4-DHB in the absence (A) and the presence (B) of 1.0 mM NADH.

Based on these observations, a deposition time of 3 min was chosen as optimal.

From the results presented above, a solution concentration of 3,4-DHB of 0.5 mM and a deposition time of 3 min at a constant potential of +0.20 V in pH 7 Tris/nitrate buffer were employed in subsequent studies.

5. Electrocatalysis on NADH Oxidation. One of the objectives of these investigations was the development of modified electrodes capable of the electrocatalytic oxidation of NADH. This, in part, was responsible for the choice of 3,4-DHB as a modifying agent since it has an *o*-quinone moiety which, as mentioned earlier, has been identified as one that is capable of catalytically oxidizing NADH. In order to test for the potential electrocatalytic activity of these electropolymerized films, their cyclic voltammetric responses were obtained in the absence and presence of 1 mM NADH, and the data are presented in Figure 8. In the absence of NADH (Figure 8A), a well-behaved redox response for the polymer film on the electrode can be observed at a formal potential value of +0.18 V. Upon the addition of 1 mM NADH, there is a dramatic enhancement of the anodic current peak (Figure 8B), and, in addition, no current is observed in the return (cathodic) wave, consistent with a very strong electrocatalytic effect. Under identical conditions, NADH is oxidized at about +0.50 V at an unmodified but activated glassy carbon electrode. However, it should also be mentioned that, whereas for electrodes that are only activated, the oxidation peak potential for NADH progressively shifts to more positive values, in the case of the 3,4-DHB-modified electrodes, the electrocatalytic response is quite persistent (vide infra).

6. Optimization of Electrocatalytic Response for the Oxidation of NADH. In order to optimize the electrocatalytic response of the modified electrodes for NADH oxidation, we determined the effect of potential and pH during deposition on the electrocatalytic oxidation of NADH at 1 mM concentration. As mentioned earlier, these two variables affect the surface coverage of the polymer on the electrode surface as well as the electrocatalytic oxidation of NADH.

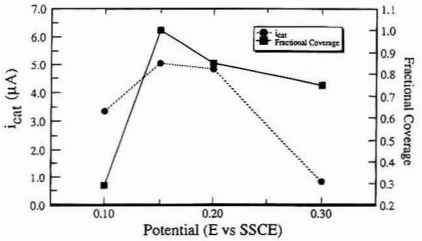


Figure 9. Dependence of fractional coverage and catalytic activity for NADH oxidation ([NADH] = 1mM) on the potential of electrodeposition of 3,4-DHB in Tris/nitrate buffer (pH 8.0). Deposition time for each potential was 3 min.

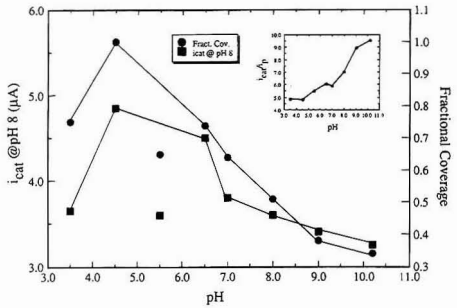


Figure 10. Dependence of fractional coverage and catalytic activity for NADH oxidation ([NADH] = 1mM) on the pH used in the electrodeposition buffer. The optimal deposition potentials for each pH were taken from Table 1. Inset: plot of normalized catalytic current vs pH.

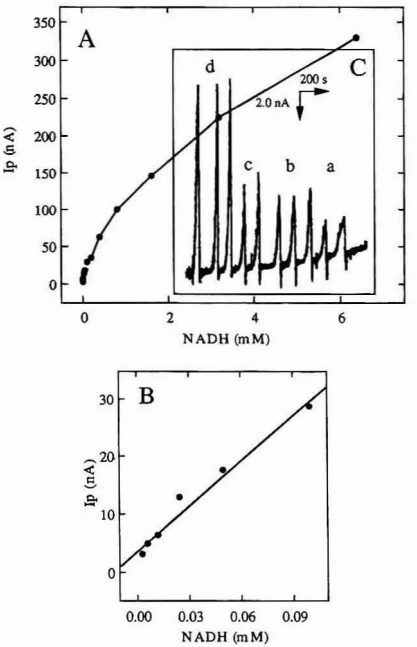


Figure 11. (A) Calibration curve for a 3,4-DHB-modified glassy carbon electrode in a FIA system in Tris/nitrate buffer solution (pH 8.0) at 0.70 mL·min^{-1}. (B) Response in the lower concentration range (3.2×10^{-6} to 1.0×10^{-4} M). (C) Recorder tracings for a series of replicate injections of NADH at concentrations of (a) 3.2×10^{-6}, (b) 6.2×10^{-6}, (c) 1.2×10^{-5}, and (d) 2.5×10^{-5} M.

Figure 9 presents the results for the effects of the applied potential (for 3 min in pH 8.0 Tris/nitrate buffer) on the fractional coverage (Γ_E/Γ_{max}) as well as on the catalytic current for NADH oxidation. As would be anticipated from the results presented earlier in Table 1, the highest coverage is obtained at an applied potential of +0.15 V. On the other hand, the catalytic current had a broad maximum over the range of +0.15 to +0.20 V. There was also a dramatic decrease both in the surface coverage and on the catalytic activity at potentials below +0.10 V and above +0.30 V, respectively. Thus, an applied potential of +0.20 V was deemed as most appropriate for maximizing the electrocatalytic response of the modified electrodes. These results are also consistent with those presented earlier in Table 1.

The effects of pH during deposition on the fractional coverage and the catalytic activity are presented in Figure 10. As had been described earlier and as also seen in Figure 10, the highest coverages were obtained in slightly acidic media. The decrease in coverage at pH values above 7 could again be due to deprotonation.[28] The catalytic activity follows a similar trend, and this might reflect the fact that, at these slightly acidic pH values, there is more material on the electrode surface and thus a larger catalytic current. In order to account for this, the catalytic current was normalized by dividing by the peak current for the electropolymerized film in the absence of NADH. The results are presented in the inset to Figure 10, where it is apparent that the normalized catalytic activity is higher at higher pH. Based on this observation, a pH value of 8.0 was chosen as representative of a compromise among the various dependencies.

Based on these studies as well as on the results presented in Table 1, we chose a pH of 8.0, an applied potential of +0.20 V (for 3 min), and a solution concentration of 3,4-DHB of 0.5 mM as representing the best compromise for the modification of glassy carbon electrodes with electropolymerized films of 3,4-DHB for their subsequent use in the electrocatalytic oxidation of NADH.

7. Calibration and Limit of NADH Detection of 3,4-DHB-Modified Electrodes. The effect of increasing concentrations of NADH on the voltammetric response of the 3,4-DHB-modified electrodes was investigated. The response was linear from 5.0×10^{-6} to 1.0×10^{-3} M NADH. Hydrodynamic voltammetry under flow injection conditions, which possesses a much higher current sensitivity than cyclic voltammetry, was used to estimate the lower limit of detection for the electrocatalytic oxidation of NADH at a 3,4-DHB-modified glassy carbon electrode. A calibration curve for NADH oxidation by continuous flow monitoring of the current at a fixed potential over the concentration range of 3.2×10^{-6} to 6.0×10^{-3} M is shown in Figure 11A. At higher concentrations, there appears to be a leveling off of the response, likely due to kinetic limitations. On the other hand, at the lower concentrations, a linear correlation is observed. For example, Figure 11B depicts the response over the range of concentrations of 3.2×10^{-6} to 1.0×10^{-4} M. In all cases the response was rapid and reproduc-

ible. Figure 11C shows the recorder tracings for a series of replicate injections of NADH at the lower concentrations from 3.2 $\times$ 10^{-6} M (a) to 2.5 $\times$ 10^{-5} M (d). From analysis of these data, we estimate that the limit of detection of NADH is of the order of 5.0 $\times$ 10^{-7} M.

Although we have not carried out extensive stability studies, we typically employ the same electrode during the course of a day in numerous determinations such as a complete calibration (in replicate determinations). As mentioned earlier, after an initial loss of activity, the electrodes exhibit a very stable response during hours of continuous potential cycling. In addition, the electrode is quite stable at high NADH concentrations, conditions under which many other electrodes that exhibit electrocatalytic activity for NADH oxidation fail. For example, in replicate determinations of NADH at near saturation (1–5 mM), we observe less than 5% loss in activity. Although in principle a single electrode could be employed for long periods of time (days), due to the ease of preparation we typically modify an electrode and employ it in all determinations in the course of a day including calibration and other determinations. In addition, if a calibration curve is normalized to the surface coverage of the polymer, a universal calibration curve is obtained. Such an approach can be quite valuable, especially in sensor applications.

It is likely that materials similar to 3,4-DHB will also undergo electropolymerization to give rise to redox-active polymer films that are also catalytically active in the oxidation of NADH. We are in the process of studying such materials, and the results of those investigations will be reported on elsewhere.

CONCLUSIONS

The oxidation of 3,4 dihydroxy benzaldehyde (3,4-DHB) on glassy carbon electrodes gives rise to stable redox-active electropolymerized films. Film deposition by controlled potential gives consistently results superior to those obtained from films prepared by potential cycling. The permeability of the resulting films is such that rapid rates of transport are always obtained. The redox response of the films is that anticipated for a surface-immobilized redox couple, and the pH dependence of the redox activity of these films is 60 mV/pH unit. These films exhibit potent and persistent electrocatalytic behavior toward NADH oxidation. We have optimized the film growth conditions (in order to maximize the electrocatalytic activity) in terms of the solution concentration of 3,4-DHB, the potential for deposition, the time of deposition, and the pH. In a flow injection analysis determination, the limit of detection of NADH was estimated to be of the order of 5.0 $\times$ 10^{-7} M.

ACKNOWLEDGMENT

This work was supported by the National Science Foundation (DMR-9107116), a NATO Collaborative Research Grant (91-0047), and the DGICYT of Spain (BIO 93-0660-C04-02). We thank the reviewers for calling to our attention refs 19, 26, and 28.

Scientific Parentage of the Author. H. D. Abruña, Ph.D. under R. W. Murray, Ph.D. under R. C. Bowers, Ph.D. under I. M. Kolthoff.

Received for review May 20, 1994. Accepted August 25, 1994.[⊗]

[⊗] Abstract published in *Advance ACS Abstracts,* October 15, 1994.

Anal. Chem. **1994,** *66,* 4345–4353

Measurement in Vitro of Human Plasma Glycerol with a Hydrogen Peroxide Detecting Microdialysis Enzyme Electrode

Lindy J. Murphy* and Peter T. Galley

Unit of Metabolic Medicine, The Mint Wing, St. Mary's Hospital, Paddington, London, W2 1NY, UK

Human plasma glycerol was determined with a microdialysis electrode, containing the enzymes glycerol kinase and glycerol phosphate oxidase held stationary within the electrode. A microdialysis electrode is essentially a conventional microdialysis probe, with a platinum working electrode inserted into the tip of the dialysis fiber and reference and counter electrodes contained in the upper compartment. The linear range of response to glycerol was directly dependent on the concentration of ATP. At 4 mM ATP, the linear range was 0.5–500 μM. A fast response time of 20 s was obtained. Two types of interferences were observed when plasma glycerol was measured: direct oxidation of interferents at the electrode and attenuation of response to glycerol by reaction with hydrogen peroxide and/or poisoning of the platinum electrode. Ascorbate, urate, and acetaminophen were removed from plasma samples by a pretreatment step involving peroxidase and catalase. Any remaining interferent current was reduced by electropolymerizing *o*-phenylenediamine onto the platinum electrode. Adsorption of plasma proteins on the dialysis fiber was minimal and was not reduced by the preadsorption of human serum albumin. Very good correlation was obtained between the electrode and the standard spectrophotometric technique for the variation in glycerol concentration with time.

The determination of plasma glycerol is clinically desirable in the study of lipolysis in diabetics. Lipolysis is the process by which triglycerides in fatty tissue are broken down into free fatty acids and glycerol. Plasma glycerol concentration is therefore a measure of the rate of lipolysis. In healthy subjects, lipolysis is much more sensitive to low doses of insulin than glucose metabolism. The loss of the sensitivity of lipolysis to insulin results in increased levels of free fatty acids, which are oxidized in preference to glucose.[1] This could be an early indicator of type II diabetes (non-insulin-dependent diabetes mellitus). A technique called a glycerol clamp, analogous to the euglycaemic clamp[2] but using much lower insulin levels, has been proposed to measure the insulin resistance of fatty tissue. This technique requires accurate measurement (±1 μM) of plasma glycerol every 10 min. At present, glycerol is measured routinely in clinical laboratories by enzymatic spectrophotometric techniques, using deproteinized samples of whole blood.[3] The measurement time using these techniques is too slow for the performance of the glycerol clamp.

This paper reports the accurate determination of plasma glycerol using a microdialysis electrode, enabling the glycerol clamp to be performed. The microdialysis electrode is a novel configuration of the frequently used hydrogen peroxide detecting enzyme electrode. The measurement of glycerol[4] and glutamate[5,6] with the microdialysis electrode has been reported previously. A microdialysis electrode is shown in Figure 1, and a schematic diagram is given in Figure 2. Enzyme solution can be infused into the dialysis electrode by means of inlet tubing at the top of the electrode which extends into the tip of the dialysis fiber. The lifetime of the electrode can be extended by infusing in fresh enzyme solution when required. The electrode has a fast response time of 20 s.

The glycerol microdialysis electrode contains the enzymes glycerol kinase and L-glycerol-3-phosphate oxidase within the dialysis fiber, next to the platinum electrode. The enzymes catalyze the reactions

$$\text{glycerol} + \text{ATP} \xrightarrow{\text{glycerol kinase}} \text{glycerol phosphate} + \text{ADP}$$

$$\text{glycerol phosphate} + \text{O}_2 \xrightarrow[\text{oxidase}]{\text{glycerol phosphate}} \text{glycerone phosphate} + \text{H}_2\text{O}_2$$

ATP, the cofactor for glycerol kinase, must be added to the bulk solution. The hydrogen peroxide produced by the second reaction is oxidized at the platinum electrode.

The nonspecific oxidation of interferents, in particular ascorbate, urate, and acetaminophen, is a problem common to all hydrogen peroxide detecting enzyme electrodes for measurements in plasma.[7] Electropolymerized coats of phenylenediamine have been shown to significantly decrease interference currents.[8–10]

(1) Randle, P. J.; Garland, P. B.; Hales, C. N.; Newsholme, E. A. *Lancet* **1963,** 785–789.
(2) Defronzo, R. A.; Tobin, J. D.; Andres, R. *Am. J. Physiol.* **1979,** *237,* E214–E223.
(3) Harrison, J.; Hodson, A. W.; Skillen, A. W.; Stappenbeck, R.; Agius, L.; Alberti, K. G. M. M. *J. Clin. Chem. Clin. Biochem.* **1988,** *26,* 141–146.
(4) Albery, W. J.; Galley, P. T.; Murphy, L. J. *J. Electroanal. Chem.* **1993,** *344,* 161–166.
(5) Albery, W. J.; Boutelle, M. G.; Galley, P. T. *J. Chem. Soc., Chem. Commun.* **1992,** *12,* 900–901.
(6) Galley, P. T.; Errington, M. L.; Bliss, T. V. P. *Brain Res. Assoc.* **1993,** *10,* 34.4P.
(7) Palleschi, G.; Rahni, M. A. N.; Lubrano, G. J.; Ngwainbi, J. N.; Guilbault, G. G. *Anal. Biochem.* **1986,** *159,* 114–121.
(8) Malitesta, C.; Palmisano, F.; Torsi, L.; Zambonin, P. G. *Anal. Chem.* **1990,** *62,* 2735–2740.
(9) Sasso, S. V.; Pierce, R. J.; Walla, R.; Yacynych, A. M. *Anal. Chem.* **1990,** *62,* 1111–1117.
(10) Moussy, F.; Harrison, D. J.; O'Brien, D. W.; Rajotte, R. V. *Anal. Chem.* **1993,** *65,* 2072–2077.

0003-2700/94/0366-4345$04.50/0 © 1994 American Chemical Society

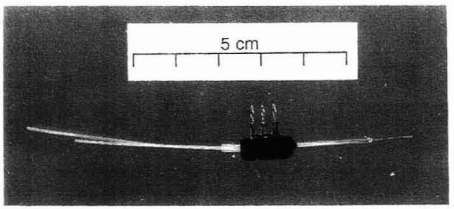


Figure 1. Microdialysis electrode.

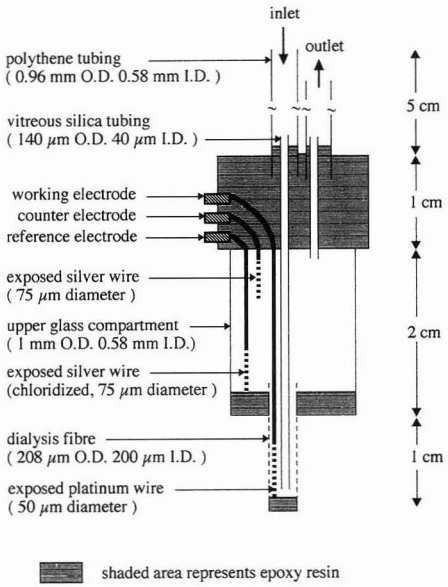


Figure 2. Schematic diagram of the microdialysis electrode (not drawn to scale). The electrodes are formed from lengths of Teflon-coated wire, with 4 mm of Teflon stripped from either end to expose the metal. One end is soldered to a gold contact, while the other end is used as the electrode. The contacts are held at the top of the electrode in a block formed from epoxy resin set in a rectangular mould.

Unfortunately, mixing of hydrogen peroxide and interferents in the internal solution of the dialysis fiber can still take place. Ascorbate has been observed to cause attenuation of the hydrogen peroxide response, either by direct reaction with hydrogen peroxide,[11] as frequently observed in spectrophotometric enzymatic determination,[12] or by fouling the electrode surface, thereby blocking it to hydrogen peroxide oxidation.[13] A pretreatment step for plasma samples is reported here for the elimination of major interferents before measuring the glycerol concentration. The pretreatment step was necessary because this second type of interference caused significant error in the measurement of plasma glycerol at the low glycerol concentrations found in human plasma. In addition, *o*-phenylenediamine was electropolymerized onto the electrode to reduce any interferent current remaining after the pretreatment step. The adsorption of albumin onto the outside of the dialysis fiber is also reported. It is hoped that by blocking the adsorption sites on the outside of the dialysis fiber with albumin, adsorption of plasma proteins will be reduced.

Only a small number of enzyme electrodes have been reported for the determination of glycerol. Merchie et al.[14] coimmobilized glycerol kinase and glycerol phosphate oxidase on nylon membrane which was held next to a platinum electrode detecting H_2O_2. However, they employed a laborious differential measurement for determining serum glycerol, involving measurement of serum response in the presence and absence of the enzymatic membrane. Glycerol dehydrogenase has been used in both potentiometric[15] and amperometric[16] determinations of glycerol using ferricyanide and 1,1′-dimethylferrocene as mediators, respectively, although the determination of plasma glycerol by either of these methods was not reported.

EXPERIMENTAL SECTION

Chemicals and Solutions. Glycerol kinase from *Cellulomonas sp.* (lyophilized, 45 units/mg), horseradish peroxidase type II (185 units/mg), catalase from bovine liver (1600 units/mg), human serum albumin (fraction V), ATP (magnesium salt from equine muscle), hydrogen peroxide (30% solution), glycerol, ascorbic acid, acetaminophen, uric acid, and L-cysteine were obtained from Sigma Chemical Co. L-Glycerol-3-phosphate oxidase from microorganisms (lyophilized, 52 units/mg) was obtained from Boehringer Mannheim. *o*-Phenylenediamine (99+%) was obtained from Aldrich Chemical Co. All buffer reagents were AnalaR grade. All solutions were made up with deionized water obtained from an Elgastat Option 4 water purifier.

All experiments were carried out in pH 7.4 phosphate buffer containing K_2HPO_4 (0.1 M) and KCl (0.15 M). The buffer was balanced with concentrated HCl. All solutions were prepared with this buffer. Enzyme solutions were prepared by dissolving known weights of each enzyme in the same buffer solution (30 μL). Enzyme solution was 500 units/mL in each enzyme unless otherwise stated. Stock solutions used were 1 mM glycerol, 100 mM ATP, 10 mM ascorbate, 10 mM acetaminophen, 10 mM L-cysteine, 3 mM urate, and 100 mg/mL for both peroxidase and catalase. Hydrogen peroxide solution was 100-fold dilute (88.2 mM) for the pretreatment of plasma and 1000-fold dilute (8.82 mM) for all other experiments.

Apparatus and Procedures. Microdialysis electrodes were purchased from Sycopel International Limited, Boldon, Tyne and Wear, UK. The electrodes were constructed to our design and specifications. Cuprophan dialysis fibers, MWCO 5−10 000, were obtained from a Gambro dialysis cartridge (Gambro Ltd). The electrodes were supplied dry. Immediately prior to use, buffer was infused into the electrode at a flow rate of 0.5 μL/min by use of a Carnegie Medicin syringe drive. When the electrode had been filled, enzyme solution was then infused into the electrode using the same flow rate. The flow was stopped once the electrode was full of enzyme solution. Note that the internal electrode solution was held stationary throughout the experiment. The dialysis fiber of the filled electrode was then completely immersed in buffer solution (4 mL) held in a small beaker. The

(11) Lowry, J. P.; O'Neill, R. D. *Anal. Chem.* **1992**, *64*, 456−459.
(12) Nagele, U.; Ziegenhorn, J.; Klose, S. In *Methods of Enzymatic Analysis*, 3rd ed.; Academic Press: New York, 1974; Vol. 7, pp 140−146.
(13) Palmisano, P. G.; Zambonin, P. G. *Anal. Chem.* **1993**, *65*, 2690−2692.
(14) Merchie, B.; Girard, A.; Maisterrena, B.; Michalon, P.; Couturier, R. *Anal. Chim. Acta* **1992**, *263*, 85−91.
(15) Chen, A. K.; Starzmann, J. A. *Biotechnol. Bioeng.* **1982**, *24*, 971−975.
(16) Davis, G.; Hill, H. A. O. Eur. Pat. Appl. EP 125867, 1984.

platinum working electrode was held at +650 mV with respect to the Ag/AgCl reference electrode. The external solution was stirred with a magnetic flea. When not in use, electrodes were stored with the dialysis fiber immersed in buffer at 4 °C.

Electrode potentials were held and currents measured by use of modules constructed in-house by Mr. John Hooper. Current–time transients were measured using a Gould series 60000 XYT chart recorder. Currents are given, rather than current densities, since the precise area of the platinum electrode was unknown. However, since the diameter of the platinum wire was 50 μm, and the length of exposed platinum was approximately 4 mm, the area of the electrode is estimated to be 6×10^{-3} cm^2.

Calibration. Stock ATP solution was added to the external buffer to give a concentration of 1 mM, unless otherwise stated. Additions of stock glycerol solution were then made to the external buffer. The external solution was replaced by exchanging the beaker containing the buffer. The electrode was polarized while the beaker was exchanged and could be kept out of external solution for some time, the limiting factor being the drying out of the dialysis fiber, which is irreversibly altered on dehydration.

Electropolymerization. If a poly(*o*-phenylenediamine) coat was required, the electropolymerized coat was grown directly onto the platinum electrode in situ within the dialysis fiber, following the method of Malitesta et al.[8] Polymer coats were always grown prior to infusing enzyme solution into the electrode, since immobilization of enzyme was not desired. The dialysis fiber of the electrode was immersed in *o*-phenylenediamine solution (5 mM in buffer) and nitrogen was bubbled through the solution for 15 min. Electropolymerization took place at +650 mV vs Ag/AgCl for 15 min, while nitrogen was bubbled through the buffer. The electrode was placed in fresh external buffer after electropolymerization, and enzyme solution then infused into the electrode.

Adsorption of Albumin. If the albumin coat was required, human serum albumin was adsorbed onto the external wall of the dialysis fiber by dipping the dialysis fiber into a 4% solution of albumin in buffer for 30 min. The electrode was then placed in buffer as usual. If both electropolymerization and adsorption of albumin were required, electropolymerization was always performed first, followed by adsorption.

pH Dependence. The electrode was prepared in the usual manner with the electropolymerized poly(*o*-phenylenediamine) coat and the adsorbed albumin coat. The electrode was initially calibrated in pH 7.4 buffer. The pH dependence was then determined for the response to 10 μM glycerol. The buffers used were phosphate (pH 6.0–8.0), tris (pH 7.5–10.0), and succinate (pH 6.0–4.0) in that order. All buffers were 0.1 M in the buffer species and 0.15 M in KCl and balanced with either concentrated HCl or KOH where appropriate.

Identification of Interferents in Plasma. The electrode was prepared as usual, without enzyme solution, the poly(*o*-phenylenediamine) coat, or adsorbed albumin. The background current was allowed to settle, and approximately 5 mg of solid of a species naturally present in plasma was added to the bulk buffer solution. The response to the species was measured when all the solid had dissolved. The buffer was replaced and the process repeated for all other species. Responses to 10 μM ascorbate, 300 μM urate, and 10 μM acetaminophen were determined by addition of a known volume of stock solution.

Long-Term Stability of Poly(*o*-phenylenediamine). An electrode, filled with buffer, was calibrated for response to hydrogen peroxide with 8.82 μM aliquots of 8.82 mM hydrogen peroxide stock solution. The responses to 100 μM ascorbate, 100 μM acetaminophen, 100 μM cysteine, and 300 μM urate were also determined by addition of a single aliquot of stock solution to fresh external buffer solution. The electrode was then placed in fresh external buffer for 10 min, prior to electropolymerization of *o*-phenylenediamine in the usual manner. The electrode was then placed in fresh buffer and the background current allowed to settle. The response of the electrode to hydrogen peroxide and interferents was determined as before, immediately after electropolymerization and on subsequent days. The electrode was stored in buffer at 4 °C when not in use.

Effect of Interferents on Hydrogen Peroxide Response. The electrode was prepared as usual with the poly(*o*-phenylenediamine) coat but without the adsorbed albumin coat. The remainder of this experiment was performed with buffer containing 10 mM Na_2EDTA. The response to hydrogen peroxide was determined by addition of aliquots of stock solution (8.82 mM) to the bulk solution in steps of 8.82 μM. This calibration plot was repeated five times before the electrode was placed in buffer containing 300 μM urate. The background current was allowed to settle, and the electrode was calibrated for response to hydrogen peroxide in the presence of urate. The electrode was then placed in fresh buffer and the calibration repeated for response in the absence of urate. This process was repeated for buffer containing 100 μM creatinine, 100 μM acetaminophen, and 100 μM ascorbate.

Effect of Exposure to Plasma on Response. The working electrode was not coated with poly(*o*-phenylenediamine). The electrode was calibrated at least five times for response to glycerol. The electrode was then placed in 10-fold-diluted plasma for 2 h, followed by several further calibrations in fresh buffer. This same procedure was followed for the effect of plasma on an electrode prepared with the adsorbed albumin coat.

Measurement of Plasma Glycerol. The working electrode was coated with poly(*o*-phenylenediamine), and albumin was adsorbed onto the outside of the dialysis fiber. The electrode was prepared the day before the clamp was performed and stored overnight at 4 °C. On the day of the clamp experiment, the electrode was switched on and allowed to settle for 1–2 h before commencing measuring samples.

Glycerol clamps were performed on healthy volunteers. Plasma samples were taken and measured every 10 min for 3–4 h. EDTA was used as anticoagulant on fresh whole blood samples (4 mL). The treated blood (1.5 mL) was spun in a microcentrifuge for 20 s. Plasma (0.4 mL) was extracted, and peroxidase solution (10 μL) and hydrogen peroxide solution (35 μL) were added. The sample was mixed with a whirly mixer for 5 s and left to stand for 1 min. Catalase solution (10 μL) was added and the sample mixed as before.

The glycerol concentration of the treated plasma sample was then determined as follows: (1) 0.3 mL of treated sample was added to the external buffer solution (4.0 mL); (2) 10 μL of ATP solution (0.25 mM) was added; (3) 10 μL of glycerol solution was added (approximately 5 μM).

The current was allowed to steady after each of the above stages. The electrode was placed in buffer containing 20 μM glycerol after each measurement for 2–3 min. This was necessary to remove any ATP retained inside the dialysis fiber. The electrode was then placed in fresh buffer (4 mL) and left for at

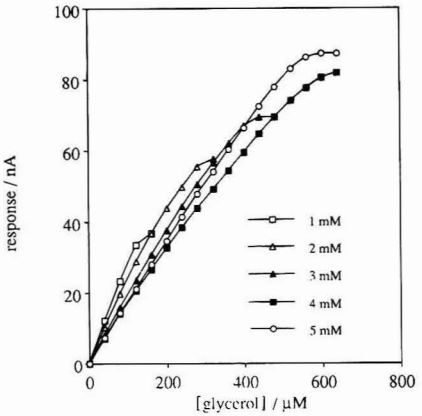


Figure 3. Response to glycerol at different ATP concentrations (bare working electrode and albumin not adsorbed). The response to aliquots of glycerol was determined in buffer containing a known concentration of ATP. The calibrations were performed in order of increasing ATP concentrations.

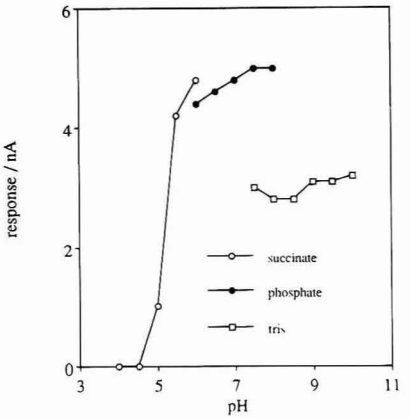


Figure 4. pH dependence of the response to 10 μM glycerol (unsaturated response). The electrode was coated with poly(*o*-phenylenediamine), and albumin was adsorbed onto the outside of the dialysis fiber.

least 1 min before adding the next treated plasma sample. A plasma sample was measured every 10 min.

Plasma samples, taken at the same time as those for the electrode, were deproteinized with perchloric acid and were tested with an automatic analyzer using the standard enzymatic spectrophotometric technique.[3] This uses glycerol kinase and glycerol phosphate dehydrogenase and measures the production of NADH at 340 nm.

RESULTS AND DISCUSSION

Optimization of the Electrode Response. Initially the electrode response was investigated for variation with ATP and enzyme concentrations and with pH in order to optimize the electrode and determine its suitability for measurement of plasma glycerol during the glycerol clamp. In a previous paper,[4] the electrode response to glycerol was analyzed according to the membrane electrode theory developed by Albery and Bartlett.[17] This indicated the unsaturated response of the electrode was determined by the rate of diffusion of glycerol through the dialysis fiber.

Dependence on ATP Concentration. The dependence of the electrode response on ATP concentration is shown in Figure 3. At 4 mM ATP and below, the linear range of the unsaturated region of response is dependent on the concentration of ATP, the cofactor for glycerol kinase. This suggests the saturated response is determined by the glycerol kinase kinetics. Glycerol kinase can convert glycerol more efficiently at higher ATP concentrations. Above 4 mM ATP, no further increase in linear range is observed, suggesting that glycerol kinase is now saturated with respect to ATP. The saturated electrode response is now determined by either the saturated enzyme kinetics (either glycerol phosphate oxidase or glycerol kinase) or by the electrode kinetics. An increase in the glycerol kinase or glycerol phosphate oxidase concentration did not result in any increase in saturated response (not shown), indicating that the saturated electrode response at high ATP concentration is determined by the electrode kinetics. Note that, with 4 mM ATP, the electrode response is linear up to 500 μM glycerol, which is more than adequate for the measurement of plasma glycerol (27–137 μM in normal subjects[18] and raised levels in diabetics[19]).

Dependence on Enzyme Concentration. The dependence of the response on enzyme concentration was determined, with glycerol kinase and glycerol phosphate oxidase in the ratio 1:1 by activity. No response could be detected below 10 units/mL, and above 100 units/mL, the response became approximately independent of enzyme concentration. This supports the conclusion that the unsaturated response is controlled by the rate of diffusion of glycerol through the dialysis fiber. A concentration of 500 units/mL was adopted as the standard concentration for experiments.

pH Dependence. The pH dependence of the electrode response to 10 μM glycerol (unsaturated response) is shown in Figure 4. The response to glycerol was approximately independent of pH above pH 6.0 for the phosphate buffer. However, although the response was approximately constant from pH 7.5 to 10 in Tris buffer, there was a fall in response of 40% compared to phosphate buffer. The response time remained fast, suggesting that the response was still controlled by diffusion through the dialysis fiber. This is expected since the permeability of the dialysis fiber is not thought to vary with pH. Below pH 6.0, the response decreases since the enzymes are no longer active. Glycerol kinase is stable over the pH range 6.0–9.8, exhibiting maximum activity at pH 9.8,[20] while glycerol phosphate oxidase exhibits broad optimum activity over the pH range 6.5–9.0.[21]

The odd drop in response observed with tris buffer was also observed with borate buffer (pH 8.0–10.0), although pyrophos-

(17) Albery, W. J.; Bartlett, P. N. *J. Electroanal. Chem.* **1985**, *194*, 211–222.

(18) Foster, K. J.; Alberti, K. G. M. M.; Hinks, L.; Lloyd, B.; Postle, A.; Smythe, P.; Turnell, D. C.; Walton, R. *Clin. Chem.* **1978**, *24*, 1568–1572.

(19) Skowronski, R.; Hollenbeck, B. B.; Varasteh, Y.-D. I. Chen; Reaven, G. M. *Diabetes Med.* **1991**, *8*, 330–333.

(20) Hiyashi, S.-I.; Lin, E. C. C. *J. Biol. Chem.* **1967**, *242*, 1030–1035.

(21) Esders, T. W.; Michrina, C. A. *J. Biol. Chem.* **1979**, *254*, 2710–2715.

phate buffer (pH 8.0–9.5) gave a slightly higher response compared to phosphate. These effects were observed whether or not the electrode was coated with poly(*o*-phenylenediamine) and in response to aliquots of hydrogen peroxide rather than glycerol, suggesting that the drop in response is due to some effect of buffer species on hydrogen peroxide oxidation.

The pH range of the electrode is more than satisfactory for the measurement of glycerol in plasma, since the pH of plasma varies very little and plasma samples are diluted 13-fold during the glycerol clamp.

Effect of Buffer Purity on Response. The response of the electrode during repeated calibrations to glycerol was observed to fall continuously by up to 50% over several hours, although the speed of the response was unchanged and remained fast, indicating that control of the response by diffusion of glycerol through the dialysis fiber was still occurring. However, if a new electrode was calibrated repeatedly using buffer made from AristaR grade reagents, the response remained stable. The concentration of calcium in AristaR buffer is much less than in AnalaR buffer (0.2 vs 25 μM). Calcium and other divalent and polyvalent cations form insoluble phosphate salts, and it is thought that these salts precipitate within the dialysis fiber, blocking the pores to some extent and causing the diffusion of glycerol through the dialysis fiber to be greatly reduced. Calibrations carried out in AnalaR buffer with 10 mM Na_2EDTA also gave a stable response, supporting the idea that insoluble phosphate salts block the dialysis fiber.

Identification of Interferent Species in Plasma. An advantage of using the ATP-dependent glycerol kinase is that the electrode response to a plasma sample can be measured in the absence and presence of ATP, giving the interferent and glycerol response, respectively. However, if the interferent current could be eliminated, plasma glycerol can be measured in one step. The large, nonspecific oxidation current due to interferents in plasma is particularly detrimental to the measurement of glycerol, since glycerol concentrations in plasma are in the micromolar range. The interferent current can be 1 order of magnitude larger than the response due to glycerol (approximately 80–180 nA vs 6–25 nA). Clearly the nonspecific oxidation current must be reduced if plasma glycerol is to be measured accurately.

Ascorbate, urate, and acetaminophen are known to be oxidized at hydrogen peroxide detecting platinum electrodes.[7] A number of other species present in plasma[22] were also tested for electrooxidation at the electrode. Species that gave rise to oxidation currents are given in Table 1, along with their normal concentrations in human plasma. As can be seen, a large number of species can be oxidized. However, if the magnitude of the oxidation current is considered in relation to the concentration in plasma for each individual species, then only ascorbate and urate are of major importance, contributing 50–80% of the oxidation current. Acetaminophen is of equal importance to ascorbate and urate if present in plasma. L-Cysteine is of secondary importance compared to ascorbate and urate, contributing 20–40% of the oxidation current (this assumes no cystine present—the relative importance of L-cysteine decreases on storage at room temperature due to dimerization to cystine). The remainder (up to 10%) is made up of the other interferents. Determination of the individual interferents is particularly important in the measurement of glycerol, since even if the oxidation currents due to ascorbate, urate, and acetaminophen are totally suppressed, the magnitude of the remaining oxidation current can still be equal in size to the response due to glycerol.

Table 1. Species Present in Plasma That Produce a Measurable Oxidation Current at a Platinum Electrode Held at +650 mV vs Ag/AgCl[a]

species[22]	current per unit concn (nA/mM)	concn in plasma[22] (μM)
L-alanine	0.03	338–419
L-arginine	0.13	58–92
L-asparagine	0.065	41–49
L-citrulline	0.02	29
L-cysteine	36.0	89–107[b]
L-glutamine	0.05	570
glycine	0.02	179–230
L-histidine	0.04	46–85
L-lysine	0.02	137–165
L-methionine	1.0	22–29
L-ornithine	0.23	47–61
L-serine	0.02	96–119
taurine	0.13	33–66
L-tryptophan	9.7	55
L-tyrosine	0.77	45–80
imidazole	0.05	0–440
urinary indican	48.4	9.4–34
uric acid	235	160–390
ascorbic acid	420	5.7–119
guanidoacetic acid	0.02	20–24
sialic acid	0.04	1.29–2.10
riboflavin	0.24	69–98
thiamine	0.14	30–445
acetaminophen	280	200[30]

[a] The working electrode was bare and albumin was not adsorbed onto the dialysis fiber. [b] Assuming no cystine present. Note that cystine is not electroactive.

Reduction of Interferent Response with Poly(*o*-phenylenediamine). *o*-Phenylenediamine was electropolymerized onto the platinum electrode in order to reduce the interference current. It is pleasing that the platinum electrode of the microdialysis electrode can be coated in situ simply by placing the dialysis fiber part of the electrode into a solution of *o*-phenylenediamine. This reduces the possibility of damaging the coat during construction of the microdialysis electrode. Table 2 shows the poly(*o*-phenylenediamine) coat was found to be effective at reducing the oxidation currents of the major interferents. However, Figure 5 shows that the long-term stability of the coat was poor, particularly toward acetaminophen. The response to acetaminophen greatly increased over the period of 3 days, while the response to hydrogen peroxide also increased. This is consistent with deterioration of the coating, with a concomitant increase in the available electrode surface. This deterioration, in particular for acetaminophen, has been observed by other workers.[10] The results suggest the poly(*o*-phenylenediamine) coat is not sufficient to eliminate the interferent current.

Attenuation of Response by Interferents. The attenuation of the electrode response by interferents was also investigated. Ascorbate, urate, and creatinine are all known to react with hydrogen peroxide, causing interference in enzymatic spectrophotometric assays.[12] The effect of interferents on the gradients obtained from consecutive calibration runs for hydrogen peroxide is shown in Figure 6. This experiment was performed in buffer containing 10 mM Na_2EDTA, since this stabilized the electrode

(22) *Blood and Other Body Fluids*, 3rd ed.; Altman, P. L., Dittmer, D. S., Eds.; Federation of American Societies for Experimental Biology: Washington, DC, 1971.

Table 2. Efficiency of Poly(*o*-phenylenediamine) Coat in Preventing Oxidation of Species Present in Plasma[a]

species	concn of species tested[b] (mM)	% reduction	calcd interference current[c] with poly(*o*-phenylenediamine) coat (nA)
L-cysteine	0.1	72	0.89–1.1[d]
L-methionine	6.5	38	0.014–0.018
L-ornithine	8.0	78	0.0024–0.0031
L-tryptophan	3.4	82	0.093
L-tyrosine	4.7	75	0.009–0.015
imidazole	11.1	0	0–0.022
urinary indican	4.4	96	0.017–0.063
uric acid	0.3	95	2.0–4.6
ascorbic acid	0.1	97	0.06–1.3
acetaminophen	0.1	91	4–16

[a] Albumin was not adsorbed onto the dialysis fiber. [b] An aliquot of stock solution was made to the external buffer for L-cysteine, ascorbate, urate, and paracetamol. For the other interferents, approximately 5 mg of solid was added to the external buffer. [c] Calculated from (1 – % reduction/100) multiplied by (current per unit concentration × concentration in plasma given in Table 1). [d] Assuming no cystine present.

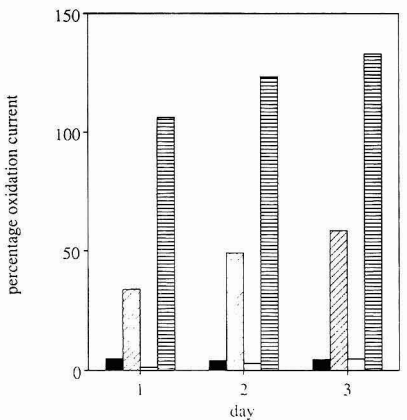


Figure 5. Deterioration of the poly(*o*-phenylenediamine) coat with time (albumin not adsorbed). Day 1 is the day of coating the electrode. Percentage oxidation current is given by (i_{coated}/i_{bare}) × 100% for each species. Species tested were 100 μM ascorbate (solid), 100 μM acetaminophen (diagonal hatched), 300 μM urate (open), and 8.82 μM hydrogen peroxide (horizontal hatched).

response (see above). This allowed any changes in gradient due to the effect of interferents to be determined more accurately. Similar results were obtained for the effect of interferents on glycerol response. Typical physiological concentrations of creatinine, acetaminophen, urate, and ascorbate caused 6%, 12%, 13%, and 18% reduction in hydrogen peroxide response, respectively. A plasma sample containing these concentrations of interferents would cause a 49% drop in glycerol response, although dilution of the plasma sample would result in much smaller attenuation of glycerol response. Note that urate and ascorbate, and to a lesser extent acetaminophen, caused some permanent suppression of the hydrogen peroxide response after the electrode was placed in fresh solution, suggesting these species cause poisoning of the electrode surface in addition to the solution reaction with hydrogen peroxide.

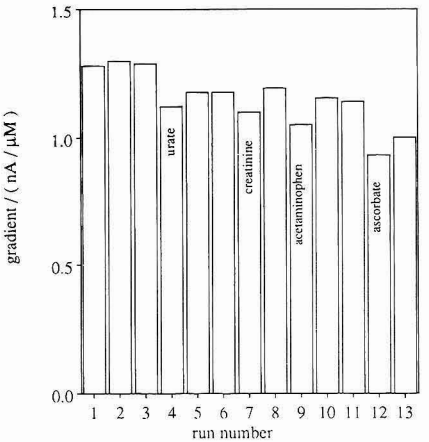


Figure 6. Effect of interferents on gradient of calibration runs. The working electrode was coated with poly(*o*-phenylenediamine), and albumin was not adsorbed. The buffer contained Na_2EDTA (10 mM). The gradients of a series of consecutive calibration runs are shown. For each calibration run, the electrode response was measured at 8.82, 17.64, 26.46, 35.28, and 44.10 μM hydrogen peroxide. Runs 4, 7, 9, and 12 were in the presence of 300 μM urate, 100 μM creatinine, 100 μM acetaminophen, and 100 μM ascorbate, respectively.

The presence of interferents also caused the glycerol response to drift slightly, making the determination of plasma glycerol concentration less accurate and extending the response time. The effect of the interferents during measurement of plasma glycerol could be reduced by diluting the sample and using the poly(*o*-phenylenediamine) coat. However, the need for an accurate measurement of plasma glycerol (accurate to within 1 μM) every 10 min, together with the drift in response, and the instability of the poly(*o*-phenylenediamine) coat, suggest that another method, which can overcome the interferent effects more successfully, is preferred.

The effect of the interferents on glycerol response would be eliminated if the interferents could be prevented from entering the internal solution of the dialysis fiber. Diffusion of ascorbate and urate is greatly reduced through anion exclusion membranes made from cellulose acetate[23] or Nafion.[24] However, this is not suitable for the glycerol electrode because ATP, the cofactor for glycerol kinase, is negatively charged and so would be unable to pass through the dialysis fiber. An alternative is to remove the interferents from the plasma sample prior to sampling for glycerol.

Sample Pretreatment. Peroxidase can oxidize certain interferents in the presence of hydrogen peroxide:[25]

$$DH_2 + H_2O_2 \xrightarrow{\text{peroxidase}} D + 2H_2O$$

Peroxidase and excess hydrogen peroxide can be added to the

(23) Sittampalam, G.; Wilson, G. S. *Anal. Chem.* **1983**, *55*, 1608–1610.
(24) Harrison, D. J.; Turner, R. F. B.; Baltes, H. P. *Anal. Chem.* **1988**, *60*, 2002–2007.
(25) Aebi, H. E. *Methods of Enzymatic Analysis*, 3rd ed.; Academic Press: New York, 1974; Vol. 2, pp 267–268.

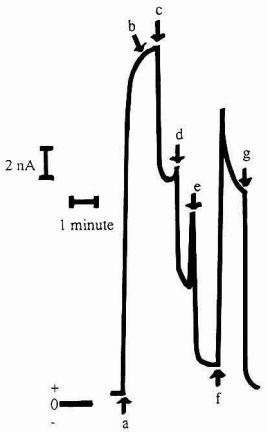


Figure 7. Eliminating acetaminophen with peroxidase and hydrogen peroxide (bare working electrode and albumin not adsorbed). Addition of (a) 100 μM acetaminophen, (b) 10 μL of peroxidase solution, (c–f) 44.1 μM hydrogen peroxide, and (g) μL of catalase solution.

plasma sample to ensure that all interferents have been removed. The excess hydrogen peroxide can be removed by the addition of catalase:[26]

$$2H_2O_2 \xrightarrow{\text{catalase}} 2H_2O + O_2$$

Both peroxidase and catalase are relatively cheap enzymes, with fast kinetics and high activity, and so it is feasible to treat each plasma sample in this manner. Such an approach has been reported previously for the measurement of glucose with an iodide selective electrode,[27] and a similar method is reported by Maidan and Heller,[28] who immobilized peroxidase directly onto a glucose-sensing electrode.

The enzymatic elimination of acetaminophen with peroxidase and hydrogen peroxide, followed by catalase to remove the excess hydrogen peroxide, is shown in Figure 7. Ascorbate and urate could also be eliminated by this method, although L-cysteine, L-tryptophan, and L-tyrosine were unaffected. A pretreatment step for plasma was developed (see Experimental Section), which gave a great reduction in the oxidation current due to interferents. However, a small oxidation current still remained (3–15 nA), which was observed to decrease on leaving the plasma sample at room temperature for 1 h. It was concluded that L-cysteine was probably the major cause of the remaining oxidation current, since it was not affected by the enzymatic pretreatment. L-Cysteine is known to dimerize to L-cystine, a nonelectroactive product, on standing. The reduction in interference current due to the dimerization of L-cysteine has been observed previously.[9] Note that peroxidase and catalase, at the concentrations used in the pretreatment step, produced a 1–2% reduction in glycerol response.

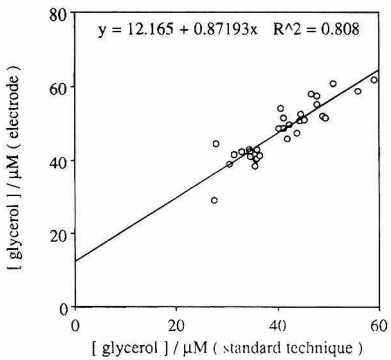


Figure 8. Correlation between plasma glycerol concentration obtained by the electrode and by the standard spectrophotometric technique (n = 31). The electrode was coated with poly(o-phenylenediamine), and albumin was adsorbed onto the outside of the dialysis fiber. The limit of detection for the electrode technique was 0.1 μM glycerol.

Adsorption of Albumin. Exposure of the glycerol electrode to 10-fold-diluted plasma for 2 h was found to result in a 1–4% decrease in glycerol response, presumably due to adsorption of plasma proteins on the outside of the dialysis fiber. It was hoped that preadsorption of albumin onto the membrane surface could prevent any further adsorption taking place. A similar approach using adsorption of polymer has been reported recently.[29] However, the reduction in response on exposure to plasma was unchanged. It is possible that the reduction in response is due to the poisoning of the electrode surface by interferents, as observed above. Note that preadsorption of albumin caused a 5% decrease in electrode response, compared to the response before adsorption of albumin. Also, the background current of the electrode took longer to steady after being placed in fresh buffer, compared to an electrode with no adsorbed albumin coat. After 5 min settling time in fresh buffer, the electrode behaved as usual.

The response to glycerol was observed to have decreased by 15–20% at the end of a glycerol clamp. While the adsorption of plasma proteins is expected to have contributed 1–4% decrease in response, the most likely cause of the remainder of the decrease is the formation of insoluble phosphate salts in the dialysis fiber as mentioned above. It is hoped that the use of AristaR buffer in future experiments will eliminate this drop in response.

Measuring Plasma Glycerol Concentrations. The electrode has been used to successfully carry out glycerol clamps. The electrode was prepared the day before the clamp with the poly(o-phenylenediamine) coat and the adsorbed albumin coat and stored in buffer overnight at 4 °C. Plasma samples were pretreated with peroxidase and catalase.

Results are shown in Figure 8 for the correlation between plasma glycerol concentrations obtained by the electrode and by the standard Cobas automatic analyzer technique. Higher glycerol

(26) See ref 25, pp 273–286.
(27) Nagy, G.; Von Storp, L. H.; Guilbault, G. G. *Anal. Chim. Acta* **1973**, *66*, 443–455.
(28) Maidan, R. and Heller, A. *Anal. Chem.* **1992**, *64*, 2889–2896.
(29) Oliveira Brett, A. M.; Pereira, J. L. C.; Dejardin, P. *Bioelectrochem. Bioenerg.* **1993**, *31*, 311–322.
(30) Moatti-Sirat, D.; Velho, G.; Reach, G. *Biosens. Bioelectron.* **1992**, *7*, 345–352.

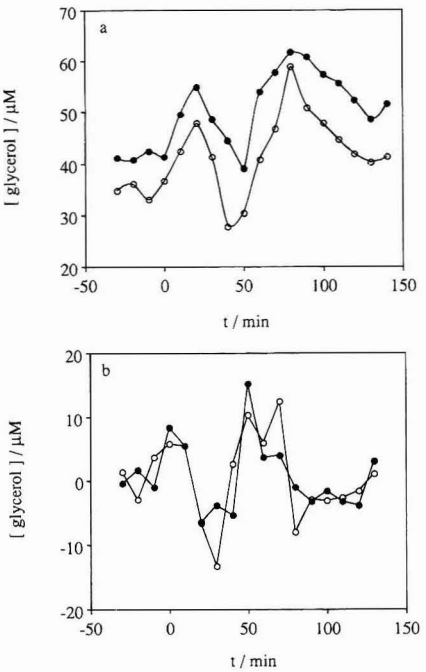


Figure 9. Glycerol concentrations during a glycerol clamp. The electrode was coated with poly(*o*-phenylenediamine), and albumin was adsorbed onto the outside of the dialysis fiber. (a, top) shows the correlation in behavior of plasma glycerol concentrations obtained by the electrode (solid dots) and the standard spectrophotometric technique (open dots). (b, bottom) shows the change in glycerol concentration with time (change in glycerol concentration = glycerol concentration at t + 10 min − glycerol concentration at t min).

concentrations were obtained with the electrode technique compared to the spectrophotometric technique, with an average ratio of the spectrophotometric to electrode glycerol concentration for the data in Figure 8 of 0.85. The two techniques are expected to give different concentrations, since the electrode technique gives the plasma glycerol concentration, while the spectrophotometric technique gives the whole blood glycerol concentration. This difference between the whole blood and plasma glycerol concentrations has been reported previously,[18] and the ratio of whole blood to plasma glycerol concentration was 0.86, in good agreement with the results above. The concentration of glycerol in whole blood is lower because although the concentration of glycerol in the water of the cells and plasma is the same, the water content of the cells is lower than plasma (73% vs 93%).

The results from a typical glycerol clamp are shown in Figure 9a. The variation of glycerol concentrations with time was very similar for the two techniques. In Figure 9b, the change in glycerol concentrations with time is shown. It is very pleasing that this change in glycerol concentration is not significantly different for the electrode and Cobas techniques (Student's t-test, $|t| = 0.0055$, $P = 0.001$, $n = 17$).

A number of steps were employed in the determination of the glycerol concentration of a plasma sample to ensure the accuracy

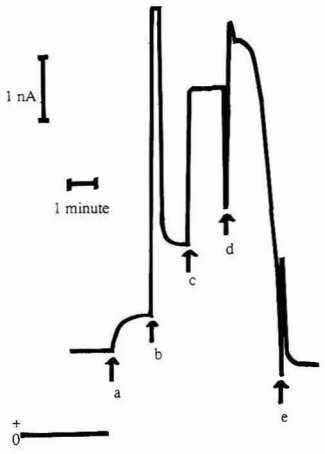


Figure 10. Typical measurement of plasma glycerol concentration. The electrode was coated with poly(*o*-phenylenediamine), and albumin was adsorbed onto the outside of the dialysis fiber. The electrode was initially in buffer containing no ATP or glycerol. The following step were made: (a) addition of 0.3 mL of treated plasma, (b) addition of 10 μL of ATP solution, (c) addition of 10 μL of glycerol solution, (d) electrode placed in buffer containing 20 μM glycerol, and (e) electrode placed in fresh buffer containing neither glycerol nor ATP.

of the measurement. A typical measurement of a plasma sample is shown in Figure 10. The electrode was initially placed in buffer held in a beaker, containing no ATP. The pretreated plasma sample was added to the buffer, giving rise to a small oxidation current (<1 nA), probably due primarily to L-cysteine. ATP was then added, giving rise to an oxidation current, the magnitude of which is proportional to the glycerol concentration in the beaker. Finally, an aliquot of glycerol solution was added to give a calibration measurement for each sample. The fast response time of the electrode made this calibration possible for each sample. This increased the accuracy of the measurement, which is particularly important for the glycerol clamp, since only small changes in plasma glycerol concentration (a few micromolar) are observed. The electrode was then placed in fresh buffer containing 20 μM glycerol for 2–3 min, to consume any ATP retained with the dialysis fiber, followed by fresh buffer containing no ATP and no glycerol, ready for the next plasma sample.

It was necessary to remove any ATP retained within the dialysis fiber, since if the ATP was not removed, some glycerol response was observed in addition to the interferent current in step a in Figure 10, giving a misleadingly low value for plasma glycerol on addition of the ATP aliquot in step b. The amount of ATP retained in the dialysis fiber was quite small, and could be liberated on placing in fresh buffer after 5–10 min, although such a long stabilization time is not possible during the glycerol clamp. An alternative would be to have a low background concentration of glycerol, say 10–20 μM, always present in the buffer.

CONCLUSIONS

This paper highlights the difficulties encountered when one attempts to accurately measure analyte in plasma with a hydrogen peroxide detecting enzyme electrode. While the nonspecific

oxidation current due to plasma interferents is well-known, the attenuation of the response by the homogeneous reaction between hydrogen peroxide and interferents, or by poisoning the electrode surface, is not considered so frequently. The nonspecific oxidation current and the attenuation of response most probably cancel each other out to some extent, disguising the true magnitude of each. Although coating an electrode can greatly reduce the oxidation of interferents, the interferents are still free to mingle with hydrogen peroxide generated by the enzyme held in the electrolyte layer next to the electrode. Awareness and consideration of the attenuation of response by interferents should lead to the formulation of better strategies for overcoming the effect of interferents.

ACKNOWLEDGMENT

We gratefully acknowledge Glaxo for financial support of L.J.M.

Received for review April 22, 1994. Accepted August 31, 1994.[⊗]

[⊗] Abstract published in *Advance ACS Abstracts,* October 1, 1994.

Correspondence

Anal. Chem. **1994,** *66,* 4354–4358

Determination of ppb-Level CO, CO_2, CH_4, and H_2O in High-Purity Gases Using Matrix Isolation FT-IR with an Integrating Sphere

Yoshimasa Ogawara,* Albert Bruneau, and Takako Kimura

Air Liquide Laboratories 5-9-9 Tokodai, Tsukuba, Ibaraki, 300-26 Japan

Parts per billion-level CO, CO_2, CH_4, and H_2O are determined in high-purity argon and nitrogen gases by using matrix isolation Fourier transform infrared spectrometry with an integrating sphere. A linear response was observed in the corrected absorbance vs concentration of CH_4 and H_2O in both matrices. While a linear response was also observed for CO and CO_2 in argon matrix, a nonlinear response was found in nitrogen matrix. The latter is probably due to internal vibration–phonon interaction. Addition of argon into the nitrogen matrix resulted in a linear response. Comparison with gas-phase FT-IR shows that the combination of the matrix isolation FT-IR technique with an integrating sphere allows an enhanced sensitivity with a reduced sample volume.

Gas-phase Fourier transform infrared spectrometry (FT-IR) is often used in the analysis of trace impurities in high-purity gases. Routine analysis at the levels of a few parts per billion (ppb) is possible for typical impurities in high-purity gases such as N_2, Ar, He, and H_2 by using a gas cell with a long optical path length. There are, however, some drawbacks in gas-phase FT-IR:

When the sample gas itself is infrared active, absorption peaks of interest can be interfered with by those of the main gas. In addition, analytical precision for the ppb-level moisture is affected by the unstable background due to the residual moisture in the spectrometer and in the gas cell. Moreover, a large volume of the sample gas and spectral treatment such as least-squares fitting are required for high-sensitivity analysis.

Matrix isolation (MI) FT-IR is an alternative technique to overcome such drawbacks. MI was first proposed by Whittle et al. as a sampling method for radicals and reactive species in gas phase for spectroscopic studies.[1] In this technique, the sample gas containing one or more species of interest is frozen on a flat substrate (e.g., a mirror or window), and the molecules of interest are isolated from each other in the solid matrix formed. FT-IR can be used as one of the spectroscopic methods to detect the species trapped in the matrix.[2] In such a matrix, rotational motions of the molecules are hindered, and their IR absorption concentrates into a smaller number of enhanced peaks corresponding to vibrational modes only. The majority of the MI-FT-IR studies have been directed toward the spectroscopic band assignments, force constant estimations, molecular interaction studies, and the identification of intermediates and unstable species.[3] MI-FT-IR has been also applied in the analysis of stable species such as in the analysis of atmospheric trace species[4] and also as a detector of gas chromatography (GC/MI-FT-IR) to identify the eluted species.[5]

MI with a flat substrate, however, has a very short path length since the IR radiation beam passes through a thin matrix media only once or twice, and the sensitivity is not sufficient for trace-level analysis in many cases. Berger et al. improved the sensitivity by using an integrating sphere (IS)[6] in which the IR radiation was reflected many times within the sphere, equivalent to a longer path length. They applied the method for the analysis of trace N_2O in the CO_2 matrix at sub parts per million (sub-ppm) levels.

In the present study, MI-FT-IR with an integrating sphere is applied to analyze CO, CO_2, CH_4, and H_2O at ppb levels in high-purity argon and nitrogen gases.

EXPERIMENTAL SECTION

Instrumentation. (A) Gas Introduction System. A schematic flow diagram of the gas introduction system is shown in Figure 1. The gas feeding system is always operated in a dynamic-flow mode to minimize the effect of adsorption/desorption of gaseous components. The inner surfaces of all the components upstream of the MI unit are made of electropolished stainless steel (SS316), and integrated valves are employed extensively in order to minimize the dead legs in the system.

Sub-ppm level standard mixtures are prepared for calibration from a gas cylinder which contains CO, CO_2, and CH_4 at $1 \pm 0.02\%$ each in helium gas prepared by weight (Teisan KK). This gas is dynamically diluted in two stages with a purified matrix gas (either

(1) Whittle, E.; Dows, D. A.; Pimentel, G. C. *J. Chem. Phys.* **1954**, *22*, 1943.
(2) Mamantov, G.; Garrison, A. A.; Where, E. L. *Appl. Spectrosc.* **1982**, *36*, 339–47.
(3) *Chemistry and Physics of Matrix-Isolated Species;* Andrews, L., Moskovits, M.. Eds.; North-Holland: Amsterdam, 1989. *Spectroscopy of Matrix Isolated Species;* Clark, R. J. H.; Hester, R. E., Eds.; Advances in Spectroscopy 17; John Wiley & Sons: Chichester, UK, 1989.
(4) Griffith, D. W. T.; Schuster, G. *J. Atmos. Chem.* **1987**, *5*, 59.
(5) Griffiths, P. R.; Pentoney, S. L.; Giorgetti, A.; Shafer, K. H. *Anal. Chem.* **1986**, *58*, 1349A.
(6) Berger, E.; Griffith, D. W. T.; Schuster, G.; Wilson, S. R. *Appl. Spectrosc.* **1989**, *43*, 320–4.

0003-2700/94/0366-4354$04.50/0 © 1994 American Chemical Society

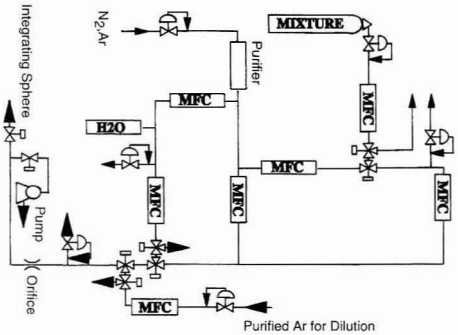


Figure 1. Gas introduction system: MFC, mass flow controller; H_2O, moisture permeation device.

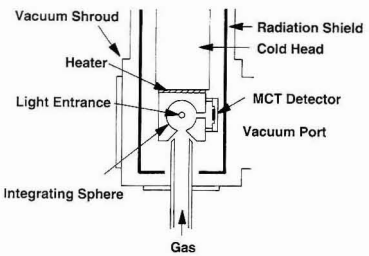


Figure 2. Matrix isolation unit (MI).

nitrogen or argon gas), using calibrated mass flow controllers. The purified argon and nitrogen gases are analyzed by an atmospheric pressure ionization mass spectrometer (APIMS) to confirm that they contain less than 1 ppb of any of the above impurities.[7] A water permeation device (GC Industries) is used as a moisture source, and it has been calibrated against a chilled mirror-type hygrometer (Hygro- M3, General Eastern). The flow rate over the permeation device is maintained constant to create a wet gas flow of a stable moisture concentration, and the mixing ratio of the wet gas with the purified matrix gas is varied to obtain desired sub-ppm moisture concentrations in the analyzed gas.

In the downstream of the two-stage dilution point, a calibrated orifice combined with a back-pressure regulator is used to introduce the mixed gas into the IS at a constant flow rate. The use of a mass flow controller is avoided here in order to minimize the surface area and thus the possible influence of adsorption/desorption of the impurities (particularly moisture) on the final concentration of the mixture. While no deposition is performed, the purified gas flow is maintained through the gas introduction system, but it is discarded through a rotary pump. The low-pressure side in the gas introduction system is all contained in an oven which is maintained at 50 °C.

(B) MI Unit. The design of the integrating sphere (Connecticut Instrument Corp., Figure 2) is similar to the one described by Berger et al.[6] A sphere of 12.5 mm in diameter has been milled from an oxygen-free copper block, and its internal surface is gold-coated. It has three orthogonal apertures. Two of them (2 mm in diameter) serve as the IR radiation beam entrance and exit while the third (4 mm in diameter) is for sample gas introduction via an electropolished SS316L tubing ($^3/_8$ in. in diamter). While Berger et al.[6] used a movable plug to close the sphere after the injection of the gas, no such movable plug is used in the present system. This is to avoid any trace air contamination into the IS by potential microleaks upon the movement of the plug since the impurities of our interest typically exist in air.

A 2 × 2 mm middle-band MCT detector is mounted on the radiation exit aperture. While Berger et al.[6] used liquid nitrogen to cool the MI unit, a closed-cycle helium cryostat is used in the present system to achieve a temperature low enough to solidify nitrogen and argon. The sphere detector block is attached to the cold head of this cryostat. A resistive heater allows control of the temperature in the sphere from 15 to 320 K. A turbomolecular pump is used in order to evacuate the cryostat chamber to 10^{-6} Torr prior to deposition, and it is maintained in vacuum whenever it is not in use.

(C) Spectrometer. The experiments are carried out with an FT-IR spectrometer (JIR-100. JEOL) with a globar power as an infrared radiation source. The inside of the spectrometer is continuously purged with dry nitrogen gas. Two off-axis paraboloidal reflectors allow focusing of the infrared radiation beam on the small entrance aperture of the IS.

Mathematical software (LAB CALC, Galactic Inc.) is used for data treatment. The investigated spectral region is typically between 400 and 4000 cm^{-1}.

Experimental Procedure. (A) Deposition Conditions. Deposition conditions (gas composition, flow dynamics, cooling rate, etc.) are known to affect the matrix structure and possibly to cause unwanted spectral broadenings.[8] In the present experiments, the gas is injected into the IS continuously for 100 s at 300 cm^3(STD) min^{-1}. No significant optical scattering of the deposited matrix is observed under this condition.

(B) IR Spectra Acquisition. Spectra are normally obtained with 1 cm^{-1} resolution and 100 scans in approximately 5 min with a triangular apodization function. The intensity spectrum of the deposit is divided by a reference intensity spectrum obtained before each deposition, and it is transformed into the absorbance spectrum. Since both argon and nitrogen gases used in the present study contain less than 1 ppb each of the impurities, the absorbance spectrum of the blank argon and that of the blank nitrogen are used to determine the base line of the absorbance peaks in the respective matrix to obtain the observed absorbance A_{obs} for each impurity. This A_{obs} is corrected for the optical parameters of an IS using eq 1 proposed by Berger et al.[6]

$$A_1 = \log(1 + b \times 10^{(A_{obs} + B)}) - \log(1 + b \times 10^{B}) \quad (1)$$

where A_1 is the linearized absorbance, A_{obs} is the observed absorbance, and B is the observed absorbance at the base line $b = 1/[(1 - h)\varrho] - 1$, where h is the fractional surface area of the sphere occupied by entrance and exit holes (=0.0384) and ϱ is the reflectivity of the gold sphere (=0.98). Thus, calculated A_1 is expected to follow the Lambert–Beer law and is therefore proportional to the concentration of the impurity in the matrix.

RESULTS AND DISCUSSIONS

Spectra of Impurities Isolated in Argon and Nitrogen Matrices. Table 1 lists the absorption peaks observed in the two

(7) Kimura, T.; Mettes, J.; Schack, M. *Proc. Inst. Environ. Sci.* **1993**, *1*, 14.

(8) Nelander, B. *J. Phys. Chem.* **1985**, *89*, 827–30.

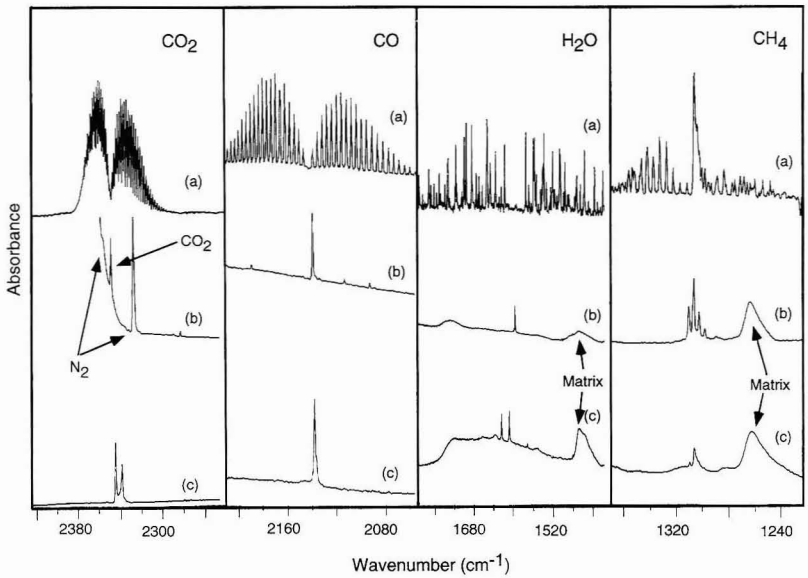


Figure 3. Absorption spectra of CO_2, CO, H_2O, and CH_4 at a few hundred ppb in the (a) gas phase, (b) nitrogen matrix, and (c) argon matrix.

Table 1. Main Absorption Peaks of CH_4, CO, CO_2, and H_2O in the Argon and Nitrogen Matrices Observed by IS-MI-FT-IR

impurity	mode attribution		peaks (cm^{-1}) in Ar matrix	peaks (cm^{-1}) in N_2 matrix
CH_4	υ_4	deg deform	*1306.0*	*1306.1*
	υ_3	deg stretch		3030.0
CO	υ_1	stretch	*2133.2*	*2139.6*
CO_2	υ_2	bend	665.0/666.5	662.5
	υ_3	antisym stretch	2339.0/*2345.0*	*2349.9*
H_2O	υ_2	bend	*1607.7*/*1623.9*	*1596.6*
	υ_1	sym stretch	3707.6	3711.6
	υ_3	antisym stretch	3753.6/3772.7	3727.1

matrices of four impurities under consideration, and their spectra are shown in Figure 3 together with gas-phase spectra for comparison.

If rotational motions of the impurities are hindered in the matrix, the absorption should be limited to a few sharp and intense vibrational peaks. This was indeed observed for CO, CO_2, and H_2O in the N_2 matrix and CO in the argon matrix. Calibrations were performed using the most intense peak of their vibrational modes (italic in Table 1) in these cases.

More complex absorption features were observed in other cases due to steric or polar interactions of the trapped impurities with the matrix. The absorption peak corresponding to the deformation mode υ_4 of CH_4 was a multiplet in both argon and nitrogen matrices due to rotational tunneling transitions of the CH_4 molecules in the solid matrices.[9] For CO_2 and H_2O in the argon matrix, a set of doublet peaks were observed for the antisymmetric stretching (υ_3) and bending (υ_2) modes due to the existence of two different substitutional sites in the argon matrix.[10]

(9) Frayer, F. H.; Ewing, G. E. *J. Chem. Phys.* **1968**, *48*, 781–92.

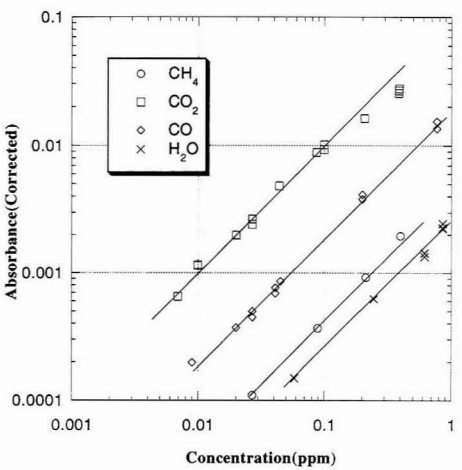


Figure 4. Calibration curves of CH_4, CO, CO_2, and H_2O in an argon matrix in the range of 10 ppb–1 ppm.

There is an advantage for H_2O analysis by MI-FT-IR compared with gas-phase FT-IR since the H_2O absorption peak in a solid matrix can be clearly distinguished from those in the gas phase, which are due to moisture in the spectrometer.

Calibration of Impurities in Argon. The observed peak heights (A_{obs}) were transformed into linearized absorbance A_l with eq 1. Calibration curves of all four impurities are shown in Figure 4 in a log–log plot. Note that the absorbance of the blank argon

(10) Irvine, M. J.; Mathieson, J. G.; Pullin, A. D. E. *Aust. J. Chem.* **1982**, *35*, 1971–7.

Table 2. Comparison of Detection Limits for CO_2, CO, CH_4, and H_2O in Argon and Nitrogen between IS-MI-FT-IR and Gas-Phase FT-IR

	detection limits (ppb)			
conditions	in gas phase[a]	in Ar matrix	in N_2 matrix	in N_2/Ar mixed matrix[b]
CH_4	8	38	23	
CO	8	8	1[c]	1
CO_2	2	2	0.05[c]	0.1
H_2O	50	50	14	
sample vol cm^3(STD)	11000	500	500	500
sampling time	a few minutes	100 s	100 s	100 s

[a] N_2, Ar at 1 kg/cm^2, 40 m path length. [b] Mix, 90%/10%. [c] Obtained by extrapolating the nonlinear calibration curves.

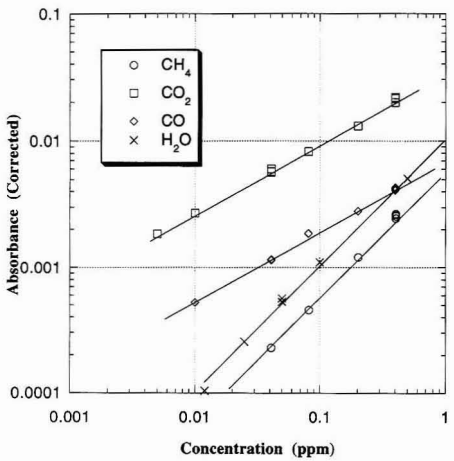


Figure 5. Calibration curves of CH_4, CO, CO_2, and H_2O in a nitrogen matrix in the range of 10 ppb−1 ppm.

gas is already subtracted. The slope of the curves were all at 45°, indicating the linear relationship in the argon matrix. Detection limits (defined as S/N = 3) thus obtained are listed in Table 2. These results show that IS-MI-FT-IR can offer detection limits for impurities such as CO, CO_2, and H_2O in argon at the same level as those of 40 m path-length gas-phase FT-IR but with much less sample volume. The CO_2 calibration curve was found to deviate from linearity at high concentrations (>0.1 ppm) because of high absorbance.

Calibration of Impurities in Nitrogen Matrix. The calibration curves of CH_4 and H_2O were linear (Figure 5) as in the argon matrix. The corresponding detection limits (definition as S/N = 3) were 14 and 23 ppb for H_2O and CH_4, respectively (Table 2). Calibration curves of CO_2 and CO were, however, found to be nonlinear (i.e., slope not being at 45° in the log−log scale). Although not shown here, the calibration curve of CO_2 obtained by using the absorption peak at 662.50 cm^{-1} was also nonlinear. An annealing treatment of the matrix did not improve the linearity. Measurement at a higher resolution (0.125 cm^{-1}) found that the half-widths of the CO and CO_2 peaks were 0.18 and 0.24 cm^{-1}, respectively, but the nonlinearity was maintained even at high-resolution measurement. This nonlinearity might be due to the interactions between the internal motions of the impurities and

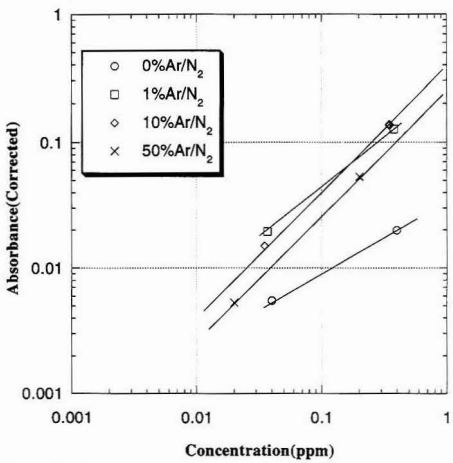


Figure 6. Calibration curves of CO_2 in the range of 10 ppb−1 ppm in an argon-doped nitrogen matrix.

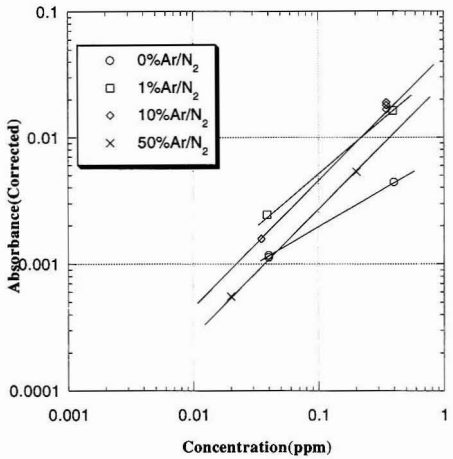


Figure 7. Calibration curves of CO in the range of 10 ppb−1 ppm in an argon-doped nitrogen matrix.

the phonons of the matrix since CO and CO_2 molecules have physical properties similar to those of the nitrogen molecule.[11]

Calibration of Impurities in Nitrogen When Doped with Ar. Modification of the matrix structure by adding another component into the matrix is one way to reduce the interactions causing the nonlinearity mentioned above. When argon was added into the nitrogen matrix at concentrations of approximately 10% or above, CO_2 and CO calibrations were found to become linear (Figures 6 and 7), respectively. Peaks of CO and CO_2 in a nitrogen matrix and an argon-doped nitrogen matrix are compared in Figure 8. The 10% concentration of argon approximately corresponds to the matrix structure in which the trapped CO or

(11) Langel, W. *Spectrochim. Acta* **1992**, *48A*, 405–27.

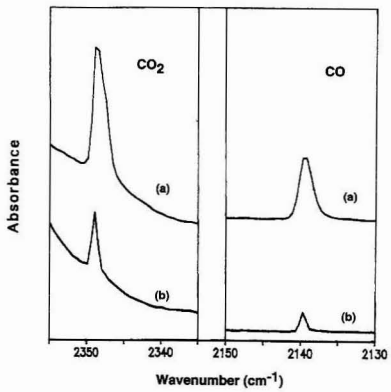


Figure 8. Effect of the Ar doping on the infrared absorption of 1 ppm CO and CO_2 in (a) a 10% argon-doped nitrogen matrix and (b) a nitrogen matrix.

CO_2 would have at least one Ar atom in its first surrounding layer of nitrogen molecules. This ratio seems to be sufficient to remove the strong interaction of the CO and CO_2 molecules with the nitrogen matrix. Detection limits for CO and CO_2 (S/N = 3) in nitrogen thus obtained were estimated to be 1 and 0.1 ppb, respectively (Table 2). Thus, lower detection limits are possible for CO and CO_2 in an argon-doped nitrogen matrix than in an argon matrix, and even with much less sample volume compared with gas-phase FT-IR.

CONCLUSION

The present study has demonstrated the ability of the IS-MI-FT-IR to analyze impurities at the ppb level in high-purity argon and nitrogen gases. While gas-phase FT-IR requires a long path length cell with a large sample volume and mathematical spectral treatment for the ppb-level analysis, IS-MI-FT-IR can achieve equivalent or better sensitivity with a significantly reduced sample volume and even without a special spectral treatment. As for CH_4, there is no improvement in sensitivity by IS-MI-FT-IR due probably to its rotational tunneling transitions. It has been shown that there is no spectral interference in the measurement of moisture in the sample gas by IS-MI-FT-IR with the residual moisture in the spectrometer, which is a limiting factor in H_2O analysis by gas-phase FT-IR. This is another advantage of IS-MI-FT-IR. Simplified spectra in MI-FT-IR would allow the resolution of two species whose absorbance peaks are very close to one another or overlap in gas-phase FT-IR. There are, however, several other analytical instruments which are simpler and faster with an equivalent sensitivity for the analysis of the impurities in nitrogen and argon gases studied here. The IS-MI-FT-IR, therefore, might be a more promising method for the analysis of impurities in high-purity infrared-active gases of small sample volumes for which the analytical methods are limited.

Received for review April 13, 1994. Accepted July 27, 1994.[⊗]

[⊗] Abstract published in *Advance ACS Abstracts*, September 15, 1994.

Anal. Chem. **1994,** *66,* 4359–4365

Detection of Alkylated Cellulose Derivatives in Several Archaeological Linen Textile Samples by Capillary Electrophoresis/Mass Spectrometry

Dmitri A. Kouznetsov,* Andrey A. Ivanov, and Pavel R. Veletsky

S. A. Sedov Biopolymer Research Laboratories, Inc., 4/9 Grafski Per., Moscow 129626, Russia

Eight different known-age samples of light, nondyed linen textile dated between 1200 B.C. and A.D. 1500 were studied by combined capillary electrophoresis/mass spectrometry analysis of the textile cellulose enzymatic hydrolysates. Both field ionization and field desorption variants of mass spectrometry have been used for identification of each electrophoretic fraction. High-resolution patterns were obtained using the 100 mM tetraborate (pH 9.0) zone electrophoresis system and the on-column laser-based refractive index detector. It has been shown that all archaeological textiles tested contain *alkylated* cellulose sequences. Thus, these textile samples differ from each other by alkyl groups (acetyl, carboxy, or methyl) as well as by the structure and abundance of the alkylated glucose residues. A possible origin and meaning of the character of this alkylation is under discussion which includes a special reference to correlations between such a parameters as (1) alkylation peculiarities, (2) geographical area of the textile manufacturing, and (3) the textile calendar age values.

There is currently a great deal of interest in the development of new approaches to chemical investigations of archaeological textile relics.[1,2] The importance of these studies stems from their potential utility in determining the chemical mechanisms of the textile "aging" and, therefore in for further improving of the accuracy of the ancient textile dating procedures. Besides, detailed chemical studies on archaeological textiles could provide important information about the lost, "archaic" technological processes practiced long ago in different geographical areas.[2,3] Finally, any information on the historic textile chemical aging should be important for development of methods for conservation of the relics.

The chemical investigation of the old textiles can be performed by a number of methods, including near-infrared/infrared reflectance spectrometry of undisintegrated textile, high-resolution electron microscopy, atomic absorption spectrophotometry for element analysis, and several chromatographic (both gas chromatography and HPLC) and electrophoretic techniques for fractionation and quantification of the textile cellulose enzymatic hydrolysate products.[1,2,4]

In our opinion, an optimal way to carry out efficient comparison between cellulose sequences of many different museum textile samples is to compare the HPLC or electrophoretic patterns obtained as a result of fractionation of low molecular weight compounds (nonmodified and modified β-D-glucose, plus cellobiose) of the enzymatically digested cellulose pool isolated from the textiles.

Thus, a combination of capillary electrophoresis and mass spectrometry should be very efficient for analysis of textiles: capillary electrophoresis provides significant separation efficiency and high analytical speed for a broad range of substances in solution, while mass spectrometry provides peak identification. Furthermore, the flow rates from the capilllary column are compatible with on-line coupling to a mass spectrometry.[4,5]

Capillary zone electrophoresis (CZE), in its numerous variants, is an alternative separation technique to HPLC. Remarkable performance of this analytical tool has been demonstrated by unprecedented separation efficiencies in many studies, including the most recent research on carbohydrates.[6,7]

Two significant problems have been identified for the analysis of sugars by CZE. First carbohydrates are not charged species under normal conditions; second, they have poor detectability. Nevertheless, it is easy to reach efficient separation results with the additon of borate ions to the separation medium, promoting the formation of ionic derivatives of sugars. This simple approach permits the formation of negatively charged sugar–borate complexes that can be separated by CZE.[7]

The low sample volumes injected in CZE make detection of carbohydrate a difficult task. Enhancements in sensitivity by UV absorbance (at 195 nm) have been obtained with the formation of the sugar–borate complex. The increase in sensitivity, however, is relatively small (2–20-fold), and the detection of sugars is limited to the nanomole range. At the same time, alternative methods of detection, such as electrochemical (am-

* All correspondence should be sent to: Dr. D. A. Kouznetsov, S.B.R.L., 25–44 Menzhinski St., Moscow 129327, Russia. Tel/FAX: 011-7095-186-7409.

(1) Cardamone, J. M.; Brown, P. Evaluation of Degradation in Museum Textiles Property Kinetics. In *Historic Textile and Paper Materials: Conservation and Characeterization*; Needles, H. L., Zeronian, S. H., Eds.; American Chemical Society Press: Washington, DC, 1986; pp 41–76.

(2) Ageyev, D. T. *Chemical Methods in Archaeology*; Moldova State University Press: Kishinev, 1992 (in Russian).

(3) Lee, J. S. *Elementary Textiles*; Prince Hall, Inc.: New York, 1953; pp 47–59.

(4) Yakimov, S. S.; Zheltkov, R. T. Field Ionization/Field Desorption Mass Spectrometry in Chemistry and Biochemistry of Carbohydrates. In *Appied Chemistry of Cellulose*; Samarin, L. K., Bakhurov, V. L., Eds.; Novosibirsk University Press: Novosibirsk, 1990; pp 126–148 (in Russian).

(5) Thompson, T. J.; Foret, F.; Vouros, P.; Karger, B. L. Capillary Electrophoresis/Electrospray Ionization Mass Spectrometry: Improvement of Protein Detection Limits Using On-Column Transient Isotachophoretic Sample Preconcentration. *Anal. Chem.* **1993**, *65*, 900–906.

(6) Bruno, A. E.; Krattiger, B.; Maystre, F.; Widmer, M. H. On-Column Laser-Based Refractive Index Detector for Capillary Electophoresis. *Anal. Chem.* **1991**, *63*, 2689–2697.

(7) Colon, L. A.; Dadoo, R.; Zare, R. N. Determination of Carbohydrates by Capillary Zone Electrophoresis with Amperometric Detection at a Copper Microelectrode. *Anal. Chem.* **1993**, *65*, 476–481.

0003-2700/94/0366-4359$04.50/0 © 1994 American Chemical Society

perometric) methods or refractometric methods based on the refractive index changes, are able to reach much better sensitivity levels in the CZE experiments with mono- and oligosaccharides.[2,6,7]

As for the cellulose chains in the ancient textile relics, some of them contain a significant number of chemically modified β-D-glucose residues, like hemiacetal derivatives of glucose or its carbonyl (conjugated) derivatives.[8,9]

Taking into account everything stated above, we have decided to carry out a comparative study on the possible chemical modification of cellulose from eight archaeological textiles dated between 1200 B.C. and A.D. 1500 which were kindly provided by several European museums (see Acknowledgment). For this study, we have used capillary zone electrophoresis of the purified cellulose enzymatic hydrolysates with mass spectrometric identification of each peak (see Experimental Section and Figure 3).

EXPERIMENTAL SECTION

Materials and Reagents. Light (nondyed) portions of the linen textile archaeological samples (75–200 g each) were purchased with a narrow calendar age certification from Russian and Ukrainian state museums and from one individual owner, Prof. Mario Moroni of Robbiate, Italy (see the Acknowledgment).

The following known-age archaeological linen textile samples were purchased: A1, Egyptian relic, 1200–1270 B.C. (from the Russian National Historical Museum, Moscow, Russia, museum no. 34118KL9); A2, Coptic relic, A.D. 380–450 (from the Russian National Historial Museum, museum no. 20014AE3); B, Israeli relic, 100 B.C.–A.D. 100 (from the Israel Antiquities Authority, Jerusalem, Israel, courtesy of Prof. M. Moroni, Robbiate, Italy); C1, Irish relic, A.D. 350–400 (from the Moscow State Institute of Textile Museum, Moscow, Russia, museum no. S411); C2, Southern English relic, A.D. 1100–1140 (from the Moscow State Institute of Textile Museum, museum no. R832); D, Middle Russian relic, A.D. 1460–1520 (from the Museum of Slavic Applied Art, Vladimir, Russia, museum no. 655E); E, Northern Greek relic, A.D. 860–930 (from the Crimean State Archaeological Museum, Simpheropol, Ukraine museum no. TK 4451); and F, Eastern Polish relic, A.D. 1280–1330 (from the West Ukrainian Museum of Ethnography and Archaeology, Ternopol, Ukraine, museum no. A8026).

Cellulase (1,4-[1,3;1,4]-β-D-glucan-4-glucanohydrolase; EC 3.2.1.4.) was purchased from Sigma Chemical Co. (St. Louis, MO). One unit of this enzyme was able to liberate 1.0 mol of glucose from cellulose in 1 h at pH 5.0 at 37 °C (2 h incubation time).

Diaflo YM-1 ultrafiltration membranes with an exclusion limit of 1000 Da were purchased from Amicon B.V. (Holland).

The capillary electrophoresis columns were fused-silica capillaries with the following parameters: i.d., 50 μm; o.d., 365 μm, where 5 mm of the polyamide coating was removed for detection; capillary length, 70 cm, 55 cm to detector (Polymicro Technologies, Inc., Phoenix, AZ).

All chemicals used were of analytical grade (Serva Heidelberg, GmbH, Germany).

Cleaning of Textile. The textile samples were defatted with an alcohol–benzene (1:2 v/v) mixture for 6 h and air-dried. The defatted samples were then submerged into a soluton containing 7.7% formaldehyde, 7.7% borax, and 0.5 sodium dodecyl sulfate for 3 min and dried in an electric oven at 100 °C for 2 h. Finally, all the samples were washed extensively with demineralized (deionized chromatographically on Amberlyte resins) water, 120 mL/cm^2, at room temperature. For this purpose, a textile sample was applied as a filter on the water flow. The cleaned and washed textile samples (up to 2.8 cm^2 each) were air-dried and kept in sealed, dry flasks for further studies.

Emzymatic Hydrolysis of the Textile Cellulose. Samples of 2.0–2.8 g of the mechanically desintegrated texiles (crude fibrous material) were incubated at 37 °C for 6 h in 20 mL of 15 mM Tris–borate (pH 6.40) buffer containing 4.5–5.0 units of cellulase per milliliter. These conditions were enough for 98% cellulose depolymerization.[1] After the incubation, the low molecular weight compounds pool was separated from the hydrolysate by ultrafiltration though the Diaflow YM–1 membranes in an Amicon MMC-10 apparatus (Amicon B.V.) at 2000 psi and then either concentrated in a rotar evaporator or lyophylized.

Capillary Zone Electrophoresis (CZE). The Elma 2000 CZE apparatus was used (manufactured by the NPO-Electron Instruments, Russia, 1992). This apparatus includes a 35 kV high-voltage power supply. Very similar equipment was used by Bruno et al.[6] in their CZE experiments. However, we have modified this apparatus with homemade microcylindrical electrodes. The microcylindrical Cu electrodes were constructed with 25-μm-diameter copper wire. One end of a 2–3-cm piece of the fine wire was attached to another piece of Cu wire (3–7 cm length, 380 μm diameter) by means of gold paint, providing electrical connection. A glass capillary (Precision Instruments, Inc., Sarasota, FL) was pulled with a vertical pipet puller, resulting in two capillary pieces with microtip at one end of each. The tip of the glass micropipet was gently cut to allow passage of the fine Cu wire. The fine wire was carefully introduced into the glass capillary through the end opposite the microtip, exposing 300–400 μm of the Cu microwire. Under a microscope, epoxy (Epoxy Technology, Inc., Billerica, MA) was applied to the tip of the glass capillary to seal the fine Cu wire to it. The electrical wire protruding at the other end of the glass capillary was also epoxied to support the electrical connection. The electrode was then mounted on a microscope slide and manipulated into the electrochemical cell by micromanipulators. Before the microelectrode was used in combination with CZE, it was cycled between 0.0 and 0.8 V for approximately 4–5 min.

New fused–silica capillaries (see the Materials and Reagents section) were treated by flushing first with 150 mM NaOH soluton and then with a separation electrolyte (100 mM tetraborate buffer, pH 9.0). Before each run, the capillary was flushed with the separation electrolyte. In addition, the electrolyte solution at the electrochemical cell was also replaced before each run. This procedure was necessary since the separation current was observed to decrease by approximately 10% during 1 h of continuous running. The capillaries were filled with deionized water for overnight storage.

The sample was siphon injected by inserting the column into the sample vial and elevating the vial by 20 cm for 10–150 s, producing an injection volume of 50–750 nL, corresponding to 40.0–500.0 ng of pure glucose.

The separation regime includes the following parameters: voltage, 14.0 kV; current, 50 μA; thermocooler temperature, 27

(8) Heller, J. H.; Adler, A. D. A Chemical Investigation of the Shroud of Turin. *Can. Soc. Forensic Sci. J.* **1981**, *14*, 81–102.

(9) Jumper, E. J.; Adler, A. D.; Jackson, J. P.; Pellicorni, S. F.; Heller, J. H.; Druzik, J. R. A Comprehensive Examination of the Various Stains and Images of the Shroud of Turin. *Archaeological Chemistry, III*; Advances in Chemistry Series 205; Americam Chemical Society: Washington, DC, 1984; pp 447–475.

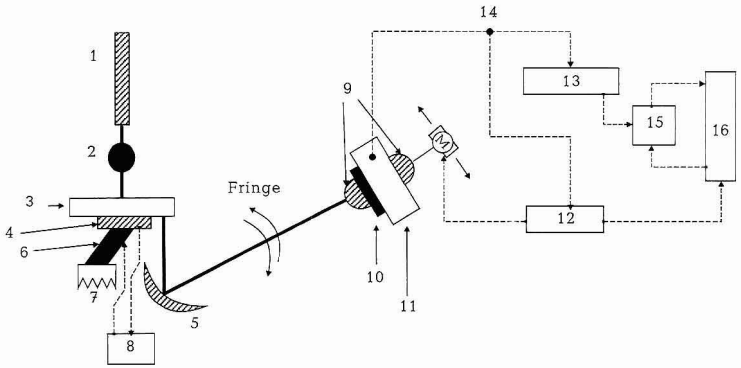


Figure 1. General scheme of the CZE refractive index detector design. (1) He–Ne laser; (2) optical unit; (3) capillary cell; (4) temperature sensor; (5) mirror; (6) Peltier element; (7) radiator; (8) temperature control unit; (9) motorized translation stage; (10) positron-sensitive diode; (11) analog electonics unit; (12) autozero control unit; (13) data conversion acquisition unit; (14) output; (15) CZE pattern recorder; (16) MultiScan DX600 unit for computerized comparative analysis of numerous (multiple similar) electrophoretic profiles (NPO-Electron Instruments, Inc., Russia).

°C; interference fringe, $n - 2$; separation time, up to 40 min; separation medium, 100 mM tetraborate, pH 9.0; capillary column geometry, see above (Materials and Reagents); applied electric field, E, 25 V cm^{-1} at the maximal current, 57.0 μA.

The on-column laser-based refractive index (RI) detector has been used designed according to recommendations given by Bruno et al.[6] A general scheme of the RI detector opticomechanical unit is presented in Figure 1. This RI detector is based on the positron-sensitive diode (PSD) and includes the surrounded liquid (RIMF) cooling system.

As for the RI cell itself, the best thermal stability in the cell is achieved when the thermocooler system is set at a temperature slightly higher than ambient. The resulting ca. 1 °C temperature gradient is localized near the cell windows and is directly correlated to an n gradient in the RIMF and fused silica according to their dn/dT thermal coefficients. Small fluctuations in the temperature around the exit air/window/RIMF interface, in contact with the environment, introduce an additional source of noise if a flat exit window is employed.

In a cell constructed with two plane parallel windows, the incoming laser beam crosses the entrance air/window/RIMF interface at 90°, and the n gradient does not alter the light-propagating path (i.e., no refraction).

The capillary tube and the flat entrance window are mounted and sealed with a pair of O rings and screws, whereas the cylindrical exit window is epoxied to the cell body. The capillary is coiled into a groove around the external part of the aluminum block before it enters the chamber filled with RIMF after crossing a region in contact with the Peltier element. The Peltier element is in contact with the capillary tube 5 mm before it enters the chamber filled with RIMF. A calibrated thermistor is placed on the opposite side of the thermocooler, in close contact with the capillary tube in a small hole in the aluminum block. Both elements are driven by a thermoelectric system. When no electrical current flows through the buffer, the short-term thermal stability ($\tau = 1$ s) of the system is better than 2×10^{-4} °C and has a typical drift of less than 1×10^{-2} deg h^{-1}.

A good RIMF should have a small dn/dT coefficient, not be photodegrade, and have a good transmittance. We employed a commerical RIMF oil (Nos. 19569 and 19571, R. P. Cargille Laboratories Inc., Cedar Grove, NJ) having $n = 1.4571$ and $dn/dt = 3.86 \times 10^{-4}$ RIU K^{-1} at 25 °C.

In all our RIMF-cooling CZE separation experiments, at the center of the bore, $T(r = 0) = 26.10$ °C.

The RI detector we used measures Δn originated not only at the capillary bore but also at any point of the optical path from the laser output coupler to the PSD. The laser (Uniphase No. 1103P), optical isolator (constructed with a polarizing filer and a $\lambda/4$ plate (Drs. Steeg and Reuter, Germany), focusing optics, and cell are mounted on four sliding stainless steel rods (S & H NO. 061216) in contact with each other to prevent air flows in the beam path. The laser beam has a diameter of 600 μm and is focused into the capillary bore with a $f = 40$ cylindrical lens producing a beam waist of ca. 23 × 600 μm in the capillary bore. The cell volume, defined by the capillary i.d. and the beam waist, for a 50-μm-i.d. tube is 1.2 nL. An autozero for the instrument is constructed by feeding the output of the PSD into a servo system which drives the PSD to the desired position by means of a motor (NPO-Electron Instruments).

The applied RI detection system makes it possible to reach a high level of thermal stability, $\Delta T = 2.0 \times 10^{-4}$ °C, as described earlier by Bruno et al.[6] This is a result of a highly symmetric design intended to ensure fast thermal response from the thermoelectric system. In this efficient RI detector, the linear dynamic range extends to more than 3 orders of magnitude, with a typical root-mean-square noise level of 3×10^{-8} RIU and baseline drifts of 2×10^{-8} RIU h^{-1} at 1 Hz.

Data acquisition was performed with the Nelson software package (Perkin-Elmer, Switzerland) on an IBM AT380 computer.

The CZE system was unified (connected) with the mass spectrometer by an on-line coupling link using the capillary electrophoresis/mass spectrometry interface in our modification of the technical approach described by Thompson et al.[5]

This electrophoresis/mass spectrometry interface diagram is presented on Figure 2; in all our studies, the MK80 field ionizaton (FI)/field desorption (FD) mass spectrometer (NPO-Electron Instruments) was employed.

The stainless needle supplied with the instrument was replaced with a polyimide-coated fused-silica capillary used in CE. This change was made to eliminate any junctions that could abe

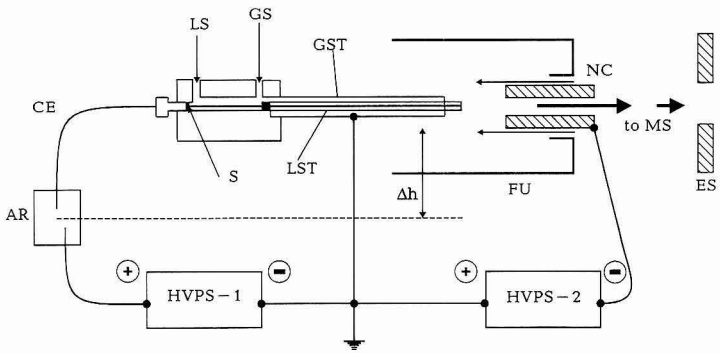


Figure 2. General scheme of the capillary electrophoresis/FI(FD) mass spectrometry interface. S, septum; LST, liquid shealth tube; LS, liquid shealth entry port; GST, gas shealth tube; GS, gas shealth entry port; AR, anode reservoir; Ce, CZE column (capillary); NC, nitrogen curtain drying gas; FU, FI(FD)-MS focusing unit (ion source compartment element); ES, entrance slit to mass analyzer; HVPS-1, high-voltage power supply for CZE; HVPS-2, high-voltage power supply for MS; Δh, height difference between the anode and cathode ends of the CZE column.

detrimental to the separation and to enable the end of the capillary to be located at the electrospray needle tip. The interface utilized a coaxial liquid sheath, as shwon previously, as well as a coaxial gas sheath. The liquid sheath tube was replaced by stainless steel tubing of ~0.4 mm i.d. and ~0.7 mm o.d., and the gas sheath tip was also replaced with a tip having an orifice of 1.0 mm i.d. The liquid sheath tip was narrowed to ~0.5 mm. The fused silica separation capillary terminated 0.5 mm inside the liquid sheath tip. A silicone septum was also added to prevent back flow of sheath liquid along the capillary.

Figure 2 shows that the differnce in height (Δh) between the anode reservoir and the tip of the MS needle (the cathode end of CZE column) was ~10 cm. A partial vacuum was created due to the flow of the gas sheath at the capillary tip, and, with the ends of the capillary at equal height, a significant bulk liquid flow toward the cathode took place. In order to compensate for this pressure drop, the level of the anode reservoir was lowered. The capillary was first filled with the leading electrolyte, and then ~150 nL of 10^{-3} M Methyl Green dye was siphon injected. The injection end of the capillary was then placed in the terminating electrolyte reservoir, and the current was applied. The current was turned off when the dye had focused into a narrow 2-mm-long band. Movement of the zone could easily be observed through the polyimide coating of the capillary, due to the high concentration of this focused dye. The height of the reservoir was adjusted until no movement of the dye was observed in either the forward or the reverse direction.

The MS needle, as shown in Figure 2, was maintained at ground potential, while the sampling orifice was at about −4000 V when the system was operated in the positive ion mode. The drying gas (nitrogen curtain) for the MS was maintained at about 100 °C at a flow rate of 6 L/min, while the sheath gas flow was set at approximately 2 L/min. The liquid sheath consisted of 1% acetic acid in 50% 2-propanol/water, flowing at a rate of 4.0 μL/min. Tuning and calibration of the mass spectrometer were performed using a 5 pmol/μL glucose solution.

Mass Spectromery. Due to the functioning of the CZE/MS interface described above (Figure 2), all electrophoretic fractions were transferred into the MK80 mass spectrometer for further analysis of the chemical structure. The pure glycerol was used as a matrix material. In our observation, the final glucose concentration range in the applied sample was equal to 1.0−30.0 mM, depending on individual CZE fraction, which normally corresponds to 1.0−5.0 μL of the postelectrophoretic solution. Before the sample was introduced into the ion source cell, it was briefly degassed to remove most of the water. Each of the MK80 internal copper probe tips contained of 2 μL of matrix material.

The MK80 mass spectrometer (NPO-Electron Instruments) contained two separate independent ion source units specially designed for both field ionizatin and field desorption versions of mass spectrometry.[4]

For both FI and FD versions, the anode/cathode potential was equal to 8.0 kV difference, and the potential gradient developed was equal to 10^8 V cm^{-1}. A conventional version of both FI and FD techniques was used: in both cases, ionization occurred when a molecule was subjected to a high potential gradient while close to an anode, which can accept electrones. The positive ions are drawn toward a cathode and then into the mass analyzer. In FI, the sample is evaporated, and molecules come very close to or impinge upon the anode (emitter), where they are ionized. In FD, the sample is coated onto the emitter, and the ions are desorbed from the solid state.[2,4]

The ion current has been monitored on the rear trapping plate of the analyzer cell and usually is between 1.0 and 10.0 nA. The ion production/injection time is variable and is typically between 5 and 500 ms, although pulses as narrow as 1 ms are sufficient to obtain signals. Frequencies ranged between 0.5 and 1.5 MHz.

Ions were collected linearly by increasing the length of the injection until saturation (space charge limit) was reached. Saturation was registered normally between 100 and 1000 ms, depending on the strength of the signal.

The pumping speed was equal to 170 L/s due tothe turbo pump which operates on the source. Two cryopumps each with a pumping speed of 2000 L/s (for N_2) operate on the ion transport region and on the analyzer region. Pressures in the source during the experiment were normally in the range 10^{-4}−10^{-5} Torr, while pressures in the analyzer region were maintained at 10^{-9}−10^{-10} Torr.[10] As it may be seen from above, a *conventional* MS-FI/FD analysis has been used.[2]

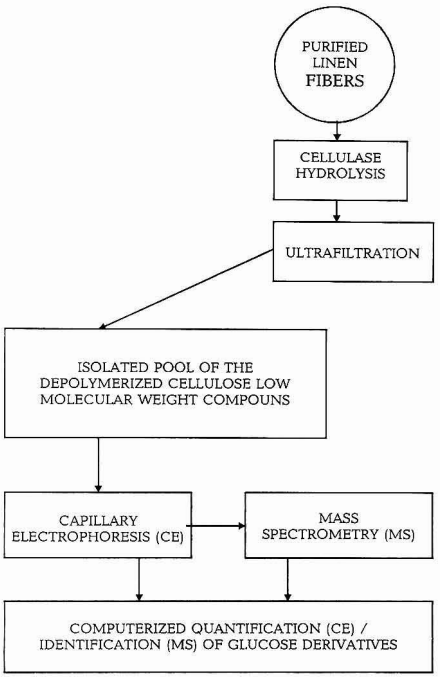
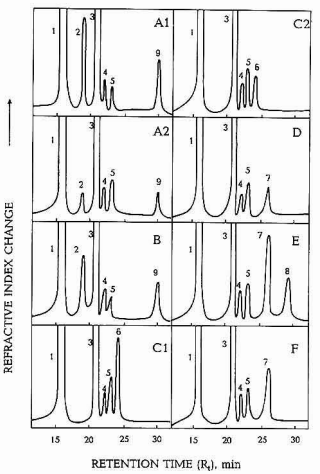


Figure 3. General scheme illustrating the consequence of steps and the final aim of the experimental procedures.



PEAK	Rt	IDENTIFIED STRUCTURE
2	16	BUFFER
2	19	2-ACETYL-6-METHYL-β-D-GLUCOSE
3	21	β-D-GLUCOSE
4	22	CELLOBIOSE
5	23	IMPURITY (NON-PYRANOSES/FURANOSES POOL)
6	24	2-CARBOXY-6-METHYL-β-D-GLUCOSE
7	26	2-CARBOXY-β-D-GLUCOSE
8	29	2,6-DICARBOXY-β-D-GLUCOSE
9	30	6-METHYL-β-D-GLUCOSE

Figure 4. Separation of products of enzymatic digestion of the fibrous cellulose from eight archaeological textile samples by capillary electrophoresis with simultaneous mass spectrometric identification of each fraction. For experiment record codes (A1–F), and technical details, see the Experimental Section.

All mass spectra were normalized to the protonated glycerol peak with subsequent computerized interpretation (chemical structure estimate) using a conventional FORTRAN/PAD algorithm in the IBM AT380 computer connected with a data bank of the Russian National Center for Ecology Studies at Moscow, Russia. For this purpose, the RNCES software for furanose/pyranose compounds identification was used.[4]

A series of scans were accumulated for each spectrum. The numbers of accumulated scans vary: for long ion injection time (e.g., 500 ms), only 10 scans were accumulated, while for the short injection time (e.g., 5 ms), up to 100 scans were accumulated. A routine analysis usually lasts several minutes.

NOTE: a general scheme of the whole experimental procedure is presented in Figure 3.

RESULTS AND DISCUSSION

As seen from our data presented in Figures 4 and 5, all eight archaeological textiles we tested contain the alkylated cellulose chains. Thus, this alkylation phenomenon includes formation of such derivatives of the glucose residues as 2-acetyl-6-methyl-β-D-glucose and 6-methyl-β-D-glucose (textiles, A1, A2, and B); 2-carboxy-6-methyl-β-D-glucose (textiles C1 and C2); 2-carboxy-β-D-glucose (textiles D, E, and F); and 2,6-dicarboxy-β-D-glucose (textile E). Furthermore, the presence and abundance of these clearly identified acetyl-, carboxy-, or methyl-containing glucose residues in the cellulose chains depend on the individual textile sample (Figures 4 and 5, Table 1, see Materials and Reagents).

For example, the content of both 2-acetyl-6-methyl-β-D-glucose and 6-methyl-β-D-glucose residues in the textile cellulose does increase with the age of the relic (A1 > B > A2, Table 1). It is also interesting to note that all these textiles (A1, A2, and B) were founded and possibly manufactured in one geographical region, Israel and Egypt. As for the other six textiles tested, they had other ages and geographical origins (see Materials and Reagents), and they contain other chemical modifications of cellulose based on permethylation and carboxylation of the latter (Figures 4 and 5).

In a group relatively young Western European textiles (C1 and C2) and in the Eastern European medieval textiles (D, E, and F), the same regularity should be noted: cellulose alkylation extent increases with the increasing calendar ages (Figure 4, Table 1).

All CZE patterns we obtained were clear and well reproducible. It seems the character of alkyl groups and the the chemical structure of alkylated glucose residues depend on the geographical (regional) origin of the textile (compare C1/C2 and D/E/F; see Figure 4, Table 1). Mass spectromeric identification of each alkylated glucose fraction presented in the CZE pattern is beyond any doubt (Figure 5).

(10) Carrol, J. A.; Ngoka, L.; McCullough, S.; Gard, E.; Jones, D. A.; Lebrilla, C B. Quadrupole Fourier Transform Mass Spectrometry of Oligosaccharides. *Anal. Chem.* **1991**, *63*, 2526–2529.

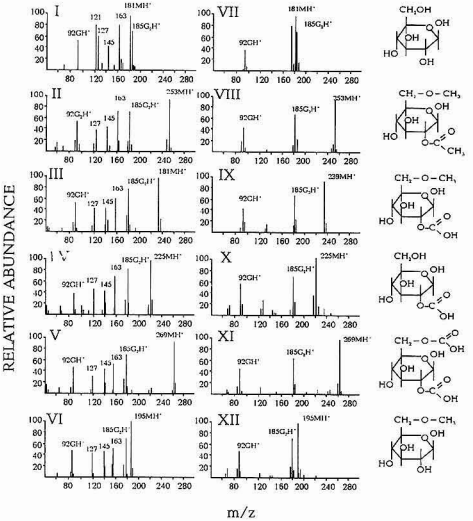


Figure 5. Mass spectra of monosaccharide fractions isolated by capillary electrophoresis of the textile cellulose hydrolysates. Spectra I–Vi, field ionization technique; VII–XII, field desorption technique; I and VII, nonmodified glucose fraction isolated from and textile sample tested (A1–F); II and VIII, fraction 2 isolated from samples A1, A2, and B; III and IX, fraction 6 isolated from samples C1 and C2; IV and X, fraction 7 isolated from samples D, E, and F; V and XI, fraction 8 isolated from sample E; VI and XII, fraction 9 isolated from samples A1, A2, and B. Two matrix peaks are labeled corresponding to protonated glycerol (*m/z* 92, GH^+) and the protonated dimer (*m/z* 185, G_2H^+). The fragment ions at *m/z* 163, 145, and 127 respresent successive losses of H_2O from (MH^+). For experiment record codes (A1–F), see the Experimental Section.

Table 1. Abundance of Alkylated Glucose Derivatives in Cellulose Chains from Several Archaeological Textile Samples[a]

sample[b]	content of minor glucose derviatives[c]	
A1	2-acetyl-6-methyl-β-D-glucose	5.40 ± 0.08
	6-methyl-β-D-glucose	6.12 ± 0.04
A2	2-acetyl-6-methyl-β-D-glucose	2.01 ± 0.007
	6-methyl-β-D-glucose	1.99 ± 0.006
B	2-acetyl-6-methyl-β-D-glucose	4.25 ± 0.02
	6-methyl-β-D-glucose	5.12 ± 0.02
C1	2-carboxy-6-methyl-β-D-glucose	5.98 ± 0.08
C2	2-carboxy-6-methyl-β-D-glucose	2.74 ± 0.02
D	2-carboxy-β-D-glucose	2.88 ± 0.03
E	2-carboxy-β-D-glucose	6.33 ± 0.07
	2,6-dicarboxy-β-D-glucose	3.27 ± 0.02
F	2-carboxy-β-D-glucose	4.18 ± 0.02

[a] These data were obtained using the refractive index change detection in capillary electrophoresis (see the Experimental Section). [b] For experiment record codes (A1–F), see the Experimental Section. [c] Percentage of total cellulose hydrolysate (M ± SEM, $n = 6$).

Summarizing the data on the cellulose alkylation extent (CAE) listed in the Table 1, we have found a crude but clear enough correlation between the calendar age values of the textiles tested and their CAE values. In our opinion, this type of dependence could be a subject for further fruitful investigations leading to the improvement of accuracy of the existing dating methods in archaeology and archaeological chemistry.

In fact, all modern archaeological textile dating techniques need to be improved and developed for better accuracy and efficiency. It seems that detailed chemical study of cellulose structure in different old textiles is a right way for creation of the efficient additional dating approach. In spite of the existence of the radiocarbon dating method, such additional and sometimes alternative dating techniques as stylistic detailed studies including microscopic research[1,3,11,12] are still important as elements of interdisciplinary approaches to the dating accuracy problem.

It is known that there are a number of unique morphological markers for textiles manufactured in several regions during limited historical periods.[3,11,12] Obviously, these markers should be taken into account in each archaeological dating procedure with objects from corresponding sites. It should not be excluded that it is possible to find not only morphological but also *molecular* markers for ancient textiles of different geographical origins and/or calendar ages. We believe that our data (Table 1, Figures 4 and 5) demonstrate the great significance of this kind of research.

As for the mechanism of cellulose alkylation in the old textiles, we could note at least two possibilities. First, it is logical to assume that the cellulose alkylation we have found in our work is a result of some unknown (lost, "archaic") technological processes for textile manufacturing. This assumption looks especially logical in the light of our data, which show that the most similar chemical structures of the alkyl derivatives were found in textile samples with common or close geographical origins (compare A1/A2/B and C1/C2; see Figures 4 and 5). Second, it should not be excluded that the cellulose alkylation process is a result of microbial contribution to the chemical modificaton of textiles. Thus, the carboxylating enzymes of bacterial carboxysomes are active even in bacterial lysates in wet alkali conditions and in the presence of oxygen.[13] The carboxylation of polyglucose can be easily promoted at pH 9.0 and in aerobic conditions by the destroyed (lysated) cells of several environmentally common bacteria of the *Desulfovibrio* genus.[14] Finally, the normal autolysis of air and soil microorganisms may lead to significant carboxylation and/or methylation processes with different substrates directed by the released active bacterial enzymes.[13–5] Thus, alkylation of the old textile cellulose could be the consequence of accumulation of the results of a great number of such a microbial treatments during the very long historic time interval. As for the alkali conditions for bacterial enzyme activity, all common soap-foaming washing procedures create this kind of pH change. Besides, alkalis were used as ingredients in some technological schemes of the past for rewashing of textile after its dyeing.[3,11]

(11) Cramer, M. Das Christlich-Koptische Agipten Einst und Heute, Eine Orientierung GmbH: Wiesbaden, Germany, 1959; pp 46–88.
(12) Bresee, R. R.; Chandrashekar, V.; Jones, B. W. Age Determination of Textiles from Single-Fiber Creep Measurements. In *Historic Textile and Paper Materials: Conversation and Characterization*; Needles, H. L., Zeronian, S. H., Eds.; Americal Chemical Society Press: Washington, DC, 1986; pp 19–40.
(13) Price, G. D.; Hewitt, S. M.; Harrison, M.; Badger, M. R. Analysis of a Genomic DNA Region from the Cyanobacterium Synechococcus sp. Strain PCC7942 Involved in Carboxysome Assembly and Function. *J. Bacteriol.* **1993**, *175*, 2871–2879.
(14) Hensgens, C. M. H.; Vonk, J.; Van Beeumen, J.; Van Bruggen, E. F. J.; Hansen, T. A. (1993) Purification and Characterization of an Oxygen-Labile NAD-Dependent Alcohol Dehydrogenase from Desulfovibrio gigas. *J. Bacteriol.* **1993**, *175*, 2859–2863.
(15) Doyle, R. J.; Koch, A. L. The Function of Autolysis in the Growth and Division of Bacillus subtilis. *Crit. Rev. Microbiol.* **1987**, *15*, 169–222.

To the best of our knowledge, the present study is the first report on the discovery of alkylated cellulose sequences in archaeological textiles. Further extensive studies on this subject could help to *classify* a great number of different archaeological textile relics using such a criterion as the *cellulose chemical modification types*. The classification mentioned would be an important tool for both dating research in archaeological chemistry and studying ancient textile technology.

CONCLUSION

The capillary zone electrophoresis equipped with the on-column laser (He–Ne)-based RI detector is an efficient approach to investigation of chemical modifications of the cellulose, including the studies in archaeological textile chemistry.

ACKNOWLEDGMENT

This work was supported by the Guy Berthault Foundation, Meulan, France. We are especially grateful to Prof. Mario Moroni of Robbiate, Italy, for sending us a fragment of linen cloth form a burial at En Gedi site, Israel, historically dated to the Early Roman Period (100 B.C.–A.D. 100) by the Israel Antiquities Authority. We would like to express our deep gratitude to Dr. Ivan Kappel, Assistant Keeper at the Russian National Historical Museum (Moscow, Russia), Dr. Oleg Krutov, Keeper at the Moscow State Institute of Textile Musemm (Moscow, Russia), Mrs. Olga Nenasheva, Deputy Director at the Museum of Slavic Applied Art (Vladimir, Russia), Mr. Sergey Bychkov, Deputy Director at the Crimean State Archaeological Museum (Simpheropol, Ukraine), and Mr. Ignat Tyshko, Keeper at the West Ukrainian Museum of Ethnography and Archaeology (Ternopol, Ukraine) for their remarkable courtesy in giving us a set of light, nondyed, known-age samples of archaeological linen textiles. We thank Dr. Alan Adler of the University of Western Connecticut at Danbury, CT, Prof. Witold Brostow of the University of North Texas at Denton, TX, and Dr. Alexander Volkov of Moscow State University for their critical remarks and fruitful participation in the discussion of our preliminary results. Mr. Timophey Palevich of the Moscow State University is especially to be thanked for his continued assistance in the preparation of samples for capillary electrophoresis.

Received for review March 7, 1994. Accepted August 9, 1994.[⊗]

[⊗] Abstract published in *Advance ACS Abstracts*, September 15, 1994.

Anal. Chem. **1994,** *66,* 4366–4369

Determination of Absolute Mass Values in MALDI-TOF of Polymeric Materials by a Method of Self-Calibration of the Spectra

Giorgio Montaudo* and Maurizio S. Montaudo

Dipartimento di Scienze Chimiche, Università di Catania, Viale A. Doria, 6-95125 Catania, Italy

Concetto Puglisi and Filippo Samperi

Istituto per la Chimica e la Tecnologia dei Materiali Polimerici, Consiglio Nazionale delle Ricerche, Viale A. Doria, 6-95125 Catania, Italy

A novel calibration procedure is introduced that allows one to obtain absolute mass values in MALDI-TOF spectra of polymeric materials. The masses of the oligomers are written as the sum of two masses: $\mu_n = \sigma_n + \theta$, where θ is the mass of the first oligomer and σ_n is a multiple of the polymer repeat unit and represents the distance in daltons from the first oligomer. The new calibration procedure considers θ as a variable parameter and performs a best-fit minimization. Two examples of application of the new procedure are given. Two synthetic polymers, poly(caprolactone) and poly(Bisphenol A carbonate), were analyzed by MALDI-TOF, and complex spectra showing one or more mass series up to 20 kDa were obtained. Application of this procedure allowed the interpretation of each single peak in the mass spectra and established that none of the peaks in the spectrum corresponds to fragments. It was found that the poly(caprolactone) sample consists of a series of oligomers with H and OH as terminal groups, which form sodium-cationized ions in the MALDI process. The composition of the poly(Bisphenol A carbonate) sample was more complex, since it contains a series of cyclic oligomers desorbing as sodium-cationized ions, plus two series of oligomers bearing H/phenol and phenyl/phenol as terminal groups, respectively, which form ions by capturing a proton in the MALDI process.

Matrix-assisted laser desorption ionization time-of-flight mass spectrometry (MALDI-TOF MS) is a recently introduced[1–9] soft ionization technique that allows desorption and ionization of very large molecules even if in complex mixtures, such as the wide molecular weight distributions present in synthetic polymers[3,6,7] and also in some natural macromolecules.[8,9]

Since TOF measures only *differences* of masses, the determination of absolute masses appears a difficult task, and calibration procedures using external and internal standards of known mass are currently used.[4,5]

However, the use of external standards may lead to ambigous results in the case of polydisperse polymeric materials constituted of one or more series of oligomers extending over a large mass range. Furthermore, internal standards are difficult to find since each synthetic polymer class would need structurally identical species, possibly monodisperse, with mass values such to avoid isochrony with the mass series displayed by the polymer sample. The task of obtaining absolute mass values in MALDI-TOF spectra of synthetic polymeric materials is of outmost importance, since it would make possible the direct determination of the species contained in each polymer sample and also of different end groups present in the oligomer series. End group identification and determination of the actual composition of a polymer sample are so crucial in polymer analysis that their importance cannot be overemphasized.

At the present time, calibration problems in MALDI-TOF analysis of polymers are such that often workers are able to obtain good spectra of polymeric samples but are unable to interpret them because of the difficulties in making the correct mass assignments and in discerning whether the polymer molecules desorb intact or not.

In the present paper, we report an attempt to solve this problem by introducing a new self-calibration method for the MALDI-TOF spectra of polymers. To this purpose, two samples of polydisperse

(1) Karas, M.; Hillenkamp, F. *Anal. Chem.* **1988,** *60,* 2299.
(2) Hillenkamp, F.; Karas, M.; Beavis R. C.; Chait, B. T. *Anal. Chem.* **1991,** *63,* 1193A.
(3) Bahr, U.; Deppe, A.; Karas, M.; Hillenkamp, F.; Giessman, U. *Anal. Chem.* **1992,** *64,* 2866.
(4) Cotter, R. A. *Anal. Chem.*, **1992,** *64,* 1027A.
(5) Bruker, User Software Manual, Reflex MALDI-TOF.
(6) Danis, P. O.; Karr, D.E.; Mayer, F.; Holle, A.; Watson, C. H. *Org. Mass Spectrom.* **1992,** *27,* 843. Danis, P. O.; Karr,D.E. *Org. Mass Spectrom.* **1993,** *28,* 923.
(7) Danis, P. O.; Karr, D.E.; Westmoreland, D.; Piton, M. C.; Christie, D. I.; Clay, P. A.; Kable, S. H.; Gilbert, R. G. *Macromolecules* **1993,** *26,* 6684.
(8) Burger, H.M.; Muller, H.M.; Seebach, D.; Bornsen, K. O.; Schar, M.; Widmer, H. M. *Macromolecules* **1993,** *26,* 4783.
(9) Abate, R.; Ballistreri, A.; Montaudo, G.; Garozzo, D.; Impallomeni, G.; Critchley, G.; Tanaka, K. *Rapid Commun. Mass Spectrom.* **1993,** *7,* 1033. Garozzo, D.; Spina, E.; Sturiale, L.; Montaudo, G.; Rizzo, R. *Rapid Commun. Mass Spectrom.* **1994,** *8,* 358.

0003-2700/94/0366-4366$04.50/0 © 1994 American Chemical Society

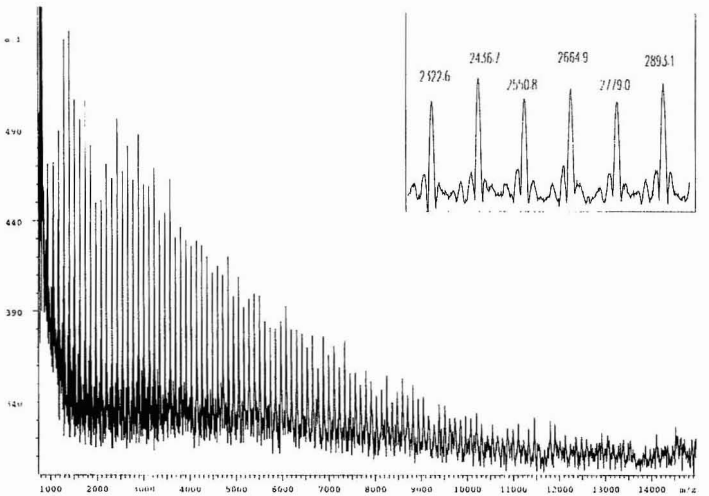


Figure 1. MALDI-TOF mass spectrum of poly(caprolactone).

synthetic polymers, poly(caprolactone) and poly(Bisphenol A carbonate), were analyzed by MALDI-TOF, and spectra up to 20 kDa were obtained. To our best knowledge, MALDI-TOF spectra of the two polymers are unreported. Application of the new calibration procedure allowed us to establish that the poly(caprolactone) sample consists of oligomers having H and OH as terminal groups, which form sodium-cationized ions in the MALDI process. The composition of the poly(Bisphenol A carbonate) sample was more complex, since it contains a series of cyclic oligomers desorbing as sodium-cationized ions, plus two series of oligomers bearing H/phenol and phenyl/phenol as terminal groups, respectively.

EXPERIMENTAL SECTION

Materials. 2-(4-Hydroxyphenylazo)benzoic acid (HABA), poly(caprolactone), and poly(Bisphenol A carbonate) were purchased from Aldrich and used without further purification.

Sample Preparation. Probe tips were loaded with 100 pmol of polymer sample and 300 nmol of matrix.

MALDI-TOF Mass Spectra. A Bruker Reflex mass spectrometer was used to obtain the matrix-assisted laser desorption/ionization time-of-flight mass spectra. The spectrometer was equipped with a nitrogen laser (337 nm, 5 ns), a double-plate microchannel detector, and a flash ADC (time base 10 ns). Accelerating voltage was 30 kV. The laser irradiance was not measured. However, it was slightly above threshold ($\sim 10^6$–10^7 W/cm^2). The detection was in the reflected mode. Ions below m/z 350 were removed with pulsed deflection, and 100 transients were summed. The resolution was ~300 at 5000 Da.

FAB Mass Spectra. A double-focusing Kratos MS 50S equipped with the standard FAB source and a DS90 data system was used. The FAB gun was operated with a 7 keV Xenon beam. The instrument was scanned from m/z 3000 to 100 with a scan rate of 10 s/decade. The accelerating voltage was 8 kV. FAB MS spectra were obtained in positive and negative modes using 3-nitrobenzyl alchol as matrix. Cesium iodide was used to calibrate the instrument.

RESULTS AND DISCUSSION

The correspondence between the time needed for an ion of mass μ to fly through the tube and the mass of the ion itself is a quadratic relationship,[4,5] as shown in eq 1, where α and β are

$$\mu_n = \alpha(t + 10^{-6}\beta)^2 \quad (1)$$

two calibration constants. The knowledge of at least two absolute mass values is therefore necessary to determine the two constants. In order to yield correct results, this procedure requires that the absolute mass values used are *exact*. Unfortunately, even in the most favorable case (i.e., using an internal standard of known mass), the mass value is uncertain because of the effect of the desorption ionization in MALDI. In fact, a particular species can be desorbed as a cation associated with H^+, Li^+, Na^+, K^+, or Cs^+, or it can form a matrix adduct. The ambiguity in the mass value used reflects itself on the calibration constants, yielding erroneous mass assignments and complicating the interpretation of the TOF spectra. To illustrate the pitfalls of the conventional calibration procedure, some calibration attempts using eq 1 will be illustrated below.

Figure 1 reports the MALDI-TOF mass spectrum of poly(caprolactone). The spectrum is constituted of a single mass series (see inset), with no evidence for ion fragmentation. Thus, the peaks correspond to caprolactone oligomers, but their exact structure is unknown.

The spectrum was initially obtained as a temporal spectrum, which reports the number of ions arriving at each time. The temporal spectrum displays a first peak at 0.033 58 ms, followed by a second one at 0.035 52 ms, a third one at 0.037 39 ms, and so on. The total number of peaks is 97; the last peak is at 0.109 11 ms.

In a first calibration attempt, it was assumed that the peak at 0.033 58 ms corresponds to the oligomer $H[O(CH_2)_5CO]_9OHLi^+$ (i.e., to a poly(caprolactone) nonamer bearing H and OH as end groups and cationized with lithium), making in fact a largely wrong assumption, since the peak actually corresponds to an octamer (see below).

Similarly, it was assumed that the peak at 0.035 52 ms corresponds to the compound $H[O(CH_2)_5CO]_{10}OHLi^+$, that the peak at 0.037 39 ms corresponds to the compound $H[O(CH_2)_5CO]_{11}OHLi^+$, and so on, up to the compound $H[O(CH_2)_5CO]_{105}OHLi^+$. These assumptions were used to calibrate the MALDI-TOF spectrum according to eq 1, as follows: (i) A set of data was built containing the square roots of the mass numbers (μ_n) and the corresponding times of flight. The vector μ_n contained the following mass numbers: 1051.9, 1166.0, 1280.1, ..., 12 005.8. It was assumed that the oligomer mass numbers are equally spaced and they were computed using the formula $\mu_n = n114.1 + 25$; (ii) The above set of data was fitted with a straight line by a linear regression procedure. The calibration contants turned out to be $\alpha = 825\,899$ and $\beta = 1691.7$ with a good coefficient of regression $r^2 = 0.999\,985$.

It is apparent that, even in the case of large errors in the assignment, the conventional calibration procedure may be misleading.

In a series of successive attempts, other more reasonable assignments were made. Each calibration attempt yielded different sets of calibration constants, each with a good regression value, leading to ambiguous mass values for the 97 caprolactone oligomers detected in the MALDI spectrum in Figure 1.

In order to overcome these difficulties, and to obtain the absolute mass values of the oligomers, a novel calibration procedure was adopted, which takes advantage of a unique property of polymers. Considering that the mass of a homopolymer results from the sum of identical units, eq 1 can be rewritten imposing the condition that the total mass of each oligomer results from the sum of the two masses:

$$\mu_n = \sigma_n + \theta \tag{2}$$

where θ is the mass of the first oligomer and σ_n is a multiple of the polymer repeat unit and represents the distance in daltons from the first oligomer. Using the above formula, eq 1 becomes

$$\sigma_n = \alpha(t + 10^{-6}\beta)^2 - \theta \tag{3}$$

This equation is more useful than eq 1. In fact, the set of parameters has been enlarged to include θ. If one fixes the value of θ, one can minimize over α and β and calibrate the spectrum. However, when θ is held constant, eq 3 is of very limited utility. In fact, it reproduces exactly the results obtained with conventional calibration procedures. An alternative consists in letting θ vary. As a matter of fact, the novel calibration procedure consists of considering θ as a variable parameter.

A new set of data for poly(caprolactone) was built, in which the nth time of flight corresponds to the distance $\sigma_n = (n - 1)$ 114.1 Da. In this way, time-of-flight 0.033 58 corresponds to the distance 0 Da, time-of-flight 0.035 52 corresponds to the distance 114.1 Da, time-of-flight 0.037 39 corresponds to the distance 228.2 Da, and so on. The data set was given, along with eq 3, as input to a computer program which performs a least-squares minimization. The iterative process converged quickly toward a sharp minimum. The parameters at the minimum were $\alpha = 843\,745.6$, $\beta = 44.8$, and $\theta = 953.8$ with a coefficient of regression $r^2 = 0.999\,998\,5$.

This allowed us to calculate the absolute mass values associated with the experimental times of flight.

Thus, it was found that the absolute mass of the peak at 0.033 552 is 953.8 Da and corresponds to the ion $H[O(CH_2)_5CO]_8OHNa^+$. This analysis therefore ascertained that the poly(caprolactone) sample consists of a series of oligomers with H and OH as terminal groups, which form sodium-cationized ions in the MALDI process.

Figure 2 shows the MALDI TOF mass spectrum of poly(Bisphenol A carbonate). The spectrum is constituted of three mass series (see inset).[11] The first (S_1) ranges from about m/z 3000 to 13 000, the second (S_2) ranges from m/z 2000 to 20 000, the third (S_3) ranges from m/z 2000 to 8000, (the repeat unit of poly(Bisphenol A carbonate) is 254.2 Da).

The complexity of this MALDI spectrum does not allow unambiguous interpretation of the structure corresponding to the peaks observed, and furthermore, ion fragmentation cannot be a priori excluded.

An inspection of the temporal spectrum associated with the mass spectrun showed that the first peak of the mass series S_2 is at 0.043 74 ms, the second peak is at 0.047 08 ms, and the third one is at 0.050 19 ms. The total number of peaks in the mass series is 74; the last peak is at 0.154 55 ms.

Assuming that the calibration constants found for poly(caprolactone) ($\alpha = 843\,745.6$, $\beta = 44.8$) were also valid for the polycarbonate spectrum, it was found that the peak at 0.043 74 ms corresponds to mass 1617.6, which is meaningless in terms of molecular structure. Therefore, the TOF calibration constants cannot be transferred.[10] This is likely due the geometry of MALDI-TOF instruments, since the time of flight of desorbing species varies with the distance between the point of desorption from the crystal matrix and the accelerating plate. In fact, the point of desorption varies from a probe tip to another and also from spot to spot within the same tip. For the above reasons, a new set of calibration constants, specific for the spectrum in Figure 2, were sought.

A set of data for poly(Bisphenol A carbonate) was built, in which the nth time of flight corresponds to mass number $\sigma_n = (n - 1)$ 254.2. The data set was given, along with eq 3, as input to the least-squares minimization program. The iterative process converged toward the parameters $\alpha = 844\,736.4$, $\beta = 6.8$, and $\theta = 1620.2$ with a coefficient of regression $r^2 = 0.999\,997\,7$. These values were used to compute absolute mass values associated with the experimental times of flight.

Thus, it was found that the absolute mass of the peak at 0.043 70 is 1620.2 Da, which corresponds to the ion $HO[BPA\text{-}OCOO]_6Ph\cdot H^+$ (BPA = Bisphenol A; Ph = phenyl).

This allows us to establish that peaks belonging to mass series S_2 are poly(Bisphenol A carbonate) oligomers having OH and

(10) However, this is not strictly true in the case of MALDI-FT mass spectra. See, for example: Castoro, J. A.; Wilkins, C. L. *Anal. Chem.* **1993**, *65*, 2621.

(11) FAB-MS spectra of the polycarbonate were recorded and there were no peaks present up to 2000 Da. The same was found for poly(caprolactone). Manifacturers do eliminate the low molecular weight tail of the distribution curve in order to obtain useful materials.

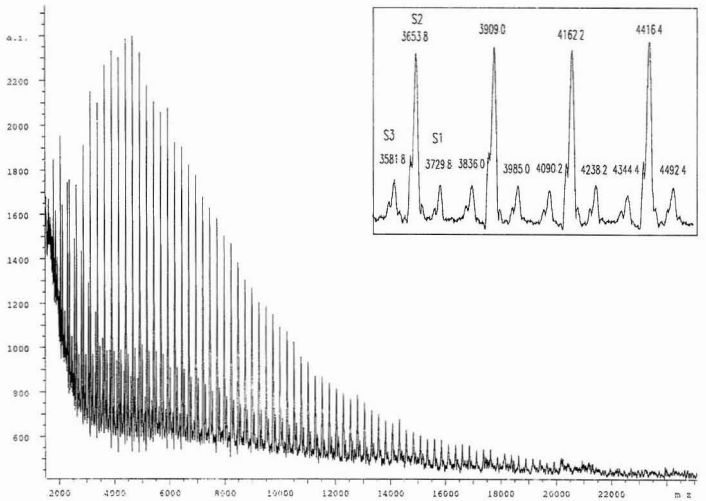


Figure 2. MALDI-TOF mass spectrum of poly(Bisphenol A carbonate).

phenyl terminal groups, which form ions by capturing a proton in the MALDI process. The mass calibration also allowed the determination that peaks belonging to mass series S_1 consist of ions having the general formula $PhO[BPA\text{-}OCOO]_nPh{\cdot}H^+$ and that peaks belonging to mass series S_3 consist of carbonate cyclic oligomers which form sodium-cationized ions in the MALDI process. Since none of the three mass series corresponds to ion fragments, it was concluded that the experimental conditions allowed the desorption of intact polymer molecules.

Summarizing our results, we note that synthetic polymers are not monodispersed as proteins and therefore ambigous peak assignments are the rule in MALDI-TOF spectra, when the conventional calibration procedure is used. One should use our method when the former has led to ambigous results.

Our calibration procedure can be applied, as such, to mixtures of polymers and to copolymers. The procedure can be applied only when the repeat unit of at least one component in the polymeric material analyzed is known.

ACKNOWLEDGMENT

Partial financial support from the Italian Ministry for University and for Scientific and Technological Research (MURST) and from the National Council of Research (CNR, Rome) is gratefully acknowledged.

Received for review April 5, 1994. Accepted August 11, 1994.[⊗]

[⊗] Abstract published in *Advance ACS Abstracts*, September 15, 1994.

Anal. Chem. **1994,** *66,* 4370–4374

Monitoring Formation of a Diamine Process Intermediate by Reversed-Phase Liquid Chromatography

Barbara S. Lord* and Rodger W. Stringham

Process Research Facility, The DuPont Merck Pharmaceutical Company, Chambers Works (S1), Deepwater, New Jersey 08023-0999

A successful separation of solutes in a reaction mixture that includes a hydrophobic solvent and precursor, a relatively hydrophobic intermediate, and a product containing two primary amine groups was performed on several different reversed-phase column packings. The problem was complicated by the presence of two labile triethylsilyl ether protecting groups which dominate hydrophobic retention. Resolution was found to require both ionic and hydrophobic interactions. Ionic interactions appear to be necessary to reorient the amine portion of the molecules toward the chromatographic surface, allowing selectivity. These interactions must be moderated to minimize peak broadening. The strength of ionic interactions was successfully modulated by varying pH and mobile-phase ionic strength for each of the three different chromatographic supports.

I is an unstable intermediate in the synthesis of a new drug entity under development at DuPont Merck Pharmaceutical Co. A schematic representation of this molecule is given in Figure 1 showing two triethylsilyl (TES) protecting groups and two deprotected primary amines attached to a core. **I** is produced from a structurally similar precursor by the reductive removal of two carboxybenzyl (Z) ester protecting groups. It is critical for the next synthetic step that this reaction proceed to completion without loss of the TES protecting groups. Monitoring this reaction requires resolution of **I** (fw ~500) not only from its di-Z-di-TES precursor (fw ~800), but also from the monoamine di-TES intermediate, the deTESylated versions of **I**, and the reaction solvent, toluene.

Initial attempts at monitoring this reaction using silica-based reversed-phase LC columns were unsuccessful due to extremely broad triangular peaks (Figure 2) obtained for both the diamine diester **I** and the mono-Z intermediate. Removal of the Z groups yields primary amines which interact with residual silanols of the stationary phase. Use of a low-pH mobile phase to suppress ionization of the stationary phase was precluded by the acid lability of the TES protecting groups. Inclusion of an ion-pairing agent (octanesulfonic acid) was unsuccessful at ameliorating the problem of broad peaks and limited detector sensitivity by contributing to background absorbance.

This challenging separation is further complicated by the possibility of blind portions of the molecule. Modern drug candidates are often peptide mimetics of sufficient size, rigidity, and complexity that portions of the molecule dominate chromatographic behavior. Regnier[1] described such behavior for proteins where a small portion of the protein's surface determines the specificity and strength of interaction between the protein and the support. The size and location of this contact region vary depending upon the mode of separation employed. Peptide mimetics are small enough that their contact region would comprise a large portion of the molecule. Chromatographic interaction could then be visualized as a preferred binding orientation where one "side" of the molecule is in contact with the stationary phase and the other "side" is exposed only to the mobile phase. Differences in the mobile-phase "side" of the molecule would not be detected without alteration of this binding orientation.

In a reversed-phase separation, **I** and its precursors would be expected to orient themselves to maximize contact between the TES groups and the hydrophobic stationary phase, destroying resolution of similarly protected impurities. Ionized groups would also favor this orientation by preferring exposure to the mobile phase. The broad peak shapes in Figure 2 indicate that the primary amines do interact with the stationary phase. That these amines interact with the stationary phase suggests that **I** will reorient itself to achieve this interaction. The chromatographic contact region induced by ionic interactions would be different from that favored by hydrophobic interactions. If the strength of the ionic interaction could be controlled, it might be possible to induce a larger contact region combining both the ionic and hydrophobic contact regions.

Control of the strength of ionic interactions could also allow chromatography of the primary amine compounds with acceptable peak shape. We hypothesized that mixed-mode chromatography offered the potential to modulate ionic interactions. These supports contain both hydrophobic alkyl ligands and titratable charged ligands. They have been used to enhance selectivity in the resolution of oligonucleotides,[2–4] peptides,[5] and proteins.[6] Mixed-mode supports have also been used to resolve mixtures of dissimilar analytes such as inorganic ions and carboxylic acids[7]

(1) Regnier, F. E. *Science* **1987**, *238*, 319.
(2) Bischoff, R.; McLaughlin, L. W. *J. Chromatogr.* **1983**, *270*, 117.
(3) Crowther, J.; Fazio, S.; Hartwick, R *J. Chromatogr.* **1983**, *282*, 619.
(4) Bischoff, R.: McLaughlin, L. W. *J. Chromatogr.* **1984**, *296*, 329.
(5) Hirata, N.; Kasai, M.; Yanagihara, Y.; Noguchi, K. *J. Chromatogr.* **1988**, *434*, 71.
(6) Kopaciewicz, W.; Rounds, M. A.; Regnier, F. E. *J. Chromatogr.* **1985**, *318*, 157.
(7) Saari-Nordhaus, R.; Anderson, J. *Anal. Chem.* **1992**, *64*, 2283.

0003-2700/94/0366-4370$04.50/0 © 1994 American Chemical Society

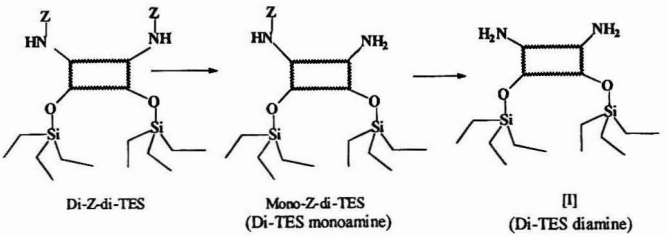


Figure 1.

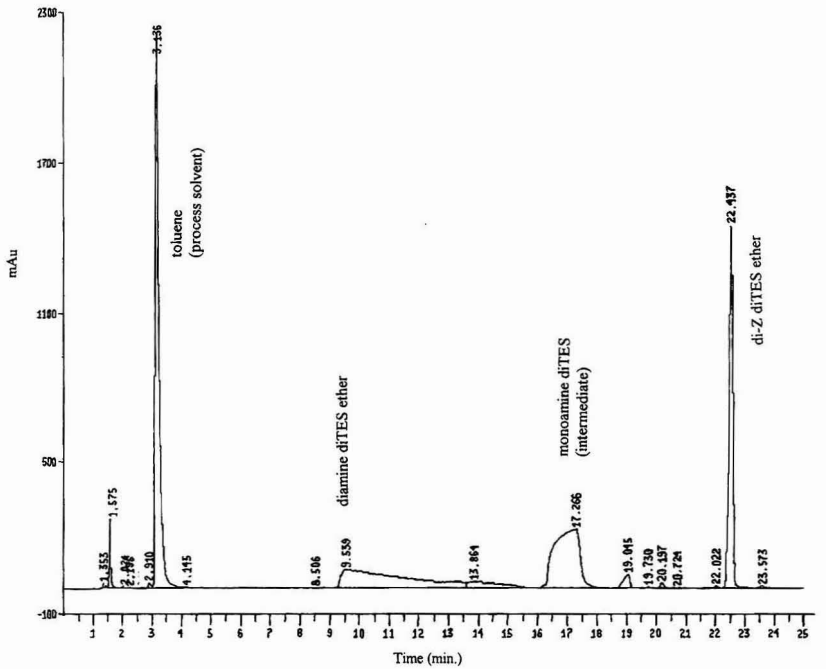


Figure 2. Conditions: column, 250 mm ZORBAX RX C18; mobile phase, 20 min linear gradient, 80–100% methanol versus 10 mM sodium phosphate (pH 3.5).

that would otherwise require two different supports. Ionic interactions in mixed-mode chromatography are modulated by titrating the fixed charges in the support or by altering the ionic strength of the mobile phase. Although this approach worked initially (Figure 3), difficulties with column reproducibility and availability prompted a search for a more rugged chromatographic approach.

The 3M Z-18 column is a relatively new column packing material that allows the use of mobile phase pH's where the amines would not be charged, possibly allowing us to separate all components based solely on hydrophobicity, without the deterioration of peak shapes observed in Figure 2. There are indications[8–11] that use of a phosphate buffer mobile phase would give this column the desired cation exchange character. Although an adequate separation was achieved in this mode, an unexpectedly high ionic strength was needed in the mobile phase to moderate the ionic interaction. Use of this high ionic strength buffer also proved successful in moderating ionic interactions with silica reversed-phase columns.

EXPERIMENTAL SECTION

Instrumentation. The liquid chromatograph used in this work was a Hewlett-Packard HP1090M diode array detector/liquid chromatograph. The temperature of the column oven was

(8) Schafer, W. A.; Carr, P. W.; Funkenbusch, E. F.; Parson, K. A. *J. Chromatogr.* **1991**, *587*, 137.

(9) Schafer, W. A.; Carr, P. W. *J. Chromatogr.* **1991**, *587*, 149.

(10) Rigney, M. P.; Funkenbusch, E. F.; Carr, P. W. *J. Chromatogr.* **1990**, *499*, 291.

(11) Rigney, M. P.; Weber, T. P.; Carr, P. W. *J. Chromatogr.* **1989**, *484*, 273.

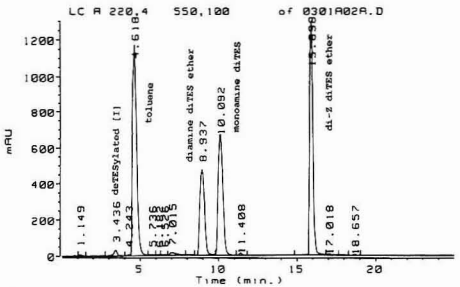


Figure 3. Conditions: column, 150 mm mixed-mode RP18/Cation; mobile phase, 20 min linear gradient, 50–100% methanol versus 10 mM sodium phosphate (pH 3.5).

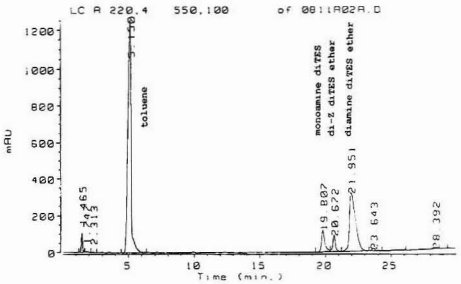


Figure 4. Conditions: column, 150 mm 3M Z-18; mobile phase, 25 min linear gradient, 50–100% methanol versus 25 mM sodium phosphate plus 100 mM ammonium chloride (pH 5.8).

Table 1. Effect of pH on Solute Retention for Mixed-Mode C18 Column

compound	retention time (min) pH 2.1	pH 3.5	pH 5.3
toluene	5.2	4.7	4.6
diamine di-TES **I**	9.3	9.2	10.3[a]
monoamine di-TES	9.3	10.3	12.0
di-Z-di-TES ether	16.4	16.0	15.9

[a] Broad peak.

Table 2. Effect of pH on Solute Retention for 3M Z-18 Column

compound	retention time (min) pH 3.0	pH 5.8	pH 8.0
toluene	5.2	5.2	5.4
monoamine di-TES	19.7	19.8	19.8
di-Z-di-TES	20.6	20.7	20.3
diamine di-TES **I**	25.2[a]	22.0	20.3

[a] Broad, triangular peak.

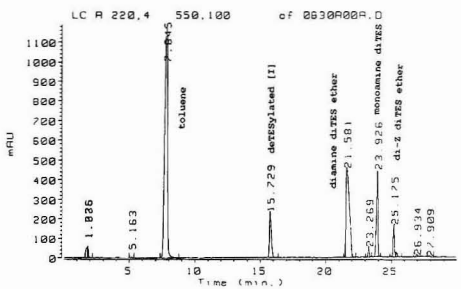


Figure 5. Conditions: column, 150 mm ZORBAX RX C8; mobile phase, 25 min linear gradient, 50% to 100% methanol versus 25 mM sodium phosphate plus 100 mM ammonium chloride (pH 5.8).

maintained at 40 °C. All data were recorded on a Hewlett-Packard HP79994A data station using Pascal Revision 3.25 software.

Columns. (1) Alltech (Deerfield, IL) Mixed-Mode RP18/Cation column (150 mm × 4.6 mm, 5 μm). The column is packed with a multifunctional support that consists of a 100 Å, 5 μm spherical silica substrate which is bonded with a single ligand containing both reversed-phase (C18) and cation (carboxylate) functionalities in a fixed 1:1 ratio. The material is not end capped. (2) Cohesive Technologies Inc. (Acton, MA) 3M Z-18 column (150 mm × 4.6 mm, 6 μm). The support material is zirconia (ZrO_2) microspheres coated with polybutadiene. The Z-18 packing is chemically stable in solvents ranging from pH 1 to pH 14. (3) DuPont (Wilmington, DE) ZORBAX RX C8 column (150 mm × 4.6 mm, 5 μm) and ZORBAX RX C18 column (250 mm × 4.6 mm, 5 μm).

Reagents. Eluants were prepared from HPLC grade methanol and ACS reagent grade sodium dihydrogen phosphate, disodium hydrogen phosphate, and ammonium chloride from J. T. Baker and Co. and HPLC grade water. The pH of the eluant was adjusted with phosphoric acid or aqueous sodium hydroxide solution as needed.

RESULTS AND DISCUSSION

Alltech Mixed-Mode RP-18/Cation Column. An aqueous 10 mM sodium phosphate buffer at pH 3.5 was used with a linear 20 min 50–100% methanol gradient to produce the separation shown in Figure 3. Eluant pH affects the degree of ionization of the stationary-phase carboxylate groups and of the ionizable groups in the solute. With decreasing pH, the stationary phase should become less ionic while the di-TES diamine **I** and the monoamine intermediate become more ionic. Three different pH's were tested, and results are presented in Table 1. Between pH 3.5 and 2.1, retention of toluene increased, reflecting the loss of support ionization and concomitant increase in hydrophobicity. At pH 3.5, the mono- and diamine di-TES ethers were resolved, while at pH 2.1, they were not. Resolution of this pair at pH 3.5 by increased retention of the monoamine indicates that the Z group is interacting with the stationary phase. At pH 2.1, the Z group must be exposed only to the mobile phase. This is unexpected in view of the increased hydrophobicity of the stationary phase. Ionic interactions could induce this orientation by turning the amine into the stationary phase and the Z group outward, but ionic interactions should be minimal at pH 2.1. Possibly the increased strength of hydrophobic interaction restricts the orientation of both molecules such that both TES groups are firmly turned into the stationary phase leaving the Z and amine groups exposed to the mobile phase. At pH 5.3, the di-TES diamine peak was overly broad, reflecting excess ionic

Table 3. Effect of pH and Ionic Strength for ZORBAX RX C8

compound	retention time (min)					
	pH 3.0 100 mM NH_4Cl	pH 5.8 100 mM NH_4Cl	pH 5.8 100 mM NaCl	pH 5.8 50 mM NH_4Cl	pH 5.8 25 mM NH_4Cl	pH 5.8 0 mM NH_4Cl
toluene	7.8	7.9	7.9	7.8	7.8	7.8
deTESylated diamine	14.5	15.7	16.0	15.6	17.9	17.6
diamine di-TES **I**	21.2	21.6	22.2	21.6	22.1[a]	25.8[b]
monoamine di-TES	21.6	23.9	24.4	24.0	24.3	24.6
di-Z-di-TES ether	25.3	25.2	25.2	25.3	25.3	25.3

[a] Peak somewhat broadened and slightly split. [b] Broad, triangular peak.

interaction. A pH of 3.5 was selected and used with fair success for monitoring this reaction.

Unfortunately this separation could not be reproduced with several columns that were purchased later. Since a problem with column-to-column reproducibility was evident, other approaches to the analysis were investigated.

3M Z-18 Columns. This column is reputed to be an inert reversed-phase packing that produces symmetrical peaks for basic compounds. Previous work indicated that surface hydroxyl groups present on zirconia microspheres adsorb phosphate. The packing then exhibits cation exchange properties.[8-11] Therefore, if a phosphate buffer is used with these columns, beneficial ionic interactions may be observed for the amines in the reaction mixture. These ionic interactions proved difficult to control. The diamine **I** was retained longer (Figure 4) than its more hydrophobic precursors, indicating the dominance of these interactions. Modulation of ionic interactions required addition of at least 80 mM ammonium chloride to the mobile phase. Below this level, the diamine peak broadened or did not elute.

Effect of pH. One of the advantages of using zirconia supports is the ability to use alkaline pH's where amines would not be expected to be charged. Mobile phases containing 100 mM ammonium chloride in 25 mM sodium phosphate buffers at three different pH's were tested, using a linear 25 min 50–100% methanol gradient. Results are shown in Table 2. The impact of ionic interactions is shown by the longer retention of **I** relative to its more hydrophobic precursors. At pH 3.0, these interactions led to excessively broad peaks for **I** even in the presence of 100 mM ammonium chloride. As pH increased this interaction moderated, resulting in acceptable chromatography at pH 5.8 but loss of resolution between **I** and the di-Z-di-TES precursor at pH 8.0. This suggests that, in the absence of ionic interactions, only the TESylated portion of these molecules interacts with the hydrophobic stationary phase.

Column-to-Column Reproducibility. The second 3M Z-18 column on which these solutes were chromatographed produced a separation similar to Figure 4 after conditioning with 25 mM phosphate plus 100 mM ammonium chloride at pH 3.5. The mechanism by which this low-pH buffer conditions the Z-18 columns is unclear. It possibly facilitates the process of binding phosphate groups to the zirconia hydroxyl groups. Retention of the di-TES diamine increased after this treatment.

Acceptable chromatography with this column was obtained at pH 5.8. A loss of resolution between toluene and de-TESylated **I** was observed for both columns at all pH values tested. This shortcoming led to the examination of another potential solution.

Zorbax RX C8 and C18 Columns. The ability of ammonium chloride to moderate ionic interactions between the amines and the 3M Z-18 column led to testing the same approach on silica-based reversed-phase columns. A 15 cm ZORBAX RX C8 column was used with the linear 25 min 50–100% methanol gradient versus 25 mM phosphate plus 100 mM ammonium chloride buffer at pH 5.8. Under these conditions, reasonable peak shapes and good resolution of all components were observed (Figure 5). A pH of 3.0 was also tested as was the effect of substituting sodium chloride for ammonium chloride. Decreasing levels of ammonium chloride were examined. Data are presented in Table 3.

The unchanging retention of toluene shows that the mobile phase does not alter stationary-phase hydrophobicity. Under the selected condition of 25 mM phosphate plus 100 mM ammonium chloride buffer at pH 5.8, solutes elute in order of hydrophobicity as well-resolved, well-shaped peaks. At pH 3.0, the di-TES diamine and the di-TES monoamine are barely resolved, suggesting that the Z protecting group is turned out to the mobile phase. At this pH there should be some residual silanol charge and a strong amine charge. The resulting ionic interaction is apparently strong enough to favor the undesired orientation (amine into the stationary phase, Z group out) but not strong enough to distort peak shapes.

No significant change was observed when sodium chloride was substituted for ammonium chloride. Buffer containing 50 mM ammonium chloride was also sufficient to produce the same separation. However, when only 25 mM ammonium chloride was added to the buffer, the di-TES diamine peak broadened noticeably and was slightly split. In the absence of added ammonium chloride, the Di-TES diamine peak shape deteriorated to a very broad, triangular peak.

CONCLUSION

The successful separation of a reaction mixture containing a hydrophobic solvent and precursor, a relatively hydrophobic intermediate, and a product containing two primary amine groups was demonstrated on several different reversed-phase column packings. The key to this reversed-phase separation proved to be the ability to moderate ionic interaction via selection of mobile-phase and stationary-phase conditions. Incorporation of moderate levels of ammonium chloride into a simple mobile phase allowed generation of acceptable peak shapes for amine-containing intermediates on a simple reversed-phase HPLC column.

Elimination of all ionic interactions destroyed the required resolution as did overly strong ionic interactions. The requirement for moderated ionic interaction can be interpreted in terms of the

need to disturb preferred binding orientations, corroborating the premise that peptide mimetics exhibit chromatographic contact regions as described by Regnier (1) for proteins. Strong ionic interaction appeared to induce its own preferred binding orientation that disallowed resolution of a process intermediate. The implication of this goes beyond the prediction of chromatographic approaches to monitoring synthetic processes. Evaluation of peptide mimetic pharmaceuticals under a single set of chromatographic conditions may lead to a failure to detect significant impurities.

Received for review April 25, 1994. Accepted September 2, 1994.[⊗]

[⊗] Abstract published in *Advance ACS Abstracts*, October 1, 1994.

Anal. Chem. **1994,** *66,* 4375–4381

Evaluation of an Automated Thermospray Interface for Coupling Electrothermal Atomization Atomic Absorption Spectrometry and Liquid Chromatography

C. Bendicho*

Universidad de Vigo, Campus de Ourense, Departamento de Química Analítica y Alimentaria, As Lagoas s/n, 32004 Ourense, Spain

An automated thermospray interface is used to couple an electrothermal atomizer and a liquid chromatograph for speciation studies. The thermospray interface allows the periodical deposition in real time of the eluent from the chromatographic column into a graphite tube equipped with a curve-shaped platform. The time required between consecutive measurements is drastically reduced since the chromatographic eluent is dried on impact onto the preheated platform at 150 °C. A total thermal program time of 40 s is feasible (15 s for the furnace cycle plus 25 s for cooling down). This thermal program time is shorter when compared to that used for conventional sample introduction in a graphite atomizer (e.g., 85 s). Relative standard deviation values of about 6% are reached for an arsenate solution when integrated absorbance measurements are used. The applicability of the interface is shown for speciation of arsenate, arsenite, and dimethylarsinate using reverse-phase isochratic separations.

The coupling of different separation techniques with atomic spectrometric detectors constitutes the most suitable approach to carrying out speciation studies.

Among separation techniques, high-pressure liquid chromatography (HPLC) has emerged as a powerful tool for speciation, since it allows the handling of both volatile and nonvolatile compounds and therefore shows a wider applicability as compared to other chromatography techniques. HPLC can be easily connected to continuous atomization systems such as flames and plasmas, since the eluent flow rate closely approaches the uptake rate of the conventional nebulizers used for sample introduction. However, these couplings share the same drawbacks that are inherent to conventional sample introduction systems in atomic spectroscopy (i.e., low nebulization efficiency) for sample introduction.[1] Additionally, undesirable effects such as dispersion and peak distortion frequently occur, which degrades further the detection limit.[2,3] Since the actual concentration range for speciation falls in the parts per billion to sub-parts per billion region, most couplings between HPLC and atomic spectroscopy techniques do not provide the appropriate detection capability.

Improvement in the performance of these couplings can be achieved by using postcolumn hydride generation for species forming volatile hydrides[4] or thermospray introduction.[3,5]

Graphite furnace atomic absorption spectrometry (GF-AAS) fulfills the detection capability requirements, but the discontinuous nature of a conventional electrothermal atomizer makes it troublesome when used in combination with continuous flow systems. These atomizers are designed to accept low sample volumes, which have to be dried, pyrolyzed, and atomized before the measurement can be obtained. This clearly departs from the concept of monitoring continuously the chromatographic eluent.

Several attempts have been made with the interface between a graphite atomizer and a liquid chromatograph, many of them using indirect couplings. Early couplings were based on a collection of the chromatographic effluent at a fixed time in autosampler cups[6] or using flow-through cells.[6,7] The indirect couplings (e.g., collection in autosampler cups) do not provide real-time chromatograms, only a small fraction of the total effluent emerging from the column is sampled, and, more importantly, optimization of the chromatographic process is troublesome to perform. On-line couplings require the atomizer to be maintained at atomization temperatures for the time necessary to monitor the whole chromatogram. Such an approach represents a direct coupling, but dilution of the analyte in the vapor phase takes place, and therefore, the residence time in the absorption volume of the furnace is small. In addition, specially designed atomizers have to be used to avoid overheating the furnace housing.[8] A few couplings of HPLC and electrothermal atomizers have been carried out using sophisticated injectors controlled by a microprocessor.[9,10] These interfaces can be considered as direct couplings in which only a fraction of the chromatographic effluent is monitored (i.e., pulsed mode operation). Therefore, the resolution of the chromatographic peak depends on the time interval between consecutive measurements.

(1) Ebdon, L.; Hill, S.; Ward, R. W. *Analyst* **1987**, *112*, 1.
(2) Katz, E. D.; Scott, R. P. W. Analyst **1985**, *110*, 253.
(3) Laborda, F.; de Loos-Vollebregt, M. T. C.; de Galan, L. *Spectrochim. Acta* **1991**, *46B*, 1089.
(4) Ebdon, L.; Hill, S.; Walton, A. P.; Ward, R. W. *Analyst* **1988**, *113*, 1159.
(5) Roychowdhury, S. B.; Koropchak, J. A. *Anal. Chem.* **1990**, *62*, 484.
(6) Brinckman, F. E.; Blair, W. R.; Jewett, K. L; Iverson, W. P. *J. Chromatogr.* **1977**, *15*, 493.
(7) Brinckman, F. E.; Jewett, K. L.; Iverson, W. P.; Irgolic, K. J.; Ehrhardt, K.C.; Stockton, R. A. *J. Chromatogr.* **1980**, *191*, 31.
(8) Nygren, O.; Nilsson, C.-A.; Frech, W. *Anal. Chem.* **1988**, *60*, 2204.
(9) Stockton, R. A.; Irgolic, K. J. Int. *J. Environ. Anal. Chem.* **1979**, *6*, 313.
(10) Haswell, S. J.; Stockton, R. A.; Bancroft, K. C. C.; O'Neill, P. O.; Rahman, A.; Irgolic, K. J. *J. Autom. Chem.* **1987**, *9*, 6.

0003-2700/94/0366-4375$04.50/0 © 1994 American Chemical Society

Though thermospray interfaces were originally designed for sample introduction into a mass spectrometer,[11] recently they have been widely used as a sample introduction system for flame and plasma atomizers.[12,13] Thermospray vaporization has been successfully used for sample introduction into a commercial electrothermal atomizer.[14,15] When the aerosol formed upon heating makes an impact on the wall of a graphite tube, a considerable savings in time is achieved, which results in shorter furnace thermal programs.

In this work, the use of an automated thermospray interface for the coupling of a commercial atomizer and an HPLC system is described. The interface is evaluated for speciation of three As species using ion-pairing chromatography.

EXPERIMENTAL SECTION

Reagents. All chemicals were of analytical grade. Water was obtained from a Milli-Q water purifier. Stock solutions (1000 μg mL^{-1}) of As were prepared in deionized water from sodium arsenate, sodium arsenite (Merck), and dimethylarsinic acid (Fluka). For the reverse-phase separations, a mixture of 95% water and 5% methanol buffered with ammonium citrate (2 mM, pH = 6.8) was used as a mobile phase. The ion-pairing reagent was tetrabutylammonium bromide (5 mM). Nickel nitrate (5000 μg mL^{-1}) and palladium nitrate (1000 μg mL^{-1}) were used as matrix modifiers when required. Mobile-phase solutions as well as arsenium standards were filtered through a 0.45-μm filter prior to use.

Instrumentation. (a) HPLC System. A Model 510 solvent delivery pump (Waters) was used in combination with an eight-port injection valve (Dionex) and a reverse-phase chromatography column (Waters). The chromatographic column consisted of a Delta Pak C18–100 Å, with dimensions of 3.9 mm diameter and 150 mm length. The stationary phase is formed by spherical particles of 5 μm diameter. The high-pressure pump was modified by using plastic material in several components in order to avoid potential sources of contamination. To load the sample into the injection valve 200 μL volume loops were used.

(b) Thermospray Interface. The thermospray interface used in this work has been previously evaluated for sample introduction into a graphite furnace[14,15] as well as for inductively coupled plasma atomic emission spectrometry.[3,13] It consists of a fused silica capillary (0.1 mm i.d., 0.2 mm o.d.) inserted into a stainless steel tube (0.5 mm i.d., 1.6 mm o.d.). The steel tube is electrically heated with a current of about 20 mA, which is regulated by a phase angle temperature controller. The temperature is controlled at the entrance of the vaporizer by a Cr–Al thermocouple attached to the input end. Another thermocouple attached near the exit of the vaporizer permits temperature measurements to be taken at this point, thereby preventing the capillary from overheating. A steel cover surrounds the outlet end of the stainless steel capillary so that the vapor cannot enter the space that exists between the two capillary tubes and cause fluctuations in the tip temperature. Two electrical connectors are welded to the stainless steel tube for power supply. The vaporizer is enclosed in a metallic probe for electrical isolation and mounted onto a holder that can move backward and forward into the furnace housing by way of a pneumatic actuator. When no sample is to be introduced into the furnace, the outlet end of the vaporizer is kept in a vacuum chamber made of plastic and located in front of the furnace housing. This chamber is necessary to prevent liquid and vapor from entering the furnace.

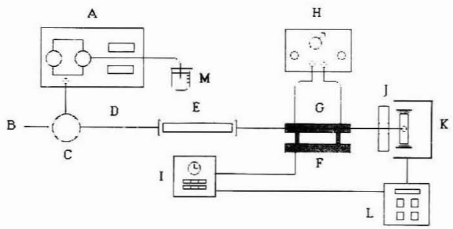


Figure 1. Coupling of GF-AAS and HPLC. (A) HPLC pump. (B) Sample. (C) Injection valve, 200 μL loop. (D) Silica capillary, 100 μm internal diameter. (E) HPLC column. (F) Thermospray holder. (G) Thermospray vaporizer. (H) Temperature controller. (I) Sequence controller. (J) Vacuum chamber. (K) Electrothermal atomizer. (L) Graphite furnace programmer. (M) Buffer.

The operation of the thermospray interface is controlled by a sequence controller (Omron, Scy-PO). Every individual action can be programmed independently using one of the 12 channels available. The sample is loaded onto the sample loop in the injection valve and metered in the chromatographic column. The action is performed by two pneumatic valves. The first pneumatic actuator moves the probe containing the vaporizer forward or backward into the furnace housing, depending on the action required (i.e., whether the chromatographic eluent is going to be introduced into the graphite furnace or not). A second pneumatic actuator moves a plastic shield located at the back of the vacuum chamber upward or downward, so that the outlet end of the vaporizer can be introduced into the furnace. The effluent that comes out the column is then introduced through the thermospray vaporizer and injected for a period of 2 s (timer accuracy is about ±10 ms) in the graphite tube. The start of the thermal program is initialized by the sequence controller. The program switches off when the furnace cycle is completed. A repetitive sequence is programmed onto the sequence controller that permits sampling of the chromatographic effluent, actioning of the different pneumatic actuators, and a delay time for the furnace to cool down as many times as required to collect the chromatographic peaks. The direction of flow in the injection valve is changed once the chromatogram is developed to permit the loading of a new sample if required. The system configuration is shown in Figure 1.

(c) Graphite Furnace Atomizer. A Perkin-Elmer absorption spectrophotometer, Model 1100, is fitted with an HGA-500 graphite furnace. For the coupling to HPLC, the atomizer was slightly modified. First, the dosing hole located in the contact cylinders is enlarged so that sample introduction can be performed parallel to the furnace plate. When a thermospray is introduced into the furnace a common problem arises, i.e., the vapor formed upon heating the liquid can condense on the optical windows located on the side of the furnace house, hence causing irreproducible absorbance measurements and high background. To avoid this

(11) Blakley, C. R.; McAdams, M. J.; Vestal, M. L. *J. Chromatogr.* **1978**, *12*, 574.
(12) Choi, D. S.; Robinson, J. W. *Spectrosc. Lett.* **1989**, *22*, 69.
(13) Peng, R.; Tiggelman, J. J.; de Loos-Vollebregt, M. T. C. *Spectrochim. Acta* **1990**, *45B*, 189.
(14) Bank, P. C.; de Loos-Vollebregt, M. T. C.; de Galan, L. *Spectrochim. Acta* **1988**, *43B*, 983.
(15) Bank, P. C.; de Loos-Vollebregt, M. T. C.; de Galan, L. *Spectrochim. Acta* **1989**, *44B*, 571.

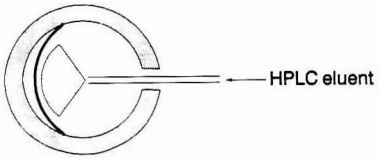


Figure 2. Curve-shaped platform used for sample deposition in the coupling of HPLC–ETA-AAS.

Table 1. Influence of the Distance between the Platform Surface and the Capillary Tip

instance from platform (mm)	peak area (A·s)
0.5	0.491
1.5	0.520
2.5	0.586
3.5	0.508
4.5	0.514
5.5	0.508

problem, the furnace housing is kept at 80 °C by recirculating water heated in a bath. Second, in contrast to the original design by Bank et al.,[15] no vacuum system is used inside the furnace to prevent vapor condensation on the optical windows. This vacuum is thought to cause fast removal of excess vapor produced during sample introduction, and, in turn, analyte losses can occur in the vacuum line when no instantaneous drying of the droplets takes place. Therefore, the internal gas (argon) is preheated before entering the furnace so that vapor can be efficiently removed. Curve-shaped platforms, specially designed for thermospray deposition (Figure 2), were used instead of the conventional rectangular-shaped platforms. In this case, the platform remains in front of the dosing hole.

Optimization of the Thermospray Interface. The performance of the interface was evaluated using a 0.1 μg mL^{-1} As(V) solution. For preliminary optimization experiments, the interface was operated in continuous mode, i.e., neither injection valve nor chromatographic column was used, and the sample was delivered directly by the HPLC pump to the thermospray vaporizer. Typically, liquid flow rates in the range of 0.2–0.6 mL min^{-1} were used.

RESULTS AND DISCUSSION

Influence of the Capillary Tip Temperature. The thermospray vaporizer temperature is adjusted so that a stable spray is formed at the outlet end. A critical aspect in the operation of the thermospray vaporizer is the formation of droplets at the silica capillary tip which impairs precision of the sample introduction. This phenomenon was observed when using low vaporizer temperatures and silica capillary tubes with an internal diameter larger than 0.2 mm. Figure 3 shows the integrated absorbance for 2 ng of As(V). At a temperature below 150 °C, the sample deposition is incomplete. At a temperature above 200 °C, a decrease in the integrated absorbance is observed, which can be attributed to analyte losses. This behavior is also displayed by As(III) and DMA, and it is believed to be caused by decreased nebulization efficiency.

Influence of the Platform Temperature. The influence of the platform temperature for sample deposition is presented in Figure 4. For As(V), a steady integrated absorbance is observed between 100 and 350 °C. Integrated absorbance drops from a temperature above 350 °C as a result of uncontrollable boiling processes occurring on the surface of the platform. The Ni matrix modifier mixed with the As solution was used to determine whether the absorbance decrease was due to the volatilization of As or to the loss of sample droplets when they impact on the hot graphite surface. As can be seen, integrated absorbance decreases at a temperature of about 450 °C, which means that Ni does not modify to a large extent As stabilization during the deposition process. For As(III) and DMA, losses start at temperatures significantly lower than for As(V). Integrated absorbance drops at 200 °C for As(III) and 180 °C for DMA. It can be concluded that the effective deposition of the three As species requires deposition temperatures below 180 °C.

Influence of the Capillary Tip Distance from the Platform. Whereas thermospray deposition on the wall of a graphite tube is almost independent of the capillary distance from the wall, deposition on the platform needs to be optimized. Table 1 shows the influence of the distance between the platform surface and the capillary tip. No critical influence is seen in the region from 0.5 to 5.5 mm when the 100 μm diameter capillary and an introduction time of 2 s are used. When an introduction time longer than 2 s was used at a pump flow rate of 0.6 mL min^{-1}, a decreasing integrated absorbance is observed with increasing

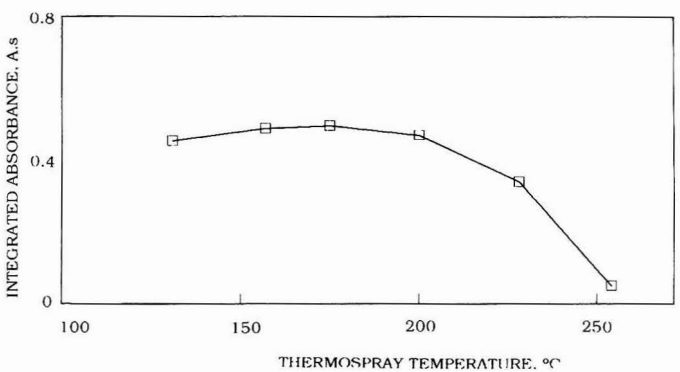


Figure 3. Influence of the capillary tip temperature on the integrated absorbance for an As(V) solution.

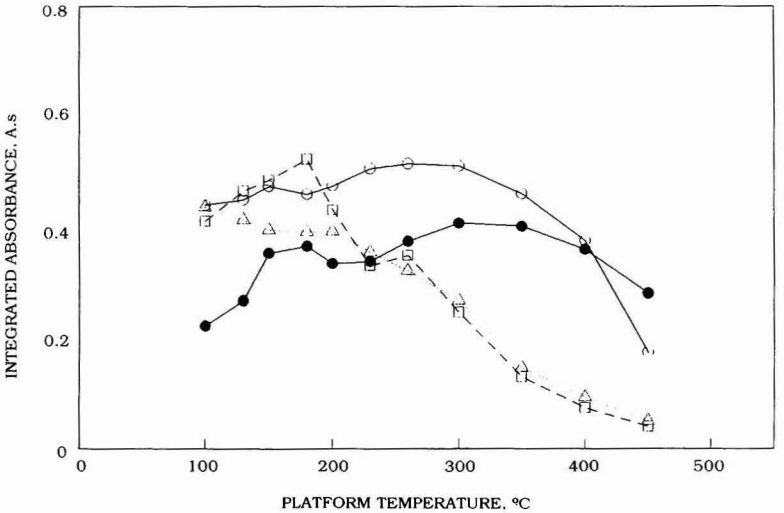


Figure 4. Influence of the deposition temperature on As(V) (○, without matrix modifier; ●, with nickel nitrate as matrix modifier), As(III) (△, without matrix modifier), and DMA (□, without matrix modifier).

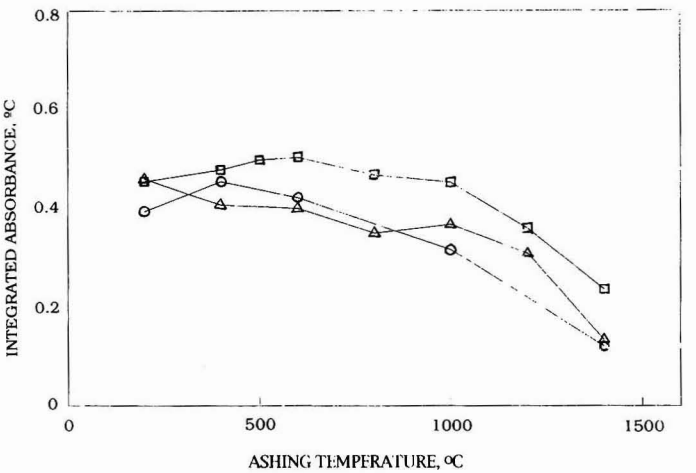


Figure 5. Influence of the ashing step on As(V) (□), As(III) (○) and DMA (△).

deposition distance from the platform. The partial deposition of the sample on the wall, which occurs in these conditions, was confirmed by the presence of two peaks in the atomic absorption signals.

Influence of the Ashing Step. The need for an ashing step has to be considered to establish whether this step should be retained or, if it can be omitted. The removal of the ashing step can provide two advantages when electrothermal atomizers are coupled to a liquid chromatograph. First, the possibility of analyte loss is reduced. This is critical when volatile species are involved (e.g., As species). Second, the total time for the thermal program is shortened, and, therefore, a larger number of individual samples can be monitored along the chromatographic separation. Figure 5 shows the ashing curves for 1.2 ng of As(V), 1.1 ng of As(III), and 1.1 ng of DMA. In all cases, a deposition temperature of 150 °C was used. The hold time for the ashing step was 10 s. As can be seen, As(V) displayed the lowest volatility. Integrated absorbance decreases at a temperature of 600 °C for DMA, which is the most volatile species. The influence of the Ni matrix modifier was studied for As(V). This matrix modifier increases considerably the thermal stability of As(V) up to temperatures of about 1300 °C. No differences in integrated absorbance are observed for As(V) when a matrix modifier is used in comparison to those obtained without the use of a matrix modifier, provided that the ashing temperature is maintained below 900 °C. It appears that in all cases the ashing step can be omitted without

the deterioration of sensitivity. The integrated absorbance values are virtually the same for the three As species when an atomization temperature of 2500 °C is used.

Thermal Program. In contrast to the on-line interface between an electrothermal atomizer and a liquid chromatograph, a direct coupling operated in the pulsed mode allows the use of small sample volumes and gas stop for atomization. However, the number of individual measurements carried out while the chromatograph is running should be as high as possible to describe the actual peak concentration profile. Therefore, the thermal program should be kept to a minimum, to increase the total number of measurements. Bearing in mind this prerequisite, the time required for each step of the thermal program was optimized accordingly.

A time of 6 s for drying (1 s ramp, 5 s hold time) was seen to be sufficient for achieving an effective deposition of the sample at 150 °C. This time is much shorter than that used for conventional sample introduction at room temperature, since the sample is dried on impact on the preheated platform. When the ashing step was skipped, background was detected at the beginning of the atomization step, which indicated that water vapor remained partially in the absorption volume of the graphite tube. Therefore, a short step at a temperature of 300 °C was included between the deposition and the atomization step (1 s ramp, 5 s hold time) to remove the water vapor. The sample was then atomized at 2500 °C for 3 s. No clean-out step was seen to be required. According to this thermal program, a total time of 15 s is obtained. When the furnace is operated at these conditions, a repeatability expressed as a relative standard deviation of 6.3% was reached by measuring the integrated absorbance. Further shortening of the time between consecutive measurements was mainly limited by the time required for the cooling-down of the platform. Temperature measurements of the platform were made in the range of 2500 °C and 80 °C using an optical pyrometer and a Cr–Al thermocouple. The experimental decay curve of temperature versus time indicated that at least 25 s was required for the platform to reach 150 °C. It should be noted that faster cooling-down of the wall takes place. In addition, external cooling by blowing gas permits a fast cooling of the graphite tube,[10] although it is less successful when the platform is to be cooled as a result of the bad thermal contact with the wall. For a sample introduction time of 2 s and a total thermal program of 40 s, 5% of the total chromatographic eluent is sampled. Further shortening of the thermal program can be achieved when the sample is deposited at higher temperatures. As(V) can be deposited at 300 °C without losses, which permits the use of a cooling-down time of 20 s. However, the more volatile As species are lost at this temperature, unless a matrix modifier is used. Another possibility to increase the total amount of chromatographic eluent that is actually sampled is to use longer introduction times. For the above mentioned introduction time, the fraction of eluent sampled is 20 μL when the HPLC pump is operated at 0.6 mL min^{-1}.

Figure 6 shows the saving in time achieved with the use of thermospray deposition and omitting both preheating of the platform and the ashing step. A conventional thermal program for As (Figure 6a) including dry step (31 s), ashing step (21 s), atomization step (3 s), and clean-out (4 s) and a 25 s cooling-down (e.g., when using platform atomization) requires about 85 s. This total time is shortened to about 70 s when thermospray deposition is used and the system is operated in flow injection

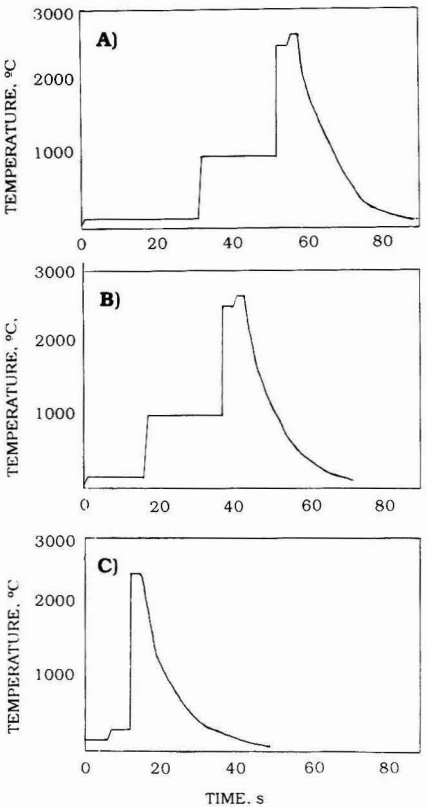


Figure 6. Thermal program for (A) conventional sample introduction, (B) thermospray deposition and flow injection introduction, and (C) thermospray deposition in the coupling of HPLC and ETA-AAS.

mode (Figure 6b). In spite of the time saved for drying, the introduction of the sample from the sample loop requires an additional time, so that all the sample is quantitatively transferred into the graphite tube.[14,15] A fraction of this time is spent in preheating the platform to the selected deposition temperature. The omission of the pyrolysis step and the use of cooling only until the platform is at the deposition temperature (e.g., 150 °C) provide further saving of time, and a total time of about 40 s is feasible (Figure 6c).

Characteristic Masses for As(V), As(III), and DMA. The characteristic masses (m_0, pg/0.0044 A·s) for As(V), As(III), and DMA using thermospray deposition as well as manual deposition at room temperature have been determined. The results are presented in Table 2. When the sample is manually introduced and dried, similar m_0 values are observed for As(V) and DMA, but significantly higher m_0 values are observed for As(III) when no matrix modifier is used. When Pd is used as a matrix modifier, the m_0 values are similar for As(V) and DMA, which are in turn very similar to those obtained without the matrix modifier. The m_0 for As(III) is improved when this species is atomized in the presence of Pd and it approaches those observed for the other

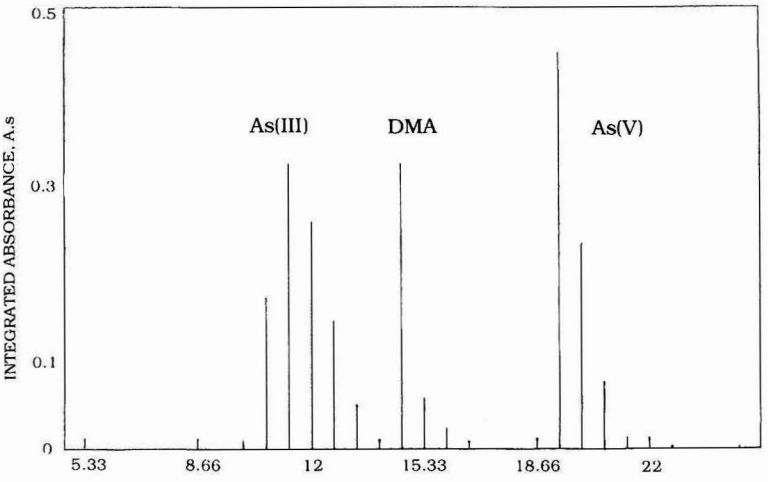


Figure 7. Chromatogram obtained for As(V) (0.25 μg), As(III) (0.18 μg), and DMA (0.27 μg) using ion-pairing chromatography. The sample containing the three As species was loaded into a 200 mL loop. The thermal program shown in Table 3 is used. The deposition time is 2 s, and the pump flow rate is 0.2 mL min^{-1}.

Table 2. Characteristic Masses (m_0 pg/0.0044 A·s) for Different As Compounds Using Both Manual Introduction and Thermospray Deposition

As species	no modifier	Pd modifier[a]	thermospray[b]	literature
As(V)	14	13	18	17 (ref 16)
As(III)	24	16	22	
DMA	15	14	18	

[a] For the Pd modifier experiment, 20 μL of 1000 μg mL^{-1} Pd solution were introduced by micropipet, dried, and pyrolyzed at 1000 °C for 20 s. [b] A 2-s deposition time at a pump flow rate of 0.6 mL min^{-1} was used. Neither matrix modifier nor pyrolysis step was used. The deposition temperature was kept at 150 °C.

Table 3. Thermal Program Used for the Coupling of Electrothermal Atomization AAS and Liquid Chromatography

	step[a]		
	1	2	3
t (°C)	150	300	2500
ramp (s)	1	1	0
hold time (s)	5	5	3
flow rate (mL/min)	300	300	0
read			*b*

[a] Step 2 was used for faster removal of water vapor before atomization. [b] Reading in the spectrophotometer was activated at this step.

As species. For thermospray deposition, neither matrix modifier nor the pyrolysis step was used. As can be seen, the m_0 values for the three As species are very similar, and, moreover, they are in close agreement to the value of 17 pg reported in the literature for As.[16] In view of these results, the validity of the approach used for atomization of As species separated by liquid chromatography is acceptable, considering the nonsignificant differences of sensitivity obtained compared to the conventional procedure.

Speciation of As(V), As(III), and DMA. The separation of the three As species considered in this work was carried out using an ion-pairing chromatographic column. The thermal program is shown in Table 3. The HPLC pump was operated at a flow rate of 0.2 mL min^{-1}, so that the dispersion of the system was increased. This condition was seen to be necessary to collect an appropriate number of fractions during the chromatographic running and thus avoid missing the chromatographic peak. Whereas good separations are reported for As on ion-exchange columns with phosphate buffers, the addition of phosphates is seen to cause spectral interference on As.[17] Ammonium carbonate buffers have been recommended since they require minimum thermal pretreatment and do not cause interference.[18] For reverse-phase separations, sodium heptanesulfonate,[9] tetraheptylammoium nitrate, and tetrabutylammonium phosphate[7] have seen used as ion-pair reagents. The use of these reagents usually required Zeeman background correction.[9] Tetrabutylammonium bromide (5 mM) was used in this work as an ion-pair reagent, since no background interference is caused at the concentration used. For a mobile phase formed by 95% water and 5% methanol, good separation was observed for As(V) and As(III), but poor resolution was observed for As(III) and DMA. The addition of a citrate buffer at low concentration (2 mM) was found to be helpful to resolve the two peaks. A chromatogram run in these conditions required less than 25 min to resolve the three As species (Figure 7). The quantification of each As compound was carried out by summation of all individual peak areas obtained during elution of the correspondent chromatographic peak, according to the ap-

(16) Slavin, W. *Graphite Furnace AAS. A source book*; The Perkin Elmer Corp.: 1984.

(17) Letourneau, V. A.; Joshi, B. M.; Butler, L. C. *At. Spectrosc.* **1987**, *5*, 145.
(18) Woolson, E. A.; Aharonson, N. *J. Assoc. Off. Anal. Chem.* **1980**, *63*, 523.

proach established by Woolson and Aharonson.[18] Only integrated absorbance values higher than 3-fold the standard deviation of the blank were considered in these calculations. The chromatographic detection limits, defined as 3-fold the standard deviation of the blank, were 5, 8, and 15 ng/mL for As(III), As(V), and DMA, respectively. Detection limits are improved by a factor of 15–50-fold when compared to those obtained using a flow-through cup for discontinuous coupling between HPLC and ETA-AAS.[18] Better detection limits can be achieved using HPLC–ICPMS. A detection limit of 2 ng/mL was reported for As(III) and arsenobetaine[19] after chromatographic separation and ICPMS detection.

CONCLUSIONS

An automated thermospray vaporizer was used as an interface for coupling electrothermal atomization AAS and liquid chromatography in As speciation studies. The chromatographic eluent can be sampled every 40 s with good reproducibility and sensitivity using deposition of the thermospray on a preheated platform. The sensitivity for thermospray deposition is comparable to that obtained by manual introduction of the sample. Further shortening of the thermal program, although it is mainly limited by the cooling-down step, would permit the monitoring of larger eluent fractions, thereby improving chromatographic detection limits. So far, the results shown for speciation of As(V), As(III), and DMA are promising and would permit the extensive application of this interface to other speciation studies.

ACKNOWLEDGMENT

The author thanks the Delft University of Technology (The Netherlands) for allowing the use of the instrumentation and Dr. M. T. C. de Loos-Vollebregt for helpful discussions.

Received for review December 8, 1993. Accepted July 7, 1994.[⊗]

[⊗] Abstract published in *Advance ACS Abstracts,* October 1, 1994.

(19) Beauchemin, D.; Siu, K. W. M.; McLaren, J. W.; Berman, S.S. *J. Anal. Atom. Spectrom.* **1989**, *4*, 285.

Anal. Chem. **1994,** *66,* 4382–4383

Labeling of Double-Stranded DNA by ROX-Dideoxycytosine Triphosphate Using Terminal Deoxynucleotidyl Transferase and Separation by Capillary Electrophoresis

Daniel Figeys, Annika Renborg, and Norman J. Dovichi*

Department of Chemistry, University of Alberta, Edmonton, Alberta T6G 2G2, Canada

Terminal transferase is used to add a single fluorescently labeled dideoxynucleotide to double-stranded DNA prepared by restriction endonuclease action on a bacteriophage. The product is separated by capillary electrophoresis with both hydroxypropylmethylcellulose and non-cross-linked polyacrylamide. The reaction products generate single peaks for each fragment with hydroxypropylmethylcellulose. However, the higher resolution separation produced by non-cross-linked polyacrylamide shows that the product contains two components for each restriction digest fragment. This labeling technique should be useful in restriction fragment length polymorphism studies.

Capillary electrophoresis is a powerful technique for the rapid separation of minute amounts of double-stranded DNA. Sensitive detection has been based on laser-induced fluorescence. Intercalating dyes, such as Thiazole Orange, POPO-3, YOYO-3, and YOYO-1, have been used to detect double-stranded DNA separated by capillary electrophoresis.[1-2] While intercalating dyes are very convenient to use, they suffer from one important limitation. Because there is a rapid equilibrium between free and bound dye, it is not possible to label selectively different strands of DNA with different dyes. This limitation is particularly acute in capillary electrophoresis, where it is very useful to include a size marker along with the unknown DNA for analysis in a single capillary; of course, the throughput of each capillary is also increased if several samples, labeled with different fluorescence label, are analyzed simultaneously. We have attempted to use different intercalating dyes to label double-stranded DNA originating from two different restriction endonuclease digests; inevitably, exchange of the dyes was observed, resulting in the inability to distinguish the fluorescence from the two digests. As a further property of intercalating dyes, the structure and stiffness of the DNA are changed, modifying the mobility of the oligonucleotide. Instead, it appears necessary to label covalently DNA with fluorescent dye; the covalently bound dye is unable to exchange between strands, allowing analysis of two (or more) different analytes simultaneously in a single capillary.

While it is possible to use fluorescently labeled primers in PCR generation of double-stranded DNA, these primers are expensive. Labeled primers are not useful in analysis of restriction endonuclease digests.

We report the use of terminal deoxynucleotidyl transferase to label covalently both blunt and sticky-end DNA fragments with a fluorescently labeled dideoxynucleotide. Terminal deoxynucleotidyl transferase is widely used for 3′-end labeling of DNA or RNA with radioisotopically labeled nucleotides.[3,4] A fluorescently labeled deoxynucleotide has been used to label RNA with terminal deoxynucleotidyl transferase.[5] Trainor and Jensen used succinylfluorescein-labeled dideoxynucleoside triphosphate to label a 17-base-pair oligonucleotide.[6] Igloi and Schiefermayr used terminal deoxynucleotidyl transferase to incorporate a fluorescently labeled dUTP to a single-stranded primer.[7] However, to the best of our knowledge, terminal deoxynucleotidyl transferase has not been used to fluorescently label restriction fragment digests.

EXPERIMENTAL SECTION

One microliter of DNA [ΦX174 RF/*Hae*III(Gibco BRL), 0.6 μg/μL, or M13mp18 RF1(Sigma)/*Taq*I(Gibco BRL), 0.045 μg/μL], 4 μL of a 5× reaction buffer (Boehringer Mannheim), 1 μL of ROX-ddCTP (90 pmol, ABI), 2 μL of $CoCl_2$ (2.5 mM, Boehringer Mannheim), 10 μL of water, and 1 μL of terminal deoxynucleotidyl transferase (10 units, Boehringer Mannheim) from calf thymus are mixed together. The mixture is incubated at 37 °C for 1 h. EDTA is added to terminate the reaction. The sample is ethanol precipitated and resuspended in 10 μL of 1× TBE (0.54 g of Tris, 0.275 g of boric acid, and 0.100 mmol of disodium EDTA, diluted to 50 mL with deionized water). The labeled product was separated by capillary electrophoresis in a locally constructed instrument.[2,8,9] A yellow He–Ne laser (594 nm) is used for excitation of fluorescence. The separation was performed with 0.4% hydroxypropylmethylcellulose at an electric field of 100 V/cm. The 32-μm-i.d. capillary is 28.6 cm long.

RESULTS AND DISCUSSION

We used ROX-dideoxycytosine triphosphate (Applied Biosystems Division of Perkin-Elmer) to labeled blunt and sticky-end restriction fragments. We successfully labeled ΦX174 RF/*Hae*III

(1) Schwartz, H. E.; Ulfelder, K. J. *Anal. Chem.* **1992,** *64,* 1737–1740.
(2) Figeys, D.; Arriaga, E.; Renborg, A.; Dovichi, N. J. *J. Chromatogr.* **1994,** *669,* 205–216.
(3) Tu, C.-P. D.; Cohen, S. N. *Gene* **1980,** *10,* 177–183.
(4) Roychoudhury, B.; Jay, E.; Wu, R. *Nucleic Acids Res.* **1976,** *3,* 863–877.
(5) Dirks, R. W.; Van Gijlswiljk, R. P. M.; Vooijs, M. A.; Smit, A. B.; Bogerd, J.; Van Minnen, J.; Raap, A. K.; Van Der Ploeg, M. *Exp. Cell Res.* **1991,** *194,* 310–315.
(6) Trainor, G. L.; Jensen, M. A. *Nucleic Acids Res.* **1988,** *16,* 11846.
(7) Igloi, G. L.; Schiefermayr, E. *BioTechniques* **1993,** *15,* 486.
(8) Chen, D. Y.; Harke, H. R.; Dovichi, N. J. *Nucleic Acids Res.* **1992,** *20,* 4873–4880.
(9) Chen, D. Y.; Swerdlow, H. P.; Harke, H. R.; Zhang, J. Z.; Dovichi, N. J. *J. Chromatogr.* **1991,** *559,* 237–246.

0003-2700/94/0366-4382$04.50/0 © 1994 American Chemical Society

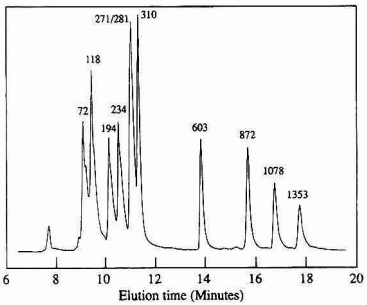


Figure 1. Separation of ΦX174 RF/*Hae*III on hydroxypropylmethylcellulose, 0.4%, at an electric field of 100V/cm. The running buffer is 1× TBE plus 0.1 M NaCl.

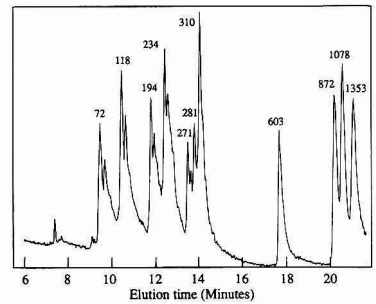


Figure 2. Separation of ΦX174 RF/*Hae*III on polyacrylamide (5%T, 0%C) at an electric field of 200 V/cm. The running buffer is 1× TBE plus 0.1 M NaCl.

and M13mp18/*Taq*I restriction fragments. We have reported the use of hydroxypropylmethyl cellulose for the separation of double stranded DNA (2). This material is very easy to use and produces good separations. Figure 1 shows the separation of ΦX174 RF/*Hae*III fragments on hydroxypropylmethylcellulose. Similar results were obtained with M13mp18/*Taq*I.

While hydroxypropylmethylcellulose is convenient for analysis of double-stranded DNA, non-cross-linked polyacrylamide solutions provide higher resolution separations. Figure 2 presents the separation of ΦX174 RF/*Hae*III fragments on polyacrylamide. Each fragment generates a major peak and a smaller satellite peak; presumably, the first peak is due to fragments that have incorporated a single label at one 3′-end, and the second peak is associated with fragments that have been labeled at both 3′-ends. For the largest peaks, the resolution presumably is insufficient to resolve the satellite peaks. Clearly, more work is required to minimize the formation of the satellite peaks. As suggested by a reviewer, the decrease in the relative amount of dideoxynucleotide should reduce formation of the satellite peaks.

The use of fluorescent dideoxynucleotides is attractive for labeling of double-stranded DNA. In particular, the labeling procedure will be of value in the analysis of restriction endonuclease digested DNA; alternative technology based on the use of intercalating dyes does not easily allow analysis of mixed samples. There are at least four different dideoxynucleotides labeled with unique fluorescent probes. In principle, a mixture containing three samples plus an internal standard can be analyzed simultaneously in a single capillary.

ACKNOWLEDGMENT

This work was supported in part by the U.S. Department of Energy Human Genome Initiative Grant No. DE-FGO2-91ER61123. Support by DOE does not constitute an endorsement of the views expressed in this article. This work was also supported by the Natural Sciences and Engineering Research Council of Canada (NSERC). D.F. acknowledges a graduate fellowship, and N.J.D. acknowledges a Steacie fellowship from NSERC.

Received for review May 26, 1994. Accepted September 12, 1994.[⊗]

[⊗] Abstract published in *Advance ACS Abstracts,* October 15, 1994.

Author Index

Abrigo, C., 4229
Abruña, H. D., 4337
Armstrong, D. W., 4278

Barshick, C. M., 4154
Bartle, K. D., 4253
Bartsch, R. A., 4332
Bauer, J. F., 4283
Bemgård, A., 4288
Bendicho, C., 4375
Bennett, G. E., 4166
Berger, T. A., 4253
Black, G. E., 4171
Bortolin, S., 4302
Bruneau, A., 4354

Cai, Z., 4202
Camilleri, P., 4121
Cassada, D. A., 4202
Chen, H., 4150
Chen, N., 4243
Chen, S., 4278
Cheng, J., 4210
Christopoulos, T. K., 4302
Clifford, A. A., 4253
Clifford, A. J., 4177
Colmsjö, A., 4288
Cornwell, J. C., 4166

Dadachova, E., 4272
Darkangelo, C., 4166
DeGraff, B. A., 4133
Demas, J. N., 4133
Dinardo, A., 4229
Dovichi, N. J., 4382
Dueker, S. R., 4177

Elrod, L., Jr., 4283
Endo, I., 4243

Figeys, D., 4382
Fox, A., 4171
Fox, K., 4171
Fréchet, J. M. J., 4308

Galley, P. T., 4345
Gennaro, M. C., 4229
Giddings, J. C., 4215
Gross, M. L., 4202

Hage, D. S., 4265
Heaton, D. M., 4253
Hergenröder, R., 4127
Hetherington, E. L., 4272
Hill, H. H., Jr., 4195
Hu, P., 4190
Huang, X., 4332
Hunt, M. D., 4166
Hybenová, A., 4258

Inoue, T., 4150
Irth, H., 4295
Ivanov, A. A., 4359

Jacobson, S. C., 4127
Jones, A. D., 4177
Jones, R. F. D., 4121

Kagan, M. R., 4159
Kana, T. M., 4166
Kaniansky, D., 4258
Keely, C. A., 4236
Kimura, T., 4354
Kirby, A. J., 4121
Klee, M. S., 4253
Knapp, F. F., Jr., 4272
Kouznetsov, D. A., 4359
Kuwano, H., 4316

Lambrecht, R. M., 4272
Langsdorf, B., 4133
Larsen, P. R., 4195
Le, K., 4278
Lee, Y.-H., 4142
Loo, J. A., 4190
Lord, B. S., 4370
Lorenzo, E., 4337
Lu, J. P., 4332

Manabe, T., 4243
Marengo, E., 4229
Maus, R. G., 4142
McCreery, R. L., 4159
McDonough, R. C., III, 4133
McManigill, D., 4236
McMinn, D. G., 4195
Mirzadeh, S., 4272
Mitchelson, K. R., 4210
Monson, S. J., 4202
Montaudo, G., 4366
Montaudo, M. S., 4366
Moore, A. W., Jr., 4127
Morley, J. A., 4283
Murphy, L. J., 4345

Nakamura, M., 4316

Ogawa, T., 4150
Ogawara, Y., 4354
Ohki, A., 4332
Okafo, G. N., 4121
Oldham, J. B., 4166
Onuska, F. I., 4258
Oosterkamp, A. J., 4295

Pariente, F., 4337
Puglisi, C., 4366

Ramanujam, V. M. S., 4202
Ramsey, J. M., 4127, 4154
Renborg, A., 4382
Rowlen, K. L., 4324
Ruhn, P. F., 4265

Salters, V. J. M., 4186
Samperi, F., 4366
Semin, D. J., 4324
Shaw, R. W., 4154
Siems, W. F., 4195
Smigol, V., 4308
Smith, B. W., 4142
Smith, G. M., 4177
Smith, P. B. W., 4171
Snyder, A. P., 4171
Spalding, R. F., 4202
Stringham, R. W., 4370
Sugimoto, I., 4316
Svec, F., 4308

Tang, Y., 4278
Tarver, E. E., 4195
Taylor, J. D., 4265
Terabe, S., 4243
Tickle, D. C., 4121
Tjaden, U. R., 4295

van de Goor, T. A. A. M., 4236
van der Greef, J., 4295
Veletsky, P. R., 4359

Williams, P. S., 4215
Winefordner, J. D., 4142
Wrangskog, K., 4288
Wu, C., 4195

Xu, W., 4133

Ye, Q.-Z., 4190
Yohda, M., 4243
Young, J. P., 4154

Zelenský, I., 4258
Zhou, E. Y., 4278

Great Research Is Surfacing...

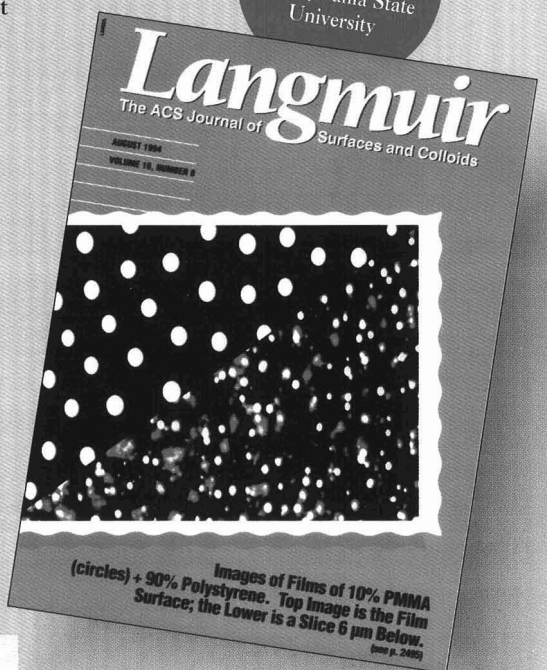
...every month in *LANGMUIR*, the Journal of Surfaces and Colloids

For people involved with surface and colloid chemistry, *Langmuir* is required reading! Published by the American Chemical Society, this monthly journal presents cutting-edge primary research as well as applied and theoretical perspectives on all aspects of this dynamic, multidisciplinary field.

Benefit from original, peer-reviewed research on...

- **Liquid State Surface Chemistry**—surface tension; spread monolayers; wetting and contact angle; adsorption from solution; nucleation; fundamental aspects of flotation, detergency emulsions, foams, lubrication
- **Surface Chemical Physics**—solid surfaces in ultra-high vacuum, including surface structure, composition, and spectroscopy; fundamental papers in heterogeneous catalysts
- **Disperse Systems**—colloidal suspensions including aerosols, microemulsions, biological and polymeric colloids, and membrane systems
- **Electrochemistry**—as related to interfacial structure and reactivity
- **Surface Structure, Tunneling Electron Microscopy, Atomic Force Microscopy**

Langmuir Editor: Dr. William A. Steele, Pennsylvania State University



Plus..letters to the editor, book reviews, symposia and more!

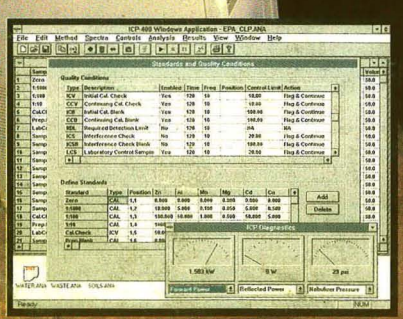
Stay on top of the latest developments...subscribe today!

☎ Phone Toll-free: 1-800-333-9511 (U.S. only) or ☎ (614) 447-3776 (outside the U.S.)
Fax: (614) 447-3671
✉ Mail: American Chemical Society ✉ Member and Subscriber Services, P.O. Box 3337, Columbus, OH 43210

	U.S.	Canada and Mexico	Europe Air Service Included	All Other Countries Air Service Included
ACS Members				
One Year *(12 issues)*	$ 69	$ 93	$125	$140
Two Years *(24 issues)*	$124	$172	$236	$266
Nonmembers *(One year only)*	$874	$898	$930	$945

ACS PUBLICATIONS
Essential Resources for the Chemical Sciences

SIMPLE and AFFORDABLE...
"SIMULTANEOUSLY"



LECO Corporation asked the question, "What if an ICP were simple to use?" Now let us show you **the answer**. LECO's **ICP-400** brings together both simplicity and affordability in a new, simultaneous inductively-coupled plasma spectrometer designed to a new standard--**yours!** It features the throughput of a polychromator, at the price of a typical sequential ICP. Computer-controlled hardware and simple-to-use ***WINDOWS™*** software make the ICP-400 the instrument of choice regardless of the complexity of your application. In addition, the random access auto-sampler, together with the ICP-400 software, conform to US Environmental Protection Agency (EPA) protocol. For more information on the ICP-400 or any of LECO's line of spectrometers, contact...

ISO-9002
No. FM 24045
(BSI - British Standards Institute)

LECO Corporation • 3000 Lakeview Avenue
St. Joseph, MI 49085-2396, U.S.A.
Phone: (616) 982-2390 • Facsimile: (616) 982-8977

LECO is a registered trademark of LECO Corporation

CIRCLE 2 ON READER SERVICE CARD